

**REVIEW COPY**

**DO NOT CITE OR QUOTE**

ISBN 0-7743-7584-1

0-7743-7587-6

MODELS FOR LONG-RANGE AND MESOSCALE TRANSPORT  
AND DEPOSITION OF ATMOSPHERIC POLLUTANTS

PHASE I: MODELING SYSTEM DESIGN

VOLUME II

August 1982

ARB-38-82-AQM

Prepared for

ONTARIO MINISTRY OF THE ENVIRONMENT  
AIR RESOURCES BRANCH  
880 Bay Street, 4th Floor  
Toronto, Ontario M5S 1Z8 Canada

Prepared by

MOE  
MOD  
ANXC

Environmental Research &  
Technology, Inc.  
696 Virginia Road  
Concord, MA 01742, USA

Meteorological and Environmental  
Planning Limited  
850 Magnetic Drive  
Downsview, Ontario  
M3J 2C4, Canada

c.1  
a aa

### Copyright Provisions and Restrictions on Copying:

This Ontario Ministry of the Environment work is protected by Crown copyright (unless otherwise indicated), which is held by the Queen's Printer for Ontario. It may be reproduced for non-commercial purposes if credit is given and Crown copyright is acknowledged.

It may not be reproduced, in all or in part, for any commercial purpose except under a licence from the Queen's Printer for Ontario.

For information on reproducing Government of Ontario works, please contact ServiceOntario Publications at [copyright@ontario.ca](mailto:copyright@ontario.ca)



## DISCLAIMER

This report was prepared by consultants under contract to the Air Resources Branch, Ontario Ministry of the Environment. The views and findings expressed herein and the quality and accuracy of the text are the sole responsibilities of the contractor. Opinions and recommendations expressed are those of the contractor and should not be construed to represent policy of the Ministry of the Environment or the Government of Ontario. Mention of specific brand or trade names does not constitute an endorsement by the Government of Ontario.



*Environment Ontario*  
Laboratory Library  
125 Resources Rd.  
Etobicoke, Ontario M9P 3V6  
Canada  
ANXC

## INTRODUCTION

This volume describes our approach to the modeling of the major processes involved in the mesoscale and long-range transport of pollutants. The wind field model is treated in Volume I of this report. As Phase I of this project is a design effort, we have found it necessary to be specific in our recommendations on modeling the relevant processes. However, in view of our incomplete understanding of long-range transport, we expect to modify these models to accommodate progress in the state-of-the-art during the course of Phase II of this project.

Chapter 4 describes the general structure of the long-range transport and mesoscale models. Here we provide the details of the grid system used in the two models. Then we examine the structure of the general mass conservation equation which forms the basis of the models. Details of the associated boundary conditions are then discussed. This chapter also provides estimates of the computer resources required to run these models.

Chapter 5 examines the numerical methods currently available for the solution of the advection diffusion equation. Several of these methods were tested for qualities such as advection fidelity and computer resource optimization. On this basis we recommend the flux-corrected cubic spline advection routine for incorporation into the numerical framework of the models.

Chapter 6 discusses the atmospheric chemistry associated with acid precipitation. It deals with the principal reactions in both the gaseous and aqueous phases. Recommendations are made on the reaction mechanisms to be used in the models. This chapter also discusses the results of a numerical experiment conducted to investigate chemical reactions in cloud water. These results have an important bearing on current research on the in-cloud oxidation of  $\text{SO}_2$  and  $\text{NO}_x$ .

Chapter 7 recommends methods to estimate the wet scavenging of gases and aerosols. We point out that the most important gap in our understanding is the wet removal of reactive gases such as  $\text{SO}_2$ . It is concluded that further research will be required to formulate a model for the wet deposition of these gases.

# TABLE OF CONTENTS

## VOLUME II

	Page
INTRODUCTION	iii
4. STRUCTURE OF THE ONE LONG-RANGE TRANSPORT AND MESOSCALE MODELS	4-1
4.1 Introduction	4-1
4.2 The LRT Grid and Its Limitations	4-1
4.3 Computer Resources	4-5
4.4 Vertical Structure of the Model	4-6
4.5 The Governing Differential Equation	4-7
4.5.1 Transformation to Spherical Coordinates	4-9
4.5.2 Transformation to Terrain-Following Coordinates	4-12
4.5.3 Differences Between the Mesoscale and LRT Model	4-14
4.6 Boundary Conditions	4-15
4.6.1 Inflow Conditions	4-15
4.6.2 Outflow Conditions	4-17
5. NUMERICAL METHODS	5-1
5.1 Introduction	5-1
5.2 Advection Schemes	5-2
5.2.1 SURADS Development	5-4
5.2.2 SHASTA Formulation	5-4
5.2.3 SHASTA Advection Tests	5-7
5.2.4 Multi-Dimensional FCT Formulation	5-10
5.2.5 MFCT Advection Tests	5-17
5.2.6 Cubic Spline Formulation	5-20
5.2.7 Cubic Spline Advection Tests	5-22
5.2.8 Recommended Advection Scheme	5-28
5.3 Diffusion Schemes	5-32

# TABLE OF CONTENTS (Continued)

## VOLUME II

	Page
5.4 Numerical Methods for Integration of Chemical Kinetics	5-35
5.4.1 The Asymptotic Integration Scheme	5-37
5.4.2 The Psuedo-Steady-State Approximation	5-39
6. ATMOSPHERIC CHEMISTRY ASSOCIATED WITH ACID PRECIPITATION	6-1
6.1 Introduction	6-1
6.2 Gas Phase Chemistry	6-4
6.2.1 Homogeneous Process	6-4
6.2.2 Heterogeneous Oxidation	6-60
6.3 Aqueous Phase Chemistry and Related Processes	6-63
6.3.1 Equilibrium Processes	6-63
6.3.2 Kinetic Processes	6-68
6.3.3 Mass Transport	6-82
6.3.4 Review of Previous Modeling Studies	6-84
6.3.5 Summary of the Recommended Approach	6-88
6.4 Selected Case Studies of Combined Gas/Aqueous Phase Chemistry	6-93
6.4.1 The Chemical Mechanism	6-93
6.4.2 Sensitivity Test Results	6-98
6.4.3 Summary and Recommendations	6-108
6.5 Subgrid-Scale Chemical Effects	6-109
6.6 Conclusions and Recommendations	6-112
7. WET DEPOSITION	7-1
7.1 Introduction	7-1
7.1.1 Aerosol Scavenging by Rain	7-2
7.1.2 Aerosol Scavenging by Snow	7-4
7.1.3 Washout Ratio	7-8
7.1.4 Wet Scavenging of Gases	7-14
7.1.5 Washout of Gases Which React in Water	7-15
7.2 Summary	7-20

# TABLE OF CONTENTS (Continued)

## VOLUME II

	Page
8. DRY DEPOSITION	8-1
8.1 Introduction	8-1
8.2 Dry Deposition of Gases	8-2
8.3 Dry Deposition of Particles	8-9
9. DISPERSION	9-1
9.1 Introduction	9-1
9.2 Vertical Dispersion	9-1
9.3 Horizontal Dispersion	9-3
9.4 Calculation of Micrometeorological Variables	9-4
9.4.1 Surface Friction Velocity, $u_*$	9-4
9.4.2 Monin-Obukhov Length, $L$	9-9
9.4.3 Mixed Layer Height, $z_i$	9-9
10. MODEL SENSITIVITY ANALYSIS	10-1
10.1 LRT Model Sensitivity Analysis	10-2
10.1.1 LRT Model Formulation	10-2
10.1.2 LRT Model Sensitivity Analyses	
Description	10-6
10.1.3 Complex LRT Model Results	10-11
10.1.4 LRT Model Sensitivity to Model Formulation	10-24
10.1.5 Sensitivity of Long-Range Transport Model	
to Emission Reductions	10-65
10.1.6 Sensitivity of the Long-Range Transport	
Model to Sulfate Deposition Velocity	10-83
10.1.7 Sensitivity of Long-Range Transport Model	
to Advection Scheme	10-86
10.1.8 Summary of LRT Model Sensitivity Analyses	10-93
10.2 Mesoscale Model Sensitivity Analysis	10-97
10.2.1 Mesoscale Model Formulations	10-97
10.2.2 Mesoscale Model Sensitivity Run Description	10-112
10.2.3 The Complex Mesoscale Model Results	10-122

# TABLE OF CONTENTS (Continued)

## VOLUME II

	Page
10.2.4 Mesoscale Model Sensitivity to Model Formulation	10-133
10.2.5 Mesoscale Model Sensitivity to Emission Reduction	10-159
10.2.6 Mesoscale Model Sensitivity to Sulfate Deposition Velocity	10-177
10.2.7 Summary of Mesoscale Model Sensitivity Study	10-179
10.3 Comparison of Findings from the LRT and Mesoscale Sensitivity Studies	10-183
10.4 Implications of Sensitivity Analyses Results	10-186
11. CONCEPTS OF MODEL EVALUATION	11-1
11.1 Overview	11-1
11.2 The Framework	11-1
11.3 Model Evaluation Protocol	11-6
11.4 An Example	11-10
11.5 Error Statistics	11-17
11.6 Evaluation of the Mesoscale and Long-Range Transport Models	11-20

#### 4. STRUCTURE OF THE OME LONG-RANGE TRANSPORT AND MESOSCALE MODELS

##### 4.1 Introduction

The present design for the OME Long Range Transport (LRT) model consists of a multispecies, multilayer grid model covering the  $32^\circ \times 32^\circ$  region shown in Figure 4-1a, extending from  $29^\circ\text{N}$  to  $60^\circ\text{N}$  and from  $65^\circ\text{W}$  to  $96^\circ\text{W}$ . Accommodating up to 48 chemical species, the model allows for emission, advection, dispersion, deposition, and chemical interactions of each species on a spherical coordinate terrain following grid with a lateral resolution of  $1^\circ$  in latitude and longitude and a vertical resolution of up to 12 unequal thickness layers extending from 1 meter (i.e., ground level) to an upper limit of 5,000 meters. The vertical resolution of the model will be variable in that species for which little or no information is available can be modeled with box (1 layer) or low-level (4 layer) resolution, somewhat better understood species with moderate (6 layer) resolution, and species for which a detailed, height-dependent inventory is available (e.g.,  $\text{SO}_2$ ,  $\text{NO}_x$ ) with the full 12 layer resolution. The particular resolution mix a user would choose would be governed by the availability of data as well as computer size (e.g., available memory) and cost (e.g., CPU time) constraints. Additional cost saving features, such as a  $2^\circ$  (i.e., half) resolution option and an adjustable "well-mixed assumption" threshold for reducing the number of costly, daytime-chemistry calculation points, have been added to make this an affordable research and analysis tool.

The planned mesoscale grid is identical in all respects except for a ten-fold greater lateral resolution (i.e.,  $\Delta\lambda = \Delta\phi = 0.1$  degree). Figure 4-1b shows this grid superimposed over a portion of Ontario and the Great Lakes.

##### 4.2 The LRT Grid and Its Limitations

A glance at Figure 4-1a indicates the enormosity of the region to be modeled. With an area in excess of  $8 \times 10^6 \text{ km}^2$ , even a

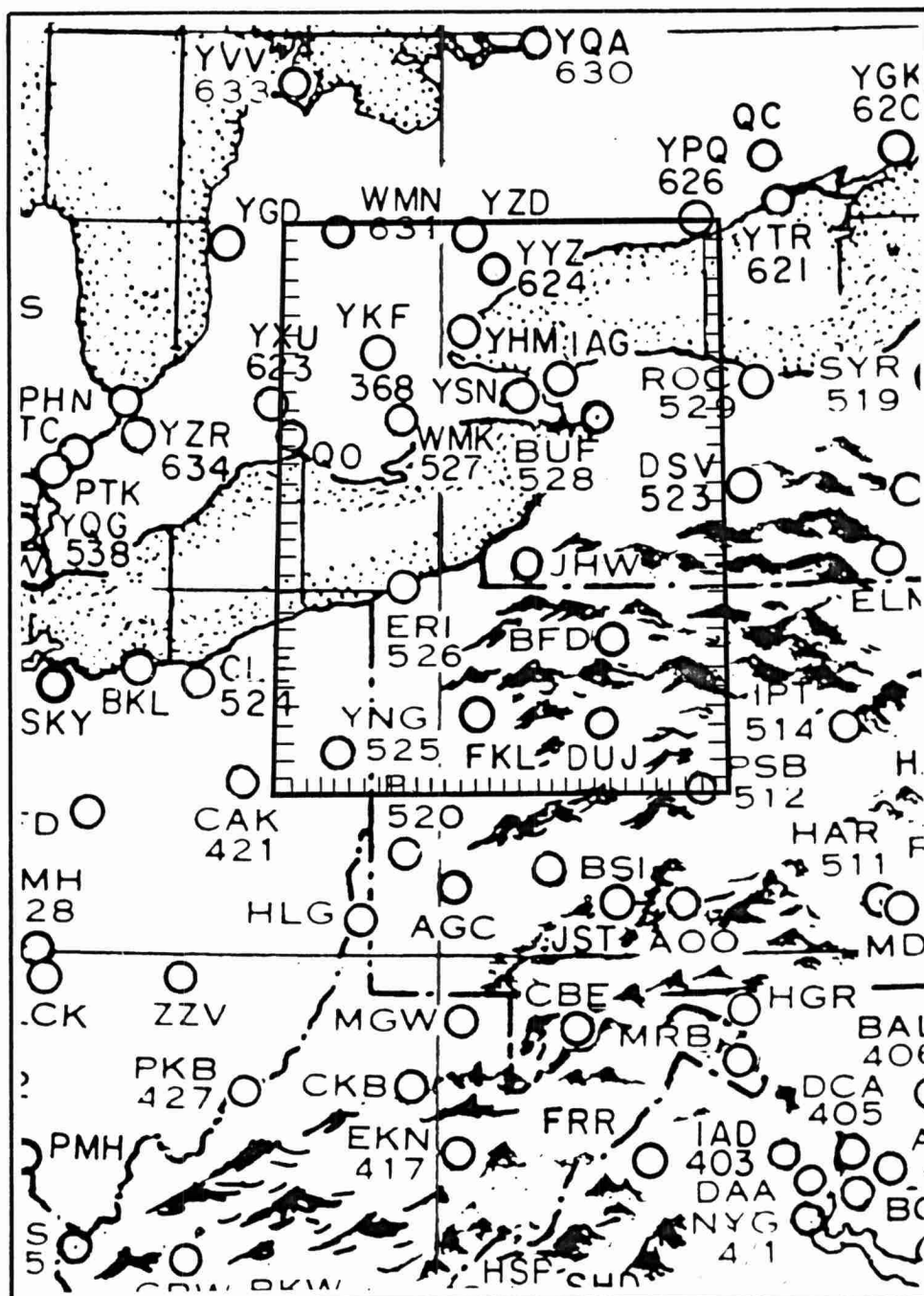


Figure 4-1b Possible Boundary of the OME Mesoscale Model Grid. The 0.1° x 0.1° Grid Resolution is Indicated by Tick Marks on the Boundary. Surface Meteorological Stations are also Indicated.



### 4.3 Computer Resources

The 2 MB maximum size of the pollutant concentration array is one of the chief determinants of the final code's size. Added to this are a number of meteorological variables at each grid point such as: u, v, and w wind components; lateral and vertical diffusivities; temperature and dew point temperature. Other meteorological variables related to surface deposition, rainfall rate, and clouds would occupy smaller 32 x 32 arrays. Thus the total memory requirements for the arrays plus program could approach 3 MB. This approaches the size of the physical memory in ERT's Data General MV-8000 computer and represents a significant fraction of the typical 16 MB size of an IBM 3033. With the advent of virtual operating systems (VOS), however, program size is not the limitation it once was. Both the MV-8000 and the 3033 have a directly addressable space exceeding 4,000 MB, and even the small supermicro computers (e.g., an Apollo Domain based on the MC 68000 chip) have 16 MB of virtual memory. Actually running a program of such size may proceed at full speed (i.e., as though virtual memory equaled physical memory) or at a small fraction of that speed if shuffling of pieces of the program\* between physical memory and the virtual memory on disk becomes a limiting factor. How the program has been structured determines how fast it will run on a virtual machine. This statement is doubly true for a machine like the 3033, which has a three-level memory hierarchy--a small (e.g., 4 KB) but rapidly accessible "cache" memory, the normal physical memory of 16 MB, and the very large, but potentially slow to access, virtual memory pages resident on disk.

Another key issue is the amount of CPU time required to simulate an episode. The present SURADS model deals with two pollutant species,  $SO_2$ , and  $SO_4$ , on a 23 x 30 x 5 grid and requires about 1,600 CPU seconds on the MV-8000 or about 350 CPU seconds on the IBM 3033 for one 24-hour episode simulation. Just on the basis of total number of species times grid points, the OME model will multiply

---

\*These program pieces are referred to as "pages" and are usually fairly small (e.g., 4,096 bytes).

this time requirement by a factor of order 100, and the full nonlinear treatment of chemistry will cost another factor of 2-10. This means that, without extensive streamlining (e.g., vectorization) of the code and implementation of previously mentioned computation saving measures, 20-100 hours of CPU time on an IBM 3033 will be needed for each 24 hours simulated. Equivalently, the unoptimized code is estimated to take 0.8 to four times real time. While the computation saving measures could reduce the CPU time by a factor of 3, vectorization of the advection, diffusion, and chemistry modules could save an additional factor of 10 (Winsor 1981). Thus, the completed OME code could be expected to run at a rate of 0.025 to 0.10 of real time on a 3033.

If computer time were to be purchased at a rate of \$1,000/CPU hour, a single, typical three-day simulation could cost from \$1,800 to \$7,000. Clearly the expense of running the model could quickly grow out of hand. An alternative solution would be to buy a small, dedicated supermicro (e.g., the Apollo with 3 MB of memory) or mini for under \$100,000 and allow the model to run at a computation rate approximately comparable to (i.e., 0.25 to 1.0) the real time period being simulated.

#### 4.4 Vertical Structure of the Model

While arbitrary heights above terrain could be used to define the vertical layers, it is computationally advantageous to use a regular grid or at least a grid which can be transformed to a regular grid via a differentiable transform. Given the intent to have greater resolution near the surface it is reasonable to define a transformed variable  $\rho$  as

$$\rho \equiv \ln \left[ 1 + \alpha \left( \frac{z - z_{1/2}}{z_{N+1/2} - z_{1/2}} \right) \right] / \ln (1 + \alpha) \quad (4-1)$$

where  $z = z_i$  specifies the midpoint of the  $i^{\text{th}}$  level and  $z_{i-1/2}$  and  $z_{i+1/2}$  the lower and upper cell faces. The fact that the  $z_i$

may be functions of  $x$ ,  $y$ , and  $t$  in a terrain following coordinate system will be considered later.

Choosing a lower boundary of  $z_{1/2} = 1$  m and an upper boundary of  $z_{N+1/2} = 5$  km still leaves the parameter  $\alpha$  to be determined, thus giving additional flexibility over the transformation advocated by McKee et al. (1982). A convenient way to choose  $\alpha$  for  $N$  even is to force  $z_{(N+1)/2}$  to correspond to  $\rho = 0.5$ . In this way, one can choose the height, above and below which there will be an equal number of levels. Choosing  $\hat{z} \equiv z_{(N+1)/2} = 600$  m and computing  $\alpha$  as

$$\alpha = (1 - 2\beta)/\beta^2, \quad (4-2)$$

where  $\beta \equiv (\hat{z} - z_{1/2})/(z_{N+1/2} - z_{1/2})$  then completely defines the scheme shown in Figure 4-2. Also shown are the level pairings used to produce the intermediate resolution six layer model, and the threefold and twelvefold groupings used to produce the low resolution four layer and box resolution models, respectively. A less ambitious scheme might involve defining the six layer model as the high resolution scheme.

#### 4.5 The Governing Differential Equation

The atmospheric diffusion equation for the concentration  $C$  is generally written as:

$$\frac{\partial C}{\partial t} + \underline{V} \cdot (\underline{V}C) = \nabla \cdot (K \underline{\nabla} C) + S - D \quad (4-3)$$

where  $\underline{V}$  is the advective velocity vector,  $K$  is the diffusivity tensor,  $S$  represents the sources, and  $D$  represents the sink or depletion terms. However, in order to use Equation 4-3 within the model structure one must:

- transform the equation to spherical coordinates corresponding to the Earth's latitude  $\phi$ , longitude  $\lambda$ , and local normal coordinate  $r$ ;

- transform from the local normal coordinate  $r$  to the transformed coordinate  $\rho$ , where  $z \equiv r-a$  and  $a$  is the Earth's radius;
- make the necessary approximations to ensure that operator splitting is still possible; and
- write the individual equations describing the development of  $C$  as the appropriate finite difference equations.

#### 4.5.1 Transformation to Spherical (Latlong) Coordinates

Defining the unit vectors  $e_\lambda$ ,  $e_\phi$ , and  $e_r$  to point locally east, north, and vertically, respectively, Haltiner (1971) and, more recently and more comprehensively, Lamb (1982) describe the transformation. If the wind field is written as

$$\underline{V} = ue_\lambda + ve_\phi + we_r \quad (4-4)$$

then the equation for longitudinal advection and diffusion becomes

$$\frac{\partial C}{\partial t} + \frac{1}{h_\lambda} \frac{\partial}{\partial \lambda} (uC) + \frac{1}{h_\lambda} (uC) \frac{M}{\partial \lambda} \ln \tau \sim \frac{1}{h_\lambda} \frac{\partial}{\partial \lambda} \left( \frac{K_x}{h_\lambda} \frac{\partial C}{\partial \lambda} \right) \quad (4-5)$$

where  $h_\lambda = a \cos \phi$  is just the Jacobian,  $\tau = a^2 \cos \phi d\lambda d\phi dr$  is the size of the local volume element, and  $a$  is the Earth's radius. If the thickness of the vertical layer  $dr$  is independent of longitude (as it will be in the model) the  $\partial/\partial \lambda \ln \tau$  term will vanish. Thus, longitudinal advection and diffusion is as simple as replacing  $dx$  with  $h_\lambda d\lambda$  in the equation for advection and diffusion in Cartesian coordinates.

The case of latitudinal advection and diffusion is complicated slightly by the fact that the northern face of the region is slightly smaller than the southern face. This manifests itself in the advection diffusion equation

$$\frac{\partial C}{\partial t} + \frac{1}{h_\phi} \frac{\partial}{\partial \phi} (vC) + \frac{1}{h_\phi} (vC) \frac{\partial}{\partial \phi} \ln \tau \sim \frac{1}{h_\lambda h_\phi} \frac{\partial}{\partial \phi} \left( \frac{h_\lambda K_y}{h_\phi} \frac{\partial C}{\partial \phi} \right), \quad (4-6)$$

where  $h_\phi \equiv a$ ,

because  $\tau$  is a function of  $\phi$ . In fact, a correction of this type will affect both the advection and diffusion terms since

$$\frac{\partial}{\partial \phi} \ln \tau = \frac{1}{h_\lambda} \frac{\partial}{\partial \phi} h_\lambda = - \tan \phi.$$

The approximate equality signs in Equation 4-5 and 4-6 result from the neglect of off-diagonal diffusivity terms and small advective corrections caused by the slope of the terrain. These corrections have been shown to be negligible by McRae et al. (1982).

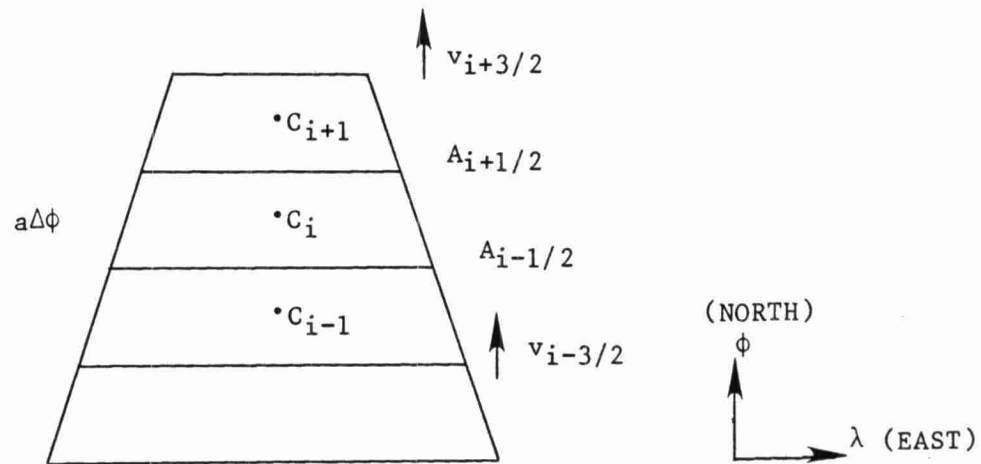
Equation 4-6 actually becomes clearer when it is rewritten in flux or mass conserving form as

$$\begin{aligned} & \tau_i \left( \frac{C_i^{n+1} - C_i^n}{\Delta t} \right) + A_i [(vC)_{i+1/2} - (vC)_{i-1/2}] + (vC)_i [A_{i+1/2} - A_{i-1/2}] \\ &= \frac{\Delta \lambda}{\Delta \phi} \Delta r [\cos(\phi_i + \Delta \phi / 2) K_{y,i+1/2} (C_{i+1} - C_i) - \cos(\phi_i - \Delta \phi / 2) K_{y,i-1/2} (C_i - C_{i-1})] \end{aligned} \quad (4-7)$$

where low-order differencing is assumed adequate for the diffusivity term. In fact, the LHS of Equation 4-7 appears even more clear if one undoes the chain rule and expresses the entire flux as the single difference

$$F_{i+1/2} - F_{i-1/2} = [(AvC)_{i+1/2} - (AvC)_{i-1/2}], \quad (4-8)$$

which is what one would write upon examination of Figure 4-3. Much of Chapter 5 will deal with the various numerical schemes used to obtain the best estimate of this advective flux difference expressed by Equation 4-8.



$A$  = area of cell interface perpendicular to Earth

$\tau$  = cell volume

$$A_{i\pm 1/2} = a \cos(\phi_i \pm \Delta\phi/2) \Delta\lambda \Delta r_{i\pm 1/2}$$

$$\tau_i = \frac{a^2}{4} [\cos(\phi_i + \Delta\phi/2) + \cos(\phi_i - \Delta\phi/2)] \Delta\lambda \Delta\phi (\Delta r_{i+1/2} + \Delta r_{i-1/2})$$

In the model  $\Delta r$  is constant with respect to  $\phi$  and  $\lambda$  so that

$$\tau_i = 1/2 (A_{i+1/2} + A_{i-1/2}) a\Delta\phi$$

Figure 4-3 Geometrical Interpretation of Latitudinal Advection

#### 4.5.2 Transformation to Terrain-Following Coordinates

The transformation to  $p$  coordinates as expressed by Equation 4-1 is quite general and includes the time-dependent layers discussed by Lamb (1982) and McRae et al. (1982); however, the previous section has already utilized the assumption that the layer thickness  $\Delta r_i$  (or alternatively  $\Delta z_i$  or  $\Delta p_i$ ) will remain constant in space and time. Thus, the surfaces will all parallel the terrain (so that differences like  $z_{N+1/2} - z_{1/2}$  will also be independent of space and time) in both the mesoscale and LRT model. This assumption has the advantage of simplifying the equations of motion and the wind field and diffusivity generation modules. The disadvantage is that one must in principle use more vertical levels to retain the same predictive accuracy. An example of this accuracy problem arises in describing the depth of the mixed layer. Whereas the dynamic layer models treat this layer exactly by allowing the layer depth to expand and contract accordingly, the static layer must be content to deal with mixing depth heights corresponding to the levels  $z_i$  shown in Figure 4-2.\*

Terrain thus only appears through the term  $z_{1/2}$  in the numerator of Equation 4-1 since  $z_{1/2} \equiv H(\lambda, \phi) + 1 \text{ m}$ , where  $H(\lambda, \phi)$  is the terrain height. This then manifests itself in the definition of the vertical velocity  $W$  of Equation 4-4 as

$$W = w - u \frac{1}{h_\lambda} \frac{\partial H}{\partial \lambda} - v \frac{1}{h_\phi} \frac{\partial H}{\partial \phi} \quad (4-9)$$

where  $w$  is the vertical wind component predicted by the three-dimensionally divergence-free, wind field generator. The advection diffusion equation is then written in differential form as

$$\frac{\partial C}{\partial t} + \frac{1}{h_p} \frac{\partial}{\partial p} (WC) + \frac{1}{h_p} (WC) \frac{\partial}{\partial p} \ln \tau \approx \frac{1}{h_p} \frac{\partial}{\partial p} \left( \frac{K_z}{h_p} \frac{\partial C}{\partial p} \right) + S-D \quad (4-10)$$

\*Some subgrid scale resolution is recovered in the fixed level scheme, however, by computing the diffusivity characterizing a layer as the (harmonic) mean of diffusivities at numerous subgrid scale intervals.

where

$$h_{\rho} = \frac{\alpha'}{\alpha} (z_{N+1/2} - z_{1/2}) e^{+\alpha' \rho} \quad (4-11)$$

and  $\alpha' = \ln(1+\alpha)$  is obtained from the differential of Equation 4-1, and the differential volume element is now expressed as  $\tau = h_{\lambda} h_{\phi} h_{\rho} d\lambda d\phi d\rho$ .

In practice, a mass-conserving, flux-form finite difference equation:

$$\begin{aligned} \tau_i \left( \frac{C_i^{n+1} - C_i^n}{\Delta t} \right) + a^2 \cos \phi_i \Delta \lambda \Delta \phi [(WC)_{i+1/2}^n - (WC)_{i-1/2}^n] = \\ a^2 \cos \phi_i \Delta \lambda \Delta \phi \alpha' \left[ \frac{K_{z,i+1/2}}{(h_{\rho,i+1} - h_{\rho,i})} (C_{i+1}^n - C_i^n) - \right. \\ \left. \frac{K_{z,i-1/2}}{(h_{\rho,i} - h_{\rho,i-1})} (C_i^n - C_{i-1}^n) \right] + \tau_i (S_i - D_i) \end{aligned} \quad (4-12)$$

where  $\tau_i = a^2 \cos \phi_i \Delta \lambda \Delta \phi (h_{\rho,i+1/2} - h_{\rho,i-1/2}) / \alpha'$

and  $h_{\rho,i} = (z_{N+1/2} - z_{1/2}) \exp(\alpha' \rho_i) \alpha' / \alpha$

will be utilized in the model. The concentrations  $C_{i+1/2}^n$  required for the advective portion of Equation 4-12 can, for example, be obtained via the spline interpolation relations:

$$C_{i-1/2} = 0.5 (C_{i-1} + C_i) + (D_{i-1} - D_i) \Delta \rho / 8$$

and

(4-13)

$$C_{i+1/2} = 0.5 (C_i + C_{i+1}) + (D_i - D_{i+1}) \Delta \rho / 8$$

where the superscript n is assumed, and the derivatives D are treated as unknowns and obtained from the solution of the tridiagonal relation:



$$D_{i-1} + 4D_i + D_{i+1} = 3 (C_{i+1} - C_{i-1})/\Delta\rho \quad (4-14)$$

While these spline forms are discussed in greater detail in Section 5 (see Equations 5-18 and 5-19), it is interesting to note that these results are identical to the high-order (i.e., third order on the boundary, fourth order in the interior) compact Hermitian method (Adam 1977), reported to give extremely accurate results.

#### 4.5.3 Differences Between the Mesoscale and LRT Model

Up to this point there is no difference in the governing equations of the mesoscale and LRT models. As discussed earlier, one major, but mathematically trivial, difference will be the latlong resolution  $\Delta\lambda = \Delta\phi$ :

- 1.0 degree in the LRT model, and
- 0.1 degree in the mesoscale model.

The only other difference arises in the treatment of the terrain induced wind component  $w_T$  in Equation 4-9, that is

$$W = w - w_T \quad \text{where } w_T = u \frac{1}{h_\lambda} \frac{\partial H}{\partial \lambda} + v \frac{1}{h_\phi} \frac{\partial H}{\partial \phi}$$

Examination of a terrain map of the entire region shows that

$$\frac{\Delta H}{\Delta X} < \frac{1 \text{ km}}{5.5 \text{ km}} \sim 0.2 \text{ on the mesoscale}$$

and

$$\frac{\Delta H}{\Delta X} < \frac{0.75 \text{ km}}{55 \text{ km}} \sim 0.015 \text{ on the LRT scale.}$$

Thus,  $w_T$  may approach a few meters per second on the mesoscale, yet is generally less than several centimeters per second on the LRT scale. On the LRT scale this small velocity  $-w_T$  is completely cancelled in the lowest layer by a  $+w_T$  term produced by the wind

field generator and cancelled to a lesser, stability dependent extent with increasing  $z$ . Thus, while the LRT wind field generator will compute the small vertical velocities needed to simulate the effect of gradual but widespread subsidence, the terrain induced  $w_T$  will be ignored in both the wind field generator and in the governing equations. This is done more to suppress computational noise than to simplify the problem since inclusion of  $w_T$  could in some cases dominate over the  $w$  from subsidence.

In summary, the main difference between the two models is that

- the LRT model and its wind field generator will ignore terrain induced winds  $w_T$  whereas
- the mesoscale model and its wind field generator will include  $w_T$ .

#### 4.6 Boundary Conditions

In an effort to keep the model as flexible as possible a set of border cells surrounding the grid will be added at the surface, or lowest level, as shown in Figure 4-4. In addition the model will have a single cell above the top level to allow for advection of pollutants in from the stratosphere. These boundary cells will function differently under inflow and outflow conditions and detailed treatment of the conditions may vary slightly with the advection routine used.

##### 4.6.1 Inflow Conditions

At the surface level each boundary cell concentration  $C_{0,j}$ ,  $C_{N+1,j}$ ,  $C_{i,0}$  and  $C_{i,N+1}$  (where  $1 \leq i,j \leq N$  and  $N = 32$ ) will be set to a predetermined value. For levels  $k$  above the surface level, the inflow concentration will be linearly interpolated as

$$C_{i,j,k} = (1 - \rho_k) C_{i,j} + \rho_k C_{BT} \quad , \quad (4-15)$$

where  $i, j$  take on only boundary cell values and  $C_{BT}$  is a single concentration value chosen to be typical of background stratospheric values. Inflow from the top of the grid is possible and the concentration  $C_{BT}$  will be assumed. Inflow (and outflow) through the bottom of the grid is prohibited by the condition  $W_{1/2} = 0$  (i.e.,  $w = w_T$ ).

The above procedure is repeated separately for each pollutant species. For species for which information is sparse there will be an option to set all surface cell inflow concentrations to a single, user determined value.

#### 4.6.2 Outflow Conditions

Advection out of the grid will be accomplished by assuming that the concentration at the boundary cell equals the concentration of the nearest computational grid point. This procedure will be extended to include advection out of the top of the box, in which case the advected flux out of the top layer will be cumulatively summed and stored in the array. This procedure should ensure minimal mass reflection problems at the grid boundary.

The same boundary conditions are used for the diffusion step, thus causing reflection of diffused material at the boundary. Whether this is genuinely preferable to using inflow conditions of mixed inflow/outflow conditions is an issue which falls into the domain of uncertainties incurred by termination of the grid.

Dry deposition at the surface is accomplished by removal of a flux

$$F_d = v_d C_1 \quad (4-16)$$

where  $C_1$  is the concentration in the lowest lying grid cell. This deposition flux reduces the concentration  $C_1$  as would an advective flux, and the  $F_d$  is cumulatively summed in the array location specified in Section 4-2.

Wet deposition is also described by a net flux  $F_w$  which is likewise cumulatively summed and stored; however, this flux constitutes removal from (and transfer between) a number of vertical layers and is discussed in greater detail in Chapter 7.

## 5. NUMERICAL METHODS

### 5.1 Introduction

Efficient and accurate numerical techniques are required for the time integration of the advection-diffusion-reaction equations for atmospheric pollutants within a large Eulerian grid model. As the individual terms (e.g., the advection, diffusion, deposition, and chemistry operators) driving the time development of the concentration field are optimally treated by specialized techniques, it is desirable to split up or "factorize" the time development operator as,

$$C^{n+1} = A_x A_y A_z A_c A_c A_z A_y A_x C^n \quad (5-1)$$

where  $A_x$ ,  $A_y$  are the horizontal transport and diffusion operators;  
 $A_z$  is the vertical transport, diffusion, source injection, and physical depletion operator; and  
 $A_c$  is the operator containing all chemical conversion terms.

In the above decomposition, each operator acts for the fractional step  $\Delta t/2$  and must therefore be applied twice to advance the solution by  $\Delta t$ . The time-consuming chemistry operation is conveniently placed in the middle and may be compressed into a single operation (i.e.,  $A_c(\Delta t) = A_c(\Delta t/2) A_c(\Delta t/2)$ ). Marchuk (1975) has shown that this particular decomposition, with operators applied in alternating forward and reverse order, causes the errors of order  $\Delta t$  which build up during the first half of the cycle to be cancelled out as the reversed operator application completes the time-marching cycle. Hence, the above decomposition is second-order accurate in time; that is, errors of order  $(\Delta t)^2$  are present. Such a decomposition is reasonable only if each suboperator  $A$  satisfies the condition  $A - 1 = \alpha \Delta t \ll 1$ . Thus, the time scale  $\tau = 1/\alpha$  of a particular process imposes a size constraint on the basic time step  $\Delta t$ . McRae et al. (1982a) recently reviewed this split operator approach and recommended using implicit (rather than explicit) time integration procedures. Although implicit time integration is extremely important for the very "stiff,"

nonlinear chemical operator  $A_c$  connecting the various species  $C_i$ , it is only marginally important for the vertical operator  $A_z$  and is optional for the advection-diffusion operators  $A_x$  and  $A_y$ .

In the discussion to follow, the detailed properties and solution methods of these various operators will be considered in detail. Particular emphasis will be placed on those methods presently incorporated into the SURADS model as well as techniques under consideration for the OME model.

## 5.2 Advection Schemes

The advection of a concentration field  $C$  is described by the partial differential equation (PDE):

$$\frac{\partial C}{\partial t} + \underline{\nabla} \cdot (\underline{V}C) = 0 \quad (5-2)$$

where  $\underline{V}$  is the vector wind field having components  $u$ ,  $v$ , and  $w$ , each of which is a function of  $x$ ,  $y$ ,  $z$ , and  $t$ . After invoking the divergenceless condition,  $\underline{\nabla} \cdot \underline{V} = 0$ , this PDE has the simple solution  $C(x,y,z,t) = C(x',y',z',0)$  for time  $t > 0$

$$\text{where} \quad x' = x - \int_0^t u(\underline{s}, t') dt'$$

and  $y'$  and  $z'$  are similarly defined. The integration in time corresponds to integration along the trajectory  $\underline{s}(t')$  of a massless particle in the flow field  $\underline{V}$ .

Unfortunately, this solution assumes that the  $C$  and  $\underline{V}$  fields are known everywhere at a particular time  $t'$ . Even if the wind field is taken as constant in time, the solution procedure is flawed by the practical necessity of introducing space discretization (i.e., the functions are known only at a finite number of grid points or are expanded as a finite sum of basis functions). Time discretization also introduces errors; however, these are not as bothersome for two

reasons. First, reducing the time step  $\Delta t$  increases the computer time proportional to  $(\Delta t)^{-1}$ , whereas reducing  $\Delta x$  also increases the required storage by a factor proportional to  $(\Delta x)^{-2}$ . Second, because operator splitting already limits the accuracy of the time-marching scheme to second order, efforts to retain higher-order accuracy in individual advection steps are wasted.

Hundreds of papers have been written describing the theoretical stability characteristics and actual performance of different advection schemes. Roache (1976) provides an extensive introduction to the subject, and Chock and Dunker (1982), Long and Pepper (1976, 1981) and Pepper et al. (1979) compare the algorithms presently considered reasonable candidates for treating the advection of atmospheric pollutants. Their performance measures can be categorized into:

- advection fidelity: conservation of mass and higher moments, conservation of peak values, and avoidance of unphysical negative concentrations; and
- resource optimization: computer storage and computation time considerations.

The design of the advection scheme for the OME models is also influenced by several factors:

- the intent to retain a variable grid or embedded subgrid option (which tends to bias against such methods as the highly accurate pseudospectral technique of Prahm and Christensen, 1977);
- the plan to include lateral atmospheric diffusion (which could bias against expensive, highly accurate schemes as some of the advected detail is subsequently diffused away; or, conversely, could bias in favor of some high-order spatial techniques because the diffusivity term acts as a nonlinear filter that removes high-frequency computational noise that can generate small negative concentrations); and

- the desire to add vertical advection (which could make the fully multi-dimensional flux-corrected transport (MFCT) technique of Zalesak (1979) prohibitively expensive if full three-dimensional advection as an unsplit operation was required).

In the remainder of this subsection, we will examine the advection routines used in the existing SURADS (Sulfate Regional Advection and Diffusion Scheme) code and, in light of the above considerations, recommend a technique for its implementation in the OME model.

#### 5.2.1 SURADS Development

The SURADS model, developed by ERT for the EPRI-funded SURE program, is an extension of the earlier SULFA3D model. The original advection scheme utilized the "method of moments" (Egan and Mahoney 1972), which exhibits excellent advection fidelity but is quite slow and requires considerably more physical storage than other methods. In addition, the original version of the algorithm leads to an anomalous redistribution of mass under strongly sheared flow situations. Although the recent moments method of Chock and Dunker (1982) may cure these shortcomings, their published tests do not include a strongly sheared flow situation, thus making it difficult to judge the success of their approach. Because of the mass redistribution problem and the slowness of the moments method algorithm, it was replaced in 1979 in SURADS with the flux-corrected transport (FCT) algorithm, SHASTA.

#### 5.2.2 SHASTA Formulation

The one-dimensional Sharp and Smooth Transport Algorithm (SHASTA) was introduced by Boris and Book (1973) as a method of advecting distributions with steep gradients (such as shock waves) without introducing the high-frequency ripples, including negative concentrations (i.e., the Gibbs phenomenon) that accompany the use of

a high-order spatial scheme. As with all FCT algorithms, SHASTA conserves mass and maintains the positivity of concentrations. The advection equation is considered to be in flux form when it can be written as:

$$C_i^{n+1} = C_i^n - [F_{i+1/2} - F_{i-1/2}] \Delta t / \Delta x_i \quad (5-3)$$

where  $F_{i+1/2}$  and  $F_{i-1/2}$  are the transportative fluxes out of and into the faces of the  $i^{\text{th}}$  grid cell and are functions of  $C$  and  $u$  at one or more levels of time and at different numbers of spatial points (depending on the spatial order of the scheme). In both the SHASTA scheme and the multi-dimensional FCT scheme (MFCT) of Zalesak (1979), the procedure consists of:

- 1) computing low-order fluxes  $F^L$  by a low-order scheme (e.g., donor cell) known to give results free of the Gibbs oscillations but subject to severe numerical diffusion;
- 2) computing high-order fluxes  $F^H$  by a high-order scheme designed to give high spatial accuracy but subject to the aforementioned Gibbs phenomenon;
- 3) defining the "antidiffusive fluxes",

$$A \equiv F^H - F^L, \quad (5-4)$$

at each cell face;

- 4) computing the time-advanced but diffused intermediate concentrations,  $C_i^*$ , by inserting the low-order fluxes  $F^L$  into Equation 5-3;
- 5) limiting the "antidiffusive fluxes,"  $A$ , such that  $C_i^{n+1}$  of Step 6 is free of unphysical oscillations (i.e., overshoots or undershoots) by multiplying by a factor  $\alpha$ , that is:

$$A_{i+1/2}^c = \alpha_{i+1/2} A_{i+1/2}, \quad (5-5)$$



where  $0 \leq \alpha \leq 1$ ; and

6) applying the "limited," antidiffusive fluxes to obtain

$$C_i^{n+1} = C_i^* - [A_{i+1/2}^c - A_{i-1/2}^c] \Delta t / \Delta x_i. \quad (5-6)$$

This six-step procedure was originally used by Zalesak (1979) to describe his MFCT scheme and has been adopted recently (Book et al. 1981) to describe SHASTA as well. In all cases, proper design of the flux limiter,  $\alpha$ , (Step 5) represents the most crucial step.

As presently coded in the SURADS model, the SHASTA algorithm is more "traditionally" expressed explicitly as:

$$C_i^* = \frac{1}{2} \phi_-^2 (C_{i-1}^n - C_i^n) + \frac{1}{2} \phi_+^2 (C_{i+1}^n - C_i^n) + (\phi_+ + \phi_-) C_i^n \quad (5-7a)$$

where

$$\phi_{\pm} = \left( \frac{1}{2} \mp u_i^n \Delta t / \Delta x \right) / [1 \pm (u_{i+1}^n - u_i^n) \Delta t / \Delta x] \quad (5-7b)$$

and the corrected antidiffusive fluxes are given as

$$A_{i+1/2}^c = S_{i+1/2} \max \left\{ 0, \min \left( \frac{1}{8} \Delta_{i+1/2}, S_{i+1/2} \Delta_{i+1/2}, S_{i+1/2} \Delta_{i+3/2} \right) \right\} \Delta x / \Delta t \quad (5-8a)$$

where

$$\Delta_{i+1/2} = C_{i+1}^* - C_i^* \quad (5-8b)$$

$$\Delta_{i-1/2} = C_i^* - C_{i-1}^* \quad (5-8c)$$

$$\Delta_{i+3/2} = C_{i+2}^* - C_{i+1}^* \quad (5-8d)$$

$$\Delta_{i-3/2} = C_{i-1}^* - C_{i-2}^* \quad (5-8e)$$

$$S_{i\pm 1/2} = \begin{array}{ll} +1 & \text{if } A_{i\pm 1/2} \geq 0 \\ -1 & \text{if } A_{i\pm 1/2} < 0 \end{array} \quad (5-8f)$$

Equation 5-6 is then used to obtain the fully time-advanced  $C_i^{n+1}$ . Boris (1976) later introduced the phenical, low-phase-error (LPE) SHASTA coded to run efficiently on vector computers; however, this algorithm was never used in SURADS. We mention it because it was designed to have a lower phase error than the original formulation and because it was tested by Dunker and Chock (1982) and eliminated as a viable algorithm for solving the two-dimensional advection equation in photochemical modeling because of its large numerical diffusion. Despite their negative conclusion regarding LPE-SHASTA, we will present some advection tests of the original SHASTA and compare its rate of diffusion with a plausible<sup>+</sup> diffusivity for LRT modeling (e.g.,  $10^4 \text{ m}^2/\text{sec}$  for  $\Delta x = 80 \text{ km}$  and  $\Delta t = 1 \text{ hr}$ ).

### 5.2.3 SHASTA Advection Tests

Figure 5-1 shows a  $2 \times 2$  block of 100's prior to circular advection on a  $\Delta x = 80 \text{ km}$  grid, a size typical of LRT grids. The advection about the center  $I = 12$ ,  $J = 16$  is designed to bring the distribution around one full revolution in 200 time steps of  $\Delta t = 1 \text{ hour}$ . After only 10 time steps (see Figure 5-2), the peak value has fallen by a factor of 3 and the equivalent, numerical diffusion diffusivity  $K_e$ , defined as

$$2K_e = K_{xe} + K_{ye} = \frac{\sigma^2(t) - \sigma^2(t_0)}{2(t - t_0)} \quad (5-9)$$

with  $\sigma^2$  equal to the spatial variance, is nearly  $10 \times 10^4 \text{ m}^2/\text{sec}$ . After

<sup>+</sup>Opinions differ widely on the physical implications of using a lateral diffusivity in a numerical model. Perhaps  $10^4 \text{ m}^2/\text{sec}$  should only be referred to as a convenient unit of diffusivity for modeling on this scale.

ADVECTION TEST: SHASTA-ERT, 2X2 BLOCK OF 100S , CIRCULAR WIND FIELD  
INITIAL CONCENTRATIONS

LEVEL #	1	2	3	4	5	6	7	8	9	10	11	12	13	14	15	16	17	18	19	20	21	22	23	24	25	26	27	28	29	30
1 1	0	0	0	0	0	0	0	0	0	0	0	0	0	0	0	0	0	0	0	0	0	0	0	0	0	0	0	0	0	0
23 1	0	0	0	0	0	0	0	0	0	0	0	0	0	0	0	0	0	0	0	0	0	0	0	0	0	0	0	0	0	0
22 1	0	0	0	0	0	0	0	0	0	0	0	0	0	0	0	0	0	0	0	0	0	0	0	0	0	0	0	0	0	0
21 1	0	0	0	0	0	0	0	0	0	0	0	0	0	0	0	0	0	0	0	0	0	0	0	0	0	0	0	0	0	0
20 1	0	0	0	0	0	0	0	0	0	0	0	0	0	0	0	0	0	0	0	0	0	0	0	0	0	0	0	0	0	0
19 1	0	0	0	0	0	0	0	0	0	0	0	0	0	0	0	100	100	0	0	0	0	0	0	0	0	0	0	0	0	0
18 1	0	0	0	0	0	0	0	0	0	0	0	0	0	0	0	100	100	0	0	0	0	0	0	0	0	0	0	0	0	0
17 1	0	0	0	0	0	0	0	0	0	0	0	0	0	0	0	0	0	0	0	0	0	0	0	0	0	0	0	0	0	0
16 1	0	0	0	0	0	0	0	0	0	0	0	0	0	0	0	0	0	0	0	0	0	0	0	0	0	0	0	0	0	0
15 1	0	0	0	0	0	0	0	0	0	0	0	0	0	0	0	0	0	0	0	0	0	0	0	0	0	0	0	0	0	0
14 1	0	0	0	0	0	0	0	0	0	0	0	0	0	0	0	0	0	0	0	0	0	0	0	0	0	0	0	0	0	0
13 1	0	0	0	0	0	0	0	0	0	0	0	0	0	0	0	0	0	0	0	0	0	0	0	0	0	0	0	0	0	0
12 1	0	0	0	0	0	0	0	0	0	0	0	0	0	0	0	0	0	0	0	0	0	0	0	0	0	0	0	0	0	0
11 1	0	0	0	0	0	0	0	0	0	0	0	0	0	0	0	0	0	0	0	0	0	0	0	0	0	0	0	0	0	0
10 1	0	0	0	0	0	0	0	0	0	0	0	0	0	0	0	0	0	0	0	0	0	0	0	0	0	0	0	0	0	0
9 1	0	0	0	0	0	0	0	0	0	0	0	0	0	0	0	0	0	0	0	0	0	0	0	0	0	0	0	0	0	0
8 1	0	0	0	0	0	0	0	0	0	0	0	0	0	0	0	0	0	0	0	0	0	0	0	0	0	0	0	0	0	0
7 1	0	0	0	0	0	0	0	0	0	0	0	0	0	0	0	0	0	0	0	0	0	0	0	0	0	0	0	0	0	0
6 1	0	0	0	0	0	0	0	0	0	0	0	0	0	0	0	0	0	0	0	0	0	0	0	0	0	0	0	0	0	0
5 1	0	0	0	0	0	0	0	0	0	0	0	0	0	0	0	0	0	0	0	0	0	0	0	0	0	0	0	0	0	0
4 1	0	0	0	0	0	0	0	0	0	0	0	0	0	0	0	0	0	0	0	0	0	0	0	0	0	0	0	0	0	0
3 1	0	0	0	0	0	0	0	0	0	0	0	0	0	0	0	0	0	0	0	0	0	0	0	0	0	0	0	0	0	0
2 1	0	0	0	0	0	0	0	0	0	0	0	0	0	0	0	0	0	0	0	0	0	0	0	0	0	0	0	0	0	0
1 1	0	0	0	0	0	0	0	0	0	0	0	0	0	0	0	0	0	0	0	0	0	0	0	0	0	0	0	0	0	0
TOTAL MASS		400																												
INITIAL		16.5																												
CURRENT		16.5																												
% CHANGE		0																												
SIGMA		71																												

Figure 5-1 SHASTA Circular Advection Test: Initial Concentrations

ADVECTION TEST SHASTA-ERT, 2X2 BLOCK OF 100S , CIRCULAR WIND FIELD  
 STEP NUMBER = 10, DELTA T= 60 MIN, DELTA X= 80KM, U= A\*(J-12)  
 V= A\*(16-I)

LEVEL =	1	2	3	4	5	6	7	8	9	10	11	12	13	14	15	16	17	18	19	20	21	22	23	24	25	26	27	28	29	30
23	1	0	0	0	0	0	0	0	0	0	0	0	0	0	0	0	0	0	0	0	0	0	0	0	0	0	0	0	0	0
22	1	0	0	0	0	0	0	0	0	0	0	0	0	0	0	0	0	0	0	0	0	0	0	0	0	0	0	0	0	0
21	1	0	0	0	0	0	0	0	0	0	0	0	0	0	0	0	1	1	1	0	0	0	0	0	0	0	0	0	0	0
20	1	0	0	0	0	0	0	0	0	0	0	0	0	0	0	1	6	7	6	3	1	0	0	0	0	0	0	0	0	0
19	1	0	0	0	0	0	0	0	0	0	0	0	0	0	0	3	21	31	30	19	3	0	0	0	0	0	0	0	0	0
18	1	0	0	0	0	0	0	0	0	0	0	0	0	0	0	3	23	33	32	20	3	0	0	0	0	0	0	0	0	0
17	1	0	0	0	0	0	0	0	0	0	0	0	0	0	0	3	21	31	30	19	3	0	0	0	0	0	0	0	0	0
16	1	0	0	0	0	0	0	0	0	0	0	0	0	0	0	1	6	10	10	6	1	0	0	0	0	0	0	0	0	0
15	1	0	0	0	0	0	0	0	0	0	0	0	0	0	0	0	1	1	1	1	0	0	0	0	0	0	0	0	0	0
14	1	0	0	0	0	0	0	0	0	0	0	0	0	0	0	0	0	0	0	0	0	0	0	0	0	0	0	0	0	0
13	1	0	0	0	0	0	0	0	0	0	0	0	0	0	0	0	0	0	0	0	0	0	0	0	0	0	0	0	0	0
12	1	0	0	0	0	0	0	0	0	0	0	0	0	0	0	0	0	0	0	0	0	0	0	0	0	0	0	0	0	0
11	1	0	0	0	0	0	0	0	0	0	0	0	0	0	0	0	0	0	0	0	0	0	0	0	0	0	0	0	0	0
10	1	0	0	0	0	0	0	0	0	0	0	0	0	0	0	0	0	0	0	0	0	0	0	0	0	0	0	0	0	0
9	1	0	0	0	0	0	0	0	0	0	0	0	0	0	0	0	0	0	0	0	0	0	0	0	0	0	0	0	0	0
8	1	0	0	0	0	0	0	0	0	0	0	0	0	0	0	0	0	0	0	0	0	0	0	0	0	0	0	0	0	0
7	1	0	0	0	0	0	0	0	0	0	0	0	0	0	0	0	0	0	0	0	0	0	0	0	0	0	0	0	0	0
6	1	0	0	0	0	0	0	0	0	0	0	0	0	0	0	0	0	0	0	0	0	0	0	0	0	0	0	0	0	0
5	1	0	0	0	0	0	0	0	0	0	0	0	0	0	0	0	0	0	0	0	0	0	0	0	0	0	0	0	0	0
4	1	0	0	0	0	0	0	0	0	0	0	0	0	0	0	0	0	0	0	0	0	0	0	0	0	0	0	0	0	0
3	1	0	0	0	0	0	0	0	0	0	0	0	0	0	0	0	0	0	0	0	0	0	0	0	0	0	0	0	0	0
2	1	0	0	0	0	0	0	0	0	0	0	0	0	0	0	0	0	0	0	0	0	0	0	0	0	0	0	0	0	0
1	1	0	0	0	0	0	0	0	0	0	0	0	0	0	0	0	0	0	0	0	0	0	0	0	0	0	0	0	0	0
		TOTAL MASS				XBAR		YBAR		SIGMA																				
INITIAL		400.				16.5		18.5		.71																				
CURRENT		397.				18.5		17.9		1.65																				
% CHANGE		-1.				---		---		133.59																				

Figure 5-2 SHASTA Circular Advection Test: After 10 Time Steps

ADVECTION TEST: SHASTA-ERT, 2X2 BLOCK OF 100S , CIRCULAR WIND FIELD

STEP NUMBER = 200, DELTA T= 60 MIN, DELTA X= 80KM, U= A\*(J-12)  
V= A\*(16-I)

LEVEL = 1

	1	2	3	4	5	6	7	8	9	10	11	12	13	14	15	16	17	18	19	20	21	22	23	24	25	26	27	28	29	30
23	1	0	0	0	0	0	0	0	0	0	0	0	0	1	2	2	2	1	1	0	0	0	0	0	0	0	0	0	0	0
22	1	0	0	0	0	0	0	0	0	0	0	0	0	2	4	4	4	3	2	1	1	0	0	0	0	0	0	0	0	0
21	1	0	0	0	0	0	0	0	0	0	0	0	2	5	7	7	7	6	4	2	1	0	0	0	0	0	0	0	0	0
20	1	0	0	0	0	0	0	0	0	0	0	1	4	7	8	8	8	8	7	4	2	1	0	0	0	0	0	0	0	0
19	1	0	0	0	0	0	0	0	0	0	0	2	5	7	8	8	8	8	7	4	2	1	0	0	0	0	0	0	0	0
18	1	0	0	0	0	0	0	0	0	0	0	2	5	7	8	8	8	8	7	4	2	1	0	0	0	0	0	0	0	0
17	1	0	0	0	0	0	0	0	0	0	0	2	5	7	8	8	8	8	6	4	2	1	0	0	0	0	0	0	0	0
16	1	0	0	0	0	0	0	0	0	0	0	1	3	5	7	7	7	7	5	2	1	0	0	0	0	0	0	0	0	0
15	1	0	0	0	0	0	0	0	0	0	0	0	1	2	4	4	5	5	3	1	1	0	0	0	0	0	0	0	0	0
14	1	0	0	0	0	0	0	0	0	0	0	0	0	1	2	2	2	2	1	0	0	0	0	0	0	0	0	0	0	0
13	1	0	0	0	0	0	0	0	0	0	0	0	0	0	0	0	0	0	0	0	0	0	0	0	0	0	0	0	0	0
12	1	0	0	0	0	0	0	0	0	0	0	0	0	0	0	0	0	0	0	0	0	0	0	0	0	0	0	0	0	0
11	1	0	0	0	0	0	0	0	0	0	0	0	0	0	0	0	0	0	0	0	0	0	0	0	0	0	0	0	0	0
10	1	0	0	0	0	0	0	0	0	0	0	0	0	0	0	0	0	0	0	0	0	0	0	0	0	0	0	0	0	0
9	1	0	0	0	0	0	0	0	0	0	0	0	0	0	0	0	0	0	0	0	0	0	0	0	0	0	0	0	0	0
8	1	0	0	0	0	0	0	0	0	0	0	0	0	0	0	0	0	0	0	0	0	0	0	0	0	0	0	0	0	0
7	1	0	0	0	0	0	0	0	0	0	0	0	0	0	0	0	0	0	0	0	0	0	0	0	0	0	0	0	0	0
6	1	0	0	0	0	0	0	0	0	0	0	0	0	0	0	0	0	0	0	0	0	0	0	0	0	0	0	0	0	0
5	1	0	0	0	0	0	0	0	0	0	0	0	0	0	0	0	0	0	0	0	0	0	0	0	0	0	0	0	0	0
4	1	0	0	0	0	0	0	0	0	0	0	0	0	0	0	0	0	0	0	0	0	0	0	0	0	0	0	0	0	0
3	1	0	0	0	0	0	0	0	0	0	0	0	0	0	0	0	0	0	0	0	0	0	0	0	0	0	0	0	0	0
2	1	0	0	0	0	0	0	0	0	0	0	0	0	0	0	0	0	0	0	0	0	0	0	0	0	0	0	0	0	0
1	1	0	0	0	0	0	0	0	0	0	0	0	0	0	0	0	0	0	0	0	0	0	0	0	0	0	0	0	0	0

TOTAL	MASS	XBAR	YBAR	SIGMA
INITIAL	400.	16.5	18.5	71
CURRENT	394.	16.5	18.4	3.15
% CHANGE	-1.	---	---	345.60

Figure 5-3 SHASTA Circular Advection Test: After 200 Time Steps

ADVECTION TEST: SHASTA-ERT, 5X5 BLOCK OF 100S , UNIFORM HORIZ WIND  
INITIAL CONCENTRATIONS

LEVEL =	1	2	3	4	5	6	7	8	9	10	11	12	13	14	15	16	17	18	19	20	21	22	23	24	25	26	27	28	29	30
23	0	0	0	0	0	0	0	0	0	0	0	0	0	0	0	0	0	0	0	0	0	0	0	0	0	0	0	0	0	0
22	0	0	0	0	0	0	0	0	0	0	0	0	0	0	0	0	0	0	0	0	0	0	0	0	0	0	0	0	0	0
21	0	0	0	0	0	0	0	0	0	0	0	0	0	0	0	0	0	0	0	0	0	0	0	0	0	0	0	0	0	0
20	0	0	0	0	0	0	0	0	0	0	0	0	0	0	0	0	0	0	0	0	0	0	0	0	0	0	0	0	0	0
19	0	0	0	0	0	0	0	0	0	0	0	0	0	0	0	0	0	0	0	0	0	0	0	0	0	0	0	0	0	0
18	0	0	0	0	0	0	0	0	0	0	0	0	0	0	0	0	0	0	0	0	0	0	0	0	0	0	0	0	0	0
17	0	0	100	100	100	100	100	0	0	0	0	0	0	0	0	0	0	0	0	0	0	0	0	0	0	0	0	0	0	0
16	0	0	100	100	100	100	100	0	0	0	0	0	0	0	0	0	0	0	0	0	0	0	0	0	0	0	0	0	0	0
15	0	0	100	100	100	100	100	0	0	0	0	0	0	0	0	0	0	0	0	0	0	0	0	0	0	0	0	0	0	0
14	0	0	100	100	100	100	100	0	0	0	0	0	0	0	0	0	0	0	0	0	0	0	0	0	0	0	0	0	0	0
13	0	0	100	100	100	100	100	0	0	0	0	0	0	0	0	0	0	0	0	0	0	0	0	0	0	0	0	0	0	0
12	0	0	0	0	0	0	0	0	0	0	0	0	0	0	0	0	0	0	0	0	0	0	0	0	0	0	0	0	0	0
11	0	0	0	0	0	0	0	0	0	0	0	0	0	0	0	0	0	0	0	0	0	0	0	0	0	0	0	0	0	0
10	0	0	0	0	0	0	0	0	0	0	0	0	0	0	0	0	0	0	0	0	0	0	0	0	0	0	0	0	0	0
9	0	0	0	0	0	0	0	0	0	0	0	0	0	0	0	0	0	0	0	0	0	0	0	0	0	0	0	0	0	0
8	0	0	0	0	0	0	0	0	0	0	0	0	0	0	0	0	0	0	0	0	0	0	0	0	0	0	0	0	0	0
7	0	0	0	0	0	0	0	0	0	0	0	0	0	0	0	0	0	0	0	0	0	0	0	0	0	0	0	0	0	0
6	0	0	0	0	0	0	0	0	0	0	0	0	0	0	0	0	0	0	0	0	0	0	0	0	0	0	0	0	0	0
5	0	0	0	0	0	0	0	0	0	0	0	0	0	0	0	0	0	0	0	0	0	0	0	0	0	0	0	0	0	0
4	0	0	0	0	0	0	0	0	0	0	0	0	0	0	0	0	0	0	0	0	0	0	0	0	0	0	0	0	0	0
3	0	0	0	0	0	0	0	0	0	0	0	0	0	0	0	0	0	0	0	0	0	0	0	0	0	0	0	0	0	0
2	0	0	0	0	0	0	0	0	0	0	0	0	0	0	0	0	0	0	0	0	0	0	0	0	0	0	0	0	0	0
1	0	0	0	0	0	0	0	0	0	0	0	0	0	0	0	0	0	0	0	0	0	0	0	0	0	0	0	0	0	0
		TOTAL MASS				XRAR		YRAR		SIGMA																				
INITIAL		2500.				5.0		15.0		2.00																				
CURRENT		2500.				5.0		15.0		2.00																				
% CHANGE		0				---		---		.00																				

Figure 5-4 SHASTA Linear Advection Test: Initial Concentrations

ADVECTION TEST: SHASTA-ERT, 5X5 BLOCK OF 100S , UNIFORM HORIZ WIND

STEP NUMBER = 4, DELTA T= 13 MIN, DELTA X= 10KM, U= 6.25M/S  
V= .00M/S

LEVEL =	1	1	2	3	4	5	6	7	8	9	10	11	12	13	14	15	16	17	18	19	20	21	22	23	24	25	26	27	28	29	30
23	1	0	0	0	0	0	0	0	0	0	0	0	0	0	0	0	0	0	0	0	0	0	0	0	0	0	0	0	0	0	
22	1	0	0	0	0	0	0	0	0	0	0	0	0	0	0	0	0	0	0	0	0	0	0	0	0	0	0	0	0	0	
21	1	0	0	0	0	0	0	0	0	0	0	0	0	0	0	0	0	0	0	0	0	0	0	0	0	0	0	0	0	0	
20	1	0	0	0	0	0	0	0	0	0	0	0	0	0	0	0	0	0	0	0	0	0	0	0	0	0	0	0	0	0	
19	1	0	0	0	0	0	0	0	0	0	0	0	0	0	0	0	0	0	0	0	0	0	0	0	0	0	0	0	0	0	
18	1	0	0	0	3	8	11	11	11	8	3	0	0	0	0	0	0	0	0	0	0	0	0	0	0	0	0	0	0	0	
17	1	0	0	0	21	68	89	89	89	68	21	0	0	0	0	0	0	0	0	0	0	0	0	0	0	0	0	0	0	0	
16	1	0	0	0	24	76	100	100	100	76	24	0	0	0	0	0	0	0	0	0	0	0	0	0	0	0	0	0	0	0	
15	1	0	0	0	24	76	100	100	100	76	24	0	0	0	0	0	0	0	0	0	0	0	0	0	0	0	0	0	0	0	
14	1	0	0	0	24	76	100	100	100	76	24	0	0	0	0	0	0	0	0	0	0	0	0	0	0	0	0	0	0	0	
13	1	0	0	0	21	68	89	89	89	68	21	0	0	0	0	0	0	0	0	0	0	0	0	0	0	0	0	0	0	0	
12	1	0	0	0	3	8	11	11	11	8	3	0	0	0	0	0	0	0	0	0	0	0	0	0	0	0	0	0	0	0	
11	1	0	0	0	0	0	0	0	0	0	0	0	0	0	0	0	0	0	0	0	0	0	0	0	0	0	0	0	0	0	
10	1	0	0	0	0	0	0	0	0	0	0	0	0	0	0	0	0	0	0	0	0	0	0	0	0	0	0	0	0	0	
9	1	0	0	0	0	0	0	0	0	0	0	0	0	0	0	0	0	0	0	0	0	0	0	0	0	0	0	0	0	0	
8	1	0	0	0	0	0	0	0	0	0	0	0	0	0	0	0	0	0	0	0	0	0	0	0	0	0	0	0	0	0	
7	1	0	0	0	0	0	0	0	0	0	0	0	0	0	0	0	0	0	0	0	0	0	0	0	0	0	0	0	0	0	
6	1	0	0	0	0	0	0	0	0	0	0	0	0	0	0	0	0	0	0	0	0	0	0	0	0	0	0	0	0	0	
5	1	0	0	0	0	0	0	0	0	0	0	0	0	0	0	0	0	0	0	0	0	0	0	0	0	0	0	0	0	0	
4	1	0	0	0	0	0	0	0	0	0	0	0	0	0	0	0	0	0	0	0	0	0	0	0	0	0	0	0	0	0	
3	1	0	0	0	0	0	0	0	0	0	0	0	0	0	0	0	0	0	0	0	0	0	0	0	0	0	0	0	0	0	
2	1	0	0	0	0	0	0	0	0	0	0	0	0	0	0	0	0	0	0	0	0	0	0	0	0	0	0	0	0	0	
1	1	0	0	0	0	0	0	0	0	0	0	0	0	0	0	0	0	0	0	0	0	0	0	0	0	0	0	0	0	0	

TOTAL MASS	2500.	XRAR	5.0	YHAR	15.0	SIGMA	2.00
INITIAL	2500.		7.0		15.0		2.17
CURRENT			---		---		8.27
% CHANGE	0						

Figure 5-5 SHASTA Linear Advection Test: After 4 Time Steps

advection operations are not split. In two dimensions one computes all four relevant fluxes into the  $i,j^{th}$  grid cell simultaneously.

Because the net flux (rather than the x or y components separately) into a cell is available, the antidiffusive flux-limiting (Step 5 of the earlier discussion) can be done in a more physical way, ensuring that more of the qualities of the high-order solution (e.g., less dispersion) can be retained by the time-advanced solution. The price paid for this accuracy in these tests is a three-fold increase in CPU time for the 23 x 30 grid point system as well as an increase in the number of two-dimensional arrays required for storage of intermediate results.

Zalesak (1979) extended the FCT concept to two dimensions by first rewriting Equation 5-3 as:

$$C_{i,j}^{n+1} = C_{i,j}^n - [F_{i+1/2,j} - F_{i-1/2,j} + G_{i,j+1/2} - G_{i,j-1/2}] \Delta t / (\Delta x_i \Delta y_j), \quad (5-10)$$

where the fluxes F in the x direction are of the form

$$F_{i+1/2,j} = u_{i+1/2,j} C_{i+1/2,j} \Delta y_i \quad (5-11a)$$

and the fluxes G in the y direction are of the form

$$G_{i,j+1/2} = v_{i,j+1/2} C_{i,j+1/2} \Delta x_i \quad (5-11b)$$

The specific form of the F's and G's depends on the desired order of the scheme. For the low-order donor cell method and first-order Euler time marching, one may obtain the following:

$$F_{i+1/2,j}^L = u_{i+1/2,j} C_{i+1/2,j}^{DC} \Delta y_j \quad (5-12a)$$

$$\text{where } u_{i+1/2,j} = \frac{1}{2} (u_{i,j}^n + u_{i+1,j}^n) \quad (5-12b)$$



and 
$$C_{i+1/2,j}^{DC} = \begin{cases} C_{i,j}^n & \text{if } u_{i+1/2,j} \geq 0 \\ C_{i+1,j}^n & \text{if } u_{i+1/2,j} < 0 \end{cases} \quad (5-12c)$$

as well as similar equations for  $F_{i-1/2,j}^L$  and  $G_{i,j+1/2}^L$ . The high-order fluxes are specified to eighth-order by Zalesak-derived expressions such as:

$$\begin{aligned} F_{i+1/2,j}^H = & \frac{533}{840} (f_{i,j} + f_{i+1,j}) - \frac{139}{840} (f_{i-1,j} + f_{i+2,j}) \\ & + \frac{29}{840} (f_{i-2,j} + f_{i+3,j}) - \frac{1}{280} (f_{i-3,j} + f_{i+4,j}) \end{aligned} \quad (5-13a)$$

where  $f_{i,j} = u_{i,j}^n C_{i,j}^n \Delta y_j \quad (5-13b)$

ERT's implementation of MFCT uses an eighth-order expression for interior points, dropping to sixth, fourth, and then second order as the edges of the grid are approached. This eliminates the need for a wasteful, four-cell-deep perimeter layer around the "useful" computational grid.

Except for the added subscript, Steps 3-6 of the one-dimensional FCT procedure follow Equations 5-4 through 5-6, which can be rewritten as follows:

$$A_{i+1/2,j} = F_{i+1/2,j}^H - F_{i+1/2,j}^L \quad (5-14a)$$

$$A_{i,j+1/2} = G_{i,j+1/2}^H - G_{i,j+1/2}^L \quad (5-14b)$$

$$A_{i+1/2,j}^C = A_{i+1/2,j} \alpha_{i+1/2,j}, \quad 0 \leq \alpha_{i+1/2,j} \leq 1 \quad (5-15a)$$

$$A_{i,j+1/2}^C = A_{i,j+1/2} \alpha_{i,j+1/2}, \quad 0 \leq \alpha_{i,j+1/2} \leq 1 \quad (5-15b)$$

$$\text{and } C_{i,j}^{n+1} = C_{i,j}^* - [A_{i+1/2,j}^C - A_{i-1/2,j}^C + A_{i,j+1/2}^C - A_{i,j-1/2}^C] \Delta t / (\Delta x_i \Delta y_j) \quad (5-16)$$

As expected, however, the definition of the flux-limiting factors  $\alpha$  becomes a bit more complicated in two dimensions. It is fully described in Equations 7'-18' of Zalesak (1979).

#### 5.2.5 MFCT Advection Tests

Advection tests were also performed on the Zalesak MFCT algorithm, which has the eighth-order spatial accuracy and first-order time accuracy described above. In all tests, the MFCT scheme exhibited substantially reduced numerical diffusion. For example, circular advection of a  $2 \times 2$  block of 100's (see Figure 5-1 for initial conditions) leads to a distribution, after 10 one-hour time steps, which retains up to 96% of the initial peak value (see Figure 5-7). The equivalent  $K_e$  of  $2.0 \times 10^4 \text{ m}^2/\text{sec}$  is still a factor of two above our reference level; however, it must be recognized that no numerical advection scheme will retain sharp structures extending over only one or two grid squares.

Figure 5-8 shows the distribution after one full revolution, which requires 200 hours. Peak concentrations have dropped by a factor of three (experienced by SHASTA after only 10 hours), corresponding to  $K_e = 0.64 \times 10^4 \text{ m}^2/\text{sec}$  over the 200-hour period or--perhaps of greater significance--a value of  $K_e = 0.57 \times 10^4 \text{ m}^2/\text{sec}$  between hour 10 and hour 200, which is well below  $10^4 \text{ m}^2/\text{sec}$ . The corresponding rate for SHASTA over this same 190-hour interval is  $1.7 \times 10^4 \text{ m}^2/\text{sec}$  or a factor of three greater than MFCT.

Figure 5-8 also exhibits the distortion discussed by Lamb (1982) (that is, an elongation perpendicular to the advection direction), as well as a slight phase lag and a minor mass gain of 2%, a gain that has since been traced to a slight error in the high-order outflow boundary conditions. None of these problems are considered of sufficient magnitude to disqualify the MFCT scheme, however.

Thus, for LRT modeling purposes, the three-fold-greater cost of using MFCT reduces the numerical diffusion  $K_e$  by a factor of three

ADVECTION TEST: FCT8-ERT, 2X2 BLOCK OF 100S , CIRCULAR WIND FIELD  
 STEP NUMBER = 10, DELTA T= 60 MIN, DELTA X= 80KM, U= A\*(J-12)  
 V= A\*(16-I)

LEVEL =	1	2	3	4	5	6	7	8	9	10	11	12	13	14	15	16	17	18	19	20	21	22	23	24	25	26	27	28	29	30
1	1	1	1	1	1	1	1	1	1	1	1	1	1	1	1	1	1	1	1	1	1	1	1	1	1	1	1	1	1	1
23	1	0	0	0	0	0	0	0	0	0	0	0	0	0	0	0	0	0	0	0	0	0	0	0	0	0	0	0	0	0
22	1	0	0	0	0	0	0	0	0	0	0	0	0	0	0	0	0	0	0	0	0	0	0	0	0	0	0	0	0	0
21	1	0	0	0	0	0	0	0	0	0	0	0	0	0	0	0	0	0	0	0	0	0	0	0	0	0	0	0	0	0
20	1	0	0	0	0	0	0	0	0	0	0	0	0	0	0	0	0	0	0	0	0	0	0	0	0	0	0	0	0	0
19	1	0	0	0	0	0	0	0	0	0	0	0	0	0	0	0	0	56	45	6	0	0	0	0	0	0	0	0	0	0
18	1	0	0	0	0	0	0	0	0	0	0	0	0	0	0	0	35	96	85	14	0	0	0	0	0	0	0	0	0	0
17	1	0	0	0	0	0	0	0	0	0	0	0	0	0	0	0	3	33	23	2	0	0	0	0	0	0	0	0	0	0
16	1	0	0	0	0	0	0	0	0	0	0	0	0	0	0	0	0	0	0	0	0	0	0	0	0	0	0	0	0	0
15	1	0	0	0	0	0	0	0	0	0	0	0	0	0	0	0	0	0	0	0	0	0	0	0	0	0	0	0	0	0
14	1	0	0	0	0	0	0	0	0	0	0	0	0	0	0	0	0	0	0	0	0	0	0	0	0	0	0	0	0	0
13	1	0	0	0	0	0	0	0	0	0	0	0	0	0	0	0	0	0	0	0	0	0	0	0	0	0	0	0	0	0
12	1	0	0	0	0	0	0	0	0	0	0	0	0	0	0	0	0	0	0	0	0	0	0	0	0	0	0	0	0	0
11	1	0	0	0	0	0	0	0	0	0	0	0	0	0	0	0	0	0	0	0	0	0	0	0	0	0	0	0	0	0
10	1	0	0	0	0	0	0	0	0	0	0	0	0	0	0	0	0	0	0	0	0	0	0	0	0	0	0	0	0	0
9	1	0	0	0	0	0	0	0	0	0	0	0	0	0	0	0	0	0	0	0	0	0	0	0	0	0	0	0	0	0
8	1	0	0	0	0	0	0	0	0	0	0	0	0	0	0	0	0	0	0	0	0	0	0	0	0	0	0	0	0	0
7	1	0	0	0	0	0	0	0	0	0	0	0	0	0	0	0	0	0	0	0	0	0	0	0	0	0	0	0	0	0
6	1	0	0	0	0	0	0	0	0	0	0	0	0	0	0	0	0	0	0	0	0	0	0	0	0	0	0	0	0	0
5	1	0	0	0	0	0	0	0	0	0	0	0	0	0	0	0	0	0	0	0	0	0	0	0	0	0	0	0	0	0
4	1	0	0	0	0	0	0	0	0	0	0	0	0	0	0	0	0	0	0	0	0	0	0	0	0	0	0	0	0	0
3	1	0	0	0	0	0	0	0	0	0	0	0	0	0	0	0	0	0	0	0	0	0	0	0	0	0	0	0	0	0
2	1	0	0	0	0	0	0	0	0	0	0	0	0	0	0	0	0	0	0	0	0	0	0	0	0	0	0	0	0	0
1	1	0	0	0	0	0	0	0	0	0	0	0	0	0	0	0	0	0	0	0	0	0	0	0	0	0	0	0	0	0
		TOTAL MASS				IBAR		JBAR		SIGMA																				
INITIAL		400.				16.5		18.5		.71																				
CURRENT		400.				18.4		18.1		.98																				
% CHANGE		0				---		---		38.52																				

Figure 5-7 FCT8 Circular Advection Test: After 10 Time Steps

5-19

[illegible]

Figure 5-8 FCT8 Circular Advection Test: After 200 Time Steps

and places it in a plausible range. Although simple to incorporate within MFCT, added x, y diffusion may not be needed for MFCT advection on the LRT grid as the numerical diffusion is still substantial. Whether this constitutes an "acceptable" level of control over numerical diffusion remains somewhat debatable, though errors incurred in the initial dilution of point source emissions over a large box of dimensions  $\Delta x$ ,  $\Delta y$  has, to some degree, already put bounds on what could be called acceptable.

#### 5.2.6 Cubic Spline Formulation

The third advection scheme to be considered is based on cubic splines. Use of cubic spline functions to obtain derivatives of the concentration field, thus enabling interpolation, has been analyzed by Rubin and Graves (1975) for Eulerian formulations of the advection equation and by Mahrer and Pielke (1978) for a quasi-Lagrangian formulation. Comparative tests by Pepper et al. (1979), Long and Pepper (1981), and Lamb (1982) indicate that:

- cubic splines should be intermediate between SHASTA and MFCT\* in computation speed,
- cubic splines preserve peak values better than MFCT, and
- cubic splines are one of the few techniques tested on variable mesh grids. In this application, they are superior to Chapeau functions and appear to be applicable to embedded mesh problems.

Spline techniques are usually not without their drawbacks, however. First, advection of sharp distributions generally leaves a trailing wake that contains small negative concentrations (on the order of a few percent of positive peak values). Though these negative concentrations can either be deleted, pushed into neighboring positive concentration cells, or eliminated by filtering, their

---

\*Lamb (1982) indicates that splines are more than a factor of two slower than fourth-order MFCT. However, it is not clear whether both routines were optimized to the same extent.

elimination generally leads to additional numerical diffusion.

Second, although mass is well conserved in practice, it is not usually conserved explicitly as it is with FCT methods.

Our extensive review of the advection scheme literature indicated that it should be possible to combine the virtues of spline techniques and FCT methods into a single algorithm. Our experimental testing of such a routine has found it to be superior to either technique.

The algorithm involves the following ingredients:

- The flux form (Equation 5-3) of the advection equation is used, thus ensuring total mass conservation.
- Splines are fit to the fluxes rather than the concentrations. This is a fundamentally more appropriate use of splines since concentrations are required physically to be non-negative, whereas neither splines nor fluxes have such a constraint.
- The spline interpolated fluxes  $F_{i\pm 1/2}$  are then strongly limited to ensure:
  - positivity of the concentration field;
  - low reflection at grid boundaries; and
  - avoidance of instabilities or generation of spurious new maxima.

The equation used to obtain the interpolated fluxes is simply the spline interpolation relation (Ahlberg et al. 1967).

$$F_{i-1/2} = 1/2 (F_{i-1} + F_i) + (D_{i-1} - D_i) \Delta x_- / 8 \quad (5-17)$$

The  $D_i$  quantities are the spline derivatives,  $(\partial F / \partial x)_i$ , obtained from the solution of the tridiagonal relation:

$$\frac{D_{i-1}}{\Delta x_-} + 2 \left( \frac{1}{\Delta x_-} + \frac{1}{\Delta x_+} \right) D_i + \frac{D_{i+1}}{\Delta x_+} = 3 \left( \frac{F_i - F_{i-1}}{(\Delta x_-)^2} \right) + 3 \left( \frac{F_{i+1} - F_i}{(\Delta x_+)^2} \right), \quad (5-18)$$

where  $\Delta x_- = x_i - x_{i-1}$  and  $\Delta x_+ = x_{i+1} - x_i$  and  $\Delta x_i$  in (5-3) are replaced with  $1/2 (\Delta x_- + \Delta x_+)$ .

The relations used to define the flux limiting step involve numerous conditional tests but may be summarized as:

- a) if  $F_{i-1} \leq F_{i-1/2} \leq F_i$  is not satisfied then (5-19a)  
reset  $F_{i-1/2} = F_{i-1}$  or  $F_i$ , whichever is closer. This prevents flux over/undershoots.
- b) if  $C_i^{n+1} < 0$  would be predicted by Equation 5-3,  
reduce both fluxes  $F_{i\pm 1/2}$  the multiplicative  
factor  $C_i^n / (C_i^n - C_i^{n+1})$  so that the "corrected" (5-19b)  
 $C_i^{n+1} = 0$ . Loop  $i = 1, N$ .
- c) if  $F_{i+1/2} > 0$  and  $C_i^{n+1} > C_{\max}$  where (5-19c)  
 $C_{\max} = \max(\alpha_{i-1/2} C_{i-1}^n, -\alpha_{i+1/2} C_{i-1}^n, C_n^i)$  and  
 $a_{i\pm 1/2}$  is the sign of  $F_{i\pm 1/2}$ , then boost  $F_{i+1/2}$   
by  $+(C_i^{n+1} - C_{\max}) \Delta t / \Delta x$ . Loop to  $i = 1$  to  $N$ .
- d) if  $F_{i-1/2} < 0$  and  $C_i^{n+1} > C_{\max}$  where  $C_{\max}$  is given (5-19d)  
above, then subtract  $(C_i^{n+1} - C_{\max}) \Delta t / \Delta x$  from  
 $F_{i-1/2}$ , thus making it more negative. Loop  $i = N$  to  $1$ .
- e) repeat Step b to prevent negative concentrations.

Finally, compute the time advanced concentrations using the above limited fluxes in Equation 5-3.

### 5.2.7 Cubic Spline Advection Tests

Initial advection tests were performed using a "bare" cubic spline model (i.e., Equations 5-17 and 5-18 with no flux limiting).

Tests on the  $2 \times 2$  block of 100's undergoing circular advection showed remarkably little diffusion and retention of up to 71% of the peak value; however, subsequent linear advection tests on larger distributions (i.e., a  $5 \times 5$  block of 100's) showed the buildup of instabilities and excessive phase lag, in that the center of mass was unable to keep up with the wind.

These problems led to the flux limiting steps defined by Equations 5-19a-d with the resulting model possessing excellent characteristics under what is essentially one-dimensional advection. Starting with the same initial conditions of Figure 5-4, Figure 5-9 shows the distribution after 4 time steps of  $u\Delta T/\Delta x = 1/2$  advection and Figure 5-10 shows the identical distribution after 36 time steps. Based on these and other linear advection tests we find:

- zero mass loss or gain;
- zero phase error for linear advection in the Courant number range 0 to 1;
- zero diffusion perpendicular to the direction of advection. This means that if there is no advection there will be no diffusion--a property highly desirable for the low velocity vertical advection;
- an initial dispersion corresponding to  $K_x = 0.32 \times 10^4 \text{ m}^2/\text{sec}$  and  $K_y = 0$  with zero subsequent diffusion if the Courant number remains constant;
- reflection-free transmission through and out of the grid; and
- slightly faster execution speed than SHASTA.

Encouraged by the linear advection tests we again ran the circular advection test on the  $2 \times 2$  block of 100's and found that the flux limiting was causing more diffusion than in the bare spline model but that even with flux limiting the spline routine performed comparably to FCT8 and at less than one-third the computing expense. Figure 5-9 shows that after 10 time steps a peak retention of up to 86% and a  $K_e = 2.9 \times 10^4 \text{ m}^2/\text{sec}$  is somewhat below FCT8 standards; however, after the full rotation of 200 time steps the peak values equal those of MFCT8 and the  $K_e = 0.43 \times 10^4 \text{ m}^2/\text{sec}$  is lower than that obtained with MFCT8. The equivalent  $K_e$  for the 190 steps between 10 and 200 of  $0.30 \times 10^4 \text{ m}^2/\text{sec}$  indicates that while the spline approach is more dispersive than MFCT for small spatial distributions (e.g.,  $2 \times 2$ ) it is less dispersive than MFCT of distributions spread over four or more grid squares. In addition, we note an overall lag of only 0.4 grid units for the spline method compared to about 2.0 grid units of phase shift for MFCT.



ADVECTION TEST: FCT3SP-ERT, 5X5 BLOCK OF 100S , UNIFORM HORIZ WIND  
 STEP NUMBER = 4, DELTA T= 13 MIN, DELTA X= 10KM, U= 6.25M/S  
 V= .00M/S

LEVEL =	1	2	3	4	5	6	7	8	9	10	11	12	13	14	15	16	17	18	19	20	21	22	23	24	25	26	27	28	29	30
23	0	0	0	0	0	0	0	0	0	0	0	0	0	0	0	0	0	0	0	0	0	0	0	0	0	0	0	0	0	0
22	0	0	0	0	0	0	0	0	0	0	0	0	0	0	0	0	0	0	0	0	0	0	0	0	0	0	0	0	0	0
21	0	0	0	0	0	0	0	0	0	0	0	0	0	0	0	0	0	0	0	0	0	0	0	0	0	0	0	0	0	0
20	0	0	0	0	0	0	0	0	0	0	0	0	0	0	0	0	0	0	0	0	0	0	0	0	0	0	0	0	0	0
19	0	0	0	0	0	0	0	0	0	0	0	0	0	0	0	0	0	0	0	0	0	0	0	0	0	0	0	0	0	0
18	0	0	0	0	0	0	0	0	0	0	0	0	0	0	0	0	0	0	0	0	0	0	0	0	0	0	0	0	0	0
17	0	0	0	10	90	100	100	100	90	10	0	0	0	0	0	0	0	0	0	0	0	0	0	0	0	0	0	0	0	0
16	0	0	0	10	90	100	100	100	90	10	0	0	0	0	0	0	0	0	0	0	0	0	0	0	0	0	0	0	0	0
15	0	0	0	10	90	100	100	100	90	10	0	0	0	0	0	0	0	0	0	0	0	0	0	0	0	0	0	0	0	0
14	0	0	0	10	90	100	100	100	90	10	0	0	0	0	0	0	0	0	0	0	0	0	0	0	0	0	0	0	0	0
13	0	0	0	10	90	100	100	100	90	10	0	0	0	0	0	0	0	0	0	0	0	0	0	0	0	0	0	0	0	0
12	0	0	0	0	0	0	0	0	0	0	0	0	0	0	0	0	0	0	0	0	0	0	0	0	0	0	0	0	0	0
11	0	0	0	0	0	0	0	0	0	0	0	0	0	0	0	0	0	0	0	0	0	0	0	0	0	0	0	0	0	0
10	0	0	0	0	0	0	0	0	0	0	0	0	0	0	0	0	0	0	0	0	0	0	0	0	0	0	0	0	0	0
9	0	0	0	0	0	0	0	0	0	0	0	0	0	0	0	0	0	0	0	0	0	0	0	0	0	0	0	0	0	0
8	0	0	0	0	0	0	0	0	0	0	0	0	0	0	0	0	0	0	0	0	0	0	0	0	0	0	0	0	0	0
7	0	0	0	0	0	0	0	0	0	0	0	0	0	0	0	0	0	0	0	0	0	0	0	0	0	0	0	0	0	0
6	0	0	0	0	0	0	0	0	0	0	0	0	0	0	0	0	0	0	0	0	0	0	0	0	0	0	0	0	0	0
5	0	0	0	0	0	0	0	0	0	0	0	0	0	0	0	0	0	0	0	0	0	0	0	0	0	0	0	0	0	0
4	0	0	0	0	0	0	0	0	0	0	0	0	0	0	0	0	0	0	0	0	0	0	0	0	0	0	0	0	0	0
3	0	0	0	0	0	0	0	0	0	0	0	0	0	0	0	0	0	0	0	0	0	0	0	0	0	0	0	0	0	0
2	0	0	0	0	0	0	0	0	0	0	0	0	0	0	0	0	0	0	0	0	0	0	0	0	0	0	0	0	0	0
1	0	0	0	0	0	0	0	0	0	0	0	0	0	0	0	0	0	0	0	0	0	0	0	0	0	0	0	0	0	0
		TOTAL MASS				XBAR		YBAR		SIGMA																				
INITIAL		2500.				5.0		15.0		2.00																				
CURRENT		2500.				7.0		15.0		2.05																				
% CHANGE		0				---		---		2.47																				

Figure 5-9 ERT-SPLINE Linear Advection Test: After 4 Time Steps

ADVECTION TEST: FCT3SP-ERT, 5X5 BLOCK OF 1008 , UNIFORM HORIZ WIND

STEP NUMBR = 36, DELTA T= 13 MIN, DELTA X= 10KM, U= 6.25M/S  
V= .00M/S

LEVEL = 1

	1	2	3	4	5	6	7	8	9	10	11	12	13	14	15	16	17	18	19	20	21	22	23	24	25	26	27	28	29	30
23	0	0	0	0	0	0	0	0	0	0	0	0	0	0	0	0	0	0	0	0	0	0	0	0	0	0	0	0	0	
22	0	0	0	0	0	0	0	0	0	0	0	0	0	0	0	0	0	0	0	0	0	0	0	0	0	0	0	0	0	
21	0	0	0	0	0	0	0	0	0	0	0	0	0	0	0	0	0	0	0	0	0	0	0	0	0	0	0	0	0	
20	0	0	0	0	0	0	0	0	0	0	0	0	0	0	0	0	0	0	0	0	0	0	0	0	0	0	0	0	0	
19	0	0	0	0	0	0	0	0	0	0	0	0	0	0	0	0	0	0	0	0	0	0	0	0	0	0	0	0	0	
18	0	0	0	0	0	0	0	0	0	0	0	0	0	0	0	0	0	0	0	0	0	0	0	0	0	0	0	0	0	
17	0	0	0	0	0	0	0	0	0	0	0	0	0	0	0	0	0	0	0	10	90	100	100	100	90	10	0	0	0	0
16	0	0	0	0	0	0	0	0	0	0	0	0	0	0	0	0	0	0	0	10	90	100	100	100	90	10	0	0	0	0
15	0	0	0	0	0	0	0	0	0	0	0	0	0	0	0	0	0	0	0	10	90	100	100	100	90	10	0	0	0	0
14	0	0	0	0	0	0	0	0	0	0	0	0	0	0	0	0	0	0	0	10	90	100	100	100	90	10	0	0	0	0
13	0	0	0	0	0	0	0	0	0	0	0	0	0	0	0	0	0	0	0	10	90	100	100	100	90	10	0	0	0	0
12	0	0	0	0	0	0	0	0	0	0	0	0	0	0	0	0	0	0	0	0	0	0	0	0	0	0	0	0	0	0
11	0	0	0	0	0	0	0	0	0	0	0	0	0	0	0	0	0	0	0	0	0	0	0	0	0	0	0	0	0	0
10	0	0	0	0	0	0	0	0	0	0	0	0	0	0	0	0	0	0	0	0	0	0	0	0	0	0	0	0	0	0
9	0	0	0	0	0	0	0	0	0	0	0	0	0	0	0	0	0	0	0	0	0	0	0	0	0	0	0	0	0	0
8	0	0	0	0	0	0	0	0	0	0	0	0	0	0	0	0	0	0	0	0	0	0	0	0	0	0	0	0	0	0
7	0	0	0	0	0	0	0	0	0	0	0	0	0	0	0	0	0	0	0	0	0	0	0	0	0	0	0	0	0	0
6	0	0	0	0	0	0	0	0	0	0	0	0	0	0	0	0	0	0	0	0	0	0	0	0	0	0	0	0	0	0
5	0	0	0	0	0	0	0	0	0	0	0	0	0	0	0	0	0	0	0	0	0	0	0	0	0	0	0	0	0	0
4	0	0	0	0	0	0	0	0	0	0	0	0	0	0	0	0	0	0	0	0	0	0	0	0	0	0	0	0	0	0
3	0	0	0	0	0	0	0	0	0	0	0	0	0	0	0	0	0	0	0	0	0	0	0	0	0	0	0	0	0	0
2	0	0	0	0	0	0	0	0	0	0	0	0	0	0	0	0	0	0	0	0	0	0	0	0	0	0	0	0	0	0
1	0	0	0	0	0	0	0	0	0	0	0	0	0	0	0	0	0	0	0	0	0	0	0	0	0	0	0	0	0	0

	TOTAL MASS	XRAR	YRAR	SIGMA
INITIAL	2500.	5.0	15.0	2.00
CURRENT	2500.	23.0	15.0	2.05
% CHANGE	0	---	---	2.47

Figure 5-10 ERT-SPLINE Linear Advection Test: After 36 Time Steps

ADVECTION TEST: FCT3SP-ERT, 2X2 BLOCK OF 1009 , CIRCULAR WIND FIELD  
 STEP NUMBER = 10, DELTA T= 60 MIN, DELTA X= 80KM, U= A\*(J-12)  
 V= A\*(16-I)

LEVEL =	1	2	3	4	5	6	7	8	9	10	11	12	13	14	15	16	17	18	19	20	21	22	23	24	25	26	27	28	29	30
23	0	0	0	0	0	0	0	0	0	0	0	0	0	0	0	0	0	0	0	0	0	0	0	0	0	0	0	0	0	0
22	0	0	0	0	0	0	0	0	0	0	0	0	0	0	0	0	0	0	0	0	0	0	0	0	0	0	0	0	0	0
21	0	0	0	0	0	0	0	0	0	0	0	0	0	0	0	0	0	0	0	0	0	0	0	0	0	0	0	0	0	0
20	0	0	0	0	0	0	0	0	0	0	0	0	0	0	0	0	0	0	0	0	0	0	0	0	0	0	0	0	0	0
19	0	0	0	0	0	0	0	0	0	0	0	0	0	0	0	13	47	40	9	0	0	0	0	0	0	0	0	0	0	0
18	0	0	0	0	0	0	0	0	0	0	0	0	0	0	0	31	86	72	15	0	0	0	0	0	0	0	0	0	0	0
17	0	0	0	0	0	0	0	0	0	0	0	0	0	0	0	5	35	35	8	0	0	0	0	0	0	0	0	0	0	0
16	0	0	0	0	0	0	0	0	0	0	0	0	0	0	0	1	2	1	0	0	0	0	0	0	0	0	0	0	0	0
15	0	0	0	0	0	0	0	0	0	0	0	0	0	0	0	0	0	0	0	0	0	0	0	0	0	0	0	0	0	0
14	0	0	0	0	0	0	0	0	0	0	0	0	0	0	0	0	0	0	0	0	0	0	0	0	0	0	0	0	0	0
13	0	0	0	0	0	0	0	0	0	0	0	0	0	0	0	0	0	0	0	0	0	0	0	0	0	0	0	0	0	0
12	0	0	0	0	0	0	0	0	0	0	0	0	0	0	0	0	0	0	0	0	0	0	0	0	0	0	0	0	0	0
11	0	0	0	0	0	0	0	0	0	0	0	0	0	0	0	0	0	0	0	0	0	0	0	0	0	0	0	0	0	0
10	0	0	0	0	0	0	0	0	0	0	0	0	0	0	0	0	0	0	0	0	0	0	0	0	0	0	0	0	0	0
9	0	0	0	0	0	0	0	0	0	0	0	0	0	0	0	0	0	0	0	0	0	0	0	0	0	0	0	0	0	0
8	0	0	0	0	0	0	0	0	0	0	0	0	0	0	0	0	0	0	0	0	0	0	0	0	0	0	0	0	0	0
7	0	0	0	0	0	0	0	0	0	0	0	0	0	0	0	0	0	0	0	0	0	0	0	0	0	0	0	0	0	0
6	0	0	0	0	0	0	0	0	0	0	0	0	0	0	0	0	0	0	0	0	0	0	0	0	0	0	0	0	0	0
5	0	0	0	0	0	0	0	0	0	0	0	0	0	0	0	0	0	0	0	0	0	0	0	0	0	0	0	0	0	0
4	0	0	0	0	0	0	0	0	0	0	0	0	0	0	0	0	0	0	0	0	0	0	0	0	0	0	0	0	0	0
3	0	0	0	0	0	0	0	0	0	0	0	0	0	0	0	0	0	0	0	0	0	0	0	0	0	0	0	0	0	0
2	0	0	0	0	0	0	0	0	0	0	0	0	0	0	0	0	0	0	0	0	0	0	0	0	0	0	0	0	0	0
1	0	0	0	0	0	0	0	0	0	0	0	0	0	0	0	0	0	0	0	0	0	0	0	0	0	0	0	0	0	0
TOTAL MASS						XBAR		YBAR		SIGMA																				
INITIAL	400.				16.5		18.5		.71																					
CURRENT	400.				18.4		18.0		1.08																					
% CHANGE	-0				---		---		53.13																					

Figure 5-11 ERT-SPLINE Circular Advection Test: After 10 Time Steps

ADVECTION TEST: FCT3SP-FHT, 2X2 BLOCK OF 100S , CIRCULAR WIND FIELD

STEP NUMBER = 200, DELTA T= 60 MIN, DELTA X= 80KM, U= A\*(J-12)  
V= A\*(16-I)

LEVEL =	1	2	3	4	5	6	7	8	9	10	11	12	13	14	15	16	17	18	19	20	21	22	23	24	25	26	27	28	29	30
23	1	0	0	0	0	0	0	0	0	0	0	0	0	0	0	0	0	0	0	0	0	0	0	0	0	0	0	0	0	0
22	1	0	0	0	0	0	0	0	0	0	0	0	0	0	0	0	0	0	0	0	0	0	0	0	0	0	0	0	0	0
21	1	0	0	0	0	0	0	0	0	0	0	0	0	0	3	5	3	0	0	0	0	0	0	0	0	0	0	0	0	0
20	1	0	0	0	0	0	0	0	0	0	0	0	0	0	17	22	19	5	0	0	0	0	0	0	0	0	0	0	0	0
19	1	0	0	0	0	0	0	0	0	0	0	0	0	9	30	36	36	13	1	0	0	0	0	0	0	0	0	0	0	0
18	1	0	0	0	0	0	0	0	0	0	0	0	0	13	31	35	33	11	0	0	0	0	0	0	0	0	0	0	0	0
17	1	0	0	0	0	0	0	0	0	0	0	0	0	5	19	23	18	4	0	0	0	0	0	0	0	0	0	0	0	0
16	1	0	0	0	0	0	0	0	0	0	0	0	0	0	0	3	3	1	0	0	0	0	0	0	0	0	0	0	0	0
15	1	0	0	0	0	0	0	0	0	0	0	0	0	0	0	0	0	0	0	0	0	0	0	0	0	0	0	0	0	0
14	1	0	0	0	0	0	0	0	0	0	0	0	0	0	0	0	0	0	0	0	0	0	0	0	0	0	0	0	0	0
13	1	0	0	0	0	0	0	0	0	0	0	0	0	0	0	0	0	0	0	0	0	0	0	0	0	0	0	0	0	0
12	1	0	0	0	0	0	0	0	0	0	0	0	0	0	0	0	0	0	0	0	0	0	0	0	0	0	0	0	0	0
11	1	0	0	0	0	0	0	0	0	0	0	0	0	0	0	0	0	0	0	0	0	0	0	0	0	0	0	0	0	0
10	1	0	0	0	0	0	0	0	0	0	0	0	0	0	0	0	0	0	0	0	0	0	0	0	0	0	0	0	0	0
9	1	0	0	0	0	0	0	0	0	0	0	0	0	0	0	0	0	0	0	0	0	0	0	0	0	0	0	0	0	0
8	1	0	0	0	0	0	0	0	0	0	0	0	0	0	0	0	0	0	0	0	0	0	0	0	0	0	0	0	0	0
7	1	0	0	0	0	0	0	0	0	0	0	0	0	0	0	0	0	0	0	0	0	0	0	0	0	0	0	0	0	0
6	1	0	0	0	0	0	0	0	0	0	0	0	0	0	0	0	0	0	0	0	0	0	0	0	0	0	0	0	0	0
5	1	0	0	0	0	0	0	0	0	0	0	0	0	0	0	0	0	0	0	0	0	0	0	0	0	0	0	0	0	0
4	1	0	0	0	0	0	0	0	0	0	0	0	0	0	0	0	0	0	0	0	0	0	0	0	0	0	0	0	0	0
3	1	0	0	0	0	0	0	0	0	0	0	0	0	0	0	0	0	0	0	0	0	0	0	0	0	0	0	0	0	0
2	1	0	0	0	0	0	0	0	0	0	0	0	0	0	0	0	0	0	0	0	0	0	0	0	0	0	0	0	0	0
1	1	0	0	0	0	0	0	0	0	0	0	0	0	0	0	0	0	0	0	0	0	0	0	0	0	0	0	0	0	0

TOTAL MASS	400.	XBAR	16.5	YBAR	18.5	SIGMA	.71
INITIAL	400.						
CURRENT	400.	16.1	18.5			1.56	
% CHANGE	-0	---	---	---	---	120.63	

Figure 5-12 ERT-SPLINE Circular Advection Test: After 200 Time Steps

Finally, to facilitate comparison with advection schemes tested by Chock and Dunker (1982), we allowed the cosine-hill distribution  $50 (1 + \cos \pi R/4)$ , where  $R^2 = (x_i - x_0)^2 + (y_i - y_0)^2$  to be advected by a circular wind field for two full revolutions at a rate of one revolution per 240 time steps\* and maximum Courant numbers of 0.42.

Figure 5-13 shows the initial distribution and Figure 5-14 shows the distribution after the two full revolutions. The peak value of 93 exceeds all methods tested by Dunker and Chock except for the pseudospectral method, which in fact they tested only at lower Courant numbers. We note that the slight net decrease in the second moment, corresponding to a negative  $K_e = -0.04 \times 10^4 \text{ m}^2/\text{sec}$ , actually indicates a slight tendency to "square-up" a distribution as can the second moment method in some cases. The remaining characteristics of these advection tests are summarized in Table 5-1 in order of increasing computational expense. Clearly, the pseudospectral method maintains the best distribution fidelity in this case but at substantially greater computational expense than the cubic spline technique developed here.

#### 5.2.8 Recommended Advection Scheme

The advection scheme tests presented in this section indicate that the SHASTA scheme will cause excessive numerical dispersion in the anticipated LRT model. The more time consuming MFCT approach of Zalesak exhibits three times less numerical diffusion in the two dimensional advection tests undertaken here and is considered adequate for that task on a regular grid. The proposed OME LRT grid, described in Chapter 4, is directly transformable to a regular grid thereby enabling MFCT to be utilized with the minor addition of a multiplicative "map factor" or Jacobian to relate grid increments to real space. The MFCT scheme would, however, have to be expanded to a full

---

\*This corresponds to Chock and Dunker's time step of  $\Delta T = 30 \pi$ .

ADVECTION TEST: FCT3SP-ERT, COSINE HILL:MAX=100, CIRCULAR WIND FIELD  
INITIAL CONCENTRATIONS

LEVEL =		1	2	3	4	5	6	7	8	9	10	11	12	13	14	15	16	17	18	19	20	21	22	23	24	25	26	27	28	29	30	31	32	33
33	1	0	0	0	0	0	0	0	0	0	0	0	0	0	0	0	0	0	0	0	0	0	0	0	0	0	0	0	0	0	0	0	0	
32	1	0	0	0	0	0	0	0	0	0	0	0	0	0	0	0	0	0	0	0	0	0	0	0	0	0	0	0	0	0	0	0	0	
31	1	0	0	0	0	0	0	0	0	0	0	0	0	0	0	0	0	0	0	0	0	0	0	0	0	0	0	0	0	0	0	0	0	
30	1	0	0	0	0	0	0	0	0	0	0	0	0	0	0	0	0	0	0	0	0	0	0	0	0	0	0	0	0	0	0	0	0	
29	1	0	0	0	0	0	0	0	0	0	0	0	0	0	0	0	0	0	0	0	0	0	0	0	0	0	0	0	0	0	0	0	0	
28	1	0	0	0	0	0	0	0	0	0	0	0	0	0	0	0	0	0	0	0	0	0	0	0	0	0	0	0	0	0	0	0	0	
27	1	0	0	0	0	0	0	0	0	0	0	0	0	0	0	0	0	0	0	0	0	0	0	0	0	0	0	0	0	0	0	0	0	
26	1	0	0	0	0	0	0	0	0	0	0	0	0	0	0	0	0	0	0	0	0	0	0	0	0	0	0	0	0	0	0	0	0	
25	1	0	0	0	0	0	0	0	0	0	0	0	0	0	0	0	0	0	0	0	0	0	0	0	0	0	0	0	0	0	0	0	0	
24	1	0	0	0	0	0	0	0	0	0	0	0	0	0	0	0	0	0	0	0	0	0	0	0	0	0	0	0	0	0	0	0	0	
23	1	0	0	0	0	0	0	0	0	0	0	0	0	0	0	0	0	0	0	0	0	0	0	0	0	0	0	0	0	0	0	0	0	
22	1	0	0	0	0	0	0	0	0	0	0	0	0	0	0	0	0	0	0	0	0	0	0	0	0	0	0	0	0	0	0	0	0	
21	1	0	0	0	0	0	0	0	0	0	0	0	0	0	0	0	0	0	0	0	0	0	0	0	0	0	0	0	0	0	0	0	0	
20	1	0	0	0	0	2	10	15	10	2	0	0	0	0	0	0	0	0	0	0	0	0	0	0	0	0	0	0	0	0	0	0	0	
19	1	0	0	0	2	20	41	50	41	20	2	0	0	0	0	0	0	0	0	0	0	0	0	0	0	0	0	0	0	0	0	0	0	
18	1	0	0	0	10	41	72	85	72	41	10	0	0	0	0	0	0	0	0	0	0	0	0	0	0	0	0	0	0	0	0	0	0	
17	1	0	0	0	15	50	85	100	85	50	15	0	0	0	0	0	0	0	0	0	0	0	0	0	0	0	0	0	0	0	0	0	0	
16	1	0	0	0	10	41	72	85	72	41	10	0	0	0	0	0	0	0	0	0	0	0	0	0	0	0	0	0	0	0	0	0	0	
15	1	0	0	0	2	20	41	50	41	20	2	0	0	0	0	0	0	0	0	0	0	0	0	0	0	0	0	0	0	0	0	0	0	
14	1	0	0	0	0	2	10	15	10	2	0	0	0	0	0	0	0	0	0	0	0	0	0	0	0	0	0	0	0	0	0	0	0	
13	1	0	0	0	0	0	0	0	0	0	0	0	0	0	0	0	0	0	0	0	0	0	0	0	0	0	0	0	0	0	0	0	0	
12	1	0	0	0	0	0	0	0	0	0	0	0	0	0	0	0	0	0	0	0	0	0	0	0	0	0	0	0	0	0	0	0	0	
11	1	0	0	0	0	0	0	0	0	0	0	0	0	0	0	0	0	0	0	0	0	0	0	0	0	0	0	0	0	0	0	0	0	
10	1	0	0	0	0	0	0	0	0	0	0	0	0	0	0	0	0	0	0	0	0	0	0	0	0	0	0	0	0	0	0	0	0	
9	1	0	0	0	0	0	0	0	0	0	0	0	0	0	0	0	0	0	0	0	0	0	0	0	0	0	0	0	0	0	0	0	0	
8	1	0	0	0	0	0	0	0	0	0	0	0	0	0	0	0	0	0	0	0	0	0	0	0	0	0	0	0	0	0	0	0	0	
7	1	0	0	0	0	0	0	0	0	0	0	0	0	0	0	0	0	0	0	0	0	0	0	0	0	0	0	0	0	0	0	0	0	
6	1	0	0	0	0	0	0	0	0	0	0	0	0	0	0	0	0	0	0	0	0	0	0	0	0	0	0	0	0	0	0	0	0	
5	1	0	0	0	0	0	0	0	0	0	0	0	0	0	0	0	0	0	0	0	0	0	0	0	0	0	0	0	0	0	0	0	0	
4	1	0	0	0	0	0	0	0	0	0	0	0	0	0	0	0	0	0	0	0	0	0	0	0	0	0	0	0	0	0	0	0	0	
3	1	0	0	0	0	0	0	0	0	0	0	0	0	0	0	0	0	0	0	0	0	0	0	0	0	0	0	0	0	0	0	0	0	
2	1	0	0	0	0	0	0	0	0	0	0	0	0	0	0	0	0	0	0	0	0	0	0	0	0	0	0	0	0	0	0	0	0	
1	1	0	0	0	0	0	0	0	0	0	0	0	0	0	0	0	0	0	0	0	0	0	0	0	0	0	0	0	0	0	0	0	0	
		TOTAL MASS					XBAR		YBAR		SIGMA		CMDR																					
INITIAL		1496.					7.0		17.0		1.93		1.00																					
CURRENT		1496.					7.0		17.0		1.93		1.00																					
% CHANGE		0					---		---		.00		.00																					

Figure 5-13 ERT-SPLINE Cosine Hill Circular Advection Test:  
Initial Concentrations

ADVECTION TEST: FCT3SP-ERT, COSINE HILL:MAX=100, CIRCULAR WIND FIELD

STEP NUMBER = 480, DELTA T= 60 MIN, DELTA X= 80KM, U= A\*(J-17)  
V= A\*(17-I)

LEVEL =	1	2	3	4	5	6	7	8	9	10	11	12	13	14	15	16	17	18	19	20	21	22	23	24	25	26	27	28	29	30	31	32	33
33	1	0	0	0	0	0	0	0	0	0	0	0	0	0	0	0	0	0	0	0	0	0	0	0	0	0	0	0	0	0	0	0	
32	1	0	0	0	0	0	0	0	0	0	0	0	0	0	0	0	0	0	0	0	0	0	0	0	0	0	0	0	0	0	0	0	
31	1	0	0	0	0	0	0	0	0	0	0	0	0	0	0	0	0	0	0	0	0	0	0	0	0	0	0	0	0	0	0	0	
30	1	0	0	0	0	0	0	0	0	0	0	0	0	0	0	0	0	0	0	0	0	0	0	0	0	0	0	0	0	0	0	0	
29	1	0	0	0	0	0	0	0	0	0	0	0	0	0	0	0	0	0	0	0	0	0	0	0	0	0	0	0	0	0	0	0	
28	1	0	0	0	0	0	0	0	0	0	0	0	0	0	0	0	0	0	0	0	0	0	0	0	0	0	0	0	0	0	0	0	
27	1	0	0	0	0	0	0	0	0	0	0	0	0	0	0	0	0	0	0	0	0	0	0	0	0	0	0	0	0	0	0	0	
26	1	0	0	0	0	0	0	0	0	0	0	0	0	0	0	0	0	0	0	0	0	0	0	0	0	0	0	0	0	0	0	0	
25	1	0	0	0	0	0	0	0	0	0	0	0	0	0	0	0	0	0	0	0	0	0	0	0	0	0	0	0	0	0	0	0	
24	1	0	0	0	0	0	0	0	0	0	0	0	0	0	0	0	0	0	0	0	0	0	0	0	0	0	0	0	0	0	0	0	
23	1	0	0	0	0	0	0	0	0	0	0	0	0	0	0	0	0	0	0	0	0	0	0	0	0	0	0	0	0	0	0	0	
22	1	0	0	0	0	0	0	0	0	0	0	0	0	0	0	0	0	0	0	0	0	0	0	0	0	0	0	0	0	0	0	0	
21	1	0	0	0	0	0	0	0	0	0	0	0	0	0	0	0	0	0	0	0	0	0	0	0	0	0	0	0	0	0	0	0	
20	1	0	0	0	0	0	8	9	0	0	0	0	0	0	0	0	0	0	0	0	0	0	0	0	0	0	0	0	0	0	0	0	
19	1	0	0	0	1	18	63	72	68	23	0	0	0	0	0	0	0	0	0	0	0	0	0	0	0	0	0	0	0	0	0	0	
18	1	0	0	0	12	57	92	92	89	59	6	0	0	0	0	0	0	0	0	0	0	0	0	0	0	0	0	0	0	0	0	0	
17	1	0	0	0	12	61	93	92	91	65	12	0	0	0	0	0	0	0	0	0	0	0	0	0	0	0	0	0	0	0	0	0	
16	1	0	0	0	5	40	80	88	75	38	8	0	0	0	0	0	0	0	0	0	0	0	0	0	0	0	0	0	0	0	0	0	
15	1	0	0	0	0	3	14	24	15	4	1	0	0	0	0	0	0	0	0	0	0	0	0	0	0	0	0	0	0	0	0	0	
14	1	0	0	0	0	0	0	0	0	0	0	0	0	0	0	0	0	0	0	0	0	0	0	0	0	0	0	0	0	0	0	0	
13	1	0	0	0	0	0	0	0	0	0	0	0	0	0	0	0	0	0	0	0	0	0	0	0	0	0	0	0	0	0	0	0	
12	1	0	0	0	0	0	0	0	0	0	0	0	0	0	0	0	0	0	0	0	0	0	0	0	0	0	0	0	0	0	0	0	
11	1	0	0	0	0	0	0	0	0	0	0	0	0	0	0	0	0	0	0	0	0	0	0	0	0	0	0	0	0	0	0	0	
10	1	0	0	0	0	0	0	0	0	0	0	0	0	0	0	0	0	0	0	0	0	0	0	0	0	0	0	0	0	0	0	0	
9	1	0	0	0	0	0	0	0	0	0	0	0	0	0	0	0	0	0	0	0	0	0	0	0	0	0	0	0	0	0	0	0	
8	1	0	0	0	0	0	0	0	0	0	0	0	0	0	0	0	0	0	0	0	0	0	0	0	0	0	0	0	0	0	0	0	
7	1	0	0	0	0	0	0	0	0	0	0	0	0	0	0	0	0	0	0	0	0	0	0	0	0	0	0	0	0	0	0	0	
6	1	0	0	0	0	0	0	0	0	0	0	0	0	0	0	0	0	0	0	0	0	0	0	0	0	0	0	0	0	0	0	0	
5	1	0	0	0	0	0	0	0	0	0	0	0	0	0	0	0	0	0	0	0	0	0	0	0	0	0	0	0	0	0	0	0	
4	1	0	0	0	0	0	0	0	0	0	0	0	0	0	0	0	0	0	0	0	0	0	0	0	0	0	0	0	0	0	0	0	
3	1	0	0	0	0	0	0	0	0	0	0	0	0	0	0	0	0	0	0	0	0	0	0	0	0	0	0	0	0	0	0	0	
2	1	0	0	0	0	0	0	0	0	0	0	0	0	0	0	0	0	0	0	0	0	0	0	0	0	0	0	0	0	0	0	0	
1	1	0	0	0	0	0	0	0	0	0	0	0	0	0	0	0	0	0	0	0	0	0	0	0	0	0	0	0	0	0	0	0	
		TOTAL MASS				XBAR		YBAR		SIGMA		CMDR																					
INITIAL		1496.				7.0		17.0		1.93		1.00																					
CURRENT		1496.				7.0		17.3		1.79		1.20																					
% CHANGE		-0				---		---		-7.58		20.39																					

Figure 5-14 ERT-SPLINE Cosine Hill Circular Advection Test:  
After Two Rotations

TABLE 5-1  
COSINE-HILL CIRCULAR ADVECTION RESULTS SUMMARY\*

<u>Algorithm</u>	<u>Time Marching</u>	<u>Execution Time**</u>	<u>Max. Value</u>	<u>Min. Value</u>	$\Sigma c^2 / \Sigma c_0^2$
ERT-Spline	Explicit Euler	0.60	93.	0.	1.20
SHASTA (LPE)	Explicit Euler	1.0	27.	0.	0.32
Chapeau Functions	Implicit Crank-Nicholson	1.2	91.	-10.	1.00
Chapeau Functions (Filtered)	Implicit Crank-Nicolson	2.3	60.	-1.	0.63
Zalesak MFCT (Fourth Order)	Modified Euler Predictor- Corrector	3.1	58.	0.	0.60
Second Moment	Explicit	4.3	60.	0.	0.68
Pseudospectral (Periodic Boundaries)	Explicit Leapfrog	4.3	99.	-1.	1.00

---

\*Adapted from Chock and Dunker (1982) with ERT-Spline results added.  
 \*\*Normalized by SHASTA.



three-dimensional scheme to accommodate vertical advection or be supplemented by a separate z advection module. The latter option would be preferable since three-dimensional MFCT would be very computationally expensive and, given the unexplored modeling benefits of including vertical advection in an LRT model, it is recommended as a modeler-selectable option.

The flux-corrected, cubic-spline algorithm developed and tested during this program has been found to perform as well or better than the MFCT scheme and at computation speed several times faster than MFCT. Since this spline scheme already utilizes operator splitting, extension to three dimensions would be trivial and should not increase overall advection computation time by more than a factor of two. Adaptation to the OME latlong grid should not be a problem and the proven applicability of spline techniques to truly variable grids ensures maximum flexibility for future code development and modification. Thus, further testing and incorporation of a vectorized version of this flux-corrected cubic spline advection algorithm (with added lateral diffusion) into the OME LRT and mesoscale models are recommended.

### 5.3 Diffusion Schemes

The diffusion of a concentration field C is described by the partial differential equation

$$\frac{\partial C}{\partial t} = \nabla \cdot (K \nabla C) \quad (5-20)$$

where K is the 3 x 3 diffusivity matrix with elements  $K_{xx}$ ,  $K_{xy}$ , ...  $K_{yz}$ ,  $K_{zz}$  which are functions of x, y, z, and time. Within a split operator framework the off-diagonal terms (e.g.,  $K_{xz}$ ), usually assumed insignificant, would have to be ignored in any case, and the problem reduces to three partial differential equations in time and x, y, and z, respectively. The z equation is written

$$\frac{\partial C}{\partial t} = \frac{\partial}{\partial z} K_z(x, y, z, t) \frac{\partial C}{\partial z} \quad (5-21)$$

where the redundant z subscript on  $K_{zz}$  is now dropped. Since in the above equation only the value of K and its derivative in z are important, variations in x and y are averaged over the grid cell of concern as are variations over the time step  $\Delta t$  of concern. The same considerations apply to the x and y equations and the final set of three differential equations is then

$$\frac{\partial C}{\partial t} = \frac{\partial}{\partial x} K_x(x) \frac{\partial C}{\partial x} \quad (5-22a)$$

$$\frac{\partial C}{\partial t} = \frac{\partial}{\partial y} K_y(y) \frac{\partial C}{\partial y} \quad (5-22b)$$

$$\frac{\partial C}{\partial z} = \frac{\partial}{\partial z} K_z(z) \frac{\partial C}{\partial z} + S - D \quad (5-22c)$$

where source terms S and depletion terms D have been added to 5-22c to ensure completeness.

In the conversion of these equations to finite difference form, low-order accuracy is usually adequate. For example, if  $K_x(x)$  does not vary significantly in x, and  $\Delta x_j$  is a constant  $\Delta x$ , then Equation 22a becomes:

$$(c_j^{n+1} - c_j^n)/\Delta t = (K_x \Delta x^2) [\gamma (\delta^2 C)_j^{n+1} + (1-\gamma)(\delta^2 C)_j^n] \quad (5-23a)$$

where  $\delta C_j \equiv C_{j+1/2} - C_{j-1/2}$  and  $\delta^2 C$  is the simple three-point differencing expression  $\delta^2 C = C_{j+1} - 2C_j + C_{j-1}$ .

Equation 5-23a has been written such that a fraction  $\gamma$  is done implicitly (i.e., unknown values  $C_j^{n+1}$  at the next time step are utilized) and a fraction  $1 - \gamma$  is done explicitly in terms of the known  $C_j^n$ . Equation 5-23a thus encompasses the Euler explicit scheme ( $\gamma = 0$ ), the Crank-Nicolson scheme ( $\gamma = 1/2$ ), the fully implicit scheme ( $\gamma = 1$ ), as well as all other mixed implicit - explicit schemes. The explicit form of 5-23a is stable only for  $K_x \Delta t / (\Delta x)^2 < 1$  whereas the implicit form is unconditionally stable.

In the horizontal direction simple three-point finite difference expressions and Crank-Nicolson time differencing provide accurate numerical solutions (Roache 1976), though the Euler scheme may be adequate given the phenomenological nature of  $K_x, K_y$ . Horizontal transport on the mesoscale or LRT grids is dominated by advection rather than diffusion, so that the time step limitation ( $\Delta t < \Delta x^2/K_x$ ) is rarely a problem. For  $\Delta t = 1$  hour,  $\Delta x = 80$  km, and  $K_x = 10^4 \text{ m}^2/\text{sec}$ , the stability parameter  $K_x \Delta t / (\Delta x)^2 = 0.006$  and is indeed much less than unity. Similarly, reflective boundary conditions can be used for the horizontal diffusion step without compromising the solution or generating significant numerical noise.

In contrast, vertical diffusion generally dominates the vertical transport step and greater care must be exercised in selecting a numerical scheme. Numerical integration of the vertical diffusion equation is inherently more noisy because (1) variable mesh spacing is required to resolve concentration gradients, (2)  $\Delta z^2/K_z$  can be quite small, and (3) the source emissions terms can act as a strong forcing function, particularly in the shallow surface cell. In fact, the rationale for including the deposition term in the vertical diffusion calculation is to partially dampen the noise induced by the source emissions term.

Three-point finite difference methods perform fairly well on the vertical diffusion equation providing the mesh spacing varies gradually. In this case the finite difference form of Equation 5-22c becomes

$$(c_j^{n+1} - c_j^n) / \Delta t = \gamma \Delta_j^{n+1} + (1-\gamma) \Delta_j^n + s_j^{n+1/2} - D_j^{n+1/2} \quad (5-23b)$$

where

$$\Delta_j \equiv \frac{(K_{j+1} - K_{j-1})(C_{j+1} - C_{j-1})}{[\Delta z_j + (\Delta z_{j+1} + \Delta z_{j-1})/2]^2} + 2K_j \frac{(C_{j+1} - C_j)}{(\Delta z_{j+1} + \Delta z_j)} - \frac{(C_j - C_{j-1})}{(\Delta z_j + \Delta z_{j-1})} / \Delta z_j ,$$

$$\Delta z_j = z_{j+1/2} - z_{j-1/2} , \quad K_j \equiv K_z^{n+1/2}(z_j)$$

and  $n + 1/2$  indicates that the time  $t_n + \Delta t/2$  is used in both explicit and implicit terms. LRT has found that a hybrid time differencing scheme which uses the Crank-Nicolson method when  $K_z$  is small or moderate, and the fully implicit method when  $K_z$  is large, is more accurate than the fully implicit method alone.

Higher accuracy can be obtained for the vertical diffusion equation by using compact differencing methods (Adam 1975, Hirsh 1975, Adam 1977). These are finite difference methods where the functions and their derivatives are considered unknowns. These provide fourth-order accuracy while keeping the tridiagonal structure of the schemes. Boundary conditions can be written with the compact differencing schemes which provide either second- or third-order accuracy. Furthermore, the methods work well with nonuniform mesh spacing and have only slightly greater computational expense than simple three-point finite difference schemes. These compact differencing schemes are very similar to spline techniques and should be further assessed in terms of cost versus accuracy of the diffusion operator evaluation.

#### 5.4 Numerical Methods for Integration of Chemical Kinetics

Like the advection and diffusion terms, the rate of change of species concentration resulting from the chemical kinetics term requires a numerical integration procedure designed to accommodate the specific form and characteristics of its equations. The chemical rate of change of concentration can be described as a set of nonlinear, coupled ordinary differential equations:

$$\left(\frac{dC_j}{dt}\right)_{\text{CHEM}} = R_j = f_j(C_1, C_2, \dots, C_n, k_1, k_2, \dots, k_r, t), \quad i=1, 2, \dots, n \quad (5-24)$$

and an associated set of initial concentrations,  $C_j(0)$ . Given a set of chemical reactions defined by:

$$\sum_{j=1}^n V_{ij} M_j \xrightarrow{k_i} \sum_{j=1}^n U_{ij} M_j, \quad i=1, 2, \dots, r \quad (5-25)$$

where  $M_j$  = chemical formula of the  $i^{\text{th}}$  species,  
 $k_i$  = rate of  $i^{\text{th}}$  chemical reaction,  
 $V_{ij}$  = stoichiometric coefficient of  $j^{\text{th}}$  reactant in  $i^{\text{th}}$   
 chemical reaction,  
 $U_{ij}$  = stoichiometric coefficient of  $j^{\text{th}}$  product in  $i^{\text{th}}$   
 chemical reaction,  
 $r$  = number of chemical reactions,  
 $n$  = number of species,

the specific form of the chemical kinetic function is:

$$R_j = \sum_{i=1}^r (U_{ij} - V_{ij}) k_i \prod_{m=1}^n C_m^{V_{im}}, \quad j=1,2,\dots,n \quad (5-26)$$

where  $C_m$  is the concentration of the  $j^{\text{th}}$  species. The primary difficulty associated with solving this system for atmospheric reactions is that there are reactions whose characteristic time scales differ by 5 to 10 orders of magnitude. This condition is often referred to as stiffness in the equations and it occurs when the real parts of the eigenvalues of the Jacobian ( $\partial f / \partial C$ ) are negative and differ by orders of magnitude.

Numerous general purpose algorithms have been developed in the last decade to solve stiff differential equations (Gear 1971, Bryne and Hindmarsh 1975, Curtis 1978). Perhaps the most widely used algorithms for chemical kinetics are the Gear-type algorithms employing variable order, variable-step-backwards differencing, multi-step schemes. These methods are quite accurate, reliable, and efficient for solving problems of chemical kinetics alone. However, the Gear-type methods have relatively high start-up overheads. For a typical 8- to 12-hour photochemical mechanism calculation, over half the computational costs are associated with obtaining the solution for the first hour. The high start-up costs of the Gear-type methods detract from their usefulness in multi-grid point calculations, where transport, diffusion, and chemistry are time-split.

#### 5.4.1 The Asymptotic Integration Scheme

A solution method that ERT and others (McRae et al. 1982) have found to be well suited to multi-point calculations is an asymptotic integration scheme developed by Boris and Young (1977). The method was designed to solve reaction kinetics in large hydrodynamic problems. It is not quite as accurate as the Gear-type schemes, but it has low start-up costs and is computationally fast. Comparisons between the Gear scheme and the Boris and Young scheme for photochemical kinetic problems have shown the latter to be 5 to 10 times faster during the first 15 minutes of integration and accurate to within 5% of the Gear solution for major species. Furthermore, the method has been found to be quite reliable in ERT's PLMSTAR reactive plume model and the CalTech air shed model (McRae 1981).

The Young and Boris method is a second-order, predictor-corrector method which takes special notice of those particular equations which are determined to be stiff. The derivatives  $f_j$  are computed from Equation 5-27 or equivalently Equation 5-26.

$$f_j(t) = a_j(t) - b_j(t) C_j(t) \quad (5-27)$$

An initial trial time step size is chosen independent of the stiffness criterion and is determined such that none of the concentrations will change by more than a prescribed amount (which is typically a few percent). The actual step size is chosen so that:

$$\Delta t \leq \epsilon_1 \min \begin{bmatrix} C_j(0)/f_j(0) \\ 1/b_j(0) \end{bmatrix} \quad \begin{matrix} \text{if } C > 0 \\ \text{if } C \approx 0 \end{matrix}, \quad j=1, \dots, N$$

where  $\epsilon_1$  is a scale factor usually equal to the convergence criteria. This time step may be larger than some or all of the equilibrium times, in which the corresponding equations would be called stiff. Nevertheless, when solved by asymptotic integration, this time step ensures that accuracy can be maintained. When a stiff equation is close to equilibrium, the changes in concentration over

the time step will be small even though the adjustment rate toward equilibrium can be very much shorter than the time step. When the stiff equation is far from an equilibrium, the time step should be scaled down to the equilibrium time to ensure that the transition to equilibrium can be followed accurately. Readjustment, because of the very fast rate, generally occurs very rapidly, after which much longer time steps may be taken.

After a time step has been selected, the equations are designated stiff or nonstiff, according to the criterion:

$$\begin{array}{ll} b_j \Delta t > \epsilon_2 & \text{stiff} \\ b_j \Delta t \leq \epsilon_2 & \text{nonstiff} \end{array}$$

where  $\epsilon_2$  is typically unity. The two types of equations are then integrated using separate predictor-corrector formulas. The usual predictor-corrector formula is used for the nonstiff equations and a simple asymptotic formula is used for the stiff equations.

The predictor part of the step is performed as follows:

$$C_j(1) = C_j(0) + \Delta t f_j(0) \quad (\text{nonstiff})$$

$$C_j(1) = \frac{C_j(0)(2 - \Delta t b_j(0)) + 2\Delta t a_j(0)}{2 + \Delta t b_j(0)} \quad (\text{stiff})$$

where the integer in parentheses denotes the iteration number. The function is then evaluated using the results,  $C_j(1)$ , of the predictor step and the following corrector formulas are applied:

$$C_j(m+1) = C_j(0) + \frac{\Delta t}{2} [f_j(0) + f_j(m)] \quad (\text{nonstiff})$$

$$C_j(m+1) = \frac{0.5 \alpha \Delta t (a_j(m) + a_j(0)) + C_j(0)(\alpha - \Delta t)}{\alpha + \Delta t} \quad (\text{stiff})$$

where

$$\alpha = \frac{1}{b_j(m)} + \frac{1}{b_j(0)}$$

After each corrector step, the relative error ( $E_j$ ) in each equation is calculated from:

$$E_j = \frac{C_{j(m+1)} - C_{j(m)}}{\max(C_{j(m+1)}, C_{\min_j})}$$

where  $C_{\min_j}$  is the lower bound concentration for each species. If the relative error on the corrector step is less than the prescribed convergence criteria  $\epsilon_2$  (typically 0.005 to 0.001) for all equations, the step is complete. If the convergence test fails, the corrector step is repeated iteratively until convergence is reached or in practice, until the maximum number of iterations (typically 2 or 3) is reached. When the latter occurs, the time step is reduced sharply and the whole procedure is repeated with the smaller step. When convergence is obtained, a new time step is selected based on the number of corrector iterations taken in the last step. In practice, the method is most efficient when the maximum number of iterations is kept small, ( $\leq 3$ ) and when the time steps are increased gradually after steps requiring only one or two iterations.

#### 5.4.2 The Pseudo-Steady-State Approximation

Even with fast integration, the computational costs of solving the chemical kinetics is high. The costs can be substantially reduced by treating the fast reacting species with the pseudo-steady-state approximation (PSSA). The PSSA assumes the rates of formation and destruction of fast reacting species are essentially equal. This allows their concentrations to be calculated from algebraic equations, i.e.,:

$$f_j = 0 = a_j - b_j C_j, \text{ which is solved to yield}$$

$$C_j = a_j / b_j$$

where  $a_j$  and  $b_j$  are functions of other integrated and/or steady-state concentrations.



The species treated with the PSSA must be carefully selected to ensure that solutions of the chemical kinetics with and without the PSSA are in agreement. The first step in the selection procedure involves computing the eigenvalues of the Jacobian of the full kinetic system over a wide range of conditions. The relative stiffness of the species are then ranked according to the magnitude of their eigenvalues. Testing is then carried out to identify the largest subset of steady-state species for which the full and partial PSSA solutions are in agreement. The procedure is initiated with a trial subset of steady-state species which include only the stiffest species. Depending on the degree of agreement in the solutions, subsequent testing is performed on either larger or smaller subsets of steady-state species, until the largest subset is identified. The importance of this testing cannot be overemphasized, because solutions with too many steady-state species diverge rather rapidly from the true solutions.

# REFERENCES: SECTION 5

- Adam, Y. 1975. A Hermitian finite difference method for solution of parabolic equations. Computers and Mathematics with Appls. 1: 393-406.
- Adam, Y. 1977. Highly accurate compact implicit methods and boundary conditions. J. Comp. Phys. 24: 10-22.
- Ahlbert, J.H., E.N. Nilson, and J. Walsh 1967. The Theory of Splines and Their Applications. Academic Press, 284 pp.
- Book, D.L., J.P. Boris, and K. Hain 1975. Flux-corrected transport II: Generalizations of the method. J. Comp. Phys. 18: 248-283.
- Book, D.L., J.P. Boris, and S.T. Zalesak 1981. Flux-corrected transport. In: D.L. Book (ed.), Finite-Difference Techniques for Vectorized Fluid Dynamics Calculations. New York: Springer-Verlag. 226 pp.
- Boris, J.P. and D.L. Book 1973. Flux-corrected transport. I. SHASTA, a fluid transport algorithm that works. J. Comp. Phys. 11: 38-69.
- Boris, J.P. 1976. Flux-Corrected Transport Modules for Solving Continuity Equations. Naval Research Laboratory Memo. Report 3237.
- Boris, J.P. and D.L. Book 1976. Flux-corrected transport III: Minimal-error FCT algorithms. J. Comp. Phys. 20: 397-431.
- Chock, D.P. and A.M. Dunker 1982. A Comparison of Numerical Methods for Solving the Advection Equation. General Motors Report No. GMR-3603/ENV#100.
- Curtis, A.K. 1978. Solution of Large, Stiff Initial Value Problems--The State of the Art. In: Numerical Software--Needs and Availability. London: Academic Press.
- Egan, B.A. and J.R. Mahoney 1972. Numerical modeling of advection and diffusion of urban-area source pollutants. J. Appl. Meteor. 11: 312-322.
- Gear, C.W. 1971. Numerical Initial Value Problems in Ordinary Differential Equations. Englewood Cliffs, N.J.: Prentice Hall.
- Hirsch, R.S. 1975. Higher order accurate difference solutions of fluid mechanics problems by a compact differencing technique. J. Comp. Phys. 99: 90-109.
- Hindmarsh, A.C. and G.D. Byrne 1975. EPISODE: An experimental program for the integration of systems of ordinary differential equations. Lawrence Livermore Laboratory Report UCID-30112.

- Lamb, R.G. 1982. A regional scale (1,000 km) model of photochemical air pollution. Part I: Theoretical formulation. U.S. EPA Report.
- Long, P.E. and D.W. Pepper 1976. A comparison of six numerical schemes for calculating the advection of atmospheric pollution. Third Symposium on Atmospheric Turbulence, Diffusion, and Air Quality, Raleigh, NC. Oct. 19-22, 1976.
- Long, P.E. and D.W. Pepper 1981. An examination of some simple numerical schemes for calculating scalar advection. J. Appl. Meteor. 20: 146-156.
- Mahrer, Y. and R.A. Pielke 1978. A test of an upstream spline interpolation technique for the advection terms in a numerical mesoscale model. Mon. Wea. Rev. 106: 818-830.
- Marchuk, G.I. 1975. Methods of Numerical Mathematics. New York: Springer-Verlag. 316 pp.
- McRae, G.J. 1981. Mathematical Modeling of Photochemical Air Pollution. Ph.D. Thesis, California Institute of Technology, Pasadena, CA.
- McRae, G.J., W.R. Goodin, and J.H. Seinfeld 1982a. Numerical solution of the atmospheric diffusion equation for chemically reacting flows. J. Comp. Phys. 45: 1-42.
- McRae, G.J., W.R. Goodin, and J.H. Seinfeld 1982b. Development of a second-generation mathematical model for urban air pollution - I. Model formulation. Atmos. Environ. 16: 679-696.
- Pepper, D.W., C.D. Kern, and P.E. Long 1979. Modeling the dispersion of atmospheric pollution using cubic splines and chapeau functions. Atmos. Environ. 13: 223-237.
- Prahn, L.P. and O. Christensen 1977. Long-range transmission of pollutants simulated by a two-dimensional pseudospectral dispersion model. J. Appl. Meteor. 16: 896-910.
- Roache, P.J. 1976. Computational Fluid Dynamics (2nd Edition). Albuquerque, NM: Hermosa Publishers. 434 pp.
- Rubin, S.G., and R.A. Graves 1975. A cubic spline approximation for problems in fluid mechanics. NASA TR R-436.
- Young, T.R. and J.P. Boris 1977. A numerical technique for solving stiff ordinary differential equations associated with the chemical kinetics of reactive flow problems. J. Phys. Chem. 8: 25.
- Zalesak, S.T. 1979. Fully multidimensional flux-corrected transport algorithms for fluids. J. Comp. Phys. 31: 335-362.

## 6. ATMOSPHERIC CHEMISTRY ASSOCIATED WITH ACID PRECIPITATION

### 6.1 Introduction

This section of the report addresses the chemical processes controlling the formation of sulfates and nitrates in the atmosphere from the precursors, sulfur oxides ( $\text{SO}_x$ ) and nitrogen oxides ( $\text{NO}_x$ ), respectively. The recent upsurge in the interest in acid precipitation has presented a significant challenge to atmospheric chemists. It is necessary to understand the chemical processes of sulfate and nitrate formation under ambient conditions sufficiently well that predictive models can be formulated for these products of  $\text{SO}_x$  and  $\text{NO}_x$  emissions. The atmospheric chemistry processes occurring should be viewed as an integrated system as shown in Figure 6.1-1. The reaction pathways shown in this figure are those which should be considered in the atmospheric chemical transformations of  $\text{NO}_x$  and  $\text{SO}_x$ . Each possible class of reaction is discussed in this section, namely:

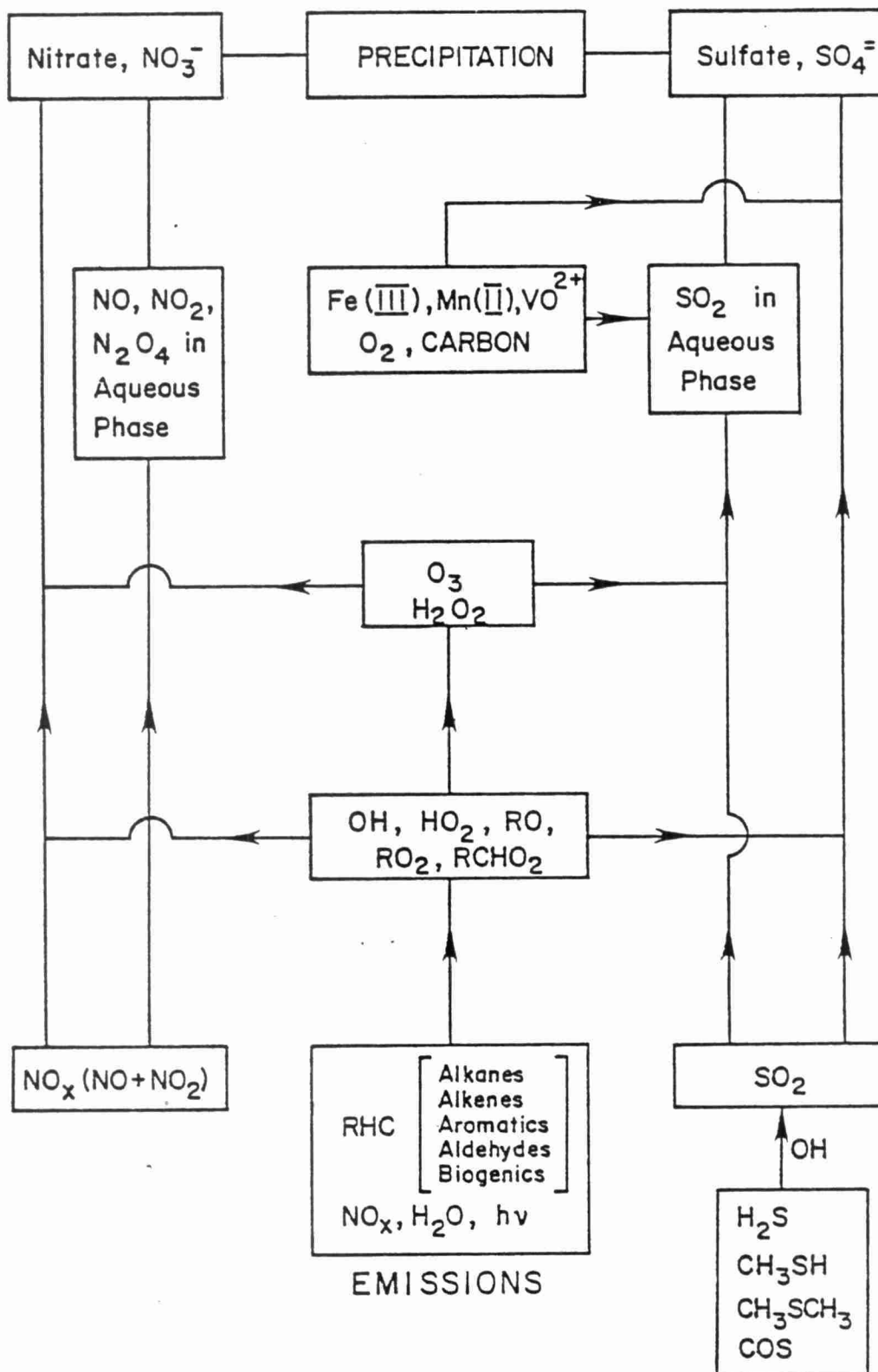
- homogeneous gas phase photochemical reactions involving hydrocarbons,
- heterogeneous reactions occurring on particles, and
- aqueous chemistry occurring in aerosol droplets or on wetted aerosols.

The relationship between the various reactions is illustrated by hydrogen peroxide ( $\text{H}_2\text{O}_2$ ).  $\text{H}_2\text{O}_2$  is formed photochemically from the interaction of reactive hydrocarbons (RHC) and  $\text{NO}_x$ , and can oxidize  $\text{SO}_2$  to sulfate in the aqueous phase after dissolving in a water droplet or aerosol. This example illustrates the need to treat the total system for the formulation of a predictive model. For the purposes of this review, various chemical processes are discussed separately.

The remainder of this section contains discussions of the broad categories of reactions. These categories include discussion of many subelements:

Figure 6.1-1

# MAJOR PATHWAYS FOR SO<sub>2</sub> AND NO<sub>x</sub> OXIDATION



- gas phase photochemical processes
  - $\text{NO}_x$ 
    - inorganic reactions
    - organic reactions involving different hydrocarbon classes
    - peroxyacyl nitrates as  $\text{NO}_x$  sinks
    - nighttime chemistry
    - role of biogenic hydrocarbon emissions
  - $\text{SO}_x$ 
    - inorganic radical reactions
    - organic radical reactions
    - role of biogenic sulfur emissions
- heterogeneous oxidation on dry particles for  $\text{NO}_x$  and  $\text{SO}_x$
- aqueous-phase reactions
  - $\text{SO}_x$ 
    - oxidation by  $\text{O}_3$
    - oxidation by  $\text{H}_2\text{O}_2$
    - catalytic oxidation by  $\text{O}_2$  in presence of  $\text{Fe}^{3+}$ , and  $\text{Mn}^{2+}$
  - $\text{NO}_x$ 
    - oxidation of  $\text{NO}$  and  $\text{NO}_2$  in solution
    - reactions of peroxyacetyl nitrate (PAN) in solution

Following this review of the current state of chemical knowledge of  $\text{NO}_x$  and  $\text{SO}_x$  oxidations under atmospheric conditions, this section of the report concludes with the recommendations for treating and parameterizing the atmospheric chemical transformation processes in the proposed atmospheric models. Several reactions are deleted from those shown in Figure 6.1-1 on the basis of conclusions reached from discussions in this section.

## 6.2 Gas Phase Chemistry

### 6.2.1 Homogeneous Process

#### 6.2.1.1 Nitrogen Oxides ( $\text{NO}_x$ )

##### Overview of $\text{HNO}_3$ Formation

The product of concern from emissions of nitrogen oxides ( $\text{NO}_x = \text{NO} + \text{NO}_2$ ) is nitric acid,  $\text{HNO}_3$ . This is converted to particulate nitrate,  $\text{NO}_3^-$ , if the nitric acid interacts with other atmospheric species to form nitrate, e.g., reaction of  $\text{HNO}_3$  with ammonia,  $\text{NH}_3$  will produce ammonium nitrate  $\text{NH}_4\text{NO}_3$ .  $\text{HNO}_3$  is formed from  $\text{NO}_2$  by the following inorganic processes.



Reaction (1) is considered the more important of the two reactions - Reaction (1) and (4) - producing  $\text{HNO}_3$ , although the uncertainty in the heterogeneous nature of reaction (4) makes the prediction of its rate under atmospheric conditions highly uncertain.  $\text{HNO}_3$  can also be formed by reaction of  $\text{NO}_3$  with aromatics as discussed in Section 6.2.1.4. The above reactions illustrate that  $\text{HNO}_3$  production depends on  $\text{NO}_2$ ,  $\text{NO}_3$ ,  $\text{OH}$  and  $\text{O}_3$ . Since emissions of  $\text{NO}_x$  are largely in the form of  $\text{NO}$ , the processes oxidizing  $\text{NO}$  to  $\text{NO}_2$  must be considered. In essence, this incorporates the inorganic reactions of major importance in atmospheric chemistry. As shown in Figure 6.1-1, hydrocarbons also must be considered since they participate in the oxidation of  $\text{NO}$  through the reactions of alkylperoxy radicals ( $\text{RO}_2$ ) and provide temporary sinks for  $\text{NO}_2$  through the formation of peroxyacyl nitrates

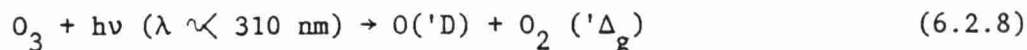
as discussed below. There is also evidence that peroxy radicals formed from long chain alkanes react with  $\text{NO}_2$  to form organic nitrates (Darnall et al. 1976; Niki et al. 1980; Atkinson et al. 1982).

#### Inorganic Reactions of $\text{NO}_x$

The inorganic reaction mechanisms applicable to the lower troposphere and air pollution chemistry now appear to be reasonably well understood (Atkinson et al. 1980; Hampson and Garvin 1978; NASA 1979; Atkinson and Lloyd 1980).



followed by the important tropospheric OH radical production steps from the inorganic cycle:



$\text{O}_3$  also reacts with  $\text{NO}_2$  leading to  $\text{NO}_3$  and  $\text{N}_2\text{O}_5$  chemistry as discussed in reactions 6.2.(2)-(5) above.

Reaction of hydroxyl radicals with CO:

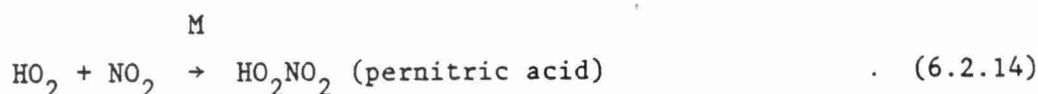
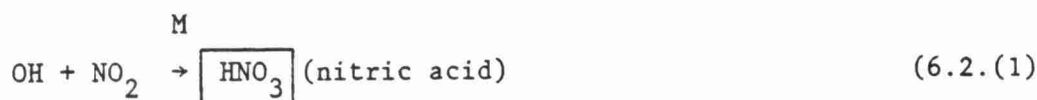
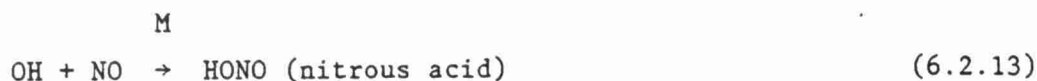


followed by





leads to regeneration of OH, and this chain oxidation of CO was first postulated around 1969 (Heicklen et al. 1969; Stedman et al. 1970). The inorganic chemistry is completed by reactions of OH and HO<sub>2</sub> with O<sub>3</sub> and by the termination reactions of OH with NO and NO<sub>2</sub> and of HO<sub>2</sub> with NO<sub>2</sub>:



Because of the efficient regeneration of OH + NO from HONO by photolysis and of HO<sub>2</sub> + NO<sub>2</sub> from HO<sub>2</sub>NO<sub>2</sub> by thermal decomposition, under ambient lower tropospheric conditions the OH + NO<sub>2</sub> termination reaction is the most important of these three and is the reaction of most interest for the prediction of acid precipitation from NO<sub>x</sub> emissions.

#### Hydrocarbon Participation in HNO<sub>3</sub> Formation

The need to consider the different hydrocarbon classes is shown by the illustrative data obtained for Tulsa and shown in Table 6.2-1 (Arnts and Meeks 1980). These data illustrate the type and variety of hydrocarbons present in urban atmospheres. Similar compounds, though at higher concentrations, have been identified in the larger urban areas such as Los Angeles (Grosjean et al. 1982). The organics present in ambient air can be categorized into three general classes of hydrocarbons, as shown in the table: alkanes, such as n-butane, isobutane, and the pentanes; alkenes (ethene, propene, butenes); and aromatics (benzene, toluene, and xylenes). Oxygenates are another

TABLE 6.2-1

HYDROCARBON COMPOSITION OF TULSA AREA AIR [27]<sup>a</sup>

<u>Hydrocarbons</u>	<u>Concentration (ppbc)</u>	<u>Hydrocarbons</u>	<u>Concentrations (ppbc)</u>	<u>Hydrocarbons</u>	<u>Concentration (ppbc)</u>
<u>Alkanes</u>		<u>Alkenes</u>		<u>Aromatics</u>	
ethane	7.2	ethene	7.3	toluene	14.8
propane	8.9	propene	2.8	ethylbenzene	2.5
isobutane	12.9	isobutene	4.3	p-xylene	2.0
n-butane	48.7	trans-2-butene	4.7	m-xylene	5.4
isopentane	65.9	cis-2-butene+butadiene	0	o-xylene	2.5
n-pentane	40.9	1-pentene	2.2	isopropylbenzene	0
cyclopentane	4.6	2-methyl-1-butene	3.1	n-propylbenzene	0.9
2-methylpentane	19.6	trans-2-pentene	7.3	m+p-ethyltoluene	0
3-methylpentane	13.0	cis-2-pentene	5.6	1,3,5-trimethylbenzene	1.0
n-hexane	14.0	2-methyl-2-butene	6.0	o-ethyltoluene	0
n-heptane	5.8	isoprene	0.3	1,2,4-trimethylbenzene	1.3
nonane	1.3	4-methyl-2-pentene	0.8	m-ethyltoluene	1.3
decane	1.8	trans-2-hexene	1.3		
<b>Σ ALKANES</b>	<b>230.6</b>	<b>Σ ALKENES</b>	<b>45.8</b>	<b>Σ AROMATICS</b>	<b>31.7</b>

a) 10:33-11:03 A.M., Tulsa Post Office, 7-27-1978.

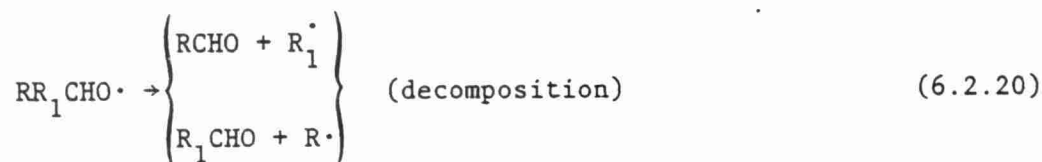
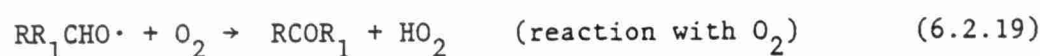
class. They are mostly composed of aldehydes, but smaller amounts of ketones, alcohols, ethers, and esters are also present. Of these, only the aldehydes and ketones are photoactive, but the other species can also react to form radicals. The major reactions of these hydrocarbon classes are discussed briefly in the following sections.

#### 6.2.1.2 Alkanes

Under ambient atmospheric conditions the sole chemical loss process of the alkanes is via reaction with the OH radical (Demerjian et al. 1974; Falls and Seinfeld 1978; Carter et al. 1979; Atkinson and Lloyd 1980).



following by, for the simple ( $\leq \text{C}_3$ ) alkanes:



followed by the regeneration of the chain carrier, the OH radical:



The formation of alkylperoxynitrates appears to be of minimal importance due to their short ( $\sim 1$  sec at 298°K) lifetime with respect

to thermal decomposition back to reactants (Carter et al. 1979; Edney et al. 1979; Hendry and Kenley 1979). Hence, this scheme leads to the ultimate degradation of the original carbon skeleton via the intermediate formation of carbonyl compounds; these carbonyls then react with OH radicals or photodecompose further. The key intermediate organic radicals in these  $\text{NO}_x$  photooxidations are alkyl peroxy ( $\text{RO}_2$ ) and alkoxy (RO) radicals -- hence, their reactions under ambient atmospheric conditions are of prime importance.

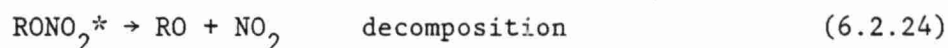
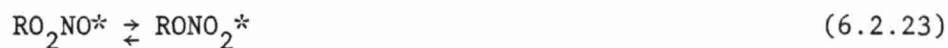
While the above reaction scheme is applicable to the lower carbon number alkanes, i.e., methane, ethane, and propane, two other processes involving  $\text{RO}_2$  and RO reactions can occur for the longer chain alkane systems. These reactions, particularly the alkyl nitrate formation reaction, should be taken into account in developing a photochemical model for long range transport, since they influence the fate of  $\text{NO}_x$  and the concentration of key radical intermediates.

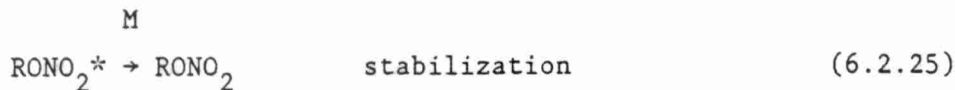
1) Alkyl nitrate formation from  $\text{RO}_2 + \text{NO}$

This reaction pathway:



was postulated by Darnall et al. (1975) from smog chamber product studies of the  $\text{NO}_x$  photooxidations of n-butane, n-pentane and n-hexane. It was proposed that the reaction of  $\text{RO}_2$  radicals with NO proceeds via





with the ratios  $k_a/(k_a + k_b)$  derived being given in Table 6.2-2, where  $k_a$  and  $k_b$  are the rate constants for the overall reactions (a) and (b):



As expected from unimolecular theory, the stabilization/decomposition ratio  $k_a/k_b$  increases with the number of degrees of freedom of the RO radical, and this ratio is less for branched than unbranched alkylperoxy radicals.

Recent work of Atkinson et al. (1982) has confirmed the importance of this reaction pathway. Their results are summarized in Table 6.2-3. An additional dimension to the possible importance of this reaction pathway has been found since results show that the reaction rate is pressure and temperature dependent. The percentage of nitrate formation decreases as the temperature is increased. Studies on the magnitude of this dependence and on the pressure effect are in progress (Atkinson, private communication, July 1982).

This reaction pathway forming alkyl nitrates from  $\text{RO}_2 + \text{NO}$  is both a substantial sink for  $\text{NO}_x$  and a radical termination process. Consequently, it should be included in the photochemical model for  $\text{HNO}_3$  and  $\text{H}_2\text{O}_2$  prediction, since it will impact the proportion of  $\text{NO}_x$  going to  $\text{HNO}_3$ . More work is needed to provide detailed information on rates at lower than ambient temperatures.

TABLE 6.2-2

RATE CONSTANT RATIOS  $k_a/(k_a + k_b)$  DERIVED FOR THE  
REACTION OF  $RO_2^a$  RADICALS WITH NO

Alkane, RH	$k_a/(k_a + k_b)$
propane	$0.04^a$
n-butane	$0.08_3 \pm 0.02^b$ ; $0.08^6_a$
n-pentane	$0.14 \pm 0.05^b$ ; $0.11^c$
n-hexane	$0.37 \pm 0.88^b$ ; $0.11^c$
n-hexane	$0.37 \pm 0.88^b$ ; $0.15 \pm 0.03^c$
2,3-dimethylbutane	$\sim 0.1^c$

<sup>a</sup>Carter et al. 1979a.

<sup>b</sup>Darnall et al. 1976.

<sup>c</sup>Carter 1979, cited in Atkinson and Lloyd 1980.

TABLE 6.2-3

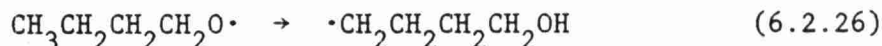
PERCENTAGE ALKYL NITRATE FORMATION FROM PERCENT ALKANE  
(at room temperature and pressure) (Atkinson et al. 1982)

<u>Alkane</u>	<u>Percentage Nitrate Formation</u>
$C_2H_6$	<1.4
$C_3H_8$	$3.6 \pm 0.5$
$C_4H_{10}$	$7.7 \pm 0.9$
$C_5H_{12}$	$12.9 \pm 1.9$
$C_6H_{14}$	$22.3 \pm 3.5$
$C_7H_{16}$	$30.9 \pm 5.0$
$C_8H_{18}$	$33.2 \pm 3.4$

## 2) Alkoxy Radical Isomerization

Isomerization of alkoxy radicals, known from studies of cool-flames and hydrocarbon oxidations at elevated temperatures (Mulcahy 1973) was first proposed, on the basis of smog chamber product studies, as being of importance in room temperature  $\text{NO}_x$  photooxidations by Carter et al. (1976) and subsequently by Baldwin et al. (1977).

Thermochemical calculations by both groups (Carter et al. 1976, Baldwin et al. 1977) have shown that under ambient atmospheric conditions only the 1.4- and 1.5-H shifts of alkoxy radicals (via 5- and 6-membered ring transition states) are of importance (alkyl and alkyl peroxy radicals react with  $\text{O}_2$  and  $\text{NO}_2$ , respectively, much faster than the corresponding isomerizations). Thus, the simplest alkoxy radical isomerization is that of the n-butoxy radical:



Alkoxy radicals formed during the  $\text{NO}_x$  photooxidation of  $\geq \text{C}_4$  alkanes can then react via four routes: reaction with  $\text{O}_2$ , unimolecular decomposition, isomerization, and reaction with  $\text{NO}_2$  to form alkyl nitrates. For the simple ( $\leq \text{C}_4$ ) alkoxy radicals, rate constants for reaction with  $\text{O}_2$  and for unimolecular decomposition are now available from experimental studies (Batt 1979a, b; Batt and Robinson 1979; Gutman et al. 1982), and thermochemical estimation procedures are also available, especially for the unimolecular decompositions and isomerizations (Batt 1979a, b; Baldwin et al. 1977). These latter estimation procedures have been discussed in detail by Golden and coworkers (Baldwin et al. 1977; Golden 1979), by Carter et al. (1976), and by Batt (1979a, b), and will not be dealt with in detail here. As an indication of the relative importance of the various alkoxy radical reaction routes under atmospheric conditions, Table 6.2-4 summarizes the experimental



TABLE 6.2-4a  
REACTION RATES FOR SELECTED ALKOXY RADICALS  
AT 298°K AND 760 TORR OF AIR

Alkoxy Radical	Reaction Rate, sec <sup>-1</sup>		
	Reaction with O <sub>2</sub> <sup>a</sup>	Decomposition <sup>b</sup>	Isomerization <sup>c</sup>
CH <sub>3</sub> O·	7 x 10 <sup>3</sup>	Negligible	NO isomerization possible
CH <sub>3</sub> CH <sub>2</sub> O·	4 x 10 <sup>4</sup>	2 x 10 <sup>-5</sup>	Negligible
$\begin{array}{c} \text{O} \\   \\ \text{CH}_3\text{CHCH}_3 \end{array}$	2 x 10 <sup>5</sup>	20	Negligible
CH <sub>3</sub> CH <sub>2</sub> CH <sub>2</sub> CH <sub>2</sub> O·	4 x 10 <sup>4</sup>	0.3	1.2-1.5 x 10 <sup>5</sup> <sup>c</sup> 6 x 10 <sup>4</sup> - 2 x 10 <sup>5</sup>
$\begin{array}{c} \text{O} \\   \\ \text{CH}_3\text{CH}_2\text{CHCH}_3 \end{array}$	2 x 10 <sup>5</sup>	5 x 10 <sup>3</sup>	~40 - 150 <sup>d</sup>
(CH <sub>3</sub> ) <sub>3</sub> CO·	No Reaction Possible	2 x 10 <sup>3</sup>	Negligible

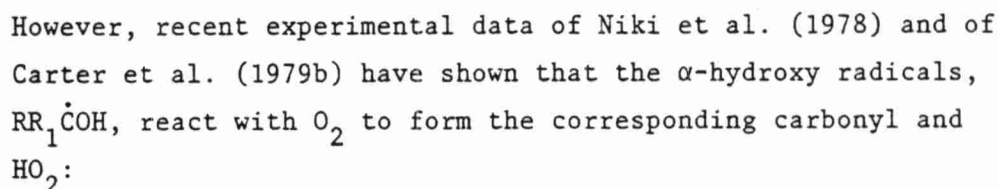
a. D. Gutman, N. Sanders and J.E. Butler, J. Phys. Chem., 86, 66 (1982).

b. Baldwin et al. 1977, Batt 1979a, b.

c. Experimental value; Carter et al. 1979a, R.A. Cox, K.F. Patrick and S.A. Chant, Environ. Sci. Technol. 15, 587 (1981); H. Niki, P.D. Maker, C.M. Savage and L.P. Breitenbach, J. Phys. Chem., 85, 2698 (1981).

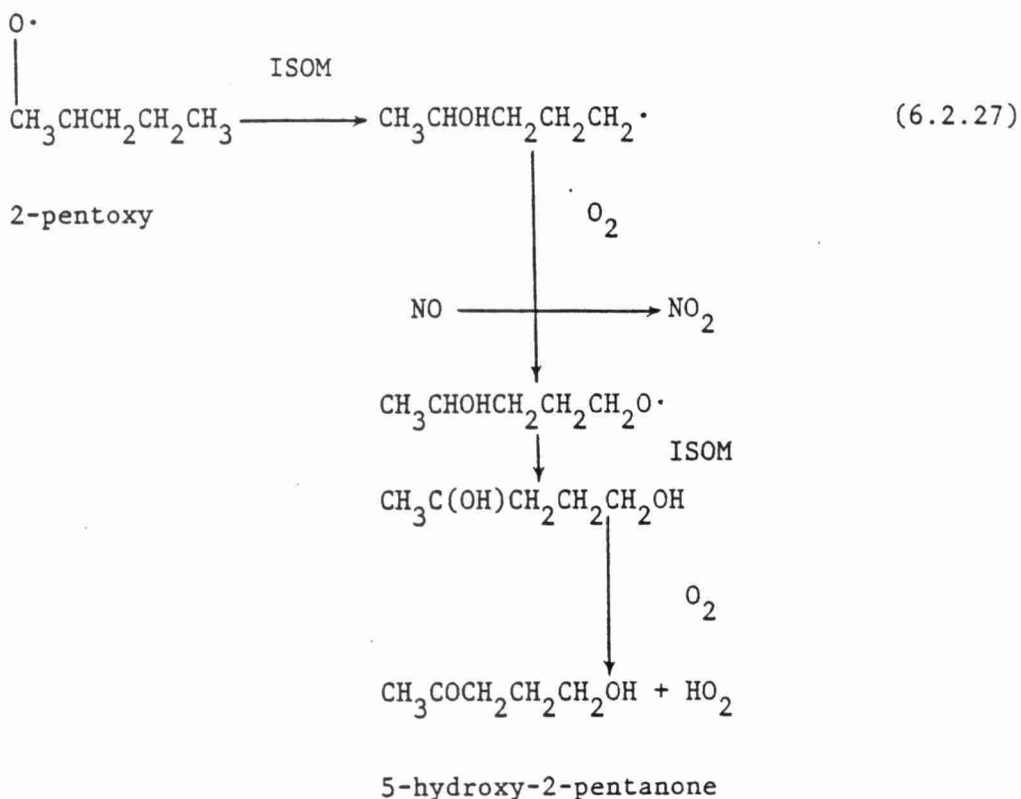
d. Carter et al. 1976, Baldwin et al. 1977, estimate.

For n-butane, the isomerization pathway only affect ~ 15% of the total reaction pathway with the OH radical, since the initial radicals are ~15% n-butyl and ~85% sec-butyl (Carter et al. 1979a; Atkinson et al. 1979); while for the higher alkanes such as n-pentane, of the total number of alkoxy radicals formed ~70% can undergo isomerization (Carter et al. 1976), and alkoxy radical isomerization probably dominates for the  $\geq C_5$  straight chain alkanes (Carter et al. 1976). The reactions subsequent to the first isomerization have been a matter of conjecture until fairly recently - since in theory the hydroxy alkoxy radical formed subsequent to the first isomerization could isomerize further, as for example:





and so terminate the isomerization sequence after a total of two isomerizations. This is illustrated below for the 2-pentoxy radical which forms a  $\delta$ -hydroxy carbonyl:



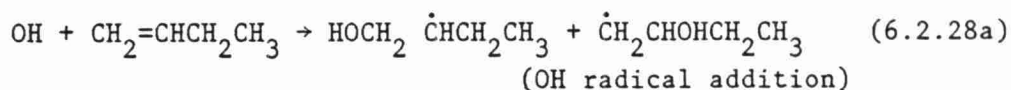
(competing reactions, i.e., decomposition and reaction with  $O_2$ , of these alkoxy radicals are expected to be minor; reaction with  $NO_2$  to form  $RONO_2$  can also occur.

Since these species retain the carbon skeleton, then, at least for the  $\delta$ -hydroxyketones, further reaction with the OH radical will lead to progressively more polyfunctionality and may ultimately lead to aerosol formation.

### 6.2.1.3 Alkenes

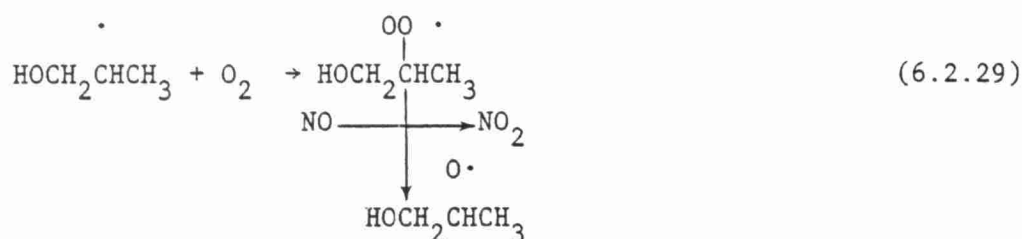
Alkenes are the most reactive of the hydrocarbon classes. They are precursors of the radical intermediates important in the oxidation of  $\text{NO}_x$  emissions. The Criegee intermediates, formed in reaction of alkenes with  $\text{O}_3$  (Niki et al. 1977; Calvert et al. 1978; Su et al. 1980; Kan et al. 1981; Herron and Huie 1977, 1978; Martinez et al. 1982), may also react with both  $\text{NO}_x$  and also oxidize  $\text{SO}_2$ . The reactions of alkenes are thus important to discuss and should be included in the photochemical model for both nitrate and sulfate formation.

Alkenes react predominately with ozone and with OH radicals under ambient atmospheric conditions. The OH radical rate constants are now reasonably well known to within  $\pm 20\text{-}25\%$  for most alkenes, (Atkinson et al. 1979; Atkinson and Lloyd 1980), and the initial reaction pathway for ethene and the methyl-substituted ethenes proceeds essentially totally via OH radical addition to the double bond (Atkinson et al. 1979). However, for alkenes containing longer ( $>\text{C}_2$ ) side chains, a substantial amount ( $20 \pm 5\%$  for the case of 1-butene (Biermann et al. 1980) of the overall OH radical reaction proceeds via H atom abstraction from the weak allylic C-H bonds:

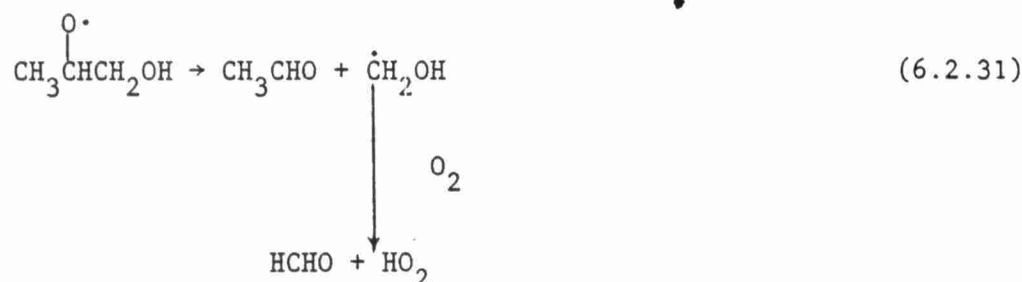
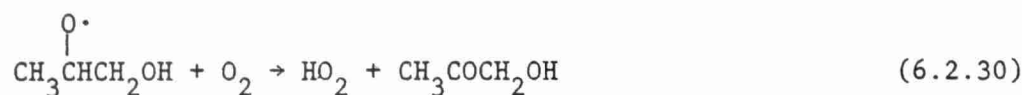


(H atom abstraction, with  
 $k_b/(k_a + k_b) = 0.20 \pm 0.05$   
 at room temperature.)

The major uncertainty is between theoretical calculations (Baldwin et al. 1977, Batt 1979 a,b; Golden 1979) and experimental data (Niki et al. 1978, 1981) concerning the fate of the  $\beta$ -hydroxyalkoxy radicals formed from the OH-alkene adducts:



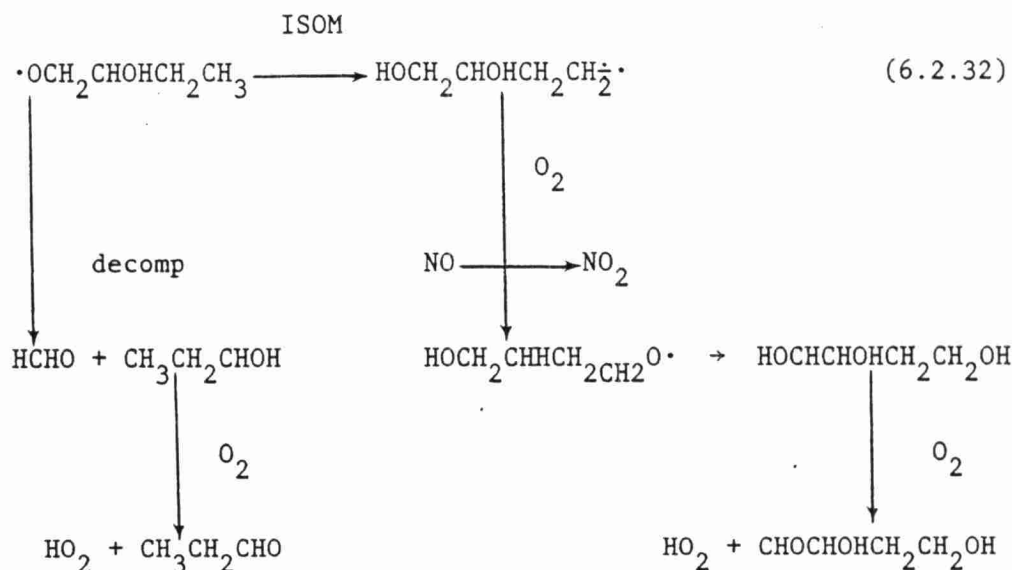
As with the simple alkoxy radicals, these  $\beta$ -hydroxyalkoxy radicals can react with  $\text{O}_2$  or unimolecularly decompose:



Theoretical estimates of Baldwin et al. (1977), Golden (1979), and Batt (1979a,b) indicate that reaction of  $\text{O}_2$ , at least for  $\leq \text{C}_4$   $\beta$ -hydroxyalkoxy radicals, should predominate, while the experimental data, from smog chamber studies (Carter et al. 1979a) and from irradiated RONO-alkene-NO-air mixtures (Niki et al. 1981) shows conclusively that decomposition of these  $\beta$ -hydroxy-alkoxy radicals predominates. For ethene, Niki et al. (1981) have shown that decomposition to two HCHO molecules occurs ~80% of the time at room temperature and pressure, while reaction with  $\text{O}_2$  to yield glycolaldehyde occurs 20% of the time.

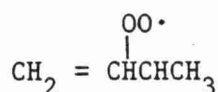
Two further reactions of interest concern:

- 1) The possibility of isomerization of these  $\beta$ -hydroxyalkoxy radicals (Atkinson et al. 1979), the simplest case being the 2-hydroxy-1-butoxy radical derived from internal OH radical addition to 1-butene:

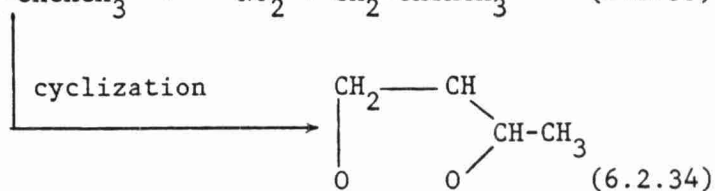
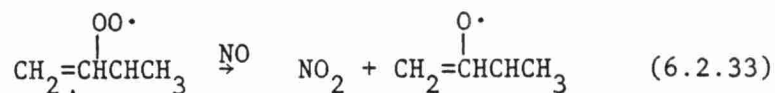


Whether these isomerizations in general can compete with the decompositions is not known at present, but appears unlikely (Atkinson and Lloyd 1980).

- 2) The reactions subsequent to H atom abstraction from alkenes. Thus, taking 1-butene as an example, ~20% of the OH radical reaction yields the allylic radical  $\text{CH}_2=\text{CHCHCH}_3$  (Biermann et al. 1980), which can presumably add  $\text{O}_2$  to form the peroxy radical:



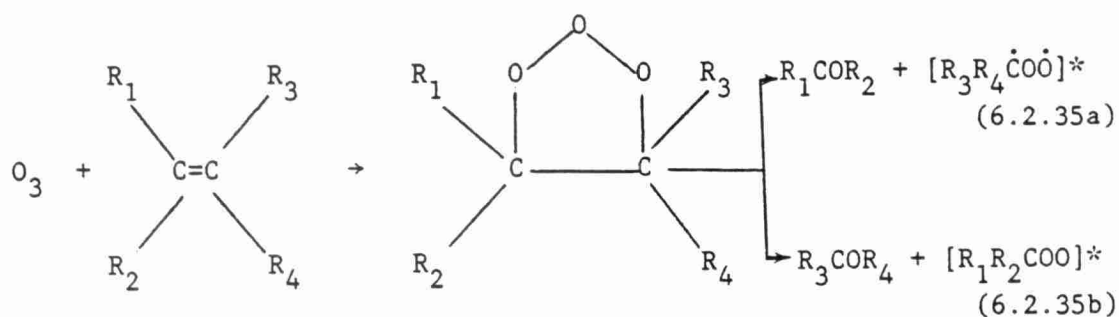
This radical can, besides reacting with NO to yield (mainly) the corresponding alkoxy radical, cyclize:



Despite earlier estimates (Demerjian et al. 1974; Atkinson et al. 1980) that cyclization should dominate under atmospheric conditions, recent experimental data on the  $\text{NO}_x$  photooxidation of isoprene (Arnts and Gay 1979), where methylvinylketone and methacrolein are produced in the early stages, i.e., before significant amounts of  $\text{O}_3$  are formed, indicates that, at least for these particular radicals  $[\text{CH}_2=\text{C}(\text{OO}\cdot)\text{R}_1\text{CH}_2\text{OH}]$  where  $\text{R}$ ,  $\text{R}_1=\text{H}$  and  $\text{CH}_3$  or  $\text{CH}_3$  and  $\text{H}$ , formed after reaction of  $\text{OH}$  radicals with isoprene), the reaction with  $\text{NO}$  predominates.

For the reactions of  $\text{O}_3$  with the alkenes, despite well over a decade of investigation, there are still significant areas of uncertainty (Herron et al. 1979). While the rate constants for the initial reactions of  $\text{O}_3$  with the 1-alkenes seem to be reasonably well known, larger uncertainties exist for the internal alkenes. For instance, the rate constants at  $298^\circ\text{K}$  for trans-2-butene from two studies are  $1.76 \times 10^{-16}$  (Huie and Herron 1975) and  $2.60 \times 10^{-16}$  (Japar et al. 1974)  $\text{cm}^3 \text{ molecule}^{-1} \text{ sec}^{-1}$ . The recent study of Adeniji et al. (1981) reports a value of  $2.88 \times 10^{-16} \text{ cm}^3 \text{ molecule}^{-1} \text{ sec}^{-1}$ .

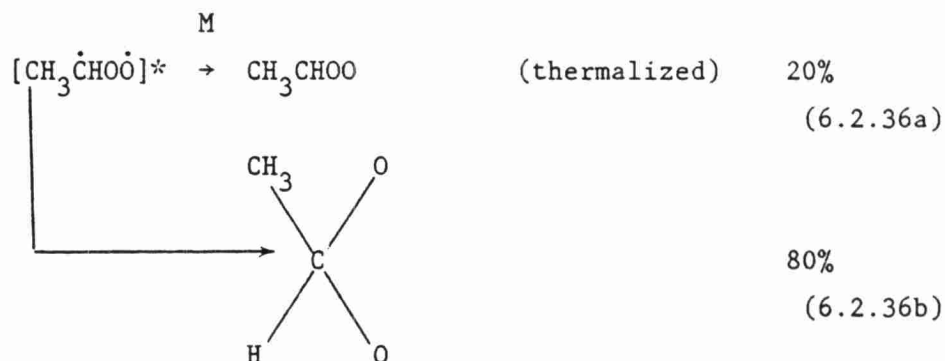
Recent work by Niki et al. (1977), Calvert and coworkers (Su et al. 1980), and by Herron and Huie (1977, 1978; Herron et al. (1982); Martinez (1982) has shown that the  $\text{O}_3$ -alkene reactions proceed mainly by the Criegee route:



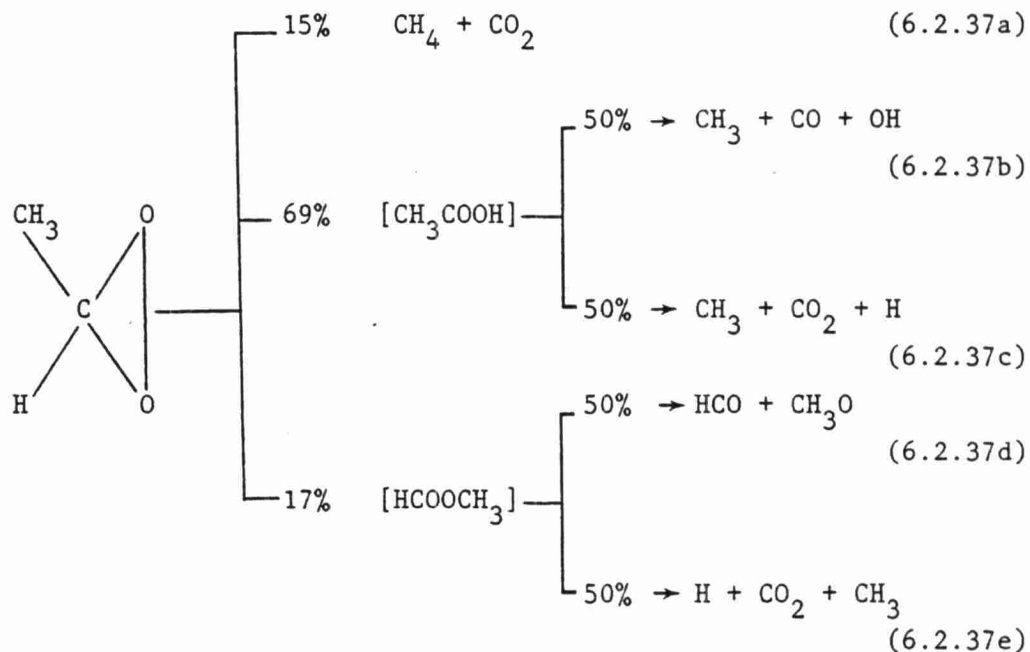
where the symbol  $[\cdot]^*$  denotes an initially energy rich species.

The observation of significant yields of secondary ozonide formation (Niki et al. 1977), including secondary ozonide formation from the ozone-ethene reaction (Su et al. 1980) shows that a

significant fraction (~20-40%) of the initially energy rich biradicals are thermalized under atmospheric conditions, with rearrangement and/or decomposition accounting for the other reaction pathways of the biradicals. Thus, for example, some of the recently proposed reactions (Dodge and Arnts 1979) of the  $\text{CH}_3\dot{\text{C}}\text{HO}\dot{\text{O}}$  biradical are shown below:



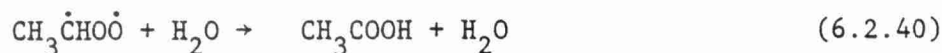
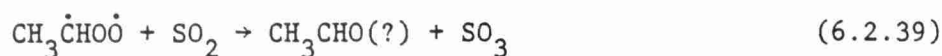
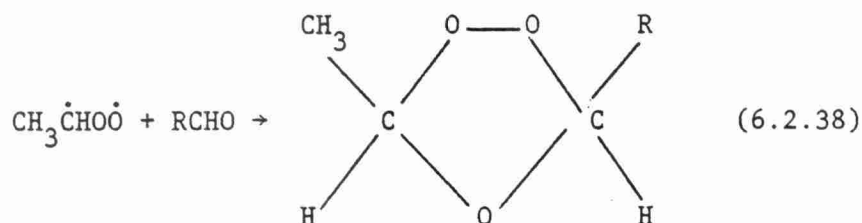
followed by:



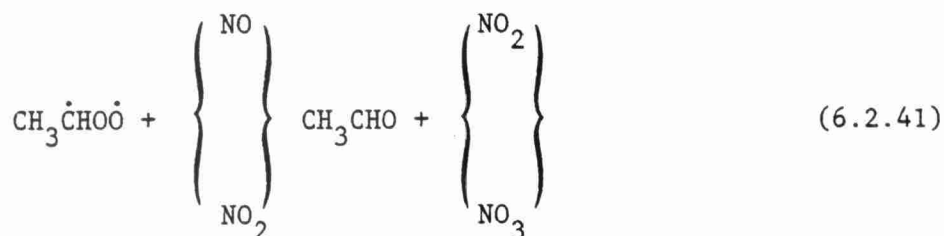
The reactions of the thermalized biradicals ( $\text{CH}_2\text{OO}$ ,  $\text{CH}_3\text{CHOO}$ , etc.) need further investigation. They have been postulated to react with aldehydes to form secondary ozonides (Niki et al. 1977, Su et al. 1980), with  $\text{SO}_2$  to form  $\text{SO}_3$  and the corresponding aldehydes (Niki et



al. 1977, Su et al. 1980, Calvert et al. 1978), and with  $H_2O$  (Calvert et al. 1978) to rearrange into the corresponding carboxylic acid as shown below:



Further possible important reactions with NO and  $NO_2$  need to be studied (Atkinson and Lloyd 1980):



Most recently a series of papers by Herron, Martinez and Huie has presented additional studies of  $O_3$ -alkene reactions (Int. J. Chem. Kin., March 1982). Their results are generally consistent with the above observations.

In summary, the reactions of alkenes under ambient conditions are complex. Currently, there is a reasonably good qualitative, and in some cases semi-quantitative, understanding of the  $O_3$ -alkene systems in the absence of  $NO_x$ . In the presence of low levels of  $NO_x$ , there remains uncertainty for the precise splits between different mechanistic pathways, and the relevant rate constant data for these pathways. In the interim, the reactions and rate constants published by Atkinson et al. (1982) based on the review of available data by Atkinson and Lloyd (1980), will be used.

#### 6.2.1.4 Aromatic Hydrocarbons

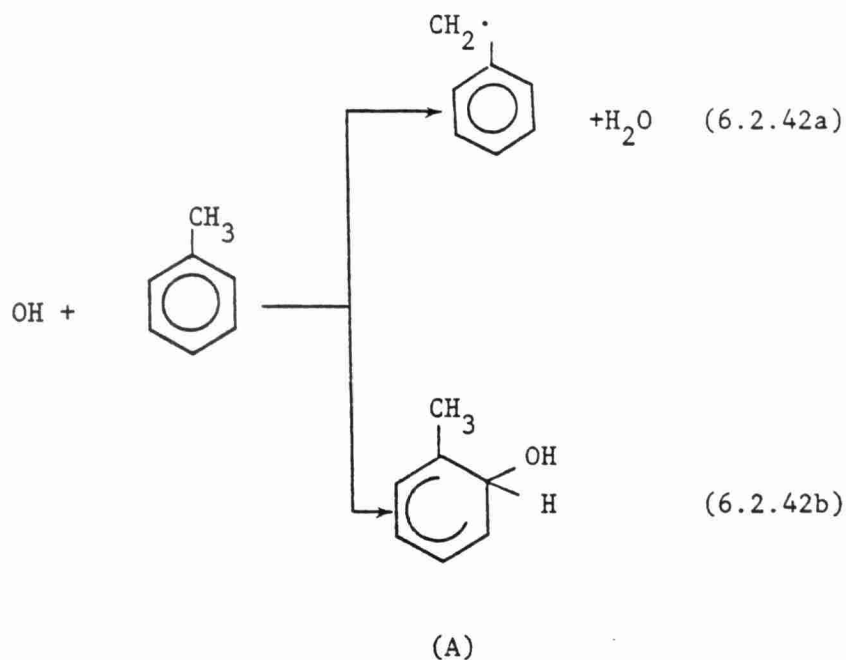
The chemistry of aromatic hydrocarbons continues to be less well understood than that of the three classes discussed above - inorganics, alkanes and alkenes. However, the aromatic content of gasoline has increased during the last decade and appears to be reflected in increased fraction of aromatic hydrocarbons in the hydrocarbon concentration of urban areas (Grosjean et al. 1982).

The fraction of aromatic hydrocarbons in the total nonethene hydrocarbon inventory will likely vary considerably from minor and low levels (e.g., in the Tulsa atmosphere data shown in Table 6.2-1) to the higher levels in the automobile dominated Los Angeles area (Grosjean et al. 1982) which is more typical of the major urban areas. Aromatic hydrocarbons are important for consideration and should be included in the chemical module (in spite of significant mechanistic uncertainties) because they:

- are precursors to radical intermediates,
- react with the OH radical, and
- can react with  $\text{NO}_x$  to form nitrogen containing products. These  $\text{NO}_x$  sinks are important when one is predicting  $\text{HNO}_3$  formation.

A brief discussion of the major reaction processes is provided below. More experimental data may change or modify the proposed reaction scheme which is based on the best available data (reviewed by Atkinson and Lloyd 1980) and tested against smog chamber data.

It has been known since the early 1970s that the only important chemical loss process of the aromatic hydrocarbons under atmospheric conditions is via reaction with the OH radical. Data are now available concerning both the overall OH radical rate constants (Atkinson et al. 1979), and the relative amounts of the two reaction pathways (Atkinson et al. 1979, Hendry 1979, Bignozzi et al. 1981): OH radical addition to the ring, and H atom abstraction, mainly from the substituent groups

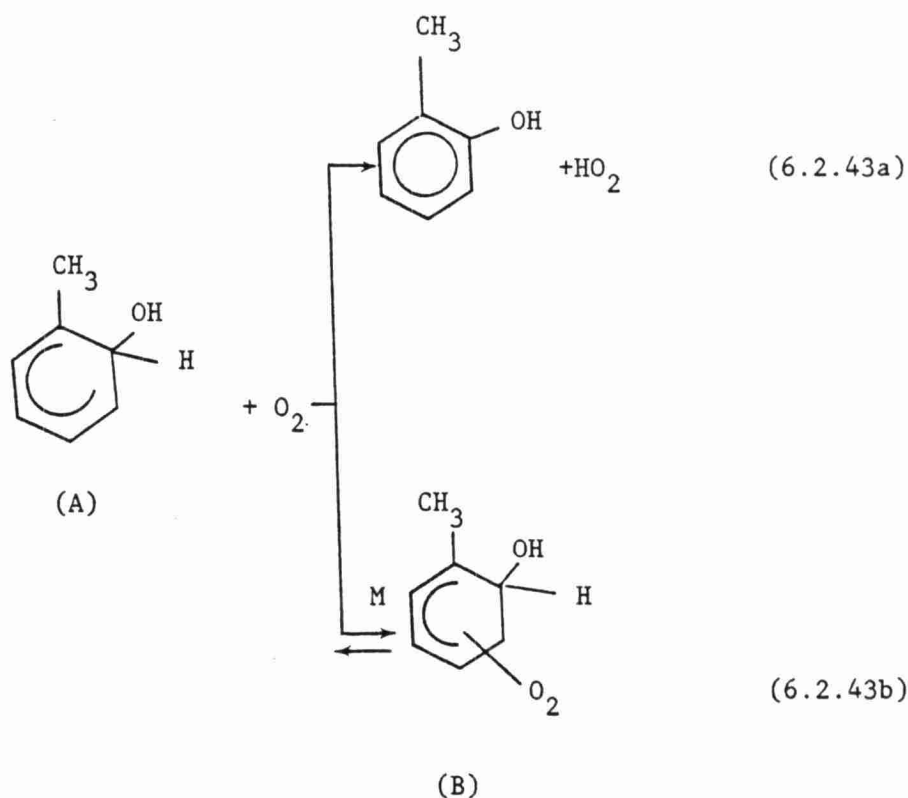


for toluene,  $k_{42a}/(k_{42a} + k_{42b}) \approx 0.15$  (Atkinson et al. 1979, 1980).

Under atmospheric conditions the benzyl radical will react to form benzaldehyde and benzyl nitrate - these reaction pathways have been discussed in detail previously (Atkinson et al. 1980; Atkinson and Lloyd 1980) and are analogous to the relatively well known alkyl radical reactions.

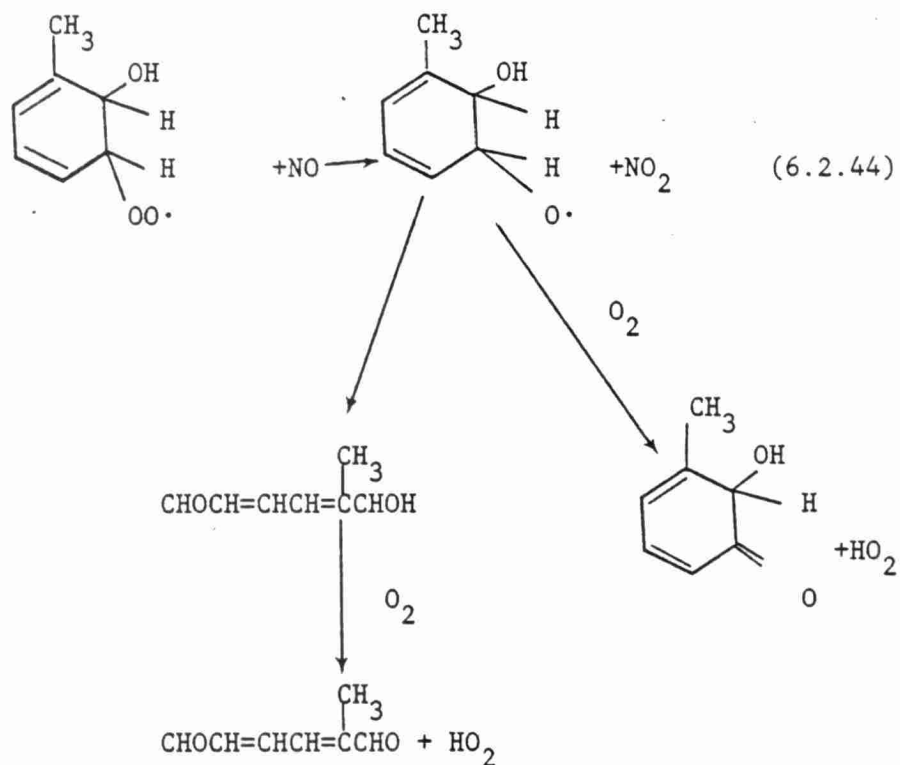
The uncertainties in the aromatic  $\text{NO}_x$ -photooxidation mechanisms lie in the fate of the addition adducts (A). Both experimentally and theoretically the situation is unclear, but some data are available which allow a reasonable mechanism to be postulated (Atkinson et al. 1980; Atkinson and Lloyd 1980) (it should be emphasized that much experimental data are needed before this suggested mechanism can be regarded as anything but tentative).

The OH-aromatic adducts can react with  $\text{O}_2$  via two pathways; H atom abstraction to form cresols or reversible  $\text{O}_2$  addition to the adduct (Atkinson et al. 1979, 1980);

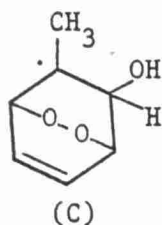


At low total pressures and low  $\text{NO}_x$  concentrations, cresols and benzaldehyde are essentially the sole products (Kenley et al. 1978; Hendry 1979) with ~85% cresol and ~15% benzaldehyde, while at atmospheric pressure, cresol yields of  $\lesssim 20\%$  have been derived from smog chamber studies (Atkinson et al. 1980; O'Brien et al. 1979), these data then being consistent with a pressure-dependent  $\text{O}_2$  addition pathway.

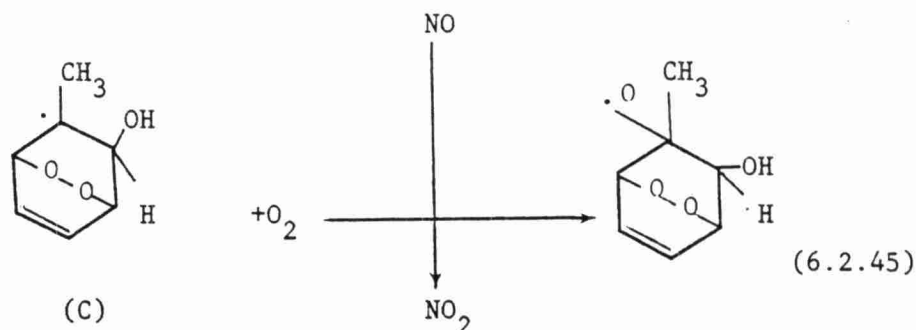
The structure and atmospheric fate of the adduct (B) is not known at present; however, certain conclusions can be drawn from recent smog chamber studies, which are applicable to ambient conditions. The rapid formation of biacetyl and other  $\alpha$ -dicarbonyls in the  $\text{NO}_x$  photooxidation of o-xylene (Darnall et al. 1979; Takagi et al. 1980) eliminates the reaction sequence (and others analogous to it):



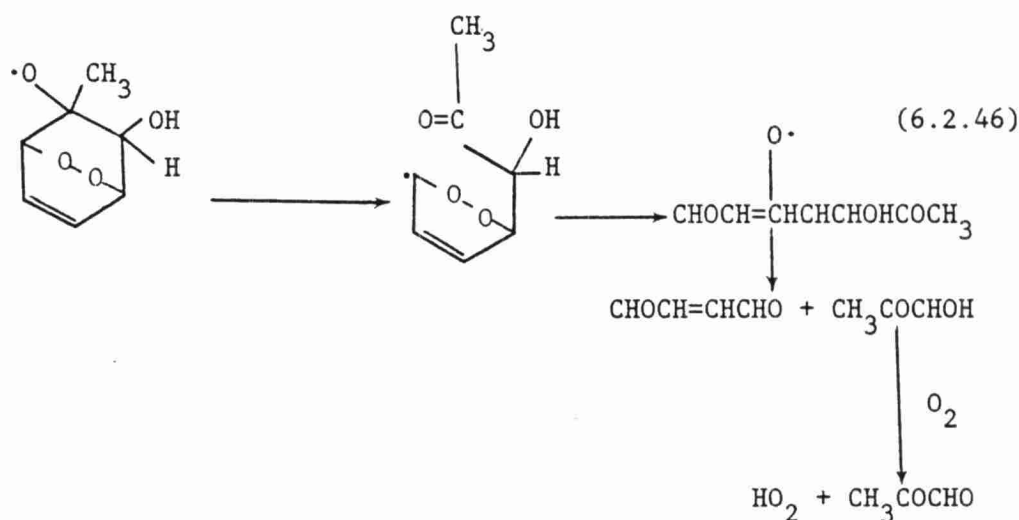
It appears (Atkinson et al. 1980), that in order to fit the experimental data and to be consistent with thermochemical evaluations, the only plausible route is the formation of bicyclic radicals of the form:



These bicyclic radicals can then add O<sub>2</sub> and react with NO similarly to alkyl radicals:



followed by spontaneous decomposition of the bicyclic oxy radicals:



followed by the subsequent reactions (Atkinson et al. 1980; Atkinson and Lloyd 1980) of the  $\alpha$ -dicarbonyls [glyoxal, methylglyoxal and biacetyl, depending on the parent aromatic hydrocarbon and the precise structure of the bicyclic intermediates (C)], and  $\gamma$ -unsaturated dicarbonyls (CHOCH=CHCHO and CH<sub>3</sub>COCH=CHCHO, for example).

Extension of this plausible mechanism to the cresols yields an explanation for their low reactivity, in terms of NO to NO<sub>2</sub> conversion and O<sub>3</sub> forming potential, in that, instead of the formation of the  $\alpha$ -dicarbonyls, methylglyoxal and biacetyl, which either photolyse rapidly or react rapidly with OH, the cresols should instead lead to the formation of carbonyl acids, such as pyruvic acid, CH<sub>3</sub>COCO<sub>2</sub>H, which is expected to be much less photoreactive (Atkinson et al. 1980). Indeed, Grosjean (1982) has identified pyruvic acid in irradiations of o-cresol/NO<sub>x</sub>/air mixtures. This compound, along with

2-butene-1,4 dial is expected to be formed from o-cresol as shown in Figure 6.2-1.

The chemical reactivity and fate of these dicarbonyl products under typical atmospheric conditions have not been studied experimentally. Pyruvic acid, which does not readily photolyze and is probably unreactive towards the hydroxyl radical, may accumulate as "stable" reaction product. The unsaturated dialdehyde, 2-butene-1, 4-dial, may react with OH to form glyoxal and formaldehyde as shown in Figure 6.2-2.

In terms of reactivity of the present aromatic hydrocarbons, benzene should be less reactive than toluene (as regards NO to NO<sub>2</sub> conversion and O<sub>3</sub> forming potential) than may be expected solely on the basis of its OH radical rate constant. This is believed to occur because glyoxal, from benzene, apparently does not photodissociate rapidly, if at all, in the actinic region to form radicals [but rather photodissociates to yield HCHO + CO (Calvert and Pitts 1966)]. For the purposes of our current modeling study, it may be possible to neglect the chemistry of benzene and concentrate all the aromatic hydrocarbon chemistry in toluene. From a strict chemical viewpoint, this incorporates additional uncertainties, but these are a necessary trade-off to satisfy the need to incorporate the chemistry of a representative aromatic and yet minimize the computing requirements required for additional species.

#### 6.2.1.5 Additional Organic Reactions Influencing HNO<sub>3</sub> Formation

Peroxyacyl nitrates, RCO<sub>3</sub>NO<sub>2</sub>, play an important role in the atmospheric chemistry of NO<sub>x</sub> emissions (Hendry and Kenley 1977; Cox and Roffey 1977). The best known of the species is peroxyacetyl nitrate, PAN, formed by the reaction of acetylperoxy radicals with NO<sub>2</sub>.



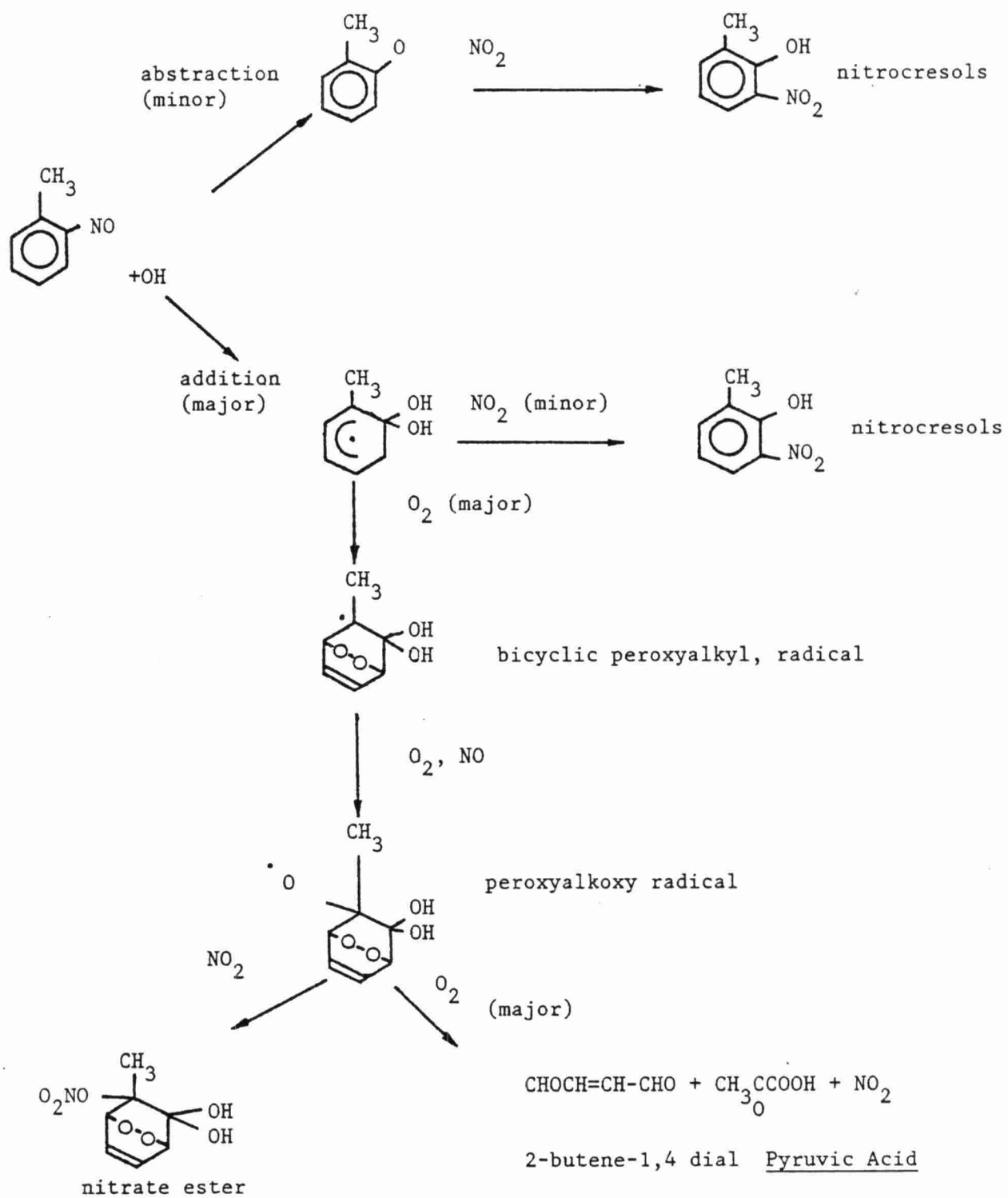
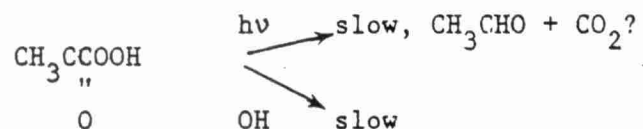


Figure 6.2-1. Simplified photooxidation mechanism for o-cresol.



1. Pyruvic acid



2. 2-butene-1, 4-dial

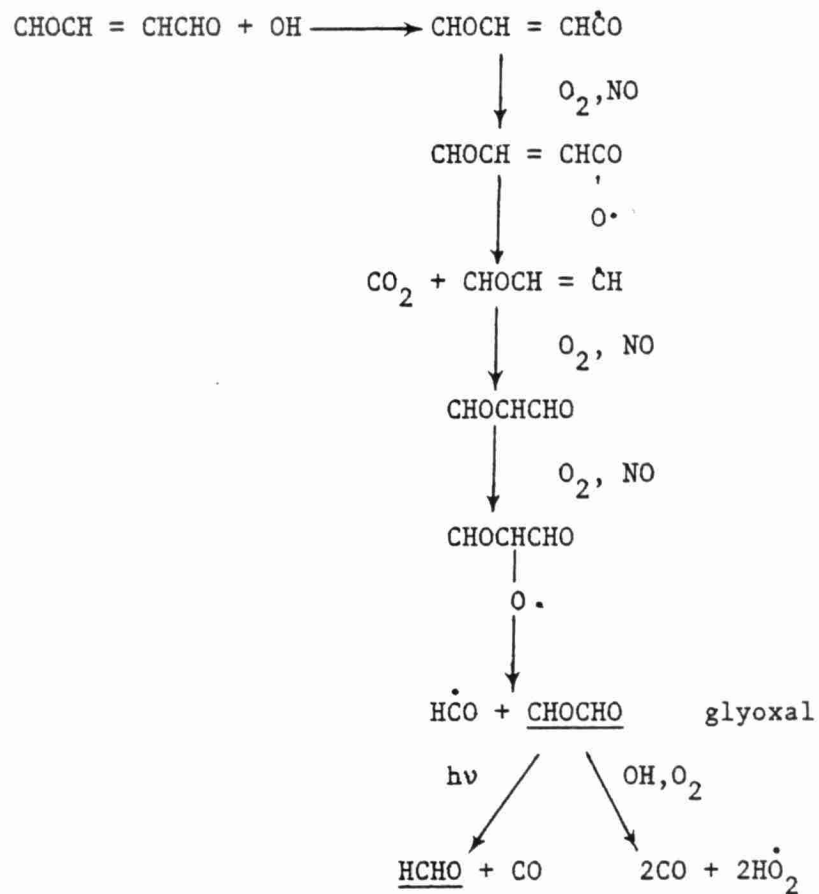


Figure 6.2-2. Tentative reaction pathways for o-cresol dicarbonyl products.

The acetyl peroxy radicals are formed by the reactions of  $O_2$  with acetyl radicals formed from acetaldehyde by reaction with the OH radical:



PAN is a temporary sink for  $NO_2$  since it thermally decomposes to the initial species:



The variation of the rate constant data as a function of temperature has been studied by several workers (Pate et al. 1976; Hendry and Kenley 1977; Cox and Roffey 1977; Nieboer and Duyzer 1978). The results from these workers show general agreement and Atkinson and Lloyd (1980) recommend the rate constant expression obtained by Hendry and Kenley (1977) of

$$k_{6.2.49} = 1.95 \times 10^{16} e^{-13543/T} \text{ sec}^{-1}.$$

Due to the temperature dependence, this sink for  $NO_2$  is likely to be more significant at the lower temperatures. Pernitric acid,  $HO_2NO_2$ , also may act as a temporary sink for  $NO_2$ , but it is thermally less stable than PAN.

Since peroxy radicals may remain at high levels during nighttime hours, peroxy nitrates such as pernitric acid and peroxyacyl nitrates (PAN and higher homologues) become especially important, since their thermal lifetimes increase rapidly as the temperature falls. Table 6.2-4b gives the thermal lifetimes at atmospheric pressure and at various temperatures which may be encountered under long range transport conditions. The results shown in this table shows that PAN (and by analogy, other peroxyacyl nitrates) becomes increasingly important as a temporary sink for  $NO_x$  as the temperature falls. PAN, acting as a nighttime reservoir for  $NO_x$  (and peroxyacyl radicals)

TABLE 6.2-4

THERMAL LIFETIMES OF PEROXY- AND PEROXYACYL-NITRATES  
AT ATMOSPHERIC PRESSURE

Temperature °K	Thermal Lifetime		
	$\text{HO}_2\text{NO}_2^*$	$\text{C}_5\text{H}_7\text{O}_2\text{NO}_2^{**}$	$\text{PAN}^\dagger$
305 (90°F)	5 sec	0.3 sec	16 minutes
294 (70°F)	17 sec	1.0 sec	37 minutes
283 (50°F)	69 sec	4.0 sec	8.6 hours

\* Graham et al. (1977)

\*\* Edney et al. (1979)

† Hendry and Kenley (1977)

will, as the morning temperatures rise, release  $\text{NO}_2$  back for continuation of the photochemistry. To a lesser extent, pernitric acid,  $\text{HO}_2\text{NO}_2$ , will act in a similar manner. However, from the available (though sparse) data, the alkyperoxynitrates,  $\text{RO}_2\text{NO}_2$  have [at least for peroxypropionynitrate (Edney et al. 1979)] too short a thermal lifetime, even at temperatures on the order to  $50^\circ\text{F}$ , to act as  $\text{NO}_x$  sinks of any significance. In conclusion, it appears that the formation and thermal decomposition of peroxyalkynitrates may be neglected. However, such reactions for pernitric acid and peroxyacylnitrates must be considered, although the former species will be of importance only at temperatures well below  $50^\circ\text{F}$ .

Most recently, interest in the role of PAN in acid precipitation has increased, not only because of its role in photochemical reactions, but also due to its potential importance in aqueous phase chemistry. This aspect will be discussed in the section on aqueous phase reactions of  $\text{NO}_x$ .

#### 6.2.1.6 Importance of Nighttime Chemistry in $\text{NO}_x$ Transformations

The chemistry of  $\text{NO}_x$  occurring during the nighttime is important for multiday events encountered in acid precipitation modeling. Several chemical phenomena take place during the evening and nighttime which are important for consideration:

- Reactions of  $\text{NO}_3$  and  $\text{N}_2\text{O}_5$  may be more important at the end of a day's irradiation when  $\text{O}_3$  and  $\text{NO}_2$  may be consumed and  $\text{HNO}_3$  formed via the reaction sequence:



- As the solar irradiation intensity falls, the production rates of radical species such as  $\text{OH}$  and  $\text{HO}_2$  also fall. For

radicals such as the OH radical, for which the destruction rates remain essentially unaltered, their concentrations fall rapidly to near-zero levels (Hov and Isaksen 1979). Peroxy radicals ( $\text{HO}_2$  and  $\text{RO}_2$ ), however, remain at high levels because of a drop in both production and loss rates, and hence their reactions, such as the combination reactions:



become of more importance in that such photoinitiators as HCHO may build up during nighttime hours. For example, Grosjean et al. (1981) measured the diurnal variation in the concentration of aldehydes at Claremont in the Los Angeles basin in 1980. Figure 6.2-3 shows that significant concentrations were measured at night. These aldehydes generate more radical species the following day to propagate the oxidation of  $\text{NO}_x$  and  $\text{SO}_x$  emissions.

The ambient concentrations of  $\text{H}_2\text{O}_2$  are not well established. The method used by Kok who measured ppb levels in the Los Angeles basin and elsewhere has subsequently been questioned and shown to respond to other oxidants in addition to  $\text{H}_2\text{O}_2$ . Calculations presented in Section 10 show that the photochemical model can predict sufficient  $\text{H}_2\text{O}_2$  to act as a significant potential species for the aqueous oxidation of  $\text{SO}_2$ .

- Nitrous acid, HONO, has been observed at the 1-10 ppb level in the Los Angeles nighttime and early morning hours (Harris et al. 1982). The mechanism for HONO formation is uncertain, but since HONO is a significant precursor to the OH radical, any model must incorporate this species in the chemistry module.

DIURNAL PROFILES FOR O<sub>3</sub>, PAN AND SELECTED CARBONYLS,  
CLAREMONT, CA, 9/25-26/80

WB102123

6-35

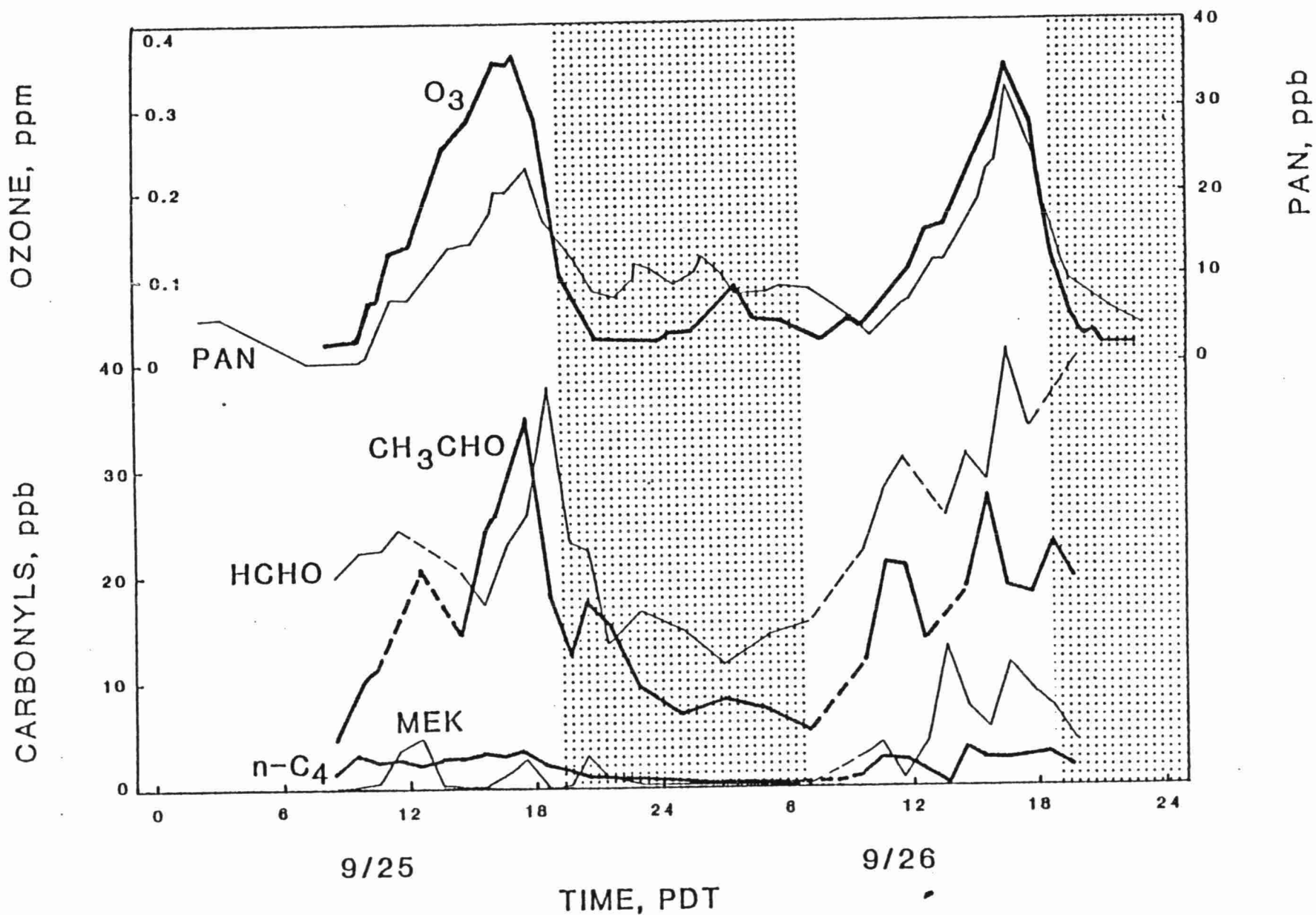


Figure 6.2-3

The above examples illustrate that nighttime chemistry can influence radical production and nitrogen containing products including  $\text{HNO}_3$ . While most understanding of these processes is incomplete, sufficient is known to present a reasonable chemical scheme to incorporate the major processes expected to occur at night. These reactions, and those discussed in the earlier sections are continued in the chemical mechanism constructed and listed by Atkinson et al. 1982. This is shown in Table 6.2-5. It is recommended that this form the basis for the photochemical mechanism under concentration for the acid precipitation model formulation.

#### 6.2.1.7 Role of Biogenic Hydrocarbons

The discussions above demonstrate that hydrocarbons play a key role in generating radical species under atmospheric conditions. These radicals participate in the photooxidation of  $\text{NO}_x$  and  $\text{SO}_x$  emissions. For parts of the geographic area of concern for long range transport and acid precipitation modeling, biogenic hydrocarbon emissions may provide a much lower, but significant contribution than anthropogenic emissions to the hydrocarbon atmospheric loading. Our current understanding of the role of biogenic hydrocarbons in atmospheric chemistry is briefly discussed below.

The role of biogenic hydrocarbons [mainly isoprene and the monoterpenes (Graedel 1979)] in influencing atmospheric ozone concentrations has been of interest for many years (Dimitriades and Altshuller 1977; Coffey 1977; Westberg 1977; Graedel 1979; Dimitriades 1981). Recent field and laboratory studies (Rasmussen et al. 1976; Lonneman et al. 1978; Holdren et al. 1979; Zimmerman 1979; Arnts and Gay 1979; Arnts and Meeks 1980; Kamens et al. 1981) have contributed significantly to the understanding of the emission rates, ambient concentrations, and the atmospheric chemistry of these naturally emitted hydrocarbons. Nevertheless, considerable controversy and uncertainty still exists as to the role of these compounds on ozone formation/destruction in rural and urban regions and the uncertainties have been discussed elsewhere (Dimitriades 1981).

TABLE 6.2-5

Reactions and rate constants used in the basic standard model. Rate constants etc. from Atkinson et al. (1981) unless otherwise noted.

<u>Reaction</u>	<u>Notes</u>	<u>Rate Constant (ppm min units)</u>
<u>Inorganics</u>		
1. $\text{NO}_2 + h\nu \xrightarrow{\text{O}_2} \text{NO} + \text{O}_3$	1.	$k_1$ variable
2. $\text{NO} + \text{O}_3 \rightarrow \text{NO}_2 + \text{O}_2$		$k_2 = 1.0 \times 10^6 \text{ T}^{-1} e^{-1450/\text{T}}$
3. $\text{O}_3 + h\nu \rightarrow 2 \text{ OH}$	2.	$k_3 = \beta_1 k_1 \times 7.5 \times 10^{-6} [\text{H}_2\text{O}]$
4. $\text{OH} + \text{NO} \xrightarrow{\text{M}} \text{HONO}$	3.	$k_4 = 8.7 \times 10^8 \text{ T}^{-2}$
5. $\text{OH} + \text{NO}_2 \xrightarrow{\text{M}} \text{HNO}_3$	3.	$k_5 = 1.5 \times 10^9 \text{ T}^{-2}$
6. $\text{HONO} + h\nu \rightarrow \text{OH} + \text{NO}$		$k_6 = \beta_2 k_1$
7. $\text{HO}_2 + \text{NO} \rightarrow \text{OH} + \text{NO}_2$	4.	$k_7 = 3.7 \times 10^6 \text{ T}^{-1}$
8. $\text{HO}_2 + \text{NO}_2 \xrightarrow{\text{M}} \text{HO}_2\text{NO}_2$	3.	$k_8 = 1.5 \times 10^8 \text{ T}^{-2}$
9. $\text{HO}_2\text{NO}_2 \xrightarrow{\text{M}} \text{HO}_2 + \text{NO}_2$	5.	$k_9 = 7.8 \times 10^{15} e^{-10420/\text{T}}$
10. $\text{HO}_2 + \text{HO}_2 \rightarrow \text{H}_2\text{O}_2 + \text{O}_2$	6.	$k_{10} = 3.4 \times 10^4 \text{ T}^{-1} e^{1100/\text{T}}$ $+ 5.8 \times 10^{-5} \text{ T}^{-2} e^{5800/\text{T}}$ $[\text{H}_2\text{O}]$
11. $\text{H}_2\text{O}_2 + h\nu \rightarrow 2\text{OH}$		$k_{11} = \beta_3 k_1$
12. $\text{OH} + \text{CO} \xrightarrow{\text{O}_2} \text{HO}_2$		$k_{12} = 1.3 \times 10^5 \text{ T}^{-1}$
13. $\text{NO}_2 + \text{O}_3 \rightarrow \text{NO}_3$		$k_{13} = 5.3 \times 10^4 \text{ T}^{-1} e^{-2450/\text{T}}$
14. $\text{NO} + \text{NO}_3 \rightarrow 2\text{NO}_2$		$k_{14} = 8.4 \times 10^6 \text{ T}^{-1}$
15. $\text{NO}_2 + \text{NO}_3 \xrightarrow{\text{M}} \text{N}_2\text{O}_5$	7.	$k_{15} = 3.1 \times 10^7 \text{ T}^{-1} e^{-1100/\text{T}}$
16. $\text{N}_2\text{O}_5 \xrightarrow{\text{M}} \text{NO}_2 + \text{NO}_3$	7.	$k_{16} = 3.5 \times 10^{18} e^{-12280/\text{T}}$
17. $\text{N}_2\text{O}_5 + \text{H}_2\text{O} \rightarrow 2\text{HNO}_3$	8.	$k_{17} \sim 1.33 \times 10^{-3} \text{ T}^{-1}$
18. $\text{NO}_3 + h\nu \rightarrow 0.3 \text{ NO} + 0.7 \text{ NO}_2$ $+ 0.7 \text{ O}_3$	9.	$k_{18} = \beta_4 k_1$



TABLE 6.2-5 (Continued)

Reaction	Notes	Rate Constant (ppm min units)
19. $\text{OH} + \text{O}_3 \rightarrow \text{HO}_2$		$k_{19} = 7.0 \times 10^5 \text{ T}^{-1} e^{-940/\text{T}}$
20. $\text{HO}_2 + \text{O}_3 \rightarrow \text{OH}$		$k_{20} = 4.8 \times 10^3 \text{ T}^{-1} e^{-580/\text{T}}$
<u>Formaldehyde</u>		
21. $\text{HCHO} + \text{h}\nu \xrightarrow{\text{O}_2} \text{HO}_2 + \text{HO}_2 + \text{CO}$	10.	$k_{21} = 8_5 k_1$
22. $\text{HCHO} + \text{h}\nu \rightarrow \text{CO} + \text{H}_2$		$k_{22} = 8_6 k_1$
23. $\text{OH} + \text{HCHO} \xrightarrow{\text{O}_2} \text{HO}_2 + \text{CO}$	10.	$k_{23} = 4.4 \times 10^6 \text{ T}^{-1}$
<u>Acetaldehyde</u>		
24. $\text{CH}_3\text{CHO} + \text{h}\nu \xrightarrow{\text{O}_2} \text{CH}_3\text{O}_2 + \text{HO}_2$ + CO	10.	$k_{24} = 8_7 k_1$
25. $\text{OH} + \text{CH}_3\text{CHO} \xrightarrow{\text{O}_2} \text{CH}_3\text{CO}_3$		$k_{25} = 3.0 \times 10^6 \text{ T}^{-1} e^{250/\text{T}}$
26. $\text{CH}_3\text{CO}_3 + \text{NO}_2 \rightarrow \text{PAN}$		$k_{26} = 2.1 \times 10^6 \text{ T}^{-1}$
27. $\text{PAN} \rightarrow \text{CH}_3\text{CO}_3 + \text{NO}_2$		$k_{27} = 1.2 \times 10^{18} e^{-13543/\text{T}}$
28. $\text{CH}_3\text{CO}_3 + \text{NO} \xrightarrow{\text{O}_2} \text{NO}_2 + \text{CH}_3\text{O}_2$	11.	$k_{28} = 3.1 \times 10^6 \text{ T}^{-1}$
29. $\text{CH}_3\text{O}_2 + \text{NO} \rightarrow \text{HCHO} + \text{HO}_2$ + NO <sub>2</sub>	12.	$k_{29} = 3.1 \times 10^6 \text{ T}^{-1}$
<u>Propane</u>		
30. $\text{OH} + \text{PROPANE} \rightarrow \text{PO}_2$		$k_{30} = 6.6 \times 10^6 \text{ T}^{-1} e^{-680/\text{T}}$
31. $\text{PO}_2 + \text{NO} \rightarrow \text{HO}_2 + \text{NO}_2$ + CH <sub>3</sub> COCH <sub>3</sub>	13.	$k_{31} = 3.1 \times 10^6 \text{ T}^{-1}$
<u>Alkanes</u>		
32. $\text{OH} + \text{Alkane} \rightarrow \text{AO}_2$	14.	$k_{32} = 8.0 \times 10^6 \text{ T}^{-1} e^{-560/\text{T}}$ for explicit n-butane $k_{32} = 6.6 \times 10^6 \text{ T}^{-1} e^{-400/\text{T}}$ for lumped $\geq \text{C}_4$ alkane

TABLE 6.2-5 (Continued)

Reaction	Notes	Rate Constant (ppm min units)
33. $\text{AO}_2 + \text{NO} \rightarrow 1.3 \text{NO}_2 + -0.4 \text{NO} + 0.9 \text{HO}_2 + 0.6 \text{CH}_3\text{CHO} + 0.1 \text{RCHO}$ + 0.5 MEK		
	14. Explicit n-butane	
$\rightarrow 1.7 \text{NO}_2 + -0.8 \text{NO} + 0.9 \text{HO}_2 + 0.15 \text{HCHO} + 0.3 \text{CH}_3\text{CHO}$ + 0.1 RCHO + 0.3 $\text{CH}_3\text{COCH}_3$ + 0.45 MEK		
	14. Lumped $\geq \text{C}_4$ alkane mechanism	
		$k_{33} = 3.1 \times 10^6 \text{ T}^{-1}$ for both systems
<u>Higher Aldehydes</u>		
34. $\text{OH} + \text{RCHO} \xrightarrow{\text{O}_2} \text{RCO}_3$	15.	$k_{34} = 9.2 \times 10^6 \text{ T}^{-1}$
35. $\text{RCO}_3 + \text{NO}_2 \rightarrow \text{PPN}$	15.	$k_{35} = 2.1 \times 10^6 \text{ T}^{-1}$
36. $\text{PPN} \rightarrow \text{RCO}_3 + \text{NO}_2$	16.	$k_{36} = 1.2 \times 10^{18} e^{-15543/\text{T}}$
37. $\text{RCO}_3 + \text{NO} \rightarrow \text{C}_2\text{H}_5\text{O}_2 + \text{NO}_2$	15.	$k_{37} = 3.1 \times 10^6 \text{ T}^{-1}$
38. $\text{C}_2\text{H}_5\text{O}_2 + \text{NO} \xrightarrow{\text{O}_2} \text{CH}_3\text{CHO}$ + $\text{HO}_2 + \text{NO}_2$	15.	$k_{38} = 3.1 \times 10^6 \text{ T}^{-1}$
39. $\text{RCHO} + \text{h}\nu \xrightarrow{\text{O}_2} \text{C}_2\text{H}_5\text{O}_2 + \text{CO}$ + $\text{HO}_2$		$k_{39} = 8k_1$
<u>Ketones</u>		
40. $\text{OH} + \text{MEK} \xrightarrow{\text{O}_2} \text{XO}_2$	17.	$k_{40} = 4.4 \times 10^6 \text{ T}^{-1} e^{-330/\text{T}}$
41. $\text{XO}_2 + \text{NO} \rightarrow \text{NO}_2 + \text{CH}_3\text{CHO}$ + $\text{CH}_3\text{CO}_3$		$k_{41} = 3.1 \times 10^6 \text{ T}^{-1}$
42. $\text{MEK} + \text{h}\nu \xrightarrow{\text{O}_2} \text{CH}_3\text{CO}_3 + \text{C}_2\text{H}_5\text{O}_2$		$k_{42} = 8k_1$
43. $\text{CH}_3\text{COCH}_3 + \text{h}\nu \xrightarrow{\text{O}_2} \text{CH}_3\text{CO}_3$ + $\text{CH}_3\text{O}_2$	18.	$k_{43} = 8k_1$

TABLE 6.2-5 (Continued)

Reaction	Notes	Rate Constant (ppm min units)
<u>Alkenes</u>		
44. $\text{OH} + \text{Ethene} \xrightarrow{\text{O}_2}$	19.	$k_{44} = 9.7 \times 10^5 \text{ T}^{-1} e^{380/\text{T}}$
$2\text{HCHO} + \text{NO}_2 \rightarrow \text{NO} + \text{HO}_2$		
45. $\text{OH} + \text{Propene} \xrightarrow{\text{O}_2}$	19.	$k_{45} = 1.8 \times 10^6 \text{ T}^{-1} e^{540/\text{T}}$
$\text{HCHO} + \text{CH}_3\text{CHO} + \text{HO}_2$		
$+ \text{NO}_2 \rightarrow \text{NO}$		
46. $\text{OH} + \text{Butene} \xrightarrow{\text{O}_2}$	19.	$k_{46} = 5.0 \times 10^6 \text{ T}^{-1} e^{540/\text{T}}$
$1.8 \text{ CH}_3\text{CHO} + 0.9 \text{NO}_2$		
$+ 0.9 \text{HO}_2 \rightarrow \text{NO}$		
47. $\text{O}_3 + \text{Ethene} \rightarrow \text{HCHO} + 0.4$		$k_{47} = 4.2 \times 10^3 \text{ T}^{-1} e^{-2560/\text{T}}$
$\dot{\text{CH}}_2\dot{\text{O}}_2 + 0.4 \text{CO} + 0.12 \text{HO}_2$		
48. $\text{O}_3 + \text{Propene} \rightarrow 0.5 \text{HCHO} + 0.5 \text{CH}_3\text{CHO} + 0.2 \dot{\text{CH}}_2\dot{\text{O}}_2 + 0.2 \text{CH}_3\dot{\text{C}}\text{HOO}$		
$+ 0.3 \text{CO} + 0.2 \text{HO}_2 + 0.1 \text{OH} + 0.2 \text{CH}_3\text{O}_2$		
		$k_{48} = 3.1 \times 10^3 \text{ T}^{-1} e^{-1900/\text{T}}$
49. $\text{O}_3 + \text{Butenes} \rightarrow \text{CH}_3\text{CHO} + 0.4 \text{CH}_3\dot{\text{C}}\text{HOO} + 0.3 \text{HO}_2 + 0.2 \text{OH} + 0.45$		
$\text{CH}_3\text{O}_2 + 0.2 \text{CO}$		
		$k_{49} = 3.3 \times 10^3 \text{ T}^{-1} e^{-1050/\text{T}}$
50. $\dot{\text{CH}}_2\dot{\text{O}}_2 + \text{NO} \rightarrow \text{HCHO} + \text{NO}_2$		$k_{50} = 3.1 \times 10^6 \text{ T}^{-1}$
51. $\dot{\text{CH}}_2\dot{\text{O}}_2 + \text{NO}_2 \rightarrow \text{HCHO} + \text{NO}_3$		$k_{51} = 3.1 \times 10^5 \text{ T}^{-1}$
52. $\dot{\text{CH}}_2\dot{\text{O}}_2 + \text{SO}_2 \rightarrow \text{HCHO} + \text{SO}_4^-$	20.	$k_{52} = 3.0 \times 10^4 \text{ T}^{-1}$
53. $\dot{\text{CH}}_2\dot{\text{O}}_2 + \text{H}_2\text{O} \rightarrow \text{Product}$		$k_{53} = 1.5 \text{ T}^{-1}$
54. $\text{CH}_3\dot{\text{C}}\text{HOO} + \text{NO} \rightarrow \text{CH}_3\text{CHO} + \text{NO}_2$		$k_{54} = 3.1 \times 10^6 \text{ T}^{-1}$
55. $\text{CH}_3\dot{\text{C}}\text{HOO} + \text{NO}_2 \rightarrow \text{CH}_3\text{CHO} + \text{NO}_3$		$k_{55} = 3.1 \times 10^5 \text{ T}^{-1}$
56. $\text{CH}_3\dot{\text{C}}\text{HOO} + \text{SO}_2 \rightarrow \text{CH}_3\text{CHO} + \text{SO}_4^-$	20.	$k_{56} = 3.0 \times 10^4 \text{ T}^{-1}$
57. $\text{CH}_3\dot{\text{C}}\text{HOO} + \text{H}_2\text{O} \rightarrow \text{Product}$		$k_{57} = 1.5 \text{ T}^{-1}$

TABLE 6.2-5 (Continued)

<u>Reaction</u>	<u>Notes</u>	<u>Rate Constant (ppm min units)</u>
<u>Aromatics</u>		
58. OH + Benzene $\rightarrow$ 0.25 Cresol + 0.25 HO <sub>2</sub> + 0.75 ADD	21.	$k_{58} = 5.3 \times 10^5 \text{ T}^{-1}$
59. OH + Toluene $\rightarrow$ 0.15 ARO <sub>2</sub> + 0.20 Cresol + 0.20 HO <sub>2</sub> + 0.65 ADD	21.	$k_{59} = 2.7 \times 10^6 \text{ T}^{-1}$
60. OH + Xylene $\rightarrow$ 0.25 Cresol + 0.25 HO <sub>2</sub> + 0.75 ADD	21.	$k_{60} = 7.9 \times 10^6 \text{ T}^{-1}$ for lumped xylenes $= 1.05 \times 10^7 \text{ T}^{-1}$ for explicit m-xylene
61. ADD + NO $\rightarrow$ 0.75 NO <sub>2</sub> + 0.75 HO <sub>2</sub> + 0.75 DIAL + $\alpha_1$ (CHO) <sub>2</sub> + $\alpha_2$ CH <sub>3</sub> COCHO	22.	$k_{61} = 3.1 \times 10^6 \text{ T}^{-1}$
62. OH + DIAL $\rightarrow$ E1	23.	$k_{62} = 1.3 \times 10^7 \text{ T}^{-1}$
63. E1 + NO <sub>2</sub> $\rightarrow$ E1 NO <sub>2</sub>		$k_{63} = 2.1 \times 10^6 \text{ T}^{-1}$
64. E1 NO <sub>2</sub> $\rightarrow$ E1 + NO <sub>2</sub>	16.	$k_{64} = 1.2 \times 10^{18} e^{-13543/T}$
65. E1 + NO $\rightarrow$ 3 NO <sub>2</sub> - 2 NO + $\alpha_3$ HO <sub>2</sub> + $\alpha_3$ (CHO) <sub>2</sub> + $\alpha_4$ CH <sub>3</sub> CO <sub>3</sub> + $\alpha_4$ CH <sub>3</sub> COCHO + $\alpha_3$ CO	24.	$k_{65} = 3.1 \times 10^6 \text{ T}^{-1}$
66. OH + (CHO) <sub>2</sub> $\xrightarrow{\text{O}_2}$ HO <sub>2</sub> + CO		$k_{66} = 8.8 \times 10^6 \text{ T}^{-1}$
67. (CHO) <sub>2</sub> + hv $\rightarrow$ HCHO + CO		$k_{67} = \beta_{11}k_1$
68. OH + CH <sub>3</sub> COCHO $\xrightarrow{\text{O}_2}$ CH <sub>3</sub> CO <sub>3</sub> + CO		$k_{68} = 6.6 \times 10^6 \text{ T}^{-1}$
69. CH <sub>3</sub> COCHO + hv $\xrightarrow{\text{O}_2}$ CH <sub>3</sub> CO + HO <sub>2</sub> + CO		$k_{69} = \beta_{12}k_1$
70. OH + Cresol $\rightarrow$ ADD2	25.	$k_{70} = 1.9 \times 10^7 \text{ T}^{-1}$
71. ADD2 + NO $\rightarrow$ 0.75 NO <sub>2</sub> + 0.75 HO <sub>2</sub> + 0.75 DIAL	26.	$k_{71} = 3.1 \times 10^6 \text{ T}^{-1}$

TABLE 6.2-5 (Continued)

<u>Reaction</u>	<u>Notes</u>	<u>Rate Constant (ppm min units)</u>
<u>Aromatics</u>		
72. $\text{NO}_3 + \text{Cresol} \rightarrow \text{HNO}_3 +$ Phenoxy	27.	$k_{72} = 6.6 \times 10^6 \text{ T}^{-1}$
73. Phenoxy + $\text{NO}_2 \rightarrow$ Products (o-, p-nitrophenols)	27.	$k_{73} = 6.6 \times 10^6 \text{ T}^{-1}$
74. $\text{ARO}_2 + \text{NO} \rightarrow 0.75 \text{ NO}_2$ + $0.75 \text{ HO}_2 + 0.75 \text{ ARCHO}$	27.	$k_{74} = 3.1 \times 10^6 \text{ T}^{-1}$
75. $\text{ARCHO} + \text{h}\nu \rightarrow$ Products		$k_{75} = \beta_{13} k_1$
76. $\text{OH} + \text{ARCHO} \xrightarrow{\text{O}_2} \text{ARCO}_3$	27.	$k_{76} = 5.7 \times 10^6 \text{ T}^{-1}$
77. $\text{ARCO}_3 + \text{NO}_2 \rightarrow \text{PBZN}$	27.	$k_{77} = 2.1 \times 10^6 \text{ T}^{-1}$
78. $\text{PBZN} \rightarrow \text{ARCO}_3 + \text{NO}_2$		$k_{78} = 1 \times 10^{17} e^{-13025/\text{T}}$
79. $\text{ARCO}_3 + \text{NO} \rightarrow \text{PhO}_2 + \text{NO}_2$	27.	$k_{79} = 3.1 \times 10^6 \text{ T}^{-1}$
80. $\text{PhO}_2 + \text{NO} \rightarrow \text{Phenoxy} + \text{NO}_2$		$k_{80} = 3.1 \times 10^6 \text{ T}^{-1}$
<u>SO<sub>2</sub></u>		
81. $\text{OH} + \text{SO}_2 \xrightarrow{\text{M}} \text{SO}_4^=$	20.	$k_{81} = 1.5 \times 10^{15} \text{ T}^{-4}$
<u>Chamber Dependent Reactions</u>		
82. $? \rightarrow \text{OH}$	28.	$k_{82} = \sim 1.5 \times 10^{-4}$
83. $\text{O}_3 \rightarrow \text{Wall}$	29.	$k_{83} = 1.7 \times 10^{-3}$
84. General Dilution	29.	

Since the first publication of natural hydrocarbon (HC) emission estimates (Went 1960), researchers have debated whether natural HCs act as sources or sinks for ozone and as to the magnitude of such sources or sinks (Dimitriades and Altshuller 1977; Coffey 1977; Sandberg et al. 1978; Bufalini 1980; Dimitriades 1981). Their role has been difficult to assess because of uncertainties in the chemistry as well as discrepancies between measurements of ambient concentrations and emissions (Graedel 1979, Dimitriades 1981).

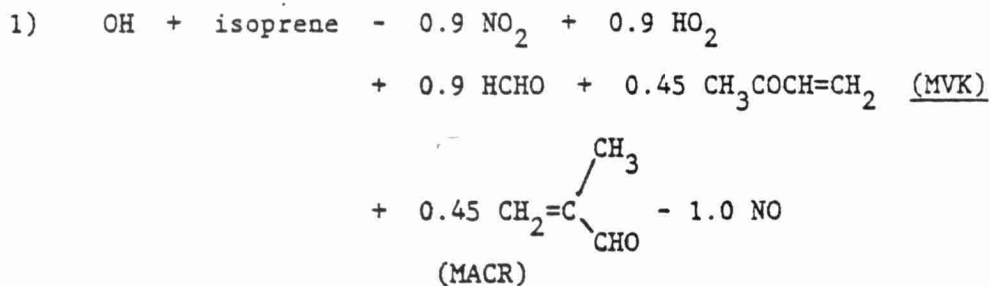
Many of the natural hydrocarbons (HCs) have been shown to react rapidly with ozone (Grimsrud et al. 1975, Japar et al. 1974, Atkinson et al. 1982a) and with OH radicals (Atkinson et al. 1979, 1982b). Smog chamber experiments have shown that these natural hydrocarbons are efficient at forming ozone when photooxidized in the presence of  $\text{NO}_x$  (Arnts and Gay 1979; Kamens et al. 1981).

Two naturally emitted hydrocarbons (isoprene and  $\alpha$ -pinene) have received most study to date. Isoprene, a hemiterpene, is emitted in significant amounts from deciduous trees such as oaks and sycamore and the evergreen eucalyptus (Rasmussen 1972; Sanadze 1961; Sanadze and Kalandadze 1966), while  $\alpha$ -pinene is more commonly emitted from evergreen trees such as pines and firs (Rasmussen 1972; Tingey et al. 1978; Westberg 1980). Field measurements of emissions from trees have shown these two compounds frequently comprise large fractions of the measured HC emissions (Zimmerman 1979). Laboratory studies have shown these two compounds are perhaps the most efficient ozone producers among the known biogenic HCs (Arnts and Gay 1979; Kamens et al. 1981).

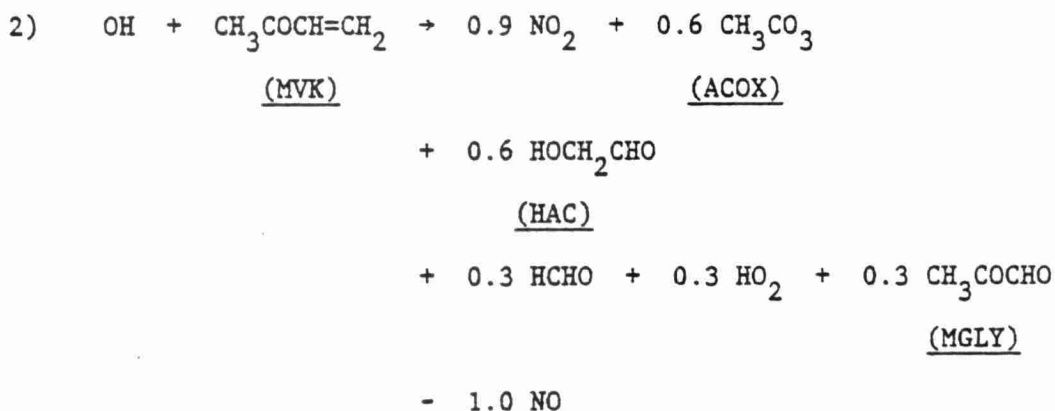
Lloyd et al. (1982) and Lurmann et al. (1982) have carried out a modeling study to develop a chemical mechanism for isoprene and  $\alpha$ -pinene and to assess their potential importance in generating  $\text{O}_3$  under various atmospheric conditions. Two of the major products of isoprene ( $\text{CH}_2=\text{CH}\cdot\text{C}(\text{CH}_2)$ ) photooxidation are methylvinylketone ( $\text{CH}_2=\text{CHCOCH}_3$ ) and methacrolein ( $\text{CH}_2=\text{C}(\text{CH}_3)\text{CHO}$ ) (Arnts and Gay 1979, Cox et al. 1980, Kamens et al. (1981). The proposed chemical mechanism to account for these and other products is shown in Table 6.2-6 (Lloyd et al. 1982). The reactions shown in this table illustrate that isoprene is effective in oxidizing  $\text{NO}_x$  to products through the formation of organic and inorganic radical species.

TABLE 6.2-6

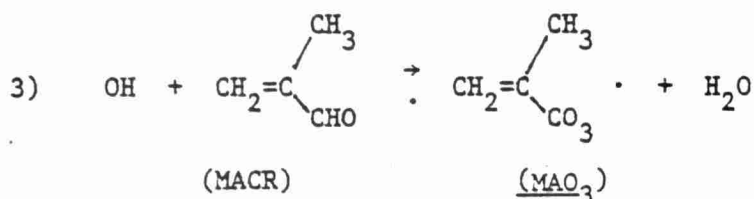
PROPOSED MECHANISM AND RATE CONSTANTS FOR ISOPRENE PHOTOOXIDATION AFTER  
LLOYD ET AL. (1982)



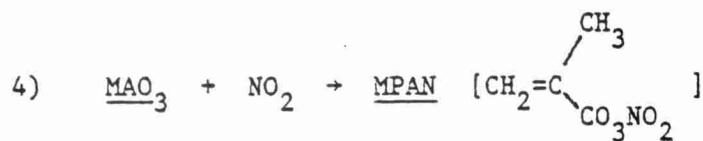
$$k = 6.6 \times 10^6 \text{ T}^{-1} e^{500/T} \text{ ppm}^{-1} \text{ min}^{-1}$$



$$k = 1.32 \times 10^6 \text{ T}^{-1} e^{500/T} \text{ ppm}^{-1} \text{ min}^{-1}$$



$$k = 4.5 \times 10^6 \text{ T}^{-1} \text{ ppm}^{-1} \text{ min}^{-1}$$



$$k = 2.1 \times 10^6 \text{ T}^{-1} \text{ ppm}^{-1} \text{ min}^{-1}$$

TABLE 6.2-6 (Continued)

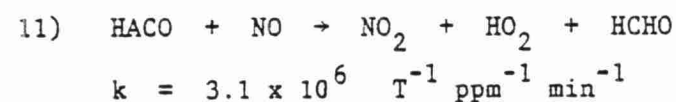
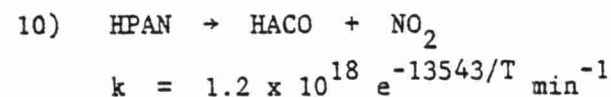
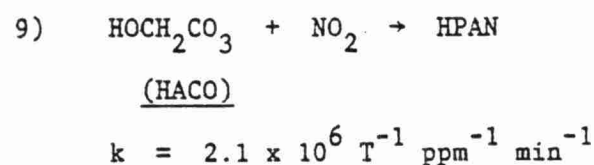
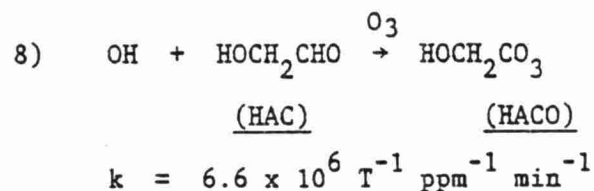
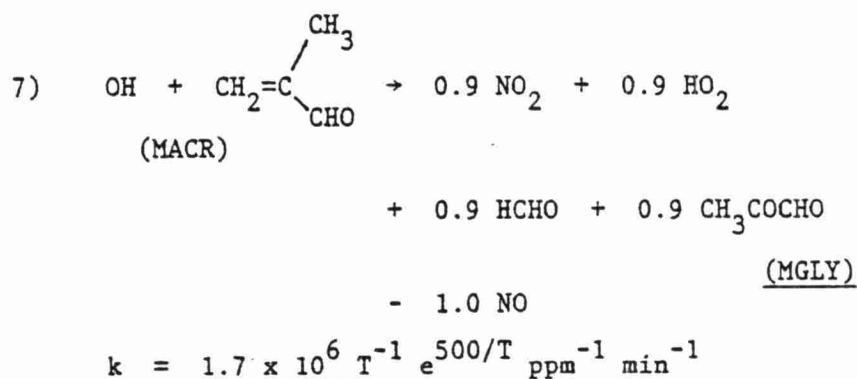
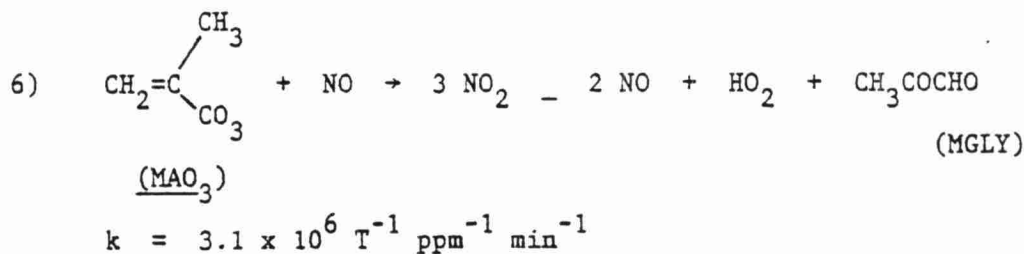
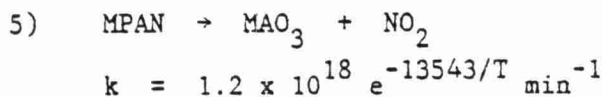
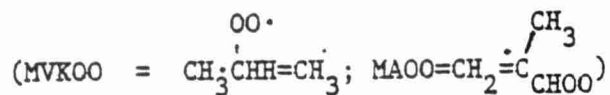
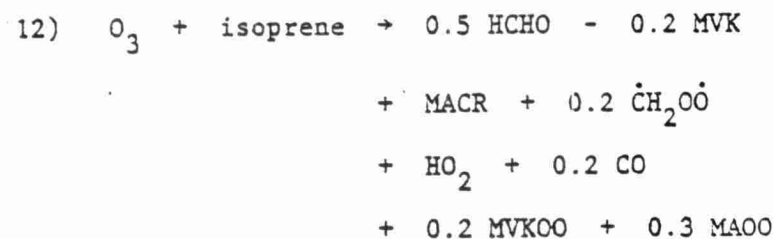
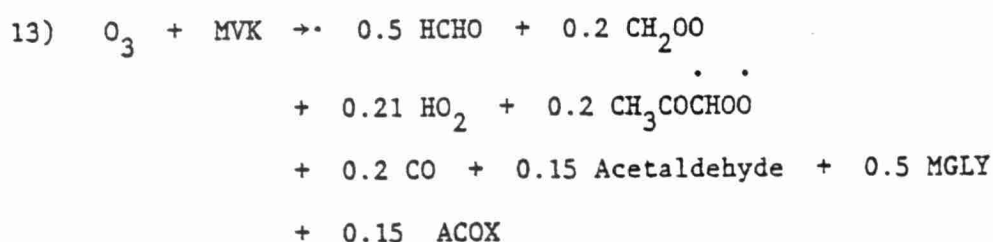




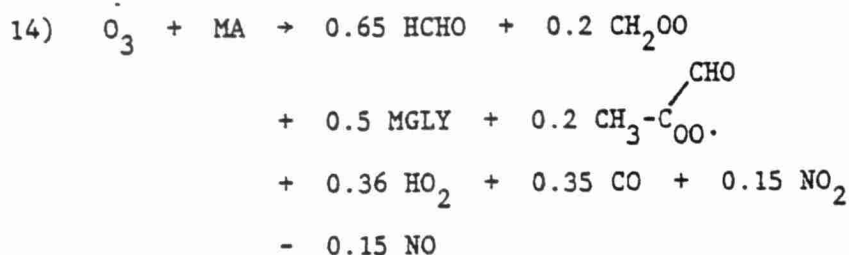
TABLE 6.2-6(Continued)



$$k = 3.1 \times 10^3 \text{ T}^{-1} e^{-1900/T} \text{ ppm}^{-1} \text{ min}^{-1}$$



$$k = 1.76 \times 10^3 \text{ T}^{-1} e^{-2000/T} \text{ ppm}^{-1} \text{ min}^{-1}$$



$$k = 1.94 \times 10^3 \text{ T}^{-1} e^{-2500/T} \text{ ppm}^{-1} \text{ min}^{-1}$$

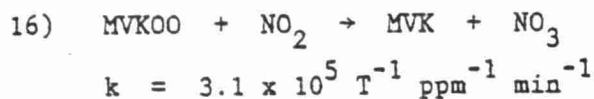
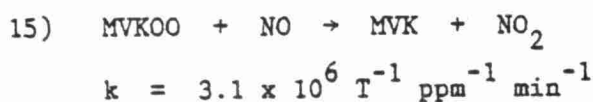


TABLE 6.2-6.(Continued)

- 17)  $\text{MVKOO} + \text{H}_2\text{O} \rightarrow \text{Product}$   
 $k = 1.5 \text{ T}^{-1} \text{ ppm}^{-1} \text{ min}^{-1}$
- 18)  $\text{MAOO} + \text{NO} \rightarrow \text{MACR} + \text{NO}_2$   
 $k = 3.1 \times 10^6 \text{ T}^{-1} \text{ ppm}^{-1} \text{ min}^{-1}$
- 19)  $\text{MAOO} + \text{NO}_2 \rightarrow \text{MACR} + \text{NO}_3$   
 $k = 3.1 \times 10^5 \text{ T}^{-1} \text{ ppm}^{-1} \text{ min}^{-1}$
- 20)  $\text{MAOO} + \text{H}_2\text{O} \rightarrow \text{Products}$   
 $k = 1.5 \text{ T}^{-1} \text{ ppm}^{-1} \text{ min}^{-1}$
- 21)  $\text{CH}_3\text{COCHO} + \text{NO} \rightarrow \text{MGLY} + \text{NO}_2$   
 $k = 3.1 \times 10^6 \text{ T}^{-1} \text{ ppm}^{-1} \text{ min}^{-1}$
- 22)  $\text{CH}_3\text{COCHO} + \text{NO}_2 \rightarrow \text{MGLY} + \text{NO}_3$   
 $k = 3.1 \times 10^5 \text{ T}^{-1} \text{ ppm}^{-1} \text{ min}^{-1}$
- 23)  $\text{CH}_3\text{COCHO} + \text{H}_2\text{O} \rightarrow \text{Products}$   
 $k = 1.5 \text{ T}^{-1} \text{ ppm}^{-1} \text{ min}^{-1}$
- 24)  $\text{HAC} + h\nu \rightarrow \text{HCHO} + 2.\text{HO}_2 + \text{CO}$   
 $k = \text{Acetaldehyde Photolysis Rate}$
- 25)  $\text{MGLY} + h\nu \rightarrow \text{ACOX} + \text{HO}_2 + \text{CO}$   
 $k = 0.15 k_1$

Isoprene, and the two major initial products of methylvinylketone and methacrolein, react with both the OH radical and  $O_3$ . A PAN type compound is predicted to be formed with a lifetime assumed to be similar to PAN. Methylglyoxal,  $CH_3COCHO$ , predicted to be formed in reactions 2, 6, 7, 13 and 14 in the table, photodissociates to produce  $HO_2$  radicals and acetylperoxy radicals which produce PAN in the presence of  $NO_x$ . A mechanism has also been developed for  $\alpha$ -pinene (Lloyd et al. 1982). However, greater uncertainties exist for its atmospheric photooxidation: these are covered in Lloyd et al. 1982 and will not be repeated here.

In summary, this brief discussion illustrates that certain biogenic hydrocarbons are quite reactive, and while their emissions are not large, they are significant and should probably be included in regional modeling studies. For our present modeling plan, rather than create a separate class for the biogenics, it is likely that their emissions and reactions could be treated within the alkene class (see summary section).

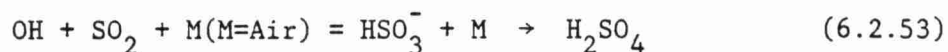
#### 6.2.1.3 Homogeneous Gas Phase Oxidation of $SO_2$

The gas phase homogeneous reactions of  $SO_2$  under atmospheric conditions have been extensively reviewed by Calvert et al. 1978. This review has been updated recently (Calvert 1982). These authors systematically reviewed all reaction pathways possible for  $SO_2$  under atmospheric conditions. They concluded that the reactions with OH,  $HO_2$  and  $RO_2$  radicals and intermediates formed in  $O_3$ -alkene reactions could be important under atmospheric conditions. The reactions of oxygen atoms, while of possible importance in power plant plumes, is surely unimportant for regional scale considerations. Based on experimental data available after the review by Calvert et al. (1978), Atkinson and Lloyd (1980) concluded that the role of  $HO_2$  and  $RO_2$  may not be as large as suggested in previous studies and could possibly be ignored for atmospheric modeling applications. However, further experimental data are needed before this conclusion can be finalized and the recent work of Kan et al. (1981) clearly indicates that significant uncertainties exist for the role of  $RO_2$  radicals.

The remainder of this section summarizes the current knowledge of the species which, based on recent reviews, may be important in the gas phase oxidation of  $\text{SO}_2$ . The section concludes with recommendations for species to be included in current modeling efforts of homogeneous gas phase oxidation of  $\text{SO}_2$ .

#### 6.2.1.8.1 Reaction of $\text{SO}_2$ with the OH Radical

The most important gas phase reaction for  $\text{SO}_2$  oxidation (Calvert et al. 1978; Altshuller 1979) is:



The reaction is in the fall-off region between second and third order kinetics at the pressures encountered under ambient conditions (Atkinson et al. 1976). From a review and evaluation of the literature data, Calvert et al. (1978) recommended a bimolecular rate constant at 1 atmosphere of air and 298°K of:

$$k_{53} = (1.1 \pm 0.3) \times 10^{-12} \text{ cm}^3 \text{ molecule}^{-1} \text{ sec}^{-1}$$

while Davis et al. (1979) have estimated, that at 1 atmosphere of  $\text{N}_2$  and at 298°K,

$$k_{53} = 9 \times 10^{-13} \text{ cm}^3 \text{ molecule}^{-1} \text{ sec}^{-1}$$

with an estimated uncertainty of a factor of -1.5, -2.5.

The data of Davis et al. (1979) were included in the review and evaluation of Calvert et al. (1978). The most recent kinetic study of the reaction was carried out by Harris et al. (1980), using a flash photolysis - resonance fluorescence technique. Rate constants were obtained for  $\text{M} = \text{Ar}$  and  $\text{SF}_6$  over the temperature range 298 - 424°K at total pressure of 98 - 653 torr total pressure the Arrhenius expressions:

$$k_{53} (M=\text{Ar}) = 1.16 \times 10^{-14} e^{(1193 \pm 150)/T} \text{cm}^3 \text{molecule}^{-1} \text{sec}^{-1}$$

and

$$k_{53} (M=\text{SF}_6) = 1.27 \times 10^{-13} e^{(752 \pm 150)/T} \text{cm}^3 \text{molecule}^{-1} \text{sec}^{-1}$$

were obtained, with bimolecular rate constants at 298°K and approximately 650 torr of:

$$k_{53} (M=\text{Ar}) = (6.5 \pm 0.8) \times 10^{-13} \text{cm}^3 \text{molecule}^{-1} \text{sec}^{-1}$$

(in excellent agreement with previous data of Atkinson et al. 1976);  
and

$$k_{53} (M=\text{SF}_6) = (1.6 \pm 0.2) \times 10^{-12} \text{cm}^3 \text{molecule}^{-1} \text{sec}^{-1}$$

By assuming that air has a third body efficiency intermediate between those for Ar and SF<sub>6</sub>, a rate constant of:

$$k_{53} (M=\text{air}) = 4 \times 10^{-14} e^{956/T} \text{cm}^3 \text{molecule}^{-1} \text{sec}^{-1}$$

at approximately atmospheric pressure was estimated, with

$$k_{53} (M=\text{air}) = 1.0 \times 10^{-12} \text{cm}^3 \text{molecule}^{-1} \text{sec}^{-1}$$

at 298°K and approximately 650 torr.

Atkinson and Lloyd (1980) recommend that at atmospheric pressure

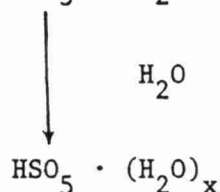
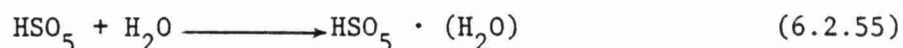
$$k_{53} (M=\text{air}) = 1.0 \times 10^{-12} \text{cm}^3 \text{molecule}^{-1} \text{sec}^{-1}$$

at 298°K with an uncertainty of  $\pm$  a factor 1.5 and (Harris et al. (1980)

$$k_{53}(\text{M=air}) = 1.0 \times 10^{-12} (\text{T}/298)^{-2.7} \text{cm}^3 \text{molecule}^{-1} \text{sec}^{-1}$$

The subsequent fate of the  $\text{HSO}_3$  radicals has been discussed by Davis et al. (1979), and investigated, using long path FTIR spectroscopy, by Niki et al. (1980).

Davis et al. (1979) suggest the following sequence of reactions of  $\text{HSO}_3$ :



followed by possible reaction with  $\text{NO}$ ,  $\text{SO}_2$ , etc. These reactions are most likely gas-aerosol in nature and would contribute to visibility degradation. The FTIR spectroscopic study of Niki et al. (1980) is consistent with such a sequence of reactions. In irradiated  $\text{Cl}_2\text{-H}_2\text{-NO-SO}_2\text{-air}$  mixtures, where the dominant reactive species is the OH radical,  $\text{SO}_2$  was observed to disappear, with the appearance of infrared absorption bands attributable to  $\text{H}_2\text{SO}_4$  (dry and ~20% hydrated) in the aerosol phase. It was suggested (Niki et al. 1980) that formation of  $\text{H}_2\text{SO}_4$  from the  $\text{HSO}_5$  radical could occur via the reaction sequence:

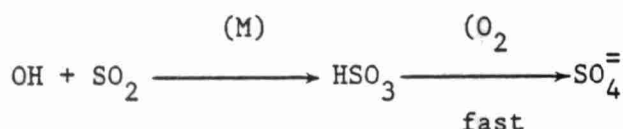


However, the study of Niki et al. (1980) was carried out at ppm ( $\sim 10^{14}$  molecule  $\text{cm}^{-3}$ ) concentrations of  $\text{H}_2\text{O}$  vapor, and under ambient atmospheric conditions, where  $\text{H}_2\text{O}$  concentrations are  $\geq 10^{17}$  molecule

cm<sup>-3</sup>, the fate of the HSO<sub>5</sub> radical may be as suggested by Davis et al. (1979), in that hydration may predominate over reaction with NO.

In summary, it appears that the rate determining step in the conversion of SO<sub>2</sub> to sulfate by reaction with OH is the initial step, i.e., the addition of OH radicals to SO<sub>2</sub>. Subsequent reactions of SO<sub>2</sub>, NO, NO<sub>2</sub>, with hydrated HSO<sub>5</sub> species are uncertain and may involve gas-liquid or gas-aerosol chemistry.

For application to sulfate modeling studies, it is reasonable to assume that the HSO<sub>3</sub> radical rapidly reacts with O<sub>2</sub> and hydrates to (ultimately) form sulfate aerosol: i.e.,



#### 6.2.1.8.2 O<sub>3</sub>-Alkene-SO<sub>2</sub> Mixtures

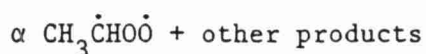
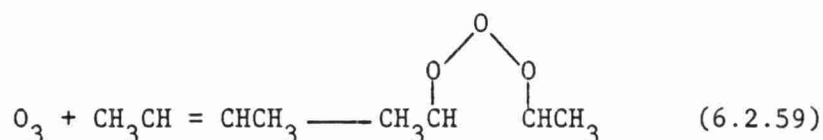
The oxidation of SO<sub>2</sub> by intermediates in O<sub>3</sub>-alkene reaction mixtures may be a significant reaction in polluted urban atmospheres under certain conditions or possibly where O<sub>3</sub> in air masses pass over areas of biogenic hydrocarbon emissions. It appears that SO<sub>2</sub> oxidation occurs via:



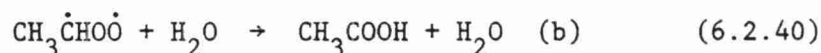
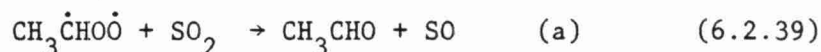
(Niki et al. 1977, Su et al. 1980).

A key earlier investigation was that of Cox and Penkett (1972) who studied O<sub>3</sub>-alkene-SO<sub>2</sub>-H<sub>2</sub>O-air systems at atmospheric pressure to elucidate the amount of thermalized biradicals found under these experimental conditions. They showed that an intermediate was capable of oxidizing SO<sub>2</sub> to (ultimately) H<sub>2</sub>SO<sub>4</sub> aerosols, and it was noted that aldehyde yields were increased in the presence of SO<sub>2</sub>, indicating that this intermediate reacts with SO<sub>2</sub> to yield the aldehyde and (presumably) SO<sub>3</sub>. A substantial effect of relative humidity was noted, with the conversion of SO<sub>2</sub> to H<sub>2</sub>SO<sub>4</sub> aerosol (relative to the O<sub>3</sub>

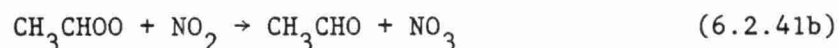
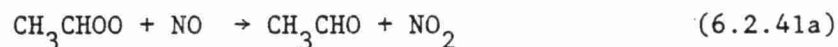
+ alkene reaction rate) decreasing with increasing relative humidity (at constant temperature). Calvert et al. (1978) have reviewed and reevaluated this data of Cox and Penkett (1972) and, by a slight extension of Cox and Penkett's (1972) suggested mechanism, postulated that [taking cis-2-butene, and an example and simplifying the mechanism of Calvert et al. (1978)]:



(where  $\alpha$  is the fraction of thermalized  $\text{CH}_3\dot{\text{C}}\text{HO}\dot{\text{O}}$  radicals (formed), followed by reactions of thermalized  $\text{CH}_3\dot{\text{C}}\text{HO}\dot{\text{O}}$  biradicals:



In the atmosphere, in addition to  $\text{H}_2\text{O}$ , other competing reactions are:



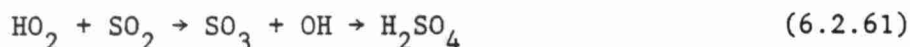
and it is not clear whether this  $\text{SO}_2$  oxidation reaction is important under atmospheric conditions. Calvert et al. (1978), neglecting any reactions of this Criegee biradical with  $\text{NO}$  or  $\text{NO}_2$ , conclude that this route for  $\text{SO}_2$  oxidation is probably minor. Conclusions from inclusion



of the  $RR'\ddot{C}OO + NO_x$  reactions are complicated because the rate constants for these reactions are not known. In the absence of experimental data, Atkinson and Lloyd (1980) assume that they are similar to those for alkylperoxy radicals, namely  $\sim 7 \times 10^{-12} \text{ cm}^3 \text{ molecule}^{-1} \text{ sec}^{-1}$  at 298°K with an uncertainty of at best a factor of 10. Based on more recent data, Kan et al. (1981) conclude that reactions of  $SO_2$  with  $CH_2O_2$  will proceed under certain atmospheric conditions, the actual importance depending on competition for  $CH_2O_2$  by HCHO, NO,  $NO_2$  and  $H_2O$ .

Based on the above discussion, it appears important for modeling to include reactions of the Criegee biradical, particularly that from the longer lived alkenes such as  $C_2H_4$ .

#### 6.2.1.8.3 Reaction of $SO_2$ with $HO_2$ Radicals



has been considered to be nearly as important as OH reactions. However, recent experimental data suggests that the previous experimental measurements upon which this conclusion was based may be too high.

At the time of the Calvert et al. (1978) review article, the sole study of the reaction of  $HO_2$  radicals with  $SO_2$  was that of Payne et al. (1973), who obtained, using an isotope labeling relative rate technique, a rate constant of:

$$k_{61} = (8.4 \pm 1.8) \times 10^{-16} \text{ cm}^3 \text{ molecule}^{-1} \text{ sec}^{-1}$$

at 300°K (relative to  $k(HO_2 + HO_2) = 3.1 \times 10^{-12} \text{ cm}^3 \text{ molecule}^{-1} \text{ sec}^{-1}$ ; see reaction 31).

More recently, Thrush and coworkers (Burrows et al. 1979) have obtained, using a discharge flow system with laser magnetic resonance (LMR) spectroscopic detection of  $HO_2$ , upper limits of

$$k_{61}^{bi} \leq 2 \times 10^{-17} \text{ cm}^3 \text{ molecule}^{-1} \text{ sec}^{-1} \text{ at } 298^\circ\text{K}$$

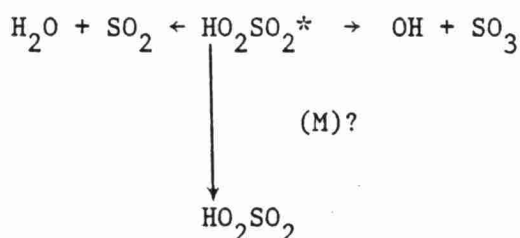
$$k_{61}^{tri}(\text{M} = \text{He} + \text{SO}_2) \leq 4 \times 10^{-34} \text{ cm}^6 \text{ molecule}^{-2} \text{ sec}^{-1} \text{ at } 298^\circ\text{K}$$

while Graham et al. (1979), from the rates of disappearance of  $\text{HO}_2\text{NO}_2$  in the presence and absence of  $\text{SO}_2$ , obtained:

$$k_{61}^{bi} \leq 1 \times 10^{-18} \text{ cm}^3 \text{ molecule}^{-1} \text{ sec}^{-1}$$

at  $300^\circ\text{K}$  and 760 torr total pressure (mainly  $\text{N}_2$ ). We recommend this upper limit. Thus, it appears that this reaction can be neglected under atmospheric conditions (Graham et al. 1979). Niki (1979a) has also reported experimental evidence which indicates that the reaction of  $\text{HO}_2$  radicals with  $\text{SO}_2$  is very slow.

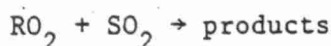
It is likely that the reaction would proceed via the sequence:



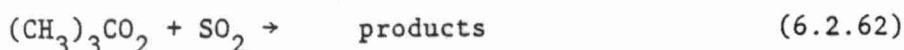
Benson (1978) estimates that  $\Delta H_f(\text{HO}_2\text{SO}_2) = -73 \pm 4 \text{ kcal mole}^{-1}$  so that formation of  $\text{HO}_2\text{SO}_2$  is approximately  $3 \pm 6 \text{ kcal mole}^{-1}$  exothermic. Hence, this intermediate adduct ( $\text{HO}_2\text{SO}_2$ ) should not be stable (even when thermalized) and should either redissociate to  $\text{HO}_2 + \text{SO}_2$  or form  $\text{OH} + \text{SO}_3$ . The low upper limit observed for the rate constant then implies either a substantial energy barrier (of the order of  $> 8 \text{ kcal mole}^{-1}$ ) in the exit channel from  $\text{HO}_2\text{SO}_2$  to  $\text{OH} + \text{SO}_3$  or that redissociation to  $\text{HO}_2 + \text{SO}_2$  is much favored over formation of  $\text{SO}_3 + \text{OH}$  (as is somewhat expected on the basis of the respective entropy changes).

#### 6.2.1.8.4 The Reaction of SO<sub>2</sub> with Alkylperoxy Radicals

The reaction



can produce sulfates. The rate constant for t-butoxy radical reaction with SO<sub>2</sub>



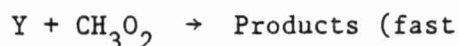
has been reviewed by Whitbeck et al. (quoted in Calvert et al. 1978) using a flash photolysis study. An upper limit value of  $7.3 \times 10^{-11} \text{ cm}^3 \text{ molecule}^{-1} \text{ s}^{-1}$  was determined making the contributions of this route to SO<sub>2</sub> oxidation negligible.

To date, experimental data for CH<sub>3</sub>O<sub>2</sub>, the most important species in terms of likely atmospheric abundance, are not definitive. Both Kan et al. (1979) and Sanhueza et al. (1979), using flash photolysis techniques, have obtained rate constants of  $1.06 \times 10^{-14} \text{ cm}^3 \text{ molecule}^{-1} \text{ sec}^{-1}$  and  $8.2 \times 10^{-15} \text{ cm}^3 \text{ molecule}^{-1} \text{ sec}^{-1}$ , respectively, at room temperature for the reaction of methylperoxy radicals with SO<sub>2</sub>.

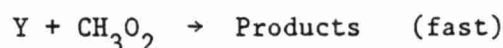
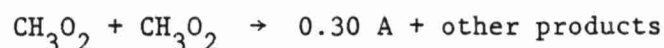
Kan et al. (1979) monitored the time dependence of CH<sub>3</sub>O<sub>2</sub> radicals after flash photolysis of CH<sub>3</sub>N<sub>2</sub>CH<sub>3</sub>O<sub>2</sub>-SO<sub>2</sub> mixtures, and ascribed the suppression of the CH<sub>3</sub>O<sub>2</sub> absorbance in the presence of SO<sub>2</sub> of reaction of CH<sub>3</sub>O<sub>2</sub> radicals with SO<sub>2</sub>. Because of the onset of aerosol formation, the range of SO<sub>2</sub> pressures studied was small ( $\leq 0.20$  torr), resulting in an effective observed extra first order rate of removal of CH<sub>3</sub>O<sub>2</sub> radicals of  $\sim 40 \text{ sec}^{-1}$ , which was a relatively small perturbation of the "average" pseudo-first order decay rate of CH<sub>3</sub>O<sub>2</sub> radicals due to self-combination of  $\sim 400 \text{ sec}^{-1}$  over the first half-life [CH<sub>3</sub>O<sub>2</sub> initial  $\sim 10^{15} \text{ molecule cm}^{-3}$ ]. The rate constant for reaction of CH<sub>3</sub>O<sub>2</sub> radicals with SO<sub>2</sub>, if any, was determined from the CH<sub>3</sub>O<sub>2</sub> decay rates at longish times after the flash.

The experimental system of Sanhueza et al. (1979) was potentially more direct involving the flash photolysis of Cl<sub>2</sub>-CH<sub>4</sub>-O<sub>2</sub>-SO<sub>2</sub> mixtures. Experiments were carried out with and

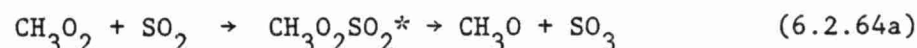
without added  $\text{SO}_2$ , and the  $\text{CH}_3\text{O}_2$  decays (initial  $[\text{CH}_3\text{O}_2] \sim [3-4] \times 10^{15} \text{ molecule cm}^{-3}$ ) were observed to change from second order to first order kinetics when  $\geq 6$  torr  $\text{SO}_2$  was added. However, a first-order plot of their data with and without  $\text{SO}_2$  shows that the increased  $\text{CH}_3\text{O}_2$  radicals in the systems with added  $\text{SO}_2$  (Atkinson and Lloyd 1980). It is possible that the increased decay of  $\text{CH}_3\text{O}_2$  radicals after  $\sim 0.3 \text{ m sec}$  is caused by secondary reactions such as:



The Sanhueza et al. (1979) data could apparently be fitted with an  $\sim 30\%$  yield of A, i.e.,



Sander and Watson (1981), from the flash photolysis of  $\text{Cl}_2\text{-CH}_4\text{-O}_2\text{-SO}_2$  mixtures (but with much reduced initial  $\text{CH}_3\text{O}_2$  concentrations), observed no reaction, such that  $k_{\text{CH}_3\text{O}_2 + \text{SO}_2} < 10^{-16} \text{ cm}^3 \text{ molecule}^{-1} \text{ sec}^{-1}$  at room temperature. Analogous to the  $\text{HO}_2$  case, any reaction sequence is expected to be :



with the formation of  $\text{RO}_2\text{SO}_2$  being  $4 \pm 4 \text{ kcal mole}^{-1}$  exothermic (Benson 1978), and hence, probably not stable under ambient



conditions. Kan et al. (1981) carried out further studies to resolve the discrepancy between the various studies. They found that the reaction was dependent on flash intensity or  $\text{CH}_3\text{O}_2$  concentrations. While it was demonstrated that  $\text{CH}_3\text{O}_2$  reacted with  $\text{SO}_2$ , lack of observation of  $\text{SO}_3$  or  $\text{H}_2\text{SO}_4$  in the primary products indicated that reaction (b) is the only pathway for this reaction under the conditions employed. The authors conclude that the net oxidation of  $\text{SO}_2$  by  $\text{CH}_3\text{O}_2$  depends on the concentration of  $\text{CH}_3\text{O}_2$  radicals, NO and other species. The implication of these results for atmospheric concentrations of NO is under investigation according to Kan et al. (1981).

Based on the above results, the role of  $\text{CH}_3\text{O}_2$  in  $\text{SO}_2$  oxidation is uncertain. Kan et al. (1981) indicate that in latter studies, Heicklen and coworkers also find  $k_{\text{CH}_3\text{O}_2+\text{SO}_2} \leq 5 \times 10^{-17} \text{ cm}^3 \text{ molecule}^{-1} \text{ sec}^{-1}$ . Until the current uncertainty is resolved, it is recommended that the reaction of  $\text{RO}_2$  radicals with  $\text{SO}_2$  under atmospheric conditions be neglected. This does introduce uncertainty into the chemical calculations.

#### 6.2.1.8.5 Biogenic Sulfur Compounds as Sources of $\text{SO}_2$

Although biogenic sulfur emissions are probably an order of magnitude less than anthropogenic sulfur emissions (Golloway and Whelpdale 1980), the biogenic emissions are important in understanding the S cycle and should be considered in the acid precipitation context. Typical compounds are hydrogen sulfide,  $\text{H}_2\text{S}$  and methyl sulfide  $\text{CH}_3\text{SCH}_3$ , both of which have been observed at significant concentrations in the atmosphere.

The major reaction route for  $\text{H}_2\text{S}$  is reactions with the OH radical in H atom abstraction. Sulfate is ultimately formed via  $\text{SO}_2$  formation in the probable sequence of reactions:





Several workers have reviewed the rate constant for the initial attack of OH on H<sub>2</sub>S, the two most recent being Liu (1982) and Wine et al. (1981). Previous work is summarized in their papers - room temperature rate constants range from 3.1 to 5.5 x 10<sup>-12</sup> cm<sup>3</sup> molecule<sup>-1</sup> sec<sup>-1</sup>. Based on an average OH radical concentration of 2 x 10<sup>6</sup> radicals cm<sup>-2</sup>, Wine et al. estimate a lifetime for H<sub>2</sub>S of 27 hours.

Similarly, based on a rate constant determination of 4.15 x 10<sup>-12</sup> cm<sup>3</sup> molecule<sup>-1</sup> s<sup>-1</sup> and the same OH radical concentration, Wine et al. (1981) calculate a lifetime of methyl sulfide CH<sub>3</sub>SCH<sub>3</sub> of 33 hours for the reaction:



This reaction has recently been studied by Grosjean and Lewis (1982) under atmospheric conditions in the presence of NO<sub>x</sub>, using environmental chambers. Methyl sulfide was introduced into an outdoor environmental chamber along with NO<sub>x</sub> and irradiated by natural sunlight. Products identified included formaldehyde, methyl nitrate and sulfur dioxide. The identification of SO<sub>2</sub> as a product differed from the results of the study by Cox and Sandells (1974). Grosjean and Lewis conclude that nonanthropogenic sources of CH<sub>3</sub>SCH<sub>3</sub> may contribute to acid precipitation in remote locations.

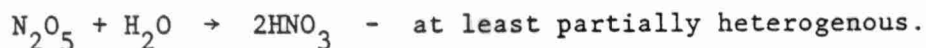
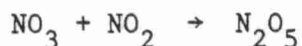
While the rate constants for the initial attack on H<sub>2</sub>S and CH<sub>3</sub>SCH<sub>3</sub> do not lead to rapid formation of SO<sub>2</sub> from this work, other natural S compounds such as methyl mercaptan and dimethyl disulfide are predicted to have significantly shorter lifetimes of 4.1 hours and 42 minutes, respectively (Wine et al. 1981). It is considered that for the purposes of the current modeling, biogenic S emission sources are of minor importance. However, the decision for their inclusion should be assessed on a regional case-by-case basis.

### 6.2.2 Heterogeneous Oxidation

This section is devoted to the oxidation of  $\text{NO}_x$  and  $\text{SO}_x$  emissions occurring on particles, i.e., oxidation of gases on dry particles. This differs from the reactions in aqueous solution (discussed in Section 6.3), which may be catalyzed by the same species discussed here. This class of reaction could be important because of anthropogenic particle emissions (e.g., fly ash, particles from diesel fuel vehicles) and natural sources of particles (e.g., wind blown soil including minerals).

#### 6.2.2.1 $\text{NO}_x$ Oxidation

The conversion of  $\text{NO}_x$  emissions to  $\text{HNO}_3$  on surfaces has not received much study. The only reaction of a heterogeneous nature of particular significance is the reaction sequence:



The importance of the heterogeneous component of the last reaction route for  $\text{HNO}_3$  formation is uncertain. The reaction is included in the basic photochemical reaction list, but the rate constant assumed is based largely on the expected homogeneous rate measurements.

#### 6.2.2.2 $\text{SO}_2$ Oxidation

Several workers have studied the oxidation of  $\text{SO}_2$  on different surfaces. In general, two types of reaction mechanisms occur: a capacity limited reaction and a catalytic reaction. In both cases the initial reaction on the surface produces a rapid loss of  $\text{SO}_2$  from the gas phase followed by:

- the reaction rate decreasing to zero for the capacity limited case, and
- the reaction rate levels off and then approaches zero for the catalytic route. This behavior is attributed to a pH decrease caused by sulfuric acid formation.

Urone et al. (1968) and Smith et al. (1969) examined the effectiveness of a number of solid particles in removing  $\text{SO}_2$ . Urone et al. (1968) exposed ferric oxide, magnetic, lead oxide, lead dioxide, calcium oxide and aluminum oxide solids to  $\text{SO}_2$  gas in a flash. Ferric oxide was the most reactive species in removing  $\text{SO}_2$ , but because of the nature of the exponents which could be diffusion controlled, little useful quantitative data can be obtained.

Benarie et al. (1972) investigated the influence of various parameters on the oxidation of  $\text{SO}_2$  in an urban atmosphere over a six-month (winter and spring) period, in the city of Rouen, France. These workers found the most significant correlation for  $\text{SO}_2$  oxidation to be with the presence of "black smoke" containing  $\text{Cr}_2\text{O}_3$ ,  $\text{Fe}_2\text{O}_3$ ,  $\text{MnO}_2$ ,  $\text{PbO}$ ,  $\text{ZnO}$ , and  $\text{CuO}$ . They found no correlation with  $\text{NO}_2$  and only a slight correlation with ammonia in the atmosphere. Novakov et al. (1974) studied the oxidation of  $\text{SO}_2$  over finely divided carbon (soot) particles and showed that increased oxidation of  $\text{SO}_2$  occurred. This catalytic formation of sulfate on soot particles was identified before similar studies were carried out in the presence of water vapor as discussed in the next section. The results showed that graphite and soot particles oxidize  $\text{SO}_2$  in air and that the process exhibits a significant saturation effect; that is, the efficiency of the catalytic conversion is considerably reduced with time. This phenomenon is attributed to the saturation of the particles by  $\text{SO}_2$  vapor.

Judeikis and coworkers (1974, 1978) have also identified such saturation effects in their work. They studied the rate of removal of gaseous  $\text{SO}_2$  over different solids whose composition was typical of those encountered in ambient aerosols. A tubular flow reactor, in which the walls of an inner, concentric cylinder were coated with the solid under investigation was used in these studies. The relative



humidity in these systems was found to be important in determining the total amount, but not the initial rate, of  $\text{SO}_2$  uptake. The  $\text{SO}_2$  uptake increases at higher humidity. The initial calculated  $\text{SO}_2$  removal rates decreased in the order of  $\text{MgO}$ ,  $\text{Fe}_2\text{O}_3$ ,  $\text{Al}_2\text{O}_3$ ,  $\text{MnO}_2$ ,  $\text{PbO}$ , and  $\text{NaCl}$ .

Tartarelli et al. (1978) studied the interaction of  $\text{SO}_2$  with carbonaceous particles collected from the flue ducts of oil burning power stations. The workers found that the amount of adsorption is increased by the presence of oxygen and water in the gas stream. No kinetic data were observed in this study.

Liberti et al. (1978) studied the adsorption and oxidation of  $\text{SO}_2$  on various particles, including soot from an oil furnace. Their results indicated that the main interaction between the  $\text{SO}_2$  and particulate matter is adsorption, with most catalytic reactions occurring at high temperature, near the combustion source. Their experiments with atmospheric particulate samples lead them to the conclusion that any heterogeneous nonphotochemical sulfate formation is strongly dependent on the reactivity of the particle surface, and hence the history (aged, freshly emitted), of the aerosol.

Baldwin (1982) studied the rate of adsorption of  $\text{SO}_2$  on a carbonaceous surface at less pressure in a flow reactor. Rapid saturation of the surface by  $\text{SO}_2$  was found, suggesting that this mechanism is of limited importance. A much slower surface reaction, enhanced by the presence of  $\text{NO}_2$  was found. Based on the experimental data, Baldwin calculates a maximum atmospheric loss of  $\text{SO}_2$  by  $\text{SO}_2$  adsorption of  $1\%/\text{hr}^{-1}$  for a particle density of  $100 \mu\text{g}/\text{m}^{-3}$ . However, this loading is recomprised as being very high and hence, the contribution of the reaction to the removal of  $\text{SO}_2$  under atmospheric conditions is probably much lower than the calculation indicates.

In summary, current information on the heterogenous surface catalyzed oxidation indicates that initial oxidation rates may be large but very quickly approach zero. For practical atmospheric applications, the only possible solid surface of importance is carbon or soot. Until more information on the reactions and the atmospheric carbon concentration becomes available, for current modeling purposes,

this class of reaction can be neglected as a significant oxidation route for  $\text{SO}_2$ .

### 6.3 Aqueous-Phase Chemistry and Related Processes

Heterogeneous oxidation rates in cloud-water droplets and hydrometeors (any aqueous cloud particle large enough to leave the cloud under the influence of gravity) are functions of the chemical composition of the aqueous phase. The chemical composition, in turn, is dependent on the concentrations and types of chemical compounds found in the gas phase and in suspended particulate matter and their chemical and physical abilities to enter the aqueous phase. In the following sections, those equilibrium, kinetic and mass-transport processes that are known to be important in determining the chemical composition at any time within cloud-water droplets and hydrometeors will be discussed. The manner in which a chemical equilibrium model with kinetic constraints will be used to describe this complex physical-chemical system will be addressed.

#### 6.3.1 Equilibrium Processes

##### 6.3.1.1 Gas/Liquid Equilibria

###### Soluble Gases

The equilibrium distribution of soluble gases between the gas and aqueous phases is defined by the Henry's law relationship. Considering sulfur compounds in the +4 oxidation state, the S(IV) system, this is expressed as follows.

$$[\text{SO}_2(\text{aq})] = K_H \cdot p_{\text{SO}_2} \quad (6.3.1)$$

where square brackets indicate aqueous concentrations in molar units, (moles  $\ell^{-1}$  or M),  $K_H$  is the Henry's law constant in units of  $\text{M atm}^{-1}$  and  $p_{\text{SO}_2}$  is the partial pressure of  $\text{SO}_2$  in the gas phase in units of atmospheres.  $K_H$  is thus the equilibrium constant for the reaction:



Schwartz (1982) has collected Henry's law constants of some important atmospheric gases capable of dissolving in water. These are shown in Table 6.3-1. The temperature dependence of Henry's law constants for  $\text{SO}_2$ ,  $\text{O}_3$ ,  $\text{H}_2\text{O}_2$  and  $\text{HNO}_2$  has been tabulated by Martin (1982) and are available for  $\text{CO}_2$  in Stumm and Morgan (1981).

### Soluble Particles

Atmospheric particulate matter can also be incorporated into cloud water droplets and hydrometeors. There are pathways, both in-cloud and below-cloud, by which this mass-transfer process occurs.

- Brownian motion,
- phoretic attachment,
- inertial impaction,
- nucleation,
- interception, and
- turbulent diffusion.

In condensing clouds, one should expect nucleation processes to be the dominant mechanism for scavenging of hygroscopic aerosols (Hidy 1973). Non-hygroscopic aerosol scavenging occurs predominantly through turbulent diffusion and inertial impaction both in-cloud and below-cloud. Aqueous-phase concentrations of aerosol-derived chemical compounds will be calculated based on estimated scavenging coefficients and total masses of each chemically distinct aerosol species according to:

$$[\text{X}] = \frac{\varepsilon(\text{X}) \cdot 10^{-3}}{M_{\text{X}} L} \quad (6.3.3)$$

where  $(\text{X})$  is the aerosol mass concentration of chemical compound X in  $\mu\text{g}/\text{m}^3$ ,  $M_{\text{X}}$  its molecular weight,  $\varepsilon$  the estimated scavenging coefficient

TABLE 6.3-1

HENRY'S LAW CONSTANTS OF ATMOSPHERIC GASES CAPABLE OF  
DISSOLVING IN WATER

<u>Gas</u>	<u><math>K_H</math> (M atm<sup>-1</sup>), 25°C</u>
O <sub>2</sub>	1.3 x 10 <sup>-3</sup>
NO	1.9 x 10 <sup>-3</sup>
C <sub>2</sub> H <sub>4</sub>	4.9 x 10 <sup>-3</sup>
NO <sub>2</sub>	1.0 x 10 <sup>-2</sup>
O <sub>3</sub>	1.3 x 10 <sup>-2</sup>
N <sub>2</sub> O	2.5 x 10 <sup>-2</sup>
CO <sub>2</sub>	3.4 x 10 <sup>-2</sup>
SO <sub>2</sub>	1.3 x 10 <sup>0</sup>
HNO <sub>2</sub>	4.9 x 10 <sup>1</sup>
NH <sub>3</sub>	6.2 x 10 <sup>1</sup>
H <sub>2</sub> CO	6.3 x 10 <sup>3</sup>
H <sub>2</sub> O <sub>2</sub>	1.0 x 10 <sup>5</sup>
HNO <sub>3</sub>	2.1 x 10 <sup>5</sup>

and  $L$  the volume fraction of liquid water per  $m^3$  of physical volume ( $cm^3/m^3$ ). This is a first approximation as most atmospheric aerosols are not chemically distinct;  $\epsilon$  is some weighted average based on the actual composition.

Details of the methods by which scavenging coefficients will be estimated for both hygroscopic and non-hygroscopic aerosols, both in-cloud and below-cloud in precipitating and nonprecipitating cloud systems, are presented in Section 7.

#### 6.3.1.2 Aqueous-Phase Equilibria

Once soluble gases and particles (or some portion of them) have dissolved in an aqueous phase, they may undergo further reaction with water itself (i.e., hydrolysis) or with other chemical species which may be present. These latter reactions fall into several broad categories.

- complex formation,
- ion-pairing,
- precipitation-dissolution, and
- adsorption-desorption.

Some reactions in the above categories can be considered in an equilibrium framework if the stoichiometry of the reaction is known (vide infra for the nonequilibrium situation), equilibrium constants are available and a set of components whose total concentrations are known can be defined. As an example, the hydrolysis reactions and corresponding equilibrium constants of a generic diprotic acid,  $H_2X$ , are shown below.



$$K_{a1} = \frac{[HX^-][H^+]}{[H_2X]} \quad (6.3.5)$$



$$K_{a2} = \frac{[\text{X}^{2-}][\text{H}^+]}{[\text{HX}^-]} \quad (6.3.7)$$

The above equations (6.3.5 and 6.3.7) along with a mass balance equation for X

$$X_T = [\text{H}_2\text{X}] + [\text{HX}^-] + [\text{X}^{2-}] \quad (6.3.8)$$

and the ion-product of water,

$$K_W = [\text{H}^+][\text{OH}^-] \quad (6.3.9)$$

allow us to completely define the speciation of  $\text{H}_2\text{X}$  at any pH in a system at equilibrium containing the components  $\text{H}_2\text{X}$  and  $\text{H}_2\text{O}$ . The addition of other components to this system requires an equilibrium constant for each new species to be considered and a mass balance equation for each new component.

The equilibrium constants written here in terms of concentration units are thermodynamically correct only in dilute solutions where activity coefficients approach unity. The manner in which activity coefficients will be corrected when the dilute solution approximation no longer applies is treated in Section 6.3.5.1.

It is extremely difficult to describe equilibrium chemistry in wetted aerosols, where solution concentrations of 8 to 26 M have been measured in Los Angeles by Stelson and Seinfeld (1981), due to the nonideal nature of these concentrated solutions. Stelson and Seinfeld (1982 a,b,c) have considered in detail the equilibrium thermodynamic properties of aqueous systems of nitrate, sulfate, ammonium, nitric and sulfuric acids at concentrations greater than 1 M where solutions are strongly nonideal. While they were able to accurately predict variations in activity coefficients at high ionic strength for these species, allowing them to predict the behavior of systems composed of these compounds, their results cannot be generalized to other

compounds. In addition to having limited knowledge of equilibrium chemistry in concentrated solutions, we know little about the effects of high ionic strengths on rate constants. Middleton et al. (1980) carried out an equilibrium and kinetic study on sulfate aerosol production mechanisms on wetted aerosols in an urban atmosphere. The major difference in the wetted-aerosol aqueous-phase modeled by these investigators and cloud-water droplets was the total amount of liquid water present. While the dilute solution approximation generally holds for cloud-water droplets, it does not apply to concentrated solutions of wetted aerosols. The application of equilibrium and rate constants measured in dilute solutions to wetted aerosols by Middleton et al. (1980) is not appropriate. It is not considered feasible at this time to rigorously attempt to describe the chemistry taking place in wetted aerosols.

#### 6.3.2 Kinetic Processes

Several types of chemical reactions are generally not amenable to an equilibrium description. The criterion for applicability of an equilibrium description to a given chemical reaction involves a comparison of its characteristic reaction time,  $\tau = k^{-1}$ , to some time,  $t$ , characteristic of the next slowest process in the system. An equilibrium treatment is valid when  $t < \tau$ . In many systems, oxidation-reduction (redox), precipitation-dissolution and adsorption-desorption, reactions do not come to equilibrium within the time frame of interest. It then becomes necessary to describe the kinetic behavior of these processes rather than to their equilibrium behavior. In the context of heterogeneous reactions in cloud-water droplets and hydrometeors, the kinetics of most redox processes must be considered. The following sections identify the redox reactions important in determining the composition of the aqueous phase and summarize their rate constants and expressions.

### 6.3.2.1 S(IV) Oxidation

Conversion of anthropogenic  $\text{SO}_2$  to sulfate is thought to be the dominant pathway for production of acidic atmospheric aerosols in eastern North America. Both homogeneous gas-phase processes and heterogeneous reactions taking place in wetted aerosols, cloud-water droplets and hydrometeors contribute to the overall transformation rate.

While scavenging of preexisting sulfate aerosol was observed to account for nearly all cloud and precipitation water sulfate in one case study (Scott and Laulainen 1979), it is usually necessary to invoke a pathway whereby sulfur dioxide gas is absorbed by cloud-water droplets and subsequently oxidized to sulfate in the aqueous phase in order to explain the observed sulfate concentrations in precipitation (e.g., Hales and Dana 1979; Hegg and Hobbs 1981).

The kinetics of aqueous-phase oxidation of S(IV) pertinent to the atmosphere have been the subject of a number of previous reviews (Hegg and Hobbs 1978; Beilke and Gravenhorst 1978; Möller 1980; Seinfeld 1980; Middleton et al. 1980; Chang et al. 1981; Martin 1982; and Schwartz 1982). Consequently, we will focus on evaluation of rate expressions, rate constants and characteristic times for three potentially important pathways, oxidation by  $\text{O}_3$ ,  $\text{H}_2\text{O}_2$  and  $\text{NO}_x$ . The effects of catalytic agents, e.g., trace metals and elemental carbon, on these reactions and on the oxidation of S(IV) by  $\text{O}_2$  is discussed. Critically chosen rate expressions and rate constants are presented. Rates of formation of S(VI) in the atmosphere due to aqueous-phase chemistry are given in the general form:

$$R_i = \frac{dS(\text{VI})}{dt} = - \frac{dS(\text{IV})}{dt} = k^{(2)} K_{H_i} p_i [S(\text{IV})(\text{aq})]_T \quad (6.3.10)$$

where  $R_i$  = is the aqueous phase rate of formation of oxidized sulfur by species  $i$  in  $\text{M sec}^{-1}$ ,

$k^{(2)}$  = is the second-order rate constant for reaction of species  $i$  with S(IV) in the aqueous phase,  $\text{M}^{-1}\text{sec}^{-1}$ ,

$K_H$  and  $p$  = are defined as before, and the term



$[S(IV)(aq)]_T$  = represents the total concentration of aqueous S(IV) species:

$$[S(IV)(aq)]_T = [SO_2(aq)] + [HSO_3^-] + [SO_3^{2-}] \quad (6.3.11)$$

$[S(IV)(aq)]_T$  is a function of the partial pressure of  $SO_2(g)$  and pH and can be defined in terms of these variables and the equilibrium constants for the S(IV) system, (Equation 6.3.1) and Equations 6.3.5 and 6.3.7 replacing X with  $SO_3$ . The results of substituting these equations in Equation 6.3.11 and simplifying yields

$$[S(IV)(aq)]_T = K_H \cdot p_{SO_2} \left[ 1 + \frac{K_{a1}}{[H^+]} + \frac{K_{a1} K_{a2}}{[H^+]^2} \right] \quad (6.3.12)$$

in the absence of mass transport limitations.  $[S(IV)(aq)]_T$  is a convenient and useful way to express the concentration of S(IV) in solution as conversion rates between  $SO_2(aq)$ ,  $HSO_3^-$  and  $SO_3^{2-}$  in solution are fast compared to all oxidation reactions considered here. When the aqueous S(IV) species which is involved in the rate-determining step was known, its concentration was used in place of  $[S(IV)aq]_T$  in equation 6.3.10.

#### Oxidation of S(IV) by $O_3$

The kinetics of the reaction of S(IV) with  $O_3$ , as determined by several investigators (Erikson et al. 1977; Larson et al. 1978; Penkett et al. 1979; Maahs 1982 and Martin 1982), can be expressed in terms of a second-order rate expression:

$$R_{O_3} = - \frac{d[S(IV)]}{dt} = k^{(2)} [O_3(aq)] [S(IV)(aq)]_T \quad (6.3.13)$$

The dependence of the second-order rate constant  $k^{(2)}$  upon solution pH is shown in Figure 6.3.1. There is considerable agreement among these data with the exception of the data of Larson et al. (1978) which are somewhat lower than the others and the data at a pH value of 5. Examination of the experimental conditions of Larson et al. suggests two explanations for their lower values. Their data were taken at much lower ozone concentrations,  $10^{-8}$  to  $10^{-9}$  M (which is more representative of ambient conditions) as compared to  $10^{-4}$  to  $10^{-5}$  M in the other studies, indicating a possible concentration sensitivity in the rate expression. Further, the convective mixing rate of their apparatus, while not specified, may not have been sufficient to eliminate mass transport as a rate-limiting process. The rate constant measured by Maahs (1982) at a pH value of 5 is approximately five times that measured by Penkett et al. (1979). Penkett et al. measured the rate constant in an unbuffered solution in which  $[O_3(aq)]$  was twice  $[H^+]$ . As S(IV) oxidation proceeds, hydrogen ions are produced, lowering the pH, which would tend to underestimate the rate constant in unbuffered experiments. The rate constant of Maahs is believed to be more accurate at a pH value of 5.

Two values for  $k^{(2)}$  are necessary to describe the data over the pH range 0 to 7. For low pH, 0 to 3, the rate constant of Martin (1982),  $1.9 \times 10^4 [H^+]^{-0.5}$ , will be used while at pH values of 3 to 7, the rate constant of Maahs (1982),  $4.19 \times 10^5 (1 + 2.39 \times 10^{-4} [H^+]^{-1})$ , is recommended.

Schwartz (1982) has evaluated oxidation rates of S(IV) by ozone under representative atmospheric conditions, 30 ppb  $O_3$ , using values of  $k^{(2)}$  between those of Erikson et al. and Penkett et al. The results of his calculations are shown in Figure 6.3.2. The aqueous-phase oxidation rate,  $R$ , per ppb  $SO_2$ , is shown on the left-hand ordinate and the gas-phase rate,  $\rho/L$ , per  $cm^3 m^{-3}$  liquid water volume fraction, is shown on the right-hand ordinate. These rates scale linearly with  $p_{O_3}$ . A strong pH dependence is seen reflecting S(IV) solubility as well as the pH dependence of  $k^{(2)}$ ,

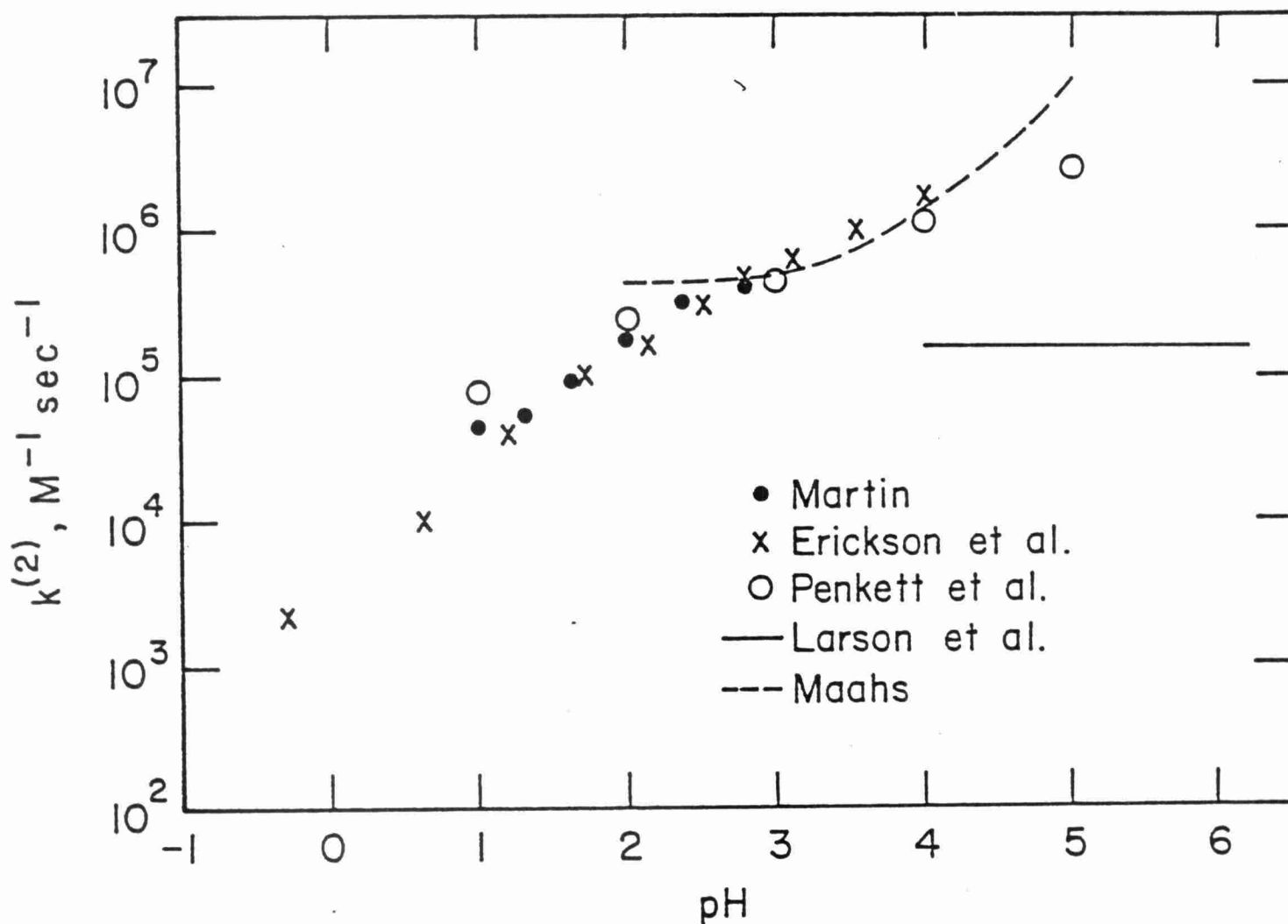


Figure 6.3.1. Second-order rate constant,  $k^{(2)}$ , for oxidation of S(IV) by  $O_3$  according to  $-d[S(IV)]/dt = k^{(2)}[O_3(aq)][S(IV)aq]_T$  as a function of solution pH. Data of Erickson (1977), Larson et al. (1978), Penkett et al. (1979), Maahs (1982) and Martin (1982). Temperature = 25°C.

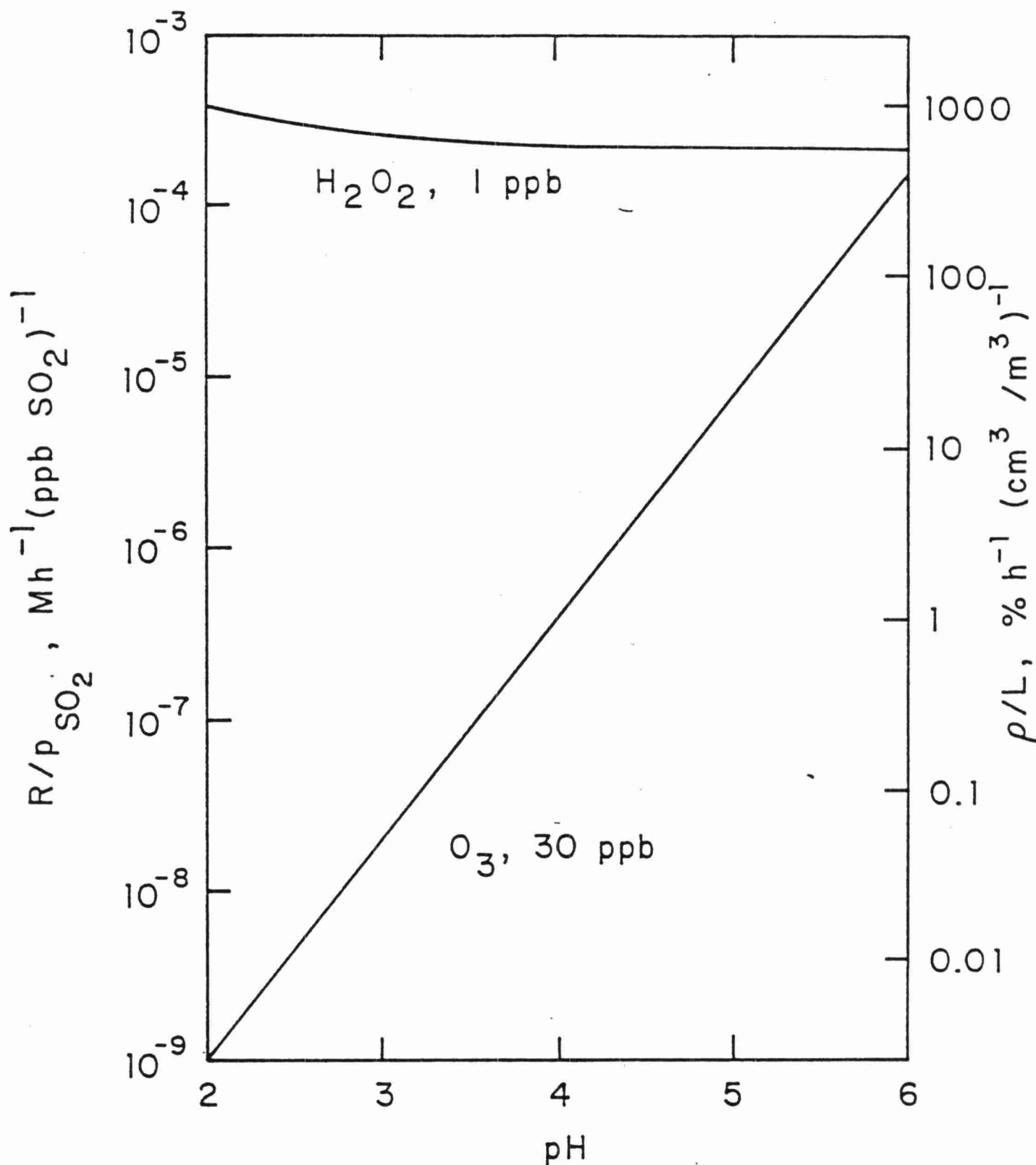


Figure 6.3.2. Rate of aqueous-phase oxidation of S(IV) by  $\text{O}_3$  (30 ppb) as a function of solution pH. Gas aqueous equilibria are assumed for all reagents.  $R/p_{\text{SO}_2}$  represents aqueous reaction rate per ppb of gas-phase  $\text{SO}_2$ .  $\rho/L$  represents rate of reaction referred to gas phase  $\text{SO}_2$  partial pressure, per  $\text{cm}^3/\text{m}^3$  liquid water volume fraction. (From S. Schwartz 1982, reproduced with permission.)

which will cause the overall reaction,  $\text{HSO}_3^- + \text{O}_3 \rightarrow \text{SO}_4^{2-} + \text{H}^+ + \text{O}_2$ , to be self-limiting due to the net acidity produced.

Martin (1982) found no sensitivity of the ozone reaction to metal ion catalysis by  $\text{Fe}^{3+}$ ,  $\text{Mn}^{2+}$ ,  $\text{VO}^{2+}$  or  $\text{Cu}^{2+}$ . A modest rate increase due to catalysis by manganese and iron has been reported by Harrison et al. (1982).

#### Oxidation of S(IV) by $\text{H}_2\text{O}_2$

The kinetics of the reaction of S(IV) with  $\text{H}_2\text{O}_2$ , again as determined by several investigators (Mader 1958; Hoffman and Edwards 1975; Penkett et al. 1979 and Martin and Damschen 1981) can be expressed in terms of a second-order rate expression.

$$R_{\text{H}_2\text{O}_2} = - \frac{d\text{S(IV)}}{dt} = k^{(2)} [\text{H}_2\text{O}_2(\text{aq})] [\text{SO}_2(\text{aq})] \quad (6.3.14)$$

The dependence of this second-order rate constant upon solution pH is shown in Figure 6.3.3, corrected for temperature and the effect of buffer catalysis. These data agree well with the solid curve generated using the rate expression of Martin and Damschen (1981) with a value of  $k^{(2)}$  of  $(8 \pm 2 \times 10^4)(0.1 + [\text{H}^+])^{-1}$ , except in the pH range 5 to 6 where the curve underpredicts the experimental data. The dashed portion of the curve includes a sulfite ion term according to Mader (1958).

Schwartz (1982) also has evaluated oxidation rates of S(IV) by  $\text{H}_2\text{O}_2$  under representative atmospheric conditions, 1 ppb  $\text{H}_2\text{O}_2$ . The results of his calculations are shown in Figure 6.3.2. Analogously to the case for  $\text{O}_3$ ,  $R$  and  $\rho$  scale linearly with  $p_{\text{H}_2\text{O}_2}$ . Under these conditions, the transformation of  $\text{SO}_2$  to sulfate is dominated by  $\text{H}_2\text{O}_2$  oxidation over the pH range 1 to 5. The lack of pH-dependent behavior in the  $\text{H}_2\text{O}_2$  system results from the balance between a decreasing  $k^{(2)}$  as a function of pH and an increasing  $[\text{S(IV)(aq)}]_T$  as a function of pH.

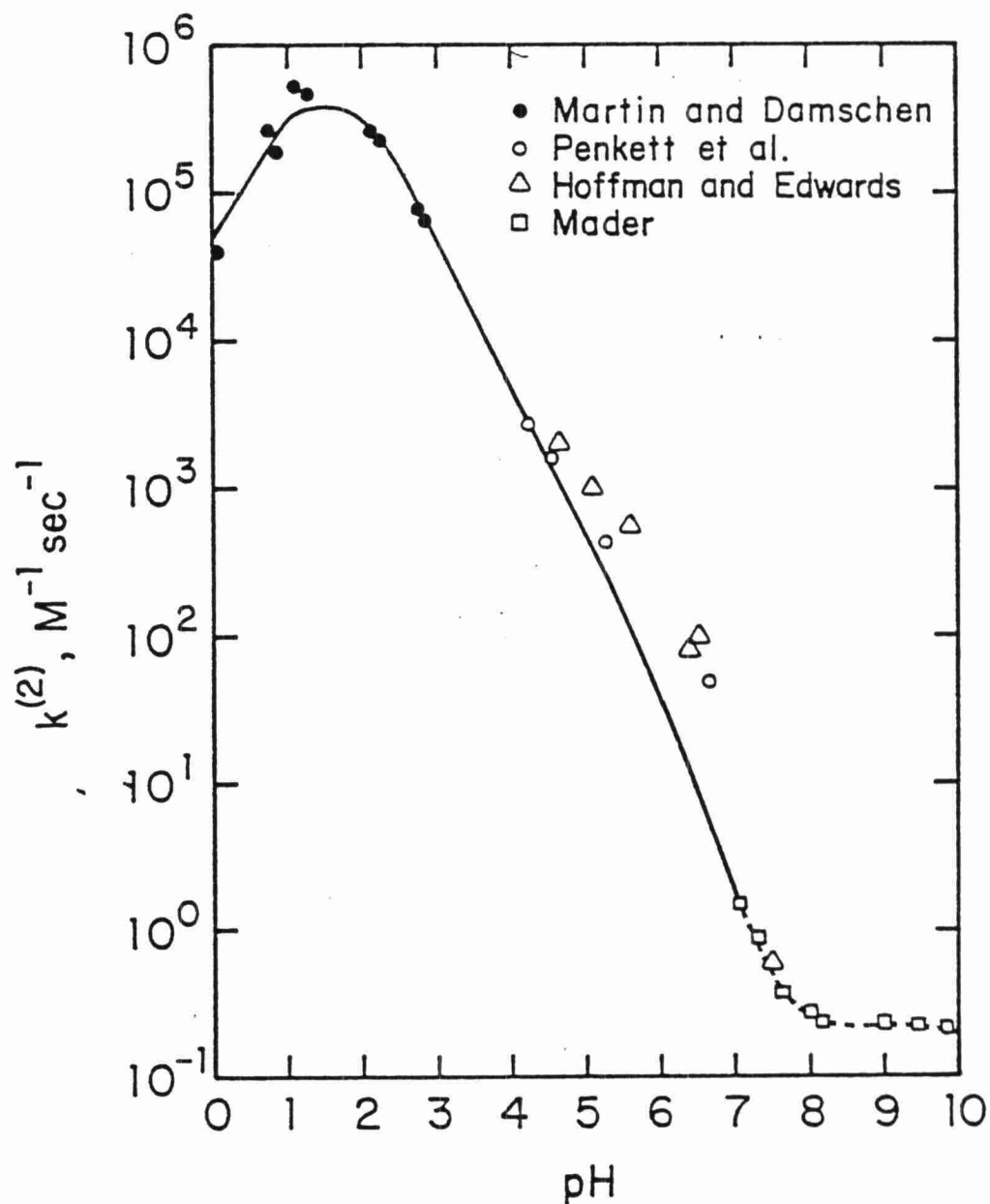


Figure 6.3.3. Second-order rate constant,  $k^{(2)}$ , for oxidation of S(IV) by  $H_2O_2$  according to  $-d[S(IV)]/dt = k [H_2O_2(aq)][S(IV)_{aq}]_T$  as a function of solution pH. Data of Mader (1958), Hoffman and Edwards (1975), Penkett et al. (1979) and Martin and Damschen (1981). Temperature = 25°C. The effect of buffer catalysis has been removed.

The concentration of  $\text{H}_2\text{O}_2$  used in this model calculation was obtained from modeling work on photochemically reactive systems by Möller (1980) and Rhode et al. (1981). The available data on measured atmospheric concentrations of  $\text{H}_2\text{O}_2$  gathered using analytical methods employing an aqueous trapping technique are now believed to be invalid (Zika and Saltzman 1982; Heikes et al. 1982). They reported  $\text{O}_3$  to be a serious interferent in these methods, reacting with water in the impingers to producing  $\text{H}_2\text{O}_2$  according to the following mechanism (Hoigne and Bader 1976).



Ozone also can react with  $\text{H}_2\text{O}_2$  which has been already captured (Marschalein 1977):



An additional aqueous-phase pathway for the formation of  $\text{H}_2\text{O}_2$  may involve direct reaction of gas-phase free radicals with the aqueous aerosol (Chameides and Davis 1982).

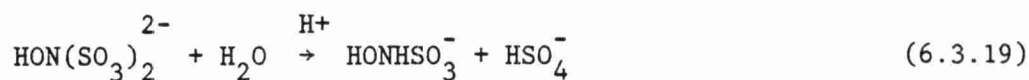
#### Oxidation of S(IV) by $\text{NO}_x$

Reactions of S(IV) with  $\text{NO}$ ,  $\text{NO}_2$ ,  $\text{HNO}_2$  and  $\text{HNO}_3$  have been studied to a much lesser degree than was the case for  $\text{O}_3$  and  $\text{H}_2\text{O}_2$ . Relevant work has been done by Takeuchi et al. (1977), Nash 1979, Sato et al. (1979), Chang et al. (1981), Martin et al. (1981), Lee and Schwartz (1981a) and Schwartz and White (1982). Martin et al. (1981) observed that  $\text{NO}(\text{aq})$  and  $\text{NO}_3^-$  are essentially unreactive with S(IV) at representative atmospheric concentrations. They set an upper limit on the second-order rate constant of  $0.01 \text{ M}^{-1} \text{ sec}^{-1}$  for both reactions. Nitric acid was also found to be unreactive with S(IV) in the presence of  $\text{Fe}^{3+}$ ,  $\text{Mn}^{2+}$ ,  $\text{Cu}^{2+}$ ,  $\text{Co}^{2+}$ ,  $\text{Pb}^{2+}$  or  $\text{VO}^{2+}$ .

Reaction of S(IV) with nitrous acid ( $\text{HNO}_2$ ), studied by Oblath et al. (1980), Martin et al. (1981) and Chang et al. (1981) is considerably faster than reaction with NO or  $\text{HNO}_3$ . For the rate expression:

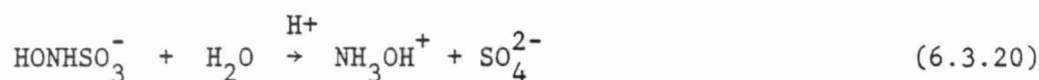
$$R_{\text{HNO}_2} = - \frac{dS(\text{IV})}{dt} = k^{(2)} [\text{N(III)(aq)}][\text{S(IV)(aq)}]_T \quad (6.3.18)$$

Martin et al. determined a value for  $k^{(2)}$  of  $142[\text{H}^+]^{0.5} \text{ M}^{-1.5} \text{ sec}^{-1}$  over the pH range 0 to 3. The reaction did not respond to catalysis by  $\text{Fe}^{3+}$ ,  $\text{Mn}^{2+}$  or  $\text{VO}^{2+}$ . Oblath et al., conducting experiments in the pH range 4.5 to 7.0, report  $k^{(2)}$  to be  $3.8 \times 10^3 [\text{H}^+]$ . These two values of  $k^{(2)}$  are consistent and indicate a change in pH dependence near pH 3. The rate expression of Oblath et al. contains a zero-order term and a second-order term in addition to the one in Equation 6.3.18. The zero-order term, whose contribution to the overall rate was found to be small under all of the conditions studied, and the second-order term, only important at S(IV) concentrations greater than 0.1 M and pH values greater than 6.5, have been neglected in this treatment. The end products of the reactions of nitrous acid with S(IV) vary with pH. Below pH 3.5, Martin et al. report nitrous oxide ( $\text{N}_2\text{O}$ ) to be the major product. Above pH 4.5, the major product as determined by Oblath et al., was hydroxylamine disulfonate,  $\text{HON}(\text{SO}_3)_2^{2-}$ , which can hydrolyze to hydroxylamine monosulfonate as shown below.

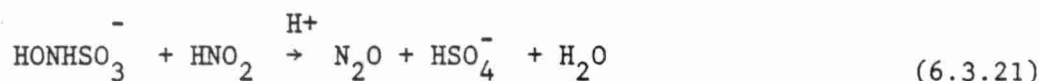


The hydrolysis product,  $\text{HONHSO}_3^-$  can either undergo further hydrolysis producing hydroxylamine cation





or react with nitrous acid to produce nitrous oxide and sulfates (Chang et al. 1981).



Kinetic studies by Naiditch and Yost (1941) and Seel and Paushmann (1962) indicate the nitrous acid reaction is much more important than the hydrolysis.

Under representative atmospheric conditions, 5 ppb  $\text{SO}_2$  and 3 ppb  $\text{HNO}_2$ , the rate of S(IV) oxidation by  $\text{HNO}_2$  is much slower than when ozone or peroxide are present (Martin et al. 1981). This reaction may be important at night if atmospheric droplet lifetimes are long.

The fastest reactions in this group are observed for S(IV) oxidation by  $\text{NO}_2$ . Takeuchi et al. (1977), Nash (1979); Sato et al. (1979); Lee and Schwartz (1981a) and Schwartz and White (1982) have studied this system; however, details of the stoichiometry, order of reagent concentrations and pH dependence of the rate are not known. Estimates of the second-order rate constant have been made by Schwartz and White based on the data of Takeuchi et al. They suggest values for  $k^{(2)}$  of  $3 \times 10^5$  and  $1 \times 10^7 \text{ M}^{-1} \text{ sec}^{-1}$  for reaction of  $\text{NO}_2(\text{aq})$  with  $\text{HSO}_3^-$  and  $\text{SO}_3^{2-}$ , respectively.

#### Catalytic Oxidation of S(IV) by $\text{O}_2$

In the absence of catalysis, oxidation of S(IV) by molecular oxygen is unimportant when compared to oxidation by  $\text{O}_3$  or  $\text{H}_2\text{O}_2$  at representative atmospheric concentrations (Penkett et al. 1979). Catalysis of this reaction by trace metals, e.g.,  $\text{Fe}^{3+}$ ,  $\text{Mn}^{2+}$  and  $\text{Fe}^{3+}$  plus  $\text{Mn}^{2+}$ , can substantially increase the rate of this reaction such that it becomes competitive with the stronger oxidants  $\text{O}_3$  and  $\text{H}_2\text{O}_2$ . Martin (1982) provides an excellent review of the work on this subject

to date and has assembled the rate expressions and rate constants valid in regimes of low (<4.5) and high (>4.5) pH for small (<10<sup>-5</sup> M) and large (>10<sup>-5</sup> M) S(IV) concentrations. Rate expressions are given in Table 6.3.2. As concentrations of iron and manganese in atmospheric aerosols and cloud-water droplets are poorly known, and reaction rates are subject to inhibition by common organic molecules, e.g., toluene, hexene,  $\alpha$ -pinene and hydroquinone (Altwicker 1979), it does not appear that these processes can be quantitatively modeled at this time.

The catalytic oxidation of S(IV) by O<sub>2</sub> on carbon particles in aqueous suspension has been investigated by Brodzinsky et al. (1980) and Chang et al. (1981). They found the reaction rate to be pH independent below pH 7.6, first-order in carbon and 0.69th-order in dissolved oxygen and a complex function of [S(IV)(aq)]<sub>T</sub>. Their rate expression is shown below for a temperature of 25°C.

$$\frac{dS(IV)}{dt} = 2.4 \times 10^{-5} [O_2(aq)]^{0.69} \cdot (C) \cdot f([S(IV)(aq)]_T) \quad (6.3.22)$$

where

$$f([S(IV)(aq)]_T) = \frac{1.5 \times 10^{12} [S(IV)(aq)]_T^2}{1 + 3.06 \times 10^6 [S(IV)(aq)] + 1.5 \times 10^{12} [S(IV)(aq)]_T^2} \quad (6.3.23)$$

(C) = carbon concentration in g/l and the rate constant has units of mole<sup>0.31</sup> l<sup>0.69</sup> g<sup>-1</sup> sec<sup>-1</sup> and is a function of the type and surface area of the carbon particles.

Chang et al. (1981) evaluated oxidation rates of S(IV) by several mechanisms under representative atmospheric conditions and found catalytic oxidation by carbon particles to be an important process close to sources and in heavily polluted areas where soot concentrations are high and when the lifetime of fog or cloud droplets is long.

TABLE 6.3-2

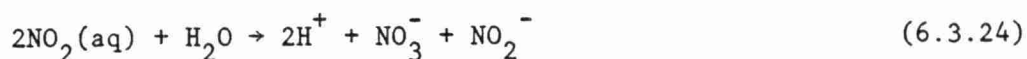
RATE EXPRESSIONS FOR Fe AND Mn CATALYZED OXIDATION  
OF S(IV) BY O<sub>2</sub> VALID OVER VARIOUS pH RANGES AND [S(IV)] CONCENTRATIONS

>10 <sup>-5</sup> M	$R = 4.7 [\text{Mn}^{2+}]^2 [\text{H}^+]^{-1}$ $+ \frac{0.82 [\text{Fe}^{3+}] [\text{S(IV)(aq)}]_T}{[\text{H}^+]}$ $+ \frac{1.7 \times 10^3 [\text{Mn}^{2+}]^{1.5}}{(6.3 \times 10^{-6}) + [\text{Fe}^{3+}]}$	$R = 4.7 [\text{Mn}^{2+}] [\text{H}^+]^{-1}$ $+ 10^7 [\text{Fe}^{3+}] [\text{S(IV)(aq)}]^2]_T$
[S(IV)]	$R = 5000 [\text{Mn}^{2+}] [\text{S(IV)(aq)}]_T$ $+ \frac{0.82 [\text{Fe}^{3+}] [\text{S(IV)(aq)}]_T}{[\text{H}^+]}$ $+ 3 \left[ \frac{1.7 \times 10^3 [\text{Mn}^{2+}]^{1.5}}{(6.3 \times 10^{-6}) + [\text{Fe}^{3+}]} \right]$	$R = 5000 [\text{Mn}^{2+}] [\text{S(IV)(aq)}]_T$
<10 <sup>-5</sup> M	pH	
	<5	>5

#### 6.3.2.2 Oxidation of Nitrogen Containing Compounds

##### NO and NO<sub>2</sub>

The aqueous-phase oxidation of nitrogen oxides (NO and NO<sub>2</sub>) has received considerable attention and until recently, investigators have not been in agreement as to the importance of the contribution of these processes to the observed nitric acid (HNO<sub>3</sub>) acidity in precipitation. Schwartz and coworkers (Schwartz and White 1981, 1982; Lee and Schwartz 1981a, 1982) have conducted equilibrium and kinetic studies within the past year on the following reactions:

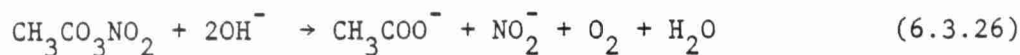


Their work is summarized in Schwartz (1982). The second-order rate constants they report for these reactions,  $7 \times 10^7$  and  $3 \times 10^7 \text{ M}^{-1} \text{ sec}^{-1}$ , respectively, coupled with representative atmospheric partial pressures of NO and NO<sub>2</sub>, indicate that these reactions are "quite slow and, consequently, unimportant on the time scales of concern."

##### PAN

There is interest in the aqueous-phase oxidative behavior of peroxyacetylnitrate (PAN) as it may serve as an additional pathway from NO to nitrate in the atmosphere. Unfortunately, information on the aqueous-phase chemistry of this compound is virtually nonexistent.

PAN is thought to be relatively insoluble. Grosjean (1982) observed no detectable loss of PAN from a gas stream which was passed through distilled water by means of an impinger. The only well-characterized aqueous-phase reaction is a base-catalyzed hydrolysis reported by Mudd (1966) and Nicksic et al. (1967) shown below.



Mudd indicates the half-life of PAN increases from 1.5 to 6.5 min as the pH drops from 8.6 to 4.5. There is no information concerning the behavior of PAN in acidic solution.

### 6.3.3 Mass-Transport

Mass-transport processes must be considered when kinetic constraints to an equilibrium situation are being evaluated. Transfer of soluble gases and particles from the gas phase to the liquid phase in small cloud-water droplets ( $<50 \mu$ ) can be accurately described by molecular diffusion (Baboolal et al. 1981) and the assumption of equilibrium between the two phases has been shown to be appropriate except under conditions of very high oxidation rates, e.g., high concentrations of  $\text{O}_3$  or  $\text{H}_2\text{O}_2$  (Beilke and Gravenhorst 1978, Freiberg and Schwartz 1982).

A general treatment of the coupled physical-chemical processes that control the characteristic times of mass-transport in spherical droplets can be found in Schwartz and Freiberg (1981). A relevant summary of that work by Schwartz (1982) is given here.

"Aqueous-phase diffusion. This characteristic time describes the approach of the aqueous-phase concentration profile to its steady-state, uniform value in the absence of chemical reaction, following initial sudden exposure of the drop to a surface concentration of the material maintained for all subsequent times:

$$\tau_{d.a.} = d^2/4\pi^2 D_{aq} \quad (6.3.27)$$

where  $D_{aq}$  is the aqueous-phase diffusion coefficient (and  $d$  is the droplet diameter).

Gas-phase diffusion. This characteristic time describes the establishment of a steady-state concentration profile in the gas-phase region local to the drop following sudden exposure of the drop to an initially uniform gas-phase concentration profile:

$$\tau_{d.g.} = d^2/4\pi^2 D_g \quad (6.3.28)$$

where  $D_g$  is the gas-phase diffusion coefficient . . .

Phase equilibrium. This characteristic time addresses the ability of the gas-kinetic collision rate of the reagent gas to supply this gas fast enough to maintain Henry's law locally at the interface:

$$\tau_{\text{phase}} = D_{\text{aq}} (4H/\bar{v}\xi)^2, \quad (6.3.29)$$

where  $\bar{v}$  is the average molecular speed  $= (8 kT/\pi m)^{1/2}$ , where  $m$  is the molecular mass and  $k$  is Boltzmann's constant, and  $\xi$  is a dimensionless sticking coefficient.

( $H$ , the ratio of gas-phase and aqueous-phase concentrations of species  $X$ , is defined as:

$$H = \frac{[X(\text{aq})]}{[X(\text{g})]} = \frac{K_{\text{Hx}} p_x}{p_x/RT} = K_{\text{Hx}} RT \quad (6.3.30)$$

where  $R$  is the gas constant and  $T$  is absolute temperature. For soluble gases which undergo rapid reversible aqueous-phase reactions such as hydrolysis or complex-formation,  $K_{\text{Hx}}$  should be replaced with an expression, written in terms of  $[H^+]$  and appropriate equilibrium constants, which defines the speciation of the entire family of products. This consideration applies to all following equations involving  $H$ .)

"For dilute solutions in the absence of surfactants,  $\xi$  appears to be close to unity (Danckwerts 1970) . . .

Reagent supply. This characteristic time addresses the ability of gas-phase diffusion to supply sufficient material to saturate the drop in the dissolved reagent:

$$\tau_{\text{reag}} = Hd^2/12 D_g \quad (6.3.31)$$

Reaction, referred to aqueous-phase reagent concentration. This characteristic time describes the rate of depletion of the dissolved reagent by aqueous-phase reaction. For a species  $X$  undergoing irreversible first-order reaction with rate  $R = k[X]$

$$\tau_{\text{r.a.}} = k^{-1} \quad (6.3.32)$$

This definition can be extended to other reaction orders by replacing  $k$  with  $k^{(1)}$  defined as

$$k^{(1)} = R/[X] \quad (6.3.33)$$

For a gaseous reagent such as  $\text{SO}_2$ , which undergoes rapid solution equilibria such as acid dissociation equilibria, the rate coefficient  $k^{(1)}$  must be defined with respect to the entire pool of dissolved reagent, i.e.,  $[X] = [\text{S(IV)}]$ .

Reaction, referred to gas-phase reagent concentration. This characteristic time describes the rate of depletion of the gas-phase reagent by aqueous-phase reaction:

$$\tau_{\text{r.g.}} = (\text{H}k^{(1)})^{-1} \quad (6.3.34)$$

In order that the aqueous-phase reaction proceed at its intrinsic rate, as evaluated assuming saturation of the cloud liquid water by the reagent gas, the system must be at steady state with uniform concentration profiles in the gas and aqueous phases and with Henry's law satisfied locally at the interface . . .

The criteria that must be satisfied (Freiberg and Schwartz 1981) in order that the diffusion reaction system be at steady state are that the period of contact of the reagent gas with the droplet substantially exceed  $\tau_{\text{d.g.}}$ ,  $\tau_{\text{reag}}$  and the lesser of  $\tau_{\text{r.a.}}$  and  $\tau_{\text{d.a.}}$  . . .

The criteria that must be satisfied in order that the droplet, at steady state, be saturated in the reagent gas are

$$\tau_{\text{phase}} \ll \tau_{\text{r.a.}} \quad (6.3.35)$$

$$\tau_{\text{d.a.}} \ll \tau_{\text{r.a.}} \quad \text{and} \quad (6.3.36)$$

$$\tau_{\text{d.a.}} \ll \tau_{\text{r.a.}} \quad (6.3.37)$$

#### 6.3.4 Review of Previous Modeling Studies

Many approaches have been taken by investigators attempting to model the processes which determine the chemical composition of precipitation. Generally, these modeling efforts fall into two categories: (1) a particular aspect of the problem is focused on and modeled in a rigorous manner. Results of these efforts are often validated by comparison to laboratory studies designed to address the same issue or selected field data collected under conditions where the modeled process is considered to be dominant; and (2) a large subset of the relevant chemical and physical processes are included in a model. The amount of sophistication applied to each process is a

function of several variables including the modelers' goals, available data, how well the process is understood on a fundamental level and computational costs. We review here a few of the many recent modeling efforts, which are examples of the two approaches above, designed to understand and/or predict the observed sulfate concentrations in precipitation in order to assess state-of-the-art in this field.

Precipitation scavenging of  $\text{SO}_2$  and sulfate both in-cloud (rainout) and below-cloud (washout) as a mechanism to account for the observed sulfate levels measured in precipitation has been extensively addressed by several authors. Hales (1978) presented an overview of sulfur scavenging calculations. He included discussions of direct sulfur dioxide scavenging, direct sulfate scavenging and  $\text{SO}_2$  scavenging combined with subsequent chemical oxidation to sulfate. Both the microphysics of mass-transport and the chemical equilibrium reactions of the S(IV) system were considered. While the calculation of direct scavenging of  $\text{SO}_2$  was found to be well understood, calculations of direct sulfate scavenging were limited by a lack of sufficient data regarding particle-size distributions of sulfate aerosols.  $\text{SO}_2$  absorption followed by aqueous-phase conversion to sulfate was expected to be rate limited by the chemical conversion step under most circumstances. At the present time, adequate particle-size distribution data are still unavailable. Although considerable progress has been made in identifying the important aqueous-phase oxidation mechanisms and their rate-limiting steps under representative atmospheric conditions (see Sections 6.3.2 and 6.3.3).

Ways of incorporating  $\text{SO}_2$  washout into sulfur cycles is discussed and an expression is derived relating  $\text{SO}_2$  washout ratios to rainwater pH and temperature by Barrie (1981). Sulfate concentrations in precipitation are predicted to be strongly dependent on the precipitation formation mechanism within a cloud (Scott 1978). Precipitation formed without an initial ice-growth stage can have sulfate concentrations 2 to 10 times as large as precipitation in the form of snow or ice or originated as snow in the upper portions of the cloud.

Durham et al. (1981) and Overton and Durham (1981) have examined the roles of chemical oxidation kinetics, mass-transport rates and



raindrop size distributions for below-cloud rain acidification. Raindrops with dissolved catalysts were assumed to form in-cloud and then fall through a stable polluted region containing  $\text{SO}_2$ ,  $\text{H}_2\text{O}_2$ ,  $\text{O}_3$  and  $\text{HNO}_3$ . It was found that  $\text{H}_2\text{O}_2$  was the dominant oxidizing agent for  $\text{SO}_2$  and that scavenging of gas-phase  $\text{HNO}_3$  was an important process contributing to the acidification of rain. Subcloud scavenging of both  $\text{H}_2\text{O}_2$  and  $\text{HNO}_3$  were mass-transport limited.

The laboratory studies of such investigators as Penkett et al. (1979), Martin and Damschen (1981) and Schwartz and coworkers designed to address the issues of  $\text{S(IV)}$  and  $\text{NO}_x$  oxidation in cloud-water droplets and hydrometeors have significantly increased our understanding of these important chemical processes as they relate to the heterogeneous formation of strong acids in the atmosphere.

Seinfeld and coworkers (Bassett et al. 1981, Gelbard and Seinfeld 1980 and Gelbard et al. 1980) have developed a mathematical model to predict the evolution of size and composition of submicron atmospheric aerosols as well as cloud droplets: a major component of any comprehensive atmospheric model.

There are several noteworthy approaches which are used to predict the chemical composition of precipitation by modeling aqueous-phase chemical processes. Charlson and Rhode (1982) used an equilibrium thermodynamic model to predict the range of acidity expected to be present in natural rainwater at remote (marine) locations. They found their predicted pH values to be most sensitive to two parameters, the amount of  $\text{H}_2\text{SO}_4$  aerosol scavenged and the liquid-water content of clouds, and estimated that pH values might range from 4.5 to 5.6 due to variability of the sulfur cycle. Middleton et al. (1980) estimated the relative importance of various sulfate aerosol production mechanisms in an urban atmosphere by incorporating photochemical reactions, vapor condensation and catalytic and noncatalytic oxidation on a wetted aerosol into their theoretical considerations. Oxidation rates were calculated in a series of kinetic and equilibrium steps. Initially, gases were assumed to be in equilibrium with the aerosols. Sulfate production due to time-variant oxidation processes was then calculated while, simultaneously, sulfuric acid vapor was condensing onto the aerosol

surface. As the increase in sulfate due to both of the above processes perturbed the initial gas/aerosol equilibrium, it was recalculated after a small time step. If the result of this calculation indicated the necessity for gas transfer into or out of the wetted aerosol, mass-transport limitations to this process were evaluated. Use of this "pseudo-kinetic" approach with appropriately small time intervals allowed these researchers to determine the overall rate-limiting step in the conversion of  $\text{SO}_2$  to sulfate at each time step. They found the dominant sulfate aerosol production mechanism in urban atmospheres to be sulfuric acid condensation during the daytime, which is consistent with the experimental observations of Hering (1982);  $\text{H}_2\text{O}_2$  oxidation on winter days; and a combination of soot and manganese catalyzed oxidation followed closely in importance by  $\text{H}_2\text{O}_2$  and iron-catalyzed oxidation at night.

The most complex of these models are long-range transport (LRT) models in which many of the above components are integrated into a framework which describes emissions, photochemistry, meteorology, transport and deposition over time scales of a few days. Examples of this type of model include the work of Rhode et al. (1981) and Carmichael and Peters (1982).

Aqueous-phase chemistry in the LRT model of Rhode et al. (1981) is incorporated into the single reaction shown below:



The rate constant for this reaction,  $6 \times 10^{-16} \text{ cm}^3 \text{ molecule}^{-1} \text{ sec}^{-1}$ , was chosen simply to make the aqueous-phase conversion of  $\text{SO}_2$  to sulfate comparable in magnitude to the gas-phase transformation for typical summertime OH concentrations.

Hong and Carmichael (1982) have developed a much more sophisticated aqueous-phase chemistry component for the LRT model of Carmichael and Peters (1982). They have included many of the important equilibrium, kinetic and mass-transport processes outlined here, and coupled them with the relevant cloud physics using a flow-through chemical reactor model approach. Model results predict sulfate production rates varying from 60% per hour to 1000% per hour

expressed in terms of S(IV) concentrations. Presently, this component is being incorporated into their LRT model.

#### 6.3.5 Summary of the Recommended Approach

The previous sections have described the equilibrium, kinetic and mass-transport processes which play important roles in defining the chemical composition of precipitation. The relative importance of the contributions of these processes change with changing atmospheric conditions. It is necessary to develop a model framework which can consider all of the above processes. The components of the aqueous-phase chemistry module which will deal with each of these are described below.

##### 6.3.5.1 Equilibrium Modeling

The chemical equilibrium model proposed to be used here was designed to calculate chemical speciation in multicomponent, multiphase aqueous systems at equilibrium. The equilibrium problem is defined by specifying the total concentrations of a set of components from which all species in the system can be formed. Concentrations of those species are then computed using stability constants, stoichiometry and mass-balance relationships by an iterative process [see Westall et al. (1976) for a detailed description of the model]. Activity coefficients for all species are calculated using the Davies equation (Stumm and Morgan 1981) which is applicable in solutions where the ionic strength is less than 0.5 M.

The effect of temperature on rate constants for redox processes will be considered when this information is available in the literature. The temperature dependence of equilibrium constants will be estimated when sufficient thermodynamic information exists. This information includes the standard enthalpy change of reaction,  $\Delta H^\circ$ , and the standard change in heat capacity,  $\Delta C_p^\circ$ , both at constant pressure. For many reactions in aqueous systems,  $\Delta C_p^\circ$  is close to zero and  $\Delta H^\circ$  is essentially independent of temperature. An

equilibrium constant,  $K_2$ , at some temperature,  $T_2$ , can be readily calculated according to

$$\ln \frac{K_2}{K_1} = \frac{\Delta H^\circ}{R} \left( \frac{1}{T_1} - \frac{1}{T_2} \right) \quad (6.3.39)$$

The application of this type of chemical model to cloud-water droplets introduces several concepts which are not generally considered. Mass balances must be carried out over gas, liquid and solid phases. Previously, partial pressures of soluble gases were fixed providing an infinite supply of mass. While this is sufficient for describing  $\text{CO}_2$  gas/aqueous equilibria in an open system, it is not appropriate for soluble gases present in trace quantities. In the latter case, under certain conditions, gas-phase concentrations can decrease when these soluble trace gases dissolve in cloud-water droplets.

In order to input total concentrations and perform mass balances for gas-phase components, it is necessary to express their concentrations in units consistent with the aqueous-phase concentration units with which the model deals, i.e., molar units. The necessary parameter which allows one to make this conversion from partial pressure to molar units is the volume fraction of liquid water in a cloud per  $\text{m}^3$  of physical volume. This parameter,  $L$ , typically has a value of 0.1 to 1  $\text{cm}^3/\text{m}^3$  (Pruppacher and Klett 1978) which corresponds to a dimensionless value of  $10^{-7}$  to  $10^{-6}$ .

The total concentration of a soluble gas on a mole per liter of cloud water basis is then calculated according to:

$$[X]_T = \frac{P_x}{LRT} \quad (6.3.40)$$

Here, the subscript T denotes a total concentration, R is the gas constant and T is temperature. Values of L for several cloud/storm types will be determined and made available for aqueous chemistry

modeling. A description of these calculations can be found in Section 7.

#### 6.3.5.2 Kinetic and Mass-Transport Constraints

Mass transport may hinder the establishment of gas/aqueous equilibria. The characteristic times for gas-phase diffusion, establishing equilibrium at the gas/liquid interface and aqueous-phase diffusion must be compared to cloud-water droplet lifetimes and aqueous-phase chemical reactions which consume species originating in the gas phase. If mass-transport or chemically-slow reactions are found to be rate-limiting in the approach to equilibrium, these processes will be modeled kinetically and the output used to define a set of mass-balance constraints for the rest of the system when rate expressions and rate constants are known or can be estimated. These constraints will change with time, permitting an equilibrium approach to describe the composition of the parts of the system that have sufficiently short chemical time scales.

#### 6.3.5.3 Recommendations and Conclusions

If the aqueous-phase chemistry module is to be as accurate as possible, input data must be reliable and representative. Several inputs which play significant roles are poorly characterized and warrant comment.

##### Hydrogen Peroxide

Hydrogen peroxide is potentially the most important aqueous-phase oxidant in wetted aerosols, cloud-water droplets and hydrometeors (Penkett et al. 1979, Middleton et al. 1980 and Durham 1981). Measurements of  $\text{H}_2\text{O}_2$  concentrations in the atmosphere are not believed to be correct due to  $\text{O}_3$ /water interactions (Zika and Saltzmann 1982) and  $\text{SO}_2/\text{O}_3$ /water interactions (Heikes et al. 1982) during aqueous trapping. Thus, until better experimental data become available, gas-phase  $\text{H}_2\text{O}_2$  concentrations may be derived from models

incorporating relevant homogeneous gas-phase reactions. Considerable effort must be expended to ensure that known gas-phase pathways resulting in peroxide formation and destruction are incorporated into the photochemistry module. These reactions are included in the recommended homogeneous photochemical model discussed in Section 6.1.

#### Cation Budget

It will be necessary to know the chemical composition and mass concentration of soluble particles that are scavenged by cloud-water droplets and hydrometeors. In particular, the cations associated with sulfate and nitrate aerosols and soil dust particles have to be specified for two reasons, (1) they maintain electroneutrality in the aqueous phase and (2) they are important in determining solution pH. The major cations to be considered here are  $H^+$ ,  $NH_4^+$ ,  $Na^+$ ,  $Ca^{2+}$  and  $Mg^{2+}$ . Hydrogen and ammonium ion dominate sulfate and nitrate aerosols and determine their acidity. Calcium, magnesium and sodium account for the majority of soil-derived cations. Basic anions associated with these cations help to neutralize the acidity of precipitation when soil dust particles are scavenged. The following approach is recommended to address this problem. The mass concentration of sulfate aerosol will be available from the photochemistry model. A seasonally and geographically dependent  $H^+/NH_4^+$  ratio will be impressed upon the sulfate aerosol data. These ratios could be generated from precipitation chemistry data available from such networks as CANSAP, NADP, UAPSP and MAP3S or sulfate aerosol chemical compositions from SURE. Seasonally averaged isopleths for the major cations in precipitation, such as those in Semonin et al. (1981), may be particularly useful for this purpose. In the same manner, seasonally and geographically averaged  $Ca^{2+}/Mg^{2+}/Na^+$  ratios and soil dust mass loadings will be generated to account for soil dust scavenging.

The cations Fe and Mn play an insignificant role in the pH determination of cloud-water droplets and hydrometeors via the electroneutrality condition due to their very low concentrations; however, their catalytic effect on S(IV) oxidation by molecular oxygen has been shown to be an important oxidative pathway at night in the

absence of the strong photochemical oxidants,  $O_3$  and  $H_2O_2$  (Middleton et al. 1980) and in fogs and urban plumes. Based on a lack of quantitative data on Fe and Mn concentrations in cloud-water droplets and hydrometeors, it is recommended that linear, first-order kinetic parameterizations, applicable at night and possibly near urban sources, are sufficient to treat these reactions.

Realizing the limitations imposed upon the modeling of aqueous-phase oxidation processes in cloud-water droplets and hydrometeors by the input data deficiencies noted above, it is nevertheless recommended that an aqueous-phase chemistry module based on an equilibrium model with kinetic constraints be constructed. The framework will be built to include all of the equilibrium, kinetic and mass-transport processes discussed here and such that future developments in this field can be readily incorporated. It is recommended that the model be independently tested for sensitivity to several estimated and poorly-known input parameters. These include, but are not limited to the following:

- $H^+/NH_4^+$  ratio in soluble particles,
- $Ca^{2+}/Mg^{2+}/Na^+$  ratio in soluble particles,
- $Fe^{3+}$  and  $Mn^{2+}$  concentrations in the aqueous phase,
- rate constants and rate expressions for catalyzed S(IV) oxidation by  $O_2$ , and
- parameters describing cloud physics such as liquid water content of clouds, particle size distributions, scavenging coefficients for soluble particles, cloud lifetimes, precipitation rates, average droplet diameters and fall velocities.

Results of these sensitivity analyses will allow for independent assessment of the importance or nonimportance of the various oxidation pathways for  $SO_2$  and  $NO_x$  under representative atmospheric conditions and for useful parameterizations to be identified and implemented. Further, experience gained in constructing and testing of the aqueous-phase chemistry module will allow it to be successfully integrated into the existing mesoscale and grid models. This

comprehensive and step-wise approach will result in a well-behaved and efficient module representing a significant improvement on current methodology.

#### 6.4 Selected Case Studies of Combined Gas/Aqueous-Phase Chemistry

Three case studies of the atmospheric chemistry of  $\text{NO}_x$  and  $\text{SO}_2$  were performed to illustrate the typical interactions between gas, aerosol, and aqueous phases. The model employed for the calculations was a fixed-volume, well-mixed reactor which included gas phase kinetics of the  $\text{HC}/\text{NO}_x/\text{SO}_x$  system, aqueous-phase kinetics of the  $\text{O}_3/\text{H}_2\text{O}_2/\text{S(IV)}$  system, and gas/aqueous phase equilibria. The conditions for the case studies were selected such that the chemical kinetics were not limited by mass transfer rates.

The case studies involved 10-hour simulations of ambient air irradiation in the summer for typical urban and rural situations using three sets of  $\text{RHC}/\text{NO}_x/\text{SO}_x$  precursor concentrations. Calculations with gas phase kinetics only were performed first. A second set of calculations was performed where water condensation was assumed to occur in the afternoon. More specifically, the calculations assumed liquid water at a volume fraction of  $10^{-6}$  in air was instantaneously formed at 1400 hours, and remained fixed thereafter. It should be pointed out that the model did not simulate the effects of dry deposition or precipitation, but rather focused only on chemical aspects of the system. It also should be noted that cloud water is believed to recycle (or evaporate) every 5 to 30 minutes so the results presented herein for longer aqueous-phase lifetimes longer than 30 minutes may not be realistic.

##### 6.4.1 The Chemical Mechanism

The gas phase  $\text{HC}/\text{NO}_x/\text{SO}_x$  chemical mechanism used in the calculations was that of Atkinson et al. (1982) (shown in Table 6.2-5), which includes 52 chemical species and 81 chemical reactions. As discussed in Section 6.2, this mechanism is believed to include the



TABLE 6.4-1

## AQUEOUS-PHASE EQUILIBRIA

SPECIES FORMATION REACTIONS AND CORRESPONDING  
EQUILIBRIUM CONSTANTS INCLUDED IN THE AQUEOUS-  
PHASE CHEMISTRY MODULE

<u>Species Formation Reaction Stoichiometry</u>	<u>Log K (25°C)</u>
1. $\text{SO}_2(\text{g}) \rightleftharpoons \text{SO}_2(\text{aq})$	$1.5 + \log L^*$
2. $\text{SO}_2(\text{g}) + \text{H}_2\text{O} \rightleftharpoons \text{HSO}_3^- + \text{H}^+$	$-0.26 + \log L$
3. $\text{SO}_2(\text{g}) + \text{H}_2\text{O} \rightleftharpoons \text{SO}_3^{2-} + 2\text{H}^+$	$-7.46 + \log L$
4. $\text{CO}_2(\text{g}) \rightleftharpoons \text{CO}_2(\text{aq})$	$-1.5$
5. $\text{CO}_2(\text{g}) + \text{H}_2\text{O} \rightleftharpoons \text{HCO}_3^- + \text{H}^+$	$-7.8$
6. $\text{CO}_2(\text{g}) + \text{H}_2\text{O} \rightleftharpoons \text{CO}_3^{2-} + 2\text{H}^+$	$-18.0$
7. $\text{NH}_3(\text{g}) \rightleftharpoons \text{NH}_3(\text{aq})$	$3.18 + \log L$
8. $\text{NH}_3(\text{aq}) + \text{H}^+ \rightleftharpoons \text{NH}_4^+$	$12.18 + \log L$
9. $\text{HNO}_3(\text{g}) \rightleftharpoons \text{HNO}_3(\text{aq})$	$6.69 + \log L$
10. $\text{HNO}_3(\text{g}) \rightleftharpoons \text{NO}_3^- + \text{H}^+$	$7.89 + \log L$
11. $\text{H}_2\text{O}_2(\text{g}) \rightleftharpoons \text{H}_2\text{O}_2(\text{aq})$	$6.39 + \log L$
12. $\text{O}_3(\text{g}) \rightleftharpoons \text{O}_3(\text{aq})$	$-0.5 + \log L$
13. $\text{Ca}^{2+} + \text{CO}_2(\text{g}) + \text{H}_2\text{O} \rightleftharpoons \text{CaHCO}_3^+ + \text{H}^+$	$-7.4$
14. $\text{Ca}^{2+} + \text{CO}_2(\text{g}) + \text{H}_2\text{O} \rightleftharpoons \text{CaCO}_3^0(\text{aq}) + 2\text{H}^+$	$-15.0$
15. $\text{Ca}^{2+} + \text{SO}_4^{2-} \rightleftharpoons \text{CaSO}_4^0(\text{aq})$	$2.3$
16. $\text{Ca}^{2+} + \text{H}_2\text{O} \rightleftharpoons \text{CaOH}^+ + \text{H}^+$	$-12.2$
17. $\text{SO}_4^{2-} + \text{H}^+ \rightleftharpoons \text{HSO}_4^-$	$2.2$
18. $\text{H}_2\text{O} \rightleftharpoons \text{H}^+ + \text{OH}^-$	$-14.0$

\*  $L$  = volume fraction of liquid water in a cloud.

TABLE 6.4-2

INITIAL PRECURSOR CONCENTRATIONS FOR  
CHEMICAL SYSTEM CASE STUDIES

	Case			Units
	<u>1</u>	<u>2</u>	<u>3</u>	
NO	10	10	0.1	ppb
NO <sub>2</sub>	10	10	0.9	ppb
RHC	100 <sup>a</sup>	200 <sup>a</sup>	50 <sup>b</sup>	ppbC
SO <sub>2</sub>	5	5	5	ppb
SO <sub>4</sub>	2	2	2	μgm/m <sup>3</sup>

<sup>a</sup>urban RHC mixture.<sup>b</sup>rural RHC mixture.

reactions of known importance for atmospheric HC/NO<sub>x</sub>/SO<sub>x</sub> chemical systems and has undergone extensive testing against smog chamber data.

Modeling aqueous-phase equilibrium chemistry was accomplished using an equilibrium constant approach in which a set of nonlinear equations provided by mass action law and mole balance equations were solved by an iterative procedure (Morel and Morgan 1972; Westall 1979). The equilibrium problem was defined by choosing a set of chemical compounds (components) from which all chemical species to be considered could be formed. Stoichiometrically correct chemical reactions were written for the formation of each species from the set of components chosen and the corresponding equilibrium constants for these reactions were evaluated. Total concentrations of each component, species formation reaction stoichiometrics and equilibrium constants were the model inputs.

The components chosen to describe the equilibrium chemistry of cloud-water droplets were SO<sub>2</sub>(g), CO<sub>2</sub>(g), HNO<sub>3</sub>(g), H<sub>2</sub>O<sub>2</sub>(g), NH<sub>3</sub>(g), O<sub>3</sub>(g), Ca<sup>2+</sup>, Na<sup>+</sup>, SO<sub>4</sub><sup>2-</sup> and H<sup>+</sup>. Formation reactions for the chemical species considered and their equilibrium constants are listed in Table 6.4-1. Neither the set of components chosen nor the species considered in this problem are unique.

Total concentrations of gas-phase components on a mole per liter of liquid water basis were calculated as described in Section 6.3.5.1. Equilibrium constants for all species which are formed from gas-phase components depend on the parameter L, the volume fraction of liquid water present. For example, for the reaction:



the Henry's law constant is:

$$K = \frac{[\text{SO}_2(\text{aq})]}{P_{\text{SO}_2}} = 1.3 \quad (6.4.2)$$

The concentration of SO<sub>2</sub>(g) on a mole per liter of liquid water basis is calculated according to:

$$[\text{SO}_2(\text{g})] = \frac{P_{\text{SO}_2}}{\text{LRT}} \quad (6.4.3)$$

The form of the equilibrium constant for reaction 1 in Table 6.4-1,  $K(1)$ , is:

$$K(1) = \frac{[\text{SO}_2(\text{aq})]}{[\text{SO}_2(\text{ag})]} \quad (6.4.4)$$

which, after substitution of equation 6.4.3 into equation 6.4.2, can be shown to be equal to

$$K(1) = K_H \text{LRT} \quad (6.4.5)$$

Thus, at 298°K and a value for  $R$  of  $0.08205 \text{ l atm mole}^{-1} \text{ }^\circ\text{K}^{-1}$ ,

$$\log K(1) = 1.5 + \log L \quad (6.4.6)$$

The total concentration of sulfate was calculated initially from its predicted gas phase concentration assuming a scavenging coefficient of unity. It was necessary to define the cationic composition of the sulfate aerosol incorporated into the aqueous phase to maintain electroneutrality and allow pH values of the aqueous phase to be calculated. For these case studies, we have assumed the following chemical composition for gas phase sulfate aerosol:

40%	$(\text{NH}_4)_2\text{SO}_4$
40%	$\text{H}_2\text{SO}_4$
10%	$\text{CaSO}_4$
10%	$\text{Na}_2\text{SO}_4$

The above percentages are on a percent total sulfate basis. The total concentration of  $\text{NH}_3(\text{g})$  was adjusted for the  $\text{NH}_3$  associated with the sulfate aerosol. Total concentrations of  $\text{H}^+$ ,  $\text{Ca}^{2+}$  and  $\text{Na}^+$  were initially calculated based on the concentration of gas phase sulfate

aerosol and its assumed chemical composition. Total concentrations of all components were adjusted after each kinetic step to reflect their formation or destruction as a result of kinetic processes.

Two aqueous-phase kinetic reactions describing the oxidation of S(IV) by  $\text{H}_2\text{O}_2(\text{aq})$  and  $\text{O}_3(\text{aq})$  were included in this analysis. The rate constants and rate expressions described in Section 6.3.2.1 for these reactions were used here.

#### 6.4.2 Sensitivity Test Results

Precursor initial concentrations for the three cases are shown in Table 6.4-2. Data for Cases 1 and 2 were selected to represent air volumes immediately downwind of small urban areas at sunrise. Twenty (20) ppb of  $\text{NO}_x$  (50% as  $\text{NO}_2$ ), 5 ppb of  $\text{SO}_2$ , and  $2 \mu\text{gm}/\text{m}^3$  (0.5 ppb)  $\text{SO}_4^{2-}$  aerosol were assumed for both cases. Reactive hydrocarbons for Cases 1 and 2 were 100 and 200 ppbC, respectively, where the urban RHC mix was assumed to be 65% alkanes, 15% alkenes, 15% aromatic, and 5% aldehydes. Case 3 initial concentrations were selected to represent a rural environment with a moderate amount of  $\text{SO}_2$  and very little  $\text{NO}_x$  and RHC. The same initial  $\text{SO}_2$  and  $\text{SO}_4^{2-}$  aerosol concentrations were used in Case 3 as Cases 1 and 2, however, only 1 ppb of  $\text{NO}_x$  (90% as  $\text{NO}_2$ ) and 50 ppbC of slowly reacting RHC (90% alkanes, 10% aldehydes) were employed in Case 3.

Figures 6.4-1 through 6.4-6 illustrate the gas and aqueous phase concentration versus time profiles for the three cases. Results for the gas phase only problem and the gas plus aqueous-phase problem are shown in the figures. The predictions for Case 1 indicated that the 20 ppb of  $\text{NO}_x$  was oxidized gradually at the HC/ $\text{NO}_x$  ratio of 5:1, such that 0.5 and 3 ppb of NO and  $\text{NO}_2$  remained at the end of the run (1700 hrs). Ozone was shown to increase from 10 to 60 ppb over the day and was virtually unaffected by the presence of liquid water after 1400 hrs. The concentration time profiles for nitric acid ( $\text{HNO}_3$ ) and PAN show that most of the  $\text{NO}_x$  was transformed to  $\text{HNO}_3$  rather than PAN at this relatively low HC/ $\text{NO}_x$  ratio. The predictions showed that gas phase nitric acid was reduced from 8 ppb to less than 1 ppt by the introduction of liquid water. The aqueous-phase chemistry of PAN was

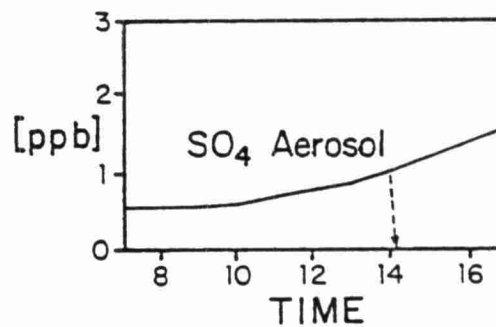
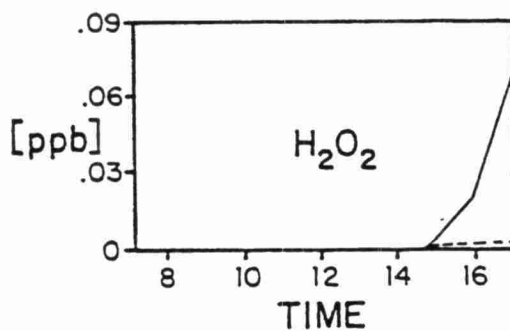
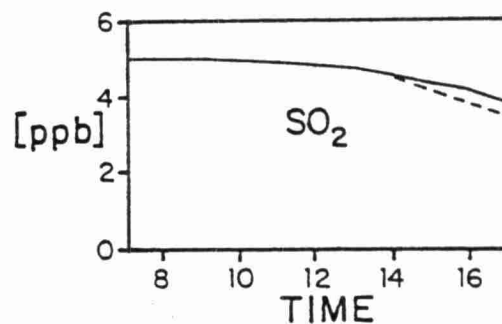
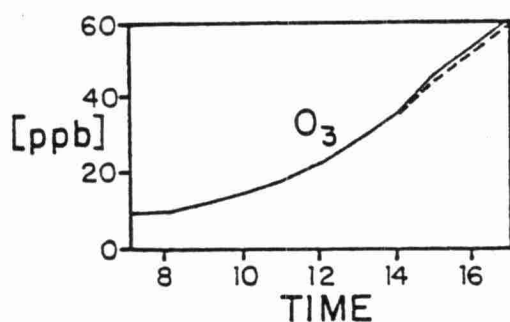
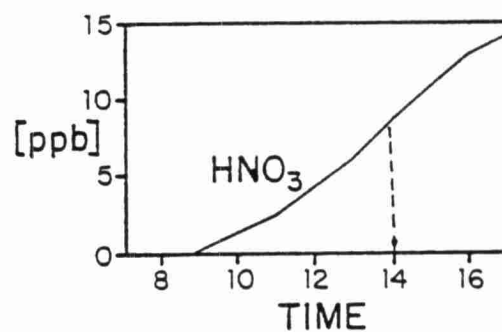
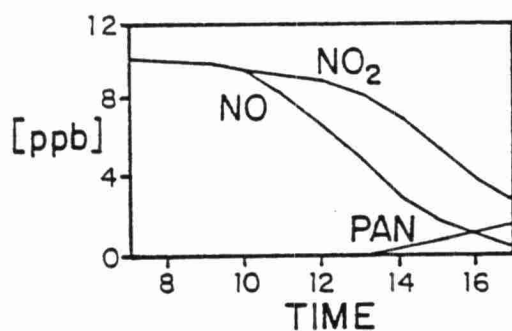


Figure 6.4-1. Gas and Aerosol Concentration-Time Profiles for Case 1. Solid lines (—) indicate gas phase only results and dashed lines (---) indicate gas plus aqueous phase results.

CASE 1

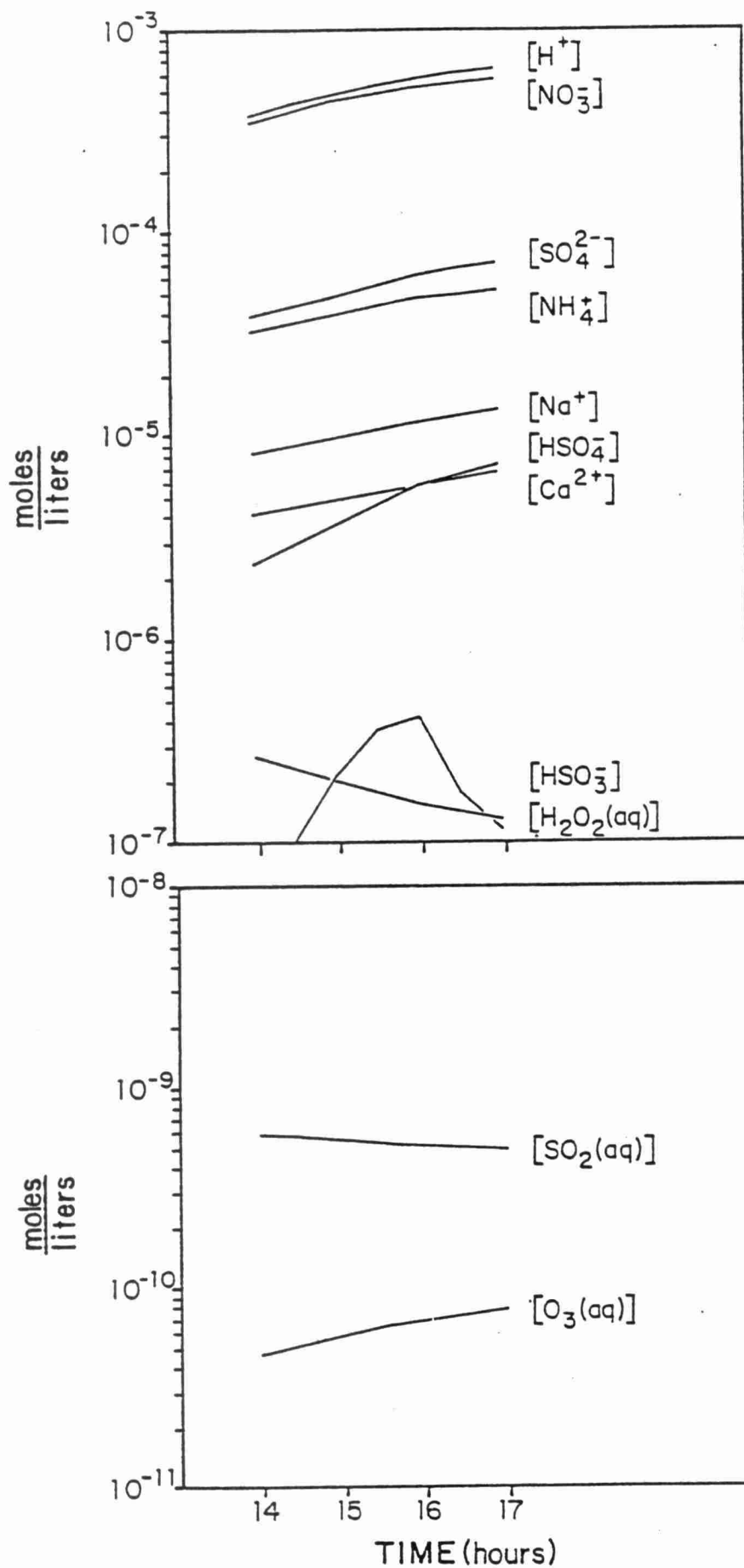


Figure 6.4-2. Aqueous-Phase Concentration-Time Profiles for Case 1.

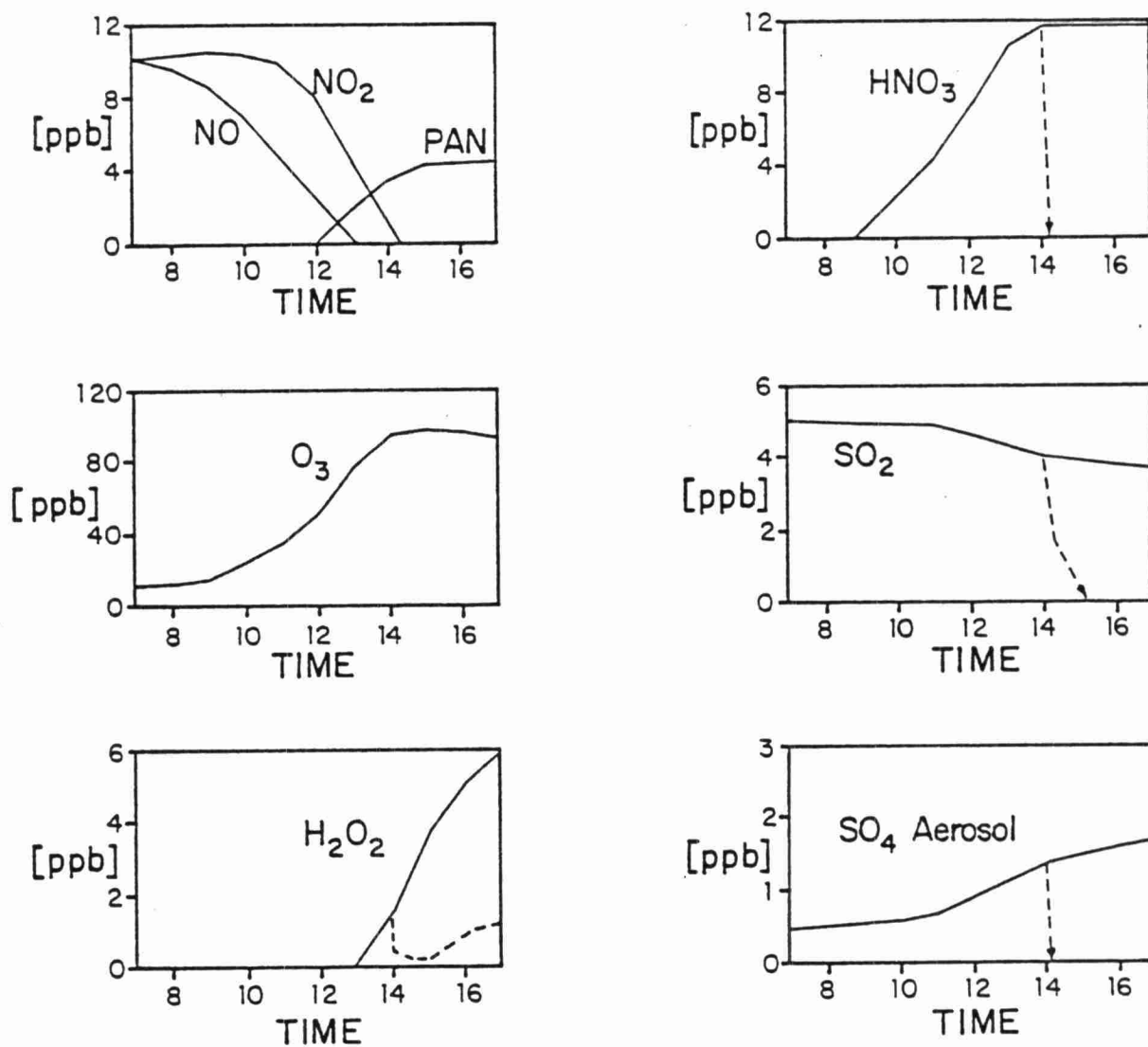


Figure 6.4-3. Gas and Aerosol Concentration-Time Profiles for Case 2. Solid lines (—) indicate gas phase only results and dashed (---) indicate gas plus aqueous-phase results.



CASE 2

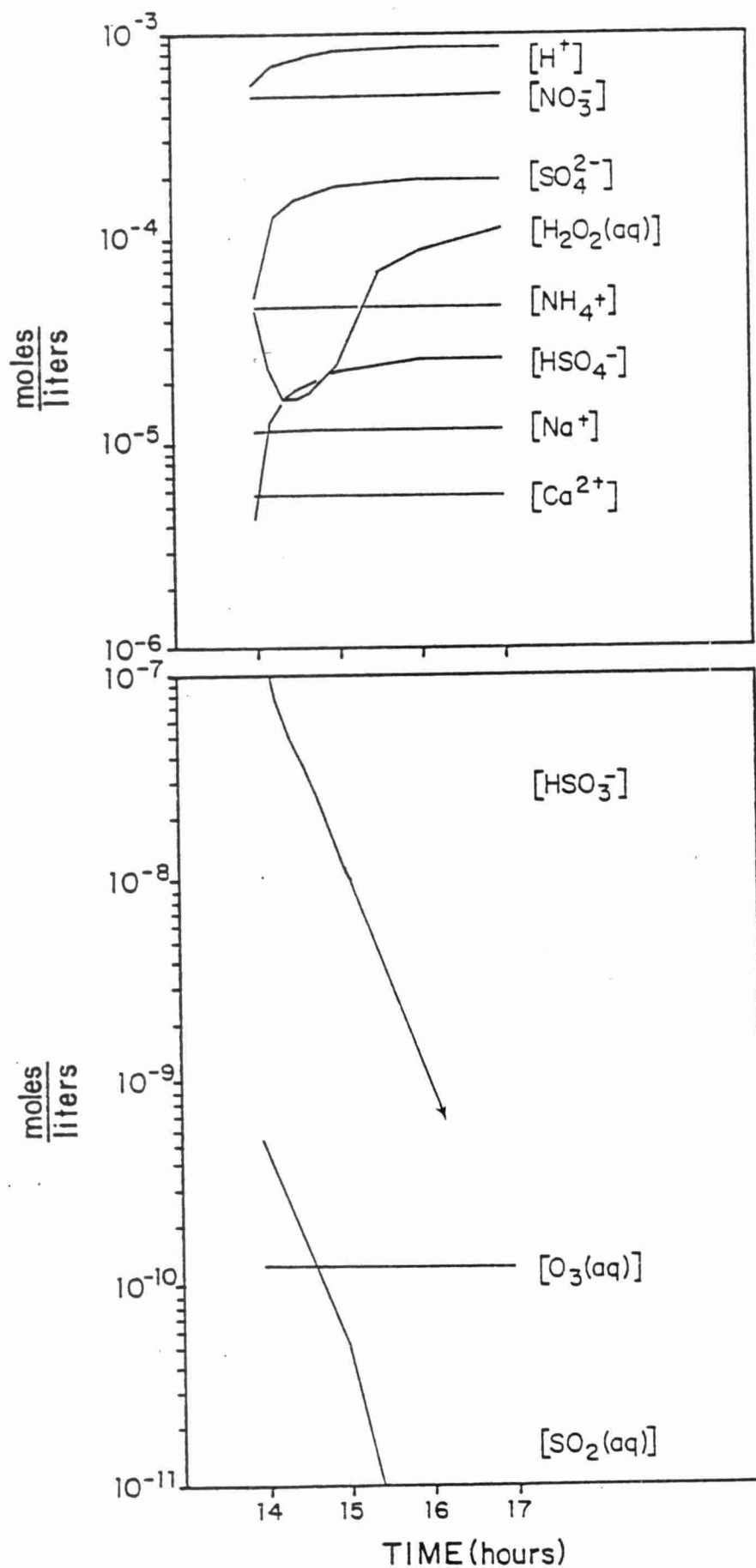


Figure 6.4-4 Aqueous-Phase Concentration-Time Profiles for Case 2.

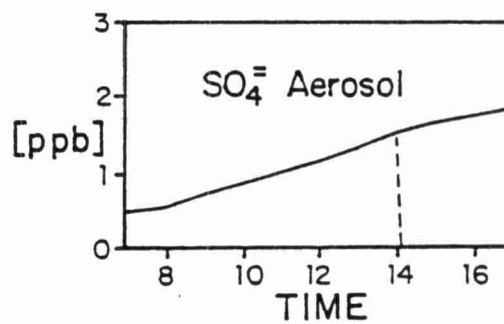
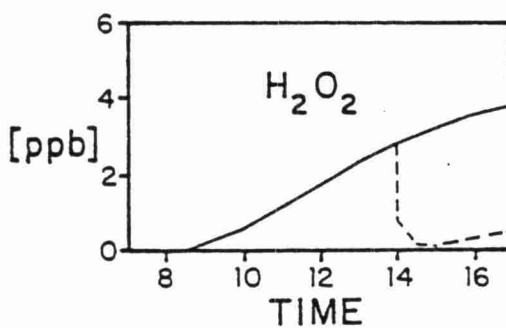
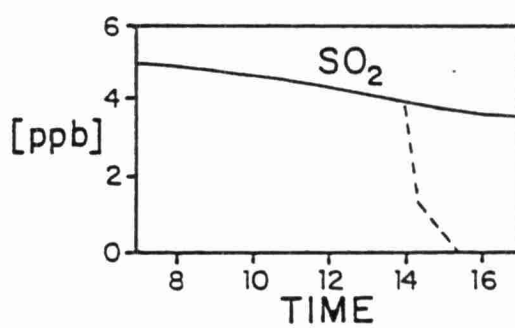
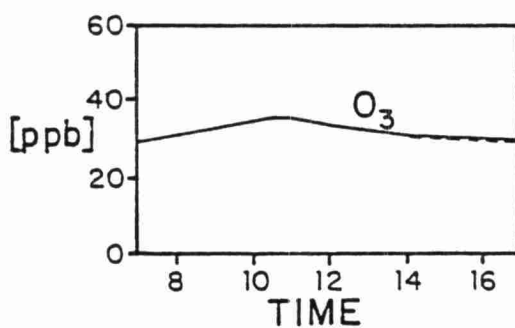
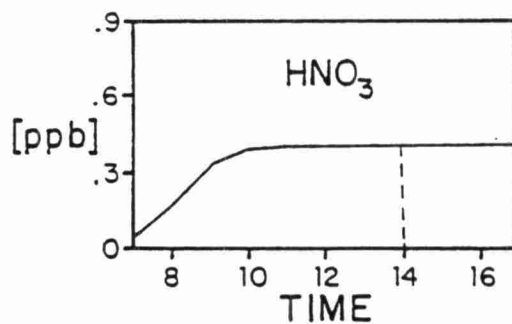
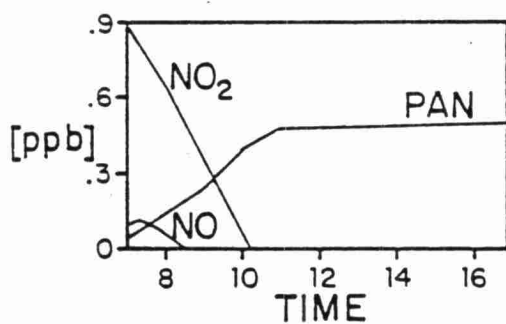


Figure 6.4-5. Gas and Aerosol Concentration-Time Profiles for Case 3. Solid line (—) indicates gas phase only results and dashed lines (---) indicate gas plus aqueous-phase results.

CASE 3

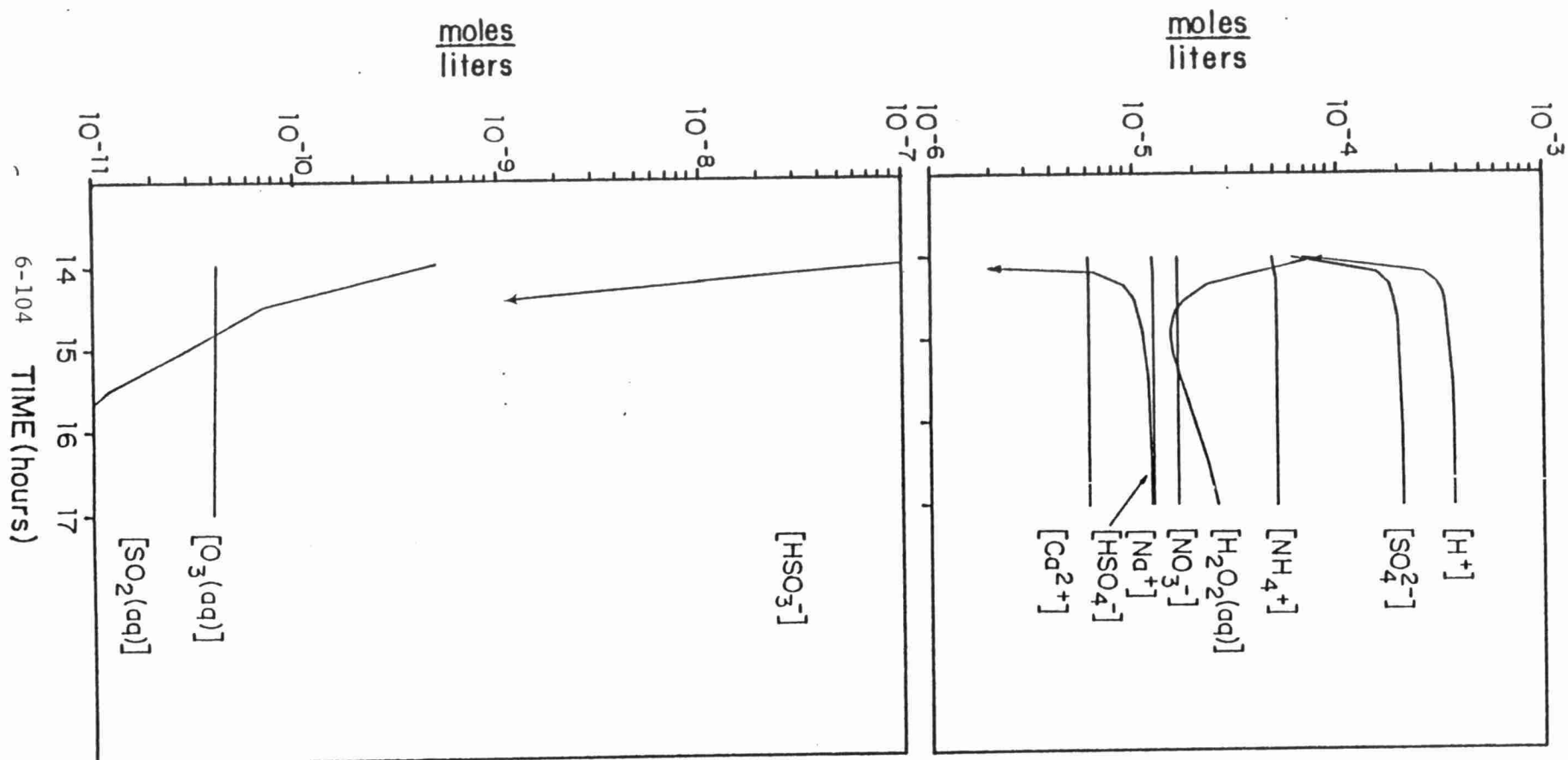


Figure 6.4-6. Aqueous-Phase Concentration-Time Profile for Case 3.

not considered per the recommendation in Section 6.3.2.1. Predicted  $\text{H}_2\text{O}_2$  gas phase concentrations were very low in this case since the  $\text{NO}_x$  was not fully oxidized in which case, the major route to  $\text{H}_2\text{O}_2$  formation ( $\text{HO}_2 + \text{HO}_2 \rightleftharpoons \text{H}_2\text{O}_2 + \text{O}_2$ ) is retarded by  $\text{NO}_x$  reactions with  $\text{HO}_2$ . Gas phase  $\text{H}_2\text{O}_2$  concentrations reached only 60 ppt by the end of the run without the cloud. In the presence of the cloud, gas phase  $\text{H}_2\text{O}_2$  concentrations remained below 5 ppt due to its high solubility and removal by aqueous-phase oxidation of S(IV). The results for  $\text{SO}_2$  gas showed that it was oxidized slowly (1.5% per hour conversion) from an initial concentration of 5 ppb to 4.5 ppb at 1400 by gas phase reactions alone. Without aqueous-phase reactions,  $\text{SO}_2$  gas concentrations were oxidized at 3.6%/hour between 1400 and 1700. With the aqueous-phase reactions included, the total  $\text{SO}_2$  conversion rate increased to 6.7% per hour between 1400 and 1700. During this time period the pH decreased from 3.4 to 3.2. It should be pointed out that these pH values are relatively low because no ammonia was associated with the  $\text{HNO}_3$  produced in the gas phase (see Figure 6.4-2 which shows that  $\text{NO}_3^-$  and  $\text{H}^+$  track quite closely). At these pH values, S(IV) oxidation by ozone was quite slow; it averaged 0.15% per hour between 1400 and 1700. The trace amounts of  $\text{H}_2\text{O}_2$  in the system were responsible for the other 3% per hour conversion of  $\text{SO}_2$  to sulfate. This result is consistent with the fact that the  $\text{H}_2\text{O}_2$  reaction with S(IV) is very fast over a wide range of pH values, yet the reaction did not dominate  $\text{SO}_2$  oxidation because it was oxidant limited. Hence, the results for Case 1 illustrated a situation where gas and aqueous-phase kinetic processes contributed comparably to  $\text{SO}_2$  conversion.

The results for Case 2 showed that  $\text{NO}_x$  was fully oxidized by 1400 and ozone concentrations were predicted to increase from 10 to 93 ppb. At the 10:1 initial HC/ $\text{NO}_x$  ratio, the results showed that 12 ppb of  $\text{HNO}_3$  and 4 ppb of PAN were formed from the  $\text{NO}_x$  by 1400. Note that the ratio of PAN to  $\text{HNO}_3$  was greater in Case 2 than Case 1 due to the higher initial hydrocarbon loading. However, when liquid water formed, the gas phase nitric acid was lost to the aqueous phase which resulted in a low pH (3.3) and decreased the gas phase  $\text{HNO}_3$  concentration to ~1 ppt. In contrast to Case 1, the Case 2 results where only gas phase processes were considered showed that significant

$\text{H}_2\text{O}_2$  concentrations (1 to 6 ppb) can be reached in the afternoon. The  $\text{H}_2\text{O}_2$  was formed from  $\text{HO}_2$  radicals which were generated from hydrocarbon oxidation in sunlight. Negligible  $\text{H}_2\text{O}_2$  gas is formed before the  $\text{NO}_x$  is fully oxidized because the  $\text{NO}$  and  $\text{NO}_2$  reactions with  $\text{HO}_2$  are much faster than  $\text{HO}_2$  recombination reactions forming  $\text{H}_2\text{O}_2$ . However, after the  $\text{NO}$  and  $\text{NO}_2$  was removed, a significant fraction of the  $\text{HO}_2$  radicals formed from the remaining hydrocarbons recombined to form  $\text{H}_2\text{O}_2$  gas. When the cloud was introduced at 1400, gas phase  $\text{H}_2\text{O}_2$  was reduced from 1.5 to 0.4 ppb owing to its high solubility. During the next half hour the concentration of gas phase  $\text{H}_2\text{O}_2$  was reduced further (to 0.16 ppb) as  $\text{S(IV)}$  was oxidized by aqueous-phase  $\text{H}_2\text{O}_2$  and mass transfer of  $\text{H}_2\text{O}_2$  gas to the aqueous-phase occurred to maintain equilibrium. This aqueous-phase reaction is quite fast over the pH range 1 to 5 and, as indicated by the  $\text{SO}_2$  gas concentration time profile, was quite effective in removing  $\text{SO}_2$  from the system. During the first half hour of combined gas and aqueous-phase processes,  $\text{SO}_2$  gas concentrations were reduced from 4.04 ppb to 1.22 ppb or at a rate of 240% per hour. Of this total rate, approximately 4% was gas phase conversion, less than 1% was aqueous-phase conversion by ozone, the remaining 235% was aqueous-phase conversion by  $\text{H}_2\text{O}_2$ . During the first half hour the pH decreased from 3.3 to 3.1 and total  $\text{S(IV)}$  increased by a factor of 3. After one hour, the gas phase  $\text{SO}_2$  concentration was reduced to 0.4 ppb or one order of magnitude below its concentration when the cloud appeared. Also, after one hour, gas phase production of  $\text{H}_2\text{O}_2$  exceeded its loss to the aqueous-phase and the  $\text{H}_2\text{O}_2$  gas concentration began to increase again. This indicated there was potential to oxidize more  $\text{S(IV)}$  if it were present. Hence, Case 2 illustrates a situation where there is a strong interaction between gas and aqueous chemistry. It shows that aqueous-phase  $\text{S(IV)}$  oxidation can overshadow gas phase oxidation when substantial amounts of  $\text{H}_2\text{O}_2$  are formed in the gas phase. Furthermore, it suggests that a knowledge of the gas phase  $\text{HC/NO}_x$  chemical system is critical in determining the overall rate of conversion of  $\text{SO}_2$  to  $\text{SO}_4^{2-}$  in the atmosphere when clouds are present.

The results for Case 3 illustrate potential chemical behavior in rural atmospheres. Figure 6.4-5 shows that the initial 1 ppb of  $\text{NO}_x$

was rapidly oxidized and that ozone was predicted to increase from 30 ppb at 0700 to a maximum of 37 ppb at 1100. At the high (50:1) initial HC/NO<sub>x</sub> ratio of this case, PAN formation was comparable to HNO<sub>3</sub> formation. By 1100, the initial 1 ppb of NO<sub>x</sub> was converted to 0.4 ppb of HNO<sub>3</sub> and 0.5 ppb of PAN.

Gas phase SO<sub>2</sub> oxidation averaged 3.3% per hour between 0700 and 1400, which was higher than that in Cases 1 and 2, because there was less NO<sub>x</sub> competing for the OH radical. Also, since the NO<sub>x</sub> was fully oxidized early in the day, the H<sub>2</sub>O<sub>2</sub> gas concentration was predicted to reach 2.8 ppb by 1400. At 1400 the H<sub>2</sub>O<sub>2</sub> gas concentration was reduced to 0.8 ppb via initial equilibrium with the cloud. Since this system had only 0.4 ppb of HNO<sub>3</sub> before the cloud was introduced, the initial pH was 4.2, substantially higher than in Cases 1 and 2. Given the high H<sub>2</sub>O<sub>2</sub> concentration, S(IV) oxidation in the aqueous-phase proceeded very rapidly. SO<sub>2</sub> gas was removed by the system at a rate of 400% per hour during the first half hour of contact with the cloud. Approximately 4% per hour occurred by gas phase reactions, 1% per hour by aqueous-phase ozone reactions, and 395% per hour by aqueous-phase H<sub>2</sub>O<sub>2</sub> reactions. Hence, most of the SO<sub>2</sub> was removed from the system in the first 30 minutes and the pH of the aqueous phase was reduced to 3.5. The results for Case 3 were very similar to those for Case 2 in that they showed that a significant amount of H<sub>2</sub>O<sub>2</sub> was produced in the gas phase after the NO<sub>x</sub> was fully oxidized which provided a source of aqueous-phase oxidant to rapidly convert S(IV) to S(VI) at pH values of 3.5 to 4.

It is important to note that in this preliminary feasibility study, a case with higher pH (5 to 6) has not been considered here due to resource constraints. We believe such a case could illustrate the importance of aqueous-phase S(IV) oxidation by ozone as the rate constant for the reaction of ozone with S(IV) increases with increasing pH. Based on the kinetic rate data for this reaction and the general abundance of ozone in the troposphere, it is obvious that the ozone reaction could play an important role in initially reducing the pH of cloud water containing S(IV).

#### 6.4.3 Summary and Recommendations

These case studies were carried out to demonstrate the feasibility of linking a detailed gas phase mechanism with aqueous-phase kinetic and equilibrium processes and to assess the relative importance of the various chemical reactions occurring in the atmospheric oxidation of  $\text{SO}_2$  and  $\text{NO}_x$  to sulfate and nitrate, respectively.

The results indicate significant interaction between the gas and aqueous-phase chemical kinetics and illustrate the need for incorporation of detailed chemical mechanisms in the proposed atmospheric models. Although gas phase  $\text{SO}_2$  oxidation could be approximated by a simple linear kinetic model, accurate predictions of  $\text{HNO}_3$ ,  $\text{O}_3$ , and  $\text{H}_2\text{O}_2$  required a more complex gas phase chemical mechanism which includes  $\text{HC/NO}_x$  reactions. Accurate estimates of  $\text{SO}_4^{2-}$  aerosol,  $\text{HNO}_3$ ,  $\text{O}_3$ , and  $\text{H}_2\text{O}_2$  from the gas phase mechanism are needed to predict chemical transformations in the aqueous phase and, ultimately, to predict precipitation composition and wet deposition rates of sulfur and nitrogen. The rapid  $\text{H}_2\text{O}_2$  oxidation of  $\text{S(IV)}$  shown in these case studies illustrates the need for an aqueous-phase chemical mechanism which includes both kinetic and equilibrium processes. Hence, these case study results for typical ambient conditions reinforce the recommendations provided in the previous three subsections.

## 6.5 Subgrid-Scale Chemical Effects

As discussed in Section 4, the proposed mesoscale and regional models have horizontal grid resolutions on the order of 10 and 100 kilometers, respectively, for the Eastern North America application. Unless algorithms are incorporated in the models to account in some manner for near field (0 to 10 km) effects of emissions from line sources and major point sources, the models will only resolve concentrations at the grid resolution. In reality, concentration variations near sources are substantial owing to the turbulent nature of atmospheric dispersion. Far downwind of the sources (100 to 300 km), concentration variations are generally small. The purpose of both proposed models is to predict average concentrations at significant distances downwind of the sources (i.e., 5 to 10 squares downwind), for which the details of the subgrid-scale concentration distribution in the source region is usually of minor importance. However, numerous researchers (Fisher 1981) have speculated that concentration variations in the near field may effect the overall rates of chemical transformation for chemical species affected by fast chemical reactions.

The classic examples of this are nitric oxide and ozone, which participate in the following fast reactions:



In the proximity of combustion sources, the atmosphere is characterized by pockets of NO-rich air from fresh emissions in O<sub>3</sub>-rich background air. Ignoring NO<sub>2</sub> photolysis for the moment, the chemical rate of changes of NO (and O<sub>3</sub>) in terms of the average ( $\bar{C}$ ) and turbulent fluctuation ( $C'$ ) components of concentration is:



$$\frac{d[\text{NO}]}{dt} = -k_1[\overline{\text{NO}}][\overline{\text{O}_3}] \left( 1 + \frac{[\text{NO}'][\text{O}_3']}{[\overline{\text{NO}}][\overline{\text{O}_3}]} \right)$$

As noted by Eschenroeder et al. (1972),  $[\text{NO}'][\text{O}_3']$  is generally negative, so that the rate of decay of NO and  $\text{O}_3$  may be decreased in an inhomogeneous concentration field, relative to the rate predicted from average concentrations alone. This phenomenon could be expected to occur for any species where the time scale for diffusion is comparable to or greater than that for chemical reactions.

Numerous researchers have discussed the effect of inhomogeneity in the  $\text{NO}/\text{O}_3/\text{NO}_2$  system in terms of apparent departures of ambient data from the photostationary state. Seinfeld (1977), Bilger (1977) and Chock and Kumar (1978) have shown that departures from photostationarity are a mathematical characteristic of time-averaging fluctuating quantities that are governed by a nonlinear constraint. These authors and Eschenroeder noted that the basic problem with using time-averaged data in the photostationary state equation is that the product of average concentrations is not equal to the average of the product of concentrations in a turbulent field, i.e.,

$$\frac{[\overline{\text{NO}}][\overline{\text{O}_3}]}{[\overline{\text{NO}_2}]} \neq \left( \frac{[\text{NO}][\text{O}_3]}{[\text{NO}_2]} \right)$$

Thus, even though the assumption of photostationarity state is locally valid, time-averaged atmospheric concentrations exhibit departures from the photostationary state due to their inhomogeneity.

Other researchers have proposed and developed models of varying complexity to treat second order reactions in turbulent flow fields (Lin and O'Brien 1972; Donaldson and Hilst 1972; Lamb and Shu 1978; Shu et al. 1978). Several of these approaches are practical for incorporation into single source models, yet none, in our opinion, are suitable for models which incorporate thousands of sources.

Lamb (1981) has formulated an approach for determining surface layer average  $\text{NO}$ ,  $\text{NO}_2$  and  $\text{O}_3$  concentrations and mass fluxes to layers aloft in a regional Eulerian photochemical model. The scale of the model is similar to those proposed herein, yet the model differs in that the surface layer is not treated with full chemical kinetics. The approach assumes the surface layer can be subdivided into an approximate volume affected by fresh  $\text{NO}$  emission and a volume of background air containing  $\text{O}_3$ . The model adjusts the average surface layer concentrations and fluxes to account for  $\text{NO}$  scavenging of ozone in the fraction of the volume containing fresh emissions. This approach has the capability of treating the coarse subgrid scale concentration inhomogeneities and essentially prevents excess scavenging of  $\text{O}_3$  by  $\text{NO}$  in grids with large sources. Nevertheless, it does require detailed knowledge of subgrid scale emissions throughout the modeling region.

Since subgrid scale emissions data is not currently available for the eastern U.S. and Canada, and probably will not be developed during the course of this study, it would be unwise for ERT and MEP to propose a model which explicitly depended on it. Nevertheless, if inhomogeneities in the source region can significantly affect the overall rate of chemical transformation, it may be worthwhile to develop a parameterization that depends on the relative emission rates in the grid squares. In order to establish the importance of this phenomenon for models with the 10 to 100 km grid scales, a Phase II task is proposed to investigate and possibly parameterize the effects of subgrid scale inhomogeneities. The proposed approach is empirical and involves exercising the ERT reactive plume model (PLMSTAR) with varying cross-wind resolution. Lurmann et al. (1982) reported a sensitivity case with the PLMSTAR model where the lateral resolution of the plume calculation was varied. As one would expect, peak concentrations were found to be a strong function of the lateral resolution, yet owing to the nonlinear coupling of chemistry and dispersion, the difference in peak concentrations were found not to be a simple linear function of grid resolution. The proposed Phase II analysis involves sensitivity analysis of this type where the average downwind concentration and average deposition rates will be employed as the criteria to establish the importance and parameterization of subgrid scale concentration fluxation effects.

## 6.6 Conclusions and Recommendations

The major homogeneous gas phase and heterogeneous oxidation mechanisms for  $\text{NO}_x$  and  $\text{SO}_x$  are discussed above. Transport of gaseous phase species to the aqueous phase followed by subsequent reaction, is discussed in Section 6.3. Based on the above discussions and information presented in recent reviews and papers (Calvert 1978, 1982; Bottenheim and Strausz 1982; Rhode et al. 1981), the following treatment is recommended for the mesoscale and regional models:

- The heterogeneous oxidation of  $\text{SO}_2$  on dry particles should be ignored for regional applications.
- The main processes for oxidizing  $\text{SO}_2$  in the gas phase are via the hydroxyl radical, Criegee intermediates and possibly alkylperoxy radicals. These species are included in the photochemical mechanism and consequently, they participate in the gas phase photooxidation.
- A photochemical mechanism should be incorporated to describe the conversion of  $\text{NO}_x$  to nitrate. This should be based on the mechanism developed by Atkinson et al. (1982), modified to include one hydrocarbon typical of each of the four classes. The output of this module will include, among others, concentrations for hydrogen peroxide and ozone which are important for aqueous-phase oxidation of  $\text{SO}_2$ .
- An equilibrium chemistry model with kinetic constraints will be used to address aqueous-phase equilibrium and oxidation processes.
- Seasonal, climatological and geographical  $\text{H}^+/\text{NH}_4^+$  and  $\text{Ca}^{2+}/\text{Mg}^{2+}/\text{Na}^+$  cation ratios will be estimated from precipitation chemistry monitoring networks.
- The importance of catalytic oxidation of S(IV) by  $\text{O}_2$  in the presence of trace metals (Fe, Mn and possibly  $\text{VO}^{2+}$ ) and carbon particles will be assessed. Parameterizations of these processes, applicable at night and near urban sources, may be sufficient to describe these reactions.

- It is recommended that aqueous-phase oxidation of NO and NO<sub>2</sub> be ignored due to our present understanding that the processes are kinetically slow.

The initial proposed gas phase chemical mechanism is presented in Table 6.6-1. This mechanism is a condensed version of the Atkinson et al. (1980) mechanism. Although maximum condensation of the mechanism is desirable to minimize computing requirements, past experience has shown that drastic elimination of reactions and specie results in an unrealistic scheme. Hence, one representative compound has been included in the proposed mechanism to represent each hydrocarbon class. The compounds are:

- Propene for the olefin class. This choice permits the formation of formaldehyde and also acetyl peroxy radicals from acetaldehyde. The choice for the value of the rate constant may be decreased to reflect the greater proportion of ethene in the atmosphere and in emissions compared to propene.
- A lumped >C<sub>3</sub> alkane for the alkanes as (is included in the Atkinson et al. (1982) mechanism) with a realistic percentage going to alkyl nitrate.
- Toluene for the chosen aromatic class. It is one of the more abundant aromatic compounds in the atmosphere and has one alkyl side group to provide some representation of the xylenes.
- Formaldehyde and acetaldehyde for the oxygenated class. The latter is representative of the higher aldehydes and the ketones such as methyl ethyl ketone.

This data set should provide a reasonably sound chemical scheme with an acceptable computing time requirement. The chemical species to be considered are shown in Table 6.6-2.

Inclusion of the hydrocarbons together with NO<sub>x</sub> and SO<sub>x</sub> represents the first time that such a comprehensive approach will be used to investigate sulfate and nitrate formation under atmospheric

conditions. The proposed approach will allow the prediction of gas phase species such as ozone and hydrogen peroxide which can enter the aqueous phase and participate in the oxidation of  $\text{SO}_2$ . The aqueous-phase oxidation of S(IV) by  $\text{O}_3$  and  $\text{H}_2\text{O}_2$  will be treated in a rigorous fashion. In-cloud and below-cloud scavenging of acidic aerosols, soil dust and soluble gases will also be considered in this approach. The above, coupled with physical descriptions of cloud processes, will allow predictions of the chemical composition of precipitation, including pH, to be made. This comprehensive approach represents a significant improvement on current methodology for modeling chemical transformations in regional models.

TABLE 6.6-1

## THE SUGGESTED CONDENSED ERT PHOTOCHEMICAL MECHANISM - GAS PHASE

<u>Reaction</u>	<u>Rate Constant (ppm min units)</u>
<u>Inorganics</u>	
1. $\text{NO}_2 + h\nu \xrightarrow{\text{O}_2} \text{NO} + \text{O}_3$	radiation dependent
2. $\text{NO} + \text{O}_3 \rightarrow \text{NO}_2 + \text{O}_2$	$1.0 \times 10^6 \text{ T}^{-1} e^{-1450/\text{T}}$
3. $\text{O}_3 + h\nu \rightarrow \text{OH}$	$\beta_1 k_1 \times 7.5 \times 10^{-6} [\text{H}_2\text{O}]$
4. $\text{OH} + \text{NO} \xrightarrow{\text{M}} \text{HONO}$	$8.7 \times 10^8 \text{ T}^{-2}$
5. $\text{OH} + \text{NO}_2 \xrightarrow{\text{M}} \text{HNO}_3$	$1.5 \times 10^9 \text{ T}^{-2}$
6. $\text{HONO} + h\nu \rightarrow \text{OH} + \text{NO}$	$\beta_2 k_1$
7. $\text{HO}_2 + \text{NO} \rightarrow \text{OH} + \text{NO}_2$	$3.7 \times 10^6 \text{ T}^{-1}$
8. $\text{HO}_2 + \text{NO}_2 \xrightarrow{\text{M}} \text{HO}_2\text{NO}_2$	$1.5 \times 10^8 \text{ T}^{-2}$
9. $\text{HO}_2\text{NO}_2 \xrightarrow{\text{M}} \text{HO}_2 + \text{NO}_2$	$7.8 \times 10^{-15} e^{-10420/\text{T}}$
10. $\text{HO}_2 + \text{HO}_2 \rightarrow \text{H}_2\text{O}_2 + \text{O}_2$	$3.4 \times 10^4 \text{ T}^{-1} e^{1100/\text{T}}$
11. $\text{H}_2\text{O}_2 + h\nu \rightarrow 2\text{OH}$	$\beta k_1$
12. $\text{HO}_2 + \text{HO}_2 + \text{H}_2\text{O} \rightarrow \text{H}_2\text{O}_2 + \text{O}_2 + \text{H}_2\text{O}$	$5.8 \times 10^{-5} \text{ T}^{-2} e^{5800/\text{T}}$
13. $\text{OH} + \text{CO} \xrightarrow{\text{O}_2} \text{HO}_2$	$1.3 \times 10^5 \text{ T}^{-1}$
14. $\text{NO}_2 + \text{O}_3 \rightarrow \text{NO}_3$	$5.3 \times 10^4 \text{ T}^{-1} e^{-2450/\text{T}}$
15. $\text{NO} + \text{NO}_3 \rightarrow 2\text{NO}_2$	$8.4 \times 10^6 \text{ T}^{-1}$
16. $\text{NO}_2 + \text{NO}_3 \xrightarrow{\text{M}} \text{N}_2\text{O}_5$	$3.1 \times 10^7 \text{ T}^{-1} e^{-1100/\text{T}}$
17. $\text{N}_2\text{O}_5 \xrightarrow{\text{M}} \text{NO}_2 + \text{NO}_3$	$3.5 \times 10^{18} e^{-12280/\text{T}}$
18. $\text{N}_2\text{O}_5 + \text{H}_2\text{O} \rightarrow 2 \text{HNO}_3$	$1.33 \times 10^{-3} \text{ T}^{-1}$
19. $\text{NO}_3 + h\nu \rightarrow 0.3 \text{ NO} + 0.7 \text{ NO}_2$ $\quad \quad \quad + 0.7 \text{ O}_3$	$\beta_3 k_1$
20. $\text{OH} + \text{O}_3 \rightarrow \text{HO}_2$	$7.0 \times 10^5 \text{ T}^{-1} e^{-940/\text{T}}$

TABLE 6.6-1 (Continued)

<u>Reaction</u>	<u>Rate Constant (ppm min units)</u>
<u>Inorganics</u>	
21. $\text{HO}_2 + \text{O}_3 \rightarrow \text{OH}$	$4.8 \times 10^3 \text{ T}^{-1} e^{-580/\text{T}}$
<u>Formaldehyde</u>	
22. $\text{HCHO} + \text{hv} \xrightarrow{\text{O}_2} \text{HO}_2 + \text{HO}_2 + \text{CO}$	$\beta_4 k_1$
23. $\text{HCHO} + \text{hv} \rightarrow \text{CO} + \text{H}_2$	$\beta_5 k_1$
24. $\text{OH} + \text{HCHO} \xrightarrow{\text{O}_2} \text{HO}_2 + \text{CO}$	$4.4 \times 10^6 \text{ T}^{-1}$
<u>Acetaldehyde</u>	
25. $\text{CH}_3\text{CHO} + \text{hv} \xrightarrow{\text{O}_2} \text{CH}_3\text{O}_2 + \text{HO}_2 + \text{CO}$	$\beta_6 k_1$
26. $\text{OH} + \text{CH}_3\text{CHO} \xrightarrow{\text{O}_2} \text{CH}_3\text{CO}_3$	$3.0 \times 10^6 \text{ T}^{-1} e^{250/\text{T}}$
27. $\text{CH}_3\text{CO}_3 + \text{NO}_2 \rightarrow \text{PAN}$	$2.1 \times 10^6 \text{ T}^{-1}$
28. $\text{PAN} \rightarrow \text{CH}_3\text{CO}_3 + \text{NO}_2$	$1.2 \times 10^{18} e^{-13543/\text{T}}$
29. $\text{CH}_3\text{CO}_3 + \text{NO} \xrightarrow{\text{O}_2} \text{NO}_2 + \text{CH}_3\text{O}_2$	$3.1 \times 10^6 \text{ T}^{-1}$
30. $\text{CH}_3\text{O}_2 + \text{NO} \rightarrow \text{HCHO} + \text{HO}_2 + \text{NO}_2$	$3.1 \times 10^6 \text{ T}^{-1}$
<u>Alkanes</u>	
31. $\text{OH} + \text{Alkane} \rightarrow 1.8 \text{ NO} + 1.7 \text{ NO}_2$ $\quad \quad \quad + .9 \text{ HO}_2 + .4 \text{ CH}_3\text{CHO}$ $\quad \quad \quad + .45 \text{ MEK} + .3 \text{ CH}_3\text{COCH}_3$	$6.6 \times 10^6 \text{ T}^{-1} e^{-400/\text{T}}$
<u>Alkenes</u>	
32. $\text{OH} + \text{Propene} \xrightarrow{\text{O}_2} \text{HCHO} + \text{CH}_3\text{CHO} + \text{HO}_2$ $\quad \quad \quad + \text{NO}_2 - \text{NO}$	$1.8 \times 10^6 \text{ T}^{-1} e^{540/\text{T}}$

TABLE 6.6-1 (Continued)

<u>Reaction</u>	<u>Rate Constant (ppm min units)</u>
<u>Alkenes</u> (Continued)	
33. $O_3 + \text{Propene} \rightarrow 0.5 \text{ HCHO} + 0.5 \text{ CH}_3\text{CHO}$ $+ 0.2 \dot{\text{C}}\text{H}_2\ddot{\text{O}}_2 + 0.2 \text{ CH}_3\dot{\text{C}}\text{HO}\ddot{\text{O}}$ $+ 0.3 \text{ CO} + 0.2 \text{ HO}_2 + 0.1 \text{ OH}$ $+ 0.2 \text{ CH}_3\text{O}_2$	$3.1 \times 10^3 \text{ T}^{-1} e^{-1900/T}$
34. $\dot{\text{C}}\text{H}_2\ddot{\text{O}}_2 + \text{NO} \rightarrow \text{HCHO} + \text{NO}_2$	$3.1 \times 10^3 \text{ T}^{-1}$
35. $\dot{\text{C}}\text{H}_2\ddot{\text{O}}_2 + \text{NO}_2 \rightarrow \text{HCHO} + \text{NO}_3$	$3.1 \times 10^5 \text{ T}^{-1}$
36. $\dot{\text{C}}\text{H}_2\ddot{\text{O}}_2 + \text{H}_2\text{O} \rightarrow \text{Product}$	$1.5 \text{ T}^{-1}$
37. $\text{CH}_3\dot{\text{C}}\text{HO}\ddot{\text{O}} + \text{NO} \rightarrow \text{CH}_3\text{CHO} + \text{NO}_2$	$3.1 \times 10^6 \text{ T}^{-1}$
38. $\text{CH}_3\dot{\text{C}}\text{HO}\ddot{\text{O}} + \text{NO}_2 \rightarrow \text{CH}_3\text{CHO} + \text{NO}_3$	$3.1 \times 10^5 \text{ T}^{-1}$
39. $\text{CH}_3\dot{\text{C}}\text{HO}\ddot{\text{O}} + \text{H}_2\text{O} \rightarrow \text{Product}$	$1.5 \text{ T}^{-1}$
<u>Aromatics</u>	
40. $\text{OH} + \text{Toluene} \rightarrow 0.11 \text{ NO}_2 - 0.15 \text{ NO}$ $0.2 \text{ Cresol} + 0.20 \text{ HO}_2 + 0.65 \text{ ADD}$	$2.7 \times 10^6 \text{ T}^{-1}$
41. $\text{ADD} + \text{NO} \rightarrow 0.75 \text{ NO}_2 + 0.75 \text{ HO}_2$ $+ 0.75 \text{ DIAL} + 0.75 \text{ CH}_3\text{COCHO}$	$3.1 \times 10^6 \text{ T}^{-1}$
42. $\text{OH} + \text{DIAL} \rightarrow \text{E1}$	$1.3 \times 10^7 \text{ T}^{-1}$
43. $\text{EL} + \text{NO}_2 \rightarrow \text{E1 NO}_2$	$2.1 \times 10^6 \text{ T}^{-1}$
44. $\text{EL NO}_2 \rightarrow \text{E1} + \text{NO}_2$	$1.2 \times 10^{18} e^{-13532/T}$
45. $\text{E1} + \text{NO} \rightarrow 3 \text{ NO}_2 - 2 \text{ NO} + \text{HO}_2$ $+ (\text{CHO})_2 + \text{CO}$	$3.1 \times 10^6 \text{ T}^{-1}$
46. $\text{OH} + (\text{CHO})_2 \xrightarrow{O_2} \text{HO}_2 + \text{CO}$	$8.8 \times 10^6 \text{ T}^{-1}$
47. $(\text{CHO})_2 + h\nu \rightarrow \text{HCHO} + \text{CO}$	$\beta_8 k_1$



TABLE 6.6-1 (Continued)

<u>Reaction</u>	<u>Rate Constant (ppm min units)</u>
<u>Aromatics (Continued)</u>	
48. $\text{OH} + \text{CH}_3\text{COCHO} \xrightarrow{\text{O}_2} \text{CH}_3\text{CO}_3 + \text{CO}$	$6.6 \times 10^6 \text{ T}^{-1}$
49. $\text{CH}_3\text{COCHO} + \text{h}\nu \xrightarrow{\text{O}_2} \text{CH}_3\text{CO} + \text{HO}_2 + \text{CO}$	$\beta_9 k_1$
50. $\text{OH} + \text{Cresol} \rightarrow -\text{NO} + 0.75 \text{ NO}_2$ $+ 0.75 \text{ HO}_2 + 0.75 \text{ DIAL}$	$1.9 \times 10^7 \text{ T}^{-1}$
51. $\text{NO}_3 + \text{Cresol} \rightarrow -\text{NO}_2 + \text{HNO}_3$	$k = 6.6 \times 10^6 \text{ T}^{-1}$
<u>SO<sub>x</sub></u>	
52. $\text{SO}_2 + \text{OH} \xrightarrow{\text{M}} \text{SO}_4^-$	$1.5 \times 10^{13} \text{ T}^{-4}$
53. $\text{SO}_2 + \dot{\text{C}}\text{H}_2\dot{\text{O}}_2 \rightarrow \text{HCHO} + \text{SO}_4^-$	$3 \times 10^4 \text{ T}^{-1}$
54. $\text{SO}_2 + \text{CH}_3\dot{\text{C}}\text{HOO} \rightarrow \text{CH}_3\text{CHO} + \text{SO}_4^-$	$3 \times 10^4 \text{ T}^{-1}$

TABLE 6.6-2

## CHEMICAL SPECIES FOR SUGGESTED CONDENSED MECHANISM

<u>Gas Phase</u>		<u>Aqueous Phase</u>
<u>Inorganic</u>	<u>Organic</u>	
SO <sub>2</sub>	Alkanes	HSO -*
SO <sub>4</sub>	Alkenes (propylene)	SO <sub>2</sub> *
NO	Aromatics (toluene)	H <sub>2</sub> O <sub>2</sub> *
NO <sub>2</sub>	HCHO	O <sub>3</sub> *
O <sub>3</sub>	CH <sub>3</sub> CHO	SO <sub>4</sub> <sup>=</sup>
H <sub>2</sub> O <sub>2</sub>	PAN	H <sup>+</sup>
HNO <sub>3</sub>	CH <sub>3</sub> COCHO* (ACOX)	
HONO	CH <sub>3</sub> O <sub>2</sub> * (MPOX)	
HO <sub>2</sub> NO <sub>2</sub>	CH <sub>3</sub> CHO <sup>•</sup> (CD)	
NO <sub>3</sub> *	CH <sub>2</sub> O <sub>2</sub> * (CHO <sub>2</sub> )	
N <sub>2</sub> O <sub>5</sub> *	ADD	
OH*	CRES	
HO <sub>2</sub> *	DIAL	
H <sub>2</sub> O*	CH <sub>3</sub> COCHO (MGLY)	
	(CHO) <sub>2</sub> (GLY)	
	EL*	
	ElNO <sub>2</sub>	

\*Potential Steady State Species.

## SECTION 6 REFERENCES

- Altwick, E.R. 1979. Oxidation Inhibition in Aqueous Solution. A.I.Ch.E. Symposium Series No. 188, 75:145-150.
- Arnts, R.R. and B.W. Gay, Jr. 1979. "Photochemistry of Some Naturally Emitted Hydrocarbons", EPA-600/3-79-081, September.
- Arnts, R.R. and S.A. Meeks 1980. "Biogenic Hydrocarbon Contribution to the Ambient Air of Selected Areas", EPA-600/3-80-023, January.
- Atkinson, R., K.R. Darnall, A.C. Lloyd, A.M. Winer and J.N. Pitts, Jr. 1979. "Kinetics and Mechanisms of the Reactions of the Hydroxy Radical with Organic Compounds in the Gas Phase." Adv. Photochem., 11, 375.
- Atkinson, R. and A.C. Lloyd 1980. "Evaluation of Kinetic and Mechanistic Data for Photochemical Smog Chamber Modeling", EPA Contract No. 68-02-3280, ERT Document No. P-A040.
- Atkinson, R., W.P.L. Carter, K.R. Darnall, A.M. Winer and J.N. Pitts, Jr., 1980. Int. J. Chem. Kinet., 12, 779.
- Atkinson, R., A.C. Lloyd, L. Wings 1982. "An Updated Chemical Mechanism for Hydrocarbon/NO<sub>x</sub>/SO<sub>x</sub> Photooxidations Suitable for Inclusion in Atmospheric Simulation Models," Atmospheric Environment, 16.
- Baboolal, L.B., H.R. Pruppacher and J.H. Toplian 1981. A Sensitivity Study of the Theoretical Model of SO<sub>2</sub> Scavenging by Water Drops in Air. J. Atmos. Sci. 38:856-870.
- Baldwin, A.C., J.R. Barker, D.M. Golden and D.G. Hendry 1977. J. Phys. Chem., 81, 2483.
- Baldwin, A.C. 1982. "Heterogeneous Reactions of Sulfur Dioxide with Carbonaceous Particles", Int. J. of Chem. Kin., 14, 269.
- Barrie, L.A. 1981. The Predicting of Rain Acidity and SO<sub>2</sub> - Scavenging in Eastern North America. Atmos. Environ. 15:31-41.
- Bassett, M., F. Gelbard, and J.H. Seinfeld 1981. Mathematical Model for Multicomponent Aerosol Formation and Growth in Plumes. Atmos. Environ. 15:2395-2406.
- Batt, L. 1979a. Int. J. Chem. Kinet., 11: 977.
- Batt, L. 1979b. "Reactions of Alkoxy Radicals Relevant to Atmospheric Chemistry", European Symposium on "Physico-Chemical Behavior of Atmospheric Pollutants", Ispra, Oct. 16-18.
- Batt, L., and G.N. Robinson 1979. Int. J. Chem. Kinet., 11: 1045.

- Beilke, S. and G. Gravenhorst 1978. Heterogeneous  $\text{SO}_2$  Oxidation in the Droplet Phase. Atmos. Environ. 12:231-239.
- Biermann, H.W., G.W. Harris and J.N. Pitts, Jr. 1980. 14th Informal Conf. Photochem., Newport, California, March 30-April 3.
- Bignozzi, C.A., A. Maldotti, C. Chiorboli, C. Bartocci, and V. Carassiti 1981. "Kinetics and Mechanisms of Reactions between Atmospheric Olefins and Hydroxyl Radicals", Int. J. Chem. Kinetics, 13: 1235.
- Bottenheim, J.W. and O.P. Strausz 1982. "Modeling Study of a Chemically Reactive Power Plant Plume", Atmos. Environ. 16, 85.
- Brodzinsky, R., S.G. Chang, S.S. Markowitz and T. Novakov 1980. Kinetics and Mechanisms for the Catalytic Oxidation of Sulfur Dioxide on Carbon in Aqueous Suspensions. J. Phys. Chem. 84:3354-3358.
- Bufalini, J.J. 1980. Impact of Natural Hydrocarbon on Air Quality. EPA-600/2-80-086, U.S. Environmental Protection Agency, Office of Research and Development, Research Triangle Park, NC.
- Calvert, J.G. and J.N. Pitts, Jr. 1966. "Photochemistry", Wiley, New York, N.Y.
- Calvert, J.G. F. Su, J.W. Bottenheim and O.P. Strausz 1978. Atm. Environ., 12: 197.
- Carmichael, G.R. and L.K. Peters 1982. Eulerian Modeling of the Transport and Chemical Processes Affecting the Long Range Transport of  $\text{SO}_2$  and Sulfate, to be published in: Modeling of Total Acid Precipitation Impacts, J.L. Schoor ed., Vol. 9 of Acid Precipitation, J.I. Teasley ed. Ann Arbor Science, Woburn, MA.
- Carter, W.P.L., K.R. Darnall, A.C. Lloyd, A.M. Winer and J.N. Pitts, Jr. 1976. Chem. Phys. Lett., 42: 22.
- Carter, W.P.L., K.R. Darnall, R.A. Graham, A.M. Winer and J.N. Pitts, Jr. 1979. J. Phys. Chem., 83: 2305.
- Carter, W.P.L., A.C. Lloyd, J.L. Sprung and J.N. Pitts, Jr. 1979. Int. J. Chem. Kinet., 11: 45.
- Chamaides, W.L. and D.D. Davis 1982. The Free Radical Chemistry of Cloud Droplets and its Impact upon the Composition of Rain. J. Geophys. Res. 87:4863-4877.
- Chang, S.G., R. Toosi and T. Novakov 1981. The Importance of Soot Particles and Nitrous Acid in Oxidizing  $\text{SO}_2$  in Atmospheric Aqueous Droplets. Atmos. Environ. 15:1287-1292.

- Charleson, R.J. and H. Rhode 1982. Factors Controlling the Acidity of Natural Rainwater. Nature 295:683-685.
- Cox, R.A. and S.A. Penkett 1971. "Photooxidation of Atmospheric SO<sub>2</sub>, Nature, 229, 486-88 (1971), "Oxidation of Atmospheric SO<sub>2</sub> by <sup>2</sup> Products of Ozone-Olefin Reaction", Nature 230: 321-22.
- Cox, R.A. and M.J. Roffey 1977. Environ. Sci. and Tech. 11: 900.
- Cox, R.A., R.G. Derwent and M.R. Williams 1980. Environ. Sci. Technol., 14:57.
- Danckwerts, P.V. 1970. Gas-Liquid Reactions (New York: McGraw-Hill, 1970).
- Darnall, K.R., W.P.L. Carter, A.M. Winer, A.C. Lloyd and J.N. Pitts, Jr. 1976. J. Phys. Chem., 80: 1948.
- Darnall, K.R., R. Atkinson and J.N. Pitts, Jr. 1979. J. Phys. Chem., 83: 1943.
- Demerjian, K.L., J.A. Kerr and J.G. Calvert 1974. "The Mechanism of Photochemical Smog Formation", Adv. Environ. Sci. Technol., 4: 1.
- Derwent, R. G. and O. Hov 1982. "The Potential for Secondary Pollutant Formation in the Atmospheric Boundary Layer in a High Pressure Situation over England," Atmos. Environ., 16 655.
- Dimitriades, B., A.P. Altshuller 1977. "International Conference on Oxidants--1976: Analysis of evidence and viewpoints, Part I. Definitions of key issues," JAPCA 27:299.
- Dimitriades, B. 1981. The Role of Natural Organics in Photochemical Air Pollution Joint Air Pollution Control Association, 31, 229.
- Dodge, M.C. and R.R. Arnts 1979. Int. J. Chem. Kinet., 11: 399.
- Durham, J.L., J.H. Overton and V.P. Aneja 1981. Influence of Gaseous Nitric Acid on Sulfate Production and Acidity in Rain. Atmos. Environ. 15:1059-1068.
- Edney, E.O., J.W. Spence and P.L. Hanst 1979. J. Air Poll. Contro. Assoc., 29: 741.
- Erickson, R.E., L.M. Yates, R.L. Clark and D. McEwen 1977. The Reaction of Sulfur Dioxide with Ozone in Water and its Possible Atmospheric Significance. Atmos. Environ. 11:813-817.
- Falls, A.H. and J.H. Seinfeld 1978. Environ. Sci. Technol., 12: 1398
- Freiberg, J.E. and S.E. Schwartz 1980. Oxidation of SO<sub>2</sub> in Aqueous Droplets: Mass-Transport Limitation in Laboratory Studies and the Ambient Atmosphere. Atmos. Environ. 15:1145-1154.

- Gelbard, F. and J.H. Seinfeld 1980. Simulation of Multicomponent Aerosol Dynamics. J. Colloid Interface Sci., 78:485-501.
- Golden, D.M. 1979. "Chemical Kinetic Data Needs for Modeling the Lower Troposphere," National Bureau of Standards Special Publication 557, August.
- Graedel, T.E. 1979. Rev. Geo. Phys. and Space Phys. 17:937.
- Grimsrud, E.P., H.H. Westberg and R.A. Rasmussen 1975. Int. J. Chem Kiu. Symp. 1:183.
- Grosjean, D. et al. 1981. Deriving EKMA Isopleths from Experimental Data: The Los Angeles Captive Air Experiment. Presented at the EKMA Workshop, EPA-ERSL, Research Triangle Park, NC, December 15-17.
- Grosjean, D., A. Lloyd, R.J. Countess, F. Lurmann, K. Fung, K. Ganesan, B.Nitta, J. Collins, J. Harrison 1982. "Captive Air Experiments in Support of Photochemical Kinetic Model Development, Draft Report for Coordinating Research Council.
- Grosjean, D. 1982. Personal communication.
- Gutman, D., N. Sanders and J.E. Butler 1982. J. Phys. Chem. 86, 66.
- Hales, J.M. 1978. Wet Removal of Sulfur Compounds from the Atmosphere. Atmos. Environ. 12:389-399.
- Hales J.M. and M.T. Dana 1979. Precipitation Scavenging of Urban Pollutants by Convective Storm Systems. J. Appl. Meteor. 18: 294-316.
- Hampson, R.F., Jr. and D. Garvin, eds. 1978. "Reaction Rate and Photochemical Data for Atmospheric Chemistry - 1977", NBS Special Publication 513, May.
- Harris, S.W., W.P.L. Carter, A.M. Winer, J.N. Pitts, Jr., N. Platt and D. Perner 1982. Environ. Sci. and Tech., in press.
- Harrison, H., T.V. Larson and C.S. Monkton 1982. Aqueous-Phase Oxidation of Sulfites by Ozone in the Presence of Iron and Manganese. Atmos. Environ., 16:1039-1041.
- Hegg, D.A. and P.V. Hobbs 1978. Oxidation of SO<sub>2</sub> Aqueous Systems with Particular Reference to the Atmosphere. Atmos. Environ. 12:241-153.
- Hegg, D.A. and P.V. Hobbs 1981. Cloud Water Chemistry and the Production of Sulfate in Clouds. Atmos. Environ., 15:1597-1604.
- Heicklen, J., K. Westberg and N. Cohen 1969. Report No. 115-69, Center for Air Environment Studies, Pennsylvania State University, University Park, PA.

- Heikes, B.G., A.L. Lazrus, G.L. Kok, S.M. Kunen, B.W. Grandrud, S.W. Gitlin and P.D. Sperry 1982. Evidence for Aqueous Phase Hydrogen Peroxide Synthesis in the Troposphere. J. Geophys. Res. 87:3045-3051.
- Hendry, D.G. 1979. "Chemical Kinetic Data Needs for Modeling the Lower Troposphere," National Bureau of Standards Special Publication 557, August.
- Hendry, D.G. and R.A. Kenley 1979. "Atmospheric Chemistry of Peroxynitrates", in Nitrogenous Air Pollutants, ed. D. Grosjean, Ann Arbor Press, Ann Arbor, Michigan.
- Hering, S.V. 1982. Inference of Formation Mechanisms From Comparison of Total and Elemental Size Distributions. Paper 23-3, presented at the First Annual Conference of the American Association for Aerosol Research. Santa Monica, CA, February 17-19.
- Herron, J.T. and R.E. Huie 1977. J. Amer. Chem. Soc., 99: 5430.
- Herron, J.T. and R.E. Huie 1978. Int. J. Chem. Kinet., 10: 1019.
- Herron, J.T., R.I. Martinez and R.E. Huie 1982. Kinetics and Energetics of the Criegee Intermediate in the Gas Phase I. The Criegee Intermediate in Ozone-Alkene Reactions Int. J. Chem. Kinet. 14: 201.
- Hidy, G. 1973. Removal of Gaseous and Particulate Pollutants. In Chemistry of the Lower Atmosphere, ed. S.I. Rasool Plenum Press, New York, NY.
- Holdren, M.W., H.H. Westberg, and P.R. Zimmerman 1979. Analysis of Monoterpene Hydrocarbons in Rural Atmospheres. J. Geophys. Res., 84:5083.
- Hoffman, M.R. and J.O. Edwards 1975. Kinetics of the Oxidation of Sulfite in Hydrogen Peroxide in Acidic Solution. J. Phys. Chem. 79:2096-2098.
- Hoigne, J. and H. Bader 1976. The Role of Hydroxyl Radical Reactions in Ozonation Processes in Aqueous Solutions. Water Res., 10:377-386.
- Hong, M.S. and G.R. Carmichael 1982. An Investigation of Sulfate Production in Clouds Using a Flow-Through Chemical Reactor Model Approach. 2nd Symposium on the Composition of the Nonurban Troposphere, Amer. Meteorological Society, Williamsburg, VA, May 1982.
- Hov O. and I.S.A. Isaksen 1979. Geophys. Res. Lett., 6:219.
- Huie, R.E. and J.T. Herron 1975. Int. J. Chem. Kinet., Symp. 1, 165.

- Judeikis, H.S., B.T. Stewart and A.G. Wren 1978. Atm. Environ. 12:1633.
- Kamens, R.M., M.W. Gery, H.J.F. Jeffries, M. Jackson, E.I. Cole 1981. Ozone Isoprene Reactions Product Formation and Aerosol Potential. Accepted by International Journal of Chemical Kinetics.
- Kan, C.S., Fu Su, J.G. Calvert and J.H. Shaw 1981. "Mechanism of the Ozone-Ethene Reaction in Dilute  $N_2/O_2$  Mixtures Near Atm Pressure," J. Physical Chem. 85:2359-63.
- Kenley, R.A., J.E. Davenport and D.G. Hendry 1978. J. Phys. Chem., 82: 1095.
- Larson, T.V., N.R. Horike and H. Harrison 1978. Oxidation of  $SO_2$  by  $O_2$  and  $O_3$  in Aqueous Solution: A Kinetic Study with Significance to Atmospheric Rate Processes. Atmos. Environ. 12:1597-1611.
- Lee, Y.-N. and S.E. Schwartz 1981a. Reaction Kinetics of Nitrogen Dioxide with Liquid Water at Low Partial Pressure. J. Phys. Chem. 85:840-848.
- Lee, Y.-N. and S.E. Schwartz 1981b. Evaluation of the Rate of Uptake of Nitrogen Dioxide by Atmospheric and Surface Liquid Water. J. Geophys. Res. 86:11971-11983.
- Lee, Y.-N. and S.E. Schwartz 1982. Kinetics of Aqueous Phase Reactions of  $NO_2$  with NO at Low Partial Pressures. In preparation, 1982.
- Liberti, A., D. Biocco and M. Possanzini 1978. Atm. Environ., 12:255.
- Lonneman, W.A., R.L. Seila and J.J. Bufalini 1978. Ambient Air Hydrocarbon Concentrations in Florida. Environ. Sci. Technol., 12:459.
- Maahs, H.G. 1982. The Importance of Ozone in the Oxidation of Sulfur Dioxide in Nonurban Tropospheric Clouds. 2nd Symposium on the Composition of the Nonurban Troposphere, Amer. Meteorological Society., Williamsburg, VA, May 1982.
- Mader, P.M. 1958. Kinetics of the Hydrogen Peroxide-Sulfite Reaction in Alkaline Solution. J. Am. Chem. Soc. 80:2634-2639.
- Martin, L.R., D.E. Damschen and H.S. Judeikis 1981. The Reactions of Nitrogen Oxides with  $SO_2$  in Aqueous Aerosols. Atmos. Environ. 15:191-195.
- Martin, L.R. and D.E. Damschen 1981. Aqueous Oxidation of Sulfur Dioxide by Hydrogen Peroxide at Low pH. Atmos. Environ., 15:1615-1621.



- Martin, L.R. 1982. Kinetic Studies of Sulfite Oxidation in Aqueous Solution, to be published in "SO<sub>2</sub>, NO and NO<sub>2</sub> Oxidation Mechanisms: Atmospheric Considerations, ed. J.G. Calvert, Ann Arbor Science, Woburn, MA.
- Martinez, R.J., J.T. Herron and R.E. Huie, 1981. "The Mechanism of Ozone-Alkene Reactions in the Gas Phase. A Mass Spectrometric Study of the Reactions of Eight Linear and Branched Chain Alkenes." J. Amer. Chem. Soc. 103:3807.
- Masschalein, W. 1977. Spectrophotometric Determination of Residual Hydrogen Peroxide. Water and Sewage Works, 124:69-73.
- Middleton, P., C.S. Kiang and V.A. Mohnen 1980. Theoretical Estimates of the Relative Importance of Various Urban Sulfate Aerosol Production Mechanisms. Atmos. Environ. 14:463-472.
- Miller, D. 1980. Kinetic Model of Atmospheric SO<sub>2</sub> Oxidation Based on Published Data. Atmos. Environ. 14:1067-1076.
- Morel, F. and J.J. Morgan 1972. A Numerical Method for Computing Equilibria in Aqueous Chemical Systems. Environ. Sci. and Technol. 6:58-67.
- Mudd, J.B. 1966. Reaction of Peroxyacetyl Nitrate with Glutathione. J. Biol. Chem. 241:4077-4080.
- Mulcahy, M. 1973. "Gas Kinetics," Halsted Press, John Wiley & Sons, New York.
- Naiditch, S. and D.M. Yost 1941. The Rate and Mechanism of the Hydrolysis of Hydroxylamine Disulfonate Ion. J. Amer. Chem. Soc., 63:2123-2127.
- Nash, T. 1979. The Effect of Nitrogen Dioxide and of Some Transition Metals on the Oxidation of Dilute Bisulphite Solutions. Atmos. Environ. 13:1149-1164.
- National Aeronautics and Space Administration 1979. "Chemical Kinetic and Photochemical Data for Use in Stratospheric Modeling", Evaluation No. 2, J.P.L. Publication 79-27, April, and revisions thereof.
- Nicksic, S.W., J. Harkins and P.K. Mueller 1967. Some Analyses for PAN and Studies of its Structure. Atmos. Environ. 1, 11-18.
- Nieboer, H. and J.H. Duyzer 1978. "Photochemical Smog Formation in the Netherlands," TNO, p 89, October.
- Niki, H., P.D. Maker, C.M. Savage and L.P. Breitenbach 1977. Chem. Phys. Lett., 46: 327.
- Niki, H., P.D. Maker, C.M. Savage and L.P. Breitenbach 1978. J. Phys. Chem., 82: 135.

- Niki, H., P.D. Maker, C.M. Savage and L.P. Breitenbach 1981. J. Phys. Chem. 85: 1024.
- O'Brien, R.J., P.J. Green, R.A. Doty, J.W. Vanderzanden, R.R. easton and R.P. Irwin 1979. "Interaction of Oxides of Nitrogen and Aromatic Hydrocarbons Under Simulated Atmospheric Conditions", in Nitrogenous Air Pollutants, ed. D. Grosjean, Ann Arbor Press, Ann Arbor, Michigan.
- Overton, J.H. and J.L. Durham 1981. Acidification of Rain in the Presence of  $\text{SO}_2$ ,  $\text{H}_2\text{O}_2$ ,  $\text{O}_3$  and  $\text{HNO}_3$ , to be published in: Energy and Environmental Chemistry: Acid Rain, J.I. Tensley, Ed., Ann Arbor Science, Woburn, MA.
- Pate, C.T., R. Atkinson and J.N. Pitts, Jr. 1976. "Rate Constants for the Gas Phase Reaction of Peroxyacetyl Nitrate with Selected Atmospheric Constituents," J. Environ. Sci. and Health, Part A 11, 19-31.
- Penkett, S.A., B.M.R. Jones, K.A. Brice and A.E.J. Eggleton 1979. The Importance of Atmospheric Ozone and Hydrogen Peroxide in Oxidizing Sulfur Dioxide in Cloud and Rainwater. Atmos. Environ. 13:123-37.
- Pruppacher, H.R. and J.D. Klett 1978. Microphysics of Clouds and Precipitation. D. Reidel Publishing Co., Boston, MA.
- Rasmussen, R.A. 1972. J. Air Poll. Control Assoc., 22:537.
- Rodhe, H., P. Crutzen and A. Vanderpol 1981. Formation of Sulfuric and Nitric Acid in the Atmosphere During Long Range Transport. Tellus 33:132-141.
- Sato, T.S. Matani and T. Okabe 1979. The Oxidation of Sodium Sulfite with Nitrogen Dioxide. With Special Reference to Analytical Methods for Nitrogen-Sulfur Compounds Produced in the Reaction System, Nippon Kagaku Kaishi 1979(7):869-878 (1979). In Japanese. Also, Amer. Chem. Soc. 177th National Meeting, Honolulu, HI, April 1, 1979, paper INDE-210, 1979.
- Schwartz, S.E. and W.H. White 1981. Solubility Equilibria of the Nitrogen Oxides and Oxyacids in Dilute Aqueous Solution, in Advan. Environ. Sci. Engng., Vol. 4, J.R. Pfafflin and E.N. Ziegler, Eds., (New York: Gordon and Breach.
- Schwartz, S.E. and J.E. Freiberg 1981. Mass-Transport Limitation to the Rate of Reaction in Liquid Droplets: Application to Oxidation of  $\text{SO}_2$  in Aqueous Solutions. Atmos. Environ. 15:11-29-1144
- Schwartz. S.E. and W.H. White 1982. Kinetics of Reactive Dosolution of Nitrogen Oxides into Aqueous Solution, in Advan. Environ. Sci. Technol., Vol. 12, S.E. Swhartz, Ed. (New York: Wiley and Sons, Inc., 1982).

- Schwartz, S.E. 1982. Gas-Aqueous Reactions of Sulfur and Nitrogen Oxides in Liquid-Water Clouds; to be published in  $\text{SO}_2$ ,  $\text{NO}$  and  $\text{NO}_2$  Oxidation Mechanisms: Atmospheric Conditions, ed. J.G. Calvert.<sup>2</sup> Ann Arbor Science, Woburn, MA.
- Scott, B.C. 1978. Parameterization of Sulfate Removal by Precipitation. J. Appl. Meteor. 17:1375-1389.
- Scott, B.C. and N.S. Laulainen 1979. On the Concentration of Sulfate in Precipitation. J. Appl. Meteor. 18:138-147.
- Seel, F. and H. Pauschmann 1962. Aum Kinetic der Umsetzung von Hydroxylaminemonosulfonat mit nitrit. Z. Natusf. 17b 347-349.
- Seinfeld, J.H. 1980. "Lectures in Atmospheric Chemistry." Amer. Inst. of Chemical Engineers Monograph 12, Vol. 76.
- Semonin, R.G., V.C. Bowersox, D.G. Gatz, M.E. Peden and G.J. Stensland 1981. Study of Atmospheric Pollution Scavenging. 19th Progress Report No. DE-AC02-76VO1199 to U.S. Department of Energy, Washington, D.C. S.W.S. Contract Report No. 252.
- Stedman, D.H., E.D. Morris, Jr., E.E. Daby, H. Niki and B. Weinstock 1970. 160th National Meeting of the American Chemical Society, Chicago, IL, Sept. 14-18.
- Stelson, A.W. and J.H. Seinfeld 1981. Chemical Mass Accounting of Urban Aerosol. Environ. Sci. and Technol. 15:671-679.
- Stelson, A.W., M.E. Bassett and J.H. Seinfeld 1982. Thermodynamic Equilibrium Properties of Aqueous Solutions of Nitrate, Sulfate and Ammonium, Atmos. Environ. in press.
- Stelson, A.W. and J.H. Seinfeld 1982a. Relative Humidity and Temperature Dependence of the Ammonium Nitrate Dissociation Constant. Atmos. Environ. 16:983-992.
- Stelson, A.W. and J.H. Seinfeld 1982b. Relative Humidity and pH Dependence of the Vapor Pressure of Ammonium Nitrate-Nitric Acid Solutions at 25°C. Atmos. Environ. 16:993-1000.
- Stelson, A.W. and J.H. Seinfeld 1982c. Thermodynamic Prediction of the Water Activity,  $\text{NH}_4\text{NO}_3$ -( $\text{NH}_4$ )<sub>2</sub> $\text{SO}_4$ -H<sub>2</sub>O System at 25°C to be published in Atmos. Environ.
- Stumm, W. and J.J. Morgan 1981. Aquatic Chemistry 2nd Ed. John Wiley & Sons, New York, NY.
- Su, F., J.G. Calvert and J.H. Shaw 1980. J. Phys. Chem., 84: 239.
- Takagi, H., N. Washida, H. Akimoto, K. Nagasawa, Y. Usui and M. Okuda 1980. J. Phys. Chem., 84: 478.

- Takeuchi, H., M. Ando and N. Kizawa 1977. Absorption of Nitrogen Oxides in Aqueous Sodium Sulfite and Bisulfite Solutions. Ind. Eng. Chem. Process Design. Dev. 16:303-308.
- Tartarelli, P. Davini, F. Morelli and P. Corsi 1978. Atm. Environ., 12,288.
- Went, F.W. 1960. Organic Matter in the Atmosphere, and Its Possible Relation to Petroleum Formation. In Proceed. N.A.S., 46 (2):212.
- Westall, J.D., J. Zachary and F.M.M. Morel 1976. MINEQL: A Computer Program for the Calculation of Chemical Equilibrium Composition of Aqueous Systems. Technical Note No. 18. Ralph M. Parsons Laboratory, Massachusetts Institute of Technology, Cambridge, MA.
- Westall, J. 1979. MICROQL I. A Chemical Equilibrium Program in BASIC. Swiss Federal Institute of Technology (EAWAG), CH-8600 Duebendorf, Switzerland.
- Zika, R.G. and E.S. Saltzman 1982. Interaction of Ozone and Hydrogen Peroxide in Water: Implications for Analysis of  $H_2O_2$  in Air. Geophys. Res. Lett., 9:231-234.
- Zimmerman, P.R. 1979. Tampa Bay Area Photochemical Oxidant Study - Appendix C. EPA 904/9-77-028, U.S. Environmental Protection Agency, Research Triangle Park.

ADDITIONAL REFERENCES FOR SECTION 6

- Bilger, R.W. 1977. The Effects of Admixing Fresh Emissions on the Photostationary State Relationship in Photochemical Smog. Atmospheric Environment, 12: 1109-1118.
- Chock, D.P. and S. Kumar 1978. Technical Note on the Photostationary State Assumption in the Atmospheric Nitric Oxide - Nitrogen Dioxide - Ozone System, Atmospheric Environment, 13: 419-420.
- Eschenroeder, A.Q., J.R. Martinez, and R.A. Nordsieck 1972. Evaluation of a Diffusion Model for Photochemical Smog Simulation. Final Report of General Research Corp. to EPA Contract No. 68-02-0336.
- Lamb, R.G. and W.R. Shu 1978. A model of second order chemical reactions in turbulent fluid - Part I. Formulation and valuation. Atmospheric Environment, 12: 1685-1694.
- Lurmann, F.W., D.A. Godden and A.C. Lloyd 1982. The Development and Selected Sensitivity Tests of the PLMSTAR Reactive Plume Model. Presented at the Third Joint Conference on Application of Air Pollution Meteorology, San Antonio, TX. Sponsored by American Meteorology Society, Boston, MA.
- Seinfeld, J.H. 1977. Environmental Science and Technology, 11: 1218.
- Shu, W.R., R.G. Lamb, and J.H. Seinfeld 1978. A Model of Second-Order Chemical Reactions in Turbulent Fluid - Part II. Application to Atmospheric Plume. Atmospheric Environment, 12: 1695-1704.

## 7. WET DEPOSITION

### 7.1 Introduction

The physical processes that govern the scavenging of pollutants by precipitation are discussed in review papers by Slinn (1982) and Hales (1980). These articles present a number of parameterizations which can be used to estimate wet removal of aerosols and gases. This section summarizes our "best" choice among these formulations. The criteria used in selecting them are:

- 1) The parameterizations are functions of variables which can be readily related to the meteorological observations used in the mesoscale and long-range transport (LRT) models.
- 2) The formulations are biased towards empiricism. Because our understanding of wet deposition is incomplete, it is prudent to avoid formulations which are based primarily on "theory."

There are two ways to treat wet deposition in models. One method uses a washout rate which appears as a loss term in the mass conservation equation for the pollutant. The model for the washout or scavenging rate needs input variables such as precipitation rate and concentrations resolved in the vertical. This type of detailed calculation might be necessary only for the mesoscale model. For the LRT model, precipitation scavenging is better handled with the concept of the washout ratio defined by

$$w_r = (C_p / C_a) \quad (7-1)$$

where  $C_p$  is the concentration of the pollutant in surface level precipitation and  $C_a$  is the corresponding concentration in air. This formulation implicitly integrates the wet removal over a vertical column of pollutant. This loss of vertical resolution is probably of minor importance in LRT models. Note that the flux of pollutants at the surface is given by

$$F = w_r \frac{C}{a} P_o \quad (7-2)$$

where  $p_o$  is surface level precipitation rate, a variable which can be derived from observations.

In the following sections we have tried to be specific in recommending formulations for wet scavenging. This is necessary for designing the models. However, we do expect to modify them in developing an operational model.

#### 7.1.1 Aerosol Scavenging by Rain

The scavenging rate  $\Lambda(a)$  for aerosols of dimensions 'a' can be approximated by (Scott 1982b)

$$\Lambda(a) = \int_0^{\infty} \frac{\pi A^2}{4} V(A) E(a, A) N(A) dA \quad (7-3)$$

In Equation 3,  $V(A)$  is the fall speed of the collecting hydrometeors of dimension  $A$  and size distribution  $N(A)$ ;  $E(a, A)$  is the collection efficiency of the collector particles for aerosols of size  $a$ .

Slinn (1982) shows that Equation 3 can be usefully approximated by

$$\Lambda(a) = c p E(a, R_m) / R_m \quad (7-4)$$

In Equation 4,  $c$  is a numerical factor of order unity,  $p$  is the space and time dependent precipitation rate, and  $R_m$  is the mass mean raindrop radius. For frontal storms, Mason (1971) suggests that  $R_m$  can be expressed as

$$R_m = 0.35 p^{1/4} \quad (7-5)$$

where  $R_m$  is in mm and  $p$  is in mm/hr. In order to use Equation 4, we have to estimate the collection efficiency  $E(a, R_m)$  which, as Slinn (1982) shows, is a function of a host of variables. Slinn has derived theoretical curves for  $E$ . Even if these results were supported by observations, lack of input information would prevent us from using

them. Therefore we propose to use "typical" values of (cE) based on observations. Slinn (1982) finds that the results of experiments conducted by Burtsev et al. (1970) can be explained by the relationship

$$\Lambda = \frac{1}{3} p^{3/4} \times 10^{-4} \quad (7-6)$$

where  $\Lambda$  is in  $s^{-1}$  and  $p$  is in mm/hr. This parameterization is applicable to convective storms.

As an alternative to using Equation 4, Scott (1982b) has derived  $\Lambda(a)$  by integrating Equation 3 after making some reasonable assumptions about  $V(A)$ ,  $E(a,A)$ , and  $N(A)$ . Firstly, he considers only soluble (hygroscopic) aerosols such as sulfates and nitrates. He assumes that these pollutant particles are activated as condensation nuclei which grow rapidly to cloud droplet sizes around 10  $\mu m$ . He then shows that for collector particles ranging from 0.2 to 2 mm,  $E(a,A)$  varies from 0.5 to 0.8 for 10  $\mu m$  particles. This allows him to take  $E(a,A) = \text{constant} = 0.65$ . For  $N(A)$ , he takes the Marshall-Palmer size distribution which depends on two parameters. Taking "typical" values for these parameters, he integrates Equation 3 yielding the result

$$\Lambda = 1.26 p^{0.78} (h^{-1}); p \text{ in } mmh^{-1} \quad (7-7)$$

Notice that using  $E(a,A) = 0.65$  in Equation 4 results in a very similar result

$$\Lambda = 1.86 p^{0.75} (h^{-1}) \quad (7-8)$$

In order to use either Equation 7 or 8, we need to know the variation of  $p$  with height. For heights below the freezing level in clouds, Scott (1982b) proposes the following parameterization

$$p(z)^{0.22} = p(g)^{0.22} - 3.1 \times 10^{-4} L (z - z_g) \quad (7-9)$$



where  $z_g$  is the height of the ground, and  $L$  is the average cloud water concentration between the ground and height  $z$ . Clearly, we expect a great deal of variation between  $p(z)$  predicted by Equation 9 and that occurring in any one cloud. Furthermore, we are unlikely to have any information on  $L$  for the rain event we are interested in. This suggests that estimation of  $\Lambda$  as a function  $z$  is always going to be associated with a great deal of uncertainty. Table 7-1 presents information which can be used to make rough estimates of  $p(z)$ .

### 7.1.2 Aerosol Scavenging by Snow

Slinn suggests that the particle snowout rate can be written as

$$\Lambda(a) = \gamma p E(a, \lambda) / D_m \quad (7-10)$$

where  $\gamma = 0(1)$  and  $E$  is the particle/ice-crystal collection efficiency based on the "capture length"  $\lambda$  of the ice crystal with a characteristic length scale  $D_m$ . In principle,  $\Lambda(a)$  can be calculated if the ice crystal type is known. However, the theory for the estimation of  $E(a, \lambda)$  has very little observational support. Figure 7-1 shows estimates of  $\Lambda(\equiv \Psi_s)$  against available data. Table 7-2 presents some empirical correlations for snow scavenging. Note again the dependence of  $\Lambda$  on the type of ice aggregate. This detailed information is unlikely to be available for practical applications.

Based on arguments similar to that used to derive rainout rates for soluble aerosols, Scott (1982b) has derived the following equation for scavenging by snow

$$\Lambda = 0.88p (h^{-1}) \quad (7-11)$$

where  $p$  is in  $\text{mmh}^{-1}$ . Although this equation is simpler to use than those described earlier, we still need to know the precipitation rate,  $p$ , as a function of height. Scott (1982b) does provide a parameterization for  $p(z)$  in terms of variables which cannot be estimated with observations generally available.

TABLE 7-1  
TYPICAL VALUES OF CLOUD PARAMETERS\*

<u>Parameter</u>	<u>Storm Type</u>	
	<u>Winter</u>	<u>Summer</u>
Cloud top (km)	8.0	4.7
Freezing level (km)	4.6	0.3
Mean cloud water content ( $\text{g/m}^3$ )		
Above freezing level	0.70	0.07
Below freezing level	0.30	0.04

---

\*Based on Scott's (1982b) kinematic model.

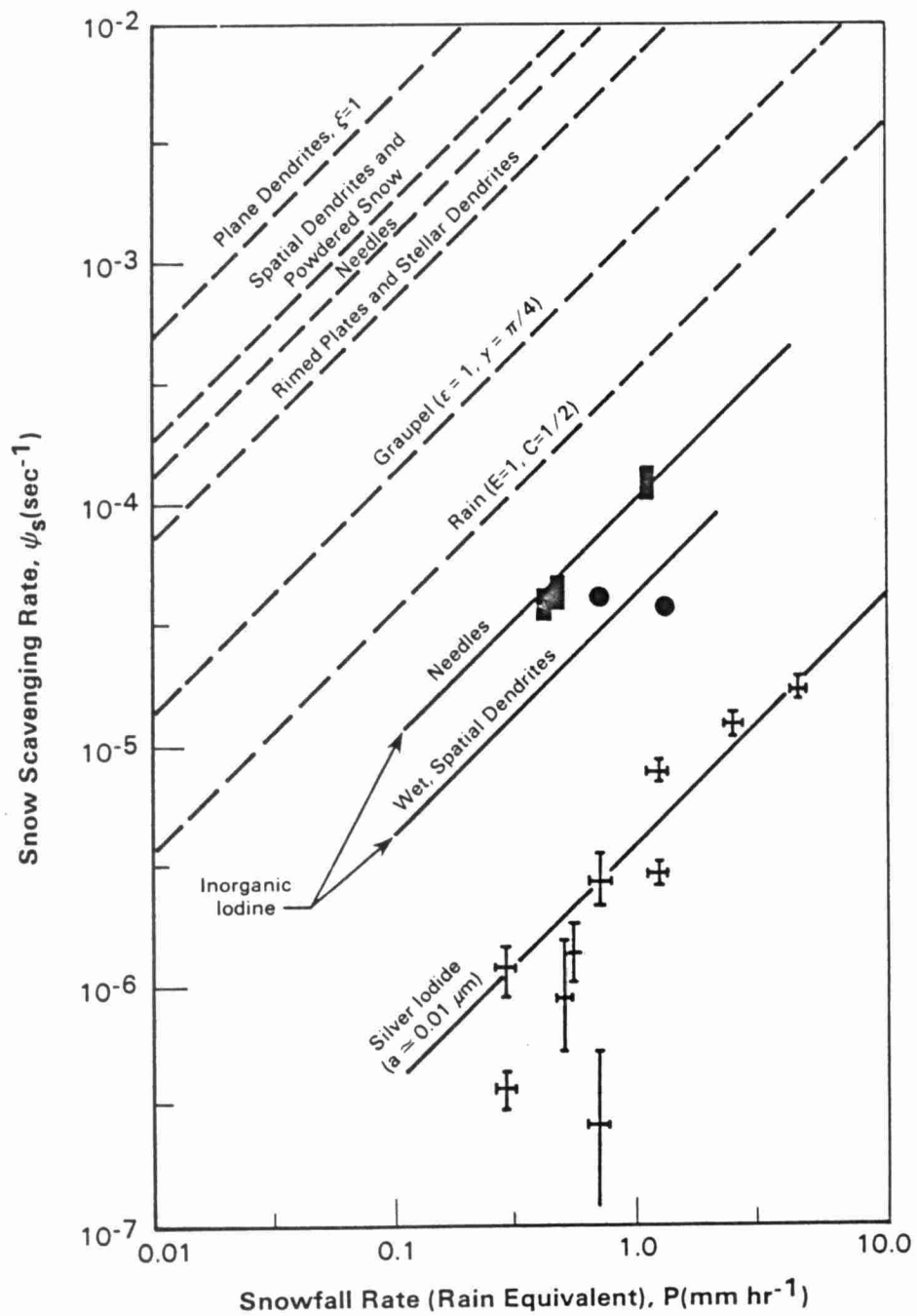


Figure 7-1 Snow Scavenging Rate (Slinn 1982)

TABLE 7-2  
EMPIRICAL EQUATIONS FOR THE SNOW SCAVENGING RATE FOR FOUR  
TYPES OF ICE AGGREGATES<sup>(a)</sup> (FROM SLINN 1982)

<u>Type of Ice Aggregate</u>	<u>Empirical Equation</u> <sup>(b)</sup>
I Lump graupel	$\psi_s = 0.21 p^{0.188} f(T, D_p)^{(c)}$
II Densely rimed dendrites	$\psi_s = 0.40 p^{0.266} f(T, D_p)$
III Densely rimed radiating assemblages of dendrites	$\psi_s = 0.32 p^{0.305} f(T, D_p)$
IV Aggregates of unrimed radiating assemblages of dendrites or dendrites	$\psi_s = 0.41 p^{0.57} f(T, D_p)$

- Notes: (a) Formulae from Knutson and Stockham (1977).  
 (b) Units are:  $\psi_s$  in sec,  $p$  in mm/hr,  $T$  in °F,  $D_p$  in  $\mu\text{m}$ ; the empirical correlations were derived from data for monodisperse particle diameter in the range  $.25 \leq D_p \leq 3.5 \mu\text{m}$  and snowflake circumscribed diameter in the range  $1 \leq D_c \leq 10 \text{ mm}$ .  
 (c)  $f(T, D_p) = \text{antilog} [-3.17 - 0.0178T + 3.41 \log D_p - 0.973 \log^2 D_p - 7.20 \log^3 D_p]$ .

Even if we could estimate  $\Lambda(z)$ , scavenging can be estimated only if the vertical concentration profile can be calculated. To do this, we have to model the dispersion (or advection) of the pollutant within a cloud system. This is an extremely complex task for a specific cloud system being considered. Currently we consider it is more useful to estimate wet scavenging via the washout ratio discussed in the next subsection. We will use the scavenging rate approach when the state-of-the-art progresses to that point.

### 7.1.3 Washout Ratio

The washout ratio is defined by the equation:

$$w_r = (C_p/C_a)_o \quad (7-12)$$

where  $C_p$  and  $C_a$  are the concentrations in precipitation and air at ground-level. In terms of the scavenging rate parameterization,  $w_r$  can be expressed as

$$w_r = \int_0^{\infty} \Lambda(z) C_a(z) dz / (pC_a)_o \quad (7-13)$$

Slinn (1982) suggests the washout ratio shows "some regularity, and therefore does have some practical value because it represents the average over many variables e.g., particle and precipitation size distributions, and vertical distributions, and sometimes even storm types." There are a number of observations to help us in estimating  $w_r$  for different aerosols. Figure 7-2 displays some measurements summarized by Slinn (1982). We see that  $w_r$  values have magnitudes ranging from  $10^5$  to  $10^6$ . Note also that in view of the large variation of  $w_r$ , the estimation of scavenging for individual storms is likely to be uncertain.

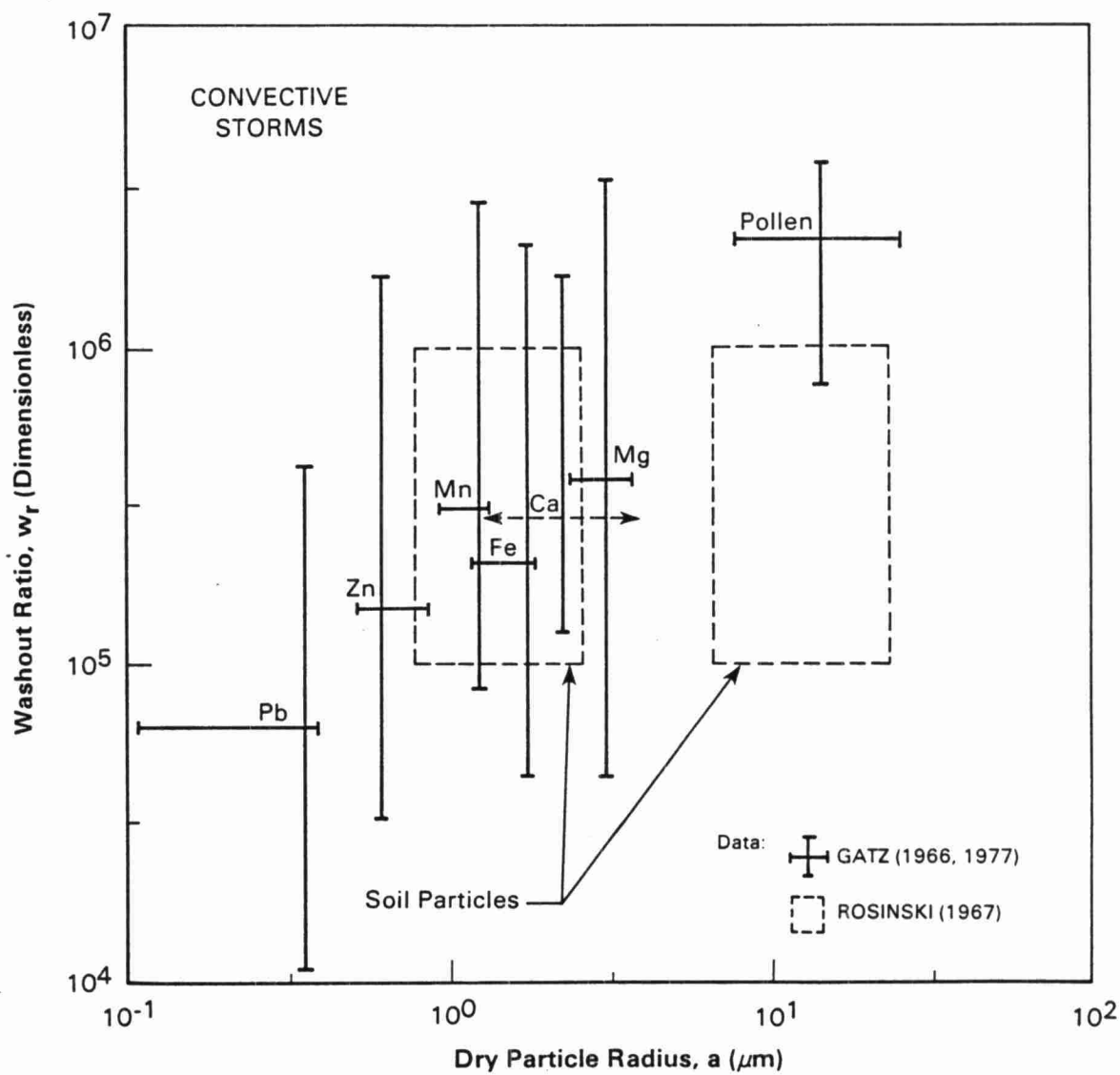


Figure 7-2 Experimental Values of  $w_r$  (Slinn 1982)

Estimates of  $w_r$  can be obtained from a simple model proposed by Junge (1963). He shows that  $w_r$  is

$$w_r = (\rho_w \epsilon_i / L) \bar{C} / C_{ao} \quad (7-14)$$

where  $\rho_w$  is the density of water,  $\epsilon_i$  is the fraction of the pollutant that enters the cloud water, and  $L$  is the condensed water content of the cloud.  $\bar{C}$  refers to the average concentration of the pollutant entering the storm, and  $C_{ao}$  is the concentration at ground-level. To use Equation 14, one would take  $\epsilon_i = 1.0$ , and  $C$  corresponds to the concentration at cloud base. In Phase II we propose to estimate  $\epsilon_i$  from a simple cloud model. The cloud water concentration  $L$  can be related to the cloud type (see Table 7-1). Additional guidance on the choice of the appropriate  $w_r$  can be obtained from Figure 7-3 drawn up by Slinn (1982).

For convective clouds, Hales and Dana (1979) show that  $w_r$  can be approximated by

$$w_r = \rho_w / H \quad (7-15)$$

where  $H$  is the concentration of water vapor entering the cloud. It is reasonable to assume that  $H$  can be related to the relative humidity at cloud base.

We realize that washout ratios provide only order of magnitude estimates of wet deposition. However, this is the best we can do without the type of detailed information needed for the scavenging rate formulation.

Figures 7-4 and 7-5 show flowcharts of the proposed approach to the calculation of the wet scavenging of aerosols.

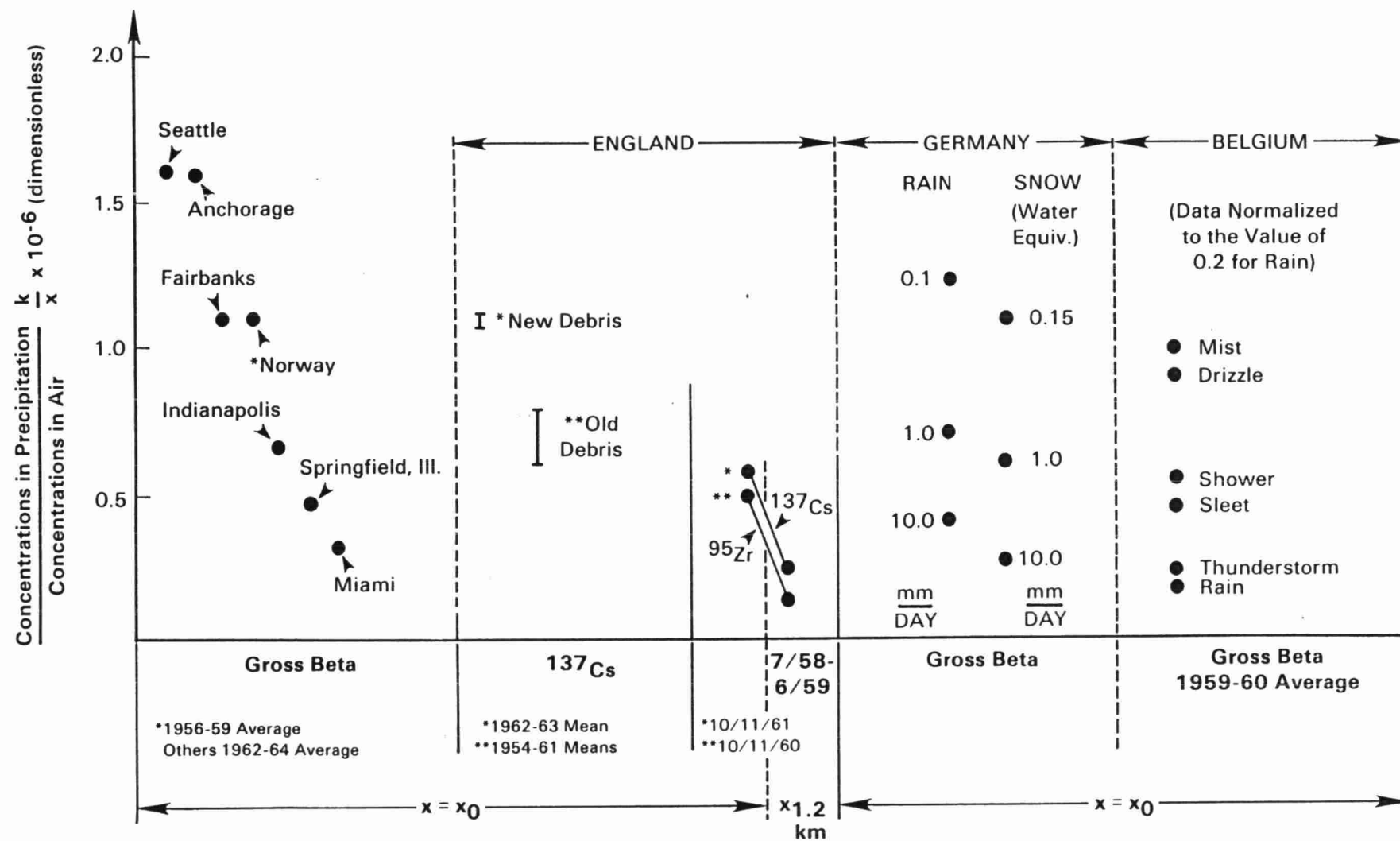


Figure 7-3 Washout Ratios for Bomb Debris (Slinn 1982)



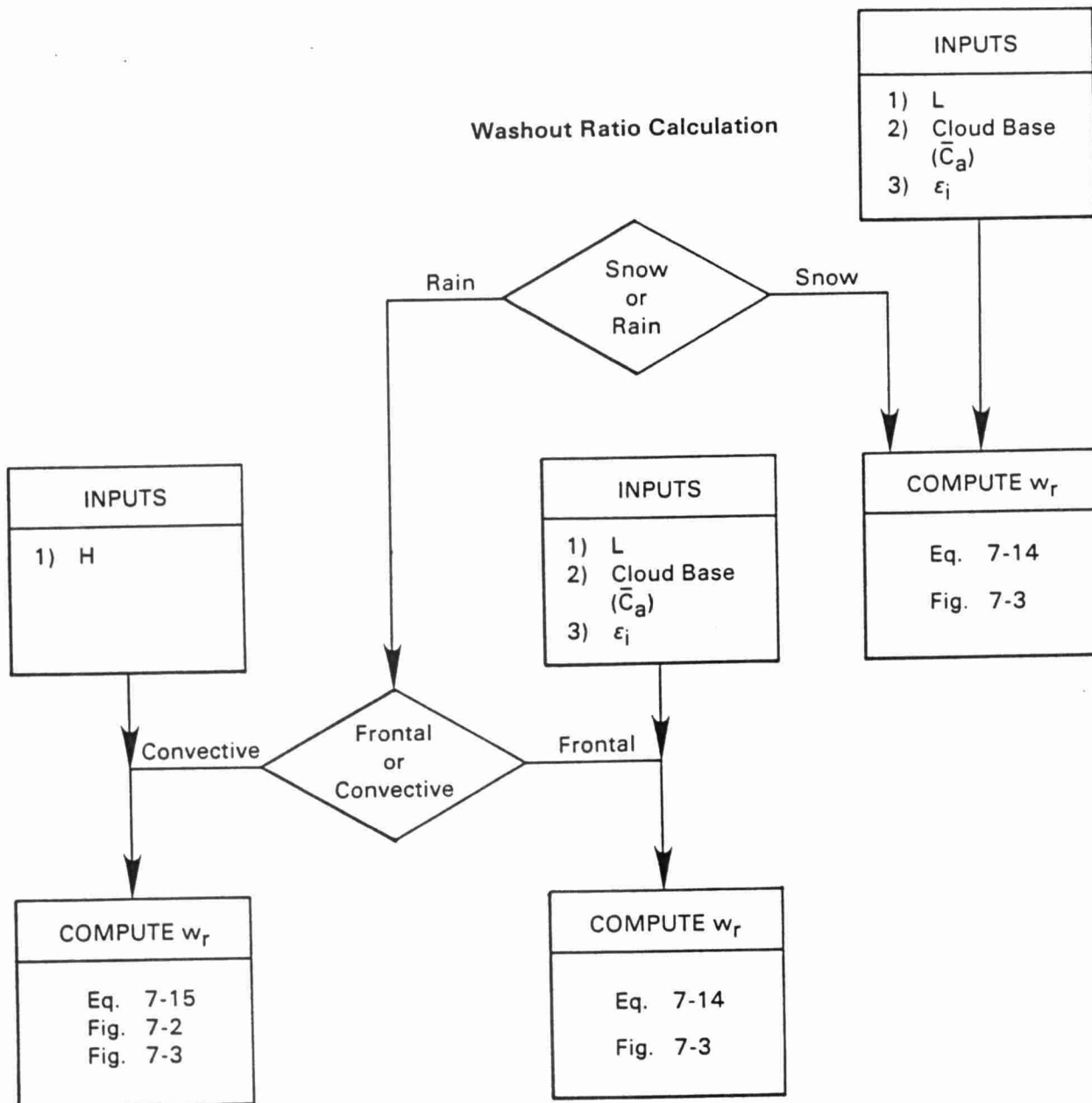


Figure 7-4 Wet Deposition of Aerosols

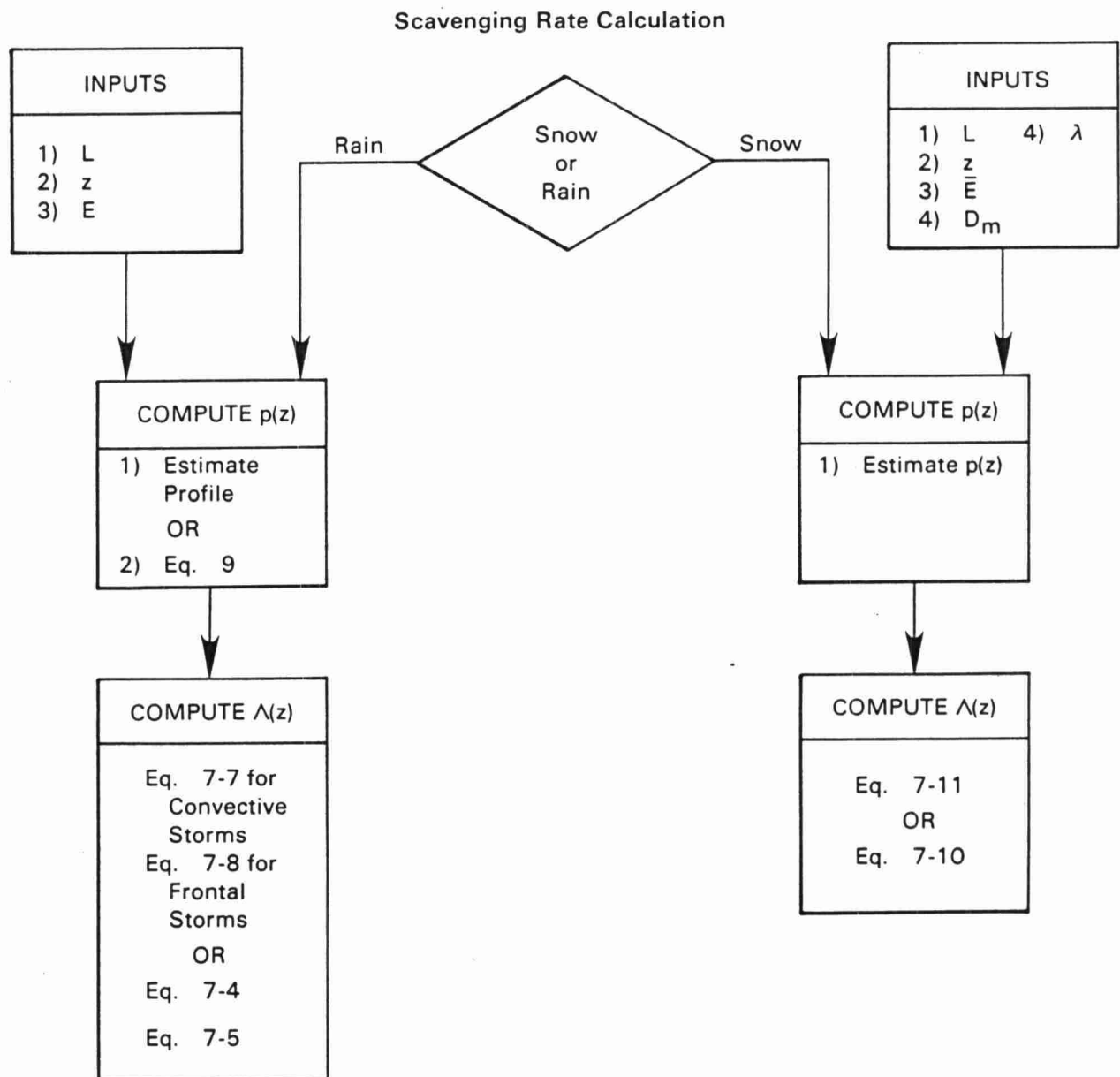


Figure 7-5 Wet Deposition of Aerosols

#### 7.1.4 Wet Scavenging of Gases

Scavenging of gases can occur in three different ways (Junge 1963):

- 1) By simple solution in cloud water according to Henry's law; examples are  $\text{NO}_2$  and  $\text{CH}_4$ .
- 2) By solution followed by ionization and recombination; examples are  $\text{CO}_2$  and  $\text{NH}_3$ .
- 3) By solution followed by reactions with other constituents in rainwater; examples are  $\text{SO}_2$  and  $\text{NO}_2$ .

In principle, gases which belong to category (1) are easiest to deal with. The mass balance for a single raindrop can be written as follows (Slinn 1982):

$$\frac{d}{dt} \left( \frac{4}{3} \pi R^3 C(R) \right) = k_m 4\pi R^2 [C_a(z) - H C(R)] \quad (7-16)$$

In Equation 16,  $R$  is the radius of the raindrop,  $k_m$  is the mass transfer coefficient, and  $H$  is the Henry's law coefficient. If  $C_a(z)$  is known, Equation 16 can be integrated to yield the concentration  $C(R,z)$  in the droplet. Then the scavenging rate  $\Lambda$  is

$$\Lambda(z) = C_a^{-1} \int_0^\infty \frac{4}{3} \pi R^3 C(R,z) N(R) V(R) dR \quad (7-17)$$

where  $N(R)$  is the cloud droplet density and  $V$  is the falling speed of the droplet of radius  $R$ . If  $C_a(z)$  is known, we can evaluate Equation 17 making reasonable assumptions about  $N(R)$  and  $V(R)$  (see Scott 1982). However, we feel that there is a great deal of uncertainty in this type of detailed calculation. It is more practical to use the assumption that the rain concentration  $C_p$  is in equilibrium with that in the air  $C_a$ ,

$$C_p = C_a / H = \alpha C_a \quad (7-18)$$

where  $\alpha = H^{-1}$  is the solubility coefficient. Equation 18 is valid when  $C_a / \partial C_a / \partial z \gg \alpha VR / k_m$ , i.e., the scale of concentration changes is large compared the height over which the droplet reaches chemical equilibrium with its surroundings. Then the washout coefficient  $w_r$  is simply

$$w_r = \alpha \quad (7-19)$$

Table 7-3 obtained from Slinn (1982) presents the solubility coefficients for a number of gases.

#### 7.1.5 Washout of Gases which React in Water

Gases like  $CO_2$  and  $NH_3$  ionize when they enter into solution. Because only the undissociated aqueous phase concentration is in equilibrium with the gas-phase concentration, these gases exhibit enhanced solubilities in water. The washout ratio is then written as

$$w_r = \alpha_* \quad (7-20)$$

where  $\alpha_*$  is now a function of the ionized products of all species in the rainwater. Clearly, the estimation of  $\alpha_*$  is an enormously complicated task. However, if the pH of the rain is known a priori, one can calculate  $\alpha_*$ . An example of this type of calculation is given by Barrie (1981). For  $SO_2$  participating only in ionization reactions, he shows

$$\ln \alpha_* = \log_{10} (K_H) + pH \quad (7-21)$$

where  $K_H$  is related to the absolute temperature through

$$K_H = 6.22 \times 10^{-8} \exp (4755.5/T) \quad (7-22)$$

TABLE 7-3  
GAS SOLUBILITIES IN WATER (SLINN 1982)

Noble Gases (10-25°C)

He		$9.4 \times 10^{-3}$
Ne		$1.1 \times 10^{-2}$
Ar		$3.6 \times 10^{-2}$
Kr		$6.3 \times 10^{-2}$
Xe		$1.4 \times 10^{-1}$
Rn		$2.3 \times 10^{-1}$

Inorganic Gases

CF <sub>4</sub>	(25°C)	$4.9 \times 10^{-3}$
SF <sub>6</sub>	(25°C)	$5.5 \times 10^{-3}$
N <sub>2</sub>	(25°C)	$1.6 \times 10^{-2}$
H <sub>2</sub>	(25°C)	$1.8 \times 10^{-2}$
CO	(25°C)	$2.6 \times 10^{-2}$
O <sub>2</sub>	(25°C)	$3.1 \times 10^{-2}$
N <sub>2</sub> O	(20°C)	$6.7 \times 10^{-1}$
COS	(13.5°C)	$6.7 \times 10^{-1}$
CO <sub>2</sub>	(25°C)	$8.3 \times 10^{-1}$
CO <sub>2</sub>	(20°C)	$9.5 \times 10^{-1}$
CO <sub>2</sub>	(10°C)	$1.2 \times 10^0$
CO <sub>2</sub>	(0°C)	$1.6 \times 10^0$
H <sub>2</sub> S	(10°C)	$3.4 \times 10^0$
Cl <sub>2</sub>	(15°C)	$3.3 \times 10^0$
SO <sub>2</sub>	(18°C)	$4.2 \times 10^1$

TABLE 7-3 (Continued)

Inorganic Gases (Continued)

HI	(0°C)	$4.9 \times 10^2$
HCl	(0°C)	$5.1 \times 10^2$
HBr	(0°C)	$6.1 \times 10^2$
NH <sub>3</sub>	(25°C)	$4.5 \times 10^2$
NH <sub>3</sub>	(0°C)	$1.2 \times 10^3$

Some Organic Gases

Methylamine, MeNH <sub>2</sub>	(20°C)	$1.26 \times 10^3$
Methylamine, MeNH <sub>2</sub>	(10°C)	$1.94 \times 10^3$
Methylamine, MeNH <sub>2</sub>	(0°C)	$4.17 \times 10^3$
Dimethylamine, Me <sub>2</sub> NH	(20°C)	$2.05 \times 10^3$
Trimethylamine, Me <sub>3</sub> N	(10°C)	$1.53 \times 10^3$
Dimethylamine, Me <sub>2</sub> O	(0°C)	$3.7 \times 10^1$
Chloromethane, MeCl	(25°C)	$2.6 \times 10^0$
Bromomethane, MeB	(25°C)	$3.9 \times 10^0$
Propylene, C <sub>3</sub> H <sub>6</sub>	(20°C)	$1.5 \times 10^{-1}$
Propane, C <sub>3</sub> H <sub>8</sub>	(15°C)	$7.7 \times 10^{-2}$

Equation 21 is useful in that if measurements of pH are available, one can estimate how much  $\text{SO}_2$  is being washed out. However, the problem is much more complicated because  $\text{SO}_2$  is oxidized by agents such as  $\text{H}_2\text{O}_2$  in water. There is good reason to believe (Scott 1980, 1982a) that in-cloud oxidation of  $\text{SO}_2$  might contribute to most of the "apparent" washout of  $\text{SO}_2$ . In fact, if this conversion is rapid enough, the "washout" of  $\text{SO}_2$  is limited by the rate at which  $\text{SO}_2$  is incorporated into precipitating clouds. Then it can be shown that  $w_r$  is given by (Smith and Hunt 1979):

$$w_r = \rho_w / H \quad (7-23)$$

which is identical to Equation 15.

It will be some time before a washout parameterization can fully account for the complex chemistry in clouds. Preliminary progress towards understanding the chemistry is described in Section 6. For present applications, Slinn (1982) suggests that we should use measured washout ratios to estimate wet deposition of reactive gases. Table 7-4, showing washout ratios, is reproduced from his review paper. He points out that these ratios have magnitudes similar to those of aerosols. This suggests that conversion of these gases to their reaction products might be complete enough to assume that washout is limited by the dynamics of the cloud. Therefore, formulations of the type (Equation 23) might be applicable to reactive gases.

We should emphasize that we have recommended the washout ratio approach for reactive gases only because a viable alternative method is not available at present. During Phase II we propose to build and perform sensitivity analyses on cloud models with chemistry and examine some of the results of recent studies on cloud chemistry. Chapter 6 describes preliminary progress ERT has made in this area. Recently, Hong and Carmichael (1982) investigated sulfate production in clouds using a simple chemical reactor model approach. Their results indicate that aqueous phase sulfate production rates, ranging from 60%/yr to 1,000%/hr, are sensitive to the chemical composition of the uptake air and the physics of the cloud. We propose to incorporate

TABLE 7-4  
 ENHANCED SOLUBILITY COEFFICIENTS,  $\alpha_*$ , AND  
 WASHOUT RATIOS,  $W_r$ , FOR REACTIVE GASES <sup>(a)</sup> (Slinn 1982)

<u>Gas</u>	<u>pH</u>	<u><math>\chi</math>(ppbv)</u>	<u><math>\alpha_*</math> (Dimensionless)</u> <sup>(b)</sup>
SO <sub>2</sub>	5.0	1	$3.7 \times 10^4$
		3	$3.0 \times 10^4$
		10	$2.2 \times 10^4$
		30	$1.5 \times 10^4$
		1	$9.0 \times 10^4$
	6.0	3	$5.5 \times 10^4$
		10	$3.2 \times 10^4$
		30	$1.9 \times 10^4$
<u>Precursor Gas</u>		<u>Mass Ratio</u>	<u><math>W_r</math> (Dimensionless)</u> <sup>(c)</sup>
NH <sub>3</sub>		(NH <sub>4</sub> <sup>+</sup> )/(NH <sub>3</sub> )	(1.2 - 2.2) $\times 10^5$ (d)
NO <sub>2</sub>		(NO <sub>3</sub> <sup>-</sup> )/(NO <sub>2</sub> )	(1.8 - 4.0) $\times 10^5$ (d)
SO <sub>2</sub>		(SO <sub>4</sub> <sup>=</sup> )/(SO <sub>2</sub> )	(0.5 - 1.5) $\times 10^5$ (d)
SO <sub>2</sub>		(SO <sub>4</sub> <sup>=</sup> )/(SO <sub>2</sub> )	(0.1 - 1.0) $\times 10^5$ (e)
SO <sub>2</sub>		(SO <sub>4</sub> <sup>=</sup> )/(SO <sub>2</sub> )	(1.5, 3.0) $\times 10^5$ (f)

- (a) Adapted from Slinn et al. (1978).  
 (b) Ratio of moles of total dissolved sulfur (other than SO<sub>4</sub><sup>=</sup>) per unit volume of air, for water and indicated pH at 20°C and for the indicated air concentrations of SO<sub>2</sub> (from Hales and Sutter 1973; Dana, personal communication).  
 (c) Ratio of reaction product mass concentration in rain to precursor-gas mass concentration in air.  
 (d) From Junge (1963) for various locations in Europe.  
 (e) Estimated from available data for the St. Louis METROMEX project; convective storm scavenging.  
 (f) Estimated from July 1972 - June 1973, National Air Sampling Network data for urban and nonurban sites, respectively, in northeastern U.S. (Dana, personal communication).



the results of such modeling studies and our sensitivity studies into a parameterization for  $w_r$  or  $\Lambda(z)$ . For example,  $w_r$  could depend on appropriate combinations of the ambient concentrations of species such as  $\text{SO}_2$ ,  $\text{NH}_3$ ,  $\text{O}_3$ ,  $\text{NO}_x$ ,  $\text{HNO}_3$ ,  $\text{CO}_2$ , and  $\text{H}_2\text{O}_2$ , and cloud parameters such as liquid water content and rain intensity. The gas-phase concentrations of these species would be calculated from a photochemical model.

It is generally believed that snow scavenging of gases is negligible (Slinn 1982). Although snow is formed from supercooled droplets, the solubility of most gases is small at the low temperatures of the clouds associated with snowstorms. Therefore, for the time being we will neglect snowout of gases.

## 7.2 Summary

This section describes a tentative selection of parameterizations for wet scavenging of aerosols and gases. Flowcharts for the actual computation of  $\Lambda(z)$  and  $w_r$  are shown in Figures 7-4 through 7-6.

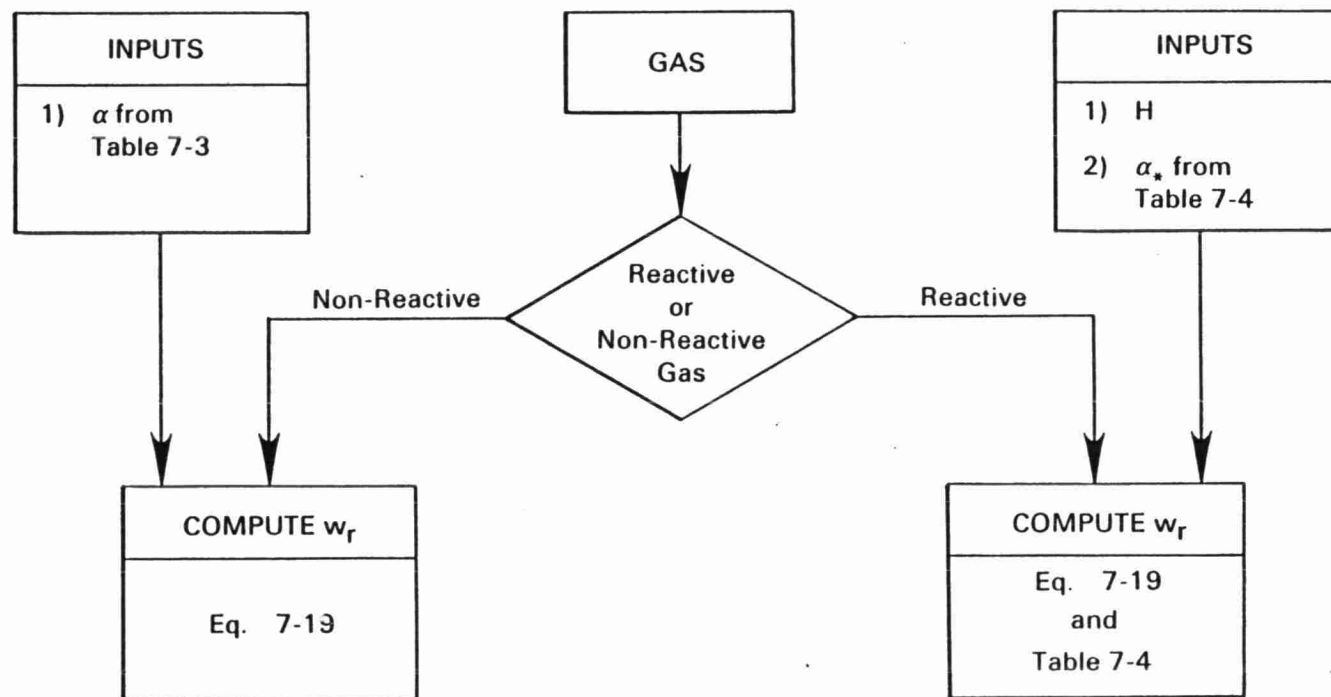


Figure 7-6 Wet Scavenging of Gases by Rain

# REFERENCES: SECTION 7

- Barrie, L.A. 1981. The prediction of rain acidity and SO<sub>2</sub> scavenging in Eastern North America. Atmos. Environ. 15: 31-41.
- Burtsev, I.I., L.V. Burtseva and S.G. Malakhov 1970. Washout characteristics of a <sup>32</sup>p aerosol injected into a cloud. In: Atmospheric Scavenging of Radioisotopes. Available as TT-69-55099 from NTIS, Springfield, VA.
- Hales, J.M. 1980. Precipitation Chemistry: Its Behavior and its Calculation. Prepared for the EPA under DOE Contract No. EY-76-C-06-1830.
- Hales, J.M. and M.T. Dana 1979. Precipitation scavenging of urban pollutants by convective storm systems. J. Appl. Meteor. 18: 294-316.
- Hales, J.M. and S.L. Sutter 1973. Solubility of sulfur dioxide in water at low concentrations. Atmos. Environ. 7:997-1001.
- Hong, M.S. and G.R. Carmichael 1981. An investigation of sulfate production in clouds using a flow-through chemical reactor model approach. In: Second Symposium on the Composition of the Nonurban Troposphere, AMS, Williamsburg, VA.
- Junge, C.E. 1963. Atmospheric Chemistry and Radioactivity. New York: Academic Press.
- Knutson, E.O. and J.D. Stockholm 1977. Aerosol scavenging by snow: Comparisons of single-flake and entire-snowfall results. In: Precipitation Scavenging. Available as CONF-741003 from NTIS, Springfield, VA.
- Mason, B.J. 1971. The Physics of Clouds (2nd Edition). Oxford: Clarendon Press. 659 pp.
- Scott, B.C. 1982a. Predictions of in-cloud conversion rates of SO<sub>2</sub> to SO<sub>4</sub> based upon a simple chemical and kinematic storm model. Atmos. Environ. Vol. 16.
- Scott, B.C. 1982b. Theoretical estimates of the scavenging coefficient for soluble aerosol particles as a function of precipitation type, rate, and altitude. Atmos. Environ. Vol. 16.
- Scott, B.C. 1980. Predictions of in-cloud conversion rates of SO<sub>2</sub> to SO<sub>4</sub> based upon a simple chemical and dynamical model. In: Second Joint Conference on Applications of Air Pollution Meteorology. 389.
- Slinn, W.G.N. 1982. Precipitation scavenging (Chapter 11). In: D. Randerson (ed.), Atmospheric Sciences and Power Production. To be published by the U.S. DOE Technical Information Center.

Slinn et al. 1978. Some aspects of the transfer of atmospheric trace constituents past the air-sea interface. Atmos. Environ. Vol. 12.

Smith, F.B. and R.D. Hunt 1979. The dispersion of sulfur pollutants over Western Europe. Phil. Trans. R. Soc. Long. A. 290: 523-542.

## 8. DRY DEPOSITION

### 8.1 Introduction

Dry deposition refers to the transfer of pollutants from the atmospheric boundary layer to the ground. Like other environmental processes, dry deposition is a function of a host of variables. A practical model for dry deposition cannot possibly include all of these variables even if we know how they are related to each other. In view of this, available models of dry deposition rely heavily on empirically derived parameterizations. These formulations are usually expressed in terms of the dry deposition velocity,  $v_d$ , which is defined by the equation:

$$F \equiv v_d C(z) \quad (8-1)$$

In Equation 8-1,  $F$  is the downward pollutant flux at a height  $z$  above the ground, and  $C(z)$  is the corresponding concentration. The parameter  $v_d$  is a complicated function of many variables. Sehmel (1980) presents a list of the important ones. The discussion to follow will highlight the processes explicitly considered in most deposition velocity formulations.

The downward flux,  $F(z)$ , can be formally written as:

$$F(z) = F_d + v_s C \equiv v_d C \quad (8-2)$$

where  $F_d$  is the diffusive flux (molecular and turbulent) and  $v_s$  is the average downward drift velocity the material might possess. It is assumed, as usual, that  $F$  corresponds to an average over the "high frequency" turbulence (see Slinn et al. 1978). To calculate  $v_d$ , it is necessary to estimate  $F_d$  and  $v_s$ . The expressions we propose to use to estimate these variables represent our best combination of the numerous methods described in the literature.

## 8.2 Dry Deposition of Gases

For gases,  $v_s$  is negligible and the flux becomes:

$$F(z) = F_d \quad (8-3)$$

To estimate  $F_d$ , it is useful to think of pollutant transfer as occurring in two distinct layers (as shown in Figure 8-1). The constant flux layer refers to the fully turbulent region in which flux gradient relationships are assumed to be valid. Pollutant transfer within the deposition layer occurs through a combination of turbulent and laminar processes. Except in the case of smooth surfaces, our understanding of mass transfer through this layer is far from complete. Transfer to the ground depends on a number of variables such as type of surface and ground cover. Our inability to model all of the processes at the surface forces us to rely primarily on empirical parameterizations.

It is generally believed that the eddy diffusivity for mass transfer in the constant flux layer is equal to that of heat. Then  $F_d$  in this layer can be written:

$$F_d = K_H \frac{\partial C}{\partial z} \quad (8-4)$$

Integrating Equation 8-4 between  $z_r$ , the reference height for wind speed, and  $\delta$ , the canopy height, results in the familiar expression:

$$(C_r - C_\delta) = \frac{F_d}{ku_*} \left[ \ln \left( \frac{z_r}{\delta} \right) - \psi_H \right] \quad (8-5)$$

where  $u_*$  is the surface friction velocity,  $k$  is the von Karman constant, and  $\psi_H$  is the stability correction function obtained by integrating the flux gradient functions (see Businger 1973). The following equations for  $\psi_H$  are suggested by Wesely and Hicks (1977).

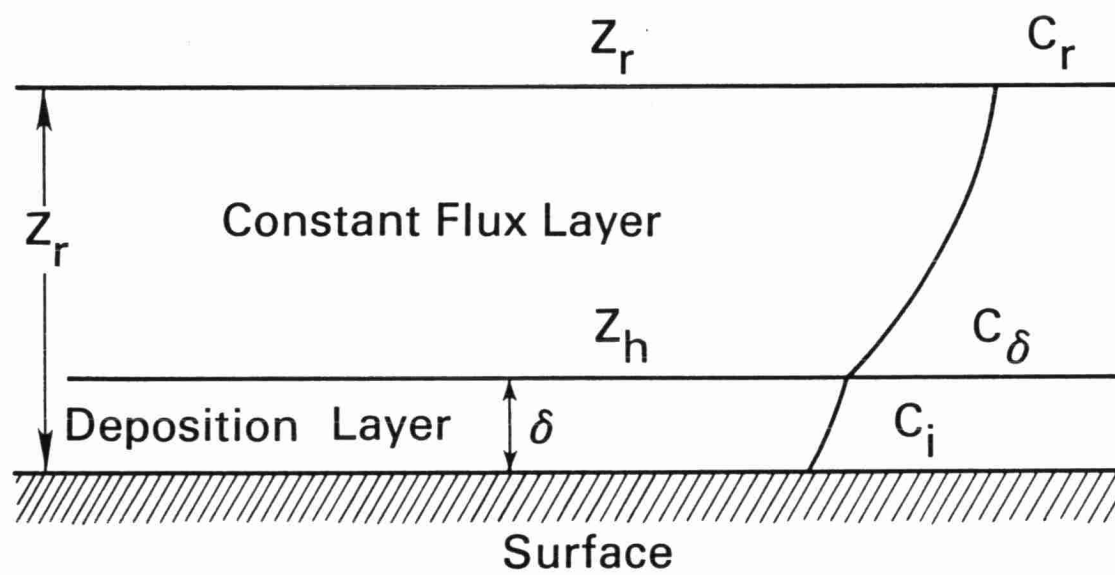


Figure 8-1 Pollutant Transfer

$$\begin{aligned}
\psi_H &= -5\zeta, \quad 0 < \zeta < 1 \text{ (stable)} \\
&= 0, \quad \zeta = 0 \text{ (neutral)} \\
&= \exp \{0.598 + 0.39 \ln(-\zeta) - 0.09 (\ln(-\zeta))^2\}, \\
&\quad -1 < \zeta < 0 \text{ (unstable)}
\end{aligned} \tag{8-6}$$

where  $\zeta = z_r/L$  and  $L$  is the Monin-Obukhov length. In deriving Equation 8-6, it is assumed that  $\delta \ll z_r$ . Equation 8-5 can be rewritten in terms of the roughness length,  $z_o$ , as follows:

$$F_d = (C_r - C_\delta) k u_* [\ln(z_r/z_o) - \psi_H + \ln(z_o/\delta)]^{-1} \tag{8-7}$$

To eliminate  $C_\delta$  in Equation 8-7, we write the expression for the mass transfer through the deposition layer:

$$F_d = h_m (C_\delta - C_i) \tag{8-8}$$

If we write  $C_i = F_d r_s$ , where  $r_s$  is a "surface resistance,"  $C_\delta$  becomes:

$$C_\delta = F_d (1/h_m + r_s) \tag{8-9}$$

where  $h_m$  is the deposition layer mass transfer coefficient. Substituting Equation 8-9 in Equation 8-7 we get:

$$F_d = \frac{C_r k u_*}{[\ln(z_r/z_o) - \psi_H + \ln(z_o/\delta) + k u_* r_s + k u_*/h_m]} \tag{8-10}$$

The form of Equation 8-10 suggests the electrical analogy in which the potential  $C_r$  drives a flux,  $F_d$ , through a sum of resistances given by:

$$r_a = [\ln(z_r/z_o) - \psi_H] / k u_* \tag{8-11a}$$

$$r_d = [\ln(z_o/\delta) + k u_*/h_m] / k u_* \tag{8-11b}$$



and  $r_s$ . From Equation 8-1, the deposition velocity can be expressed as:

$$v_d = (r_a + r_d + r_s)^{-1} \quad (8-12)$$

Note that  $v_d$  cannot be larger than  $1/r_a$ . Also, the largest resistance limits the value of  $v_d$ . For neutral conditions,  $r_a$  is simply:

$$r_a = u/u_*^2 \quad (8-13)$$

This suggests that  $v_d$  can be no greater than  $C_D u$  where  $C_D \equiv (u_*/u)^2$ . This type of simple estimate will be useful in performing sensitivity tests on the model.

As seen in Equation 8-11b, to solve for  $r_d$  it is first necessary to determine  $h_m$ . For smooth surfaces,  $\delta \sim \nu/u_*$ , where  $\nu$  is the kinematic viscosity of air, so that a surface can be considered aerodynamically smooth when  $\nu/u_* z_o > 1$ . Under these conditions, it is found that  $h_m$  can be estimated from equations of the form:

$$h_m l/D = c Sc^a Re^b \quad (8-14)$$

where  $Sc = \nu/D$  and  $D$  is the molecular diffusion coefficient of the gas with respect to air. The Reynolds number  $Re \equiv ul/\nu$  is defined with respect to a characteristic length of the surface to which mass transfer occurs and  $u$  is a velocity which scales with  $u_*$ . An unambiguous application of Equation 8-14 to estimate  $h_m$  is difficult; however, this equation provides guidance on the appropriate form of an empirical parameterization for  $h_m$ .

Most surfaces are rough ( $\nu/u_* z_o < 1$ ) in which the roughness elements stick through the viscous sublayer. Here,  $\delta$  scales with  $z_o$ , but viscous layers on the roughness elements do affect the mass transfer through the deposition layer. On the basis of a number of experiments, Wesely and Hicks (1977) suggest that:

$$r_d = 5 Sc^{2/3}/u_* \quad (8-15)$$

The surface resistance,  $r_s$ , is best estimated by using correlations (semi-quantitative) between the surface type and measurements of  $r_s$ . For plant canopies,  $r_s$  depends on factors such as stomatal activity, cuticular and mesophyll resistances, and solubility of the depositing gas. The characterization of the surface can account for only some of these factors. As pointed out earlier, even if we knew how to calculate  $r_s$ , we would never have the information to do so. We must therefore be content with rather crude parameterizations such as the one proposed by Shieh, Wesely, and Hicks (1979). Table 8-1 presents a partial list of the information presented in their paper. (Environmental factors such as sunlight are indirectly accounted for in the stability classification.) Table 8-2 presents estimates of  $r_s$  compiled by Hicks (1982) from available field observations. This list will be expanded as more information becomes available.

The surface resistance,  $r_s$ , for mass transfer to water bodies can be estimated by equating the fluxes into and away from the air-water interface. We can then write:

$$F_d = h_w (C_i/H - C_b) \quad (8-16)$$

where  $h_w$  is the mass transfer coefficient for the boundary layer inside the water surface, and  $C_b$  is the concentration of the gas in water at a distance  $\delta_w$  from the interface. In writing Equation 8-16, it is assumed that Henry's law applies at the air-water boundary. Unless  $C_b$  is known (or estimated from a model), an explicit expression for  $r_s$  cannot be written. For large bodies of water that can be considered infinite reservoirs, it might be possible to put  $C_b = 0$ . Then:

$$r_s = \frac{H\delta_w}{\alpha D_w} \quad (8-17a)$$

TABLE 8-1  
 LAND-USE TYPES AND THE ASSOCIATED ASSUMED VALUES OF  
 SURFACE ROUGHNESSES AND SURFACE RESISTANCES TO  
 $\text{SO}_2$  UPTAKE FOR CONDITIONS DURING THE SUMMER

<u>Land-Use Type</u>	$z_o$ (cm)	A,B,C	$r_s(\text{scm}^{-1})$		
			D	E	F
0: cropland and pasture	20	1.0	3.0	10.0	0.0
1: cropland, woodland, and grazing land	30	1.0	3.0	10.0	0.0
2: irrigated crops	5	1.0	3.0	10.0	0.0
3: grazed forest and woodland	90	1.0	3.0	10.0	0.0
4: ungrazed forest and woodland	100	1.0	3.0	10.0	0.0
5: sub-humid grassland and semi-arid grazing land	10	1.0	3.0	10.0	0.0
6: open woodland, grazed	20	1.0	3.0	10.0	0.0
7: desert shrubland	30	2.0	5.0	10.0	10.0
A: swamp	20	0.5	0.75	1.0	0.0
B: marshland	50	0.75	3.0	10.0	0.0
C: metropolitan city	100	10.0	10.0	10.0	0.0
F: lake or ocean	0.01	0.0	0.0	0.0	0.0

Source: Sheih, Wesely, and Hicks 1979.

TABLE 8-2  
SURFACES RESISTANCES FOR RELEVANT  
POLLUTANTS OBTAINED FROM MEASUREMENTS

<u>Pollutant</u>	<u>Type of Surface</u>	<u>Environmental Conditions</u>	<u><math>r_s</math> (cms<sup>-1</sup>)</u>
NO <sub>2</sub>	Soybean field (vegetation)	Daytime	1.3
		Night	15
O <sub>3</sub>	Range of natural surfaces	Daytime	0.8
		Night	1.8
NO	"Typical" canopies	--	5 - 20
HNO <sub>3</sub>	"Typical" canopies	--	0
NH <sub>3</sub>	"Typical" canopies	--	Similar to SO <sub>2</sub>

where  $D_w$  is the diffusion coefficient of the gas in water, and  $\alpha$  is a factor accounting for the reactivity of the gas in water. It can then be shown (Slinn et al. 1978) that:

$$\frac{h_w}{h_m} \approx \left( \frac{Sc_w}{Sc_a} \right)^{-2/3} \left( \frac{\rho_a}{\rho_w} \right)^{1/2} \frac{\alpha}{H} \quad (8-18)$$

For gases with low solubility,  $h_w < h_m$  so that the liquid-phase resistance controls the mass transfer at the air-water interface. For  $SO_2$ , the ionization of  $[SO_2 \cdot H_2O]$  results in a high value of  $\alpha$ . In this case, Hicks and Liss (1976) show that  $h_w \gg h_m$ , thereby implying that gas-phase resistance limits the dry deposition.

At the present time, there is little consensus on a formulation for  $r_d$  over water. Most of the suggested expressions are of the form:

$$u_* r_d = a Re_*^b Sc^c - d \quad (8-19)$$

where  $Re_* = u_* z_o / \nu$ . Dipprey and Sabersky (1963) suggest  $a = 10.25$ ,  $b = 0.2$ ,  $c = 0.44$ , and  $d = 8.5$  on the basis of experiments conducted with solid surfaces.

The application of Equation 8-19 to water surfaces poses problems because the effective  $z_o$  depends on the state of sea and the speed of the wind with respect to the waves. Several methods to compute  $z_o$  have been suggested. We have chosen the following:

$$z_o = \nu / (9.1 u_*) + 0.016 u_*^2 / g \quad (8-20)$$

where  $g$  is the acceleration due to gravity.

### 8.3 Dry Deposition of Particles

For particles less than  $0.1 \mu m$  in diameter, dry deposition can be estimated using the equations described in the previous sections. Particles of this size can be considered to be large gas molecules and their mass transfer across the deposition layer is dominated by

Brownian motion. For larger particles, it is necessary to account for inertial effects and gravitational settling. The expression for the downward flux can be written as:

$$F = (K_H + D) \frac{\partial C}{\partial z} + v_g C \quad (8-21)$$

where  $v_g$  is the gravitational settling velocity. Above the deposition layer, the turbulent diffusion term dominates and the formalism of the previous sections applies. In other words, the atmospheric resistance for particles can be computed from Equation 8-11a.

For aerodynamically smooth surfaces, the resistance  $r_d$  across the deposition layer is given (Slinn and Slinn 1980) by:

$$r_d = (v_g + \frac{1}{k} u_* E_j - \alpha \dot{m})^{-1} \quad (8-22)$$

where  $k \approx 0.4$ ,  $\alpha \dot{m}$  represents the contribution from diffusiophoresis, and  $\dot{m}$  is the rate of evaporation at the surface. The proportionality constant  $\alpha = 10^3 \text{ cms}^{-1} / (1 \text{ gcm}^{-2} \text{ s}^{-1})$ . The jet efficiency,  $E_j$ , is:

$$E_j = Sc^{-1/2} + 10^{-3}/St \quad (8-23)$$

where  $Sc = \nu/D$  is the Schmidt number,  $\nu$  is the kinematic viscosity of air,  $D$  is the particle's Brownian diffusivity in air, and the Stokes number  $St = \tau u_*^2 / \nu$ . Here,  $\tau$  is the particle's relaxation time,  $\tau = v_g / g$ , where  $g$  is the acceleration due to gravity.

In most cases, reentrainment of particles can be neglected. This means that  $r_s = 0.0$  and the deposition velocity  $v_d$  is then given by:

$$v_d = (r_a + r_d)^{-1} \quad (8-24)$$

This formulation would apply to surfaces such as water and snow-covered surfaces. Slinn and Slinn (1980) suggest that hygroscopic aerosol particles with mass mean radius near  $1 \mu\text{m}$  (such as sulfate particles), grow by absorbing water as they approach the water's surface. They show that their gravitational settling velocities become large enough so that  $r_d \ll r_a$  and  $v_d \approx r_a^{-1}$ .

For rough surfaces ( $z_0 v/u_* > 1$ ), the resistance of the deposition layer is:

$$r_d = (v_g + 0.2 u_* Sc^{-2/3})^{-1} \quad (8-25)$$

This formulation is tentative and is based on that for gases (see Equation 8-15).

Our understanding of deposition into canopies is far from complete. At the present time, we are forced to resort to empirical expressions of the form:

$$r_d = (v_g + \alpha u_* \epsilon / (1 + \epsilon) + u_*^2 E_j / (k u_g (1 + \epsilon)))^{-1} \quad (8-26)$$

In Equation 8-26,  $\epsilon$  is a complicated function of canopy properties, and  $u_g$  is the velocity at the top of the canopy;  $\epsilon$  increases as the canopy becomes denser. Hicks (1982) suggests that our present understanding does not warrant anything more than the use of the typical value of  $r_d$  based on measurements. He recommends  $r_d \approx 1 \text{ scm}^{-1}$  for forests and  $3 \text{ scm}^{-1}$  for mown grass for particles with a mass mean radius around  $1 \mu\text{m}$ . In our project we propose to adopt this pragmatic approach; however, the submodel for deposition will be flexible enough to allow for better formulations in the future.

The suggested formulations for  $v_d$  refer to a specific particle radius  $R$ . Therefore, to calculate the deposition velocity for a polydispersed aerosol, it is necessary to integrate  $v_d(R)$  over the particle size distribution function  $f(R)$  as follows

$$\bar{v}_d = \int v_d(R) f(R) dR \quad (8-27)$$

### Summary

As pointed out before, the equations presented in this chapter represent our "best" choice among the multitude of alternate formulations described in the literature. Therefore, they are tentative and will be modified, if necessary, during the development of the mesoscale and LRT models.

In order to help the reader through the equations, we have presented simple flowcharts in Figures 8-2 through 8-6.



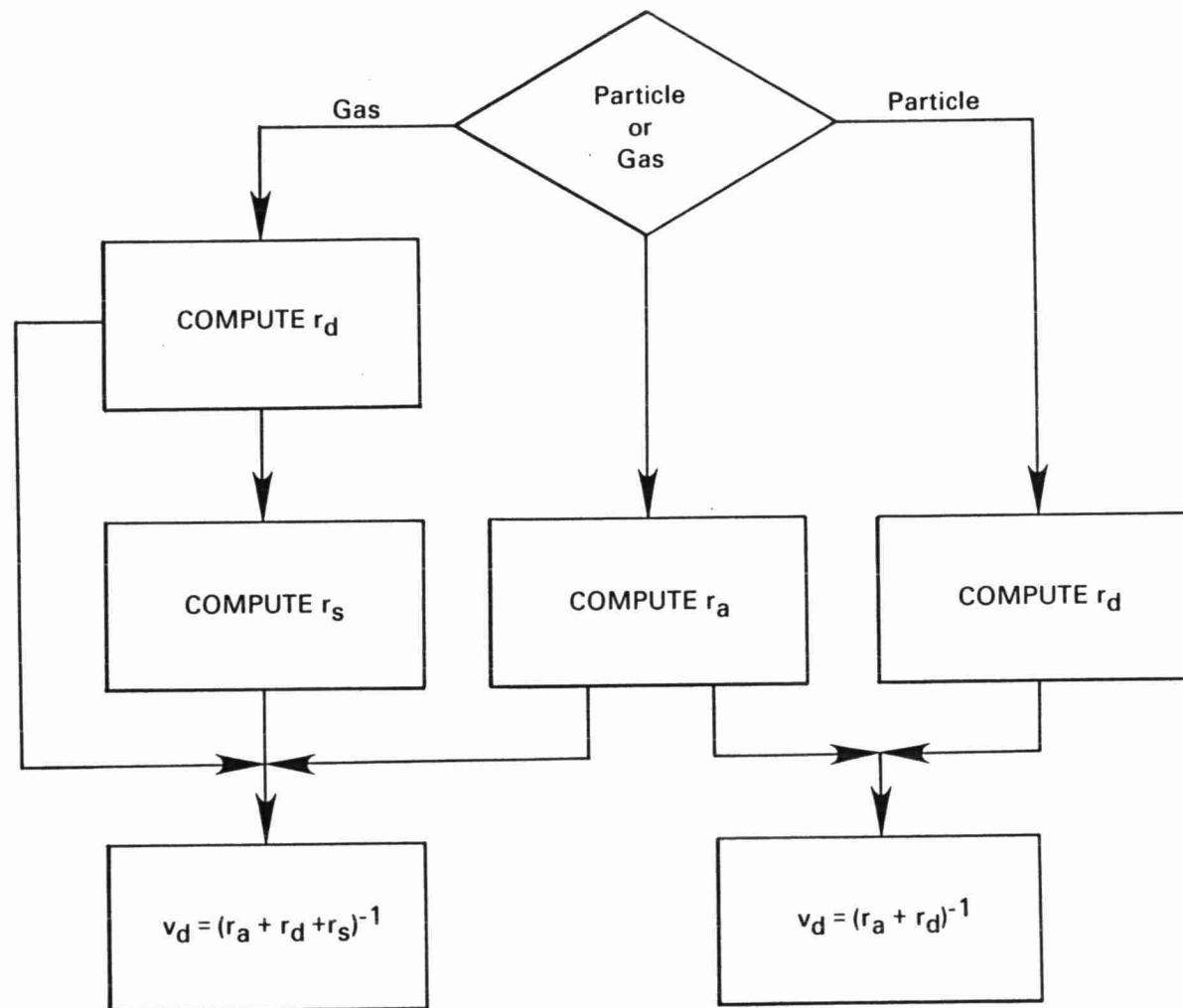


Figure 8-2 Deposition Velocity Calculation

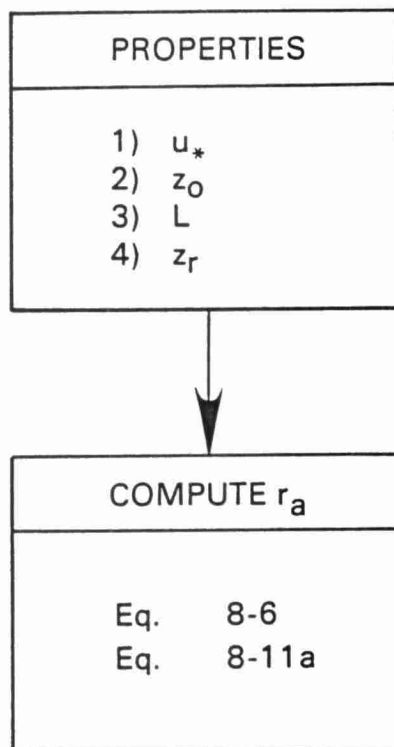


Figure 8-3 Atmospheric Resistance  $r_a$

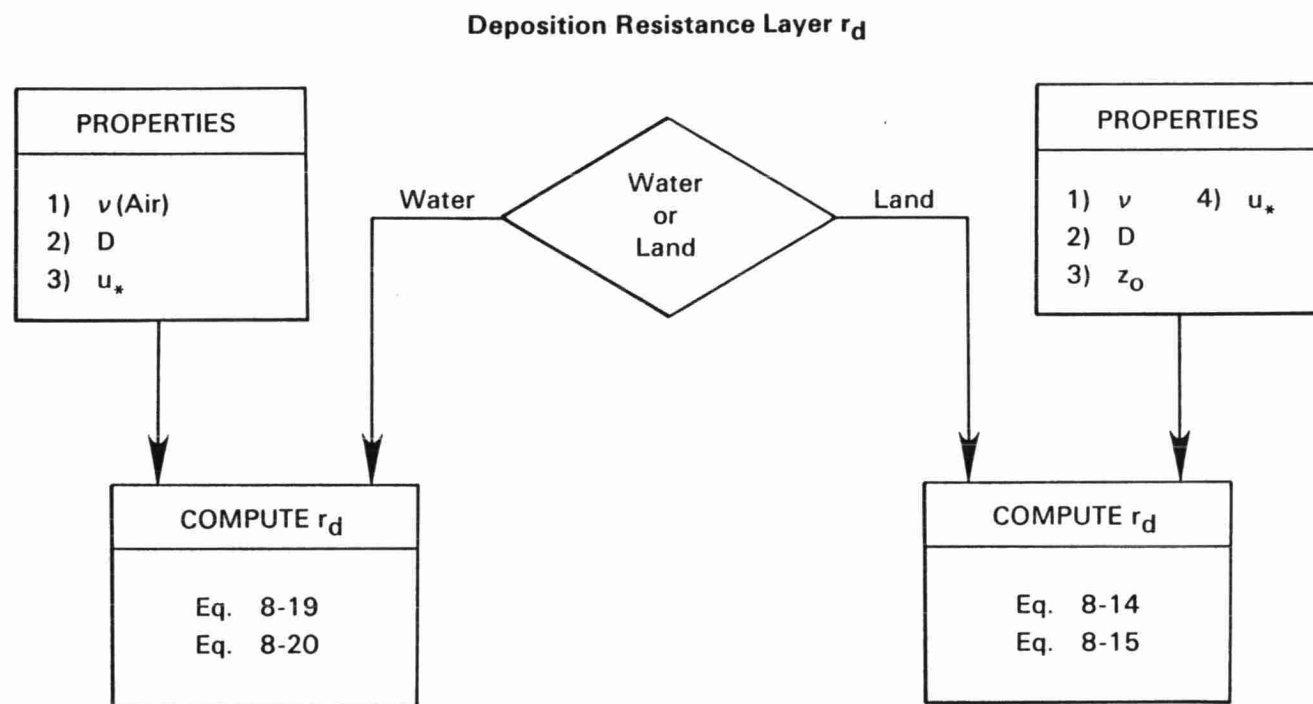


Figure 8-4 Deposition Velocity for Gases

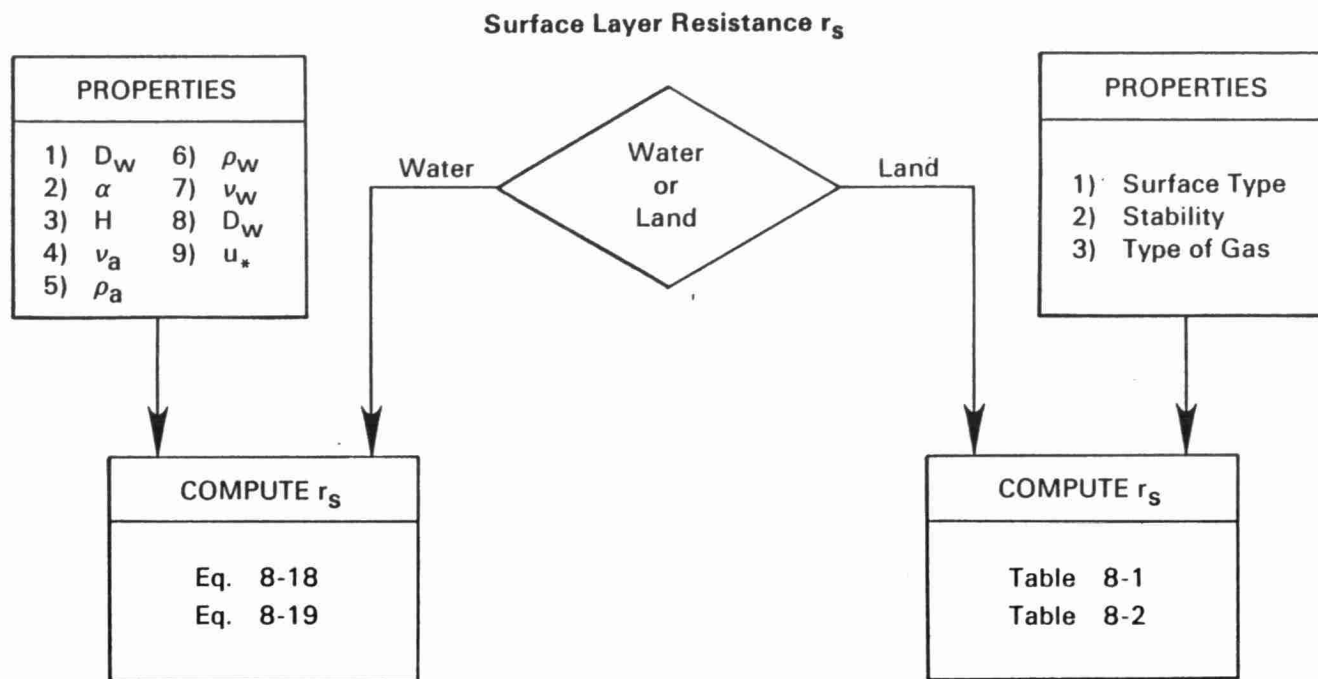


Figure 8-5 Deposition Velocity for Gases

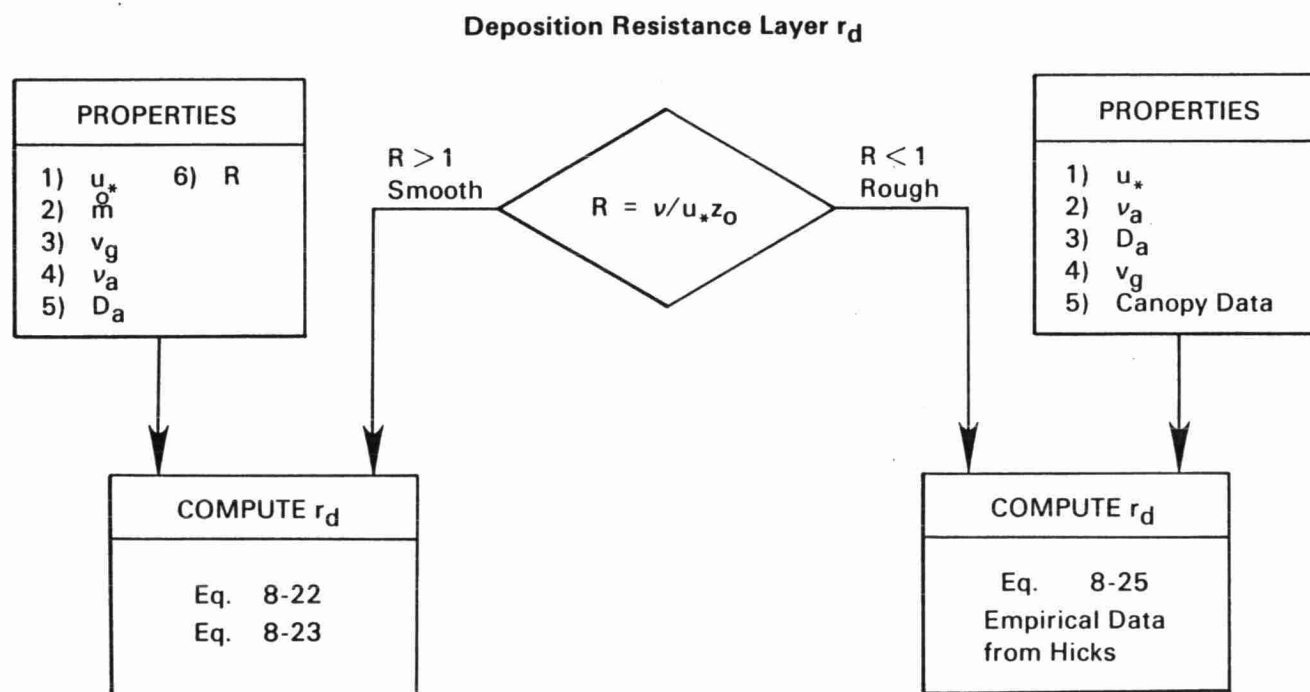


Figure 8-6 Deposition Velocity of Particles

REFERENCES: SECTION 8

- Businger, J.A. 1973. Turbulent transfer in the atmospheric surface layer. In: Workshop on Micrometeorology, pp. 67-98. American Meteorological Society, Boston, MA.
- Dipprey, D.F. and R.H. Sabersky 1963. Heat and momentum transfer in smooth and rough tubes at various Prandtl numbers. Int. J. Heat Mass Transfer 6: 329-353.
- Hicks, B.B. and P.S. Liss 1976. Transfer of SO<sub>2</sub> and other reactive gases across the air-sea interface. Tellus 28: 348-354.
- Hicks, B.B. 1982. In: Critical Assessment Document on Acid Deposition (Chapter VII). ATDL contribution File No. 81/24. Atmospheric Turbulence and Diffusion Laboratory, NOAA, Oak Ridge, TN 37830.
- Sehmel, G.A. 1980. Deposition and Reinsertion Processes. In: D. Randerson (ed.), Atmospheric Science and Power Production (Chapter 12). U.S. Dept. of Energy.
- Shieh, C.M., M.L. Wesely and B.B. Hicks 1979. Estimated dry deposition velocities of sulfur over the eastern United States and surrounding regions. Atmospheric Environment 13: 1361-1368.
- Slinn, W.G.N., L. Hasse, B.B. Hicks, A.W. Hogan, D. Lal, P.S. Liss, K.O. Munnich, G.A. Sehmel and O. Vittori 1978. Some aspects of the transfer of atmospheric trace constituents past the air-sea interface. Atmospheric Environment 12: 2055-2087.
- Slinn, S.A. and W.G.N. Slinn 1980. Predictions for particle deposition on natural waters. Atmospheric Environment 14: 1013-1016.
- Wesely, M.L. and B.B. Hicks 1977. Some factors that affect the deposition rates of sulfur dioxide and similar gases on vegetation. J. Air Poll. Control Assoc. 27: 1110-1116.

## 9. DISPERSION

### 9.1 Introduction

Dispersion refers to the transport of pollutants by the component of the velocity field which is not resolved explicitly in the model. Formally, the turbulent flux can be written as:

$$F_i = v_i' C' + v_i' \langle C \rangle \quad (9-1)$$

where  $v_i'$  is the unresolved velocity and  $C' \equiv C - \langle C \rangle$ . The ensemble average  $\langle C \rangle$  is defined in Chapter 11. Equation 9-1 can be rewritten as:

$$F_i = \langle v_i' C' \rangle + \epsilon \quad (9-2a)$$

$$\text{where } \epsilon \equiv F_i - \langle F_i \rangle \quad (9-2b)$$

It is clear from the definition of the ensemble that  $\langle v_i' \rangle = 0$ . In order to calculate  $F_i$ , we have to postulate a model for  $\langle F_i \rangle$  and estimate the statistics of  $\epsilon$  by comparing model predictions with observations. As pointed out in Chapter 11, incomplete knowledge of  $v_i$  forces us to rely on empirical methods to construct a model for  $\langle F_i \rangle$ . In the sections to follow, several available formulations for  $\langle F_i \rangle$  will be described.

### 9.2 Vertical Dispersion

Our experience with calculating dispersion in the planetary boundary layer provides some guidance on  $F_i$  in the vertical direction. When  $v_i$  and  $C$  refer to averages of velocities and concentrations over time periods of about one hour, there is empirical evidence to indicate that it is possible to develop "reasonable" estimates for  $\langle F_i \rangle$ . It is assumed here that

$$\langle F_3 \rangle = -K \frac{\partial C}{\partial z} \quad (9-3)$$

where  $K$  is the so-called eddy diffusivity. Although there is little theoretical basis for gradient transport implied by  $K$  theory, a number of studies indicate that it yields acceptable estimates of concentrations. In fact, a wide variety of  $K$  formulations appear to produce similar results; this indicates that concentrations are not very sensitive to the precise specification of the  $K$  profile. Observations on concentrations associated with pollutant releases in the surface layer indicate that  $K$  is similar to the eddy diffusivity of heat,  $K_H$ , defined by:

$$K_H \equiv -\langle w' \theta' \rangle / \partial \theta / \partial z \quad (9-4)$$

Micrometeorological studies (Businger 1973) show that  $K_H$  can be written as:

$$K_z = K_H = k u_* z / \phi_H \quad (9-5)$$

where  $\phi_H$  is the nondimensional temperature gradient which is a function of  $z/L$ . When the boundary layer is unstable,  $\phi_H$  is defined as:

$$\phi_H = 0.74 (1 - 9\zeta)^{-1/2} \quad (9-6a)$$

$$\text{where } \zeta = z/L \quad (9-6b)$$

Above  $z = |L|$ , it can be shown that the turbulent velocity fluctuations become independent of  $u_*$ , and  $K_z$  can be expressed as:

$$K_z = \beta k^{5/3} u_f z \equiv \beta k u_* z (-z/L)^{1/3} \quad (9-7a)$$

$$\text{where } u_f \equiv (g/T_0 \overline{w'\theta'}_z)^{1/3} \quad (9-7b)$$



By matching  $K_z$  from Equation 9-7 with that from Equation 9-6, we find that  $\beta = 4.3$ . For  $z > 0.1 z_i$ , we adopt the formulation suggested by Wyngaard (1981):

$$K_z = A w_* z (1 - z/z_i) \quad (9-8)$$

Ensuring that  $K_z$  is continuous across  $z = 0.1 z_i$  yields  $A = 1.56$ . This completes our prescription for  $K_z$  in the convective boundary layer.

On the basis of the work of Brost and Wyngaard (1978), we propose the following  $K_z$  formulation for the stable boundary layer:

$$K_z = k u_* z (1 - z/z_i)^{3/2} / (0.74 + 4.7\zeta) \quad (9-9)$$

These models for  $K_z$  are empirical and are based on observations taken under special conditions not likely to be similar to those we are attempting to model. It will be necessary to modify these formulations to calibrate the predictions of the model against observations. If the proposed  $K_z$  formulations prove to be inadequate during the modeling program, we will consider using eddy diffusivities derived from second-order modeling techniques (see Zeman and Lumley 1979).

### 9.3 Horizontal Dispersion

There is little theory or observation to provide guidance on the parameterization of horizontal dispersion at scales ranging from tens to hundreds of kilometers. In principle, the turbulent flux is a function of the concentration field, the scale and magnitude of the unresolved velocity field, and the grid spacing used in the model. There is now no acceptable method of estimating the horizontal fluxes. However, some empirical rules are supported in studies on momentum transport. When the scale of the unresolved velocity field  $l_v$  is larger than the grid spacing  $\Delta x$ ,  $K_h$  can be written as:

$$K_h \sim l_v^2 D \quad (9-10)$$

where  $D$  is some measure of the velocity gradient of the resolved velocity field. This type of formulation works for dispersion in the vertical direction in the planetary boundary layer. For long-range transport,  $l_v < \Delta x$  and  $K_H$  must be written as:

$$K_H = \alpha(\Delta x)^2 D \quad (9-11)$$

On the basis of experiments with a general circulation model, Smagorinsky (1963) suggests that  $D$  should be the deformation tensor given by:

$$D = \left[ \left( \frac{\partial \langle u_i \rangle}{\partial x_j} + \frac{\partial \langle u_j \rangle}{\partial x_i} \right) \left( \frac{\partial \langle u_i \rangle}{\partial x_j} + \frac{\partial \langle u_j \rangle}{\partial x_i} \right) \right]^{1/2} \quad (9-12)$$

Note that Equation 9-11 has some empirical support only if  $K_H$  applies to the velocity field averaged over the grid spacing  $\Delta x$ . It is not clear that  $K_H$  estimated from an equation of the form (9-11) can be used to model dispersion of tracers. Also, because it is difficult to interpret the velocity field constructed from available wind monitors, it will be necessary to use a trial-and-error technique to come up with a  $K_H$  that "works."

Figure 9-1 shows a flow chart for the computation of eddy diffusivities.

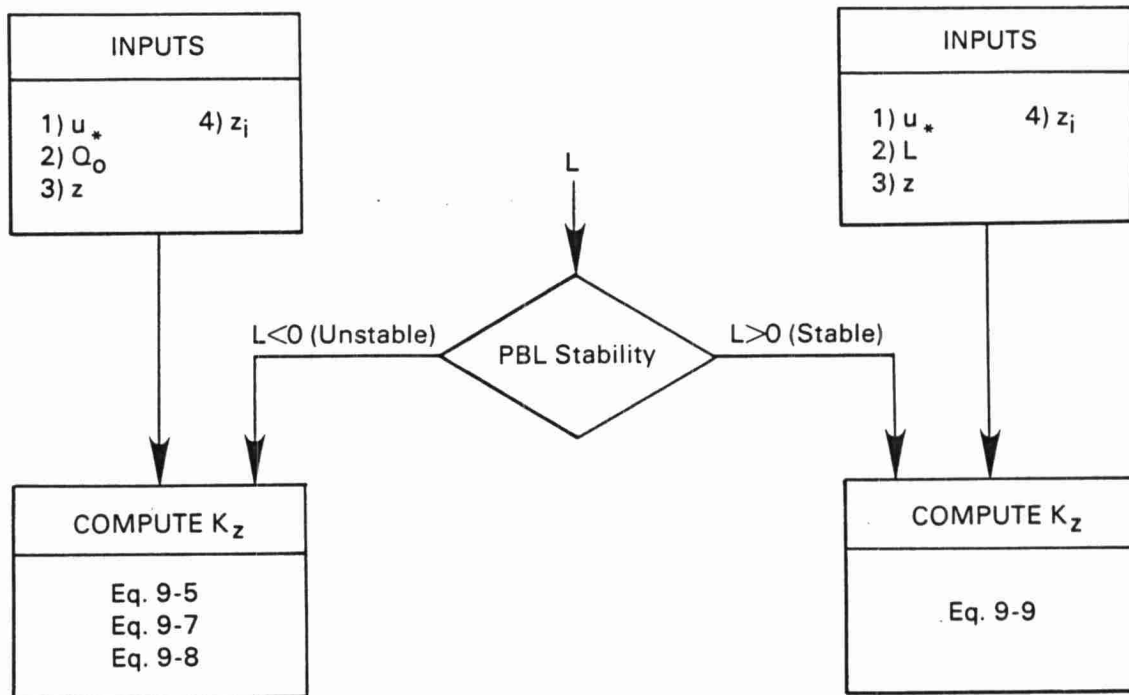
#### 9.4 Calculation of Micrometeorological Variables

The  $K_z$  formulations described in the previous sections depend on the surface friction velocity,  $u_*$ , the Monin-Obukhov length,  $L$ , and the mixed layer height,  $z_i$ . In this section, we describe methods to estimate these variables from routinely available meteorological measurements.

##### 9.4.1 Surface Friction Velocity, $u_*$

The surface friction velocity,  $u_*$ , can be estimated from routinely available meteorological data if the surface roughness characteristics are known. First, the sensible heat flux is

### Calculation of Vertical Eddy Diffusivities



### Calculation of Horizontal Diffusivities

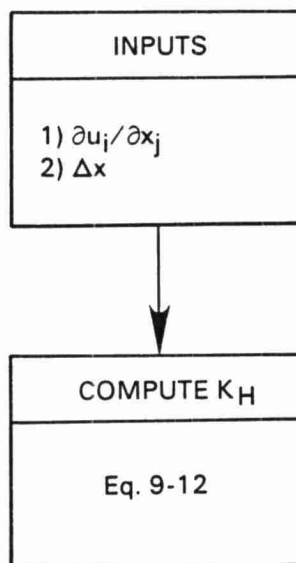


Figure 9-1 Eddy Diffusivity Calculation

calculated from an estimate of net radiation. The surface friction velocity can then be obtained using wind speed, surface roughness, and heat flux parameters.

The sensible heat flux,  $H$ , is estimated from the following equations (Maul 1980):

$$\begin{aligned} H &= \alpha R + H_o & (9-13) \\ R &= 950 \beta [\cos\phi \cos T \cos L + \sin\phi \sin L] \\ T &= \pi (\tau - U)/12 \\ \phi &= \tan^{-1} [0.4348 \sin (\pi(d-78)/180)] \end{aligned}$$

where

- $H$  is the sensible heat flux ( $Wm^{-2}$ ),
- $H_o$  is the heat flux in the absence of solar incoming radiation ( $Wm^{-2}$ ),
- $\alpha$  is a land use constant,
- $R$  is the incoming solar radiation ( $Wm^{-2}$ ),
- $\beta$  is a radiation reduction factor due to the presence of clouds,
- $U$  is the time of local noon (hours),
- $\tau$  is the time of day (hours),
- $d$  is the Julian day, and
- $L$  is latitude (degrees).

The equation for  $R$  is valid for daylight hours, i.e.,

$$U - \frac{12}{\pi} \cos^{-1}(\tan\phi \tan L) \leq t \leq U + \frac{12}{\pi} \cos^{-1}(-\tan\phi \tan L) \quad (9-14)$$

Table 9-1 contains values for the solar radiation reduction factor ( $\beta$ ) due to the presence of clouds. The values of  $\beta$  are adapted from those used by Maul (1980).

With the above estimate of sensible heat flux, the surface friction velocity,  $u_*$ , can be estimated during unstable conditions

TABLE 9-1  
SOLAR RADIATION REDUCTION FACTOR  $\beta$

<u>Cloud Cover (Tenths)</u>	<u><math>\beta</math></u>
0	1.00
1	0.91
2	0.84
3	0.79
4	0.75
5	0.72
6	0.68
7	0.62
8	0.53
9	0.41
10	0.23

by the scheme suggested by Wang and Chen (1980). The friction velocity is defined by the following equations:

$$u_* = \tilde{u}_* \{1 + a \ln [1 + b Q_o / \tilde{Q}_o]\} \quad (9-15a)$$

$$\tilde{u}_* = \frac{k u_m}{\ln (z_m / z_o)} \quad (9-15b)$$

$$Q_o = H / (\rho c_p) = \overline{w'\theta'} \quad (9-15c)$$

$$\tilde{Q}_o = \frac{\theta \tilde{u}_*}{k g z} \quad (9-15d)$$

$$a = \begin{cases} 0.128 + 0.005 \ln (z_o / z_m) & z_o / z_m \leq 0.01 \\ 0.105 & z_o / z_m > 0.01 \end{cases} \quad (9-15e)$$

$$b = 1.95 + 32.6 (z_o / z_m)^{0.45} \quad (9-15f)$$

where

$k$  is the von Karman constant,  
 $c_p$  is the specific heat of air at constant pressure ( $\text{m}^2/(\text{s}^2\text{deg})$ ),  
 $u_*$  is the surface friction velocity ( $\text{m/s}$ ),  
 $u_m$  is the wind speed ( $\text{m/s}$ ) measured at height  $z_m$  ( $\text{m}$ ),  
 $z_o$  is the surface roughness ( $\text{m}$ ), and  
 $\theta$  is potential temperature ( $^\circ\text{K}$ ).

Venkatram (1981) recommends the following method to determine  $u_*$  during stable conditions.

$$u_* = \frac{C_{DN} u_m}{2} [1 + C^{0.5}] \quad (9-16)$$

$$C_{DN} = \frac{k}{\ln (z_m/z_o)} \quad (9-17a)$$

$$C = 1 - \frac{4 u_o^2}{C_{DN}^2 u_m^2} \quad C \geq 0 \quad (9-17b)$$

$$u_o^2 = \frac{\gamma z_m}{k A} \quad (9-17c)$$

where  $\gamma$  and  $A$  are constants with values of 4.7 and 1100, respectively.

#### 9.4.2 Monin-Obukhov Length, $L$

The Monin-Obukhov length,  $L$ , is defined as:

$$L \equiv - \frac{u_*^3 T_o}{g k Q_o} \quad (9-18)$$

During unstable conditions,  $L$  is calculated directly from its definition using values of  $u_*$  and  $Q_o$  given above. During stable conditions,  $L$  is given by Venkatram (1981) as:

$$L = 1100 u_*^2$$

#### 9.4.3 Mixed Layer Height, $z_i$

During daylight hours, solar radiation reaching the ground results in a positive (upward) flux of sensible heat. This heat flux causes a well-mixed adiabatic layer to develop. If the hourly variation of surface heat flux is known, the height of the mixed layer,  $z_i$ , can be obtained in a stepwise manner from the following equation used by Maul (1980):

$$(z_i)_{t+1} = (z_i)_t^2 + \left[ \frac{2H(1+A)\Delta t}{\psi_1 \rho c_p} - \frac{2(\Delta\theta)_t (z_i)_t}{\psi_1} \right]^{1/2} + \frac{(\Delta\theta)_{t+1}}{\psi_1} \quad (9-19a)$$

$$(\Delta\theta)_{t+1} = \left[ \frac{2\psi_1 A H \Delta t}{\rho c_p} \right]^{1/2} \quad (9-19b)$$

where  $\psi_1$  is the lapse rate above the mixing height,  $A$  is a constant (0.15), and  $\Delta\theta$  is the temperature discontinuity at the top of the mixed layer. During the summer months, the OZ temperature sounding can be used to estimate  $z_i$  in the evening. This information can be used to calibrate  $\alpha$  in Equation 9-13.

In the stable boundary layer, mechanical turbulence production determines the vertical extent of dispersion. Venkatram (1980b) provides the following empirical relationship to estimate  $z_i$  during stable conditions.

$$z_i \approx 2400 u_*^{3/2} \quad (9-20)$$



REFERENCES: SECTION 9

- Brost, R.A. and J.C. Wyngaard 1978. A model study of the stably stratified planetary boundary layer. J. Atmos. Sci. 35: 1427-1440.
- Businger, J.A. 1973. Turbulent transfer in the atmospheric surface layer. In: Workshop on Micrometeorology, pp. 67-100. American Meteorological Society (AMS), Boston, MA.
- Maul, P.R. 1980. Atmospheric Transport of Sulphur Compound Pollutants. Ph.D. Thesis, University of London.
- Smagorinsky, J. 1963. General circulation experiments with the primitive equations: 1. The basic experiment. Mon. Wea. Rev. 91: 99-164.
- Venkatram, A. 1981. Estimation of turbulence velocity scales in the stable and the unstable boundary layer for dispersion applications. In: Eleventh NATO-CCMS International Technical Meeting on Air Pollution Modeling and its Application, pp. 54-64. New York: Plenum Press.
- Wang, I.T. and P.C. Chen 1980. Estimation of heat and momentum fluxes near the ground. In: Proc. 2nd Joint Conf. on Applications of Air Pollution Meteorology, New Orleans, LA, March 24-27, pp. 764-769. AMS, Boston, MA.
- Wyngaard, J.C. 1981. Wind shear in the baroclinic convective PBL. In: Fifth Symposium on Turbulence, Diffusion, and Air Pollution, pp. 78-79. AMS, Boston, MA.
- Zeman, O. and J.L. Lumley 1979. Buoyancy effects in entraining turbulent boundary layers: A second-order closure study. In: Turbulent Shear Flows I, pp. 295-306. Berlin: Springer-Verlag.

## 10. MODEL SENSITIVITY ANALYSIS

A series of computer simulations were made using air quality models to investigate differences between "simple" and "complex" models. Here "complex" refers to models in which as many parameterizations as practical are day-specific and time and space varying; "simple" refers to any model which has fewer variables than the complex model. Two complex models were employed in the analysis: ERT's SURADS Eulerian long range transport model (Lavery et al. 1980) and ERT's PLMSTAR (pronounced Plume Star) Lagrangian reactive plume model (Lurmann et al. 1982). Numerous simple models were constructed from the complex models by averaging parameters which are time and space varying in the complex models. The rationale for this exercise was that simple models generally rely on parameterizations derived from comparisons of model predictions with observations and utilize regional average, rather than time and space varying, input parameters. Because the simple models are derived indirectly from observations and, therefore, do not accurately incorporate the physics and chemistry of the atmospheric processes, they may not be suited for simulating conditions significantly different than the conditions associated with the observations. For example, they may not be accurate for simulating the effects of emission control scenarios.

The objectives of the sensitivity analysis was to first compare the predictions of alternate model formulations (i.e., simple versus complex models) and second to compare the response of the alternate model formulations to emission control scenarios. Results from the comparison of simple and complex models were used in the design of the Phase II models and are potentially useful for decision makers who commonly rely on the results of simple models only.

It is important to note that none of the simple models utilized here are truly simple models. They are still quite complex relative to many long-range transport models. Furthermore, by deriving the simple models by averaging day specific parameters in the complex models, the comparisons presented herein are believed to show the minimum differences one could expect between the simple and complex models.

## 10.1 LRT Model Sensitivity Analysis

A sensitivity analysis was performed using the SURADS Eulerian Model. The primary purpose of performing the analysis was to see the effect on calculated sulfate and  $\text{SO}_2$  concentrations and sulfur deposition of incorporating simplifying assumptions into the model formulation, and furthermore, to determine the difference in response to emission reductions between the complex and simple models.

### 10.1.1 LRT Model Formulation

The Sulfate Regional Advection and Diffusion Scheme (SURADS) is based on the numerical solution of the mass conservation of  $\text{SO}_2$  and sulfate:

$$\frac{\partial C}{\partial t} = -u \frac{\partial C}{\partial x} - v \frac{\partial C}{\partial y} + \frac{\partial}{\partial z} \left( K_z \frac{\partial C}{\partial z} \right) + Q + k_t C + k_\Delta C \quad (10-1)$$

where:

- C is a chemical composition vector with two components, each representing a species ( $\text{SO}_2$  and  $\text{SO}_4$ ) concentration,
- t is time,
- x,y,z are the components of the model grid system that follows local terrain,
- u is the east-west component of the wind,
- v is the north-south component of the wind,
- $K_z$  is the vertical diffusivity,
- Q is a source emission,
- $k_t$  is a conversion rate of  $\text{SO}_2$  to sulfate, and
- $k_\Delta$  is a deposition loss at the ground.

Equation (10-1) is a simplified version of a set of equations that are three-dimensional and that can include nonlinear terms to simulate complex chemical reactions. The simplified expression indicates that the  $\text{SO}_2$  or  $\text{SO}_4$  concentration within a grid cell can change with time by horizontal advection ( $-u \frac{\partial C}{\partial x} - v \frac{\partial C}{\partial y}$ ), vertical turbulent mixing ( $\frac{\partial}{\partial z} K_z \frac{\partial C}{\partial z}$ ), emissions, transformation or deposition.

The model is applied to a three dimensional grid region (Figure 10-1) consisting of 30 by 23 by 5 cells. Each cell has horizontal dimensions of 80 km by 80 km. The vertical dimensions of the five model layers are 0-50 m, 50-100 m, 100-300 m, 300-700 m, and 700-1500 m (AGL).

To integrate Equation (10.1), information must be provided for the following variables as functions of time and space:

- winds --  $u(x, y, z, t)$  and  $v(x, y, z, t)$ ;
- vertical turbulent diffusion coefficient --  $K_z(x, y, z, t)$ ;
- emissions --  $Q(x, y, z, t)$ ;
- first-order  $\text{SO}_2$ -to-sulfate transformation rates --  $k_t(t)$ ;  
and
- deposition velocities --  $V_d(x, y, t)$ .

These input variables were derived from the SURE data base through a series of computer programs and are specified for each grid cell and updated every hour.

Rawinsonde data collected at 29 stations twice daily (00Z and 12Z) form the data base used to develop wind inputs to the grid model. Objective analysis techniques developed by Liu and Goodin (1976), Clark and Eskridge (1977) and Endlich (1967) were used to develop an algorithm that produces gridded northward and eastward (i.e.,  $u$  and  $v$ ) components of the wind at specified vertical levels. The wind field at each level is adjusted iteratively to minimize divergence while conserving vorticity. Hourly wind fields are determined from simple linear interpolation of the fields developed for the rawinsonde times.

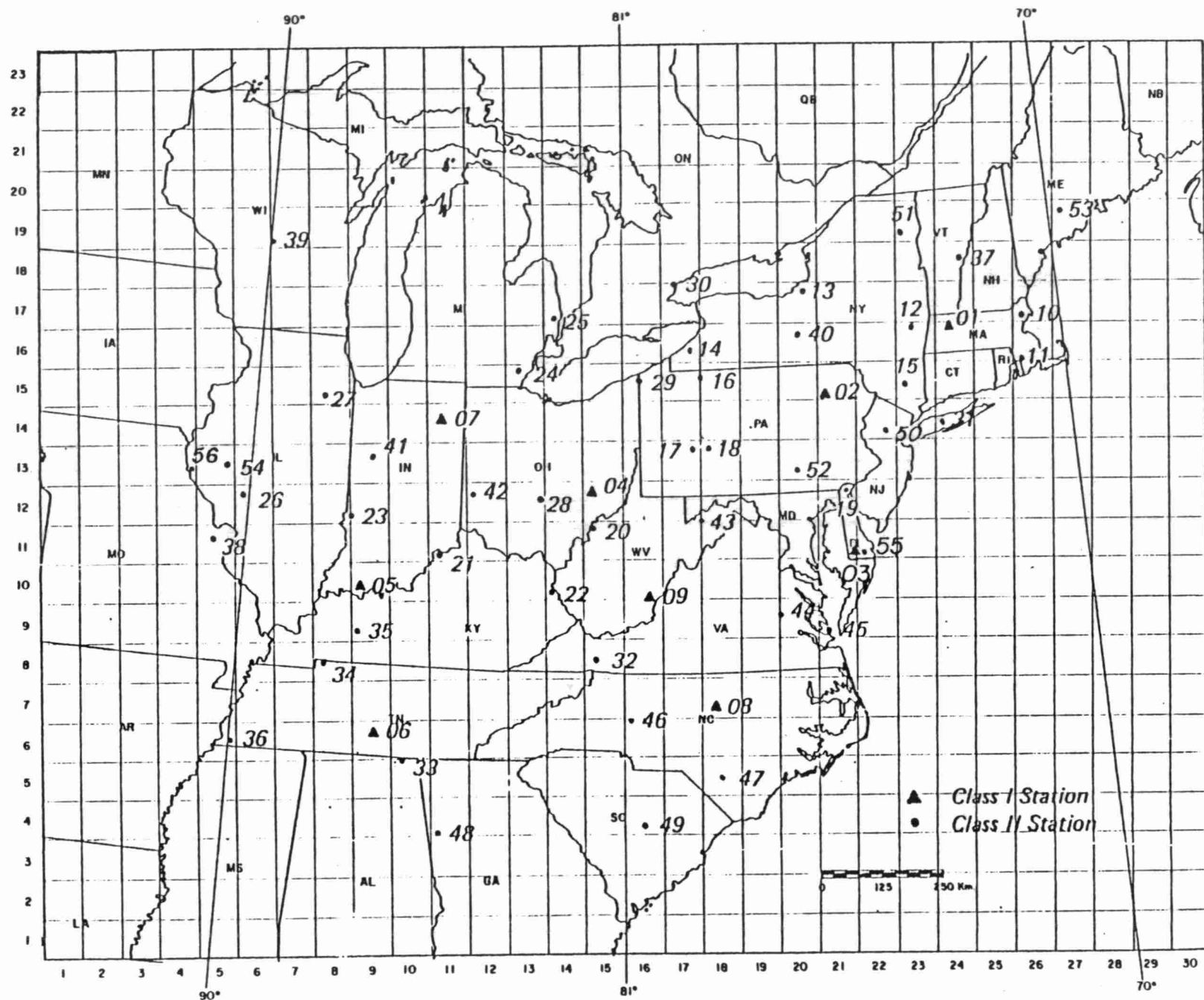


Figure 10-1. The SURE Grid Region.

In the surface layer, the vertical eddy diffusivity is given by

$$K_z = \frac{ku_*z}{\phi_m\left(\frac{z}{L}\right)} \quad (10-2)$$

where  $k$  = von Karman constant

$u_*$  = friction velocity

$z$  = height above ground

$L$  = Monin-Obukhov length

$m$  = the nondimensional wind shear.

The  $\phi$ -function is taken from Businger (1971).

The interpolation method suggested by O'Brien (1970) is used to determine diffusivities between the top of the surface layer and the top of the boundary layer.

The twice-daily soundings and hourly surface temperature and wind measurements are used to determine the vertical profile of hourly values of  $K_z$  for each radiosonde station. The surface data are used to reconstruct a sounding for each hour. The vertical temperature distribution and surface wind speed are used to determine the stability class using Fulle (1975), and Golder (1972) is used to determine  $L$ . Surface winds and values of surface roughness ( $z_0$ ), which were determined from land use and agricultural maps for the grid, are used to determine  $u_*$ . Gridded values of  $K_z$  are derived by linearly interpolating the station values with an inverse radius squared weighting procedures.

The loss of a species at the surface is simulated by use of a deposition velocity ( $V_d$ ). For  $SO_2$ ,  $V_d$  is given by

$$V_d = ku_* (\ln (z/z_0) + 2.6 - ku_* r_c)^{-1} \quad (10-3)$$

as taken from Wesley and Hicks (1977). A value of 0.7 is assigned to  $r_c$ .  $V_d$  for sulfate is taken as 10% of the  $SO_2$  deposition velocity.

To determine conversion rates, a series of EKMA-like simulations were carried out using a variety of conditions similar to those

encountered in rural, urban, and suburban locations within the SURE grid. From these, the maximum oxidation rates were determined as a function of season and initial concentrations of nonmethane hydrocarbon (NMHC) and  $\text{NO}_x$ . As a first approximation, it was assumed that the oxidation rate was constant spatially and the rates derived for St. Louis, Missouri were taken to be representative of the entire SURE region. Also, the conversion rate was assumed to have a Gaussian distribution with time about the maximum rate determined from the photochemical simulations. In mid-summer, the resultant rates used in SURADS vary from 0.2% at night to over 4% per hour at midday.

In SURADS, finite difference techniques are used to solve advection and diffusion. The advection component of the conservation equation is solved using an integration algorithm developed by Boris and Book (1973) that is called SHASTA (an acronym for "sharp and smooth transport algorithm"). An implicit integration technique is used to solve the vertical diffusion and deposition components.

Initial conditions for  $\text{SO}_2$  are based on hourly observations taken during the hour preceeding the period of simulation. Gridded initial values are calculated by linear interpolation using an inverse radius squared weighting scheme. Because 3-hour values of particulate aerosol concentrations are available from the intensive measurement months, initial values of sulfate are developed from the 3-hour concentrations measured prior to the simulation periods.

The assumed horizontal boundary conditions are 1 ppb of  $\text{SO}_2$  and  $1 \mu\text{g}/\text{m}^3$  of  $\text{SO}_4$ . No mass is allowed to escape the modeling domain through the top boundary.

#### 10.1.2 LRT Model Sensitivity Analyses Description

For the long range transport model sensitivity analyses, a total of 15 simulations were performed with eight different "models" that are variations of SURADS. Table 10-1 provides summary descriptions of the runs that were made. The number (1-8) contained in the simulation name refers to model used, whereas the letter (A,B) distinguishes additional runs made with the same model. All simulations were made with July 21, 1978 inputs derived from the SURE data base.

TABLE 10-1

## LRT MODEL SENSITIVITY ANALYSIS SIMULATIONS

<u>Simulation Name</u>	<u>Description of Run</u>
1	Complex Model (Baseline)
1A	Complex Model: Initial conditions only
1B	Complex Model: Reduced emissions
2	Average Conversion Rate ( $R_{\text{chem}}$ )
2A	Average $R_{\text{chem}}$ : Initial conditions only
3	Average Vertical Diffusivity ( $K_z$ )
3A	Average $K_z$ : Initial conditions only
4	Average Deposition Velocity ( $V_d$ )
4A	Average $V_d$ : Initial conditions only
5	Average $R_{\text{chem}}$ , $K_z$ , and $V_d$
5A	Average $R_{\text{chem}}$ , $K_z$ , and $V_d$ : Initial conditions only
5B	Average $R_{\text{chem}}$ , $K_z$ , and $V_d$ : Reduced emissions
6	Average Emission Rates
7	High $\text{SO}_4$ Deposition Velocity
8	FCT8 Advection Algorithm



The Model 1 runs are the "complex" model simulations that use SURADS in its standard form. Models 2 through 6 are "simple" models: Model 2 uses temporally averaged conversion rate; Model 3 uses temporally and horizontally averaged vertical diffusivities; Model 4 uses temporally and horizontally averaged deposition velocity; Model 5 combines average conversion rates, vertical diffusivity, and deposition velocity; and Model 6 uses temporally averaged emission rates. Model 7 is the same as Model 1, except it uses higher  $\text{SO}_4$  deposition velocities (equal to  $\text{SO}_2$  deposition velocities). Model 8 is identical to Model 1 except that an eighth order flux corrected transport algorithm (FCT8) is used in place of the SHASTA as an advection algorithm.

The "A" simulations made with Models 1 through 5 refer to runs that were made with initial conditions only, i.e., without any source emissions. These simulations were made so that the effect of initial conditions could be subtracted out. The "B" simulations made with Models 1 and 5 refer to runs in which emissions reductions were made. The emissions in levels 2 through 5 were reduced by 45% in Indiana, Ohio, and parts of neighboring states. Figure 10-2 shows the area in which the upper level emissions were reduced.

The  $\text{SO}_2$  conversion rates used in all Models except 2 and 5 vary from 0.2%/hr at night to 4.4%/hr at midday. The average value used in Models 2 and 5 is 1.6%/hr.

The  $\text{SO}_2$  deposition velocities used in all Models except 4 and 5 varied from about 0.4 cm/sec to 1.4 cm/sec depending on the time of day and location in the grid. The constant value used in Models 4 and 5 is 0.87 cm/sec, the average over x, y, and t of the variable deposition velocities.

The variation in vertical diffusivities used in all models except 3 and 5 is much greater than the variation seen in either the conversion rate or deposition velocity. The approximate range of  $K_z$  values seen at each of the four interfaces between vertical layers is shown in Table 10-2. For the upper levels,  $K_z$  can vary by almost 4 orders of magnitude, depending on time of day and grid location. Also shown in Table 10-2 are the constant values of  $K_z$  used in Models 3 and

# THE SURE GRID: JULY 21, 1978

AVERAGE SO<sub>x</sub> EMISSION RATE (METRIC TONS/HOUR/CELL)

6-01

	1	2	3	4	5	6	7	8	9	10	11	12	13	14	15	16	17	18	19	20	21	22	23	24	25	26	27	28	29	30
23 I	0	0	0	1	1	0	0	0	0	0	0	0	0	0	0	0	0	0	0	0	0	0	0	0	1	0	0	0	0	0
22 I	0	0	0	0	1	2	0	8	5	0	0	0	0	0	0	0	0	0	0	0	0	0	0	1	1	0	0	0	0	0
21 I	0	1	10	0	0	0	0	0	1	1	0	0	0	0	114	46	0	0	0	0	0	0	8	0	0	0	2	1	0	0
20 I	0	0	5	15	1	1	10	1	1	0	1	2	3	0	0	0	0	0	0	0	1	0	6	0	1	1	2	6	0	0
19 I	0	1	0	2	3	4	10	4	11	1	1	1	1	0	0	0	0	0	2	0	0	0	0	0	3	3	7	0	0	0
18 I	1	2	3	0	2	7	0	2	7	0	1	7	18	1	0	0	7	0	0	0	0	0	0	0	5	8	0	0	0	0
17 I	0	1	0	1	1	11	10	36	0	24	1	2	3	34	0	16	3	13	18	7	0	0	4	1	10	10	0	0	0	0
16 I	0	10	2	5	2	5	6	9	1	1	5	10	60	8	0	0	0	3	2	5	1	3	7	6	7	19	9	0	0	0
15 I	0	0	2	0	6	5	6	21	64	4	1	1	115	1	47	15	10	1	0	0	0	1	13	15	5	14	0	0	0	0
14 I	0	0	0	1	4	71	2	2	0	2	1	3	3	23	28	23	30	15	3	25	3	23	35	1	0	0	0	0	0	0
13 I	2	1	0	3	1	8	4	7	4	3	3	4	4	1	37	162	72	2	1	27	14	30	2	0	0	0	0	0	0	0
12 I	19	2	1	0	1	18	26	2	32	21	3	12	11	9	76	84	13	3	3	9	8	15	0	0	0	0	0	0	0	0
11 I	0	20	1	38	52	18	1	19	39	1	72	83	3	85	3	1	15	1	6	19	2	5	0	0	0	0	0	0	0	0
10 I	0	1	0	1	10	36	1	26	47	67	12	2	2	16	32	0	0	3	3	9	0	0	0	0	0	0	0	0	0	0
9 I	0	0	0	0	0	0	71	5	73	0	0	0	1	1	0	5	3	1	11	10	6	0	0	0	0	0	0	0	0	0
8 I	0	0	0	0	0	0	1	40	24	0	0	4	10	9	0	16	5	0	4	1	21	0	0	0	0	0	0	0	0	0
7 I	0	0	1	1	0	0	0	43	3	0	1	40	1	2	1	2	8	11	2	2	0	0	0	0	0	0	0	0	0	0
6 I	0	0	1	1	16	1	2	0	0	0	5	1	2	10	9	6	0	2	6	4	0	0	0	0	0	0	0	0	0	0
5 I	0	2	0	8	0	0	0	34	7	31	33	0	1	36	4	2	4	2	14	0	0	0	0	0	0	0	0	0	0	0
4 I	1	1	0	0	0	0	0	36	7	4	24	2	0	1	10	11	1	23	1	0	0	0	0	0	0	0	0	0	0	0
3 I	0	1	2	1	0	0	16	1	23	3	36	5	15	5	0	16	23	0	0	0	0	0	0	0	0	0	0	0	0	0
2 I	0	0	0	3	2	1	2	1	0	1	0	0	0	1	4	0	0	0	0	0	0	0	0	0	0	0	0	0	0	0
1 I	0	8	2	0	4	5	4	1	1	1	1	3	0	0	39	0	0	0	0	0	0	0	0	0	0	0	0	0	0	0

Figure 10-2. Average SO<sub>x</sub> emission rate on the SURE grid for July 21, 1978. The group of cells in which emissions reductions were made is outlined.

TABLE 10-2

RANGES OF  $K_z$ 's USED IN VARIABLE  $K_z$  MODELS  
 AND AVERAGE  $K_z$ 's USED IN CONSTANT  $K_z$  MODELS (2 AND 5)  
 ( $\text{cm}^2/\text{sec}$ )

<u>Vertical Interface*</u>	<u>Range of <math>K_z</math>'s</u>	<u>Average <math>K_z</math></u>
1	0.1 to 50	5.2
2	0.1 to 275	21.6
3	0.1 to 700	35.9
4	0.1 to 375	16.1

\*e.g., 1 is the interface between layers 1 and 2.

5. The constant values are averages over x, y, and t of the variable  $K_z$ 's.

The time-averaged emission rates are shown for each grid square in Figure 10-2. The values given are the sum of the five model layers of each grid column for July 21, 1978. The high emission areas include the Ohio Valley, the U.S. urban areas of St. Louis, Detroit, and New York City, and Sudbury, Ontario.

In the next subsection, the results of the Model 1 simulation for a day from the SURE is presented and compared to observations. Following that, the results of simulations for the same day using the simple models (2 through 6) are given and compared to the complex model results. Then the emissions reduction simulation (1B and 5B) results are presented and compared. Finally, the results from the higher sulfate deposition (run 7) and the FCT8 advection algorithm (run 8) simulations are presented and discussed.

#### 10.1.3 Complex LRT Model Results

A day was selected for use as a baseline for the LRT model sensitivity analysis from those modeled in the development and evaluation phase of the SURE modeling effort. As mentioned earlier, the day selected is July 21, 1978. There were two primary reasons for choosing this day over the other days modeled for SURE. First, the model performed reasonably well on this day. This, of course, lends credibility to any conclusions that are drawn from the sensitivity studies. Second, the meteorological conditions on this day were conducive to long range transport.

In this section, the meteorology and air quality of July 21, 1978 are briefly discussed. Then the modeling results are presented and comparisons are made between the calculated and measured concentrations.

July 21, 1978 was part of a widespread regional sulfate event that occurred during the period July 18, 1978 to July 23, 1978. The event began with stagnation conditions in the Ohio Valley area and evolved into channeling, or ducting, conditions which transported pollutants well beyond the Ohio Valley. The channeling conditions are

initiated by intrusion of maritime tropical air on the back side of the Bermuda high and are intensified by the physical presence of the Appalachian Mountains in the southeast and an east-west oriented cold front advancing from the northwest. July 21 was in the middle of a five-day channeling period which exposed rural areas of New England to elevated sulfate concentrations. Wind speeds and mixing heights were moderate, skies were partly cloudy, and the ambient conditions were generally warm and moist.

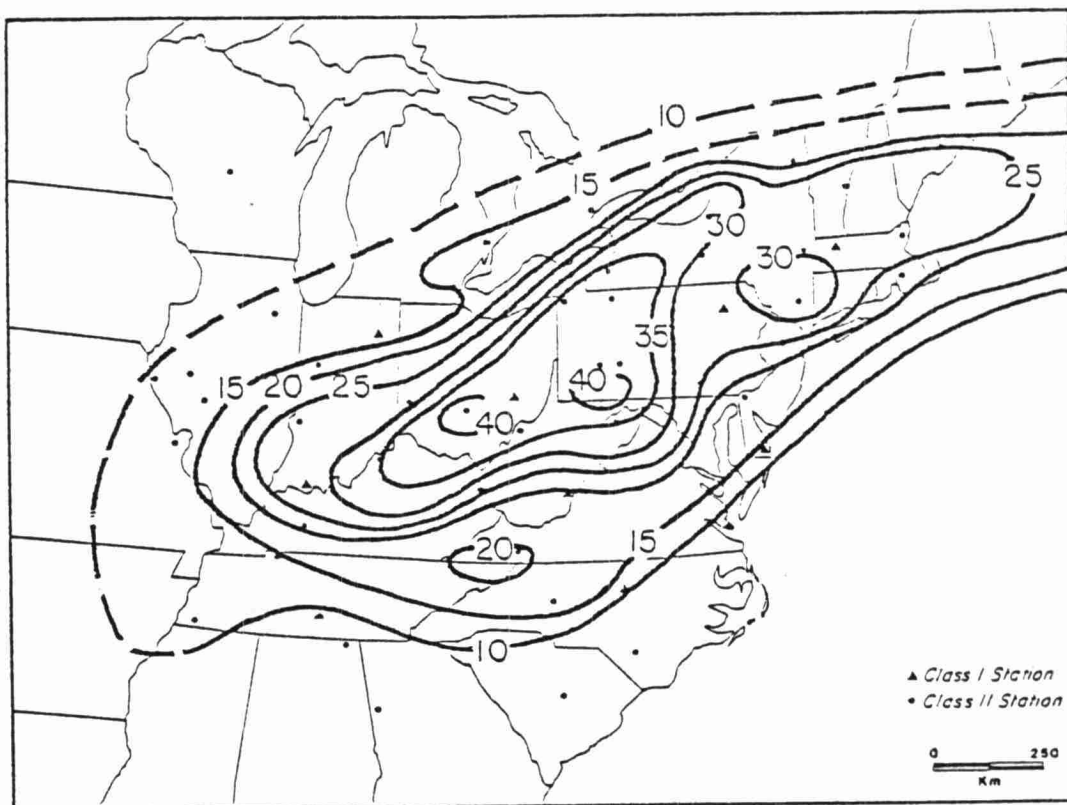
The distribution of 24-hour averaged sulfate on July 21 is shown in Figure 10-3a. The highest concentrations were measured in southwestern Pennsylvania ( $44.4 \mu\text{g}/\text{m}^3$ ) and southcentral Ohio ( $40.4 \mu\text{g}/\text{m}^3$ ). The  $35 \mu\text{g}/\text{m}^3$  isopleth encompasses all of western Pennsylvania, southern and eastern Ohio, and northern tip of Kentucky. The  $25 \mu\text{g}/\text{m}^3$  isopleth extends all the way to the New England coast.

The distribution of 24-hour average  $\text{SO}_2$  is shown in Figure 10-3b. The highest concentration (45 ppb) was measured in northeast Pennsylvania. Concentrations in excess of 10 ppb were observed as far west as Illinois and as far east as Massachusetts.

The 24-hour baseline SURADS simulation was made beginning at 0000 EST. The initial concentrations of  $\text{SO}_4$  and  $\text{SO}_2$  are shown in Figures 10-4a and 10-4b. These concentration fields were derived from hourly average  $\text{SO}_2$  and 3-hour averaged sulfate for the respective periods ending at 0000 EST. The concentrations were assumed to represent all five vertical layers of the modeling domain.

The calculated 24-hour average  $\text{SO}_4$  surface concentration distribution is shown in Figure 10-5b. For ease of comparison, the measured concentration isopleth map is provided in Figure 10-5a. Also given in Figure 10-5c is the gridded concentration field from which Figure 10-5b was derived. The agreement between the calculated and measured values is very reasonable. The major deficiency of the calculated sulfate distribution is that it is spread out more in the crosswind direction. Although the maximum calculated  $\text{SO}_4$  is almost 20% lower than the observed maximum, it is encouraging to see that the two maxima are colocated.

a.



b.

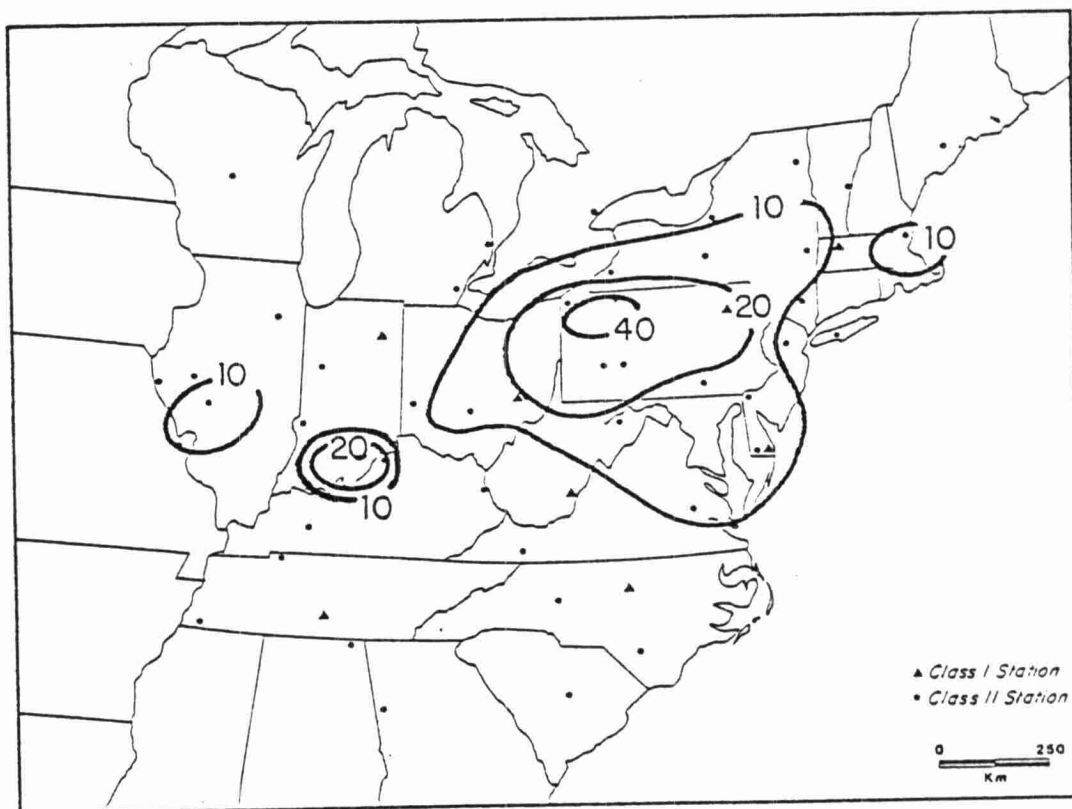


Figure 10-3. Isopleth maps of observed a. sulfate and b.  $\text{SO}_2$  for July 21, 1978.

# THE SURE GRID: JULY 21, 1978

## INITIAL SO4 CONCENTRATIONS (MICGR/M\*\*3), LEVEL 1

		1	2	3	4	5	6	7	8	9	10	11	12	13	14	15	16	17	18	19	20	21	22	23	24	25	26	27	28	29	30
	I	-----+-----																													

Figure 10-4. Initial concentrations of a. SO<sub>4</sub> and b. SO<sub>2</sub> used in July 21, 1978 SURADS simulations.

THE BURE GRID: JULY 21, 1978

INITIAL SO2 CONCENTRATIONS (PPB), LEVEL 1

		1	2	3	4	5	6	7	8	9	10	11	12	13	14	15	16	17	18	19	20	21	22	23	24	25	26	27	28	29	30
	I																														
23	I	0	0	0	0	1	1	1	1	1	1	1	1	1	1	0	0	1	1	1	1	1	1	1	1	1	1	1	1	1	1
22	I	0	0	0	0	1	1	1	1	1	1	1	1	1	1	0	0	1	1	1	1	1	1	1	1	1	1	1	1	1	1
21	I	0	0	0	1	1	1	1	1	1	1	1	1	1	0	0	0	1	1	1	2	2	2	2	1	1	1	1	1	1	1
20	I	0	0	1	1	1	1	1	2	2	2	2	2	2	1	0	0	0	1	1	2	2	3	3	2	2	2	2	3	2	2
19	I	1	1	1	1	2	2	2	2	3	3	3	3	2	2	1	0	0	2	3	2	4	5	5	3	3	5	8	5	3	3
18	I	1	1	1	1	2	3	3	4	4	4	4	4	3	2	1	1	1	8	8	3	5	9	11	8	3	5	6	5	3	3
17	I	1	1	1	2	2	3	4	5	5	5	5	6	6	4	3	5	16	26	21	10	8	12	18	12	7	5	5	4	3	3
16	I	1	1	1	2	2	4	5	7	6	5	5	7	9	6	4	7	33	57	41	16	6	8	11	9	7	5	4	3	2	2
15	I	1	1	1	1	2	4	6	8	7	5	4	6	9	7	7	17	44	98	58	23	2	3	5	6	5	4	3	3	2	2
14	I	0	0	1	1	1	2	5	7	7	5	3	5	7	5	2	5	8	46	39	20	5	4	1	3	3	3	3	2	2	2
13	I	0	0	0	0	0	1	3	6	7	8	6	5	8	7	0	1	7	18	19	11	2	1	1	2	2	2	2	1	1	1
12	I	0	0	0	0	0	1	3	6	9	12	13	9	12	17	8	5	8	4	8	6	3	2	1	1	1	1	1	1	1	1
11	I	0	0	0	1	1	1	3	5	9	15	20	14	11	9	5	3	3	3	5	5	3	1	0	1	1	1	1	1	1	1
10	I	0	0	0	1	1	1	2	3	6	11	15	12	7	1	1	0	0	2	5	6	2	0	0	0	0	0	1	1	0	0
9	I	0	0	0	0	1	1	1	1	2	7	9	9	7	4	4	1	0	2	6	8	1	0	0	0	0	0	0	0	0	0
8	I	0	0	0	0	0	0	1	1	1	4	6	7	7	7	8	2	0	2	4	5	2	1	0	0	0	0	0	0	0	0
7	I	0	0	0	0	0	0	0	0	0	2	4	5	6	6	4	0	0	1	2	3	2	1	0	0	0	0	0	0	0	0
6	I	0	0	0	1	1	0	1	1	1	2	3	4	4	4	2	0	0	0	1	1	1	1	1	1	0	0	0	0	0	0
5	I	0	0	0	1	1	1	1	1	2	2	3	4	4	3	2	0	0	1	1	1	1	1	1	1	0	0	0	0	0	0
4	I	0	0	0	1	1	1	1	1	2	3	4	4	3	2	1	1	1	1	1	1	1	1	1	0	0	0	0	0	0	0
3	I	0	0	0	0	0	1	1	1	2	3	5	4	3	2	1	1	1	1	1	0	0	0	0	0	0	0	0	0	0	0
2	I	0	0	0	0	0	0	1	1	2	3	4	3	2	2	1	1	1	1	0	0	0	0	0	0	0	0	0	0	0	0
1	I	0	0	0	0	0	0	1	1	2	3	4	3	2	2	1	1	1	1	0	0	0	0	0	0	0	0	0	0	0	0

b.

Figure 10-4. (Continued).



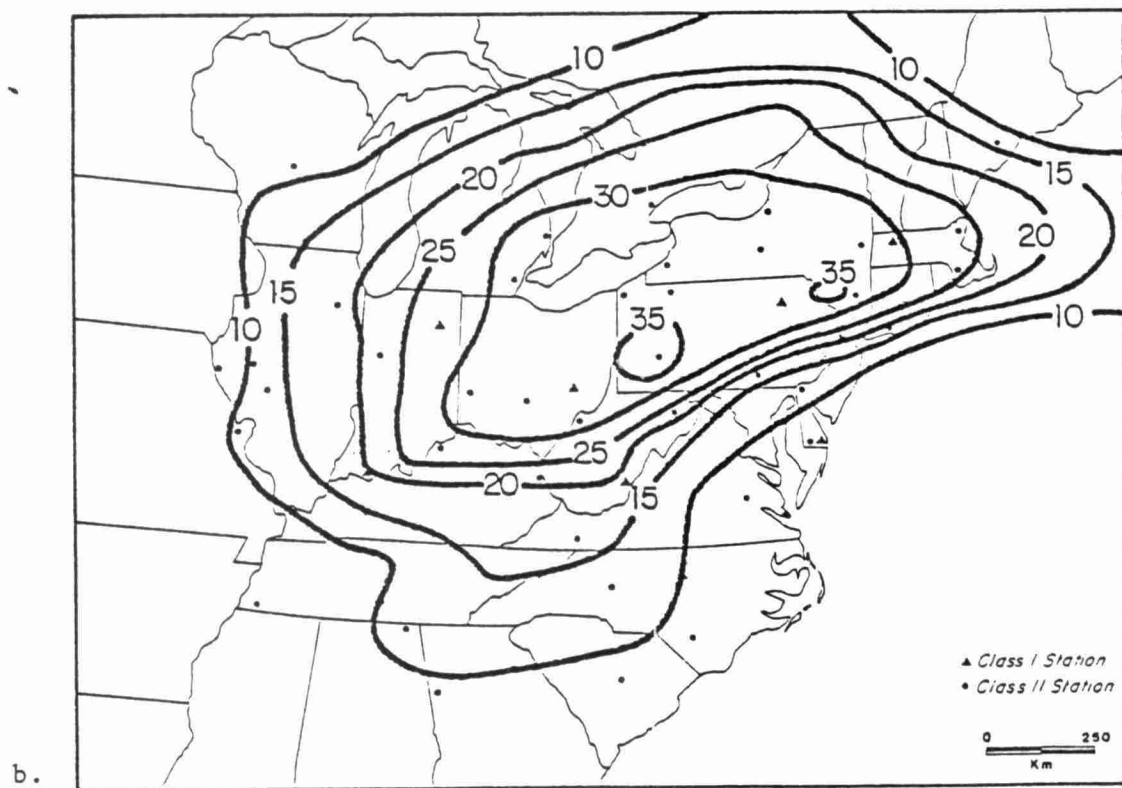
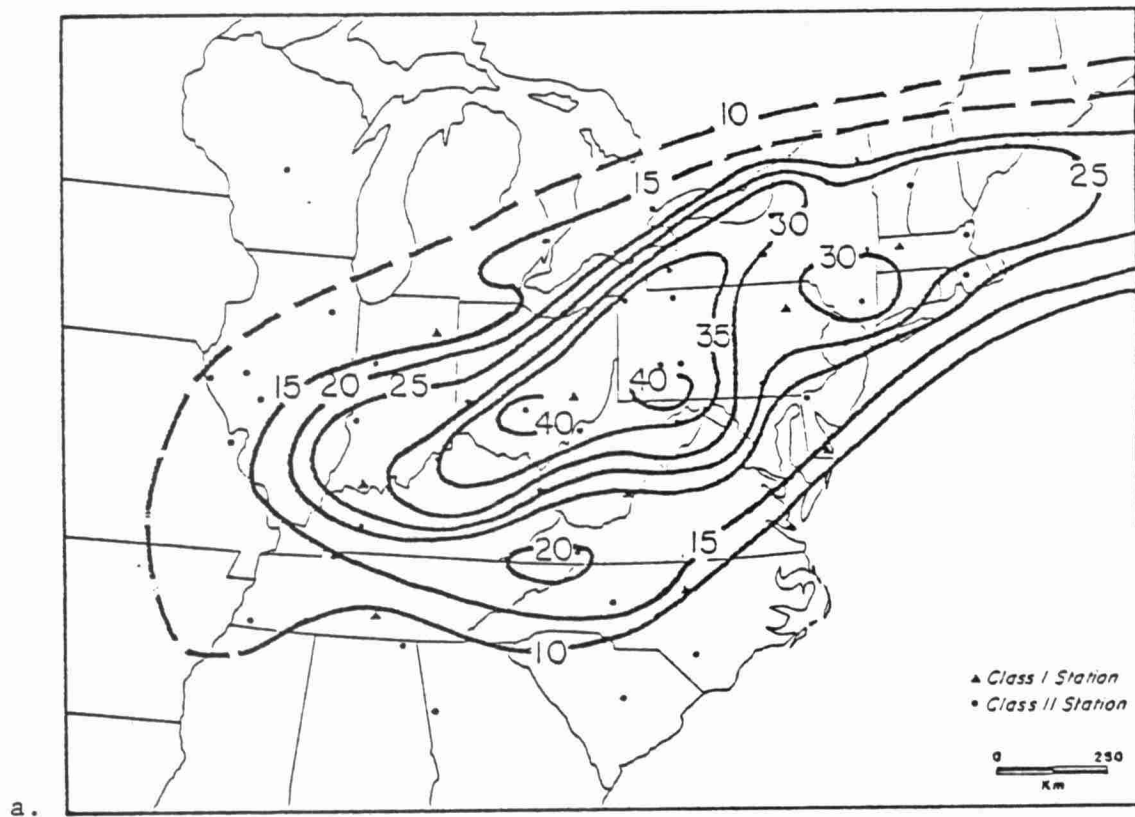


Figure 10-5. Isopleth maps of a. observed and b. calculated 24-hour average sulfate for July 21, 1978; and c. gridded values of calculated 24-hour average sulfate concentration.

# SURADS RESULTS FOR JULY 21, 1978

RUN 1: COMPLEX MODEL (BASELINE)

SURFACE CONCENTRATION OF 24-HOUR AVERAGED SO<sub>4</sub> (MICR/M\*\*3)

10-17

	1	2	3	4	5	6	7	8	9	10	11	12	13	14	15	16	17	18	19	20	21	22	23	24	25	26	27	28	29	30
23 I	1	1	1	2	2	2	2	2	2	2	3	5	5	5	6	6	8	9	10	11	11	10	9	7	6	4	3	2	2	2
22 I	1	1	1	2	2	3	3	4	4	4	4	6	6	7	7	10	12	13	14	14	14	13	11	9	7	5	4	3	2	2
21 I	1	1	2	3	3	4	5	5	5	5	6	8	8	11	16	18	19	19	20	20	21	19	18	14	11	7	6	4	3	3
20 I	2	2	3	5	6	6	6	6	6	7	9	14	15	16	18	20	22	23	24	26	26	24	21	17	14	10	8	7	5	5
19 I	3	3	4	6	8	8	8	8	8	11	16	19	20	21	23	24	26	27	29	29	28	26	24	19	17	16	15	11	9	10
18 I	4	4	4	6	8	11	13	14	15	17	19	22	25	27	28	29	30	31	31	32	30	30	29	26	23	22	20	19	16	14
17 I	3	4	4	5	8	13	15	16	18	21	23	27	30	33	33	32	32	32	32	33	32	32	31	29	28	26	22	21	17	15
16 I	3	4	4	5	7	12	16	18	21	23	26	29	33	33	33	32	31	31	32	33	34	34	34	30	28	27	22	21	17	15
15 I	3	4	4	5	7	12	16	17	22	24	27	30	33	33	33	33	33	33	32	32	34	35	34	30	26	23	20	19	15	14
14 I	3	4	4	5	7	12	16	17	21	24	27	31	33	33	33	34	35	34	32	31	31	32	30	24	16	11	10	11	11	10
13 I	4	4	4	5	7	12	16	17	21	25	28	32	34	32	33	35	36	34	29	26	21	19	16	11	8	7	7	6	6	5
12 I	4	4	5	5	10	14	16	19	22	26	30	32	33	32	32	33	33	30	19	14	11	11	9	7	5	5	5	4	4	4
11 I	3	4	5	6	11	14	15	19	23	26	28	30	31	31	30	28	20	15	11	10	9	8	6	5	4	4	4	3	3	3
10 I	3	4	5	6	9	11	14	19	22	25	24	24	24	23	23	21	16	13	10	9	8	7	6	5	4	3	3	2	2	2
9 I	3	4	5	6	7	8	13	15	16	16	17	17	18	18	18	17	13	10	9	9	8	7	5	4	3	3	2	2	2	2
8 I	3	4	5	6	7	7	9	10	11	12	14	15	17	17	17	15	13	9	8	8	8	6	5	4	3	3	2	2	2	1
7 I	3	5	6	6	7	7	8	9	9	11	13	15	15	14	14	12	10	9	8	8	7	5	4	4	3	3	2	2	1	1
6 I	3	4	5	6	7	7	8	9	10	11	13	13	14	13	13	10	10	9	8	7	5	4	3	3	2	2	2	1	1	1
5 I	3	4	4	5	5	6	7	8	10	11	12	11	10	11	10	9	9	7	6	5	3	2	2	2	2	2	1	1	1	1
4 I	3	3	3	3	4	4	5	6	8	9	10	10	9	8	8	9	7	4	3	2	2	2	2	1	1	1	1	1	1	1
3 I	3	3	3	3	3	3	3	4	5	6	7	7	7	7	7	13	5	2	2	2	2	1	1	1	1	1	1	1	1	1
2 I	2	3	2	3	2	2	2	3	4	4	5	5	4	4	3	1	1	1	1	1	1	1	1	1	1	1	1	1	1	1
1 I	2	3	2	2	2	2	2	2	2	3	4	4	3	4	4	3	2	1	1	1	1	1	1	1	1	1	1	1	1	1

c.

Figure 10-5. (Continued)

The reader should keep in mind when comparing the observed and calculated concentration fields that there is much less information available for constructing the isopleths of measurements (35-45 points) than there are for the isopleths of calculated values (690 points). Since the details of the observation maps must be filled in subjectively, there is probably more uncertainty in the measurement isopleths.

The isopleth map of calculated 24-hour average surface  $\text{SO}_2$  concentrations from SURADS are given in Figure 10-6b. The field of gridded values is also given in Figure 10-6c. Comparing this map to the map of measured  $\text{SO}_2$  concentrations (Figure 10-6a), it is apparent that the results, though reasonable, are not as good as the  $\text{SO}_4$  results. The maximum calculated concentration (26 ppb) is much less than the observed maximum (45 ppb), but the patterns are similar in many respects. The observations show an area of concentrations greater than or equal to 20 ppb of  $\text{SO}_2$  that encompasses most of Pennsylvania; the area of calculated concentration greater than 20 ppb is also in Pennsylvania though it encompasses a smaller area. The observations have relative maxima in southwestern Illinois, southern Indiana, and eastern Massachusetts; the calculated fields exhibit similar relative maxima. However, the calculated field also has relative maxima in Chicago and Detroit areas that do not appear in the observations.

Scatter plots of observed versus calculated  $\text{SO}_4$  and  $\text{SO}_2$  are given in Figure 10-7 and 10-8, respectively. The calculated values are for the grid square that contains the monitor.

As a means of quantifying the model performance, various statistical parameters have been calculated for  $\text{SO}_4$  and  $\text{SO}_2$ . These statistics are presented in Table 10-3. For sulfate, the difference between the average observed and calculated concentrations at 45 stations is  $1.2 \mu\text{g}/\text{m}^3$ ; the average absolute error is about  $5.35 \mu\text{g}/\text{m}^3$ , or 25% of the average observed value. For  $\text{SO}_2$ , the difference between the average observed and calculated values for 35 stations is less than 0.3 ppb, but the average absolute error is 5.34 ppb, or 53% of the average observed value. In addition, the standard deviation of the calculated  $\text{SO}_4$  values is comparable to that of the observations,

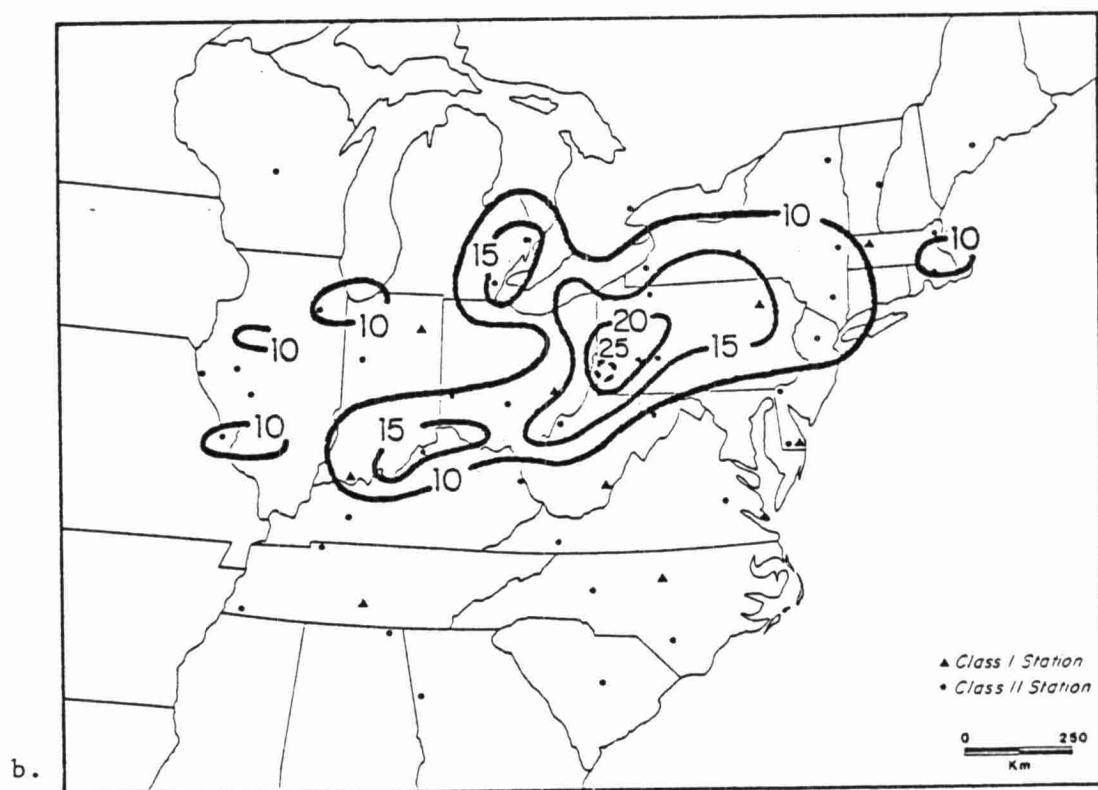
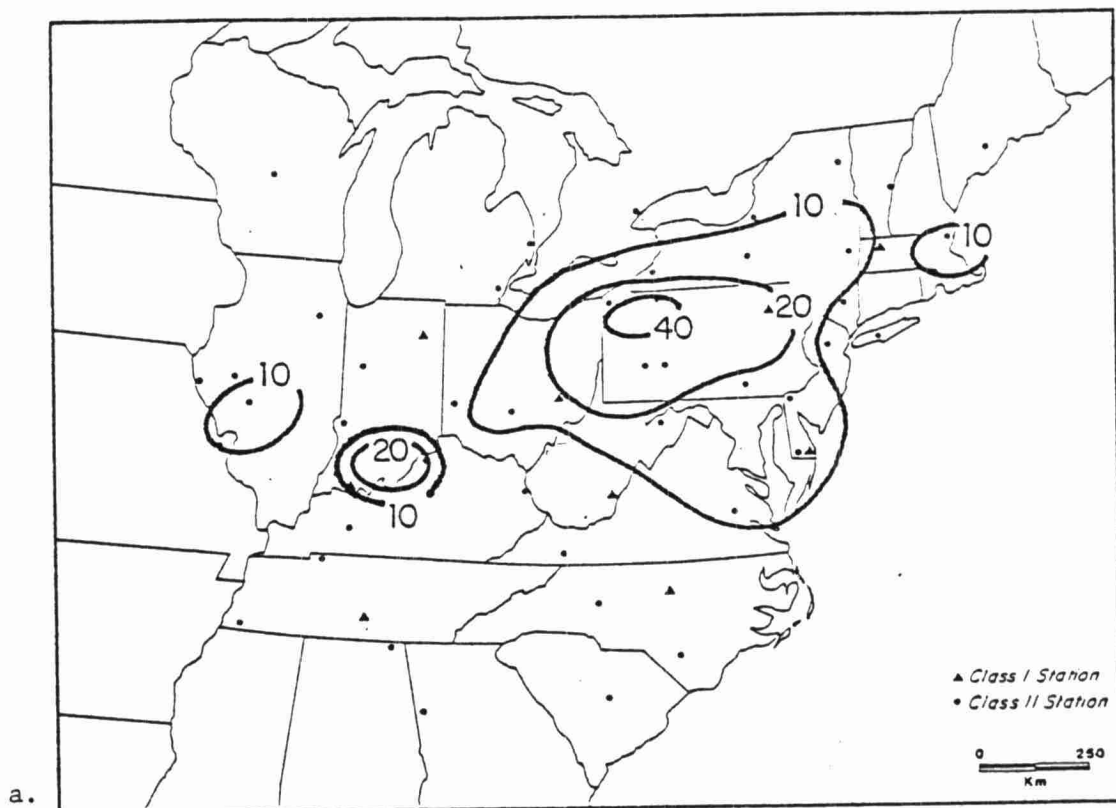


Figure 10-6. Isopleth maps for a. observed and b. calculated 24-hour average  $\text{SO}_2$  for July 21, 1978; and c. gridded values of calculated 24-hour average  $\text{SO}_2$  concentrations.

# SURADS RESULTS FOR JULY 21, 1978

RUN 1: COMPLEX MODEL (BASELINE)

SURFACE CONCENTRATION OF 24-HOUR AVERAGED SO2 (PPB)

		1	2	3	4	5	6	7	8	9	10	11	12	13	14	15	16	17	18	19	20	21	22	23	24	25	26	27	28	29	30	
	I	+	+	+	+	+	+	+	+	+	+	+	+	+	+	+	+	+	+	+	+	+	+	+	+	+	+	+	+	+	+	
10-20	23	I	0	0	0	1	1	1	1	1	1	1	0	0	0	0	0	0	0	0	0	0	0	1	1	1	1	1	1	0	0	
	22	I	0	0	0	0	1	1	2	3	3	1	1	0	0	0	1	1	1	1	1	0	1	1	1	1	1	1	1	1	0	0
	21	I	0	0	1	1	1	1	2	2	2	1	1	1	1	2	6	7	3	1	1	1	1	1	3	2	1	1	1	1	1	1
	20	I	0	1	2	3	2	2	4	2	2	2	2	2	3	3	4	4	3	2	2	2	2	3	3	2	2	2	3	3	1	1
	19	I	1	1	2	2	3	4	5	4	4	3	3	4	4	3	3	3	3	4	4	4	4	4	4	3	4	4	5	3	2	2
	18	I	1	2	2	2	3	5	5	6	6	6	6	7	8	8	5	5	5	7	8	8	7	7	6	6	6	7	5	3	3	2
	17	I	1	2	2	2	2	6	7	9	7	8	6	7	11	14	10	9	9	13	14	14	11	10	8	8	9	9	5	4	3	2
	16	I	1	3	2	3	3	5	7	8	8	7	7	8	17	12	11	10	11	15	17	16	13	11	11	9	9	10	6	4	3	2
	15	I	1	1	2	2	5	6	8	10	13	8	6	7	16	12	17	15	16	19	19	17	14	13	12	9	7	7	5	4	2	2
	14	I	1	1	1	2	5	11	7	7	7	6	6	6	9	10	16	21	21	20	18	18	15	14	14	7	4	2	1	1	1	1
	13	I	3	2	2	3	4	6	6	7	7	7	7	8	9	9	15	26	24	16	12	13	12	13	9	4	2	1	1	1	1	1
	12	I	4	2	2	3	5	7	7	8	10	11	12	14	12	12	16	20	18	10	7	8	7	7	4	2	1	1	1	0	0	0
	11	I	1	3	2	5	10	10	7	10	13	13	16	15	12	15	13	8	5	5	6	7	5	3	2	1	0	0	0	0	0	0
	10	I	0	1	1	1	5	8	7	10	14	15	13	10	9	9	10	6	4	4	6	6	4	2	1	1	0	0	0	0	0	0
	9	I	0	0	0	1	2	3	8	8	13	9	6	6	6	5	5	4	4	4	7	8	5	3	1	1	0	0	0	0	0	0
	8	I	0	0	0	1	1	2	5	7	7	5	5	5	6	6	4	4	4	3	4	4	6	3	1	1	0	0	0	0	0	0
	7	I	0	1	1	2	2	2	4	8	5	4	5	7	5	5	4	3	4	3	3	3	3	3	2	1	0	0	0	0	0	0
	6	I	0	1	1	2	3	2	4	5	5	5	6	5	5	6	5	4	3	3	3	3	3	1	1	0	0	0	0	0	0	0
	5	I	0	1	1	2	1	2	4	7	6	6	6	4	4	6	5	3	3	3	4	2	1	0	0	0	0	0	0	0	0	0
	4	I	1	1	1	1	1	1	3	6	6	5	5	4	3	4	4	3	3	3	2	1	0	0	0	0	0	0	0	0	0	0
3	I	1	1	1	1	1	1	2	1	2	2	4	3	3	3	3	3	3	1	1	0	0	0	0	0	0	0	0	0	0	0	
2	I	1	1	1	1	1	1	1	1	1	1	1	1	1	2	3	2	0	0	0	0	0	0	0	0	0	0	0	0	0	0	
c. 1	I	1	3	1	1	2	2	2	1	1	1	2	2	2	3	6	3	1	1	1	1	1	1	1	1	0	0	0	0	0	0	

Figure 10-6. (Continued).

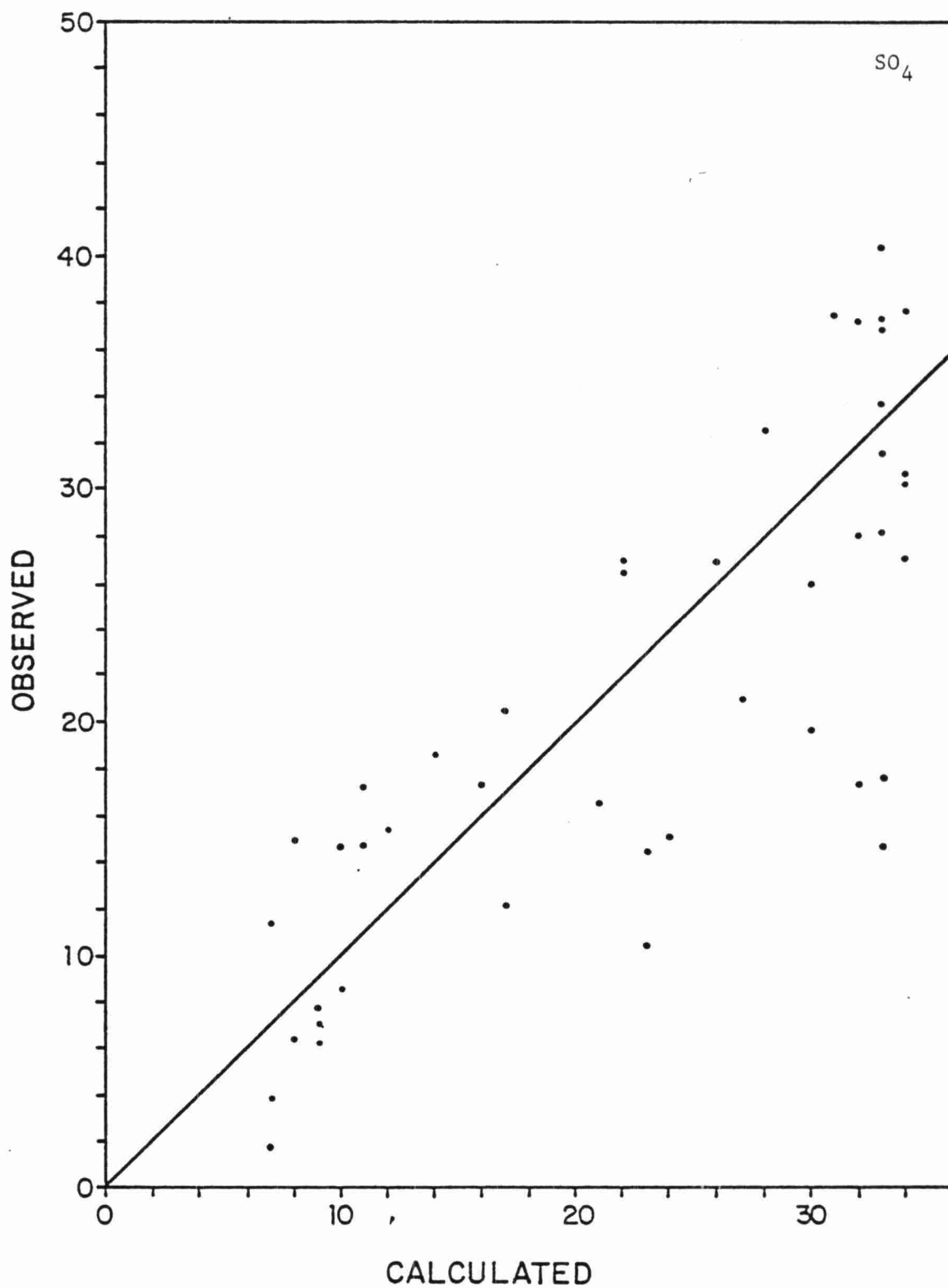


Figure 10-7. Observed versus calculated 24-hour average sulfate concentration for LRT Model baseline simulation, July 21, 1978.

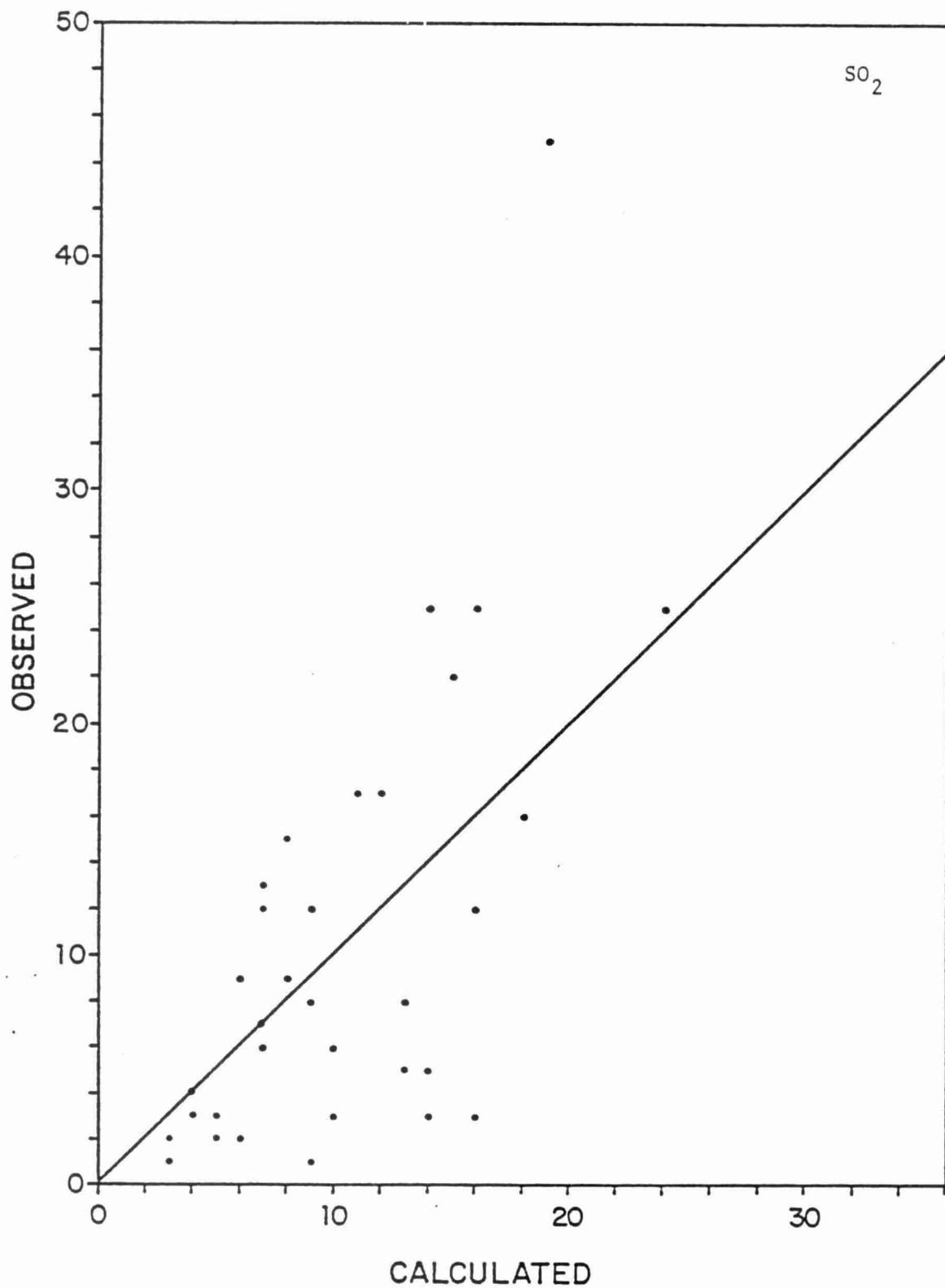


Figure 10-8. Observed versus calculated 24-hour average  $\text{SO}_2$  concentration for LRT Model baseline simulation, July 21, 1978.

TABLE 10-3

STATISTICAL EVALUATION OF THE FCT8 BASELINE  
SIMULATION RESULTS VERSUS OBSERVATIONS

Species	n	$\bar{\chi}_c$	$\sigma_c$	$\bar{\chi}_o$	$\sigma_o$	$ \bar{E} $	$E_{RMS}$	$\bar{R}_{c/o}$	$\sigma_{c/o}$	r
SO <sub>4</sub> (μg/m <sup>3</sup> )	45	22.7	10.33	21.5	11.01	5.35	6.62	1.099	0.577	0.809
SO <sub>2</sub> (ppb)	35	10.29	5.11	10.03	9.51	5.34	7.43	1.378	1.788	0.631

$\bar{n}$  = number of observations compared.

$\bar{\chi}_{c,o}$  = average of calculated (c) or observed (o) concentrations.

$\sigma_{c,o}$  = standard deviation of calculated (c) or observed (o) concentrations.

$|\bar{E}|$  = average absolute error,  $|\bar{\chi}_c - \bar{\chi}_o|$ .

$E_{RMS}$  = root mean square error,  $\sqrt{\sum(\chi_c - \chi_o)^2 / (n-1)}$ .

$\bar{R}_{c/o}$  = geometric mean ratio of calculated to observed concentrations,  $\left(\frac{\bar{\chi}_c}{\bar{\chi}_o}\right)_{geom}$

$\sigma_{c/o}$  = standard deviation of  $R_{c/o}$ ,  $\sqrt{\sum(R_{c/o} - \bar{R}_{c/o})^2 / (n-1)}$ .

r = correlation coefficient.



but for  $\text{SO}_2$ , it is much less. In short, the numbers indicate that the model performance is better for  $\text{SO}_4$  than for  $\text{SO}_2$ .

A map of sulfur deposition for the baseline simulation is given in Figure 10-9. The high deposition areas correspond to the high  $\text{SO}_2$  concentration areas.

The sulfur mass balance values for the baseline run are given in Table 10-4. Given are the initial and final mass of sulfur as  $\text{SO}_2$  and  $\text{SO}_4$  in the entire modeling domain and the emission, chemical conversion, and ground deposition contributions to changes in mass. Also given is a residual term that includes the net gain of mass through horizontal boundaries, but also contains a component of mass change due to accumulated numerical errors. The initial mass of sulfur as both  $\text{SO}_2$  and  $\text{SO}_4$  is greater than half the final mass. Emissions are the largest component of the  $\text{SO}_2$  balance, but conversion and deposition are major sinks of  $\text{SO}_2$ . Conversion of  $\text{SO}_2$  is the major source of new  $\text{SO}_4$ .

#### 10.1.4 LRT Model Sensitivity to Model Formulation

The preceding subsection presented the results of the complex model baseline simulation (run 1). In this subsection, the results of simulations 2, 3, 4, 5, and 6 -- the simple model runs -- are presented and compared to the complex model run.

##### 10.1.4.1 Comparison of Model 2 to Model 1

The 24-hour average  $\text{SO}_4$  and  $\text{SO}_2$  concentrations calculated by Model 2 (constant  $R_{\text{chem}}$ ) are shown in Figures 10-10 and 10-11, respectively. These results are very similar to the results for Model 1 (shown previously in Figures 10-5c and 10-6c). The maximum difference in  $\text{SO}_2$  concentration is 1 ppb (higher for Model 2), and the maximum difference in  $\text{SO}_4$  is  $-2 \mu\text{g}/\text{m}^3$ , or -13%.

The cumulative sulfur deposition map for run 2 is shown in Figure 10-12. It, too, is very similar to the run 1 map. The maximum differences in any grid square is 4 metric tons in southwest Pennsylvania. This represents a change of about 5%.

## SURADS RESULTS FOR JULY 21, 1978

RUN 1: COMPLEX MODEL (BASELINE)

SURFACE SULFUR DEPOSITION (METRIC TONS/DAY)

	1	2	3	4	5	6	7	8	9	10	11	12	13	14	15	16	17	18	19	20	21	22	23	24	25	26	27	28	29	30
23 I	2	2	2	5	6	4	3	4	4	3	3	4	4	4	3	4	6	5	5	5	5	6	7	6	7	6	6	6	4	4
22 I	2	1	1	4	6	13	13	20	22	11	5	4	4	4	6	11	11	10	7	7	7	8	9	9	7	6	5	6	4	3
21 I	2	3	10	10	8	10	14	14	15	12	6	5	6	16	45	58	29	15	11	10	11	16	27	17	10	8	13	11	5	5
20 I	2	5	18	24	17	16	32	18	16	10	11	19	19	20	30	33	28	19	17	18	21	24	31	21	19	17	24	30	10	9
19 I	6	9	12	18	19	33	39	30	26	19	23	31	29	22	29	30	30	30	37	36	37	37	32	26	32	38	44	21	12	12
18 I	7	14	15	12	20	34	34	43	40	40	40	51	52	52	42	40	49	56	67	65	63	61	54	46	42	48	28	22	16	14
17 I	6	14	11	14	17	43	48	71	40	54	43	45	62	95	76	75	76	117	116	124	94	82	71	66	78	75	33	25	17	15
16 I	6	22	15	20	21	38	54	68	56	49	50	57	135	92	83	75	87	123	130	128	110	101	106	84	85	88	37	27	17	14
15 I	7	9	12	13	32	41	51	85	104	56	45	50	105	81	146	116	132	152	151	140	126	121	118	80	63	48	31	25	16	13
14 I	10	8	9	13	30	70	48	48	48	47	44	53	69	81	145	175	176	152	148	148	129	140	149	69	32	13	10	10	9	9
13 I	21	14	12	16	25	39	41	45	54	57	57	65	79	78	125	217	203	128	100	111	108	128	85	33	14	8	6	5	5	4
12 I	33	17	14	16	29	41	43	49	76	94	100	124	110	101	132	161	139	73	56	68	57	62	31	12	6	4	4	4	3	3
11 I	8	20	15	32	67	60	37	62	98	94	119	131	98	108	105	62	40	28	24	51	34	23	12	6	4	3	3	3	2	1
10 I	3	7	6	10	32	42	40	62	100	121	102	77	69	71	75	45	26	20	22	26	20	12	8	5	3	2	1	1	1	1
9 I	3	4	4	6	11	18	54	57	93	67	44	44	46	42	35	34	27	21	30	34	19	10	7	5	3	1	1	1	1	1
8 I	3	3	4	6	10	14	38	52	51	36	37	43	44	41	30	30	31	19	25	21	35	13	6	4	3	1	1	1	1	1
7 I	3	5	8	12	14	15	30	61	40	32	36	49	36	34	27	23	22	22	20	20	14	9	5	3	2	1	1	1	1	1
6 I	2	7	8	14	25	18	31	38	37	38	42	35	34	43	36	26	16	18	22	24	10	3	2	2	1	1	1	1	0	0
5 I	3	8	7	11	12	15	31	53	50	48	44	30	29	42	34	21	22	21	29	16	3	2	2	1	1	1	1	1	0	0
4 I	6	9	7	7	8	12	28	47	49	39	38	27	17	24	26	24	21	24	16	3	2	1	1	1	1	1	1	0	0	0
3 I	6	9	10	8	8	10	21	13	18	19	26	17	17	25	18	22	24	8	3	2	1	1	1	1	1	1	1	0	0	0
2 I	8	11	9	11	12	9	12	9	7	7	7	7	9	17	24	11	2	1	2	2	2	2	1	1	1	1	1	1	1	1
1 I	9	22	13	8	15	17	16	10	10	10	11	17	12	23	42	14	4	3	3	3	3	3	3	3	3	2	2	2	2	2

Figure 10-9. Calculated cumulative sulfur deposition (metric tons) for run 1, the LRT Model baseline simulation.

TABLE 10-4

SULFUR MASS BALANCE FOR THE BASELINE SIMULATION  
OF JULY 21, 1978(10<sup>9</sup> grams S)

<u>Component</u>	<u>SO<sub>2</sub>-</u>	<u>SO<sub>4</sub>-</u>
Initial concentrations	26.7	20.1
Emissions	47.1	0.94
Chemical conversion	-13.4	13.4
Deposition to ground	19.9	1.4
Residual*	<u>2.4</u>	<u>-2.3</u>
Final concentrations	42.9	30.7

\*This component includes all the cumulative errors of the simulation, as well as the gains and losses of mass through the side boundaries. That is,

$$\text{Residual} = \text{Final} - \text{Initial} - \text{Emissions} - \text{Conversion} + \text{Deposition}$$

# SURADS RESULTS FOR JULY 21, 1978

## RUN 2: AVERAGE CONVERSION RATE

### SURFACE CONCENTRATION OF 24-HOUR AVERAGED SO4 (MICGR/M\*\*3)

	1	2	3	4	5	6	7	8	9	10	11	12	13	14	15	16	17	18	19	20	21	22	23	24	25	26	27	28	29	30
23 I	1	1	1	2	2	2	2	2	2	2	3	5	5	5	6	6	8	9	10	11	10	10	9	7	6	4	3	2	2	2
22 I	1	1	1	2	2	3	3	3	4	4	5	6	6	6	7	9	11	13	13	14	13	12	11	9	7	5	4	3	2	2
21 I	1	1	2	3	3	4	4	5	5	5	6	8	8	10	15	17	18	19	19	20	20	19	18	14	11	7	6	4	3	3
20 I	2	2	3	5	6	6	6	6	6	7	9	14	15	16	18	19	21	23	24	26	26	24	21	17	14	10	8	7	5	5
19 I	3	3	4	6	7	8	8	7	8	11	16	19	20	21	22	23	25	27	29	30	28	27	24	19	17	16	15	11	9	10
18 I	4	4	4	6	8	11	13	14	15	17	19	22	24	26	27	28	29	31	31	32	30	30	29	26	23	22	20	19	16	14
17 I	3	4	4	5	8	12	15	16	17	20	22	26	30	32	32	31	31	32	33	34	32	32	30	28	27	26	22	20	16	15
16 I	3	4	4	5	7	12	16	18	20	23	25	29	32	33	32	31	30	32	33	34	33	33	33	29	28	26	22	20	16	15
15 I	3	4	4	5	7	11	15	17	22	24	26	30	33	32	32	32	32	32	32	33	34	34	33	29	26	22	19	18	15	14
14 I	3	4	4	5	7	12	15	16	20	24	27	31	33	32	32	33	33	33	31	31	31	32	28	22	15	10	10	11	10	10
13 I	3	4	4	5	7	12	15	17	21	24	28	31	33	31	32	34	34	32	27	24	20	18	14	10	7	7	7	6	6	5
12 I	4	4	4	5	9	13	15	18	22	25	29	31	32	31	31	32	31	28	18	13	11	10	9	7	5	5	5	4	4	4
11 I	3	4	5	6	11	14	14	18	22	25	28	29	30	30	29	27	19	14	11	9	8	7	6	5	4	4	4	3	3	3
10 I	3	4	5	6	9	11	13	18	22	24	23	23	22	22	22	19	15	12	10	9	8	7	5	4	4	3	3	2	2	2
9 I	3	4	5	6	7	8	12	14	15	15	16	17	18	18	18	16	13	10	9	9	8	6	5	4	3	3	2	2	2	2
8 I	3	4	5	6	6	7	8	10	10	11	14	15	17	17	16	15	12	9	8	8	8	6	5	4	3	3	2	2	2	1
7 I	3	5	6	6	6	7	7	9	9	10	13	14	14	14	14	12	10	9	8	8	7	5	4	4	3	3	2	2	1	1
6 I	3	4	5	6	7	6	7	8	9	11	13	13	13	13	12	10	9	8	7	7	5	4	3	3	2	2	2	1	1	1
5 I	3	4	4	5	5	6	7	8	10	11	12	11	10	10	10	9	8	7	6	5	3	2	2	2	2	2	1	1	1	1
4 I	2	3	3	3	3	4	5	6	8	9	10	10	9	8	8	9	7	4	3	2	2	2	2	1	1	1	1	1	1	1
3 I	2	3	3	3	3	3	3	4	6	7	7	7	6	6	7	13	5	2	2	2	2	1	1	1	1	1	1	1	1	1
2 I	2	2	2	2	2	2	2	3	4	4	5	5	4	4	3	1	1	1	1	1	1	1	1	1	1	1	1	1	1	1
1 I	2	3	2	2	2	2	2	2	3	3	4	4	3	3	4	3	2	1	1	1	1	1	1	1	1	1	1	1	1	1

10-27

Figure 10-10. Calculated 24-hour average sulfate concentration ( $\mu\text{g}/\text{m}^3$ ) for wind.

SURADS RESULTS FOR JULY 21, 1978

RUN 2: AVERAGE CONVERSION RATE

SURFACE CONCENTRATION OF 24-HOUR AVERAGED SO<sub>2</sub> (PPB)

		1	2	3	4	5	6	7	8	9	10	11	12	13	14	15	16	17	18	19	20	21	22	23	24	25	26	27	28	29	30
10-28	23 I	0	0	0	1	1	1	1	1	1	1	1	0	0	0	0	0	0	0	0	0	0	0	1	1	1	1	1	1	0	0
	22 I	0	0	0	0	1	1	2	3	3	1	1	0	0	0	1	1	1	1	1	0	1	1	1	1	1	1	1	1	0	0
	21 I	0	0	1	1	1	1	2	2	2	2	1	1	1	2	6	7	3	1	1	1	1	1	3	2	1	1	1	1	1	1
	20 I	0	1	2	3	2	2	4	2	2	2	2	2	3	3	4	4	3	2	2	2	2	3	3	2	2	2	3	3	1	1
	19 I	1	1	2	2	3	4	5	4	4	3	3	4	4	3	4	4	3	3	4	4	4	4	4	3	4	4	5	3	2	2
	18 I	1	2	2	2	3	5	5	6	6	6	6	8	9	8	5	5	5	7	8	8	7	7	6	6	6	7	5	3	3	2
	17 I	1	2	2	2	3	6	7	9	7	8	6	7	11	15	10	9	9	13	14	14	11	10	8	8	9	9	6	4	3	2
	16 I	1	3	2	3	3	5	7	8	8	7	7	8	17	13	11	10	11	15	17	16	13	11	11	9	9	10	6	4	3	2
	15 I	1	1	2	2	5	6	8	10	13	8	6	7	16	12	17	16	16	20	19	17	14	13	12	9	7	7	5	4	2	2
	14 I	2	1	1	2	5	11	8	7	7	6	6	7	9	11	16	22	22	20	18	18	15	14	14	8	4	2	2	1	1	1
	13 I	3	2	2	3	4	6	7	7	7	7	7	8	9	9	16	26	24	16	12	14	12	13	9	5	2	1	1	1	1	1
	12 I	4	2	2	3	5	7	8	8	10	11	12	14	13	13	17	21	18	11	8	8	7	7	4	2	1	1	1	0	0	0
	11 I	1	3	2	5	10	11	7	10	14	13	16	15	12	15	13	8	6	5	6	7	5	3	2	1	0	0	0	0	0	0
	10 I	0	1	1	1	5	8	7	10	14	15	13	10	9	10	10	6	4	4	6	6	4	3	1	1	0	0	0	0	0	0
	9 I	0	0	0	1	2	3	8	8	13	9	6	6	6	6	5	5	4	4	7	8	5	3	1	1	0	0	0	0	0	0
	8 I	0	0	0	1	1	2	5	7	7	5	5	6	6	6	4	5	4	3	5	4	6	3	1	1	0	0	0	0	0	0
	7 I	0	1	1	2	2	2	4	8	5	4	5	7	5	5	4	4	4	4	3	3	3	2	1	0	0	0	0	0	0	0
	6 I	0	1	1	2	3	2	4	5	5	5	6	5	5	6	6	4	3	3	3	3	3	2	1	0	0	0	0	0	0	0
	5 I	0	1	1	2	2	2	4	7	6	7	6	4	4	6	5	3	3	3	4	2	1	0	0	0	0	0	0	0	0	0
	4 I	1	1	1	1	1	1	3	6	6	5	5	4	3	4	4	3	3	4	2	1	0	0	0	0	0	0	0	0	0	0
	3 I	1	1	1	1	1	1	2	1	2	2	4	3	3	3	3	3	3	1	1	0	0	0	0	0	0	0	0	0	0	0
	2 I	1	1	1	1	1	1	1	1	1	1	1	1	1	2	3	2	0	0	0	0	0	0	0	0	0	0	0	0	0	0
	1 I	1	3	1	1	2	2	2	1	1	1	2	2	2	3	6	3	1	1	1	1	1	1	1	1	1	0	0	0	0	0

Figure 10-11. Calculated 24-hour average SO<sub>2</sub> concentration (ppb) for run 2.

# SURADS RESULTS FOR JULY 21, 1978

RUN 2: AVERAGE CONVERSION RATE

SURFACE SULFUR DEPOSITION (METRIC TONS/DAY)

10-29

	1	2	3	4	5	6	7	8	9	10	11	12	13	14	15	16	17	18	19	20	21	22	23	24	25	26	27	28	29	30
23 I	2	2	2	5	6	4	3	4	4	3	3	4	4	4	4	4	6	6	5	5	5	6	6	6	7	6	6	5	4	4
22 I	2	1	1	4	6	13	13	20	23	11	5	4	4	4	6	12	12	10	8	7	7	8	9	9	7	6	5	6	4	3
21 I	2	3	10	11	8	10	14	15	15	12	6	5	6	17	45	58	30	15	11	10	11	15	27	17	10	8	13	11	5	5
20 I	2	5	18	24	18	17	32	18	17	10	12	19	19	20	31	34	29	19	18	18	21	24	31	21	19	16	24	30	10	9
19 I	6	9	12	18	19	34	39	30	27	20	23	31	29	23	30	31	30	30	38	36	38	37	34	26	32	39	44	20	12	12
18 I	7	14	15	13	20	35	35	44	41	41	41	51	52	54	43	42	50	56	67	65	63	62	54	47	42	47	28	22	16	14
17 I	6	14	12	14	17	43	49	72	41	55	43	46	64	96	78	77	77	116	116	124	94	82	72	66	79	75	34	25	17	15
16 I	6	22	15	20	21	39	54	68	57	50	51	57	136	93	85	77	88	124	131	128	110	102	107	85	85	89	37	27	17	14
15 I	6	10	12	13	33	42	51	86	105	57	46	51	106	83	146	118	133	154	151	141	127	123	119	82	64	48	32	25	16	13
14 I	10	9	9	13	31	71	49	48	48	48	44	53	70	83	146	177	178	153	148	148	130	142	152	72	33	13	9	10	10	8
13 I	21	15	12	16	26	40	42	46	54	57	58	66	81	80	128	221	207	130	102	114	110	131	87	35	14	8	6	5	5	4
12 I	33	18	14	17	30	42	45	50	77	95	101	125	113	103	134	164	142	77	58	69	57	63	32	13	6	4	4	4	3	3
11 I	9	20	15	32	68	61	38	62	100	94	121	133	100	109	106	64	41	29	25	52	35	23	12	7	4	3	3	3	2	1
10 I	3	7	6	10	32	43	41	63	101	122	104	79	71	72	76	46	25	21	23	27	21	13	9	5	3	2	1	1	1	1
9 I	3	4	4	6	12	18	55	59	95	69	45	45	46	43	35	35	27	21	31	35	19	11	7	5	3	1	1	1	1	1
8 I	3	3	4	6	10	14	38	53	52	37	37	43	45	42	31	31	32	19	25	21	35	13	7	4	3	1	1	1	1	1
7 I	3	5	8	13	15	16	31	62	41	33	37	50	37	35	27	23	22	23	20	20	15	9	5	3	2	1	1	1	1	1
6 I	2	7	8	14	25	19	31	39	38	39	43	36	35	44	36	26	16	19	22	25	10	4	2	2	1	1	1	1	0	0
5 I	3	9	7	11	12	16	32	53	51	49	45	30	29	42	34	22	23	21	29	16	3	2	2	1	1	1	1	1	0	0
4 I	5	9	7	8	8	13	28	47	49	40	38	28	18	25	26	24	22	24	15	3	2	1	1	1	1	1	1	0	0	0
3 I	5	9	10	9	8	10	21	14	18	19	26	17	17	26	18	23	24	8	3	2	2	1	1	1	1	1	1	0	0	0
2 I	7	11	8	11	11	9	11	9	7	7	7	7	9	17	25	11	2	1	2	2	2	2	1	1	1	1	1	1	1	1
1 I	9	22	13	9	15	17	16	10	10	10	11	17	12	24	42	14	4	3	3	3	3	3	3	3	2	2	2	2	2	2

Figure 10-12. Calculated cumulative sulfur deposition (metric tons) for run 2.

To get an idea of what the concentration differences are for hourly average  $\text{SO}_4$  and  $\text{SO}_2$ , Figures 10-13 and 10-14 were prepared. These bar graphs depict run 1 and run 2 concentrations plotted side-by-side each hour for grid square (16,13), which is centered on the western border of Pennsylvania. Each concentration bar is divided into emission and initial mass components. The graphs show that while the differences in hourly  $\text{SO}_2$  are generally relatively small, there are significant differences in the  $\text{SO}_4$  concentrations for the two runs.

The sulfur mass balance for run 2 is shown in Table 10-5. Slightly more  $\text{SO}_2$  is deposited ( $1\frac{1}{2}\%$ ) and converted (3%) to  $\text{SO}_4$  than in run 1.

#### 10.1.4.2 Comparison of Model 3 to Model 1

The 24-hour average concentrations of  $\text{SO}_4$  and  $\text{SO}_2$  calculated by Model 3 (average  $K_z$ ) are shown in Figures 10-15 and 10-16, respectively. The differences between these results and the Model 1 results are larger than the differences seen above for Model 2. The differences in  $\text{SO}_2$  range from +3 to -3 ppb (+15 to -38%) and the  $\text{SO}_4$  differences range from +3 to -3  $\mu\text{g}/\text{m}^3$  (+10 to -25%).

The map of sulfur deposition for run 3 are shown in Figure 10-17. The differences in individual cell values between these results and the baseline results range from +16 to -11 metric tons/day (+23 to -20%).

The hourly-averaged concentrations for grid square (16,13) are plotted for run 1 and run 3  $\text{SO}_4$  and  $\text{SO}_2$  concentrations in Figures 10-18a and 10-19a, respectively. Relatively larger differences are seen for  $\text{SO}_2$  than for  $\text{SO}_4$ , but the differences are small in both cases in this grid square. The same information for grid square (7,15) is plotted in Figure 10-18b and 10-19b and shows relatively larger differences between run 1 and run 3 results. Also, considering just the hour 24 concentrations (not shown), there are differences in the average  $\text{SO}_2$  of  $\pm 4$  ppb and differences in  $\text{SO}_4$  of +7 to -4  $\mu\text{g}/\text{m}^3$  in other parts of the grid.

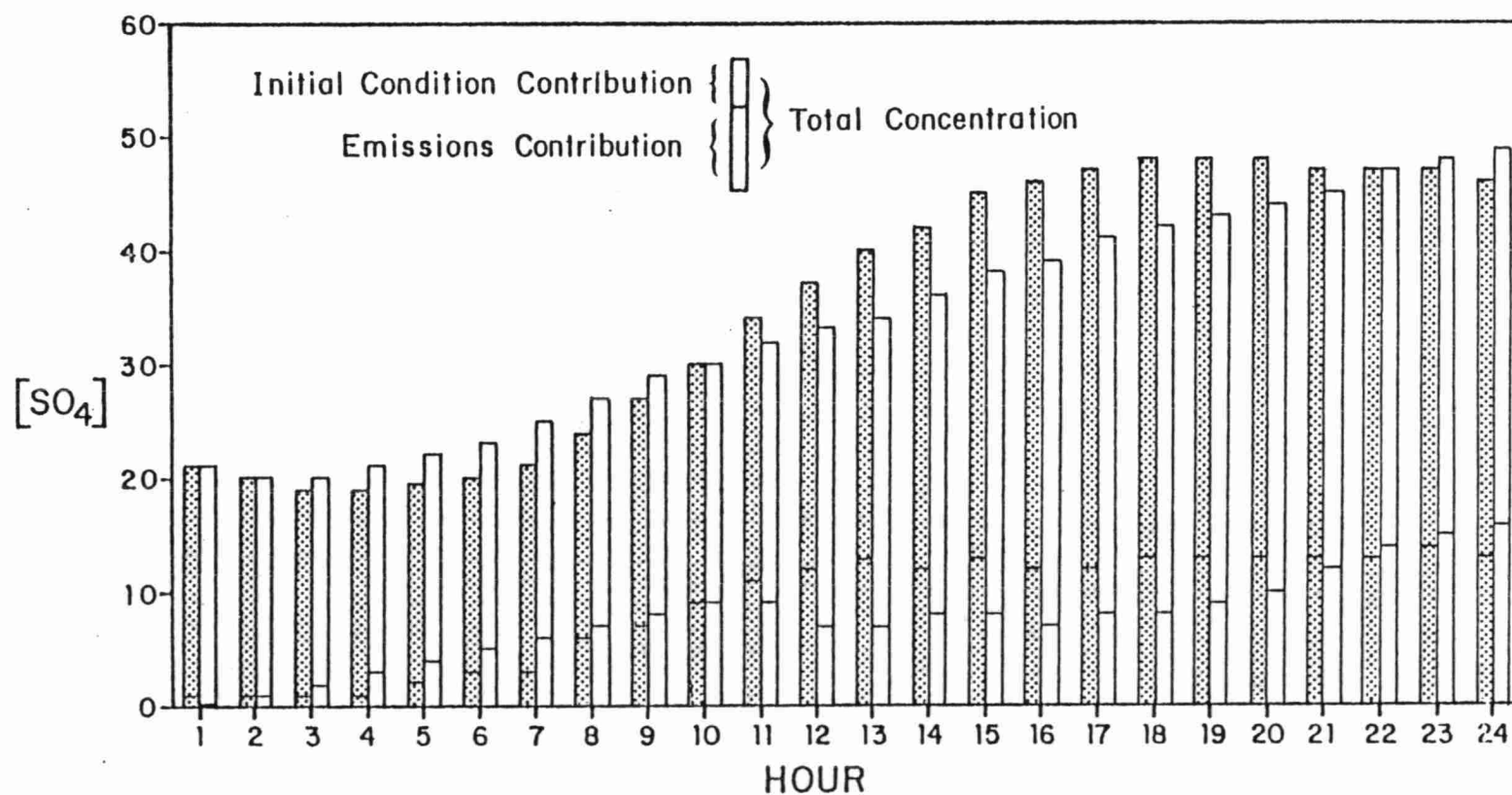


Figure 10-13. Comparison of hourly averaged  $SO_4$  from run 1 (shaded bar) and run 2 (unshaded bar) for grid square (16,13). The bars are divided, as shown, into emissions and initial condition components.



10-32

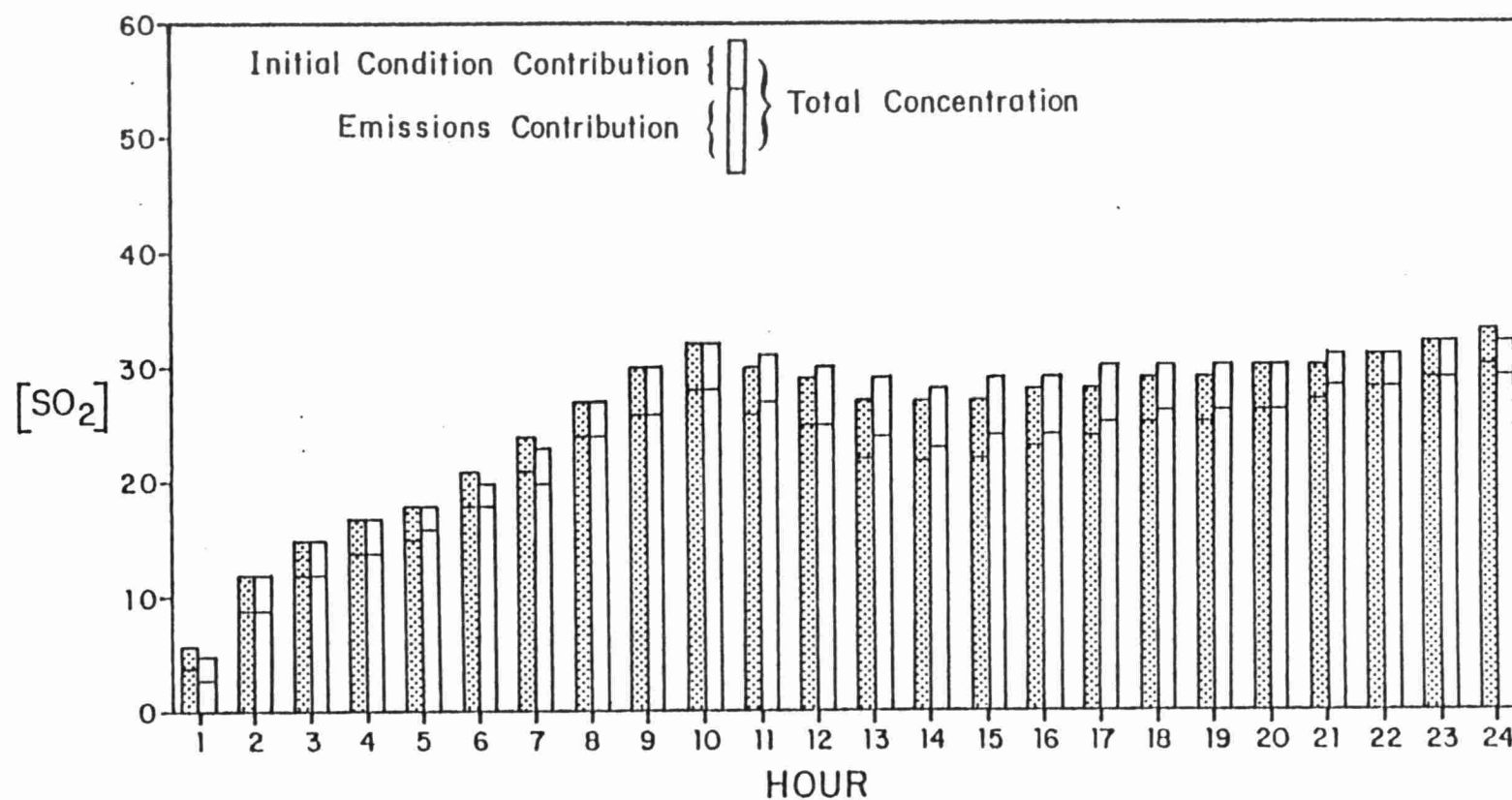


Figure 10-14. Comparison of hourly averaged SO<sub>2</sub> from run 1 (shaded bar) and run 2 (unshaded bar) for grid square (16,13). The bars are divided, as shown, into emissions and initial condition components.

TABLE 10-5  
 RUN 2 SULFUR MASS BALANCE  
 ( $10^9$  grams S)

<u>Component</u>	<u>SO<sub>2</sub>-</u>	<u>SO<sub>4</sub>-</u>
Initial concentrations	26.7	20.1
Emissions	47.1	0.94
Chemical conversion	-13.8	13.8
Deposition to ground	20.2	1.4
Residual	<u>2.5</u>	<u>-2.4</u>
Final concentrations	42.3	31.0

## SURADS RESULTS FOR JULY 21, 1978

## RUN 3: AVERAGE VERTICAL DIFFUSIVITY

SURFACE CONCENTRATION OF 24-HOUR AVERAGED SO<sub>4</sub> (MICROGRAMS/M<sup>3</sup>)

10-34

	1	2	3	4	5	6	7	8	9	10	11	12	13	14	15	16	17	18	19	20	21	22	23	24	25	26	27	28	29	30
23 I	1	1	1	2	2	2	2	2	2	2	4	5	5	5	5	6	7	9	10	11	11	10	10	8	6	5	3	3	2	2
22 I	1	1	1	2	2	3	3	3	3	4	5	6	7	7	8	10	12	13	14	14	14	13	12	10	8	6	4	4	3	2
21 I	1	1	1	3	3	4	4	5	5	5	6	7	9	11	17	18	19	19	20	21	21	20	19	16	13	9	6	5	4	4
20 I	2	2	3	5	6	6	6	6	6	6	8	13	15	16	18	19	21	23	25	26	27	25	23	19	16	11	9	7	5	6
19 I	3	3	3	5	7	8	8	7	8	11	15	17	20	21	22	24	26	27	29	30	30	28	26	21	19	17	15	12	10	10
18 I	3	4	4	5	7	10	12	13	15	17	19	22	23	26	27	29	30	30	31	33	32	32	32	28	25	23	21	20	17	15
17 I	3	4	4	5	7	11	14	15	18	21	24	28	30	33	32	32	32	31	33	34	33	33	33	31	29	27	24	22	18	16
16 I	3	4	4	5	6	10	14	17	20	24	27	30	33	34	33	32	31	31	32	34	34	35	34	32	30	28	24	22	18	16
15 I	3	4	4	5	6	9	14	17	21	25	28	31	34	33	33	33	33	33	32	33	34	34	34	31	28	25	22	21	17	16
14 I	3	4	4	5	6	9	14	16	21	25	28	32	34	33	33	34	35	34	32	31	31	31	29	24	17	13	13	13	13	12
13 I	3	4	4	5	6	10	15	17	22	26	29	33	34	32	33	35	36	34	29	26	20	18	15	10	8	7	7	7	7	6
12 I	3	4	5	5	9	12	15	18	23	27	30	32	33	32	32	33	33	29	19	13	11	10	9	7	6	5	5	5	5	4
11 I	3	4	5	6	11	13	14	18	24	27	29	30	31	31	30	28	21	14	11	9	8	7	6	5	4	4	4	4	3	3
10 I	3	4	5	6	9	10	13	18	23	25	25	25	24	24	23	21	16	12	9	8	8	7	6	5	4	3	3	3	2	2
9 I	3	4	5	6	7	8	13	15	16	15	16	17	18	19	18	17	13	9	9	8	8	7	5	4	4	3	3	2	2	2
8 I	3	5	6	6	7	7	9	10	11	11	14	15	17	17	17	16	13	9	8	8	8	6	5	4	3	3	2	2	2	1
7 I	3	5	6	6	7	7	8	9	9	11	13	15	15	14	14	12	11	9	8	8	7	5	5	4	3	3	2	2	1	1
6 I	3	4	5	6	7	7	8	9	10	11	13	13	13	13	13	11	10	9	8	7	5	4	3	3	3	2	2	2	1	1
5 I	3	4	4	5	5	6	7	9	10	12	12	12	11	11	10	9	9	8	6	5	3	3	2	2	2	2	1	1	1	1
4 I	2	3	3	3	4	4	5	7	8	10	10	10	8	7	7	7	6	4	3	2	2	2	2	1	1	1	1	1	1	1
3 I	3	3	3	3	3	3	4	4	5	7	7	7	6	6	6	10	4	2	2	2	2	2	1	1	1	1	1	1	1	1
2 I	2	3	3	3	2	2	2	3	4	4	5	5	4	4	3	1	1	1	1	1	1	1	1	1	1	1	1	1	1	1
1 I	2	3	2	2	2	2	2	2	2	3	3	3	3	3	3	2	2	1	1	1	1	1	1	1	1	1	1	1	1	1

Figure 10-15. Calculated 24-hour average sulfate concentration ( $\mu\text{g}/\text{m}^3$ ) for run 3.

# SURADS RESULTS FOR JULY 21, 1978

## RUN 3: AVERAGE VERTICAL DIFFUSIVITY

### SURFACE CONCENTRATION OF 24-HOUR AVERAGED SO<sub>2</sub> (PPB)

	1	2	3	4	5	6	7	8	9	10	11	12	13	14	15	16	17	18	19	20	21	22	23	24	25	26	27	28	29	30
23 I	0	0	0	1	1	1	1	1	1	1	1	1	1	0	0	0	0	0	0	0	0	1	1	1	1	1	1	1	1	1
22 I	0	0	0	0	1	1	1	2	2	1	1	1	1	0	1	1	1	1	1	1	1	1	1	1	1	1	1	1	0	0
21 I	0	0	1	1	1	1	1	2	2	1	1	1	1	3	8	8	3	1	1	1	1	1	2	2	1	1	1	1	1	1
20 I	0	1	2	3	2	2	3	2	2	1	2	2	3	3	4	4	3	2	2	2	2	3	3	3	2	2	2	3	2	1
19 I	1	1	1	2	2	3	4	3	3	3	3	3	3	3	3	3	3	4	4	4	4	5	5	4	4	4	5	4	3	2
18 I	1	1	2	1	2	4	4	5	5	5	5	7	7	6	5	4	5	6	8	8	8	8	8	7	7	7	5	4	3	3
17 I	1	2	1	2	2	5	6	8	7	8	6	7	9	13	9	9	9	13	16	15	13	11	10	9	9	9	7	5	4	3
16 I	1	2	2	2	2	4	6	7	8	7	7	8	16	12	10	9	11	16	18	17	14	12	12	10	9	10	7	5	3	3
15 I	1	1	1	1	3	5	6	9	13	8	6	7	17	11	16	14	16	21	20	18	14	12	12	10	8	8	6	5	3	3
14 I	1	1	1	1	3	11	6	6	6	6	6	6	8	11	15	21	21	21	19	19	14	13	13	8	4	2	2	2	2	2
13 I	3	2	1	2	3	6	6	6	7	7	7	7	8	9	16	27	25	16	12	13	11	12	9	4	2	1	1	1	1	1
12 I	4	2	2	3	4	8	8	7	10	11	13	14	12	13	18	23	20	9	7	7	6	6	3	2	1	1	1	1	1	1
11 I	1	3	2	6	9	9	7	9	14	13	17	16	12	16	14	8	6	4	5	6	4	3	2	1	0	0	0	0	0	0
10 I	0	1	1	1	5	8	7	10	16	16	14	11	9	10	10	6	3	3	5	5	4	2	1	1	0	0	0	0	0	0
9 I	0	0	0	1	1	3	10	9	14	9	6	6	6	6	5	4	3	3	5	5	5	3	1	1	0	0	0	0	0	0
8 I	0	0	0	1	1	2	5	8	7	5	5	6	6	6	4	5	4	3	4	4	5	3	1	1	0	0	0	0	0	0
7 I	0	1	1	2	2	2	4	8	5	4	5	7	6	5	4	3	3	3	3	3	3	2	2	1	1	0	0	0	0	0
6 I	0	1	1	2	3	2	4	5	5	5	6	5	5	6	5	3	2	2	3	3	1	1	1	0	0	0	0	0	0	0
5 I	0	1	1	2	1	2	4	7	6	7	7	4	4	7	4	3	3	3	3	2	1	0	0	0	0	0	0	0	0	0
4 I	1	1	1	1	1	1	4	6	5	5	6	4	3	3	4	3	3	4	2	1	0	0	0	0	0	0	0	0	0	0
3 I	1	1	1	1	1	1	3	2	3	3	5	3	3	3	2	3	3	1	1	0	0	0	0	0	0	0	0	0	0	0
2 I	1	1	1	1	1	1	1	1	1	1	1	1	1	2	3	1	0	0	0	0	0	0	0	0	0	0	0	0	0	0
1 I	1	3	1	1	1	2	1	1	1	1	1	2	2	3	6	2	1	1	1	1	1	1	1	1	0	0	0	0	0	0

Figure 10-16. Calculated 24-hour average SO<sub>2</sub> concentration (ppb) for run 3.

## SURADS RESULTS FOR JULY 21, 1978

## RUN 3: AVERAGE VERTICAL DIFFUSIVITY

## SURFACE SULFUR DEPOSITION (METRIC TONS/DAY)

10-36

		1	2	3	4	5	6	7	8	9	10	11	12	13	14	15	16	17	18	19	20	21	22	23	24	25	26	27	28	29	30
23	I	2	2	2	5	5	4	3	5	4	3	4	5	5	4	4	4	4	5	5	5	6	6	7	7	7	6	6	6	4	4
22	I	2	1	1	3	5	12	10	17	18	9	5	5	5	5	7	11	11	10	8	7	8	8	9	9	9	6	6	6	5	4
21	I	2	2	9	9	7	9	11	12	12	10	6	6	7	20	54	62	27	15	11	11	12	16	25	18	12	10	11	10	6	5
20	I	2	4	16	22	15	14	27	15	14	9	10	17	18	20	31	33	26	18	18	19	22	26	33	25	21	18	21	26	12	11
19	I	5	8	10	15	16	29	32	23	23	18	20	26	27	21	29	29	28	28	36	38	41	44	39	32	34	36	40	24	16	16
18	I	7	12	13	10	17	29	29	36	34	37	36	46	45	42	37	40	49	53	66	68	72	75	68	58	51	49	32	27	22	18
17	I	6	12	10	12	14	35	40	65	37	53	42	43	51	88	71	74	75	121	126	132	106	94	87	77	79	72	39	32	23	18
16	I	6	20	13	16	16	30	43	61	53	48	49	55	131	86	78	73	86	130	141	137	117	107	109	92	85	84	43	33	23	18
15	I	5	8	10	10	22	32	41	77	103	56	45	49	107	77	139	108	127	158	159	146	126	115	113	89	70	55	36	30	22	17
14	I	7	8	8	10	22	66	41	44	46	48	44	53	67	83	139	174	176	157	154	152	128	132	145	72	35	16	13	13	13	11
13	I	18	13	10	13	18	35	39	43	52	57	57	64	77	77	130	224	211	126	98	109	104	126	81	30	15	10	7	6	6	5
12	I	31	18	14	16	23	41	45	48	75	99	103	126	111	103	138	171	148	65	52	62	54	60	29	11	6	5	4	4	4	4
11	I	8	23	15	37	62	55	35	62	102	95	125	135	100	114	107	60	41	25	21	46	32	21	11	6	4	3	3	3	3	2
10	I	3	7	7	10	30	46	41	63	106	128	105	78	71	73	76	45	25	18	18	22	19	12	8	5	3	3	1	1	1	1
9	I	3	4	4	5	11	19	60	61	101	69	44	46	48	44	36	34	25	18	25	27	17	10	7	5	3	1	1	1	1	1
8	I	3	4	4	6	9	14	40	53	53	35	37	45	46	42	31	31	28	17	21	18	30	12	7	5	3	1	1	1	1	1
7	I	3	5	7	12	13	15	29	60	38	31	36	49	37	34	27	22	21	21	18	18	13	9	5	4	2	1	1	1	1	1
6	I	2	7	7	14	25	17	29	37	35	38	43	35	33	41	34	23	14	17	20	22	9	4	3	2	2	1	1	1	0	0
5	I	3	8	7	12	11	13	31	55	50	52	49	30	29	43	32	19	20	19	27	14	3	2	2	1	1	1	1	1	0	0
4	I	5	9	7	7	8	12	30	50	49	41	41	29	17	23	23	22	20	24	14	3	2	1	1	1	1	1	1	1	0	0
3	I	6	8	10	8	8	11	35	14	20	20	31	19	18	22	16	20	22	7	3	2	2	1	1	1	1	1	1	0	0	0
2	I	7	10	8	11	12	9	11	9	7	8	7	7	9	16	22	10	2	1	2	2	2	2	2	1	1	1	1	1	1	1
1	I	8	22	12	8	16	18	16	10	9	10	10	15	10	21	42	13	4	3	3	3	3	3	3	3	2	2	2	2	2	2

Figure 10-17. Calculated cumulative sulfur deposition (metric tons) for run 3.

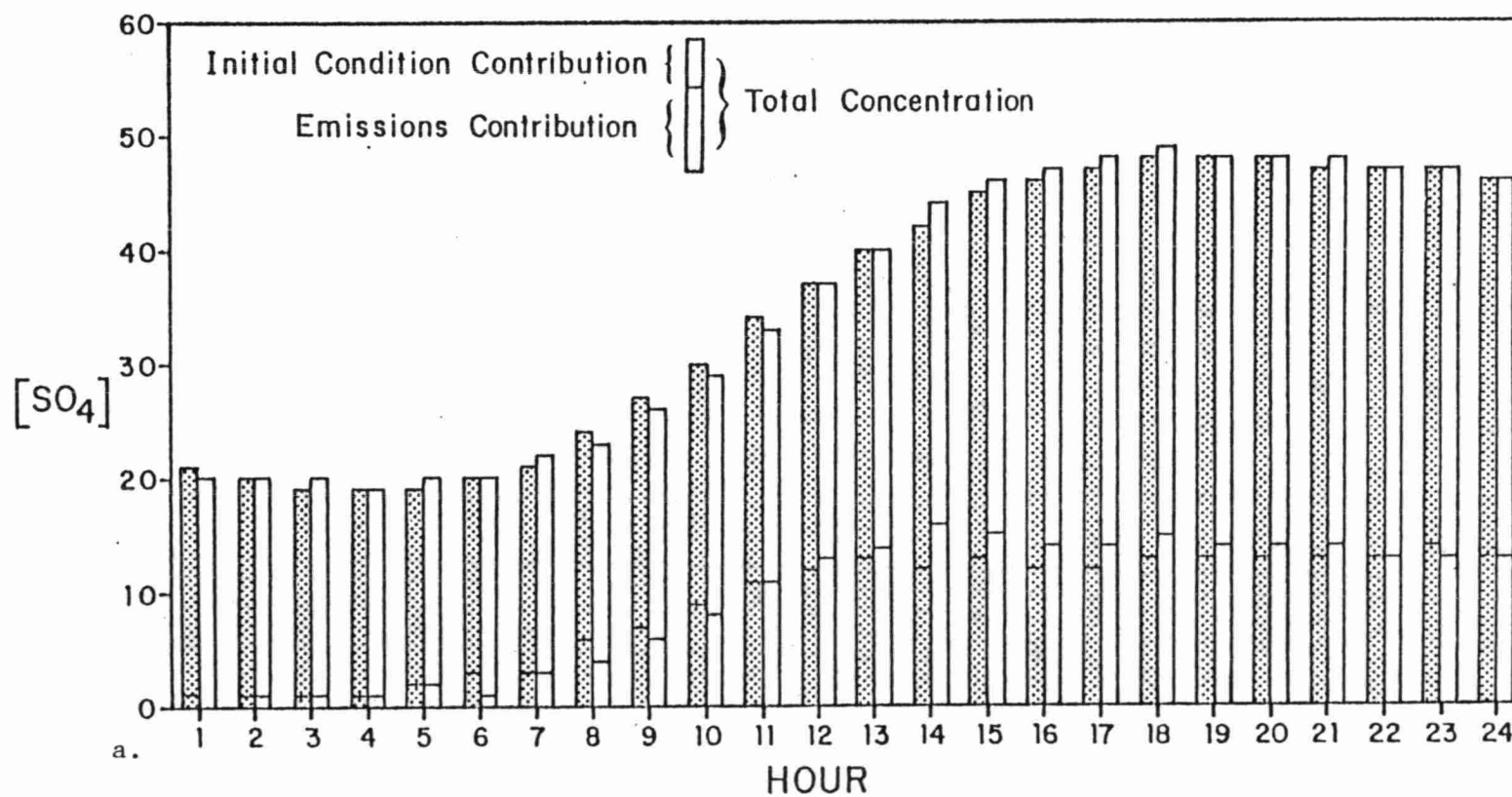


Figure 10-18. Comparison of hourly averaged SO<sub>4</sub> from run 1 (shaded bar) and run 3 (unshaded bar) for a. grid square (16,13) and b. grid square (7,15). The bars are divided, as shown, into emissions and initial condition components.

10-38

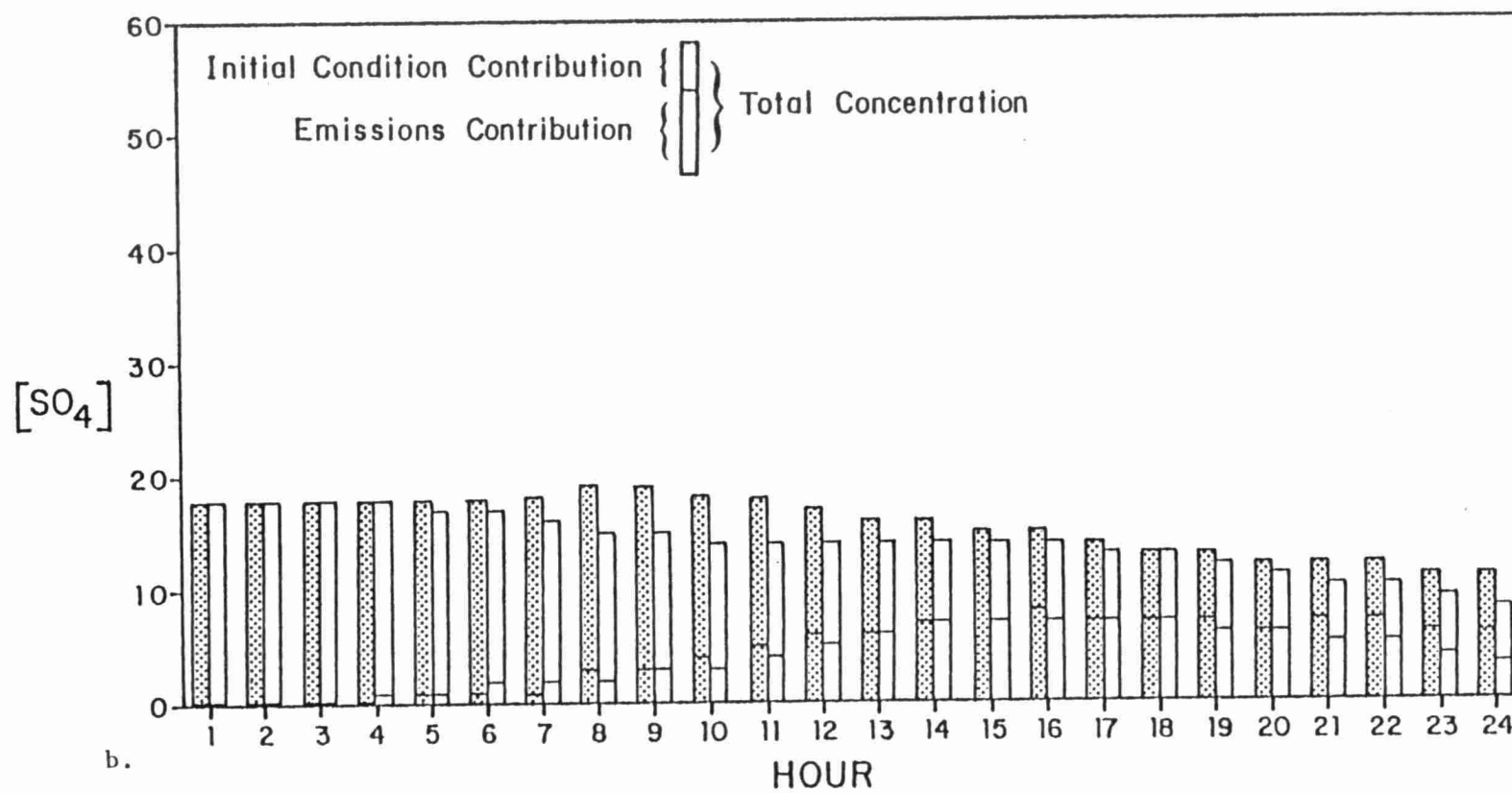


Figure 10-18. (Continued)

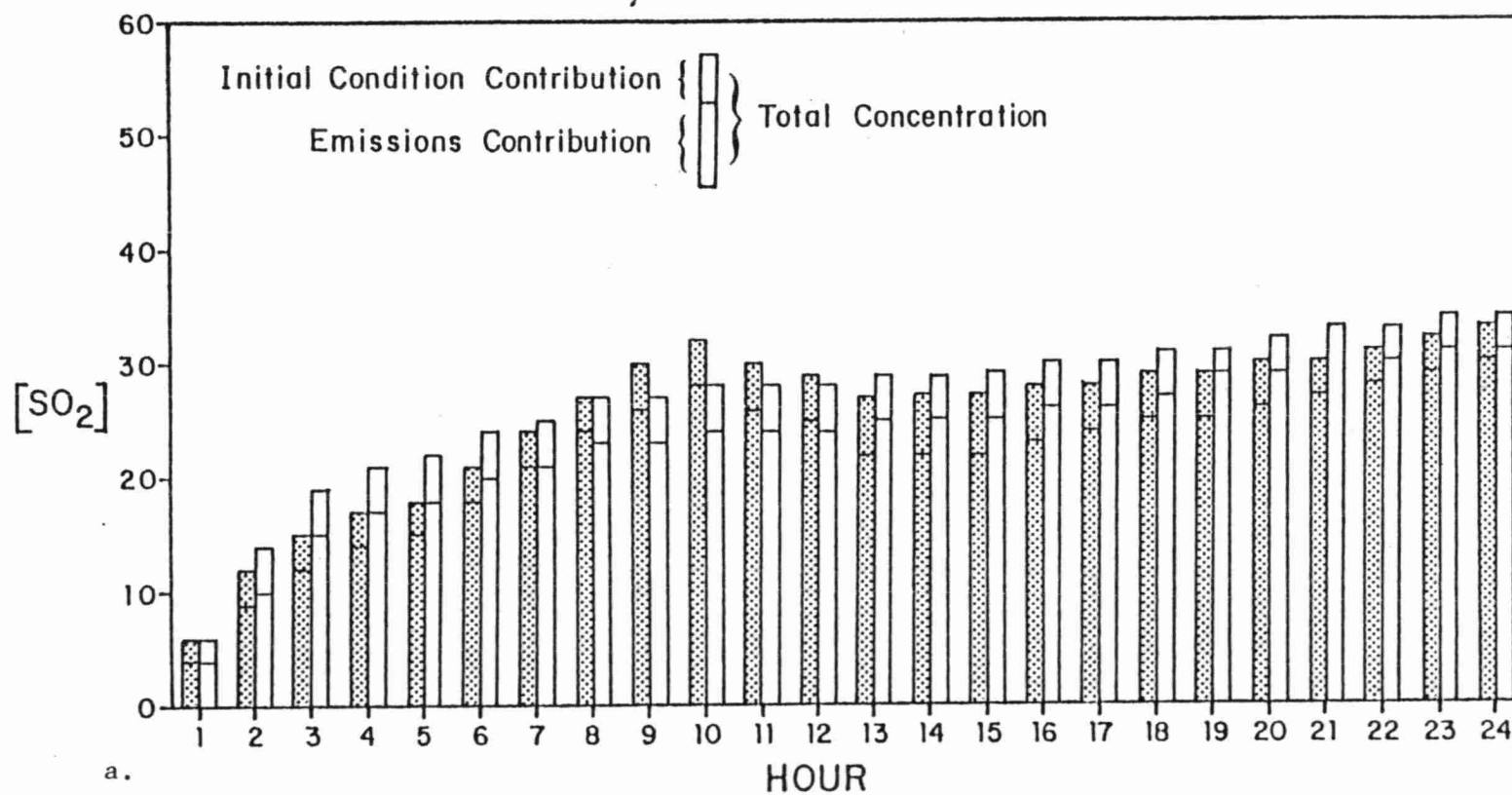


Figure 10-19. Comparison of hourly averaged SO<sub>2</sub> from run 1 (shaded bar) and run 3 (unshaded bar) for a. grid square (16,13) and b. grid square (7,15). The bars are divided, as shown, into emissions and initial condition components.



10-40

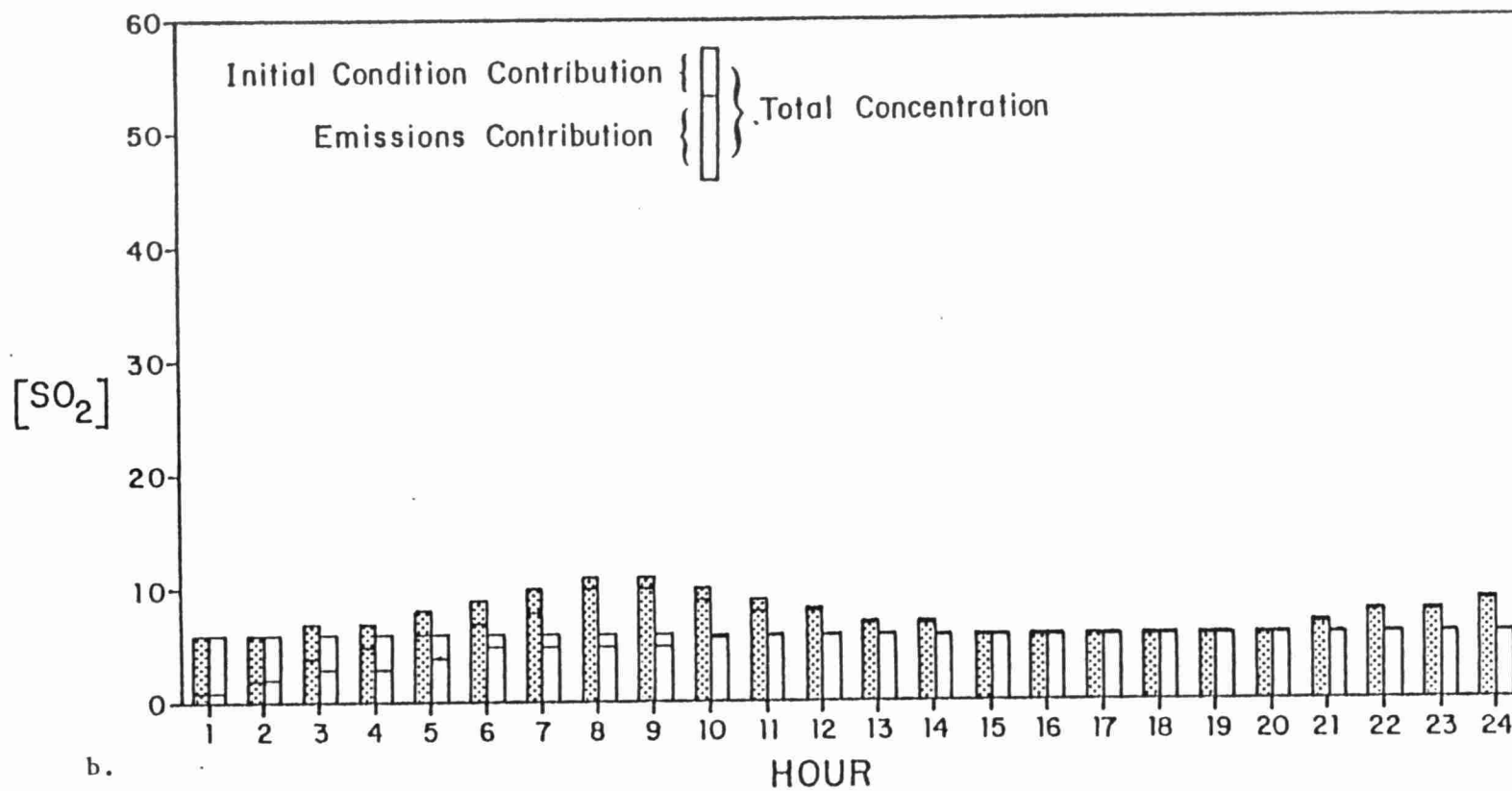


Figure 10-19. (Continued).

The sulfur mass balance for run 3 is given in Table 10-6. Compared to the run 1 values, the chemical conversion is slightly higher. Also, the residual term of  $\text{SO}_2$  is significantly larger for reasons not fully understood at this time.

#### 10.1.4.3 Comparison of Model 4 to Model 1

The 24-hour average  $\text{SO}_4$  and  $\text{SO}_2$  concentrations calculated by model 4 (average  $V_d$ ) are shown in Figure 10-20 and 10-21, respectively. The maximum difference in  $\text{SO}_2$  concentration is -2 ppb; the  $\text{SO}_4$  concentrations are all within  $\pm 1 \mu\text{g}/\text{m}^3$ .

The surface sulfur deposition map produced by run 4 is shown in Figure 10-22. The amount of deposited sulfur is less in most grid cells. The largest deficit is 39 metric tons S (-26%) in the New York City area grid square.

Plots of hour-averaged  $\text{SO}_4$  and  $\text{SO}_2$  concentrations for grid square (16,13) are shown for run 4 and run 1 together on Figures 10-23 and 10-24, respectively. The differences between the run 4 and run 1 values are relatively larger for  $\text{SO}_2$  than for  $\text{SO}_4$ . Looking at other cells, the biggest difference in the average concentrations for hour 24 are -2 to -5 ppb of  $\text{SO}_2$  and +2 to -3  $\mu\text{g}/\text{m}^3$  for  $\text{SO}_4$ .

The mass balance for run 4 is shown in Table 10-7. The  $\text{SO}_2$  sulfur lost to deposition is about 6½% less overall than for run 1. This is consistent with the results of the comparison of the cumulative sulfur deposition maps.

#### 10.1.4.4 Comparison of Model 5 to Model 1

The results of run 5 are given in Figures 10-25 and 10-26, the calculated 24-hour average  $\text{SO}_4$  and  $\text{SO}_2$ , respectively. Model 5, employed for this simulation, uses average  $R_{\text{chem}}$ ,  $K_z$  and  $V_d$ . Compared to the run 1 results (Figures 10-5c and 10-6c), the differences in  $\text{SO}_4$  concentration range from +3 to -3  $\mu\text{g}/\text{m}^3$  (+18 to -25%); the differences in  $\text{SO}_2$  concentration range from +4 to -3 ppb (+20 to -38%).

The cumulative sulfur deposition map, shown in Figure 10-27, is significantly different than the run 1 map (Figure 10-9) in many areas

TABLE 10-6  
 RUN 3 SULFUR MASS BALANCE  
 ( $10^9$  grams S)

<u>Component</u>	<u>SO<sub>2</sub>-</u>	<u>SO<sub>4</sub>-</u>
Initial concentrations	26.7	20.1
Emissions	47.1	0.94
Chemical conversion	-13.6	13.6
Deposition to ground	19.9	1.4
Residual	<u>3.3</u>	<u>-2.4</u>
Final concentrations	43.6	30.9

# SURADS RESULTS FOR JULY 21, 1978

## RUN 4: AVERAGE DEPOSITION VELOCITY

### SURFACE CONCENTRATION OF 24-HOUR AVERAGED SO4 (MICGR/M\*\*3)

	1	2	3	4	5	6	7	8	9	10	11	12	13	14	15	16	17	18	19	20	21	22	23	24	25	26	27	28	29	30
23 I	1	1	1	2	2	2	2	2	2	2	3	5	5	5	6	6	8	9	10	11	11	10	9	8	6	4	3	2	2	2
22 I	1	1	1	2	2	3	3	4	4	4	4	6	6	7	7	10	12	13	14	14	14	13	12	10	7	5	4	3	3	2
21 I	1	1	2	3	3	4	5	5	5	5	6	8	8	11	16	18	19	20	20	21	21	19	18	15	11	7	6	4	3	3
20 I	2	2	3	5	6	6	6	6	6	7	9	14	15	16	18	20	22	23	25	26	26	24	22	18	14	10	9	7	5	5
19 I	3	3	4	6	8	9	8	7	8	11	16	19	20	21	22	24	26	27	29	30	29	27	24	19	17	17	15	11	9	10
18 I	4	4	4	6	8	11	13	14	15	17	19	22	24	26	27	29	30	31	31	32	31	31	30	26	24	23	20	19	16	14
17 I	3	4	4	5	7	12	15	16	17	20	23	26	30	32	33	33	32	32	33	34	33	33	32	30	29	27	22	21	17	15
16 I	3	4	4	5	7	12	16	18	21	23	26	29	33	33	33	32	31	31	32	33	34	35	35	31	29	27	22	21	17	15
15 I	3	4	4	5	7	11	15	17	22	24	26	30	33	33	33	33	33	33	33	33	34	36	35	31	27	23	20	19	15	14
14 I	3	4	4	5	7	12	15	17	20	24	27	31	34	33	33	35	35	34	32	32	32	32	31	24	16	11	10	11	11	10
13 I	3	4	4	5	7	12	15	17	21	25	28	32	34	32	33	35	36	34	29	26	21	19	16	11	8	7	7	6	6	5
12 I	4	4	5	5	9	13	15	18	22	26	30	33	33	32	33	34	33	30	19	13	11	11	9	7	5	5	5	4	4	4
11 I	3	4	5	6	11	13	14	18	23	26	28	30	32	31	30	28	20	14	10	9	8	7	6	5	4	4	4	3	3	3
10 I	3	4	5	6	9	10	13	18	22	25	24	24	24	23	23	21	16	12	9	9	8	7	5	4	4	3	3	2	2	2
9 I	3	4	5	6	7	8	13	15	16	16	17	17	18	18	18	17	13	9	9	9	8	6	5	4	3	3	2	2	2	2
8 I	3	4	5	6	7	7	9	11	11	12	14	15	17	17	16	15	12	9	8	8	8	6	5	4	3	3	2	2	2	1
7 I	3	5	6	6	7	7	8	9	10	11	13	14	14	14	14	12	10	9	8	8	7	5	4	3	3	3	2	2	1	1
6 I	3	4	5	6	7	7	8	9	10	12	13	13	13	13	12	10	9	9	8	7	5	3	3	3	2	2	2	1	1	1
5 I	3	4	4	5	5	6	7	8	10	11	12	11	10	10	10	9	8	7	6	5	3	2	2	2	2	2	1	1	1	1
4 I	3	3	3	3	4	4	5	6	8	9	10	10	9	8	8	9	7	4	3	2	2	2	2	1	1	1	1	1	1	1
3 I	3	3	3	3	3	3	3	4	5	6	7	7	7	6	7	13	5	2	2	2	2	1	1	1	1	1	1	1	1	0
2 I	2	3	3	3	2	2	2	3	4	4	5	5	4	4	3	1	1	1	1	1	1	1	1	1	1	1	1	1	1	1
1 I	2	3	2	2	2	2	2	2	2	3	3	4	3	4	4	3	2	1	1	1	1	1	1	1	1	1	1	1	1	1

Figure 10-20. Calculated 24-hour average sulfate concentration ( $\mu\text{g}/\text{m}^3$ ) for run 4.

## SURADS RESULTS FOR JULY 21, 1978

## RUN 4: AVERAGE DEPOSITION VELOCITY

SURFACE CONCENTRATION OF 24-HOUR AVERAGED SO<sub>2</sub> (PPB)

10-44

		1	2	3	4	5	6	7	8	9	10	11	12	13	14	15	16	17	18	19	20	21	22	23	24	25	26	27	28	29	30
23	I	0	0	0	1	1	1	1	1	1	1	0	0	0	0	0	0	0	0	0	0	0	1	1	1	1	1	1	1	1	0
22	I	0	0	0	0	1	2	2	3	3	1	1	0	0	0	1	1	1	1	1	1	1	1	1	1	1	1	1	1	0	0
21	I	0	0	1	1	1	1	2	2	2	1	1	1	1	2	6	8	3	1	1	1	1	2	3	2	1	1	1	1	1	1
20	I	0	1	2	3	2	2	4	2	2	2	2	2	3	3	4	4	3	2	2	2	2	3	4	3	2	2	3	4	1	1
19	I	1	1	2	2	3	4	5	4	4	3	3	4	3	3	3	4	3	3	4	4	4	4	4	3	4	5	6	3	2	2
18	I	1	2	2	2	3	5	5	6	6	5	5	7	8	8	5	5	5	7	9	8	8	8	7	6	6	7	4	3	2	2
17	I	1	2	2	2	2	6	7	9	7	8	6	7	10	14	10	9	10	13	15	15	12	10	9	8	10	10	5	4	3	2
16	I	1	3	2	2	3	5	7	8	8	7	7	8	16	12	11	10	12	16	18	17	14	12	12	10	10	11	6	4	2	2
15	I	1	1	2	2	4	6	7	10	13	8	6	7	15	12	17	16	17	20	20	18	15	14	13	10	8	7	5	4	2	2
14	I	1	1	1	2	4	10	7	6	6	6	6	6	9	10	16	22	22	21	19	19	16	15	15	8	4	2	1	1	1	1
13	I	3	2	2	2	4	6	6	6	7	7	7	8	9	10	16	26	25	17	13	14	13	14	10	5	2	1	1	1	1	1
12	I	4	2	2	2	4	6	7	7	10	11	13	14	13	13	17	21	18	10	7	8	7	7	4	2	1	1	0	0	0	0
11	I	1	3	2	4	9	9	6	9	13	13	16	16	13	15	13	8	5	4	5	7	4	3	2	1	0	0	0	0	0	0
10	I	0	1	1	1	5	7	6	9	14	15	14	10	9	9	10	6	3	3	4	5	4	2	1	1	0	0	0	0	0	0
9	I	0	0	0	1	1	3	8	8	13	9	6	6	6	5	4	4	4	3	5	6	4	2	1	1	0	0	0	0	0	0
8	I	0	0	0	1	1	2	5	7	7	5	5	5	6	6	4	4	4	3	4	3	5	2	1	1	0	0	0	0	0	0
7	I	0	1	1	2	2	2	4	8	5	4	5	7	5	5	4	3	3	3	3	3	3	2	1	1	0	0	0	0	0	0
6	I	0	1	1	2	3	2	4	5	5	5	6	5	5	6	5	3	2	3	3	3	3	1	0	0	0	0	0	0	0	0
5	I	0	1	1	1	1	2	4	7	6	7	6	4	4	6	5	3	3	3	3	4	2	1	0	0	0	0	0	0	0	0
4	I	1	1	1	1	1	1	3	6	6	5	5	4	3	3	4	3	3	3	2	1	0	0	0	0	0	0	0	0	0	0
3	I	1	1	1	1	1	1	2	2	2	2	4	2	2	3	2	3	3	1	0	0	0	0	0	0	0	0	0	0	0	0
2	I	1	1	1	1	1	1	1	1	1	1	1	1	1	2	3	2	0	0	0	0	0	0	0	0	0	0	0	0	0	0
1	I	1	3	1	1	2	2	2	1	1	1	1	2	2	3	6	2	1	1	1	1	1	1	0	0	0	0	0	0	0	0

Figure 10-21. Calculated 24-hour average SO<sub>2</sub> concentration (ppb) for run 4.

# SURADS RESULTS FOR JULY 21, 1978

## RUN 4: AVERAGE DEPOSITION VELOCITY

### SURFACE SULFUR DEPOSITION (METRIC TONS/DAY)

10-45

	1	2	3	4	5	6	7	8	9	10	11	12	13	14	15	16	17	18	19	20	21	22	23	24	25	26	27	28	29	30
23 I	2	2	2	5	5	4	4	4	4	3	4	4	4	3	3	4	4	5	5	5	5	5	6	5	7	5	5	5	3	3
22 I	2	1	1	3	5	12	12	18	21	11	5	4	4	4	6	10	10	8	6	5	6	6	8	8	7	6	5	6	3	3
21 I	2	3	9	10	8	9	13	13	14	11	6	5	6	15	39	50	25	12	9	9	9	13	24	15	10	7	12	10	5	4
20 I	2	5	16	22	17	16	30	16	15	11	13	18	19	21	28	29	24	16	15	16	19	22	29	20	17	16	22	28	10	9
19 I	5	9	12	18	18	30	37	31	26	20	23	29	26	24	27	27	26	26	32	31	33	33	31	24	31	37	44	22	14	14
18 I	8	14	15	12	19	32	34	42	42	39	39	51	56	54	37	36	41	51	61	60	56	54	49	44	43	51	32	24	18	15
17 I	6	14	11	14	17	42	47	63	47	54	44	48	73	97	69	66	69	99	102	107	83	72	64	61	75	74	40	27	19	16
16 I	6	22	15	20	21	37	54	62	56	49	50	57	122	86	77	70	80	107	118	112	94	88	91	76	77	80	42	28	19	15
15 I	7	9	12	13	33	42	54	79	94	55	44	51	106	83	124	109	114	132	131	121	104	96	96	70	57	52	34	26	18	13
14 I	10	9	9	13	31	75	50	47	46	46	42	49	63	75	124	159	155	138	129	128	106	107	110	58	31	14	11	10	10	9
13 I	24	14	12	17	26	40	42	45	51	50	52	58	67	68	111	183	170	114	87	96	89	98	69	32	14	8	6	5	5	5
12 I	31	18	15	18	32	44	46	49	72	79	89	102	92	89	116	142	125	70	54	57	50	51	27	11	6	4	4	4	3	3
11 I	9	18	14	31	68	68	43	64	93	87	106	108	87	99	94	57	37	29	33	48	31	21	11	6	4	3	3	3	3	2
10 I	3	7	6	11	35	47	43	64	97	106	92	71	62	67	71	42	25	23	33	35	25	14	9	5	3	2	1	1	1	1
9 I	3	3	4	5	11	18	53	54	84	63	40	41	42	39	32	32	27	23	41	46	28	15	8	5	3	2	1	1	1	1
8 I	2	3	4	6	9	14	36	48	48	33	32	39	40	41	29	30	31	20	29	24	40	16	7	4	3	1	1	1	1	1
7 I	3	4	7	12	14	15	28	58	37	30	33	47	35	34	27	24	25	23	22	20	17	10	5	3	3	1	1	1	1	1
6 I	2	7	8	14	22	17	28	35	34	34	40	33	32	42	37	27	18	19	22	24	10	4	3	2	2	1	1	1	1	0
5 I	3	8	7	11	11	14	27	46	46	44	42	28	29	42	35	22	23	21	28	16	3	2	2	2	1	1	1	1	0	0
4 I	5	9	6	7	7	10	24	39	42	36	35	26	19	25	26	23	21	23	16	3	2	2	1	1	1	1	1	1	0	0
3 I	4	8	9	6	6	9	18	12	16	18	26	17	17	26	17	22	23	9	3	2	2	1	1	1	1	1	1	1	0	0
2 I	6	8	7	9	9	8	9	8	6	7	7	7	9	17	23	11	2	1	2	2	2	2	2	2	1	1	1	1	1	1
1 I	8	18	10	7	13	14	14	9	9	10	11	17	12	23	41	16	5	4	3	3	3	3	3	3	3	3	3	3	3	3

Figure 10-22. Calculated cumulative sulfur deposition (metric tons) for run 4.

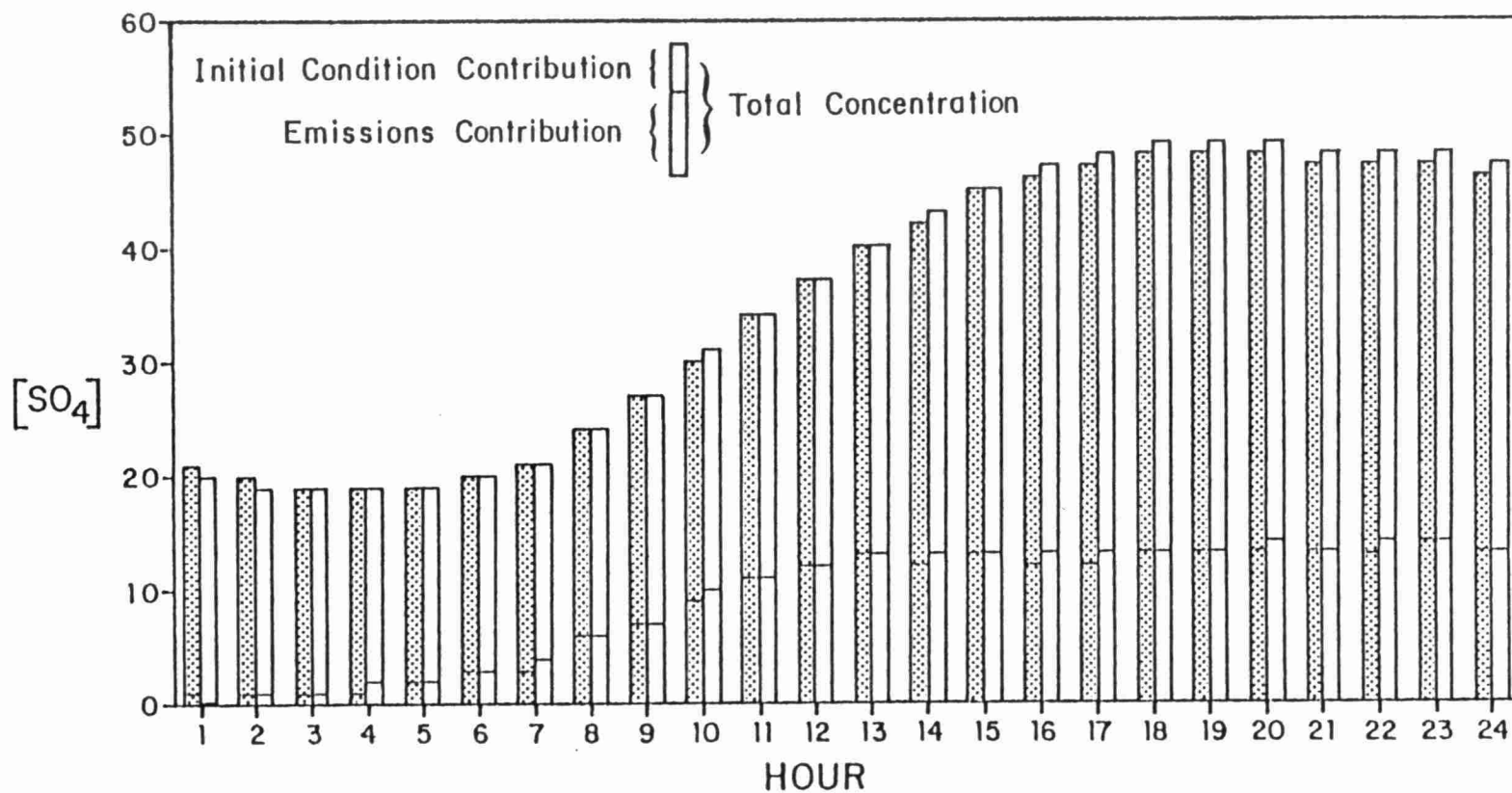


Figure 10-23. Comparison of hourly averaged  $\text{SO}_4$  from run 1 (shaded bar) and run 4 (unshaded bar) for grid square (16,13). The bars are divided, as shown, into emissions and initial condition components.

10-47

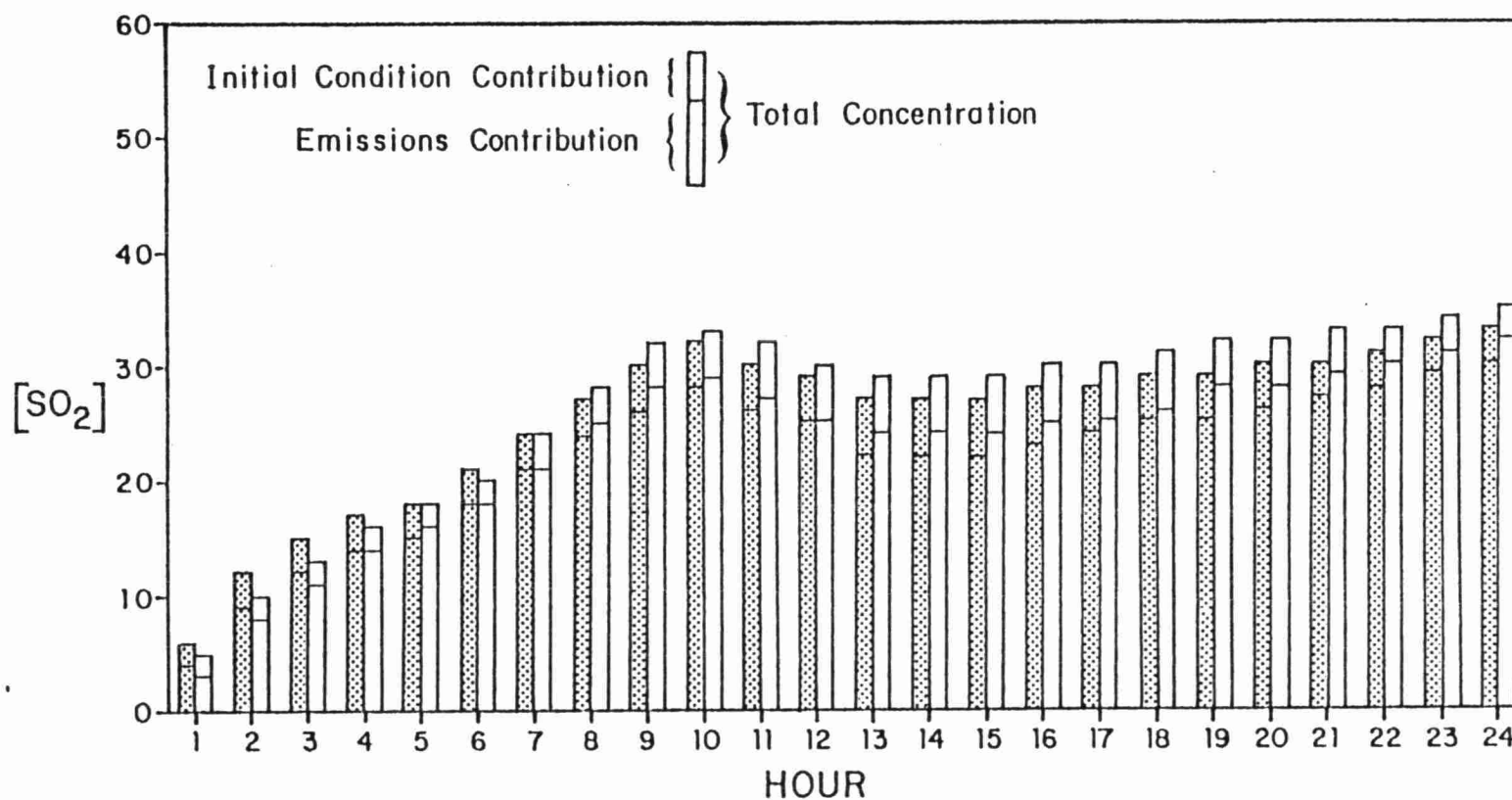


Figure 10-24. Comparison of hourly averaged  $SO_2$  from run 1 (shaded bar) and run 4 (unshaded bar) for grid square (16,13). The bars are divided, as shown, into emissions and initial condition components.



TABLE 10-7  
 RUN 4 SULFUR MASS BALANCE  
 ( $10^9$  grams S)

<u>Component</u>	<u>SO<sub>2</sub>-</u>	<u>SO<sub>4</sub>-</u>
Initial concentrations	26.7	20.1
Emissions	47.1	0.94
Chemical conversion	-13.5	13.5
Deposition to ground	18.6	1.3
Residual	<u>2.5</u>	<u>-2.3</u>
Final concentrations	44.1	31.0

# SURADS RESULTS FOR JULY 21, 1978

RUN 5: AVERAGE CONVERSION RATE, VERTICAL DIFFUSIVITY, AND DEPOSITION VELOCITY

SURFACE CONCENTRATION OF 24-HOUR AVERAGED SO<sub>4</sub> (MICRO/M\*\*3)

		1	2	3	4	5	6	7	8	9	10	11	12	13	14	15	16	17	18	19	20	21	22	23	24	25	26	27	28	29	30
23	I	1	1	1	2	2	2	2	2	2	2	4	5	5	5	5	6	7	9	10	11	11	10	10	8	6	5	3	3	2	2
22	I	1	1	1	2	2	3	3	3	3	4	5	6	7	7	8	10	11	13	14	14	14	13	12	10	8	6	5	4	3	2
21	I	1	1	1	3	3	4	4	5	5	5	5	7	9	11	16	18	18	19	20	21	21	20	19	16	12	9	6	5	4	4
20	I	2	2	3	5	6	6	6	6	6	6	8	13	15	15	17	19	21	23	24	26	27	26	24	20	16	11	9	7	6	6
19	I	3	3	3	5	7	8	8	7	8	11	15	17	19	21	21	23	25	27	29	31	30	29	26	22	19	17	15	11	10	10
18	I	3	4	4	5	7	10	12	13	14	17	18	21	22	24	26	28	29	30	32	33	32	32	31	28	25	23	21	20	17	15
17	I	3	4	4	5	7	11	13	15	17	20	23	27	29	32	31	31	31	31	33	35	33	33	33	30	29	27	23	22	18	16
16	I	3	4	4	5	6	10	13	16	20	23	26	30	33	33	32	31	30	32	34	35	35	35	34	31	29	28	23	22	18	16
15	I	3	3	4	5	6	9	13	16	21	24	27	30	33	33	32	32	32	33	33	34	35	34	33	30	28	25	21	20	17	15
14	I	3	4	4	5	6	9	14	16	20	25	28	31	33	32	32	33	33	33	32	32	31	31	28	23	17	13	12	13	13	12
13	I	3	4	4	5	6	10	14	16	21	25	29	32	34	32	32	34	34	32	27	24	19	17	14	9	8	7	7	7	6	6
12	I	3	4	4	5	8	11	14	17	22	26	29	32	33	32	32	32	32	27	18	13	11	10	8	7	6	5	5	5	5	4
11	I	3	4	5	6	10	12	13	17	22	26	28	30	31	30	29	27	19	14	10	9	8	7	6	5	4	4	4	4	3	3
10	I	3	4	5	6	9	10	13	17	22	24	24	24	23	22	22	20	15	12	9	8	8	6	5	4	4	3	3	3	2	2
9	I	3	4	5	6	7	8	12	14	15	15	16	17	18	18	18	17	12	9	8	8	8	6	5	4	3	3	3	2	2	2
8	I	3	4	5	6	7	7	8	10	10	11	13	15	17	17	17	15	12	9	8	7	7	6	5	4	3	3	2	2	2	1
7	I	3	5	6	6	7	7	7	9	9	10	13	14	14	14	14	12	10	8	8	7	7	5	4	4	3	3	2	2	1	1
6	I	3	4	5	6	7	6	7	8	9	11	13	13	13	13	12	10	9	8	7	7	5	4	4	3	3	2	2	2	1	1
5	I	2	4	4	5	5	6	7	8	10	11	12	11	10	10	9	8	8	7	6	5	3	2	2	2	2	2	1	1	1	1
4	I	2	3	3	3	4	4	5	7	8	10	10	10	8	7	7	7	6	4	3	2	2	2	2	1	1	1	1	1	1	1
3	I	2	3	3	3	3	3	4	4	6	7	7	7	6	5	5	10	4	2	2	2	2	1	1	1	1	1	1	1	1	0
2	I	2	3	2	3	2	2	2	3	4	4	5	5	4	4	3	1	1	1	1	1	1	1	1	1	1	1	1	1	1	1
1	I	2	3	2	2	2	2	2	2	2	3	3	3	3	3	3	2	1	1	1	1	1	1	1	1	1	1	1	1	1	1

Figure 10-25. Calculated 24-hour average sulfate concentration ( $\mu\text{g}/\text{m}^3$ ) for run 5.

# SURADS RESULTS FOR JULY 21, 1978

RUN 5: AVERAGE CONVERSION RATE, VERTICAL DIFFUSIVITY, AND DEPOSITION VELOCITY

SURFACE CONCENTRATION OF 24-HOUR AVERAGED SO<sub>2</sub> (PPB)

		1	2	3	4	5	6	7	8	9	10	11	12	13	14	15	16	17	18	19	20	21	22	23	24	25	26	27	28	29	30
	I	+	+	+	+	+	+	+	+	+	+	+	+	+	+	+	+	+	+	+	+	+	+	+	+	+	+	+	+	+	+
10-50	23 I	0	0	0	1	1	1	1	1	1	1	1	1	1	0	0	0	0	0	0	0	1	1	1	1	1	1	1	1	1	1
	22 I	0	0	0	0	1	1	1	2	2	1	1	1	1	1	1	1	1	1	1	1	1	1	1	1	1	1	1	1	1	1
	21 I	0	0	1	1	1	1	1	2	2	1	1	1	1	3	8	9	3	2	1	1	1	2	3	2	1	1	1	1	1	1
	20 I	0	1	2	3	2	2	3	2	2	1	2	2	3	3	4	4	3	2	2	2	2	3	4	3	2	2	3	3	2	2
	19 I	1	1	1	2	2	3	4	3	3	3	3	3	3	3	4	4	3	3	4	4	5	5	5	4	4	4	5	4	3	2
	18 I	1	1	2	1	2	4	4	5	5	5	5	7	7	6	5	5	5	7	9	9	9	9	9	8	7	7	5	4	3	3
	17 I	1	2	1	2	2	5	6	9	6	8	6	7	8	13	9	10	10	14	16	16	14	12	11	10	10	10	7	5	4	3
	16 I	1	2	2	2	2	4	6	8	8	7	7	8	16	12	11	10	12	17	19	18	15	13	13	12	10	10	7	5	3	3
	15 I	1	1	1	1	3	5	6	9	13	8	6	7	17	12	16	15	17	22	21	19	15	14	13	11	9	8	6	5	3	3
	14 I	1	1	1	1	3	11	6	6	7	7	6	7	9	11	16	22	23	22	20	20	16	15	15	9	5	3	2	2	2	2
	13 I	3	2	1	2	3	6	6	6	7	7	7	8	9	10	17	29	27	17	13	14	13	14	10	5	2	2	1	1	1	1
	12 I	4	3	2	3	4	7	8	7	10	12	13	15	13	14	19	24	21	10	7	7	7	7	4	2	1	1	1	1	1	1
	11 I	1	3	2	6	9	8	6	9	14	13	18	17	13	17	15	8	6	4	5	6	4	3	2	1	0	0	0	0	0	0
	10 I	0	1	1	1	5	8	7	10	16	17	14	11	10	10	10	6	3	3	4	5	4	2	1	1	0	0	0	0	0	0
	9 I	0	0	0	1	2	3	10	9	15	10	6	6	7	6	5	5	3	3	5	5	4	2	1	1	0	0	0	0	0	0
	8 I	0	0	0	1	1	2	6	8	8	5	5	6	7	6	4	5	4	3	3	3	5	2	1	1	0	0	0	0	0	0
	7 I	0	1	1	2	2	2	4	8	5	4	5	7	6	5	4	3	3	3	3	3	3	2	2	1	1	0	0	0	0	0
	6 I	0	1	1	2	3	2	4	5	5	5	6	5	5	6	5	3	2	2	3	3	1	1	1	0	0	0	0	0	0	0
	5 I	0	1	1	2	1	2	4	8	6	8	7	4	4	7	4	3	3	3	3	3	2	1	0	0	0	0	0	0	0	0
	4 I	1	1	1	1	1	1	4	7	6	5	6	4	3	3	4	3	3	4	2	1	0	0	0	0	0	0	0	0	0	0
	3 I	1	1	1	1	1	1	3	2	3	3	5	3	3	3	2	3	3	1	1	0	0	0	0	0	0	0	0	0	0	0
	2 I	1	1	1	1	1	1	1	1	1	1	1	1	1	1	2	3	2	0	0	0	0	0	0	0	0	0	0	0	0	0
	1 I	1	3	1	1	2	2	2	1	1	1	1	2	2	3	6	2	1	1	1	1	1	1	1	1	0	0	0	0	0	0

Figure 10-26. Calculated 24-hour average SO<sub>2</sub> concentration (ppb) for run 5.

# SURADS RESULTS FOR JULY 21, 1978

RUN 5: AVERAGE CONVERSION RATE, VERTICAL DIFFUSIVITY, AND DEPOSITION VELOCITY

SURFACE SULFUR DEPOSITION (METRIC TONS/DAY)

	1	2	3	4	5	6	7	8	9	10	11	12	13	14	15	16	17	18	19	20	21	22	23	24	25	26	27	28	29	30	
23 I	2	2	2	4	5	4	4	4	4	4	5	5	5	4	3	4	4	5	5	5	5	6	6	6	6	5	5	5	4	4	
22 I	2	1	1	3	5	10	10	16	17	9	5	5	4	4	6	11	10	8	7	6	6	7	8	9	7	6	5	6	4	3	
21 I	2	2	8	8	7	8	11	11	12	10	6	6	7	18	49	55	23	13	10	9	11	13	22	16	11	9	11	9	5	5	
20 I	2	4	14	20	15	13	25	14	13	10	12	17	19	21	30	30	23	16	16	17	20	24	29	22	19	16	20	24	12	11	
19 I	6	8	10	15	16	26	31	24	24	19	20	25	25	24	27	27	25	25	32	34	37	40	36	30	32	34	40	26	18	17	
18 I	7	12	13	11	17	28	29	36	37	37	37	48	52	45	34	36	42	49	61	63	64	65	62	54	51	53	37	30	23	19	
17 I	6	13	10	12	15	35	41	58	45	55	45	48	63	93	67	66	70	103	109	113	93	82	76	69	75	71	46	37	26	21	
16 I	5	20	13	17	17	31	43	57	54	50	51	58	120	84	75	70	80	113	127	120	101	93	94	83	76	77	50	38	25	20	
15 I	6	9	11	11	24	35	44	72	94	56	46	53	113	82	120	103	113	139	139	128	105	94	94	78	65	59	41	34	24	19	
14 I	8	8	9	11	25	75	45	45	46	48	45	50	64	79	121	160	158	146	136	133	107	104	111	62	35	18	14	14	14	12	
13 I	20	14	11	15	21	42	42	45	50	51	53	58	66	70	119	194	181	115	89	97	88	100	67	29	15	10	8	7	6	6	
12 I	29	19	15	19	28	50	54	52	73	85	94	107	95	94	127	159	140	66	50	53	48	49	24	11	7	5	5	4	4	4	
11 I	8	22	15	37	66	65	46	67	99	91	116	114	91	110	102	58	42	30	33	43	30	20	11	6	4	3	3	3	3	3	
10 I	3	7	6	11	33	56	48	69	107	115	97	75	67	72	74	44	26	23	30	33	25	15	9	5	3	3	2	1	1	1	
9 I	2	3	4	5	11	22	63	61	96	66	43	45	46	42	35	33	27	22	35	39	28	16	9	5	3	2	1	1	1	1	
8 I	2	3	4	6	10	14	39	52	52	34	34	42	45	44	31	33	29	19	26	24	37	17	8	5	3	2	1	1	1	1	
7 I	2	5	7	12	13	15	28	57	36	31	35	50	39	36	29	24	25	23	20	19	16	12	6	4	3	1	1	1	1	1	
6 I	2	7	8	14	23	17	28	33	34	36	43	35	33	42	36	24	17	18	21	22	10	5	4	3	2	1	1	1	1	0	
5 I	3	8	7	12	11	13	29	49	46	49	48	30	30	46	33	20	21	20	26	14	4	2	2	2	2	1	1	1	1	0	0
4 I	5	8	6	7	7	10	27	43	43	38	40	29	20	24	25	23	20	24	14	3	2	2	1	1	1	1	1	1	1	0	0
3 I	4	7	9	6	6	10	28	13	18	19	31	20	19	23	16	20	22	9	3	2	2	2	1	1	1	1	1	1	1	1	1
2 I	6	8	7	9	10	8	9	8	7	8	7	8	9	16	21	10	2	2	2	2	2	2	2	1	1	1	1	1	1	1	1
1 I	7	19	10	7	13	15	14	8	9	10	11	15	12	20	42	15	5	4	4	4	4	4	3	3	3	3	3	3	3	3	3

Figure 10-27. Calculated cumulative sulfur deposition (metric tons) for run 5.

of the SURE region. A map of the difference in sulfur deposition between run 5 and run 1 is given in Figure 10-28. The difference is largest in the New York City grid square where the change is -38 metric tons (-26%).

A comparison of run 1 and run 5 hourly averaged  $\text{SO}_4$  and  $\text{SO}_2$  concentrations in grid square (16,13) is given in Figures 10-29 and 10-30, respectively. Both the  $\text{SO}_4$  and  $\text{SO}_2$  results show significant differences in the hourly averages for the two runs.

The sulfur mass balance for run 5 is given in Table 10-8. Compared to run 1, there is about 4½% more conversion and 4% less deposition. The largest difference, however, is in the residual term for  $\text{SO}_2$ .

#### 10.1.4.5 Comparison of Model 6 to Model 1

The 24-hour average  $\text{SO}_4$  and  $\text{SO}_2$  concentration calculated by Model 6 (constant emission rates) is shown in Figures 10-31 and 10-32, respectively. There are only minor differences between these results and the Model 1 results: +1 to -2  $\mu\text{g}/\text{m}^3$  for  $\text{SO}_4$  and +1 to -1 ppb for  $\text{SO}_2$ .

The run 6 sulfur deposition map is shown in Figure 10-33. The differences between these values and the run 1 values are small compared to differences seen with Models 2 through 5 and are only significant in a small fraction of the modeling grid. The differences range from +8 to -2 metric tons.

The sulfur mass balances for run 6 is given in Table 10-9. As expected, there are only minor differences between these values and the run 1 values.

#### 10.1.4.6 Summary of Model Formulation Comparisons

The results presented above have yielded some important information about the sensitivity of the model output to the complexity of the input:

# SURADS RESULTS FOR JULY 21, 1978

## COMPARISON OF RUN 5 TO RUN 1

### DIFFERENCE IN SURFACE SULFUR DEPOSITION (METRIC TONS/DAY)

		1	2	3	4	5	6	7	8	9	10	11	12	13	14	15	16	17	18	19	20	21	22	23	24	25	26	27	28	29	30
10-53	23 I	0	0	0	-1	-1	0	1	0	0	1	2	1	1	0	0	0	-2	0	0	0	0	0	-1	0	-1	-1	-1	-1	0	0
	22 I	0	0	0	-1	-1	-3	-3	-4	-5	-2	0	1	0	0	0	0	-1	-2	0	-1	-1	-1	-1	0	0	0	0	0	0	0
	21 I	0	-1	-2	-2	-1	-2	-3	-3	-3	-2	0	1	1	2	4	-3	-6	-2	-1	-1	0	-3	-5	-1	1	1	-2	-2	0	0
	20 I	0	-1	-4	-4	-2	-3	-7	-4	-3	0	1	-2	0	1	0	-3	-5	-3	-1	-1	-1	0	-2	1	0	-1	-4	-6	2	2
	19 I	0	-1	-2	-3	-3	-7	-8	-6	-2	0	-3	-6	-4	2	-2	-3	-5	-5	-5	-2	0	3	4	4	0	-4	-4	5	6	5
	18 I	0	-2	-2	-1	-3	-6	-5	-7	-3	-3	-3	-3	0	-7	-8	-4	-7	-7	-6	-2	1	4	8	8	9	5	9	8	7	5
	17 I	0	-1	-1	-2	-2	-8	-7	-13	5	1	2	3	1	-2	-9	-9	-6	-14	-7	-11	-1	0	5	3	-3	-4	13	12	9	6
	16 I	-1	-2	-2	-3	-4	-7	-11	-11	-2	1	1	1	-15	-8	-8	-5	-7	-10	-3	-8	-9	-8	-12	-1	-9	-11	13	11	8	6
	15 I	-1	0	-1	-2	-8	-6	-7	-13	-10	0	1	3	8	1	-26	-13	-19	-13	-12	-12	-21	-27	-24	-2	2	11	10	9	8	6
	14 I	-2	0	0	-2	-5	5	-3	-3	-2	1	1	-3	-5	-2	-24	-15	-18	-6	-12	-15	-22	-36	-38	-7	3	5	4	4	5	3
	13 I	-1	0	-1	-1	-4	3	1	0	-4	-6	-4	-7	-13	-8	-6	-23	-22	-13	-11	-14	-20	-28	-18	-4	1	2	2	2	1	2
	12 I	-4	2	1	3	-1	9	11	3	-3	-9	-6	-17	-15	-7	-5	-2	1	-7	-6	-15	-9	-13	-7	-1	1	1	1	0	1	1
	11 I	0	2	0	5	-1	5	9	5	1	-3	-3	-17	-7	2	-3	-4	2	2	9	-8	-4	-3	-1	0	0	0	0	0	1	2
	10 I	0	0	0	1	1	14	8	7	7	-6	-5	-2	-2	1	-1	-1	0	3	8	7	5	3	1	0	0	1	1	0	0	0
	9 I	-1	-1	0	-1	0	4	9	4	3	-1	-1	1	0	0	0	-1	0	1	5	5	9	6	2	0	0	1	0	0	0	0
	8 I	-1	0	0	0	0	0	1	0	1	-2	-3	-1	1	3	1	3	-2	0	1	3	2	4	2	1	0	1	0	0	0	0
	7 I	-1	0	-1	0	-1	0	-2	-4	-4	-1	-1	1	3	2	2	1	3	1	0	-1	2	3	1	1	1	0	0	0	0	0
	6 I	0	0	0	0	-2	-1	-3	-5	-3	-2	1	0	-1	-1	0	-2	1	0	-1	-2	0	2	2	1	1	0	0	0	1	0
	5 I	0	0	0	1	-1	-2	-2	-4	-4	1	4	0	1	4	-1	-1	-1	-1	-3	-2	1	0	0	1	1	0	0	0	0	0
	4 I	-1	-1	-1	0	-1	-2	-1	-4	-6	-1	2	2	3	0	-1	-1	-1	0	-2	0	0	1	0	0	0	0	0	1	0	0
	3 I	-2	-2	-1	-2	-2	0	7	0	0	0	5	3	2	-2	-2	-2	-2	1	0	0	1	1	0	0	0	0	0	1	1	1
	2 I	-2	-3	-2	-2	-2	-1	-3	-1	0	1	0	1	0	-1	-3	-1	0	1	0	0	0	0	1	0	0	0	0	0	0	0
	1 I	-2	-3	-3	-1	-2	-2	-2	-2	-1	0	0	-2	0	-3	0	1	1	1	1	1	1	1	0	0	1	1	1	1	1	1

Figure 10-28. Difference in calculated sulfur deposition (metric tons) between run 5 and run 1.

10-54

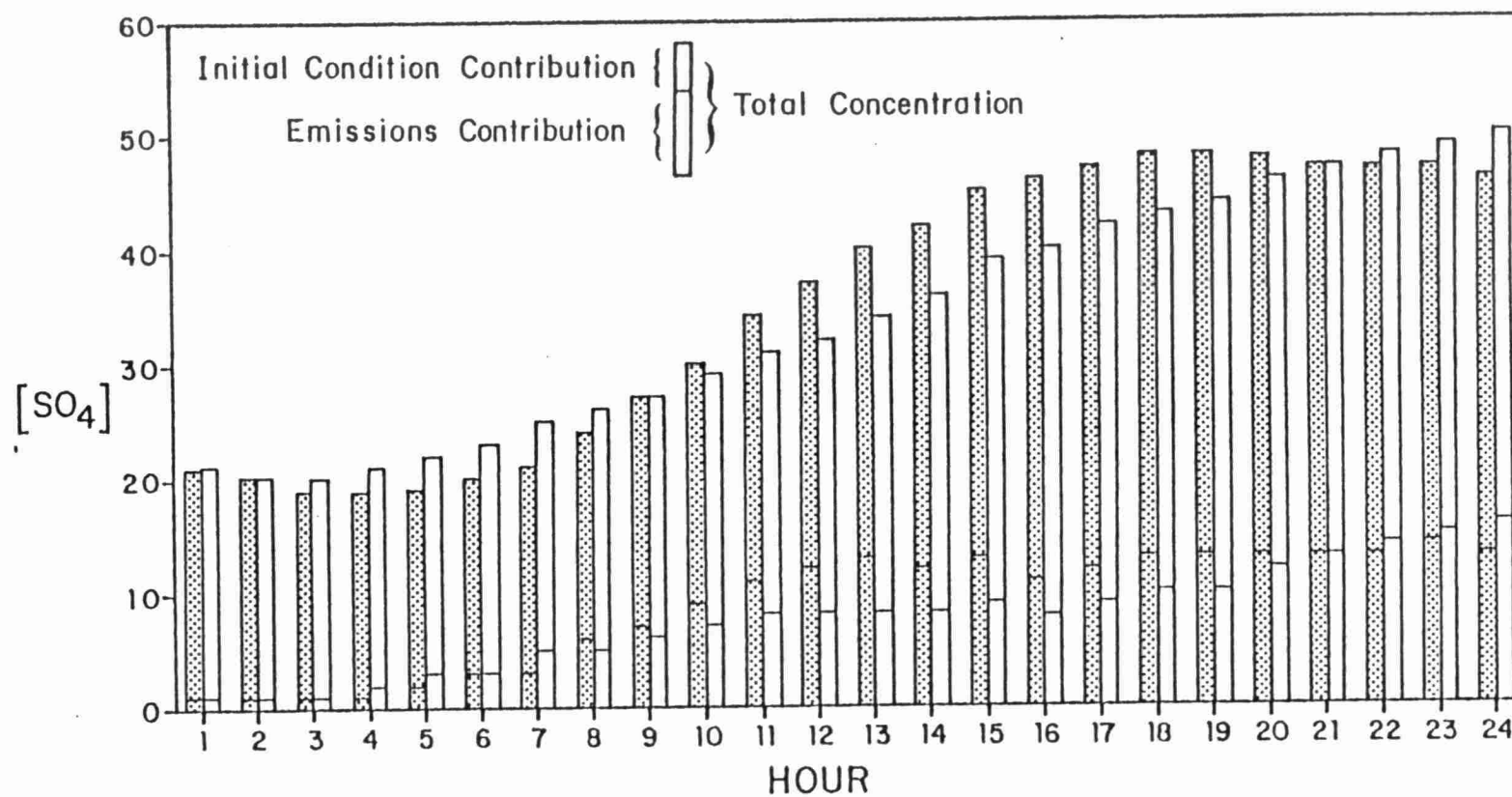


Figure 10-29. Comparison of hourly averaged  $SO_4$  from run 1 (shaded bar) and run 5 (unshaded bar) for grid square (16,13). The bars are divided, as shown, into emissions and initial condition components.

10-55

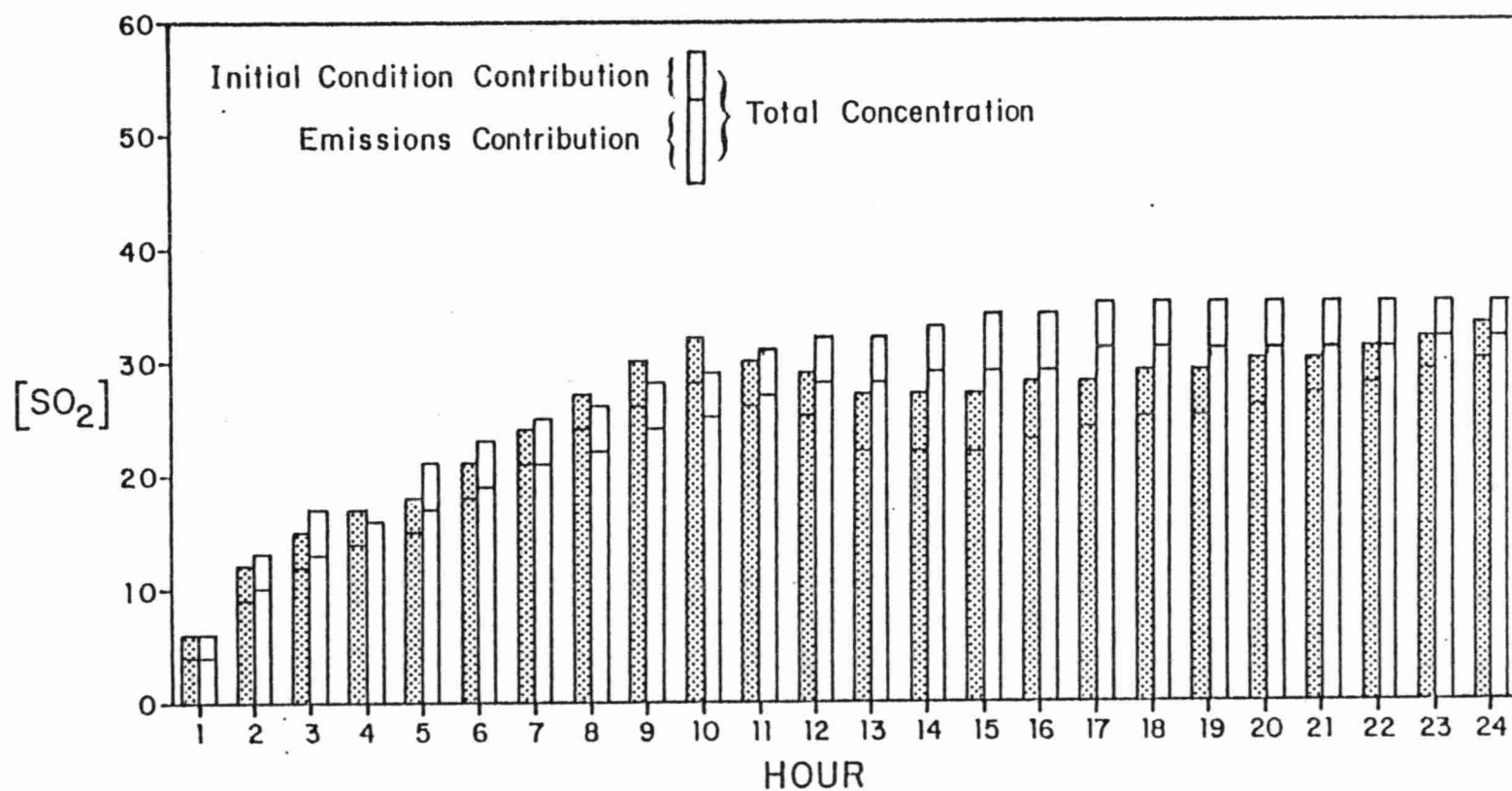


Figure 10-30. Comparison of hourly averaged SO<sub>2</sub> from run 1 (shaded bar) and run 5 (unshaded bar) for grid square (16,13). The bars are divided, as shown, into emissions and initial condition components.



TABLE 10-8  
 RUN 5 SULFUR MASS BALANCE  
 ( $10^9$  grams S)

<u>Component</u>	<u>SO<sub>2</sub>-</u>	<u>SO<sub>4</sub>-</u>
Initial concentrations	26.7	20.1
Emissions	47.1	0.94
Chemical conversion	-14.0	14.0
Deposition to ground	19.1	1.3
Residual	<u>3.4</u>	<u>-2.4</u>
Final concentration	44.0	31.4

## SURADS RESULTS FOR JULY 21, 1978

## RUN 6: AVERAGE EMISSION RATES

SURFACE CONCENTRATION OF 24-HOUR AVERAGED SO<sub>4</sub> (MICGR/M\*\*3)

	1	2	3	4	5	6	7	8	9	10	11	12	13	14	15	16	17	18	19	20	21	22	23	24	25	26	27	28	29	30
23 I	1	1	1	2	2	2	2	2	2	2	4	5	5	5	5	6	7	9	10	11	11	10	10	8	6	5	3	3	2	2
22 I	1	1	1	2	2	3	3	3	3	4	5	6	7	7	8	10	11	13	14	14	14	13	12	10	8	6	5	4	3	2
21 I	1	1	1	3	3	4	4	5	5	5	5	7	9	11	16	18	18	19	20	21	21	20	19	16	12	9	6	5	4	4
20 I	2	2	3	5	6	6	6	6	6	6	8	13	15	15	17	19	21	23	24	26	27	26	24	20	16	11	9	7	6	6
19 I	3	3	3	5	7	8	8	7	8	11	15	17	19	21	21	23	25	27	29	31	30	29	26	22	19	17	15	11	10	10
18 I	3	4	4	5	7	10	12	13	14	17	18	21	22	24	26	28	29	30	32	33	32	32	31	28	25	23	21	20	17	15
17 I	3	4	4	5	7	11	13	15	17	20	23	27	29	32	31	31	31	31	33	35	33	33	33	30	29	27	23	22	18	16
16 I	3	4	4	5	6	10	13	16	20	23	26	30	33	33	32	31	30	32	34	35	35	35	34	31	29	28	23	22	18	16
15 I	3	3	4	5	6	9	13	16	21	24	27	30	33	33	32	32	32	33	33	34	35	34	33	30	28	25	21	20	17	15
14 I	3	4	4	5	6	9	14	16	20	25	28	31	33	32	32	33	33	33	32	32	31	31	28	23	17	13	12	13	13	12
13 I	3	4	4	5	6	10	14	16	21	25	29	32	34	32	32	34	34	32	27	24	19	17	14	9	8	7	7	7	6	6
12 I	3	4	4	5	8	11	14	17	22	26	29	32	33	32	32	32	32	27	18	13	11	10	8	7	6	5	5	5	5	4
11 I	3	4	5	6	10	12	13	17	22	26	28	30	31	30	29	27	19	14	10	9	8	7	6	5	4	4	4	4	3	3
10 I	3	4	5	6	9	10	13	17	22	24	24	24	23	22	22	20	15	12	9	8	8	6	5	4	4	3	3	3	2	2
9 I	3	4	5	6	7	8	12	14	15	15	16	17	18	18	18	17	12	9	8	8	8	6	5	4	3	3	3	2	2	2
8 I	3	4	5	6	7	7	8	10	10	11	13	15	17	17	17	15	12	9	8	7	7	6	5	4	3	3	2	2	2	1
7 I	3	5	6	6	7	7	7	9	9	10	13	14	14	14	14	12	10	8	8	7	7	5	4	4	3	3	2	2	1	1
6 I	3	4	5	6	7	6	7	8	9	11	13	13	13	13	12	10	9	8	7	7	5	4	4	3	3	2	2	2	1	1
5 I	2	4	4	5	5	6	7	8	10	11	12	11	10	10	9	8	8	7	6	5	3	2	2	2	2	2	1	1	1	1
4 I	2	3	3	3	4	4	5	7	8	10	10	10	8	7	7	7	6	4	3	2	2	2	2	1	1	1	1	1	1	1
3 I	2	3	3	3	3	3	4	4	6	7	7	7	6	5	5	10	4	2	2	2	2	1	1	1	1	1	1	1	1	0
2 I	2	3	2	3	2	2	2	3	4	4	5	5	4	4	3	1	1	1	1	1	1	1	1	1	1	1	1	1	1	1
1 I	2	3	2	2	2	2	2	2	2	3	3	3	3	3	3	2	1	1	1	1	1	1	1	1	1	1	1	1	1	1

Figure 10-31. Calculated 24-hour average sulfate concentration ( $\mu\text{g}/\text{m}^3$ ) for run 6.

# BURADS RESULTS FOR JULY 21, 1978

## RUN 6: AVERAGE EMISSION RATES

### SURFACE CONCENTRATION OF 24-HOUR AVERAGED SO<sub>2</sub> (PPB)

10-53

	1	2	3	4	5	6	7	8	9	10	11	12	13	14	15	16	17	18	19	20	21	22	23	24	25	26	27	28	29	30
23 I	0	0	0	1	1	1	1	1	1	1	1	1	1	0	0	0	0	0	0	0	1	1	1	1	1	1	1	1	1	1
22 I	0	0	0	0	1	1	1	2	2	1	1	1	1	1	1	1	1	1	1	1	1	1	1	1	1	1	1	1	1	1
21 I	0	0	1	1	1	1	1	2	2	1	1	1	1	3	8	9	3	2	1	1	1	2	3	2	1	1	1	1	1	1
20 I	0	1	2	3	2	2	3	2	2	1	2	2	3	3	4	4	3	2	2	2	2	3	4	3	2	2	3	3	2	2
19 I	1	1	1	2	2	3	4	3	3	3	3	3	3	3	4	4	3	3	4	4	5	5	5	4	4	4	5	4	3	2
18 I	1	1	2	1	2	4	4	5	5	5	5	7	7	6	5	5	5	7	9	9	9	9	9	8	7	7	5	4	3	3
17 I	1	2	1	2	2	5	6	9	6	8	6	7	8	13	9	10	10	14	16	16	14	12	11	10	10	10	7	5	4	3
16 I	1	2	2	2	2	4	6	8	8	7	7	8	16	12	11	10	12	17	19	18	15	13	13	12	10	10	7	5	3	3
15 I	1	1	1	1	3	5	6	9	13	8	6	7	17	12	16	15	17	22	21	19	15	14	13	11	9	8	6	5	3	3
14 I	1	1	1	1	3	11	6	6	7	7	6	7	9	11	16	22	23	22	20	20	16	15	15	9	5	3	2	2	2	2
13 I	3	2	1	2	3	6	6	6	7	7	7	8	9	10	17	29	27	17	13	14	13	14	10	5	2	2	1	1	1	1
12 I	4	3	2	3	4	7	8	7	10	12	13	15	13	14	19	24	21	10	7	7	7	7	4	2	1	1	1	1	1	1
11 I	1	3	2	6	9	8	6	9	14	13	18	17	13	17	15	8	6	4	5	6	4	3	2	1	0	0	0	0	0	0
10 I	0	1	1	1	5	8	7	10	16	17	14	11	10	10	10	6	3	3	4	5	4	2	1	1	0	0	0	0	0	0
9 I	0	0	0	1	2	3	10	9	15	10	6	6	7	6	5	5	3	3	5	5	4	2	1	1	0	0	0	0	0	0
8 I	0	0	0	1	1	2	6	8	8	5	5	6	7	6	4	5	4	3	3	3	5	2	1	1	0	0	0	0	0	0
7 I	0	1	1	2	2	2	4	8	5	4	5	7	6	5	4	3	3	3	3	3	2	2	1	1	0	0	0	0	0	0
6 I	0	1	1	2	3	2	4	5	5	5	6	5	5	6	5	3	2	2	3	3	1	1	1	0	0	0	0	0	0	0
5 I	0	1	1	2	1	2	4	8	6	8	7	4	4	7	4	3	3	3	3	2	1	0	0	0	0	0	0	0	0	0
4 I	1	1	1	1	1	1	4	7	6	5	6	4	3	3	4	3	3	4	2	1	0	0	0	0	0	0	0	0	0	0
3 I	1	1	1	1	1	1	3	2	3	3	5	3	3	3	2	3	3	1	1	0	0	0	0	0	0	0	0	0	0	0
2 I	1	1	1	1	1	1	1	1	1	1	1	1	1	2	3	2	0	0	0	0	0	0	0	0	0	0	0	0	0	0
1 I	1	3	1	1	2	2	2	1	1	1	1	2	2	3	6	2	1	1	1	1	1	1	1	1	0	0	0	0	0	0

Figure 10-32. Calculated 24-hour average SO<sub>2</sub> concentration (ppb) for run 6.

# SURADS RESULTS FOR JULY 21, 1978

## RUN 6: AVERAGE EMISSION RATES

### SURFACE SULFUR DEPOSITION (METRIC TONS/DAY)

	1	2	3	4	5	6	7	8	9	10	11	12	13	14	15	16	17	18	19	20	21	22	23	24	25	26	27	28	29	30
23 I	2	2	2	4	5	4	4	4	4	4	5	5	5	4	3	4	4	5	5	5	5	6	6	6	6	5	5	5	4	4
22 I	2	1	1	3	5	10	10	16	17	9	5	5	4	4	6	11	10	8	7	6	6	7	8	9	7	6	5	6	4	3
21 I	2	2	8	8	7	8	11	11	12	10	6	6	7	18	49	55	23	13	10	9	11	13	22	16	11	9	11	9	5	5
20 I	2	4	14	20	15	13	25	14	13	10	12	17	19	21	30	30	23	16	16	17	20	24	29	22	19	16	20	24	12	11
19 I	6	8	10	15	16	26	31	24	24	19	20	25	25	24	27	27	25	25	32	34	37	40	36	30	32	34	40	26	18	17
18 I	7	12	13	11	17	28	29	36	37	37	37	48	52	45	34	36	42	49	61	63	64	65	62	54	51	53	37	30	23	19
17 I	6	13	10	12	15	35	41	58	45	55	45	48	63	93	67	66	70	103	109	113	93	82	76	69	75	71	46	37	26	21
16 I	5	20	13	17	17	31	43	57	54	50	51	58	120	84	75	70	80	113	127	120	101	93	94	83	76	77	50	38	25	20
15 I	6	9	11	11	24	35	44	72	94	56	46	53	113	82	120	103	113	139	139	128	105	94	94	78	65	59	41	34	24	19
14 I	8	8	9	11	25	75	45	45	46	48	45	50	64	79	121	160	158	146	136	133	107	104	111	62	35	18	14	14	14	12
13 I	20	14	11	15	21	42	42	45	50	51	53	58	66	70	119	194	181	115	89	97	88	100	67	29	15	10	8	7	6	6
12 I	29	19	15	19	28	50	54	52	73	85	94	107	95	94	127	159	140	66	50	53	48	49	24	11	7	5	5	4	4	4
11 I	8	22	15	37	66	65	46	67	99	91	116	114	91	110	102	58	42	30	33	43	30	20	11	6	4	3	3	3	3	3
10 I	3	7	6	11	33	56	48	69	107	115	97	75	67	72	74	44	26	23	30	33	25	15	9	5	3	3	2	1	1	1
9 I	2	3	4	5	11	22	63	61	96	66	43	45	46	42	35	33	27	22	35	39	28	16	9	5	3	2	1	1	1	1
8 I	2	3	4	6	10	14	39	52	52	34	34	42	45	44	31	33	29	19	26	24	37	17	8	5	3	2	1	1	1	1
7 I	2	5	7	12	13	15	28	57	36	31	35	50	39	36	29	24	25	23	20	19	16	12	6	4	3	1	1	1	1	1
6 I	2	7	8	14	23	17	28	33	34	36	43	35	33	42	36	24	17	18	21	22	10	5	4	3	2	1	1	1	1	0
5 I	3	8	7	12	11	13	29	49	46	49	48	30	30	46	33	20	21	20	26	14	4	2	2	2	2	1	1	1	0	0
4 I	5	8	6	7	7	10	27	43	43	38	40	29	20	24	25	23	20	24	14	3	2	2	1	1	1	1	1	1	0	0
3 I	4	7	9	6	6	10	28	13	18	19	31	20	19	23	16	20	22	9	3	2	2	2	1	1	1	1	1	1	1	1
2 I	6	8	7	9	10	8	9	8	7	8	7	8	9	16	21	10	2	2	2	2	2	2	2	2	1	1	1	1	1	1
1 I	7	19	10	7	13	15	14	8	9	10	11	15	12	20	42	15	5	4	4	4	4	4	3	3	3	3	3	3	3	3

Figure 10-33. Calculated cumulative sulfur deposition (metric tons) for run 6.

TABLE 10-9  
 RUN 6 SULFUR MASS BALANCE  
 ( $10^9$  grams S)

<u>Component</u>	<u>SO<sub>2</sub>-</u>	<u>SO<sub>4</sub>-</u>
Initial concentration	26.7	20.1
Emissions	47.1	0.94
Chemical conversion	-13.5	13.5
Deposition to ground	20.0	1.4
Residual	<u>2.3</u>	<u>-2.3</u>
Final concentrations	42.6	30.8

- The use of constant rather than time-varying conversion rate results in some significant ( $\sim \pm 20\%$ ) differences in hour-average concentration but generally has a much smaller ( $\lesssim 5\%$ ) effect on 24-hour average concentrations and cumulative deposition.
- The use of constant rather than horizontally- and temporally-varying  $K_z$ 's has a relatively small effect on the modeling region as a whole, but can have some very significant effects ( $\sim \pm 20\%$ ) on calculated concentrations and deposition in subregions of the grid.
- The use of constant deposition velocities results in a reduction of sulfur deposition by about  $6\frac{1}{2}\%$  overall and as much as 25% in high deposition subregions of the grid.
- The use of a model with constant conversion, vertical diffusion, and deposition has a average effect of less than 5% on the deposition and concentrations for the grid as a whole , but can have an effect that is 20% or more for individual hours and/or subregions of the grid.
- The use of constant emission rates rather than time-varying results in insignificant differences in the 24-hour concentrations and cumulative deposition.

One point should be clearly made regarding the simulation differences discussed above. The results that are compared are for one-day simulations only. Since all the models are run with the same initial concentrations (that is, have the same starting point), the differences that are seen during the first day are probably much smaller than those that would be seen during multiday simulations. This is especially true of the 24-hour average concentrations, which for a one-day simulation, are strongly influenced by the initial conditions.

To better illustrate the regional differences between the results of the complex model and the simple models, Figures 10-34 through 10-36 were prepared. These figures show the differences in hourly surface concentrations between Models 2 through 5 and Model 1 for three selected grid squares. The grid square are: (16,31), in

10-62

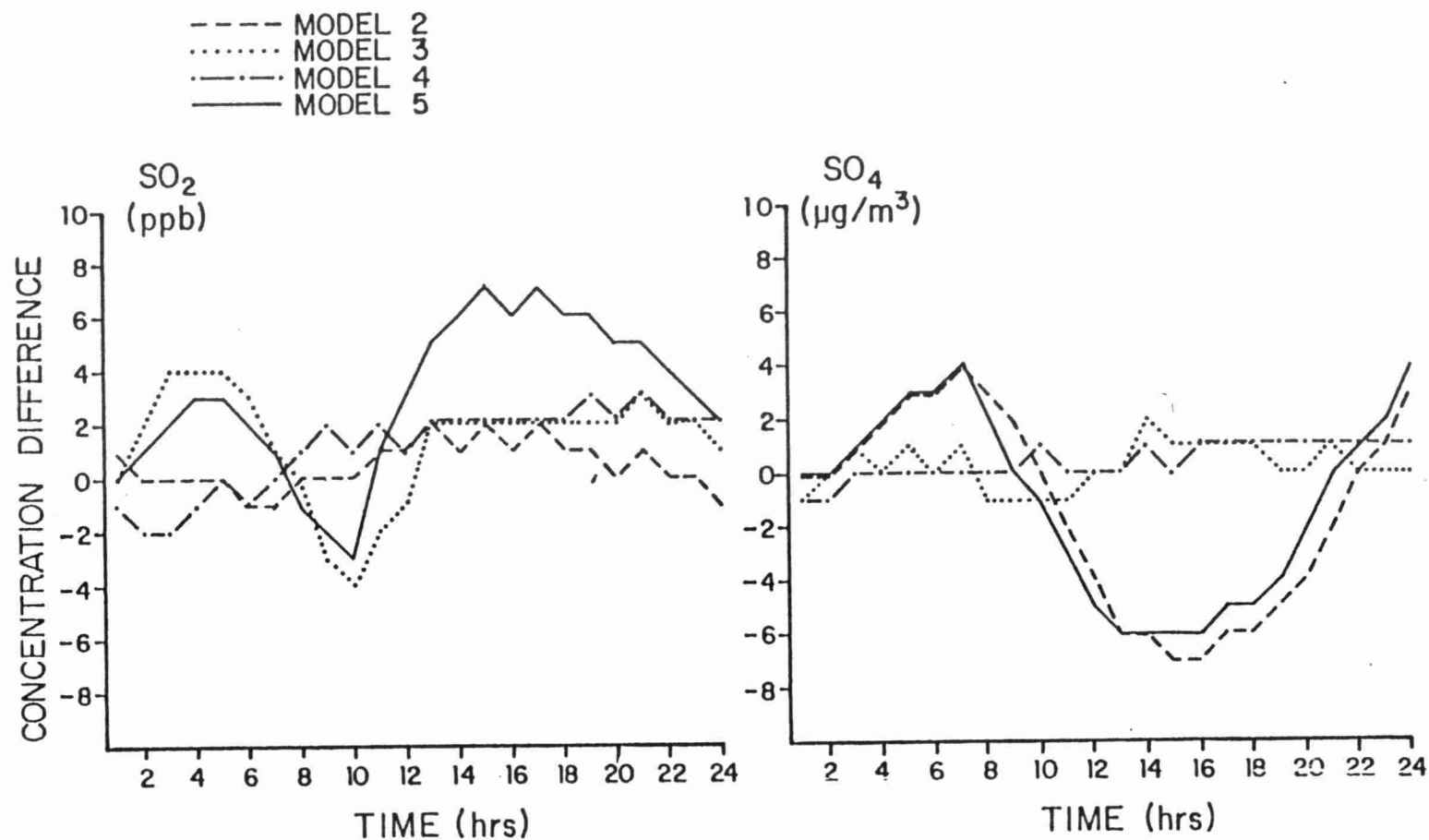


Figure 10-34. Differences in calculated hourly surface concentrations of  $\text{SO}_2$  and  $\text{SO}_4$  of the simple models' results relative to the complex model's for grid square (16,13).

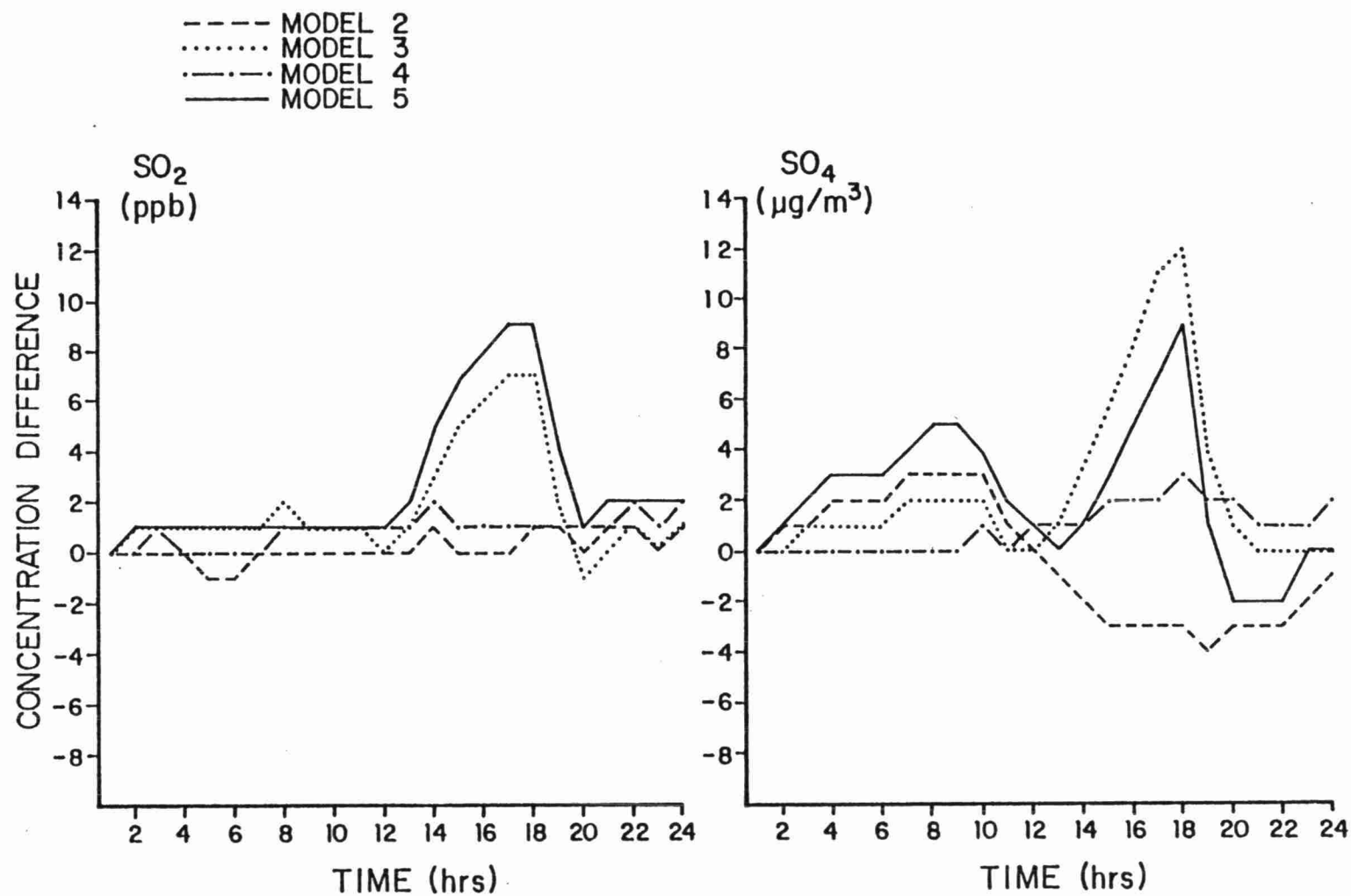


Figure 10-35. Differences in calculated hourly surface concentrations of SO<sub>2</sub> and SO<sub>4</sub> of the simple models' results relative to the complex model's for grid square (22,18).



10-64

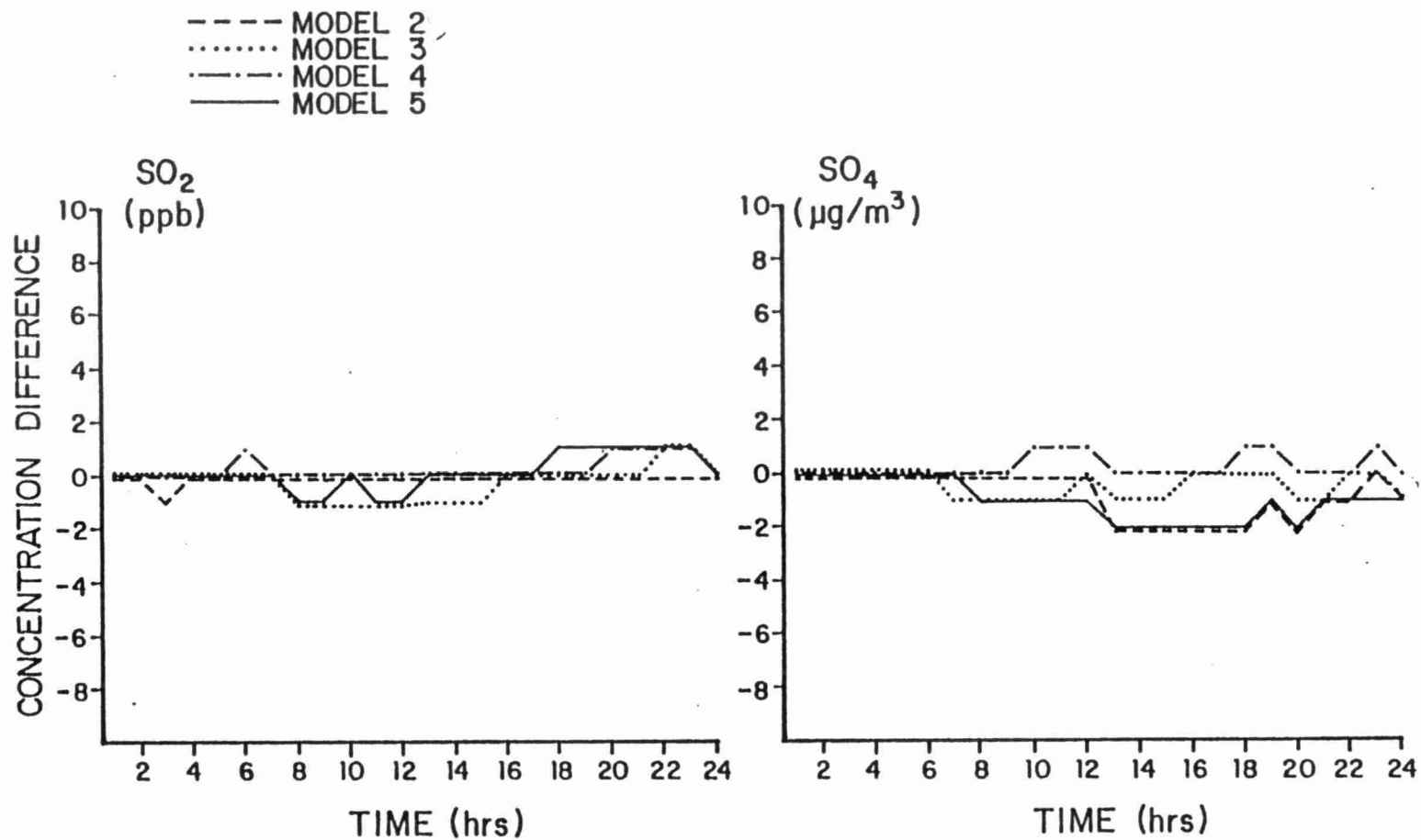


Figure 10-36. Differences in calculated hourly surface concentrations of  $\text{SO}_2$  and  $\text{SO}_4$  of the simple models' results relative to the complex model's for grid square (17,20).

northeastern Ohio Valley; (22,18), in the Adirondack Mountains of New York; and (17,20), in the Muskoka-Haliburton region of Ontario. The former grid square is in a high emissions density area, whereas the latter two squares are in sensitive receptor areas. Figure 10-34 shows that for square (16,13) the use of constant conversion rate in Models 2 and 5 appears to have the dominant effect on the calculated  $\text{SO}_4$  concentrations and the use of constant  $K_z$ 's (Model 3) effects the  $\text{SO}_2$  concentrations significantly during the first 12 hours of the simulation. The maximum differences for  $\text{SO}_4$  and  $\text{SO}_2$  with the compound simple model are seen in the afternoon. For grid square (22,18), shown in Figure 10-35, the use of constant  $K_z$ 's has the largest effect, especially on the calculated  $\text{SO}_2$  concentrations. The effects of constant conversion rate can be also seen in the calculated  $\text{SO}_4$  values, however. Again, the largest differences are seen in the afternoon. For grid square (17,20), the differences between the complex and the simple models (see Figure 10-36) are smaller than the differences seen in squares (16,13) and (22,18), but it should be noted that the absolute concentrations are also generally smaller. The use of constant conversion rate appears to have the largest effect on the calculated sulfate concentrations, whereas the use of constant  $K_z$ 's has the largest effect on the  $\text{SO}_2$  concentrations.

#### 10.1.5 Sensitivity of Long Range Transport Model to Emission Reductions

The sensitivity of the long range transport model(s) to emission reductions is one of the most important aspects of this sensitivity study. This section discusses the response of the complex model (1) and the compound simple model (5) to a substantial emission reduction (runs 1B and 5B).

As discussed in Section 10.1.2, the emission scenario considered for this test involved a 45% reduction of medium and tall stack  $\text{SO}_x$  emissions in the Ohio Valley region (primarily Ohio and Indiana). Figure 10-37 shows the percent change in total  $\text{SO}_x$  emissions for the modeling region and outlines the grid squares involved. The average reduction in emissions in this area was 36% which indicates surface

THE BURE GRID: JULY 21, 1978

PERCENT CHANGE IN SO<sub>x</sub> EMISSION RATE DUE TO REDUCTIONS IN INDIANA AND OHIO

	1	2	3	4	5	6	7	8	9	10	11	12	13	14	15	16	17	18	19	20	21	22	23	24	25	26	27	28	29	30
23 I	0	0	0	0	0	0	0	0	0	0	0	0	0	0	0	0	0	0	0	0	0	0	0	0	0	0	0	0	0	0
22 I	0	0	0	0	0	0	0	0	0	0	0	0	0	0	0	0	0	0	0	0	0	0	0	0	0	0	0	0	0	0
21 I	0	0	0	0	0	0	0	0	0	0	0	0	0	0	0	0	0	0	0	0	0	0	0	0	0	0	0	0	0	0
20 I	0	0	0	0	0	0	0	0	0	0	0	0	0	0	0	0	0	0	0	0	0	0	0	0	0	0	0	0	0	0
19 I	0	0	0	0	0	0	0	0	0	0	0	0	0	0	0	0	0	0	0	0	0	0	0	0	0	0	0	0	0	0
18 I	0	0	0	0	0	0	0	0	0	0	0	0	0	0	0	0	0	0	0	0	0	0	0	0	0	0	0	0	0	0
17 I	0	0	0	0	0	0	0	0	0	0	0	0	0	0	0	0	0	0	0	0	0	0	0	0	0	0	0	0	0	0
16 I	0	0	0	0	0	0	0	0	0	0	0	-40	-32	0	0	0	0	0	0	0	0	0	0	0	0	0	0	0	0	0
15 I	0	0	0	0	0	0	0	0	-40	-27	0	0	-42	0	-36	-33	0	0	0	0	0	0	0	0	0	0	0	0	0	0
14 I	0	0	0	0	0	0	0	0	0	0	0	0	-16	-39	-20	-22	-35	-44	0	0	0	0	0	0	0	0	0	0	0	0
13 I	0	0	0	0	0	0	0	0	0	-7	0	-9	0	0	-41	-42	-40	0	0	0	0	0	0	0	0	0	0	0	0	0
12 I	0	0	0	0	0	0	0	0	-37	-32	0	-12	-21	-32	-42	-43	-43	0	0	0	0	0	0	0	0	0	0	0	0	0
11 I	0	0	0	0	0	0	0	-41	-40	0	-45	-42	-12	-44	0	0	-42	0	0	0	0	0	0	0	0	0	0	0	0	0
10 I	0	0	0	0	0	0	0	-40	-43	-41	-44	-37	0	-40	-38	0	0	0	0	0	0	0	0	0	0	0	0	0	0	0
9 I	0	0	0	0	0	0	-43	-43	-45	0	0	0	0	0	0	0	0	0	0	0	0	0	0	0	0	0	0	0	0	0
8 I	0	0	0	0	0	0	0	-44	-44	0	0	0	0	0	0	0	0	0	0	0	0	0	0	0	0	0	0	0	0	0
7 I	0	0	0	0	0	0	0	0	0	0	0	0	0	0	0	0	0	0	0	0	0	0	0	0	0	0	0	0	0	0
6 I	0	0	0	0	0	0	0	0	0	0	0	0	0	0	0	0	0	0	0	0	0	0	0	0	0	0	0	0	0	0
5 I	0	0	0	0	0	0	0	0	0	0	0	0	0	0	0	0	0	0	0	0	0	0	0	0	0	0	0	0	0	0
4 I	0	0	0	0	0	0	0	0	0	0	0	0	0	0	0	0	0	0	0	0	0	0	0	0	0	0	0	0	0	0
3 I	0	0	0	0	0	0	0	0	0	0	0	0	0	0	0	0	0	0	0	0	0	0	0	0	0	0	0	0	0	0
2 I	0	0	0	0	0	0	0	0	0	0	0	0	0	0	0	0	0	0	0	0	0	0	0	0	0	0	0	0	0	0
1 I	0	0	0	0	0	0	0	0	0	0	0	0	0	0	0	0	0	0	0	0	0	0	0	0	0	0	0	0	0	0

Figure 10-37. Percent change in SO<sub>x</sub> emission rate due to 45% reduction in elevated source emissions in Indiana, Ohio and parts of surrounding states.

10-66

and elevated emissions contribute approximately 20 and 80% of the emissions in this area, respectively. The Ohio Valley baseline emissions represent about half the modeling region  $\text{SO}_x$  emissions, hence the scenario represents a 17% reduction in total modeling region emissions.

The response of the models to the emission reduction is best illustrated by maps of concentration differences and percent change in model outputs. The maps of 24th hour  $\text{SO}_2$  and  $\text{SO}_4$  concentrations differences are shown in Figures 10-38 through 10-43 for runs 1B and 5B (relative to runs 1 and 5). Since the baseline problem is somewhat dominated by initial concentrations, maps of the percentage change in the "emissions contribution" of model outputs are presented in Figure 10-44 through 10-49. The changes in the emissions contributions are generally 5 to 20% greater than the changes in the absolute concentrations.

The absolute reduction in  $\text{SO}_2$  and  $\text{SO}_4$  concentrations are quite similar in runs 1B and 5B. The final  $\text{SO}_2$  concentrations were reduced up to 12 and 13 ppb in runs 1B and 5B, respectively. The 24-hour average  $\text{SO}_2$  concentrations were reduced up to 9 and 10 ppb in runs 1B and 5B, respectively. The greatest differences in absolute  $\text{SO}_2$  concentration occurred in the grid squares with highest emission strengths, as would be expected. The final  $\text{SO}_4$  concentrations were reduced up to  $9 \mu\text{g}/\text{m}^3$  in run 1B and  $8 \mu\text{g}/\text{m}^3$  in 5B; the 24-hour average  $\text{SO}_4$  concentration showed somewhat smaller differences (5 to  $4 \mu\text{g}/\text{m}^3$ ). For both models, the largest absolute differences in  $\text{SO}_4$  concentration were predicted to occur just downwind of the Ohio Valley, as shown in Figure 10-36. The zone of influence extends approximately 250 km beyond the emission reduction region. Had the model been run for a longer time period, we expect the effects of the emission reduction on  $\text{SO}_4$  and  $\text{SO}_2$  concentrations could be seen much farther downwind of the Ohio Valley than shown in this test.

For the sulfur deposition, the largest absolute reduction in any grid squares was 66 metric tons for run 1B and 62 metric tons for Run 5B. In both cases, the largest absolute reduction occurred at the northern end of the Ohio Valley (at the Ohio-West

# SURADS RESULTS FOR JULY 21, 1978

## COMPARISON OF RUN 1B TO RUN 1

### DIFFERENCE IN SURFACE CONCENTRATION OF SO<sub>2</sub> (PPB) FOR HOUR 24

89-01

	1	2	3	4	5	6	7	8	9	10	11	12	13	14	15	16	17	18	19	20	21	22	23	24	25	26	27	28	29	30
23 I	0	0	0	0	0	0	0	0	0	0	0	0	0	0	0	0	0	0	0	0	0	0	0	0	0	0	0	0	0	
22 I	0	0	0	0	0	0	0	0	0	0	0	0	0	0	0	0	0	0	0	0	0	0	0	0	0	0	0	0	0	
21 I	0	0	0	0	0	0	0	0	0	0	0	0	0	0	0	0	0	0	0	0	0	0	0	0	0	0	0	0	0	
20 I	0	0	0	0	0	0	0	0	0	0	0	0	0	0	0	-1	0	0	0	0	0	0	0	0	0	0	0	0	0	
19 I	0	0	0	0	0	0	0	0	0	0	0	0	1	0	0	0	0	-1	0	0	-1	-1	0	0	0	0	0	0	0	
18 I	0	0	0	0	0	0	0	0	0	0	0	0	0	0	0	0	-1	-1	-1	0	-1	0	0	0	0	0	0	0	0	
17 I	0	0	0	0	0	0	0	-1	-1	-1	0	-1	-2	-3	-3	-2	-2	-2	-2	-1	-2	-1	0	0	0	0	0	0	0	
16 I	0	0	0	0	0	-1	0	-1	-2	-1	-1	-2	-5	-4	-3	-3	-3	-3	-2	-1	-2	-1	0	-1	0	0	0	0	0	
15 I	0	0	0	0	0	0	0	-1	-4	-2	-1	-3	-6	-4	-7	-6	-5	-7	-5	-3	-2	-2	-1	0	0	0	0	0	0	
14 I	0	0	0	0	0	0	0	-1	-1	-2	-2	-1	-2	-5	-6	-10	-10	-9	-4	-3	-2	-2	-1	0	0	0	0	0	0	
13 I	0	0	0	0	0	0	-1	0	-1	-2	-1	-2	-2	-3	-7	-12	-11	-9	-4	-3	-2	-1	-1	0	0	0	0	0	0	
12 I	0	0	1	0	0	0	-1	-2	-3	-3	-4	-5	-4	-4	-8	-10	-9	-5	-2	-1	-1	0	0	0	0	0	0	0	0	
11 I	0	0	0	0	0	-1	-1	-4	-8	-7	-7	-7	-4	-6	-6	-3	-2	-1	0	0	0	0	0	0	0	0	0	0	0	
10 I	0	0	0	0	0	-1	-2	-4	-8	-9	-8	-4	-3	-3	-3	-3	-1	0	-1	0	0	0	0	0	0	0	0	0	0	
9 I	0	0	0	0	0	-2	-3	-4	-7	-5	-2	-1	-1	-1	0	0	-1	0	0	0	0	0	0	0	0	0	0	0	0	
8 I	0	0	0	0	0	-1	-1	-2	-2	-1	0	-1	0	0	0	0	0	0	0	0	0	0	0	0	0	0	0	0	0	
7 I	0	0	0	0	0	0	0	-1	0	-1	0	0	-1	0	0	0	0	0	0	0	0	0	0	0	0	0	0	0	0	
6 I	0	0	0	0	0	0	0	0	0	0	0	0	0	0	0	0	0	0	0	0	0	0	0	0	0	0	0	0	0	
5 I	0	0	0	0	0	0	0	0	0	0	0	0	0	0	0	0	0	0	0	0	0	0	0	0	0	0	0	0	0	
4 I	0	0	0	0	0	0	0	0	0	0	0	0	0	0	0	0	0	0	0	0	0	0	0	0	0	0	0	0	0	
3 I	0	0	0	0	0	0	0	0	0	0	0	0	0	0	0	0	0	0	0	0	0	0	0	0	0	0	0	0	0	
2 I	0	0	0	0	0	0	0	0	0	0	0	0	0	0	0	0	0	0	0	0	0	0	0	0	0	0	0	0	0	
1 I	0	0	0	0	0	0	0	0	0	0	0	0	0	0	0	0	0	0	0	0	0	0	0	0	0	0	0	0	0	

Figure 10-38. Model 1 changes in calculated hour 24 SO<sub>2</sub> concentration (ppb) due to emission reductions.

# SURADS RESULTS FOR JULY 21, 1978

## COMPARISON OF RUN 1B TO RUN 1

### DIFFERENCE IN SURFACE CONCENTRATION OF SO4 (MICR/M\*\*3) FOR HOUR 24

	1	2	3	4	5	6	7	8	9	10	11	12	13	14	15	16	17	18	19	20	21	22	23	24	25	26	27	28	29	30	
23 I	0	0	0	0	0	0	0	0	0	0	0	0	0	0	0	0	0	0	0	0	0	0	0	0	0	0	0	0	0	0	
22 I	0	0	0	0	0	0	0	0	0	0	0	0	0	0	0	0	0	0	0	0	0	0	0	0	0	0	0	0	0	0	
21 I	0	0	0	0	0	0	0	0	0	0	0	0	0	0	0	-1	0	0	0	0	0	0	0	0	0	0	0	0	0	0	
20 I	0	0	0	0	-1	0	0	0	0	0	0	1	0	1	0	0	0	0	0	0	0	1	0	1	0	0	0	0	0	0	
19 I	0	0	0	0	0	0	0	0	0	0	-1	-1	-1	-1	-1	0	-1	-1	-1	-1	-1	-1	-1	0	0	0	0	0	0	0	
18 I	0	0	0	0	0	0	0	1	0	0	-1	-1	-1	-1	-2	-3	-2	-3	-3	-2	-2	-1	-1	0	-1	0	0	0	0	0	
17 I	0	0	0	0	0	0	0	0	0	0	-1	-1	-1	-2	-2	-3	-4	-4	-4	-4	-4	-2	-1	-1	-1	0	0	0	0	0	
16 I	0	0	0	0	0	0	0	0	0	-1	-1	-2	-1	-2	-2	-4	-4	-5	-5	-6	-5	-4	-1	-1	-1	0	0	0	0	0	
15 I	0	0	0	0	-1	0	0	0	-1	0	-1	-1	-2	-2	-2	-5	-6	-6	-7	-6	-5	-3	-2	-1	-1	1	0	0	1	0	
14 I	0	0	0	0	0	0	0	0	0	-1	-1	-2	-3	-3	-2	-5	-6	-6	-7	-6	-5	-4	-3	-1	1	0	0	0	0	0	
13 I	0	0	0	0	0	0	0	0	0	-2	-2	-2	-3	-4	-3	-5	-6	-6	-6	-9	-6	-3	-1	0	0	0	0	0	0	0	0
12 I	0	0	0	0	0	0	0	-2	-1	-1	-4	-4	-4	-4	-4	-6	-6	-7	-5	-2	0	0	0	0	0	0	0	0	0	0	0
11 I	0	0	0	1	0	0	0	-2	-3	-4	-5	-4	-4	-4	-3	-4	-3	-2	-1	0	0	0	0	1	0	0	0	0	0	0	0
10 I	0	0	0	0	0	0	-1	-3	-3	-3	-4	-3	-4	-4	-3	-3	-2	-2	-1	0	0	0	0	0	0	0	0	0	0	0	0
9 I	0	0	0	0	0	-1	-1	-2	-2	-3	-2	-2	-2	-1	-1	-1	0	0	1	0	0	0	0	0	0	0	0	0	0	0	0
8 I	0	0	0	0	0	0	-1	-1	-1	-1	-1	-1	-1	0	0	0	-1	0	0	0	0	0	0	0	0	0	0	0	0	0	0
7 I	0	0	0	0	0	0	-1	0	-1	0	0	0	1	1	0	1	0	0	0	0	0	0	0	0	0	0	0	0	0	0	0
6 I	0	0	0	0	0	0	0	1	0	0	1	1	0	1	-1	0	0	0	0	0	0	0	0	0	0	0	0	0	0	0	0
5 I	0	0	0	0	0	0	0	0	1	0	1	0	0	0	0	0	0	0	0	0	0	0	0	0	0	0	0	0	0	0	0
4 I	0	0	0	0	0	0	0	0	0	0	0	0	0	0	0	0	0	0	0	0	0	0	0	0	0	0	0	0	0	0	0
3 I	0	0	0	0	0	0	0	0	0	0	0	0	0	0	0	0	0	0	0	0	0	0	0	0	0	0	0	0	0	0	0
2 I	0	0	0	0	0	0	0	0	0	0	0	0	0	0	0	0	0	0	0	0	0	0	0	0	0	0	0	0	0	0	0
1 I	0	0	0	0	0	0	0	0	0	0	0	0	0	0	0	0	0	0	0	0	0	0	0	0	0	0	0	0	0	0	0

Figure 10-39. Model 1 changes in calculated hour 24 sulfate concentration ( $\mu\text{g}/\text{m}^3$ ) due to emission reductions.

# SURADS RESULTS FOR JULY 21, 1978

## COMPARISON OF RUN 1B TO RUN 1

### DIFFERENCE IN SURFACE SULFUR DEPOSITION (METRIC TONS/DAY)

10-70

		1	2	3	4	5	6	7	8	9	10	11	12	13	14	15	16	17	18	19	20	21	22	23	24	25	26	27	28	29	30
	I	+	+	+	+	+	+	+	+	+	+	+	+	+	+	+	+	+	+	+	+	+	+	+	+	+	+	+	+	+	+
23	I	0	0	0	0	0	0	0	0	0	0	0	0	0	0	0	0	0	0	0	0	0	0	0	0	0	0	0	0	0	0
22	I	0	0	0	0	0	0	0	0	0	0	0	0	0	0	0	0	1	0	0	0	0	0	0	0	0	0	0	0	0	0
21	I	0	0	0	0	0	0	0	0	0	0	0	0	0	0	0	0	0	0	0	0	0	0	0	0	0	0	0	0	0	0
20	I	0	0	0	0	0	0	0	0	0	0	0	0	1	1	0	0	0	0	0	0	1	0	1	0	0	0	0	0	0	0
19	I	0	0	0	0	0	0	0	0	1	1	1	3	0	0	0	0	0	0	0	0	-1	0	1	0	0	0	0	0	0	0
18	I	0	0	0	0	-1	0	0	0	0	-1	-2	-2	-4	-2	1	1	0	-1	-1	-1	-1	0	0	0	0	0	0	0	0	0
17	I	0	0	0	0	0	0	0	-1	-2	-3	-5	-4	-9	-12	-14	-11	-9	-9	-6	-5	-3	-1	0	-1	0	0	1	0	0	0
16	I	0	0	0	0	0	0	1	-4	-6	-6	-5	-11	-26	-18	-18	-13	-11	-10	-8	-7	-4	-2	-1	-1	0	0	0	0	0	0
15	I	0	0	0	0	0	0	1	-5	-22	-9	-6	-8	-25	-19	-37	-29	-27	-27	-20	-12	-8	-4	-3	0	0	0	0	0	0	0
14	I	0	0	0	0	0	0	1	-3	-6	-6	-6	-7	-11	-16	-30	-47	-49	-37	-22	-13	-8	-4	-2	-1	0	0	0	0	0	0
13	I	0	0	0	0	0	0	0	-2	-6	-8	-7	-7	-11	-13	-33	-66	-63	-37	-21	-14	-9	-5	-4	0	0	0	0	0	0	0
12	I	0	0	0	1	1	-2	-2	-7	-14	-18	-25	-28	-24	-23	-36	-52	-48	-23	-6	-4	-2	0	0	0	0	0	0	0	0	0
11	I	0	0	0	0	-1	-2	-5	-18	-29	-30	-37	-34	-23	-31	-29	-15	-8	-4	-1	-1	0	-1	0	0	0	0	0	0	0	0
10	I	0	0	0	1	-1	-3	-8	-19	-34	-38	-32	-18	-14	-17	-17	-11	-3	-1	0	0	0	0	0	0	0	0	0	0	0	0
9	I	0	0	0	0	0	-4	-16	-18	-36	-21	-6	-4	-5	-4	-3	-2	-2	-1	0	0	0	0	0	0	0	0	0	0	0	0
8	I	0	0	0	0	0	-1	-9	-11	-11	-3	-3	-2	-2	-1	-1	-1	-1	0	0	0	0	0	0	0	0	0	0	0	0	0
7	I	0	0	0	0	0	0	0	-1	-1	-1	-1	-1	-1	0	0	0	0	0	0	0	0	0	0	0	0	0	0	0	0	0
6	I	0	0	0	0	0	0	1	0	0	0	0	0	0	0	0	0	0	0	0	0	0	0	0	0	0	0	0	0	0	0
5	I	0	0	0	0	0	0	0	0	0	0	1	0	0	0	0	0	0	0	0	0	0	0	0	0	0	0	0	0	0	0
4	I	0	0	0	0	0	0	0	0	0	0	0	0	0	0	0	0	0	0	0	0	0	0	0	0	0	0	0	0	0	0
3	I	0	0	0	0	0	0	0	0	0	0	0	0	0	0	0	0	0	0	0	0	0	0	0	0	0	0	0	0	0	0
2	I	0	0	0	0	0	0	0	0	0	0	0	0	0	0	0	0	0	0	0	0	0	0	0	0	0	0	0	0	0	0
1	I	0	0	0	0	0	0	0	0	0	0	0	0	0	0	0	0	0	0	0	0	0	0	0	0	0	0	0	0	0	0

Figure 10-40. Model 1 changes in cumulative sulfur deposition (metric tons) due to emission reductions.

# SURADS RESULTS FOR JULY 21, 1978

## COMPARISON OF RUN 5B TO RUN 5

### DIFFERENCE IN SURFACE CONCENTRATION OF SO<sub>2</sub> (PPB) FOR HOUR 24

		1	2	3	4	5	6	7	8	9	10	11	12	13	14	15	16	17	18	19	20	21	22	23	24	25	26	27	28	29	30
23	I	0	0	0	0	0	0	0	0	0	0	0	0	0	0	0	0	0	0	0	0	0	0	0	0	0	0	0	0	0	0
22	I	0	0	0	0	0	0	0	0	0	0	0	0	0	0	0	0	0	0	0	0	0	0	0	0	0	0	0	0	0	0
21	I	0	0	0	0	0	0	0	0	0	0	0	0	0	0	0	0	0	0	0	0	0	0	0	0	0	0	0	0	0	0
20	I	0	0	0	0	0	0	0	0	0	0	0	0	1	0	0	0	0	0	0	0	1	0	0	1	0	0	0	0	0	0
19	I	0	0	0	0	0	0	0	0	0	0	0	0	1	0	0	0	0	0	-1	0	0	0	-1	1	0	0	0	0	0	0
18	I	0	0	0	0	0	0	0	0	0	0	0	0	0	1	0	0	-1	-1	-1	-1	-1	-1	0	0	0	0	0	0	0	0
17	I	0	0	0	0	0	0	0	0	0	-1	-1	-1	-1	-3	-3	-3	-2	-3	-3	-2	-2	-1	-1	0	0	-1	0	0	0	0
16	I	0	0	0	0	0	0	0	-1	-1	0	-1	-2	-5	-3	-4	-3	-3	-3	-3	-2	-2	-2	0	-1	0	0	1	0	0	0
15	I	0	0	0	0	0	0	0	0	-4	-1	-1	-2	-6	-4	-6	-6	-6	-7	-5	-4	-3	-2	-1	-1	0	0	0	0	0	0
14	I	0	0	0	0	0	0	0	0	0	-1	-1	-1	-2	-5	-5	-10	-11	-10	-5	-3	-3	-1	-2	-1	0	0	0	0	0	0
13	I	0	0	0	0	0	0	0	0	-1	-1	-1	-2	-2	-3	-7	-13	-12	-10	-5	-3	-3	-2	-1	0	0	0	0	0	0	0
12	I	0	0	0	0	0	-1	-1	-2	-3	-3	-5	-5	-4	-4	-8	-12	-10	-6	-2	-1	-1	0	0	0	0	0	0	0	0	0
11	I	0	0	0	0	0	-1	-1	-4	-6	-6	-8	-7	-5	-7	-7	-4	-3	-1	-1	-1	0	0	0	0	0	0	0	0	0	0
10	I	0	0	0	0	1	-1	-2	-5	-8	-8	-7	-4	-3	-5	-5	-3	-1	-1	0	0	0	0	0	0	0	0	0	0	0	0
9	I	0	0	0	0	0	-2	-4	-3	-7	-5	-1	-1	-1	-1	0	-1	0	0	0	0	-1	0	0	0	0	0	0	0	0	0
8	I	0	0	0	0	0	-1	-2	-2	-2	0	0	0	0	-1	0	-1	0	0	0	0	0	0	0	0	0	0	0	0	0	0
7	I	0	0	0	0	0	0	0	0	0	0	0	0	-1	0	0	1	0	0	0	0	0	0	0	0	0	0	0	0	0	0
6	I	0	0	0	0	0	0	0	0	0	-1	0	0	0	0	0	0	0	0	0	0	0	0	0	0	0	0	0	0	0	0
5	I	0	0	0	0	0	0	0	0	0	0	0	0	0	0	0	0	0	0	0	0	0	0	0	0	0	0	0	0	0	0
4	I	0	0	0	0	0	0	0	0	0	0	0	0	0	0	0	0	0	0	0	0	0	0	0	0	0	0	0	0	0	0
3	I	0	0	0	0	0	0	0	0	0	0	0	0	0	0	0	0	0	0	0	0	0	0	0	0	0	0	0	0	0	0
2	I	0	0	0	0	0	0	0	0	0	0	0	0	0	0	0	0	0	0	0	0	0	0	0	0	0	0	0	0	0	0
1	I	0	0	0	0	0	0	0	0	0	0	0	0	0	0	0	0	0	0	0	0	0	0	0	0	0	0	0	0	0	0

Figure 10-41. Model 5 changes in hour 24 SO<sub>2</sub> concentration (ppb) due to emission reductions.



# SURADB RESULTS FOR JULY 21, 1978

## COMPARISON OF RUN 5B TO RUN 5

### DIFFERENCE IN SURFACE CONCENTRATION OF SO4 (MICR/M\*\*3) FOR HOUR 24

	1	2	3	4	5	6	7	8	9	10	11	12	13	14	15	16	17	18	19	20	21	22	23	24	25	26	27	28	29	30
23 I	0	0	0	0	0	0	0	0	0	0	0	0	0	0	0	0	0	0	0	1	0	0	0	0	0	0	0	0	0	0
22 I	0	0	0	0	0	0	0	0	0	0	0	0	0	0	0	0	0	0	0	0	0	0	0	0	0	0	0	0	0	0
21 I	0	0	0	0	0	0	0	0	0	0	0	0	0	0	0	0	0	0	0	0	0	0	0	0	0	0	0	0	0	0
20 I	0	0	0	0	0	0	0	0	0	0	0	1	1	1	0	0	0	0	0	0	0	1	1	0	0	0	0	0	0	0
19 I	0	0	0	0	0	0	0	0	0	0	0	1	0	0	0	-1	0	0	-1	-1	-1	-1	0	0	0	1	0	0	0	0
18 I	0	0	0	0	0	0	0	0	0	0	-1	-1	0	0	-1	-2	-2	-3	-2	-2	-2	-1	-1	0	0	0	0	1	0	0
17 I	0	0	0	0	0	0	0	0	0	-1	-1	-1	-1	-2	-3	-3	-3	-3	-3	-3	-3	-2	-1	-1	-1	-1	0	0	0	0
16 I	0	0	0	0	0	0	0	0	0	0	0	0	-2	-3	-3	-3	-3	-4	-5	-5	-4	-2	-2	-1	-1	-1	0	0	0	0
15 I	0	0	0	0	0	0	0	0	-1	-1	-1	-2	-3	-2	-3	-5	-7	-7	-7	-5	-5	-3	-2	-1	0	0	0	0	0	0
14 I	0	0	0	0	0	0	0	0	0	-1	-1	-2	-3	-3	-3	-6	-7	-6	-7	-6	-4	-4	-3	-2	0	1	0	0	0	0
13 I	0	0	0	0	0	0	0	0	0	-2	-1	-2	-4	-3	-3	-7	-7	-7	-7	-8	-5	-2	-1	0	0	0	0	0	0	0
12 I	0	0	0	1	0	0	0	-1	-1	-2	-4	-4	-4	-4	-5	-8	-8	-8	-5	-2	-1	0	0	0	0	0	-1	0	0	0
11 I	0	0	0	0	0	0	-1	-2	-5	-4	-5	-4	-4	-4	-5	-4	-4	-2	-1	0	0	0	0	0	0	0	0	0	0	0
10 I	0	0	0	0	0	0	-1	-3	-4	-5	-4	-4	-5	-4	-2	-2	-2	-1	-1	0	0	0	0	0	0	0	0	0	0	0
9 I	0	0	0	0	0	0	-2	-2	-3	-3	-2	-2	-1	0	0	0	-1	0	0	0	0	0	0	0	0	0	0	0	0	0
8 I	0	0	0	0	0	0	-1	-2	-2	-1	-1	0	-1	-1	-1	0	0	0	0	0	0	0	0	0	0	0	0	0	0	0
7 I	0	0	0	0	0	0	0	0	-1	0	-1	-1	0	0	1	1	0	0	0	0	0	0	0	0	0	0	0	0	0	0
6 I	0	0	0	0	0	0	1	0	0	-1	0	0	0	0	0	0	0	0	0	0	0	0	0	0	0	0	0	0	0	0
5 I	0	0	0	0	1	0	0	0	0	1	1	0	0	0	0	0	0	0	0	0	0	0	0	0	0	0	0	0	0	0
4 I	0	0	0	0	0	0	0	0	0	0	0	0	0	0	0	0	0	0	0	0	0	0	0	0	0	0	0	0	0	0
3 I	0	0	0	0	0	0	0	0	0	0	0	0	0	0	0	0	0	0	0	0	0	0	0	0	0	0	0	0	0	0
2 I	0	0	0	0	0	0	0	0	0	0	0	0	0	0	0	0	0	0	0	0	0	0	0	0	0	0	0	0	0	0
1 I	0	0	0	0	0	0	0	0	0	0	0	0	0	0	0	0	0	0	0	0	0	0	0	0	0	0	0	0	0	0

Figure 10-42. Model 5 changes in calculated hour 24 sulfate concentration ( $\mu\text{g}/\text{m}^3$ ) due to emission reductions.

# SURADS RESULTS FOR JULY 21, 1978

## COMPARISON OF RUN 5B TO RUN 5

### DIFFERENCE IN SURFACE SULFUR DEPOSITION (METRIC TONS/DAY)

		1	2	3	4	5	6	7	8	9	10	11	12	13	14	15	16	17	18	19	20	21	22	23	24	25	26	27	28	29	30
	I	+	+	+	+	+	+	+	+	+	+	+	+	+	+	+	+	+	+	+	+	+	+	+	+	+	+	+	+	+	+
23	I	0	0	0	0	0	0	0	0	0	0	0	0	0	0	0	0	0	0	0	0	0	0	0	0	0	0	0	0	0	0
22	I	0	0	0	0	0	0	0	0	0	0	0	0	0	0	0	0	0	0	0	0	0	0	0	0	0	0	0	0	0	0
21	I	0	0	0	0	0	0	0	0	0	0	0	0	0	1	1	0	1	0	0	1	0	0	0	0	0	0	0	0	0	0
20	I	0	0	0	0	0	0	0	0	0	0	0	0	0	1	1	0	0	0	0	0	0	0	0	0	0	0	0	0	0	0
19	I	0	0	0	0	0	0	0	0	0	0	0	3	2	1	1	0	0	0	0	0	0	0	0	0	0	0	0	0	0	0
18	I	0	0	0	0	0	0	0	1	1	0	-1	-3	-2	3	2	-1	0	-1	-1	0	-1	-1	0	0	0	0	0	0	0	0
17	I	0	0	0	0	0	0	0	-1	-2	-3	-4	-5	-7	-13	-13	-10	-9	-7	-6	-6	-3	-1	-1	0	0	0	0	0	0	0
16	I	0	0	0	0	0	0	2	-3	-6	-6	-5	-9	-26	-17	-17	-13	-10	-9	-9	-6	-4	-1	-2	-1	0	0	0	0	0	0
15	I	0	0	0	0	0	0	0	-4	-20	-8	-6	-8	-29	-18	-30	-25	-23	-22	-15	-11	-7	-2	-1	-1	0	0	1	0	0	0
14	I	0	0	0	0	0	1	0	-2	-4	-6	-6	-5	-10	-17	-25	-45	-44	-33	-17	-11	-5	-3	-1	0	0	0	0	0	0	0
13	I	0	0	0	0	0	-1	-1	-2	-4	-5	-5	-6	-8	-12	-34	-62	-59	-33	-19	-12	-7	-4	-2	0	1	1	0	0	0	0
12	I	0	0	0	0	0	-1	-3	-7	-15	-18	-21	-23	-20	-22	-36	-51	-48	-17	-5	-3	-1	0	0	0	0	0	0	0	0	0
11	I	0	0	0	1	0	-3	-7	-19	-31	-26	-36	-30	-21	-31	-29	-14	-10	-4	-1	0	-1	0	0	0	0	0	0	0	0	0
10	I	0	0	0	0	1	-4	-11	-21	-38	-36	-30	-17	-14	-19	-18	-11	-4	-1	-1	0	0	0	0	0	0	0	0	0	0	0
9	I	0	0	0	0	0	-6	-19	-20	-36	-21	-6	-4	-4	-3	-2	-3	-2	0	-1	0	0	0	0	0	0	0	0	0	0	0
8	I	0	0	0	0	0	-1	-9	-13	-12	-3	-2	-2	-1	-1	0	-1	-1	0	-1	0	0	0	0	0	0	0	0	0	0	0
7	I	0	0	0	0	0	-1	0	-1	-1	-1	-1	-1	0	0	0	0	0	0	0	0	0	0	0	0	0	0	0	0	0	0
6	I	0	0	0	0	0	-1	0	0	0	0	0	0	0	0	1	1	0	0	0	0	0	0	0	0	0	0	0	0	0	0
5	I	0	0	0	0	0	0	0	0	0	0	0	0	0	0	0	0	0	0	0	0	0	0	0	0	0	0	0	0	0	0
4	I	0	0	0	0	0	0	0	0	0	0	0	0	0	0	0	0	0	0	0	0	0	0	0	0	0	0	0	0	0	0
3	I	0	0	0	0	0	0	0	0	0	0	0	0	0	0	0	0	0	0	0	0	0	0	0	0	0	0	0	0	0	0
2	I	0	0	0	0	0	0	0	0	0	0	0	0	0	0	0	0	1	0	0	0	0	0	0	0	0	0	0	0	0	0
1	I	0	0	0	0	0	0	0	0	0	0	0	0	0	0	0	0	0	0	0	0	0	0	0	0	0	0	0	0	0	0

Figure 10-43. Model 5 changes in cumulative sulfur deposition (metric tons) due to emission reductions.

10-73

# SURADS RESULTS FOR JULY 21, 1978

COMPARISON OF RUN 1B TO RUN 1 \*\* EMISSION CONTRIBUTION ONLY \*\*

CHANGE (%) IN SURFACE CONCENTRATION OF SO<sub>2</sub> FOR HOUR 24

	1	2	3	4	5	6	7	8	9	10	11	12	13	14	15	16	17	18	19	20	21	22	23	24	25	26	27	28	29	30
23 I	0	0	0	0	0	0	0	0	0	0	0	0	0	0	0	0	0	0	0	0	0	0	0	0	0	0	0	0	0	0
22 I	0	0	0	0	0	0	0	0	0	0	0	0	0	0	0	0	0	0	0	0	0	0	0	0	0	0	0	0	0	0
21 I	0	0	0	0	0	0	0	0	0	0	0	0	0	0	0	0	0	0	0	0	0	0	0	0	0	0	0	0	0	0
20 I	0	0	0	0	0	0	0	0	0	0	0	0	0	0	0	-20	0	0	0	0	0	0	0	0	0	0	0	0	0	0
19 I	0	0	0	0	0	0	0	0	0	0	0	0	50	0	0	0	0	-33	0	0	-33	-100	0	0	0	0	0	0	0	0
18 I	0	0	0	0	0	0	0	0	0	0	0	0	0	0	0	0	-20	-20	-17	0	-25	0	0	0	0	0	0	0	0	0
17 I	0	0	0	0	0	0	0	-9	-13	-11	0	-14	-20	-19	-30	-22	-25	-22	-22	-13	-33	-33	0	0	0	0	0	0	0	0
16 I	0	0	0	0	0	-17	0	-10	-20	-13	-13	-22	-26	-29	-27	-30	-33	-33	-22	-14	-29	-20	0	-17	0	0	0	0	0	0
15 I	0	0	0	0	0	0	0	-8	-25	-20	-14	-33	-32	-31	-37	-40	-36	-47	-42	-30	-22	-25	-13	0	0	0	0	0	0	0
14 I	0	0	0	0	0	0	0	-11	-13	-25	-29	-14	-22	-42	-32	-38	-40	-45	-31	-23	-20	-18	-8	0	0	0	0	0	0	0
13 I	0	0	0	0	0	0	-10	0	-11	-25	-14	-25	-22	-33	-39	-40	-39	-47	-31	-21	-18	-8	-10	0	0	0	0	0	0	0
12 I	0	0	33	0	0	0	-10	-17	-21	-23	-29	-33	-31	-33	-42	-38	-39	-42	-22	-13	-13	0	0	0	0	0	0	0	0	0
11 I	0	0	0	0	0	-6	-9	-27	-38	-39	-41	-39	-33	-43	-43	-33	-33	-17	0	0	0	0	0	0	0	0	0	0	0	0
10 I	0	0	0	0	0	-8	-18	-27	-36	-39	-44	-40	-38	-33	-33	-50	-25	0	-11	0	0	0	0	0	0	0	0	0	0	0
9 I	0	0	0	0	0	-33	-27	-36	-39	-42	-33	-20	-20	-20	0	0	-20	0	0	0	0	0	0	0	0	0	0	0	0	0
8 I	0	0	0	0	0	-25	-14	-22	-22	-20	0	-20	0	0	0	0	0	0	0	0	0	0	0	0	0	0	0	0	0	0
7 I	0	0	0	0	0	0	0	-8	0	-20	0	0	-20	0	0	0	0	0	0	0	0	0	0	0	0	0	0	0	0	0
6 I	0	0	0	0	0	0	0	0	0	0	0	0	0	0	0	0	0	0	0	0	0	0	0	0	0	0	0	0	0	0
5 I	0	0	0	0	0	0	0	0	0	0	0	0	0	0	0	0	0	0	0	0	0	0	0	0	0	0	0	0	0	0
4 I	0	0	0	0	0	0	0	0	0	0	0	0	0	0	0	0	0	0	0	0	0	0	0	0	0	0	0	0	0	0
3 I	0	0	0	0	0	0	0	0	0	0	0	0	0	0	0	0	0	0	0	0	0	0	0	0	0	0	0	0	0	0
2 I	0	0	0	0	0	0	0	0	0	0	0	0	0	0	0	0	0	0	0	0	0	0	0	0	0	0	0	0	0	0
1 I	0	0	0	0	0	0	0	0	0	0	0	0	0	0	0	0	0	0	0	0	0	0	0	0	0	0	0	0	0	0

Figure 10-44. Model 1 changes (%), due to emission reductions, in emission contribution to hour 24 SO<sub>2</sub> concentration.

# SURADS RESULTS FOR JULY 21, 1978

COMPARISON OF RUN 1B TO RUN 1 \*\* EMISSION CONTRIBUTION ONLY \*\*

CHANGE (%) IN SURFACE CONCENTRATION OF SO4 FOR HOUR 24

	1	2	3	4	5	6	7	8	9	10	11	12	13	14	15	16	17	18	19	20	21	22	23	24	25	26	27	28	29	30
23	0	0	0	0	0	0	0	0	0	0	0	0	0	0	0	0	0	0	0	0	0	0	0	0	0	0	0	0	0	0
22	0	0	0	0	0	0	0	0	0	0	0	0	0	0	0	0	0	0	0	0	0	0	0	0	0	0	0	0	0	0
21	0	0	0	0	0	0	0	0	0	0	0	0	0	0	0	-13	0	0	0	0	0	0	0	0	0	0	0	0	0	0
20	0	0	0	0	-33	0	0	0	0	0	0	0	0	0	0	0	0	0	0	0	0	0	0	0	0	0	0	0	0	0
19	0	0	0	0	0	0	0	0	0	0	-17	-20	-17	-20	-20	0	-20	-17	-17	-20	-17	-25	-50	0	0	0	0	0	0	0
18	0	0	0	0	0	0	0	20	0	0	-14	-20	-17	-13	-22	-30	-22	-33	-33	-25	-29	-25	-20	0	-20	0	0	0	0	0
17	0	0	0	0	0	0	0	0	0	0	-14	-20	-14	-25	-25	-33	-40	-36	-36	-36	-36	-33	-20	-20	-17	0	0	0	0	0
16	0	0	0	0	0	0	0	0	0	-14	-11	-33	-11	-29	-25	-40	-40	-38	-33	-43	-42	-44	-17	-17	-17	0	0	0	0	0
15	0	0	0	0	-33	0	0	0	-10	0	-13	-13	-22	-33	-25	-42	-46	-43	-41	-43	-38	-33	-25	-13	-13	14	0	0	25	0
14	0	0	0	0	0	0	0	0	0	-11	-13	-22	-30	-43	-22	-38	-43	-43	-39	-35	-33	-27	-20	-9	11	0	0	0	0	0
13	0	0	0	0	0	0	0	0	0	-22	-22	-20	-27	-50	-33	-38	-43	-43	-35	-41	-38	-23	-14	0	0	0	0	0	0	0
12	0	0	0	0	0	0	0	-29	-13	-11	-33	-31	-33	-40	-36	-43	-43	-47	-38	-29	0	0	0	0	0	0	0	0	0	0
11	0	0	0	100	0	0	0	-29	-30	-33	-38	-29	-36	-40	-33	-44	-43	-33	-17	0	0	0	0	50	0	0	0	0	0	0
10	0	0	0	0	0	0	-17	-33	-30	-25	-36	-25	-44	-50	-50	-60	-50	-40	-17	0	0	0	0	0	0	0	0	0	0	0
9	0	0	0	0	0	-25	-14	-25	-22	-30	-25	-25	-33	-20	-25	-25	0	0	33	0	0	0	0	0	0	0	0	0	0	0
8	0	0	0	0	0	0	-17	-14	-17	-17	-17	-17	-20	0	0	0	-25	0	0	0	0	0	0	0	0	0	0	0	0	0
7	0	0	0	0	0	0	-17	0	-17	0	0	0	25	25	0	33	0	0	0	0	0	0	0	0	0	0	0	0	0	0
6	0	0	0	0	0	0	0	25	0	0	25	25	0	25	-17	0	0	0	0	0	0	0	0	0	0	0	0	0	0	0
5	0	0	0	0	0	0	0	0	0	0	50	0	0	0	0	0	0	0	0	0	0	0	0	0	0	0	0	0	0	0
4	0	0	0	0	0	0	0	0	0	0	0	0	0	0	0	0	0	0	0	0	0	0	0	0	0	0	0	0	0	0
3	0	0	0	0	0	0	0	0	0	0	0	0	0	0	0	0	0	0	0	0	0	0	0	0	0	0	0	0	0	0
2	0	0	0	0	0	0	0	0	0	0	0	0	0	0	0	0	0	0	0	0	0	0	0	0	0	0	0	0	0	0
1	0	0	0	0	0	0	0	0	0	0	0	0	0	0	0	0	0	0	0	0	0	0	0	0	0	0	0	0	0	0

Figure 10-45. Model 1 changes (%), due to emission reductions, in emission contribution to hour 24 sulfate concentration.

10-75



Environment Ontario

Laboratory Library  
125 Resources Rd.  
Etobicoke, Ontario M9P 3V6  
Canada

# SURADS RESULTS FOR JULY 21, 1978

COMPARISON OF RUN 1B TO RUN 1 \*\* EMISSION CONTRIBUTION ONLY \*\*

CHANGE (%) IN SURFACE SULFUR DEPOSITION

10-76

	1	2	3	4	5	6	7	8	9	10	11	12	13	14	15	16	17	18	19	20	21	22	23	24	25	26	27	28	29	30
23 I	0	0	0	0	0	0	0	0	0	0	0	0	0	0	0	0	0	0	0	0	0	0	0	0	0	0	0	0	0	0
22 I	0	0	0	0	0	0	0	0	0	0	0	0	0	0	0	0	14	0	0	0	0	0	0	0	0	0	0	0	0	0
21 I	0	0	0	0	0	0	0	0	0	0	0	0	0	0	0	0	0	0	0	0	0	0	0	0	0	0	0	0	0	0
20 I	0	0	0	0	0	0	0	0	0	0	0	0	10	9	0	0	0	0	0	0	33	0	9	0	0	0	0	0	0	0
19 I	0	0	0	0	0	0	0	0	0	10	9	6	21	0	0	0	0	0	0	0	-14	0	100	0	0	0	0	0	0	0
18 I	0	0	0	0	-8	0	0	0	0	-4	-8	-6	-11	-6	5	6	0	-5	-5	-6	-9	0	0	0	0	0	0	0	0	0
17 I	0	0	0	0	0	0	0	-2	-7	-8	-19	-15	-20	-16	-27	-23	-24	-17	-15	-13	-19	-11	0	-5	0	0	6	0	0	0
16 I	0	0	0	0	0	0	2	-7	-15	-18	-16	-31	-24	-27	-32	-29	-28	-24	-22	-23	-20	-11	-3	-3	0	0	0	0	0	0
15 I	0	0	0	0	0	0	2	-7	-25	-22	-22	-27	-31	-35	-32	-35	-34	-40	-38	-32	-27	-14	-7	0	0	0	0	0	0	0
14 I	0	0	0	0	0	0	2	-8	-17	-18	-23	-25	-28	-33	-28	-33	-35	-40	-32	-22	-19	-7	-2	-3	0	0	0	0	0	0
13 I	0	0	0	0	0	0	0	-5	-14	-20	-21	-20	-27	-33	-37	-36	-37	-39	-32	-18	-12	-5	-7	0	0	0	0	0	0	0
12 I	0	0	0	7	4	-5	-5	-17	-22	-25	-35	-33	-35	-37	-37	-39	-42	-43	-16	-8	-5	0	0	0	0	0	0	0	0	0
11 I	0	0	0	0	-2	-3	-15	-32	-33	-40	-41	-37	-38	-41	-38	-38	-32	-22	-6	-3	0	-7	0	0	0	0	0	0	0	0
10 I	0	0	0	13	-3	-8	-22	-33	-37	-37	-42	-40	-38	-37	-32	-38	-19	-8	0	0	0	0	0	0	0	0	0	0	0	0
9 I	0	0	0	0	0	-27	-31	-34	-41	-38	-23	-18	-21	-18	-18	-10	-11	-7	0	0	0	0	0	0	0	0	0	0	0	0
8 I	0	0	0	0	0	-9	-26	-23	-24	-12	-14	-8	-8	-4	-7	-5	-4	0	0	0	0	0	0	0	0	0	0	0	0	0
7 I	0	0	0	0	0	0	0	-2	-3	-5	-4	-3	-5	0	0	0	0	0	0	0	0	0	0	0	0	0	0	0	0	0
6 I	0	0	0	0	0	0	4	0	0	0	0	0	0	0	0	0	0	0	0	0	0	0	0	0	0	0	0	0	0	0
5 I	0	0	0	0	0	0	0	0	0	0	3	0	0	0	0	0	0	0	0	0	0	0	0	0	0	0	0	0	0	0
4 I	0	0	0	0	0	0	0	0	0	0	0	0	0	0	0	0	0	0	0	0	0	0	0	0	0	0	0	0	0	0
3 I	0	0	0	0	0	0	0	0	0	0	0	0	0	0	0	0	0	0	0	0	0	0	0	0	0	0	0	0	0	0
2 I	0	0	0	0	0	0	0	0	0	0	0	0	0	0	0	0	0	0	0	0	0	0	0	0	0	0	0	0	0	0
1 I	0	0	0	0	0	0	0	0	0	0	0	0	0	0	0	0	0	0	0	0	0	0	0	0	0	0	0	0	0	0

Figure 10-46. Model 1 changes (%), due to emission reductions, in emission contribution to sulfur deposition.

# SURADS RESULTS FOR JULY 21, 1978

COMPARISON OF RUN 5B TO RUN 5 \*\* EMISSION CONTRIBUTION ONLY \*\*

CHANGE (%) IN SURFACE CONCENTRATION OF SO<sub>2</sub> FOR HOUR 24

		1	2	3	4	5	6	7	8	9	10	11	12	13	14	15	16	17	18	19	20	21	22	23	24	25	26	27	28	29	30
23	I	0	0	0	0	0	0	0	0	0	0	0	0	0	0	0	0	0	0	0	0	0	0	0	0	0	0	0	0	0	0
22	I	0	0	0	0	0	0	0	0	0	0	0	0	0	0	0	0	0	0	0	0	0	0	0	0	0	0	0	0	0	0
21	I	0	0	0	0	0	0	0	0	0	0	0	0	0	0	0	0	0	0	0	0	0	0	0	0	0	0	0	0	0	0
20	I	0	0	0	0	0	0	0	0	0	0	0	100	0	0	0	0	0	0	0	100	0	0	0	0	0	0	0	0	0	0
19	I	0	0	0	0	0	0	0	0	0	0	0	50	0	0	0	0	0	-25	0	0	0-100	0	0	0	0	0	0	0	0	0
18	I	0	0	0	0	0	0	0	0	0	0	0	0	20	0	0	-17	-17	-17	-17	-20	-50	0	0	0	0	0	0	0	0	0
17	I	0	0	0	0	0	0	0	0	-13	-17	-17	-14	-23	-30	-30	-22	-30	-27	-22	-29	-25	-25	0	0	-17	0	0	0	0	0
16	I	0	0	0	0	0	0	-13	-13	0	-14	-25	-29	-25	-40	-33	-33	-33	-30	-22	-25	-33	0	-14	0	0	20	0	0	0	0
15	I	0	0	0	0	0	0	0	0	-29	-13	-14	-25	-33	-33	-38	-40	-38	-41	-36	-33	-27	-22	-11	-13	0	0	0	0	0	0
14	I	0	0	0	0	0	0	0	0	0	-14	-14	-14	-25	-42	-33	-38	-41	-45	-33	-21	-25	-8	-14	-11	0	0	0	0	0	0
13	I	0	0	0	0	0	0	0	0	-13	-13	-14	-25	-25	-33	-41	-41	-40	-45	-36	-20	-23	-14	-10	0	0	0	0	0	0	0
12	I	0	0	0	0	0	-10	-9	-20	-23	-23	-36	-33	-31	-33	-42	-44	-42	-46	-25	-13	-13	0	0	0	0	0	0	0	0	0
11	I	0	0	0	0	0	-9	-11	-31	-33	-38	-38	-37	-36	-41	-47	-40	-50	-25	-20	-17	0	0	0	0	0	0	0	0	0	0
10	I	0	0	0	0	17	-9	-20	-36	-40	-38	-41	-36	-30	-45	-42	-38	-25	-33	0	0	0	0	0	0	0	0	0	0	0	0
9	I	0	0	0	0	0	-33	-33	-27	-39	-42	-17	-17	-20	-20	0	-20	0	0	0	0	-25	0	0	0	0	0	0	0	0	0
8	I	0	0	0	0	0	-33	-25	-20	-22	0	0	0	0	-20	0	-17	0	0	0	0	0	0	0	0	0	0	0	0	0	0
7	I	0	0	0	0	0	0	0	0	0	0	0	0	-17	0	0	33	0	0	0	0	0	0	0	0	0	0	0	0	0	0
6	I	0	0	0	0	0	0	0	0	0	-17	0	0	0	0	0	0	0	0	0	0	0	0	0	0	0	0	0	0	0	0
5	I	0	0	0	0	0	0	0	0	0	0	0	0	0	0	0	0	0	0	0	0	0	0	0	0	0	0	0	0	0	0
4	I	0	0	0	0	0	0	0	0	0	0	0	0	0	0	0	0	0	0	0	0	0	0	0	0	0	0	0	0	0	0
3	I	0	0	0	0	0	0	0	0	0	0	0	0	0	0	0	0	0	0	0	0	0	0	0	0	0	0	0	0	0	0
2	I	0	0	0	0	0	0	0	0	0	0	0	0	0	0	0	0	0	0	0	0	0	0	0	0	0	0	0	0	0	0
1	I	0	0	0	0	0	0	0	0	0	0	0	0	0	0	0	0	0	0	0	0	0	0	0	0	0	0	0	0	0	0

Figure 10-47. Model 5 changes (%), due to emission reduction, in emission contribution to hour 24 SO<sub>2</sub> concentration.

10-77

# SURADS RESULTS FOR JULY 21, 1978

COMPARISON OF RUN 5B TO RUN 5 \*\* EMISSION CONTRIBUTION ONLY \*\*

CHANGE (%) IN SURFACE CONCENTRATION OF SO4 FOR HOUR 24

10-78

	1	2	3	4	5	6	7	8	9	10	11	12	13	14	15	16	17	18	19	20	21	22	23	24	25	26	27	28	29	30
23 I	0	0	0	0	0	0	0	0	0	0	0	0	0	0	0	0	0	0	0	100	0	0	0	0	0	0	0	0	0	0
22 I	0	0	0	0	0	0	0	0	0	0	0	0	0	0	0	0	0	0	0	0	0	0	0	0	0	0	0	0	0	0
21 I	0	0	0	0	0	0	0	0	0	0	0	0	0	0	0	0	0	0	0	0	0	0	0	0	0	0	0	0	0	0
20 I	0	0	0	0	0	0	0	0	0	0	0	0	0	0	0	0	0	0	0	0	100	0	0	0	0	0	0	0	0	0
19 I	0	0	0	0	0	0	0	0	0	0	0	50	0	0	0	-20	0	0	-14	-14	-17	-25	0	0	0	100	0	0	0	0
18 I	0	0	0	0	0	0	0	0	0	0	-14	-17	0	0	-14	-22	-22	-33	-25	-25	-25	-25	-25	0	0	0	0	25	0	0
17 I	0	0	0	0	0	0	0	0	0	-14	-14	-17	-14	-25	-30	-30	-30	-30	-27	-30	-30	-33	-20	-20	-17	-17	0	0	0	0
16 I	0	0	0	0	0	0	0	0	0	0	0	0	-22	-33	-33	-30	-30	-33	-33	-36	-33	-25	-29	-17	-17	-14	0	0	0	0
15 I	0	0	0	0	0	0	0	0	-11	-13	-13	-22	-30	-25	-33	-36	-44	-44	-39	-36	-38	-30	-22	-11	0	0	0	0	0	0
14 I	0	0	0	0	0	0	0	0	0	-11	-11	-22	-30	-38	-33	-40	-41	-38	-39	-35	-25	-24	-18	-17	0	33	0	0	0	0
13 I	0	0	0	0	0	0	0	0	0	-22	-13	-20	-33	-38	-33	-44	-41	-41	-37	-40	-36	-17	-11	0	0	0	0	0	0	0
12 I	0	0	0	100	0	0	0	-14	-13	-20	-31	-31	-33	-36	-42	-44	-44	-47	-38	-25	-17	0	0	0	0	-100	0	0	0	0
11 I	0	0	0	0	0	0	-14	-25	-42	-31	-36	-29	-33	-36	-45	-40	-50	-40	-20	0	0	0	0	0	0	0	0	0	0	0
10 I	0	0	0	0	0	0	-14	-30	-33	-36	-33	-29	-45	-44	-33	-33	-40	-20	-25	0	0	0	0	0	0	0	0	0	0	0
9 I	0	0	0	0	0	0	-25	-22	-27	-27	-25	-22	-17	0	0	0	-25	0	0	0	0	0	0	0	0	0	0	0	0	0
8 I	0	0	0	0	0	0	-14	-25	-29	-17	-17	0	-17	-20	-20	0	0	0	0	0	0	0	0	0	0	0	0	0	0	0
7 I	0	0	0	0	0	0	0	0	-17	0	-17	-17	0	0	25	33	0	0	0	0	0	0	0	0	0	0	0	0	0	0
6 I	0	0	0	0	0	0	20	0	0	-20	0	0	0	0	0	0	0	0	0	0	0	0	0	0	0	0	0	0	0	0
5 I	0	0	0	0	0	0	0	0	0	25	25	0	0	0	0	0	0	0	0	0	0	0	0	0	0	0	0	0	0	0
4 I	0	0	0	0	0	0	0	0	0	0	0	0	0	0	0	0	0	0	0	0	0	0	0	0	0	0	0	0	0	0
3 I	0	0	0	0	0	0	0	0	0	0	0	0	0	0	0	0	0	0	0	0	0	0	0	0	0	0	0	0	0	0
2 I	0	0	0	0	0	0	0	0	0	0	0	0	0	0	0	0	0	0	0	0	0	0	0	0	0	0	0	0	0	0
1 I	0	0	0	0	0	0	0	0	0	0	0	0	0	0	0	0	0	0	0	0	0	0	0	0	0	0	0	0	0	0

Figure 10-48. Model 5 changes (%), due to emission reductions, in emission contribution to hour 24 sulfate concentration.

# SURADS RESULTS FOR JULY 21, 1978

COMPARISON OF RUN 5B TO RUN 5 \*\* EMISSION CONTRIBUTION ONLY \*\*

CHANGE (%) IN SURFACE SULFUR DEPOSITION

	1	2	3	4	5	6	7	8	9	10	11	12	13	14	15	16	17	18	19	20	21	22	23	24	25	26	27	28	29	30
23 I	0	0	0	0	0	0	0	0	0	0	0	0	0	0	0	0	0	0	0	0	0	0	0	0	0	0	0	0	0	0
22 I	0	0	0	0	0	0	0	0	0	0	0	0	0	0	0	0	0	0	0	0	0	0	0	0	0	0	0	0	0	0
21 I	0	0	0	0	0	0	0	0	0	0	0	0	0	7	2	0	6	0	0	50	0	0	0	0	0	0	0	0	0	0
20 I	0	0	0	0	0	0	0	0	0	0	0	0	0	9	5	0	0	0	0	0	0	0	0	0	0	0	0	0	0	0
19 I	0	0	0	0	0	0	0	0	0	0	0	38	22	13	8	0	0	0	0	0	0	0	0	0	0	0	0	0	0	0
18 I	0	0	0	0	0	0	0	4	4	0	-5	-11	-6	12	13	-6	0	-5	-5	0	-10	-20	0	0	0	0	0	0	0	0
17 I	0	0	0	0	0	0	0	-2	-7	-8	-17	-21	-18	-19	-30	-25	-26	-16	-17	-18	-20	-13	-9	0	0	0	0	0	0	0
16 I	0	0	0	0	0	0	6	-7	-17	-20	-17	-26	-28	-30	-36	-32	-28	-24	-27	-22	-22	-6	-7	-4	0	0	0	0	0	0
15 I	0	0	0	0	0	0	0	-7	-26	-21	-23	-27	-34	-34	-33	-35	-34	-37	-34	-32	-29	-8	-3	-3	0	0	6	0	0	0
14 I	0	0	0	0	0	1	0	-6	-13	-19	-25	-21	-29	-36	-28	-35	-36	-40	-30	-22	-14	-6	-1	0	0	0	0	0	0	0
13 I	0	0	0	0	0	-3	-3	-6	-11	-16	-18	-21	-25	-35	-40	-38	-39	-40	-33	-18	-11	-5	-4	0	17	33	0	0	0	0
12 I	0	0	0	0	0	-2	-6	-16	-25	-29	-33	-32	-35	-39	-38	-39	-41	-38	-16	-9	-3	0	0	0	0	0	0	0	0	0
11 I	0	0	0	3	0	-5	-17	-32	-36	-38	-42	-38	-39	-41	-40	-39	-38	-24	-5	0	-6	0	0	0	0	0	0	0	0	0
10 I	0	0	0	0	3	-8	-25	-33	-39	-38	-44	-41	-41	-42	-35	-38	-27	-8	-6	0	0	0	0	0	0	0	0	0	0	0
9 I	0	0	0	0	0	-32	-32	-35	-40	-39	-25	-17	-17	-15	-13	-15	-11	0	-4	0	0	0	0	0	0	0	0	0	0	0
8 I	0	0	0	0	0	-10	-26	-28	-26	-13	-11	-9	-4	-4	0	-5	-5	0	-6	0	0	0	0	0	0	0	0	0	0	0
7 I	0	0	0	0	0	-9	0	-2	-3	-5	-5	-3	0	0	0	0	0	0	0	0	0	0	0	0	0	0	0	0	0	0
6 I	0	0	0	0	0	-8	0	0	0	0	0	0	0	0	3	5	0	0	0	0	0	0	0	0	0	0	0	0	0	0
5 I	0	0	0	0	0	0	0	0	0	0	0	0	0	0	0	0	0	0	0	0	0	0	0	0	0	0	0	0	0	0
4 I	0	0	0	0	0	0	0	0	0	0	0	0	0	0	0	0	0	0	0	0	0	0	0	0	0	0	0	0	0	0
3 I	0	0	0	0	0	0	0	0	0	0	0	0	0	0	0	0	0	0	0	0	0	0	0	0	0	0	0	0	0	0
2 I	0	0	0	0	0	0	0	0	0	0	0	0	0	0	0	0	0	0	0	0	0	0	0	0	0	0	0	0	0	0
1 I	0	0	0	0	0	0	0	0	0	0	0	0	0	0	0	0	0	0	0	0	0	0	0	0	0	0	0	0	0	0

Figure 10-49. Model 5 changes (%), due to emission reductions, in emission contribution to sulfur deposition.



Virginia-Pennsylvania border). The largest relative reductions were 42% for run 1B and 44% for run 5B, in northcentral Kentucky.

The emission components of  $\text{SO}_2$  and  $\text{SO}_4$  concentrations were reduced by about 25 to 45% throughout most of the Ohio Valley for the complex model and the simple model. This indicates the response of the two models was approximately  $35 \pm 10\%$  which is a very linear response to the average emission reduction of 36%. The variability in the concentration reductions that are seen are believed to primarily reflect the nonuniformity of the emissions and emission reductions in the affected region, rather than a nonlinear model response.

The percent change in the emissions components of sulfur deposition show slightly smaller reductions than the concentration reductions in runs 1B and 5B. The emissions components of S deposition are reduced 20 to 45% throughout most of the Ohio Valley. The predicted reductions in sulfur deposition in runs 5B are almost all within 3% of the reductions in run 1B.

The sulfur mass balances for runs 1B and 5B are presented in Tables 10-10 and 10-11, respectively. Table 10-12, summarizes the percent reduction of final  $\text{SO}_2$  and  $\text{SO}_4$  mass in the modeling domain and the cumulative S deposition for runs 1B and 5B relative to runs 1 and 5. The complex model yielded a slightly larger reduction in  $\text{SO}_2$  mass due to the emission reduction but yielded slightly smaller reductions in  $\text{SO}_4$  mass and S deposition than the simple model.

In summary, the compound simple model has a overall tendency to estimate slightly larger reductions in  $\text{SO}_4$  concentration and S deposition, but slightly smaller reductions in  $\text{SO}_2$  concentration, than the complex model. The differences are quite small in the 24-hour simulations, but could be amplified in multiday simulations. The largest percent reductions in sulfur deposition occurred in the grid squares with the largest percent reductions in emissions, which further illustrates the linearity of the SURADS model response to emission reductions.

It should be pointed out that close examination of the concentration difference maps reveals a somewhat disturbing feature of the existing model. There are slightly higher concentrations (1 ppb or  $1 \mu\text{g}/\text{m}^3$ ) in several squares outside of the Ohio Valley in runs 1B

TABLE 10-10

RUN 10 SULFUR MASS BALANCE  
(10<sup>9</sup> grams S)

<u>Component</u>	<u>SO<sub>2</sub></u>	<u>SO<sub>4</sub></u>
Initial concentrations	26.7	20.1
Emissions	39.0	0.87
Chemical conversion	-12.2	12.2
Deposition to ground	17.9	1.4
Residual	1.4	-2.4
Final concentration	37.0	29.4

TABLE 10-11

RUN 5B SULFUR MASS BALANCE  
(10<sup>9</sup> Grams S)

<u>Component</u>	<u>SO<sub>2</sub></u>	<u>SO<sub>4</sub></u>
Initial concentrations	26.7	20.1
Emissions	39.0	0.87
Chemical conversion	-12.8	12.8
Deposition to ground	17.2	1.2
Residual	2.3	-2.5
Final concentration	38.0	30.0

TABLE 10-12

PERCENT (%) REDUCTION IN FINAL  $\text{SO}_2$  AND  $\text{SO}_4$  MASS  
AND SULFUR DEPOSITION MASS DUE TO EMISSION REDUCTIONS  
FOR THE COMPLEX MODEL AND THE SIMPLE MODEL

<u>Mass Component</u>	<u>Complex Model</u>	<u>Simple Model</u>
Final $\text{SO}_2$	13.8	13.6
Final $\text{SO}_4$	4.2	4.5
Sulfur deposition	9.4	9.8

and 5B. These anomalies occur two or three grid squares away from the region clearly affected by the emissions reduction. Although we are unsure of the precise cause of these anomalies, we strongly suspect the numerical advection algorithm to be responsible.

#### 10.1.6 Sensitivity of the Long Range Transport Model to Sulfate Deposition Velocity

The original SURADS model employed  $\text{SO}_4$  deposition velocities equal to 1/10 of the  $\text{SO}_2$  deposition velocities. These  $\text{SO}_4$  deposition velocities are believed to represent somewhat of a lower limit. Other researchers have conducted studies which suggest  $\text{SO}_4$  deposition velocities are comparable to those for  $\text{SO}_2$ . A SURADS sensitivity test was performed to quantify the sensitivity of the solution to this uncertainty. A additional run (#7) was made which employed  $\text{SO}_4$  deposition velocities that are equal to those for  $\text{SO}_2$ , but was otherwise identical to run 1.

The 24-hour average  $\text{SO}_4$  concentration and sulfur deposition geographic distributions for run 7 are shown in Figure 10-50 and 10-51. Comparing Figure 10-50 to 10-5c shows that calculated  $\text{SO}_4$  concentrations are approximately 2/3 of the baseline case values, which means the predictions are significantly below most of the observations. The 24-hour sulfur deposition maps show that the higher  $\text{SO}_4$  deposition velocities resulted in 15 to 200% more deposition. Larger difference occurred in the remote areas of the grid where the deposition was small in the baseline. The smallest differences occurred in the high source emission areas where  $\text{SO}_2$  deposition is dominant. For the whole grid  $\text{SO}_4$  deposition increased 650% while total sulfur deposition increased 36%.

This test shows that there is substantial uncertainty in modeling of  $\text{SO}_4$  due to the uncertainty in  $\text{SO}_4$  deposition velocities. Although the results with the lower limit deposition velocity show better agreement with the measurements than those with the upper limit, this test is insufficient to determine which is a better modeling assumption. Variations in other model parameters, such as  $\text{SO}_2$  deposition velocity or chemical conversion rates, could have

## SURADS RESULTS FOR JULY 21, 1978

RUN 7: HIGH SO<sub>4</sub> DEPOSITION VELOCITIESSURFACE CONCENTRATION OF 24-HOUR AVERAGED SO<sub>4</sub> (MICR/M\*\*3)

10-84

	1	2	3	4	5	6	7	8	9	10	11	12	13	14	15	16	17	18	19	20	21	22	23	24	25	26	27	28	29	30
23	1	1	1	1	1	1	1	1	1	2	2	3	3	3	3	4	5	5	6	6	6	5	5	4	3	2	2	1	1	1
22	1	1	1	1	1	2	2	2	2	2	3	3	4	4	4	6	7	8	8	7	7	7	6	5	4	3	2	2	1	1
21	1	1	1	2	2	2	3	3	3	3	3	4	5	7	10	12	12	12	11	11	11	10	9	7	6	4	3	2	2	2
20	2	2	2	3	4	4	4	3	4	4	6	8	9	10	12	13	14	14	15	15	15	13	11	9	7	5	5	4	3	3
19	2	2	2	4	5	5	5	4	5	7	9	11	12	14	14	15	16	17	18	18	16	14	13	10	9	8	8	6	5	6
18	2	3	3	4	5	7	8	9	10	11	12	14	16	18	18	18	19	20	20	20	17	16	15	13	11	10	11	10	9	8
17	2	3	3	4	5	8	9	10	12	13	15	17	19	22	21	21	21	20	21	22	20	19	17	15	13	12	11	11	9	8
16	2	3	3	3	4	7	10	11	13	15	17	19	21	22	22	21	20	20	21	22	22	21	20	16	14	12	11	11	9	8
15	2	2	3	3	4	7	10	11	14	16	17	20	22	22	22	22	22	22	22	22	23	24	23	18	14	12	11	10	9	8
14	2	3	3	3	4	7	10	11	13	16	18	21	22	22	22	23	23	23	22	22	22	23	21	15	10	7	7	7	6	6
13	2	3	3	3	4	7	10	11	14	16	19	22	22	21	22	24	24	23	20	18	15	14	11	8	5	5	4	4	4	3
12	2	3	3	3	6	8	10	12	15	17	20	22	22	21	21	22	22	20	13	9	8	8	7	5	4	3	3	3	3	2
11	2	3	3	4	7	9	10	12	15	18	19	20	21	20	20	18	13	10	7	6	6	5	4	4	3	3	2	2	2	2
10	2	3	3	4	6	7	9	12	15	17	16	16	15	15	15	14	11	8	7	6	6	5	4	3	3	2	2	2	1	1
9	2	3	3	4	4	5	9	10	11	11	11	11	12	12	12	11	9	6	6	6	6	5	4	3	2	2	2	1	1	1
8	2	3	3	4	4	5	6	7	7	8	9	10	11	11	11	10	8	6	5	5	5	4	4	3	2	2	2	1	1	1
7	2	3	4	4	4	5	6	6	7	7	9	10	10	10	9	8	7	6	5	5	5	4	3	2	2	2	1	1	1	1
6	2	3	3	4	5	5	5	6	7	8	9	9	9	9	8	7	6	6	5	5	3	2	2	2	2	2	1	1	1	1
5	2	2	3	3	4	4	5	6	7	8	8	7	7	7	6	6	6	5	4	3	2	2	2	1	1	1	1	1	1	0
4	2	2	2	2	3	3	4	5	6	6	7	6	5	5	5	6	5	3	2	2	1	1	1	1	1	1	1	1	0	0
3	2	2	2	2	2	2	2	3	4	4	5	5	4	4	5	10	4	2	1	1	1	1	1	1	1	1	1	0	0	0
2	2	2	2	2	2	2	2	2	3	3	3	3	3	3	3	2	1	1	1	1	1	1	1	1	1	1	1	0	0	0
1	1	2	2	1	1	1	1	1	2	2	2	2	2	2	3	2	1	1	1	1	1	1	1	1	1	1	1	1	1	1

Figure 10-50. Calculated 24-hour average sulfate concentration ( $\mu\text{g}/\text{m}^3$ ) for run 7.

## SURADS RESULTS FOR JULY 21, 1978

## RUN 7: HIGH SO4 DEPOSITION VELOCITIES

## SURFACE SULFUR DEPOSITION (METRIC TONS/DAY)

	1	2	3	4	5	6	7	8	9	10	11	12	13	14	15	16	17	18	19	20	21	22	23	24	25	26	27	28	29	30
23 I	3	3	3	7	8	6	5	6	6	5	6	7	8	9	8	10	13	14	15	15	15	15	15	13	12	10	9	8	6	6
22 I	3	2	2	6	9	15	16	23	25	14	8	8	10	10	13	20	23	22	20	19	19	19	19	16	14	11	8	9	6	6
21 I	3	4	12	12	11	13	18	19	20	17	11	11	14	27	61	78	48	35	30	28	30	33	42	29	19	15	18	15	8	7
20 I	4	8	21	29	23	22	38	23	21	15	17	31	32	34	48	53	51	43	41	42	45	44	49	35	30	25	31	36	14	13
19 I	9	12	15	23	26	41	46	36	33	28	35	48	47	39	51	54	56	59	67	65	63	61	52	41	45	50	55	29	19	20
18 I	10	17	19	17	28	45	46	55	53	55	57	69	71	75	70	71	82	87	99	96	92	90	78	66	57	60	39	34	27	24
17 I	9	17	15	19	24	54	61	87	54	72	62	67	86	126	110	111	110	152	153	163	128	114	100	90	99	91	46	38	29	25
16 I	8	26	19	25	27	48	67	85	75	69	73	83	169	125	117	109	120	160	167	167	150	139	143	111	108	108	51	40	29	24
15 I	9	12	15	17	38	50	65	103	126	78	70	77	137	113	184	152	171	191	190	180	170	167	161	111	87	63	44	37	27	23
14 I	12	11	12	17	36	79	61	63	67	70	70	85	104	116	183	213	216	190	186	188	170	186	193	96	47	21	18	18	16	16
13 I	24	18	16	20	31	48	54	60	74	83	89	101	118	115	162	259	246	166	134	143	136	157	108	45	22	14	11	10	9	8
12 I	36	21	18	20	36	50	55	64	98	124	133	163	149	137	168	198	175	103	77	84	71	77	43	20	11	8	8	7	6	6
11 I	10	24	19	37	77	70	47	77	121	121	152	168	133	139	136	90	61	40	31	61	43	31	18	11	8	6	6	5	5	4
10 I	5	10	11	15	40	50	50	77	122	148	129	103	94	93	97	65	41	29	28	32	26	17	12	9	6	4	4	3	3	3
9 I	5	8	9	12	18	25	65	72	109	83	61	62	65	60	52	50	39	29	37	40	23	13	10	8	6	4	3	3	3	3
8 I	5	7	9	12	16	21	47	63	63	49	51	59	61	56	45	45	43	27	32	27	41	17	9	7	5	4	3	3	3	2
7 I	5	9	13	18	21	22	39	71	51	44	51	64	50	47	39	33	31	30	27	27	19	13	8	5	5	4	3	3	2	2
6 I	5	11	12	19	33	26	40	48	48	51	56	49	47	56	47	35	24	26	29	31	14	6	5	4	3	3	3	3	1	1
5 I	6	11	10	15	17	22	40	63	62	61	57	41	38	51	42	29	30	28	36	20	6	4	4	3	3	3	2	2	1	1
4 I	8	12	10	10	12	17	35	56	59	49	48	35	23	31	33	33	28	27	18	5	4	3	2	2	2	2	2	1	1	1
3 I	8	12	13	11	11	13	25	18	24	26	33	23	22	31	25	36	30	10	5	4	3	2	2	2	2	2	2	1	1	0
2 I	11	14	12	14	14	12	14	12	11	11	11	10	12	20	27	13	3	2	3	3	3	3	2	2	2	2	2	2	2	2
1 I	12	25	16	11	18	20	19	13	13	13	14	20	15	26	45	17	6	4	4	4	4	4	4	4	3	3	3	3	3	3

Figure 10-51. Calculated cumulative sulfur deposition (metric tons) for run 7.

caused similar variations in the results. Hence, the only conclusion drawn from this test is the variation of the  $\text{SO}_4$  deposition velocity over its range of uncertainty results in approximately 40% variation, on the average, in  $\text{SO}_4$  concentration and in sulfur deposition in the SURADS model.

#### 10.1.7 Sensitivity of Long Range Transport Model to Advection Scheme

Numerous researchers have compared numerical advection algorithms on idealized test problems and found substantial differences between the various numerical schemes (Crowley 1968, Kreis and Oligir 1972, Pernall 1976, Long and Pepper 1976, Mahlman and Sinclair 1977, Chock and Dunker 1981, McRae 1981). Tests were carried out with the SURADS model to identify differences between two algorithms on a nonidealized case; i.e., a case where the effects of emissions, chemistry, vertical dispersion, nonuniform initial concentrations, and nonuniform winds are included. A run (#8) was carried out using an eight order flux corrected transport scheme (FCT8) of Zalesak (1979) to compare with the baseline case (Run #1) which employed SHASTA, a second order scheme (Boris and Book 1975).

The calculated 24-hour average  $\text{SO}_2$  and  $\text{SO}_4$  concentration fields and the cumulative sulfur deposition field for run 8 are shown in Figures 10-52 through 10-54. Comparison of the FCT8 predictions with the baseline results (shown in Figures 10-5c, 10-6c, and 10-9) shows some substantial differences. The greatest differences appear at or downwind of grid squares with high emission source strengths. Table 10-13 summarizes the calculations at and just downwind of the largest Canadian and U.S. emission squares. The hour 24 results are given as well as the 24-hour averages. The largest differences are seen for the more isolated Canadian sources in squares (15,21), (16,21) and (17,21);  $\text{SO}_2$  concentrations are 2 to 4 times higher and  $\text{SO}_4$  concentration are 1.3 to 4 times higher in the FCT8 solution. Similarly predicted sulfur deposition near the larger Canadian sources is 2 to 3 times higher than in the SHASTA results. In and downwind of the largest U.S. emission source grid squares, calculated  $\text{SO}_2$

## SURADS RESULTS FOR JULY 21, 1978

## RUN 8: FCT8 ADVECTION ALGORITHM

SURFACE CONCENTRATION OF 24-HOUR AVERAGED SO<sub>2</sub> (PPB)

		1	2	3	4	5	6	7	8	9	10	11	12	13	14	15	16	17	18	19	20	21	22	23	24	25	26	27	28	29	30
	I	+	+	+	+	+	+	+	+	+	+	+	+	+	+	+	+	+	+	+	+	+	+	+	+	+	+	+	+	+	+
23	I	0	0	0	1	1	0	1	1	1	1	1	0	0	0	0	1	1	1	0	0	0	0	1	1	1	1	1	1	0	0
22	I	0	0	0	1	1	2	1	3	3	1	1	0	0	0	2	5	2	1	0	0	0	0	1	1	1	1	0	1	0	0
21	I	0	1	4	1	1	1	1	2	2	1	1	1	1	0	18	22	6	1	1	0	1	1	4	2	1	1	2	1	1	1
20	I	0	1	3	8	2	1	5	1	1	1	2	2	3	1	0	0	0	0	1	1	2	2	4	2	2	2	2	4	1	1
19	I	1	1	1	1	3	4	8	4	6	2	2	3	4	3	3	2	3	2	4	3	3	3	5	2	3	4	7	3	2	2
18	I	1	2	2	1	2	6	3	3	6	5	3	9	8	9	6	4	6	5	8	7	6	6	9	5	4	7	3	3	2	2
17	I	1	2	1	2	2	8	4	17	5	11	7	6	5	21	9	10	8	11	15	15	11	10	11	7	10	10	5	4	2	2
16	I	1	4	2	3	2	4	6	6	8	6	8	3	25	15	10	9	9	14	18	18	16	13	12	11	10	11	7	6	3	2
15	I	1	0	1	1	3	7	9	8	21	12	7	3	21	10	20	18	14	21	22	21	18	16	15	12	6	6	3	2	2	1
14	I	1	1	1	2	1	18	10	6	3	2	2	4	4	8	11	16	17	23	16	19	13	13	16	6	2	1	1	1	1	1
13	I	3	2	1	3	2	4	5	6	6	8	7	9	9	10	9	35	36	28	11	15	9	13	6	2	1	1	1	1	1	1
12	I	5	3	1	1	6	9	10	8	9	13	9	14	14	13	19	24	18	4	3	6	5	7	4	2	1	0	0	0	0	0
11	I	0	3	0	6	14	16	4	8	13	13	16	28	14	23	15	4	4	5	5	11	5	4	1	0	0	0	0	0	0	0
10	I	0	0	0	0	2	3	7	9	18	25	14	5	4	4	10	6	3	2	5	6	3	1	1	0	0	0	0	0	0	0
9	I	0	0	0	0	1	1	10	5	20	2	2	4	4	5	3	3	3	2	9	11	7	3	1	0	0	0	0	0	0	0
8	I	0	0	0	1	1	1	12	4	3	2	6	7	8	4	6	5	2	4	2	9	2	1	0	0	0	0	0	0	0	0
7	I	0	0	1	2	3	1	4	13	2	4	3	11	4	3	3	2	3	4	3	3	1	1	1	0	0	0	0	0	0	0
6	I	0	1	1	2	4	1	5	6	2	8	9	2	3	10	6	4	1	1	3	4	2	1	1	0	0	0	0	0	0	0
5	I	0	1	0	1	0	1	4	13	5	9	10	1	3	13	3	3	3	4	7	2	0	0	0	0	0	0	0	0	0	0
4	I	1	1	0	0	1	1	2	4	5	3	7	2	3	2	6	4	3	7	0	0	0	0	0	0	0	0	0	0	0	0
3	I	1	1	1	1	1	2	3	1	4	3	9	2	5	3	1	2	7	0	0	0	0	0	0	0	0	0	0	0	0	0
2	I	1	1	1	1	1	1	1	1	1	1	1	1	1	2	6	0	0	0	0	0	0	0	0	0	0	0	0	0	0	0
1	I	1	2	1	1	2	2	2	1	1	1	2	2	1	3	9	1	1	1	1	1	1	1	1	1	1	0	0	0	0	0

Figure 10-52. Calculated 24-hour average SO<sub>2</sub> concentration (ppb) for run 8.



SURADS RESULTS FOR JULY 21, 1978

RUN 8: FCTB ADVECTION ALGORITHM

SURFACE CONCENTRATION OF 24-HOUR AVERAGED SO<sub>4</sub> (MICR/M\*\*3)

	1	2	3	4	5	6	7	8	9	10	11	12	13	14	15	16	17	18	19	20	21	22	23	24	25	26	27	28	29	30
23	1	1	1	2	2	2	2	2	2	2	3	5	5	5	6	8	9	10	10	10	10	10	9	7	6	4	3	3	2	2
22	1	1	1	2	2	3	2	4	3	3	4	6	6	5	9	16	15	13	13	12	13	12	11	9	7	5	4	3	2	2
21	1	2	6	5	3	3	4	5	5	4	5	8	9	7	27	36	26	20	20	19	21	19	19	15	11	7	6	5	4	3
20	2	2	6	10	6	4	6	4	4	6	10	16	16	16	15	15	17	20	23	25	26	25	23	18	13	9	7	8	5	6
19	3	3	4	5	8	7	10	7	9	13	14	19	20	21	23	26	28	28	29	30	29	29	26	17	13	15	14	11	9	10
18	4	4	5	6	9	14	13	10	11	18	17	22	22	25	27	31	32	31	31	32	29	31	34	27	19	22	16	19	14	13
17	3	4	4	6	8	15	14	20	18	21	26	29	25	35	36	37	35	33	31	33	28	35	38	29	26	27	24	24	18	16
16	3	5	4	6	8	10	16	16	22	23	29	29	35	36	36	34	30	27	26	28	33	42	45	36	33	30	24	27	21	18
15	3	3	3	5	6	11	16	16	23	23	26	26	31	33	33	33	29	30	30	33	36	44	45	34	24	18	12	15	13	12
14	3	4	4	5	5	13	15	16	19	22	24	30	32	36	32	32	30	41	35	35	29	28	26	17	10	8	7	9	8	8
13	4	4	4	4	6	11	14	19	23	27	32	35	37	37	33	36	48	50	36	30	20	19	16	10	6	6	6	7	6	6
12	4	4	4	4	9	18	18	23	21	27	28	32	35	34	34	35	34	22	11	10	9	12	10	8	5	5	4	5	4	4
11	3	4	4	5	16	15	13	15	19	30	29	37	37	35	32	27	15	11	10	10	10	9	5	4	3	4	3	4	3	3
10	3	3	5	7	8	7	12	17	26	28	28	20	21	19	20	21	16	9	5	7	8	5	4	4	3	3	3	3	2	2
9	3	4	6	8	9	6	12	14	16	10	10	14	15	19	18	17	13	9	9	12	11	8	5	4	3	3	2	2	2	2
8	3	4	5	7	7	5	6	13	5	11	10	15	18	20	18	16	13	9	7	6	8	6	4	4	4	3	2	2	1	1
7	3	4	5	7	8	7	10	10	6	14	15	16	14	14	13	10	9	10	8	9	8	5	4	4	3	3	2	2	1	1
6	2	3	5	7	8	6	10	11	9	17	19	9	12	17	13	11	9	8	8	8	6	3	3	2	2	2	2	2	1	1
5	2	3	4	4	5	5	7	10	10	13	15	9	10	12	9	11	7	8	7	5	3	2	2	2	2	2	1	1	1	1
4	2	3	3	4	4	3	4	4	8	8	12	7	10	6	9	16	5	5	2	2	2	2	2	2	1	1	1	1	1	1
3	2	2	2	3	3	3	4	4	5	8	9	6	8	6	8	34	4	2	2	2	2	1	1	1	1	1	1	1	1	1
2	2	2	2	2	2	2	2	2	3	4	4	4	3	4	5	2	2	2	1	1	1	1	1	1	1	1	1	1	1	1
1	2	2	2	2	2	2	2	2	2	3	4	3	3	4	5	2	2	1	1	1	1	1	1	1	1	1	1	1	1	1

10-88

Figure 10-53. Calculated 24-hour average sulfate concentration ( $\mu\text{g}/\text{m}^3$ ) for run 8.

## SURADS RESULTS FOR JULY 21, 1978

RUN 8: FCTB ADVECTION ALGORITHM

SURFACE SULFUR DEPOSITION (METRIC TONS/DAY)

	1	2	3	4	5	6	7	8	9	10	11	12	13	14	15	16	17	18	19	20	21	22	23	24	25	26	27	28	29	30
23 I	2	2	2	5	7	3	3	4	4	3	3	4	4	4	4	9	9	7	5	5	5	5	7	5	8	5	5	6	4	4
22 I	2	2	3	4	6	14	4	25	25	7	4	4	4	3	15	38	23	11	7	5	7	6	9	9	8	6	5	6	3	3
21 I	2	5	32	12	5	5	6	13	14	9	5	6	6	4	143	181	57	16	8	6	11	9	36	17	10	7	15	13	6	5
20 I	2	4	26	62	12	7	43	9	8	5	12	19	24	11	4	4	4	5	12	13	18	20	38	19	16	14	19	37	10	9
19 I	5	8	5	11	19	31	58	29	43	14	17	22	32	19	27	22	27	20	36	31	30	33	41	20	27	33	54	21	14	13
18 I	9	14	16	8	18	40	20	19	38	35	24	58	50	55	46	39	57	47	61	57	52	56	77	43	29	52	18	20	15	14
17 I	5	12	5	13	11	55	28	135	27	72	49	38	30	135	76	84	70	105	125	132	90	85	97	62	85	82	29	25	17	14
16 I	6	32	12	24	16	29	49	53	58	40	57	25	194	108	81	69	68	114	134	140	134	121	121	96	89	103	42	38	23	17
15 I	8	3	9	6	20	44	64	66	166	86	49	22	140	69	172	133	116	163	164	170	155	147	144	103	54	41	18	15	11	10
14 I	10	9	4	10	10	111	65	43	22	20	17	36	36	63	108	129	142	183	135	156	117	129	167	51	15	5	5	7	6	6
13 I	20	16	6	15	15	26	31	45	46	67	59	75	82	90	74	296	314	223	95	121	83	129	54	18	7	7	5	5	5	5
12 I	38	20	7	7	33	54	60	49	67	115	73	130	128	110	147	185	139	29	26	55	44	68	38	15	7	3	3	4	3	3
11 I	3	23	4	39	91	88	21	48	92	98	119	239	112	168	120	32	27	28	21	76	39	30	7	2	2	3	3	3	2	2
10 I	3	4	3	3	13	18	44	57	122	196	108	38	34	32	78	48	21	8	12	25	16	6	4	3	2	1	1	1	1	1
9 I	3	3	3	4	8	5	68	38	151	13	15	29	32	38	22	26	25	10	37	48	27	11	6	3	1	1	1	1	1	1
8 I	3	3	4	8	7	4	5	92	28	27	13	44	53	55	28	44	40	13	20	12	49	11	4	3	3	1	1	1	1	1
7 I	2	4	7	14	20	8	29	99	17	31	26	80	27	23	19	11	16	27	17	20	6	3	3	3	2	1	1	1	1	1
6 I	2	6	6	17	33	11	37	45	13	64	69	13	20	69	39	29	7	7	23	28	12	4	2	2	1	1	1	1	1	0
5 I	3	8	4	10	4	10	33	99	42	72	73	12	19	82	22	20	19	25	48	11	1	1	1	1	1	1	1	1	0	0
4 I	5	7	5	5	9	11	15	33	47	23	51	14	15	12	36	33	20	50	2	1	1	1	1	1	1	1	1	1	0	0
3 I	4	8	10	8	7	14	33	10	35	25	61	13	30	24	8	21	49	2	2	2	1	1	1	1	1	1	1	0	0	1
2 I	5	7	5	12	11	9	11	8	7	9	9	9	6	15	46	3	3	2	2	2	2	2	2	2	2	1	1	1	1	1
1 I	8	17	10	7	16	17	16	9	10	10	11	18	9	18	64	3	3	3	3	3	3	3	3	3	3	2	2	2	2	2

Figure 10-54. Calculated cumulative sulfur deposition (metric tons) for run 8.

TABLE 10-13

COMPARISON OF SHASTA AND FCT8 PREDICTIONS  
IN AND DOWNWIND OF HIGH EMISSION GRID SQUARES

<u>Advection Method</u>	<u>Grid Square</u>	<u>Final SO<sub>2</sub> (ppb)</u>	<u>Average SO<sub>2</sub> (ppb)</u>	<u>Final SO<sub>4</sub><sup>3-</sup> (μg/m<sup>3</sup>)</u>	<u>Average SO<sub>4</sub><sup>3-</sup> (μg/m<sup>3</sup>)</u>	<u>Sulfur Deposition (metric tons)</u>
SHASTA	(15,21)*	5	6	18	7	45
FCT8	(15,21)*	20	18	23	27	143
SHASTA	(16,21)	9	7	22	10	58
FCT8	(16,21)	33	22	45	36	181
SHASTA	(17,21)	5	3	22	19	29
FCT8	(17,21)	11	6	38	26	57
SHASTA	(16,13)*	33	26	46	35	217
FCT8	(16,13)*	44	35	49	36	296
SHASTA	(17,13)	31	24	47	36	203
FCT8	(17,13)	51	36	45	48	314
SHASTA	(18,13)	22	16	47	34	128
FCT8	(18,13)	38	28	65	50	223

\*High source emission grid square.

concentrations are 1.5 to 2 times higher and  $\text{SO}_4$  concentrations are 1 to 1.5 times higher with the FCT8 algorithm. Sulfur deposition is also 1.5 to 2 times higher.  $\text{SO}_2$  and  $\text{SO}_4$  concentrations far away from source areas show correspondingly lower concentrations in the FCT8 solution. Another feature of the FCT8 results is that both the final and average  $\text{SO}_4$  concentration fields show distinct peaks in the Ohio Valley and New England states in contrast to the SHASTA results which show a broad peak. The sulfur mass balance for run 8 is given in Table 10-14. Relative to run 1, the final  $\text{SO}_2$  mass is 3% higher, final  $\text{SO}_4$  mass is 1% higher, and sulfur deposition is 2% higher. The residual  $\text{SO}_2$  component is 75% higher in the FCT8 run than in the SHASTA simulation. This could be related to differences in numerical errors or it be due to less mass being advected out of the grid with FCT8.

All of these results support the contention that the SHASTA algorithm has more artificial diffusion than the FCT8 algorithm. The FCT8 maintains the peak concentrations near the high emission sources fairly well, whereas the SHASTA algorithm artificially transfers the mass of the peaks to the surrounding grid squares. The overall geographic distributions of  $\text{SO}_2$  and  $\text{SO}_4$  mass are somewhat broader and significantly smoother with the SHASTA routine, which reflect the artificial diffusion. The differences between the SHASTA and FCT8 solutions are, in fact, greater than any of the differences found for the alternate model formulation discussed in Section 10.1.4 and are also comparable to the differences found for the reduced Ohio Valley emission scenarios. Hence, the SURADS model is quite sensitive to the numerical advection algorithm incorporated into the model.

Since most advection algorithms have some artificial diffusion, the SURADS model was originally designed without an explicit lateral diffusion step. As these results show, routines such as SHASTA have ample lateral diffusion. This calls attention to an important question for models that use routines such as FCT8, which preserve concentration gradients fairly well: Should explicit treatment of lateral diffusion be included in the model? Comparison of the FCT8 results with the July 21, 1978 24-hour average observations were made to determine if the measurements would help answer this question. The

TABLE 10-14

## RUN 8 SULFUR MASS BALANCE

<u>Component</u>	<u>SO<sub>2</sub></u>	<u>SO<sub>4</sub></u>
Initial concentrations	26.7	20.1
Emissions	47.1	0.94
Chemical conversion	-13.6	13.6
Deposition to ground	20.3	1.4
Residual*	4.2	-2.2
Final concentrations	44.1	31.0

statistical evaluation data for the FCT8 results are shown in Table 10-15, along with the SHASTA results presented previously.

The FCT8  $\text{SO}_4$  concentrations are slightly higher at the monitoring sites on the average than in the SHASTA results. As a result, FCT8 overestimates the  $\text{SO}_4$  concentrations by 12% rather than 6% on the average.\* Although the correlation with observations is slightly better in the FCT8 solution, both the average absolute error and RMS error are greater. FCT8 also overpredicts the observed  $\text{SO}_2$  24-hour average more than SHASTA. The average absolute error and RMS error are about 1 ppb higher in the FCT8 solution and the correlation coefficient is lower. Hence, judging from the model performance on this one day, the FCT8 algorithm does not improve agreement with the  $\text{SO}_2$  or  $\text{SO}_4$  measurements. The differences are not large enough to conclude one algorithm is necessarily better than the other, however.

It should be stressed again that model design decisions should not be based on the results from a one-day simulation, but rather numerous case studies and more fundamental considerations such as accuracy of model subcomponents. ERT believes that algorithms such as FCT8 are preferable to lower order schemes such as SHASTA because they yield smaller advection errors due to artificial diffusion. Analyses of FCT8 presented in Section 5.1 show its artificial diffusion is comparable to the order of magnitude of  $K_y$  used in numerous modeling exercises, whereas SHASTA's artificial diffusion is 5 to 20 times greater. ERT feels that an explicit lateral diffusion step is probably unnecessary in the model as long as artificial diffusion is relatively large. Ultimately, this question will be answered in testing the improved model on numerous case studies with and without an explicit lateral diffusion step.

#### 10.1.8 Summary of LRT Model Sensitivity Analyses

The SURADS Eulerian model was employed to perform a limited sensitivity study. The study primarily involved comparison of model results using different assumptions regarding complexity of model inputs and formulation. Also, simulations were made to determine the

\*Determined from ratios of mean calculated to mean observed concentration.

TABLE 10-15

STATISTICAL EVALUATION OF THE FCT8 BASELINE  
SIMULATION RESULTS VERSUS OBSERVATIONS

Species	n	$\bar{\chi}_c$	$\sigma_c$	$\bar{\chi}_o$	$\sigma_o$	$ \bar{E} $	$E_{RMS}$	$\bar{R}_{c/o}$	$\sigma_{c/o}$	r
SO <sub>4</sub> - FCT8	45	24.0	11.81	21.5	11.01	5.50	7.15	1.161	0.623	0.835
SO <sub>4</sub> - SHASTA	45	22.7	10.33	21.5	11.01	5.35	6.62	1.099	0.577	0.809
SO <sub>2</sub> - FCT8	35	11.97	7.16	10.03	9.51	6.29	8.55	1.525	1.808	0.531
SO <sub>2</sub> - SHASTA	35	10.29	5.11	10.03	9.51	5.34	7.43	1.378	1.788	0.631

$\bar{n}$  = number of observations compared.

$\bar{\chi}_{c,o}$  = average of calculated (c) or observed (o) concentrations.

$\sigma_{c,o}$  = standard deviation of calculated (c) or observed (o) concentrations.

$|\bar{E}|$  = average absolute error,  $|\overline{\chi_c - \chi_o}|$ .

$E_{RMS}$  = root mean square error,  $\sqrt{\sum(\chi_c - \chi_o)^2 / (n-1)}$ .

$\bar{R}_{c/o}$  = geometric mean ratio of calculated to observed concentrations,  $\left(\frac{\bar{\chi}_c}{\bar{\chi}_o}\right)_{geom}$

$\sigma_{c/o}$  = standard deviation of  $R_{c/o}$ ,  $\sqrt{\sum(R_{c/o} - \bar{R}_{c/o})^2 / (n-1)}$ .

r = correlation coefficient.

difference, if any, in the response between the complex and simplest models to emissions reductions.

For the model input complexity sensitivity analyses presented in Section 10.1.4, in which simulations were made using average values of input parameters that normally vary significantly in time and/or throughout the modeling region, it was found that there can be significant effects on the model results. For example, relative to the complex model, the compound simple model, which uses average values of conversion rate, vertical diffusivities, and deposition velocities, resulted in differences of less than 5% in  $\text{SO}_2$  and  $\text{SO}_4$  concentrations and sulfur deposition for the grid as a whole, but differences of 20% or more were seen for individual hours and/or subregions of the grid. Section 10.1.4.6 contains an expanded summary of these results.

Overall, both the complex model and the compound simple model responded in a nearly linear fashion to reductions in  $\text{SO}_x$  emissions (see Section 10.1.5). The differences in response to the emissions reductions seen between the two models are not considered to be significant for the most part. The emissions reductions of up to 45% in some grid squares resulted in relative reductions of sulfur deposition of up to 42% for the complex model and 44% for the simple model. The highest absolute reduction in sulfur deposition was greater for the complex model, 66 metric tons compared to 62 metric tons. The differences in the reductions (relative and absolute) are expected to be bigger for multiday simulations than for the single day simulations performed for this study. After 24 hours the zone of influence had extended approximately 250 km beyond the region in which the emission reduction were applied.

As shown in Section 10.1.6, the use of sulfate deposition velocities equal to  $\text{SO}_2$  deposition velocities (rather than a factor of 10 lower) increased sulfate deposition by a factor of  $6\frac{1}{2}$ . However, final sulfate concentrations overall were reduced by 24% and total sulfur deposition was increased by 36%.

The use of an eighth order flux corrected transported scheme (FCT8) rather than a second order scheme (SHASTA) resulted in significantly different results. The differences seen between the two



simulations are, in fact, greater than those seen in the model formulation sensitivity analyses (Section 10.1.4). As seen in Section 10.1.7, the FCT8 scheme maintains concentration gradients and peak values better than SHASTA. The agreement with observations, however, did not appear to be as good overall with FCT8 as with SHASTA.

## 10.2 Mesoscale Model Sensitivity Analysis

Sensitivity analyses were performed using the PLMSTAR reactive plume model to primarily investigate the differences in predictions of alternate lateral dispersion and chemical submodel formulations. The PLMSTAR model employs a multicolumn K-theory approach to lateral dispersion and has a nonlinear chemical mechanism. The chemical mechanism (Atkinson et al. 1982) simulates both  $\text{SO}_2$  conversion to sulfate ( $\text{SO}_4^{=}$ ) and  $\text{NO}_x$  conversion to nitrates [primarily nitric acid ( $\text{HNO}_3$ ) and peroxyacetylnitrate (PAN)] in the presence of reactive hydrocarbons (RHC) and ozone ( $\text{O}_3$ ). Baseline and emission control scenario simulations were carried out with (1) PLMSTAR, the "complex model", (2) a special version of PLMSTAR employing a single expanding column lateral dispersion formulation, (3) a version of PLMSTAR with linear chemistry, and (4) a version of PLMSTAR with an expanding column, linear chemistry, constant deposition velocity, and constant  $K_z$  coefficients. The rationale for performing these tests in addition to those on the SURADS long range transport model was to examine a model which includes  $\text{NO}_x$  species and nonlinear chemistry for both  $\text{SO}_x$  and  $\text{NO}_x$ . In addition, several of the sensitivity tests performed on SURADS were repeated with PLMSTAR to compare the models' responses. These tests include a constant deposition velocity case, a constant vertical eddy diffusivity ( $K_z$ ) case, and a case with an order of magnitude reduction in sulfate deposition velocity.

### 10.2.1 Mesoscale Model Formulations

#### 10.2.1.1 Model 1 - The PLMSTAR Model

ERT developed the PLMSTAR Lagrangian photochemical air quality model to assess the behavior of pollutants in chemically reactive plumes in urban and rural settings. The model is suitable for predicting major point source  $\text{NO}_x$ ,  $\text{SO}_x$ , and hydrocarbon emission impacts on downwind concentrations of  $\text{O}_3$ ,  $\text{NO}_2$ , PAN,  $\text{HNO}_3$  and  $\text{SO}_4$ .

In PLMSTAR, the Lagrangian modeling concept is applied to a moving wall of computational cells. The wall is advected along a

trajectory by the mean horizontal winds at a user-specified elevation that is usually selected to coincide with the major point source plume centerline elevation. Lateral and vertical diffusion, photochemistry, and entrainment of emissions along the trajectory are accounted for in each cell. In addition, dry deposition is accounted for in the surface cells and mixing with background air is accounted for in the outermost columns. The extent of the wall in the crosswind and vertical directions is held fixed during a simulation; however, individual cells have different dimensions in order to maximize plume and surface concentration resolution as shown in Figure 10-55.

In the Lagrangian framework (i.e., moving in the x-direction with wind speed  $u$ ), the governing conservation of mass equation for PLMSTAR reduces to:

$$\frac{\partial C_i}{\partial t} = \frac{\partial}{\partial y} \left( K_y \frac{\partial C_i}{\partial y} \right) + \frac{\partial}{\partial z} \left( K_z \frac{\partial C_i}{\partial z} \right) + R_i + S_i + D_i \quad (10-4)$$

Where:

- $C_i$  = concentration of the  $i^{\text{th}}$  species,
- $K_y, K_z$  = eddy diffusivity coefficients in the crosswind (y) and vertical (z) directions,
- $R_i$  = rate of chemical transformation of the  $i^{\text{th}}$  species,
- $S_i$  = rate of emissions of the  $i^{\text{th}}$  species, and
- $D_i$  = rate of deposition of the  $i^{\text{th}}$  species.

This equation is solved numerically in PLMSTAR to provide concentration-versus-time profiles for each species in each cell along the trajectory. Actually this equation is used to compute the concentration of 30 chemical species in each cell. Concentrations of six additional species, including OH, are computed from the pseudo steady state approximation. Another species,  $H_2O$ , is assumed to be constant for a given simulation.

Horizontal diffusivity coefficients ( $K_y$ ) used in Equation 10-4 are determined from:

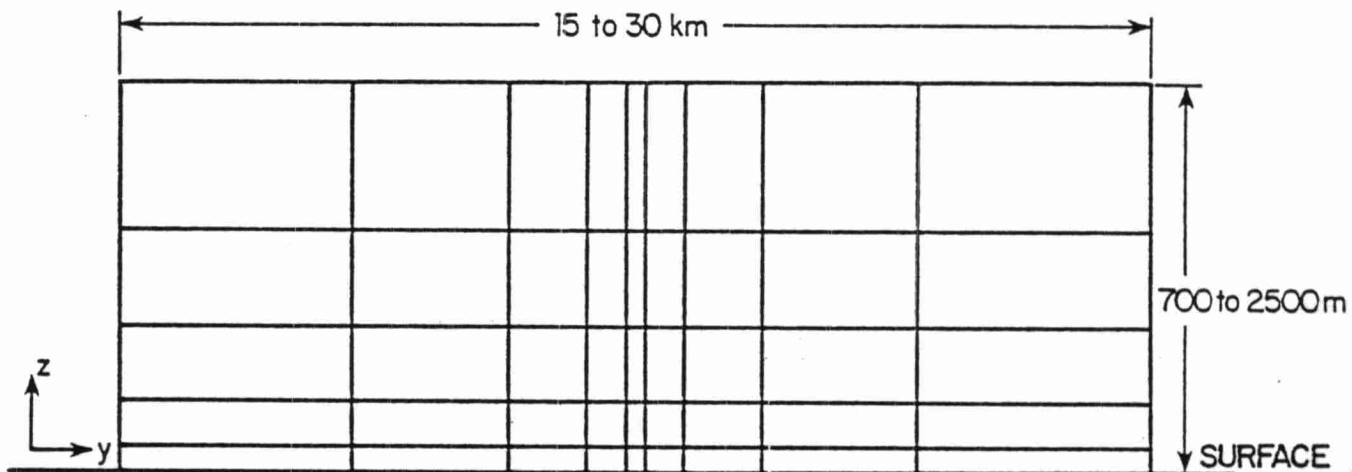


Figure 10-55. Typical PLMSTAR Computational Cell Configuration  
(drawing not to scale; actual proportions 5 to 10  
times wider than shown).

$$K_y = \frac{1}{2} \frac{\sigma_y^2}{t} \quad (10.2-2)$$

where  $\sigma_y$  is a function of atmospheric stability and downwind distance [Brookhaven National Laboratory  $\sigma_y$  data, Smith (1968)] and  $t$  is time downwind of the major point source.

Vertical diffusivity coefficients ( $K_z$ ) used in Equation 10-4 are determined from the following equations. In the unstable planetary boundary layer,

$$K_z = k u_* z \left( 1 - 15 \frac{z}{L} \right)^{1/4}, \quad z \leq |L|; \quad (10-5a)$$

$$= 2 k u_* z \left( -\frac{z}{L} \right)^{1/3}, \quad |L| \leq z \leq 0.1 z_i; \quad (10-5b)$$

$$= \frac{w_* z}{4} \left( 1 - \frac{z}{z_i} \right), \quad 0.1 \leq z \leq z_i; \quad (10-5c)$$

where  $k$  is the von Karman constant ( $=0.35$ );  $u_*$  is the surface friction velocity;  $z$  is the height above ground;  $L$  is the Monin-Obukhov length;  $z_i$  is the height of the PBL; and  $w_*$  is the convective velocity scale. For the stable PBL,

$$K_z = k u_* z \left( 1 - \frac{z}{z_i} \right)^{3/2} / \left( 1 + 4.7 \frac{z}{L} \right). \quad (10-6)$$

Above the PBL, an arbitrarily small value of  $0.01 \text{ m}^2/\text{s}$  is assigned to  $K_z$  for both stable and unstable boundary layers.

The chemical reaction rate term in Equation 10-4 based on a somewhat condensed version of the ERT photochemical mechanism (Atkinson et al. 1982). The rate for a particular species is a function of kinetic rate constants, reaction stoichiometry, and its concentrations as well as other species concentration. The distinguishing feature of this RHC/ $\text{NO}_x$ / $\text{SO}_x$  photochemical mechanism is that the hydrocarbons are partitioned into 8 classes to delineate their reactivity and reaction pathways, which is somewhat more classes than employed in other multicell photochemical models (e.g., ELSTAR, Lloyd et al. 1979). It is important to note that the PLMSTAR chemical

model does not include heterogeneous or aqueous phase reaction pathways for  $\text{SO}_x$  or  $\text{NO}_x$ . These may be particularly important for the acid rain question and will probably increase the nonlinearity of the mechanism.

The deposition rate term in Equation 10.2-1 is calculated from the product of the deposition velocity for each species and its concentration. The deposition velocity is assumed to be the inverse sum of a series of resistance to mass transfer:

$$F_d = (r_a + r_s + r_c)^{-1} \quad (10-7)$$

where  $r_a$  is the aerodynamic resistance,  $r_s$  is the surface resistance, and  $r_c$  is the canopy stomatal resistance. The deposition velocity for  $\text{SO}_2$  is calculated in PLMSTAR from the Wesley and Hicks (1977) parameterization:

$$V_d = k_{u*} [\ln(z/z_o) + 2.6 + k_{u*}r_c - \psi_c]^{-1} \quad (10-8)$$

where  $\psi_c$  is the adiabatic correction and  $r_c$  ranges from 0 to 2 s/cm (default value is 0.7 s/cm in PLMSTAR). Deposition velocities for other species are assumed to be proportional to  $\text{SO}_2$  deposition velocity. Table 10-16 lists the other species deposition velocity proportionality factors. It is important to note that only dry deposition processes are included in the model. Wet deposition processes are, of course, important for acid deposition but are not included in the current model.

#### 10.2.1.2 Model 2 - The Expanding Column Formulation

Many mesoscale trajectory models employ a single expanding column approach to lateral dispersion, rather than PLMSTAR's multicolumn K-theory approach. A special version of PLMSTAR, Model 2, was coded which employed the expanding column formulation. As in PLMSTAR, chemistry, vertical diffusion, and deposition were also calculated for a separate column representing background air. As the parcel receiving emissions is advected downwind of the major point,

TABLE 10-16

RATIO OF SPECIES DEPOSITION VELOCITIES TO  $\text{SO}_2$   $V_d$ 

<u>Species</u>	<u>Ratio</u>
$\text{SO}_4^-$	1. (1)
$\text{HNO}_3$	1. (1)
$\text{NO}_2$	.7 (2)
$\text{O}_3$	.35 (2)
PAN	.25 (3)
$\text{H}_2\text{O}_2$	.25 (3)
All others	.0

---

 (1) Hicks 1976

(2) Hill and Chamberlain 1976

(3) Garland and Penkett 1976

its width increases and its pollutant concentrations are diluted by air at background concentrations. For this application, the plume was allowed to continuously expand to the  $2.14 \sigma_y$  or 10% concentration line of a Gaussian plume, as shown in Figure 10-56.

PLMSTAR's differential equations were modified to replace the Fickian lateral diffusion term:

$$\frac{\partial C}{\partial t}(y,z,t) = \frac{\partial}{\partial y} K_y \frac{\partial C}{\partial y} + \dots \quad (10-9)$$

with

$$\frac{\partial C}{\partial t}(z,t) = -d(t) C(z,t) - C_b(z,t) + \dots \quad (10-10)$$

where  $d$  = rate of dilution,  
 $C$  = air parcel concentration, and  
 $C_b$  = background air concentration.

The dilution rate at time  $t$  was calculated from

$$d(t) = \frac{1}{\Delta t} \ln \frac{\sigma_y(t+\Delta b)}{\sigma_y(t)} \quad (10-11)$$

where  $\Delta t$  was typically one hour and BNL  $\sigma_y$  data (Smith 1968) were employed. To facilitate comparison of the expanding column model with PLMSTAR outputs, the background air was assumed to have a time-varying volume equal to the Model 1 parcel volume minus the expanding column volume. Hence, both models were initialized with the same amount of mass and deposition accumulation is calculated for the same area. The major difference between the models is that the complex model spatially resolves the crosswind concentration distribution and the simple model predicts the average concentration across the plume width.



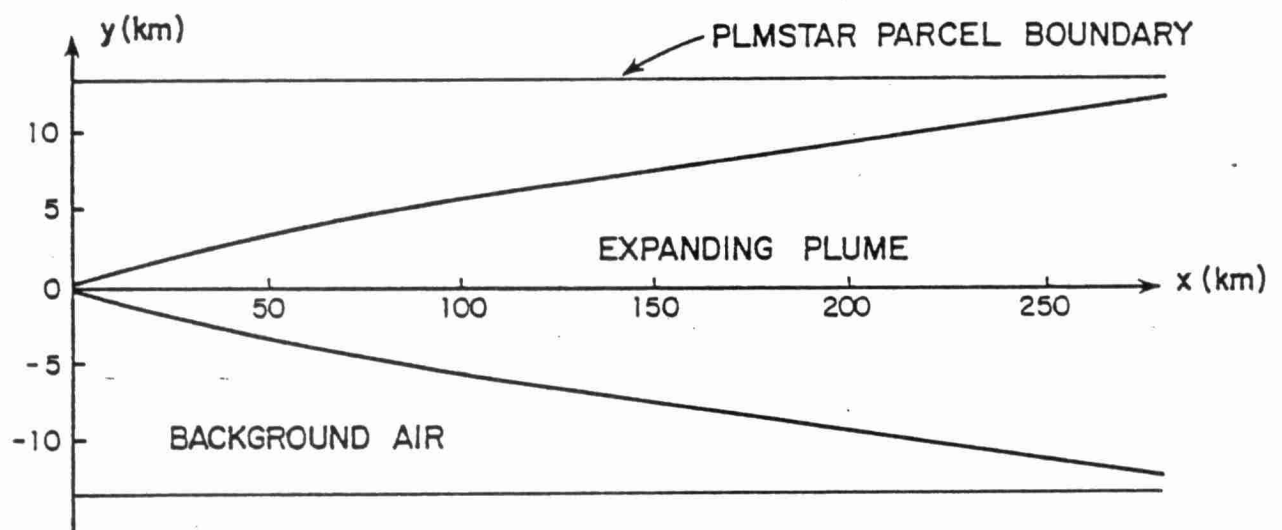


Figure 10-56. Top view of the expanding plume. This concept is used in Model 2.

#### 10.2.1.3 Model 3 - The Linear Chemistry Model

Chemical transformation of  $\text{SO}_2$  to sulfate and  $\text{NO}_x$  to nitrates are modeled as first order linear processes in most mesoscale and long range transport models. A version of PLMSTAR, Model 3, was coded with constant linear transformation rates to represent another simple model. The rates of conversion for the model were calculated from the nonlinear chemistry in the Model 1 baseline runs at 15 minute intervals. Since the cell volumes in the wall of cells typically vary by a factor of 100 or more and may have substantially different chemical transformation rates, a mass-weighted average conversion rate was computed at each interval. The diurnal variation in average conversion rates for  $\text{SO}_2$  and  $\text{NO}_x$  ( $=\text{NO} + \text{NO}_2 + \text{N}_2\text{O}_5 + \text{HNO}_4$ ) are shown in Figures 10-58 and 10-59, respectively. The apparent conversion rate for  $\text{NO}_x$  is very similar to the sum of the PAN and  $\text{HNO}_3$  formation rate shown in Figure 10-60. Summer and winter  $\text{SO}_2$  transformation rates, representative of  $40^\circ$  N latitude, were found to vary from 0 to 3.5 and 0. to 1.1 percent per hour, respectively, over the course of the day. Higher rates of conversion and a larger differential between winter and summer rates were found for  $\text{NO}_x$ . The winter  $\text{NO}_x$  conversion rates varied from 3 to 40 percent per hour, while the summer conversion rates varied from 10 to 20,000 percent per hour. It is important to note that the very high  $\text{NO}_x$  conversion rates (i.e., greater than 100%/hour) occur when the  $\text{NO}_x$  concentrations are very low. The high rates occur because of the high potential for PAN formation in the presence of RHC and sunlight. The mass-weighted conversion rates at each interval were averaged for the whole simulation to determine constant transformation rates to use in the simple model. The average  $\text{SO}_2$  transformation rates for these simulations were 0.6 and 2.0 percent per hour for winter and summer, respectively. The time-averaged  $\text{NO}_x$  transformation rates were 24 and 17,000 percent per hour for winter and summer, respectively. These  $\text{NO}_x$  loss rates, especially the summer rate, turned out to be less useful since the averages were dominated by the high apparent rates associated with very low  $\text{NO}_x$  concentrations. Hence, a trial and error approach was used to select the  $\text{NO}_x$  conversion rates. Winter

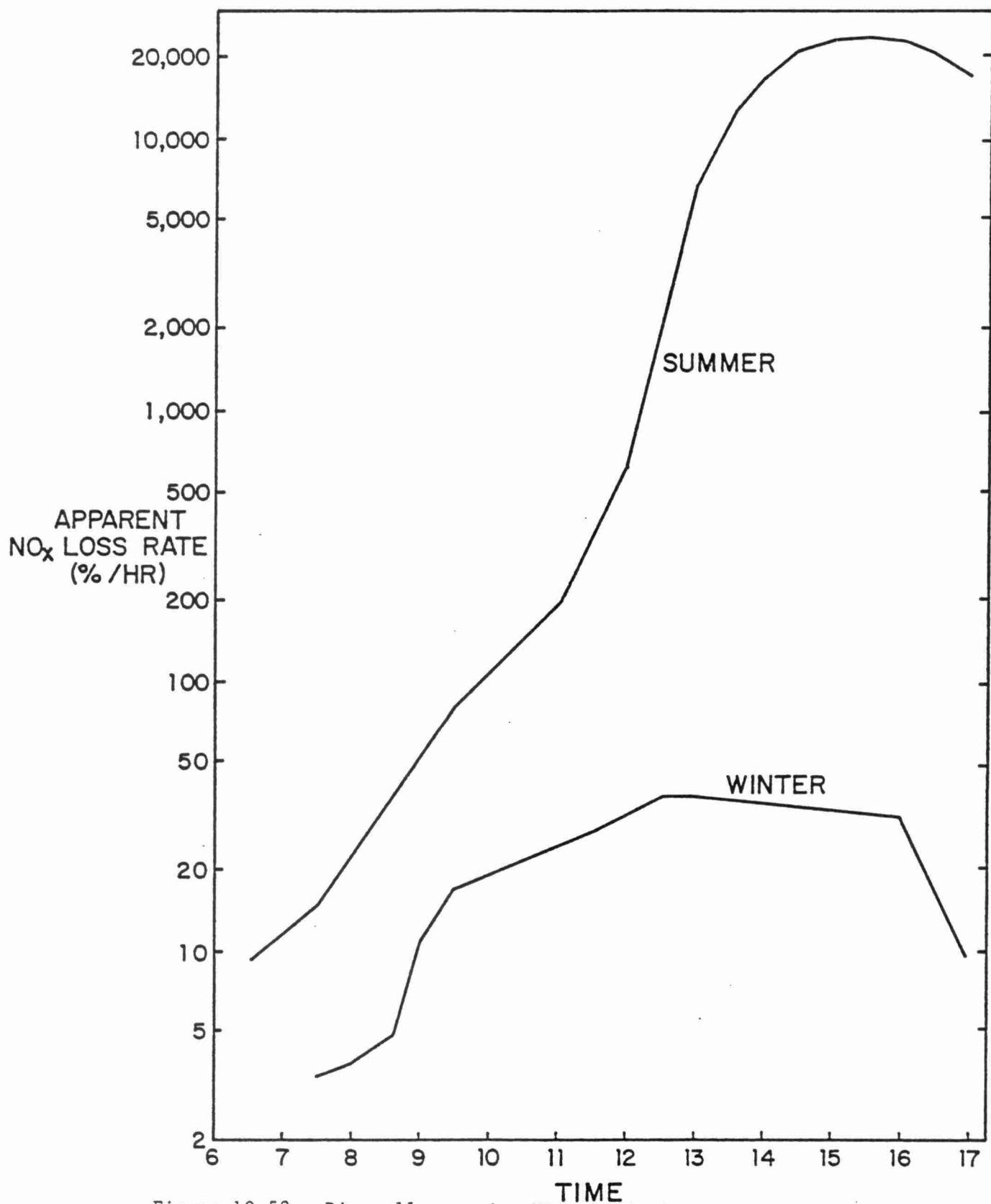


Figure 10-58. Diurnally varying NO<sub>x</sub> chemical transformation rates calculated by the PLMSTAR Model.

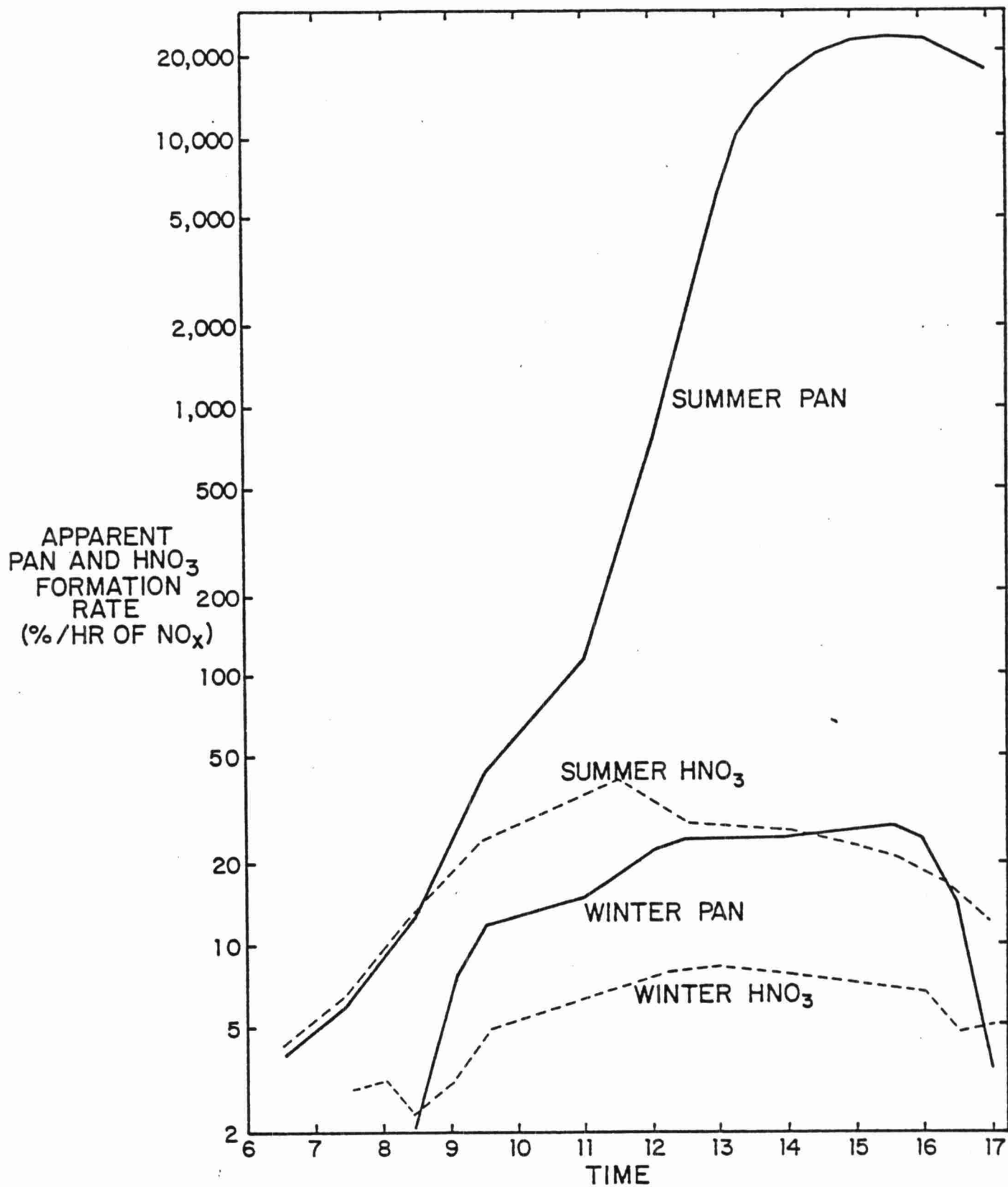


Figure 10-59. Diurnally varying PAN and HNO<sub>3</sub> formation rates calculated by the PLMSTAR Model.

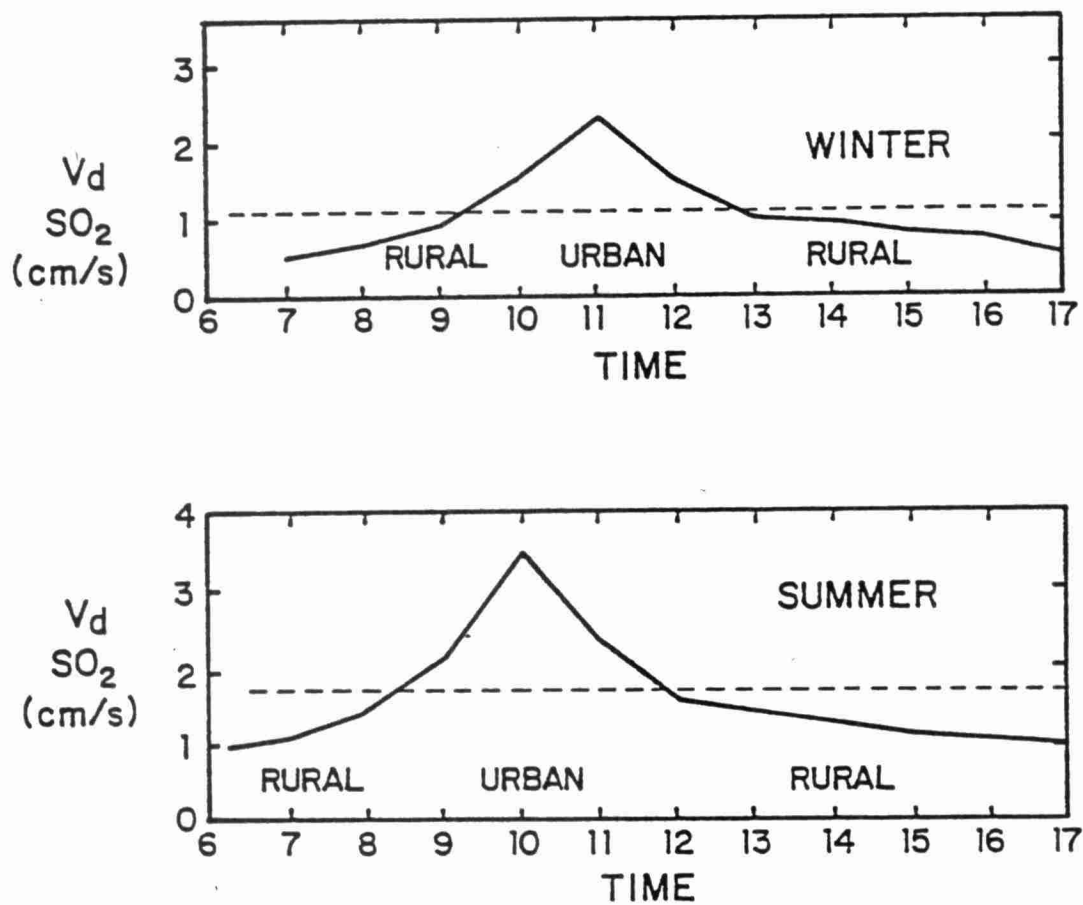


Figure 10-60. Average (---) and diurnally-Varying(—)  $\text{SO}_2$  Deposition Velocities.

simulations were carried out with 10 and 20 percent per hour rates. Summer simulations were performed with 30 and 60 percent per hour rates. The higher rates resulted in drastic overprediction of nitrates along the plume centerline relative to the complex model results, while the lower rates (10 and 30%/hour) resulted in moderate overprediction of nitrate along the centerline and moderate underprediction away from the centerline. Hence, the lower  $\text{NO}_x$  rates were selected for the simple linear chemistry model.

Deposition velocities for  $\text{NO}_x$  and total nitrates ( $\text{TNO}_3$ ) in the linear chemical model were estimated from the complex model values for  $\text{NO}$ ,  $\text{NO}_2$ , PAN, and  $\text{HNO}_3$ . In the complex model the ratios of  $\text{NO}$  and  $\text{NO}_2$  deposition velocities to  $\text{SO}_2$  deposition velocity are 0. and 0.7, respectively. Since  $\text{NO}_2$  concentrations were generally higher than  $\text{NO}$  concentrations, in these simulations, the  $\text{NO}_x$  deposition velocity was set equal to 0.5 times the  $\text{SO}_2$  deposition velocity. Nitric acid and PAN deposition velocities in the complex model are set equal to 1.0 and 0.25 times  $\text{SO}_2$  deposition velocity, respectively. Since PAN concentrations were generally higher than nitric acid in the simulations, the ratio of  $\text{NO}_3$  deposition velocity to  $\text{SO}_2$  deposition velocity was set equal to 0.5 in the linear chemical model.

#### 10.2.1.4 Other Simple Models' Formulation

Several other simple models were constructed from the complex model. A version of PLMSTAR, Model 4, was set up with time-averaged, constant deposition velocities. The average and diurnally-varying  $\text{SO}_2$  deposition velocities for the summer and winter cases are shown in Figure 10-61. Average deposition velocities of 1.6 and 1.1 cm/sec were used in summer and winter, respectively. All other features of Model 4 were identical to Model 1.

Another version of PLMSTAR, Model 5, employed average vertical eddy diffusivity ( $K_z$ ) coefficients instead of time-varying coefficients. Average  $K_z$  coefficients between each vertical layer were computed from the diurnally varying inputs to Model 1, shown in Figure 10-62. Average  $K_z$  values of 12.4, 25.9, 32.3, and 16.6  $\text{m}^2/\text{s}$  between layers 1 & 2, 2 & 3, 3 & 4, and 4 & 5, respectively, were used

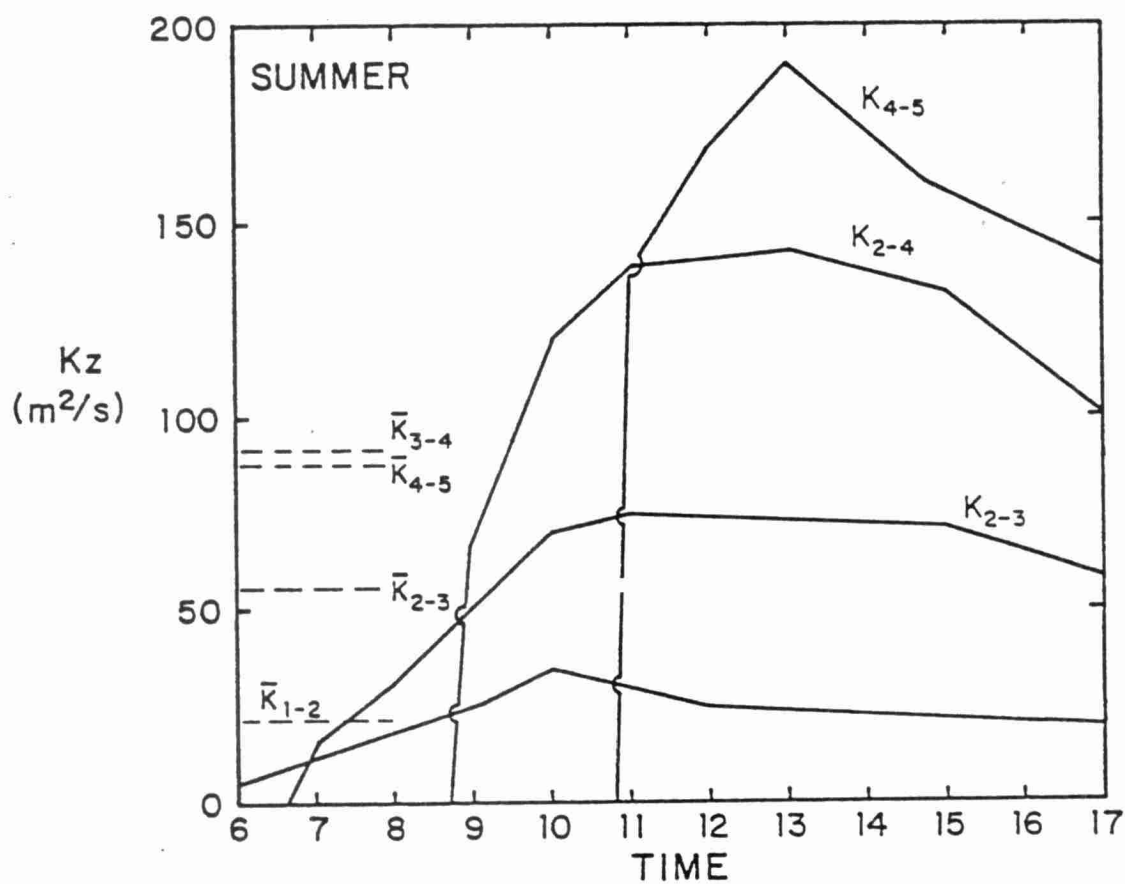
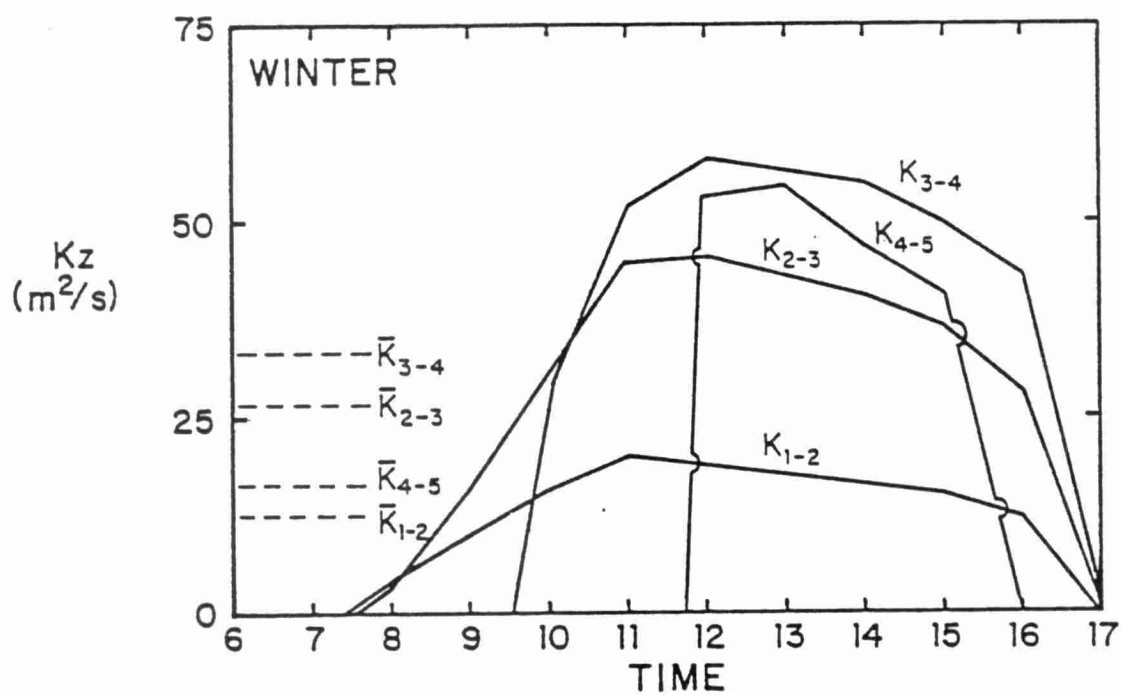


Figure 10-61. Average (---) and Diurnally-varying  $K_z$  (—) coefficients employed in Models 5 and <sup>2</sup>1.

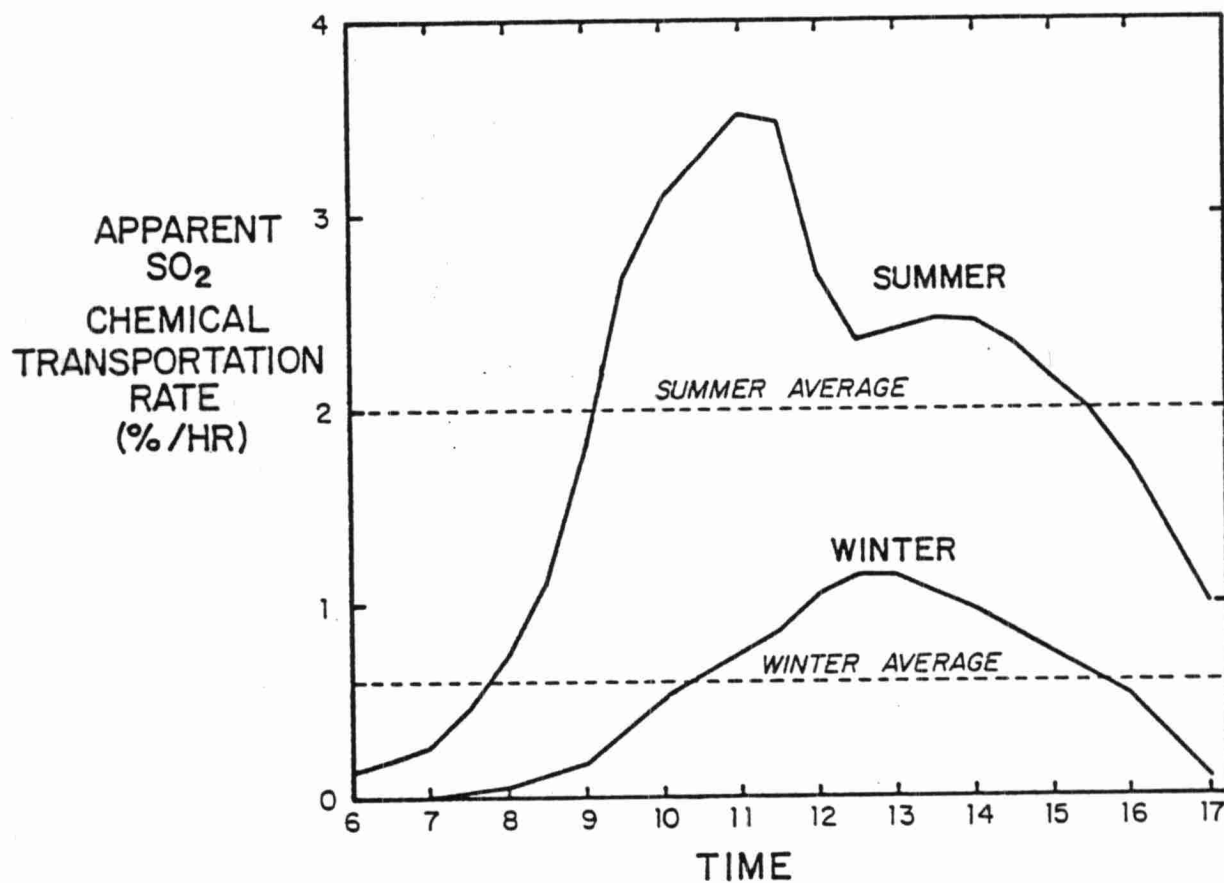


Figure 10-62. Diurnally Varying and Average SO<sub>2</sub> Chemical Transformation Rates Computed by the PLMSTAR Model.



for winter in Model 5. For summer, average  $K_z$  values of 22.2, 56.0, 92.5, and 89.0  $\text{m}^2/\text{sec}$  between layers 1 & 2, 2 & 3, 3 & 4, and 4 & 5, respectively, were used in Model 5. It is important to note that these values are dominated by the higher  $K_z$  values occurring at midday.

Lastly, Model 6 was constructed to represent the compound simple model. Its formulation was based on the combination of all of the simplifications in Models 2 through 5; i.e., the expanding column approach to lateral diffusion, the linear chemical mechanism, constant deposition velocities, and constant  $K_z$  coefficients.

#### 10.2.2 Mesoscale Model Sensitivity Run Description

##### 10.2.2.1 Baseline Case Conditions

Two hypothetical cases were established for the mesoscale model simulations. In both cases, pollutants from a generic Ohio Valley major point source passed near sunrise and from an urban area passed in midmorning were emitted into the air parcel. Meteorological conditions were selected based on two general synoptic patterns associated with elevated sulfate concentrations in eastern North America (Lavery et al. 1981). Meteorological conditions characteristic of the "channeling" synoptic situation were chosen for a summer case. Meteorological conditions resembling the "stagnation" synoptic situation were chosen for a winter case.

The assumed meteorological conditions for the summer and winter cases are listed in Table 10-17. Wind speeds, surface temperature, and mixing heights range from 6 to 8 m/s, 21 to 35°C, and 200 to 1500 m, respectively, in the summer case. Ventilation and dispersion are more restricted in the winter case. Wind speed, surface temperature, and mixing height range from 4 to 5 m/s, 5 to 15°C, and 150 to 800 m, respectively. Note that higher average temperature and solar radiation (as indicated by  $\text{NO}_2$  photolysis rates in Table 10-18) greatly enhance photochemical activity in the summer case. In fact, the primary rationale for using the two seasons was to delineate seasonal chemical differences.

TABLE 10-17  
METEOROLOGICAL CONDITIONS FOR MESOSCALE MODEL RUNS

Time (hr)	SUMMER CASE					WINTER CASE				
	Wind Speed (m/s)	Surface Temp. (°C)	Average Temp* (°C)	Mixing Height (m)	NO <sub>2</sub> Photolysis** (min)	Wind Speed (m/s)	Surface Temp. (°C)	Average Temp* (°C)	Mixing Height (m)	NO <sub>2</sub> Photolysis** (min)
6	6	21	19.2	200	.09	-	-	-	-	-
7	6	23	20.3	300	.24	4	5.0	3.7	150	.0
8	7	25	21.3	450	.37	4	6.5	4.4	250	.01
9	7	27	21.7	700	.45	4	8.0	5.3	350	.11
10	8	30	23.5	1000	.51	5	10.	6.6	500	.23
11	8	32	24.9	1250	.54	5	12.	8.2	650	.31
12	8	34	26.7	1400	.55	5	14.	10.1	750	.35
13	8	35	27.7	1500	.55	5	15.	11.1	800	.35
14	7	35	27.7	1500	.54	5	14.	10.1	750	.31
15	5	34	26.7	1400	.51	4	13.	9.1	700	.23
16	6	33	25.8	1300	.46	4	11.	7.2	650	.11
17	6	32	25.0	1200	.37	4	9.	5.3	600	.01

\*Average temperature below maximum mixing height - used to determine chemical rate constants.

\*\*For clear sky conditions.

TABLE 10-18

## MISCELLANEOUS CHARACTERISTICS OF THE MESOSCALE MODEL TRAJECTORIES

Time (hr)	SUMMER CASE				WINTER CASE			
	Travel Distance (km)	Plume* Width (km)	Surface Roughness (m)	SO <sub>2</sub> Dep. Vel (cm/sec)	Travel Distance (km)	Plume Width (km)	Surface Roughness* (m)	SO <sub>2</sub> Dep. Vel (cm/sec)
6	0	0.5	0.1	1.0	-	-	-	-
7	21.6	3.5	0.1	1.1	0	0.5	0.1	.5
8	43.2	5.8	0.1	1.4	14.4	2.6	0.1	.7
9	68.4	8.2	0.3	2.1	28.8	4.3	0.1	.9
10	93.6	10.5	1.0	3.5	43.2	5.8	0.3	1.5
11	122.	12.9	0.3	2.3	61.2	7.6	1.0	2.3
12	151.	15.2	0.1	1.5	79.2	9.2	0.3	1.5
13	180.	17.3	0.1	1.4	97.2	10.8	0.1	1.0
14	209.	19.5	0.1	1.3	115.2	12.3	0.1	0.9
15	234.	21.2	0.1	1.3	133.2	13.8	0.1	0.8
16	259.	23.0	0.1	1.1	151.2	15.2	0.1	.07
17	284.	24.7	0.1	1.1	165.6	16.3	0.1	.05

\*Plume Width = 4.28  $\sigma_y$ .

Travel distance, approximate plume width, assumed surface roughness, and calculated  $\text{SO}_2$  deposition velocities for the two trajectories are listed in Table 10-19. These data show that the winter and summer air parcels travel 165 and 284 km, respectively, and the plume spreads horizontally to approximately 16 and 25 km, respectively, in the two cases. The surface roughness height data reflects the presence of an urban area which is assumed to be passed at 1000 and 1100 in the summer and winter cases, respectively. These data show substantial increases in deposition velocities with increasing wind speed and surface roughness.

Mesh geometries for the winter and summer cases were selected to encompass the plume width ( $4.28 \sigma_y$ ) and maximum mixing height. Column widths for the multicolumn model were 6, 4, 2, 1, 0.5, 1, 2, 4, and 6 km across the wall of cells. The same column widths were used for summer and winter since the plume reaches the outermost cells by the end of the run in each case. The total width of the air mass being modeled was 26.5 km. The vertical layer depths employed were 50, 100, 150, 200, and 300 meters in the winter and 50, 100, 200, 400, 750 meters in the summer. These, of course, sum to the maximum mixing depth and provide maximum resolution near the ground.

Assumed emission rates for the simulation are shown in Table 10-19 and are identical for the summer and winter cases. The major point source has  $\text{SO}_x$ ,  $\text{NO}_x$  and reactive hydrocarbon (RHC) emissions of 4000, 1000, and 30 kg/hr, respectively, which are typical of large power plants. These emissions are injected into the center column's third layer. The urban area is assumed to emit 200, 1000, and 2000 kg/hr of  $\text{SO}_x$ ,  $\text{NO}_x$ , and RHC and have the emissions uniformly distributed over a 15 by 15 km region. The urban emissions are believed to be typical of a city with a population of about 200,000. These urban emissions are injected into the surface layer in columns 2 through 8.

All  $\text{SO}_x$  and  $\text{NO}_x$  emissions are assumed to be 97%  $\text{SO}_2$  and 3%  $\text{SO}_4$  on a molar basis.  $\text{NO}_x$  emissions are partitioned as 90% NO and 10%  $\text{NO}_2$  on a molar basis. The urban reactive hydrocarbons emissions are assumed to be 45%  $\geq \text{C}_4$  alkanes, 5% ethylene, 3% propylene, 6% butenes, 12% toluene, 18%  $\geq \text{C}_8$  aromatics, 3% aldehydes, and 8% slowly reacting

TABLE 10-19

ASSUMED EMISSION RATES FOR MESOSCALE MODEL RUNS  
(kg/hr)

<u>Pollutant</u>	<u>Major Point</u>	<u>Other Area</u>
SO <sub>x</sub> (as SO <sub>2</sub> )	4000	200
SO <sub>2</sub>	3880	194
SO <sub>4</sub>	180	9
NO <sub>x</sub> (as NO <sub>2</sub> )	1000	1000
NO	1433	1433
NO <sub>2</sub>	65	65
RHC	30	2000
>C4 Alkanes	15	900
Ethylene	0	100
Propylene	0	60
Butenes	0	120
Toluene	0	240
>C8 Aromatics	0	360
Formaldehyde	7.5	30
Acetaldehydes	7.5	30
Nonreactive	0	160

---

\*Uniformly emitted within a 15x15 km urban region.

NMHC (nonreactive in PLMSTAR) on a weight basis. Table 10-20 shows the percent of the mass entrained along the winter and summer trajectories by source category as well as the percent of emissions from the two source categories in the SURE regional inventory (Klemm and Brennan 1981). The data indicate the source category contributions in the hypothetical cases are similar to those in the regional inventory.

The PLMSTAR model requires inputs for air quality conditions at the trajectory start location. Initial concentrations assumed for the simulations are listed in Table 10-21. The assumed concentrations are basically 1.5 ppb  $\text{SO}_x$ , 5 ppb  $\text{NO}_x$ , 100 ppbC RHC, and 20 to 40 ppb  $\text{O}_3$ . These concentrations are plausible values for air quality in the Ohio Valley. They assume there are sources upwind of the trajectory start point which have contributed significantly to the air quality, especially for  $\text{NO}_x$ , RHC, and  $\text{O}_3$ . Table 10-22 shows the origin of mass in the simulations. These data clearly show that the initial pollutant mass in the air parcel often exceeds the amounts contributed by the emissions sources along the hypothetical trajectories. Initial RHC mass far exceeds the amount contributed by emissions, while initial  $\text{SO}_x$  mass is less than half the source contributions for these cases.

#### 10.2.2.2 Sensitivity Run Conditions

Table 10-23 lists the baseline and sensitivity runs characteristics for this study. The tables show the season (or meteorological case), the chemical mechanism (linear or nonlinear), the number of vertical columns in the air parcel, deposition model,  $K_z$  model, and the percentage of baseline point and area source emissions included in the simulations. Note that the first character of the run number indicates the season (S=summer, W=winter) and the second character is the model number (1-6). Three emission control scenarios were run for models 1, 2, 3, and 6. The third character in the run number indicates the emission scenario. Scenario A is a 50 percent reduction in major point source emissions of all pollutants. Scenario B is a 50% reduction in both major point and area source emissions of

TABLE 10-20

## PERCENT OF EMISSION BY SOURCE CATEGORY

	Major Point Sources (%)	Other Area Sources (%)
NO <sub>x</sub> - summer case	40	60
NO <sub>x</sub> - winter case	55	45
NO <sub>x</sub> - SURE inventory	37	63
SO <sub>x</sub> - summer case	93	7
SO <sub>x</sub> - winter case	96	4
SO <sub>x</sub> - SURE inventory	83	17
RHC - summer case	1	99
RHC - winter case	2	98
RHC - SURE inventory	8	92

TABLE 10-21

## ASSUMED INITIAL CONCENTRATIONS FOR MESOSCALE MODEL RUNS

<u>Species</u>	<u>Concentration (ppb C)</u>	
	<u>Summer</u>	<u>Winter</u>
SO <sub>x</sub>	1.5	1.5
SO <sub>2</sub>	1.0	1.0
SO <sub>4</sub>	0.5	0.5
NO <sub>x</sub>	5.0	5.0
NO	0.5	1.0
NO <sub>2</sub>	4.5	4.0
PAN	.001	.001
HNO <sub>3</sub>	.001	.001
HONO	.05	0.05
RHC*	100	100
>C4 Alkanes	60	60
Ethylene	15	15
Propylene	0	0
Butenes	0	0
Toluene	10	10
>C8 Aromatics	5	5
Formaldehyde	5	5
Acetaldehyde	5	5
O <sub>3</sub>	40	20
H <sub>2</sub> O	2 x 10 <sup>7</sup>	2 x 10 <sup>7</sup>
Other Species	0	0

\*RHC and RHC class concentrations are in ppbC.



TABLE 10-22

## MASS CONTRIBUTIONS IN MESOSCALE MODEL RUNS

Pollutant	Initial Concentration		Point Emissions		Area Emissions		Total Mass	
	(KG)	(%)	(KG)	(%)	(KG)	(%)	(KG)	(%)
NO <sub>x</sub> -summer	2790	(82)	347	(10)	260	(8)	3397	(100)
NO <sub>x</sub> -winter	1488	(61)	520	(21)	417	(17)	2425	(100)
SO <sub>x</sub> -summer	1164	(45)	1389	(53)	52	(2)	2605	(100)
SO <sub>x</sub> -winter	621	(22)	2083	(75)	83	(3)	2787	(100)
RHC-summer	16980	(97)	10	(0)	520	(3)	17510	(100)
RHC-winter	9057	(92)	16	(0)	833	(8)	9906	(100)

\*NO<sub>x</sub> and SO<sub>x</sub> weighed as NO<sub>2</sub> and SO<sub>2</sub>.

TABLE 10-23

## MESOSCALE MODEL SENSITIVITY RUNS

Run #	Chemistry	No. Columns	Deposition	K <sub>z</sub>	Season	Point	Area
S1	nonlinear	9	variable	variable	summer	100%	100%
S1A	nonlinear	9	variable	variable	summer	50%	100%
S1B	nonlinear	9	variable	variable	summer	50%	50%
S1C	nonlinear	9	variable	variable	summer	0%	0%
S2	nonlinear	1	variable	variable	summer	100%	100%
S2A	nonlinear	1	variable	variable	summer	50%	100%
S2B	nonlinear	1	variable	variable	summer	50%	50%
S2C	nonlinear	1	variable	variable	summer	0%	0%
S3	linear	9	variable	variable	summer	100%	100%
S3A	linear	9	variable	variable	summer	50%	100%
S3B	linear	9	variable	variable	summer	50%	50%
S3C	linear	9	variable	variable	summer	0%	0%
S4	nonlinear	9	constant	variable	summer	100%	100%
S5	nonlinear	9	variable	constant	summer	100%	100%
S6	linear	1	constant	constant	summer	100%	100%
S6A	linear	1	constant	constant	summer	50%	100%
S6B	linear	1	constant	constant	summer	50%	50%
S6C	linear	1	constant	constant	summer	0%	0%
W1	nonlinear	9	variable	variable	winter	100%	100%
W1A	nonlinear	9	variable	variable	winter	50%	100%
W1B	nonlinear	9	variable	variable	winter	50%	50%
W1C	nonlinear	9	variable	variable	winter	0%	0%
W2	nonlinear	1	variable	variable	winter	100%	100%
W2A	nonlinear	1	variable	variable	winter	50%	100%
W2B	nonlinear	1	variable	variable	winter	50%	50%
W2C	nonlinear	1	variable	variable	winter	0%	0%
W3	linear	9	variable	variable	winter	100%	100%
W3A	linear	9	variable	variable	winter	50%	100%
W3B	linear	9	variable	variable	winter	50%	50%
W3C	linear	9	variable	variable	winter	0%	0%
W4	nonlinear	9	constant	variable	winter	100%	100%
W5	nonlinear	9	variable	constant	winter	100%	100%
W6	linear	1	constant	constant	winter	100%	100%
W6A	linear	1	constant	constant	winter	50%	50%
W6B	linear	1	constant	constant	winter	50%	50%
W6C	linear	1	constant	constant	winter	0%	0%

all pollutants. Scenario C represents the case with zero emissions, i.e., initial concentrations only. Although Scenario C is not a very realistic scenario, its results are important for proper interpretation of the results because it reflects the lower bound for percent reduction in model output parameters for these cases.

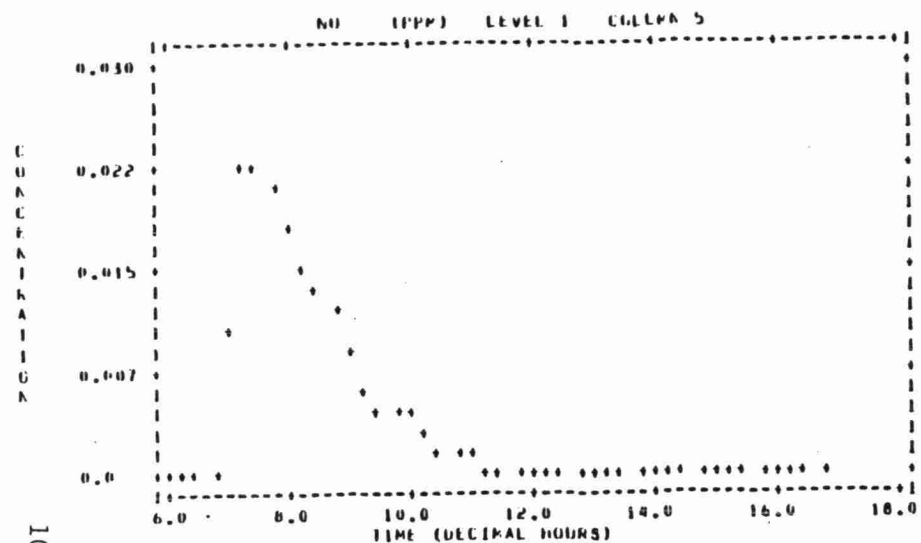
### 10.2.3 The Complex Mesoscale Model Results

The complex model's results for the baseline cases (S1 and W1) are shown in Figures 10-62 through 10-64. The predicted surface  $\text{SO}_2$ ,  $\text{SO}_4$ ,  $\text{NO}$ ,  $\text{NO}_2$ ,  $\text{O}_3$ , PAN,  $\text{HNO}_3$ , and  $\text{H}_2\text{O}_2$  centerline concentrations as a function of time are shown in Figure 10-62 and 10-63 for summer and winter trajectories, respectively. Reactive hydrocarbon (RHC) concentration profiles are shown in Figure 10-64.

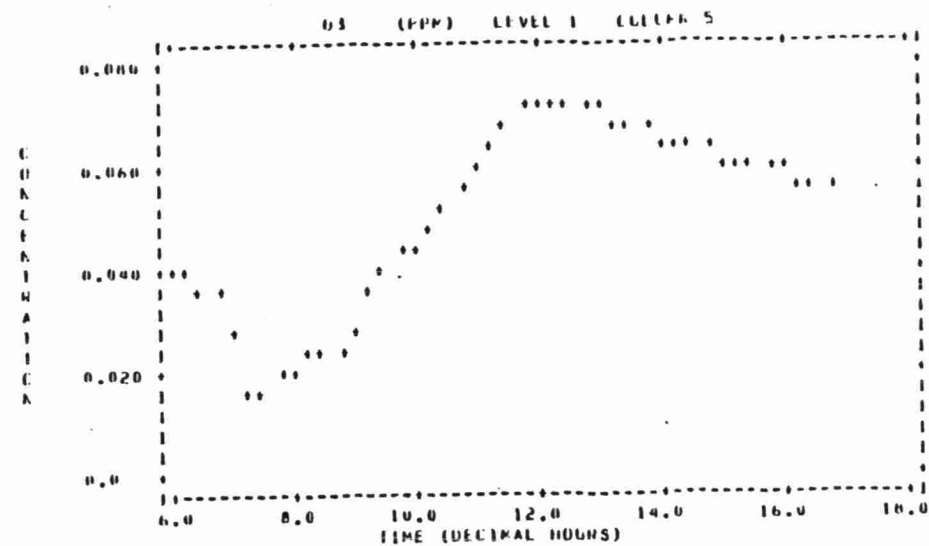
The results for the summer trajectory indicate maximum  $\text{SO}_2$ ,  $\text{SO}_4$ ,  $\text{NO}$ , and  $\text{NO}_2$  surface concentrations of 125, 4.5, 23, and 28 ppb, respectively, occurring near 0730 when the plume reaches the surface cell. The predicted ozone shows a decrease from 40 to 20 ppb in the early morning (0730-0930) as a result of scavenging by  $\text{NO}_x$  in the plume. The predicted centerline ozone increases after this period, due to photochemical production and entrainment of ambient air into the plume, to reach a maximum of 73 ppb near 1200. This predicted ozone maximum occurs 2 hours downwind of the urban area which is consistent with general trends in ambient data.

Predicted nitric acid concentrations reach a maximum of 3.5 ppb at 1130. Predicted PAN concentrations steadily increase over the run to a maximum of 7.5 ppb in late afternoon. The significantly different diurnal profiles for  $\text{HNO}_3$  and PAN are believed to be a result of different chemical formation pathways and differences in cross-plume concentration gradients. The morning  $\text{HNO}_3$  concentrations along the plume centerline are typically a factor of two higher than off-centerline values, as a result of the point source  $\text{NO}_x$  emissions. The  $\text{HNO}_3$  peak is reduced substantially by lateral diffusion and deposition in the afternoon hours. Predicted PAN concentrations, like ozone and RHC, are more uniform across the wall of cells and the effects of lateral dispersion are barely noticeable.

PLMSTAR - SUMMER - NONLINEAR CHEMISTRY - BASELINE - RUN S1



PLMSTAR - SUMMER - NONLINEAR CHEMISTRY - BASELINE - RUN S1



10-125

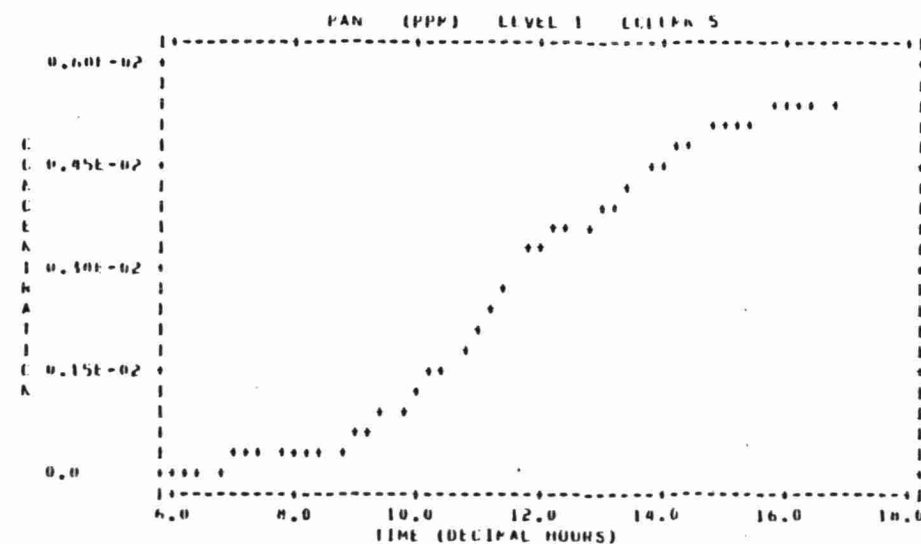
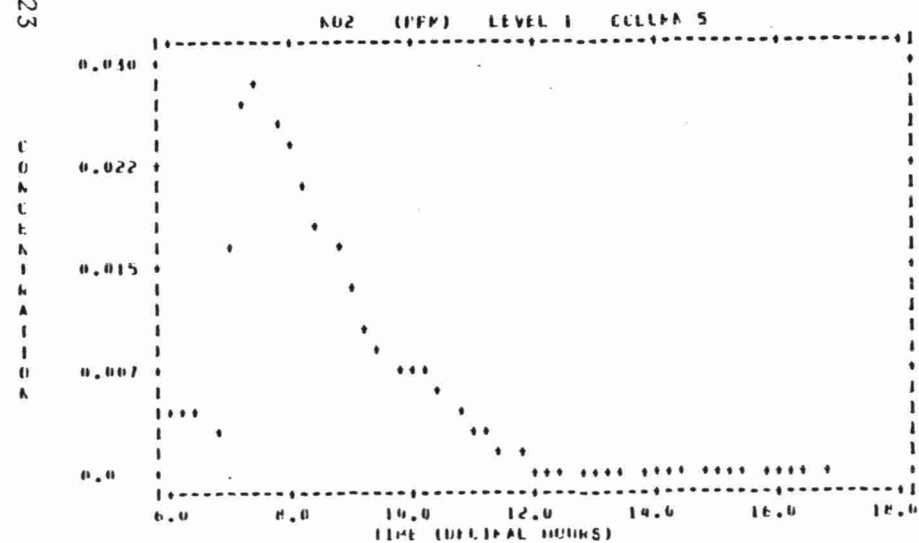
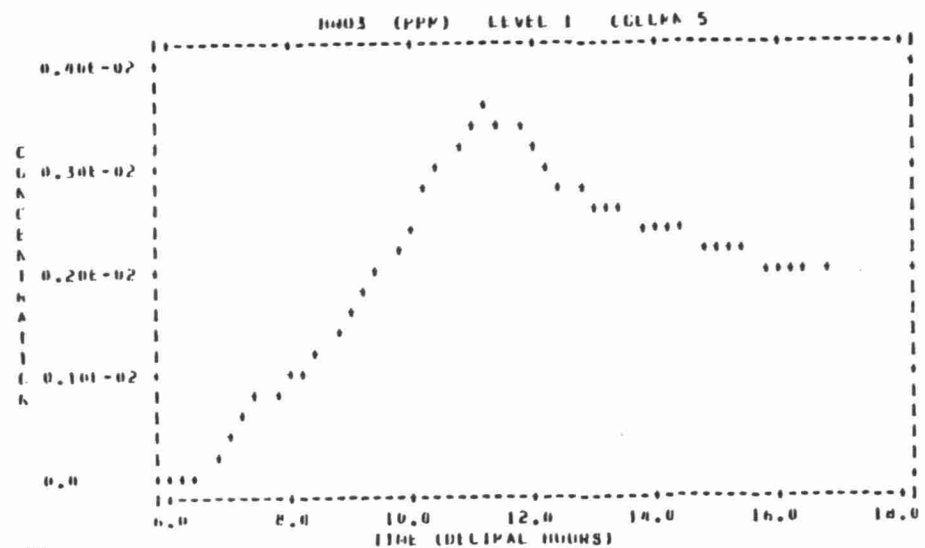
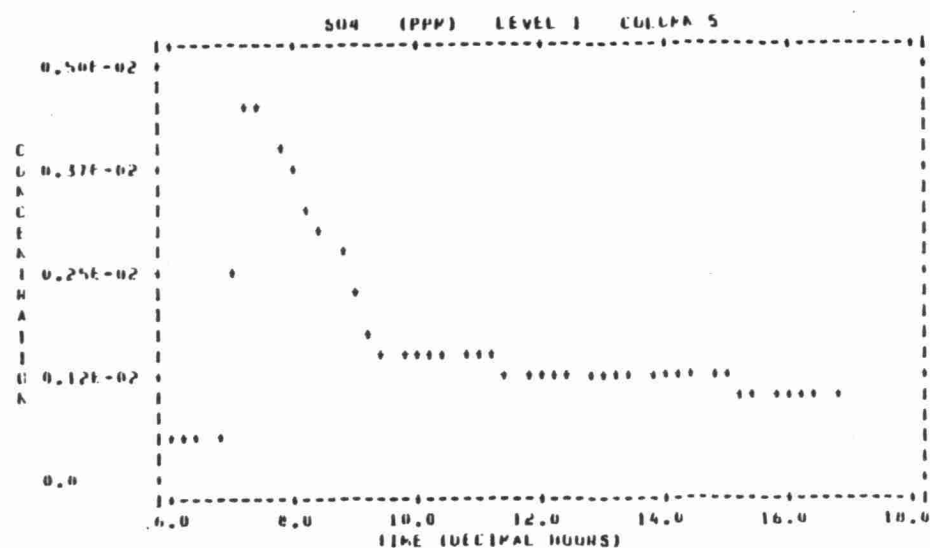


Figure 10-62. Center Column Surface Cell Concentration vs Time Profiles for PLMSTAR run S1.

PLPSTAR - SUMMER - NONLINEAR CHEMISTRY - BASELINE - RUN 51



PLPSTAR - SUMMER - NONLINEAR CHEMISTRY - BASELINE - RUN 51



10-124

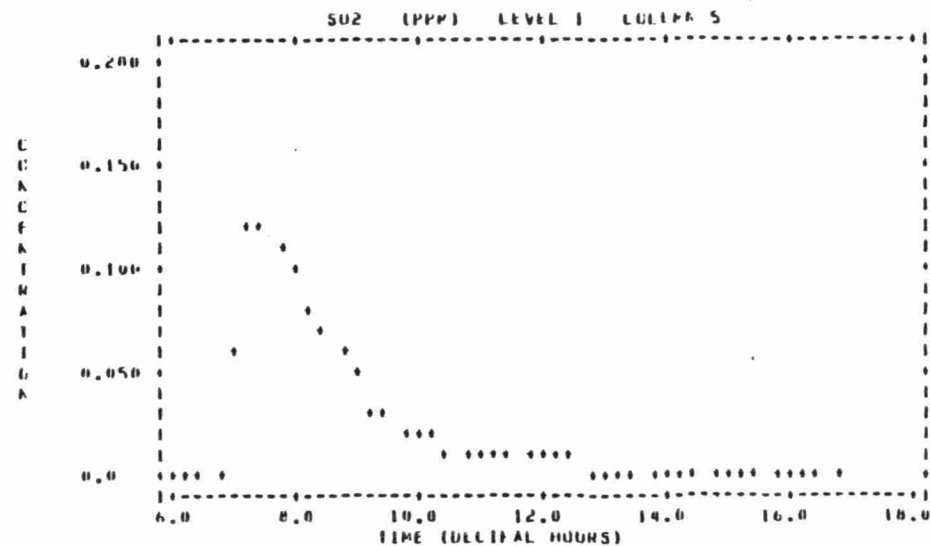
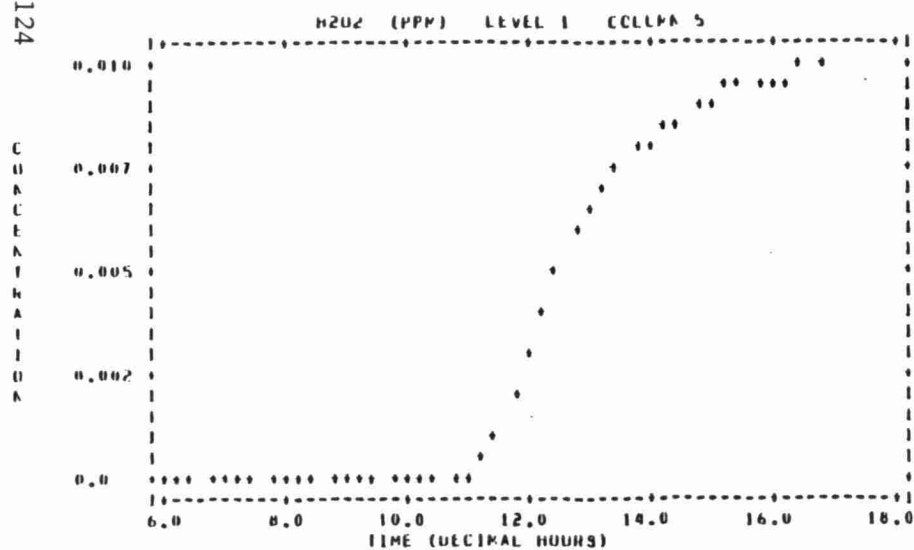
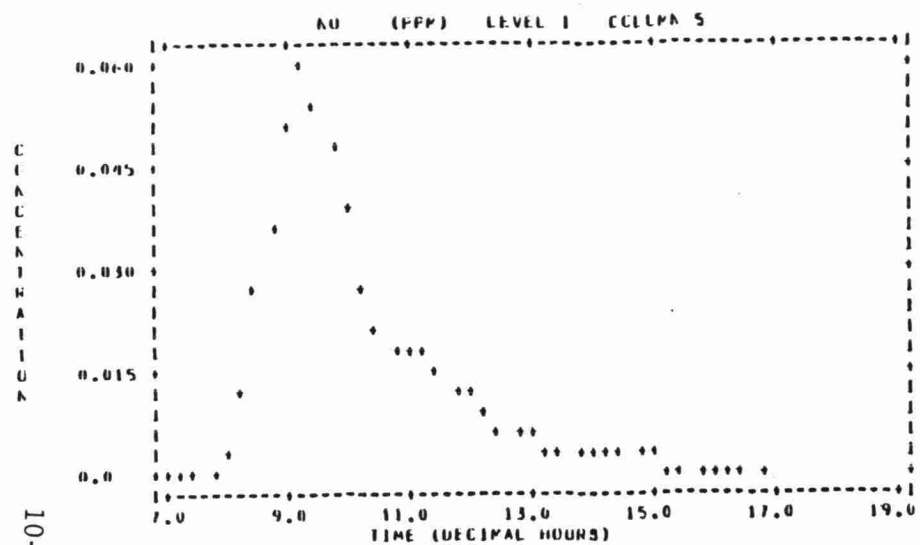


Figure 10-62 (Continued)

PLMSTAR - WINTER - NONLINEAR CHEMISTRY - BASELINE - RUN W1



PLMSTAR - WINTER - NONLINEAR CHEMISTRY - BASELINE - RUN W1

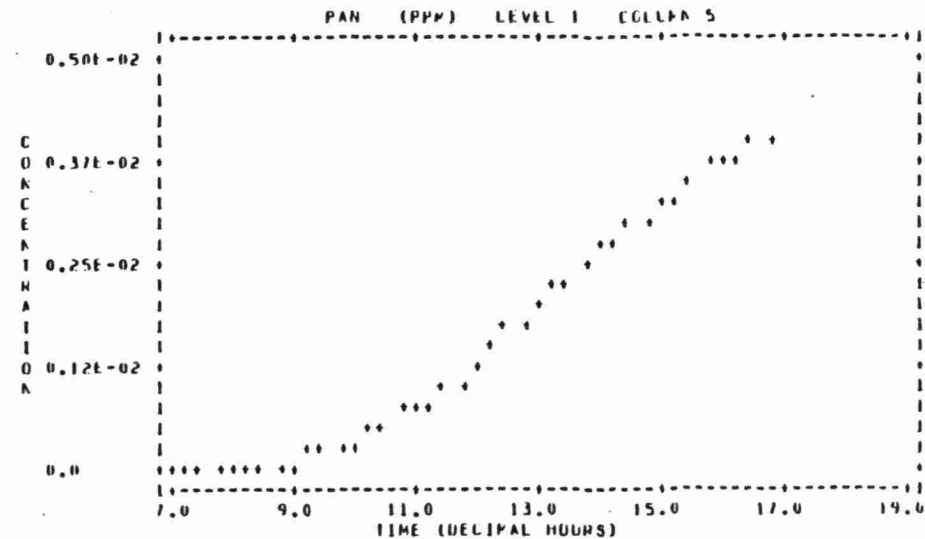
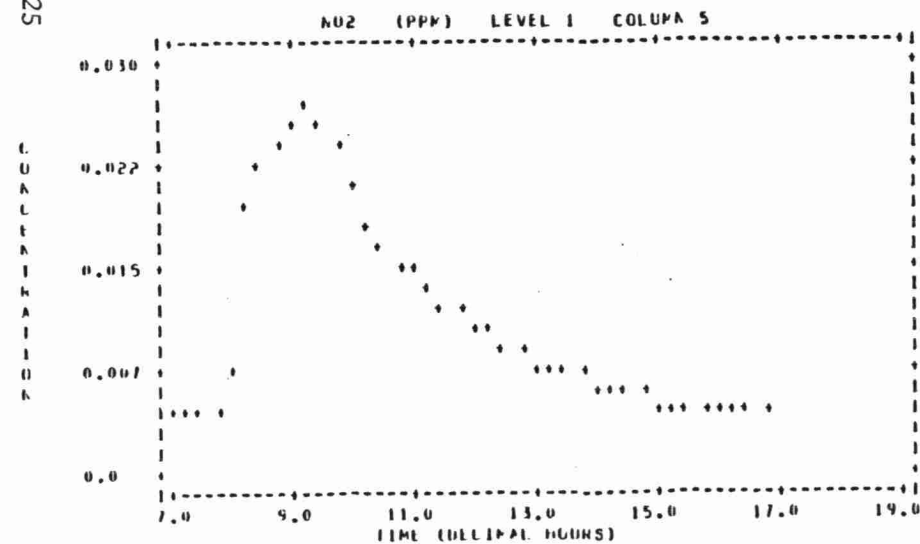
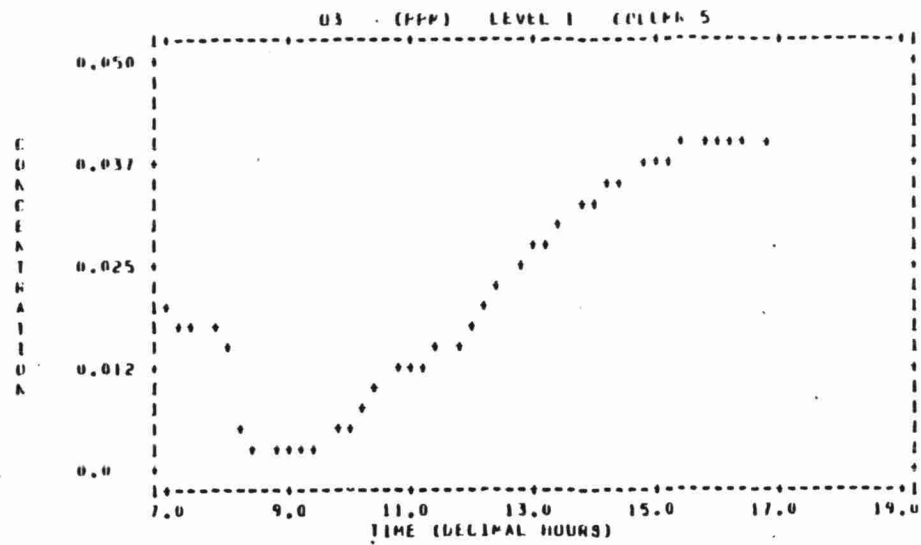
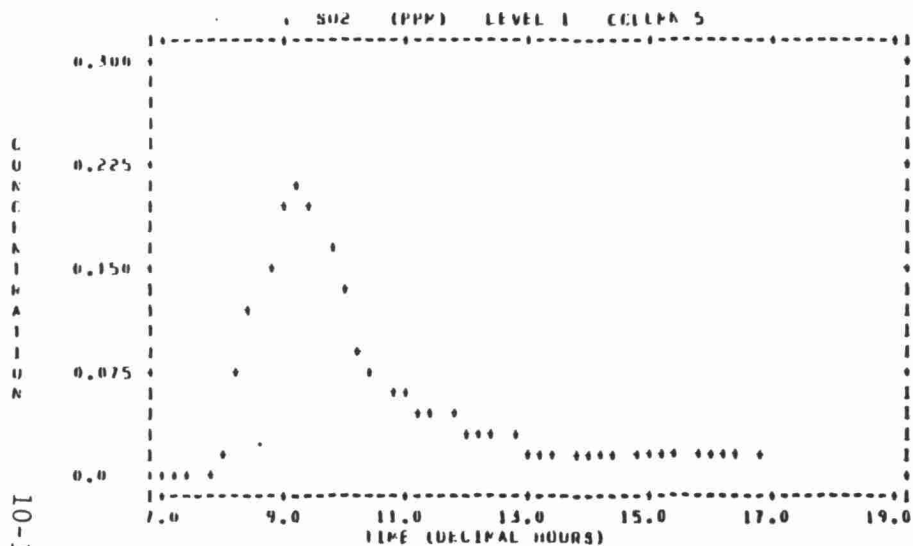
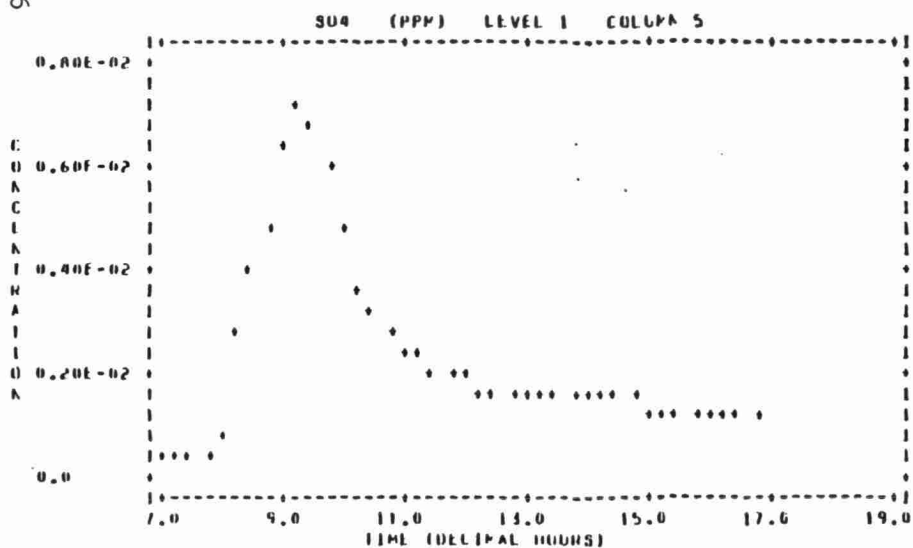


Figure 10-63. Center Column Surface Cell Concentration vs Time Profiles for PLMSTAR run W1.

PLMSTAR - WINTER - NONLINEAR CHEMISTRY - BASELINE - RUN #1



10-126



PLMSTAR - WINTER - NONLINEAR CHEMISTRY - BASELINE - RUN #1

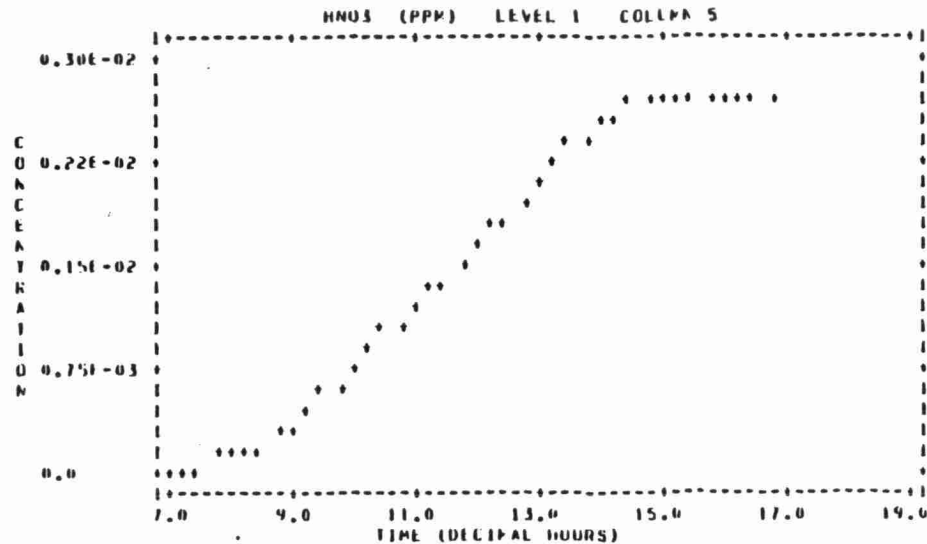
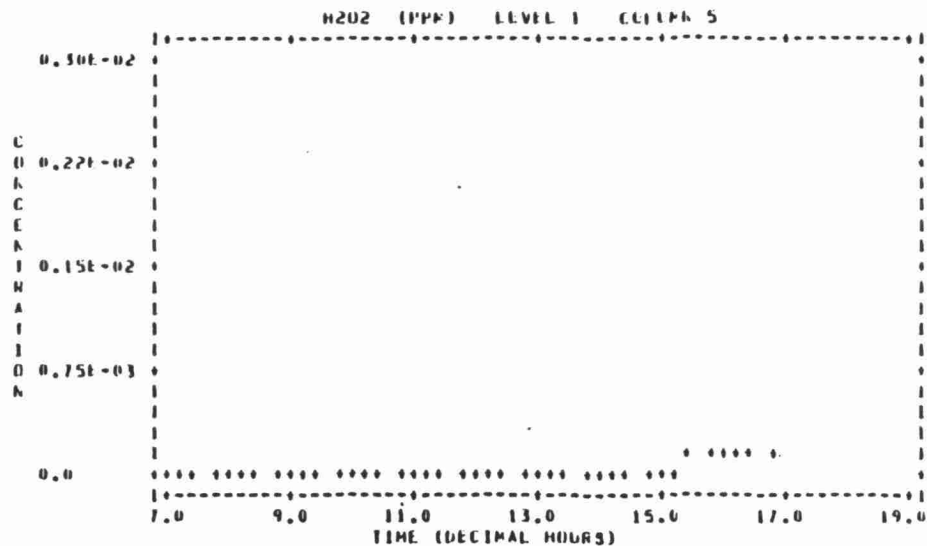


Figure 10-63. (Continued)

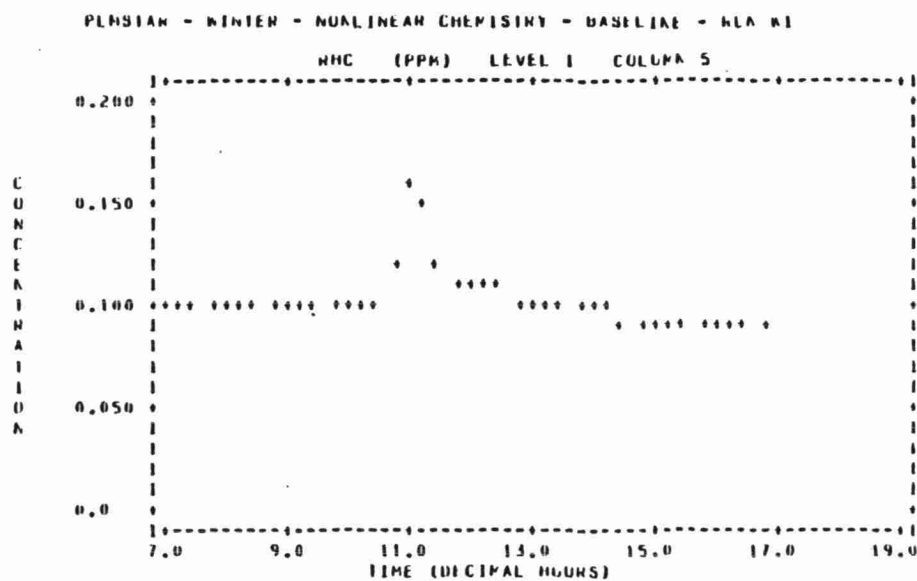
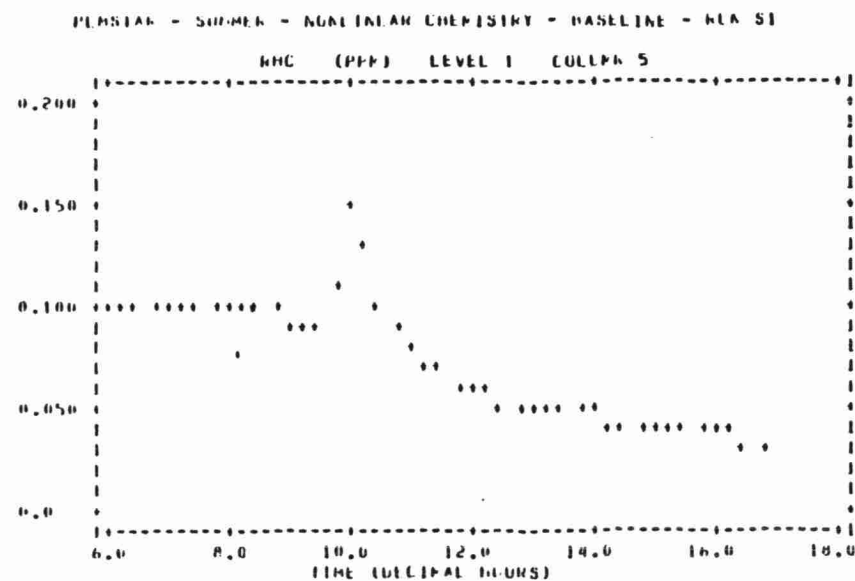


Figure 10-64. Center Column Surface Cell RHC Concentration (ppmC) vs Time Profiles for PLMSTAR runs S1 and W1.



The predictions for  $\text{H}_2\text{O}_2$  concentrations are very low until 1200, after which time the concentrations are predicted to increase steadily to a maximum of 9 ppb by the end of the run (1700). The sharp increase in  $\text{H}_2\text{O}_2$  concentration after 1200 corresponds to the decay of NO and  $\text{NO}_2$  concentrations to less than the ppt and ppb levels, respectively. Figure 10-64 shows that the RHC concentrations are still in the 30 to 60 ppbC range in the afternoon. The trends in these results are consistent with what expected from the chemical mechanism. Hydrogen peroxide is formed by recombination of  $\text{HO}_2$  radicals generated by OH attack on RHC and photolysis of carbonyls. In the presence of significant  $\text{NO}_x$ , reactions of  $\text{HO}_2$  with NO and  $\text{NO}_2$  scavenge  $\text{HO}_2$  much faster than the recombination reaction, so little  $\text{H}_2\text{O}_2$  is formed. However, in situations with RHC available and low  $\text{NO}_x$  levels, a significant potential for  $\text{H}_2\text{O}_2$  formation exists. Although these results are mechanistically consistent, the absolute magnitude of the  $\text{H}_2\text{O}_2$  concentrations are quite uncertain for several reasons. First, there is a factor of 2 uncertainty in the rate constants for the  $\text{HO}_2$  recombination reaction (Atkinson and Lloyd 1982). Second, there are no good ambient or smog chamber measurements of gas phase  $\text{H}_2\text{O}_2$  with which to compare these predictions (as there are for most other pollutants predicted here). Third, the  $\text{NO}_x$  levels in the model, especially NO, are very low and below the detectable limit of common instrumentation most frequently used. Although we strongly suspect NO and  $\text{O}_3$  do not coexist for long in aged smog, we do not know the lower extent of NO concentrations. Furthermore, the chemiluminescent  $\text{NO}_2$  measurements include interference from PAN and  $\text{HNO}_3$  (Winer et al. 1974, Joseph and Spicer 1978) so there are no data to accurately estimate low  $\text{NO}_2$  concentration. It's possible that natural sources, primarily soil emissions, could possibly maintain trace levels of  $\text{NO}_x$  high enough to inhibit significant  $\text{H}_2\text{O}_2$  production. These uncertainties and results have implications for acid deposition issues, since  $\text{H}_2\text{O}_2$  is a relatively efficient oxidant for  $\text{SO}_2$  in the aqueous phase (Penkett et al. 1979, Martin and et al. 1981). Since RHC is decayed slowly relative to  $\text{NO}_x$ , there may be a significant potential for  $\text{H}_2\text{O}_2$  formation and incorporation into the aqueous phase at locations far downwind of the source regions.

The computed concentrations for the winter trajectory show  $\text{SO}_2$ ,  $\text{SO}_4$ , NO, and  $\text{NO}_2$  maximum centerline surface concentrations of 210, 10, 60, and 17 ppb, respectively, near 0900. Lower wind speeds and mixing heights result in higher predicted winter maximum concentrations than the corresponding summer case. Note that the sulfate fraction of the  $\text{SO}_x$  peak is similar in summer and winter, probably because the assumed primary sulfate emissions are mostly responsible for the peak, while the predicted  $\text{NO}_2$  fraction of the  $\text{NO}_x$  peak is substantially lower (31 vs 55%) in the winter case due to the lower level of photochemical activity. The  $\text{SO}_2$ ,  $\text{SO}_4$ , NO, and  $\text{NO}_2$  space-time profiles for the center column show sharp peaks; however, the winter peaks are somewhat broader than the summer ones.

The profile of ozone concentrations for the center column shows substantial ozone scavenging by the plume  $\text{NO}_x$  in the morning hours. The profile shows ozone concentration decreasing from the 20 ppb initial concentration to 2 ppb and then gradually increasing to 40 ppb by the end of the run. In contrast, the off centerline ozone calculations show a very gradual increase from 20 to 40-45 ppb over the course of the run. These ozone levels are believed to be in general agreement with winter observations in the Ohio Valley (see e.g., Hidy and Mueller 1982).

The predicted maximum concentrations of  $\text{HNO}_3$  and PAN are 2.8 and 3.9 ppb, respectively. These concentrations are 20 to 30 percent lower than the summer case, yet the ratio of PAN to  $\text{HNO}_3$  is quite similar to the summer case value. Normally, the ratio of PAN to  $\text{HNO}_3$  is expected to increase in winter due to increased PAN stability at the lower winter temperatures. This increase appears to be offset by the lower effective  $\text{RHC}/\text{NO}_x$  ratios in this winter case. The winter total nitrate concentrations predicted here are believed to be slightly lower than the summer value because of the generally lower level of photochemical activity.

Hydrogen peroxide surface concentrations are predicted to reach 0.2 ppb along the centerline and 1 to 2 ppb off the centerline. The computed winter levels are lower than the summer's primarily because there are higher  $\text{NO}_x$  concentrations and slower hydrocarbon decay throughout the run.

The model's prediction for dry deposition are also important results. Figures 10-65 and 10-66 show the hourly deposition rates of sulfur and nitrogen as a function of downwind distance from the major point source for the summer and winter cases, respectively. These hourly deposition rates refer to the amount of mass deposited from the 26.5 km by 7.5 km air parcel. The general shape of the temporal deposition rate profiles is similar for the summer and winter cases and primarily reflects the source configuration and meteorology for these trajectories. The highest sulfur dry deposition rates are predicted to occur 2 to 5 hours downwind of the point source. The highest nitrogen deposition rates occur 4 to 5 hours downwind and reflect the superposition of point and urban source  $\text{NO}_x$  emissions. These predictions show higher sulfur deposition rates and more total sulfur deposition over the 165 km winter trajectory than over the 285 km summer trajectory. However, the opposite is predicted for nitrogen deposition. Summer N deposition rates and cumulative mass deposited are predicted to be significantly higher (30-50%) than for the winter case.

Figures 10-65 and 10-66 also show the  $\text{SO}_2$ ,  $\text{SO}_4$ ,  $\text{NO}_2$ ,  $\text{HNO}_3$  and PAN components of the predicted sulfur and nitrogen deposition. These predictions show that the sulfate and nitrate fractions of sulfur and nitrogen deposition are substantially higher in the summer case. This result is consistent with greater photochemical activity and secondary product formation in the summer. In fact, it appears that the majority of the difference in predicted nitrogen deposition between the summer and winter cases can be attributed to the greater nitric acid formation rates and, therefore, greater deposition in the summer case.

The differences in deposition for ozone and hydrogen peroxide for summer and winter are substantial. Approximately 3 to 10 times more  $\text{O}_3$  and  $\text{H}_2\text{O}_2$ , respectively, are predicted to be deposited in the summer, than winter case. These results are consistent with the summer-winter concentration differences and reflect the differences in photochemical activity in the two cases.

In summary, the complex model results for the winter and summer cases have plausible maximum concentrations, diurnal concentration profiles, and deposition rates. Since the cases are hypothetical,

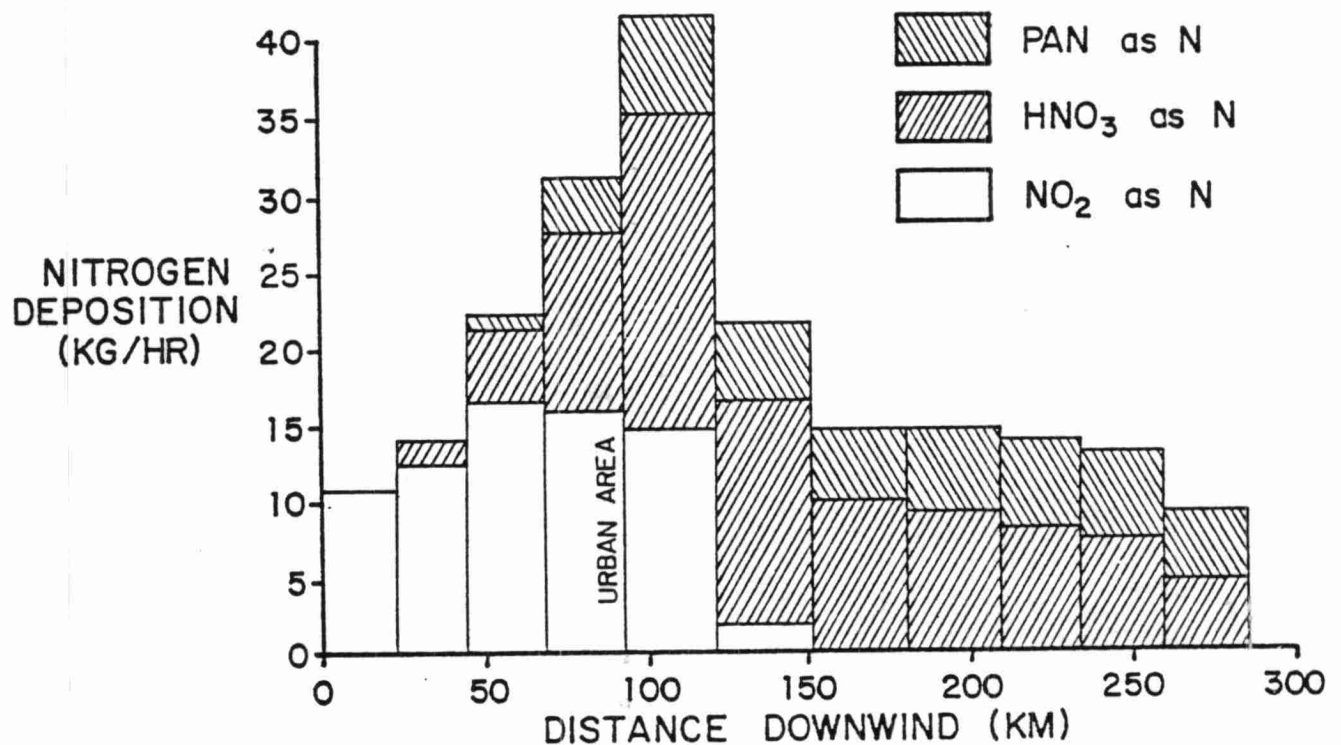
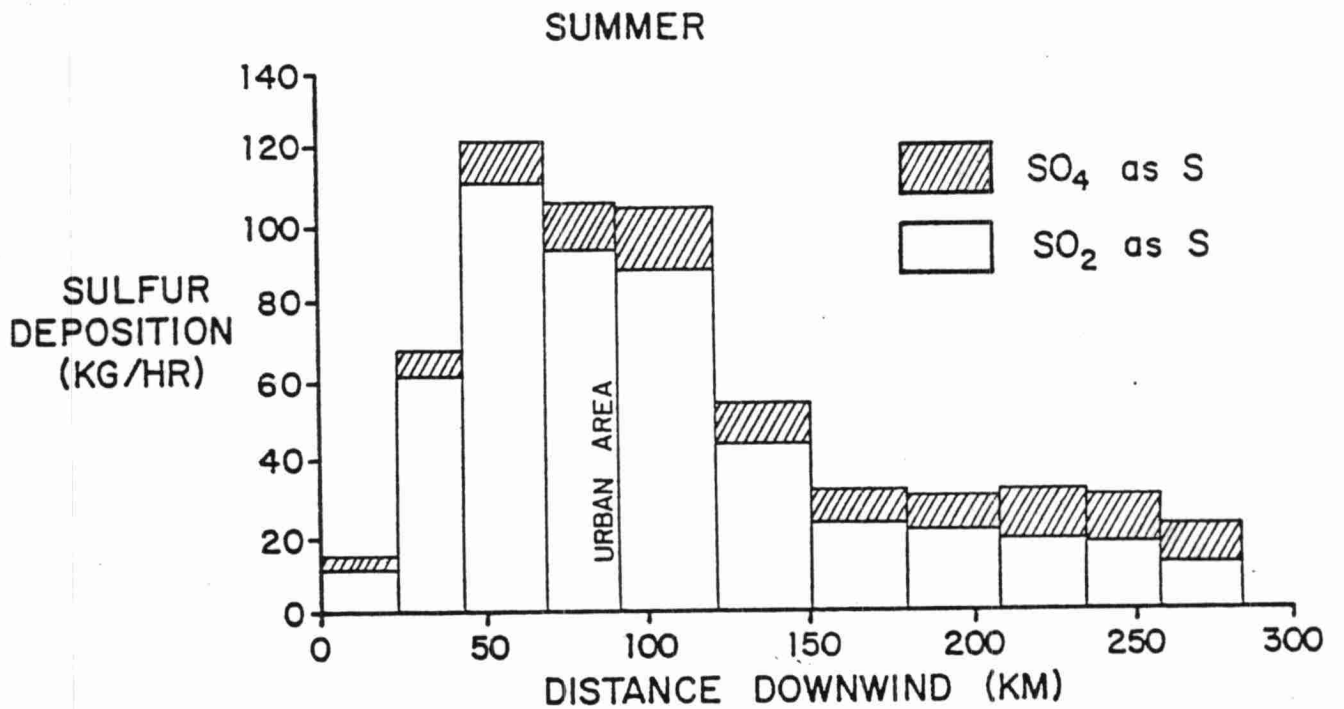


Figure 10-65. Hourly Sulfur and Nitrogen Deposition Rates Predicted by the Complex Model for the Summer Baseline Case.

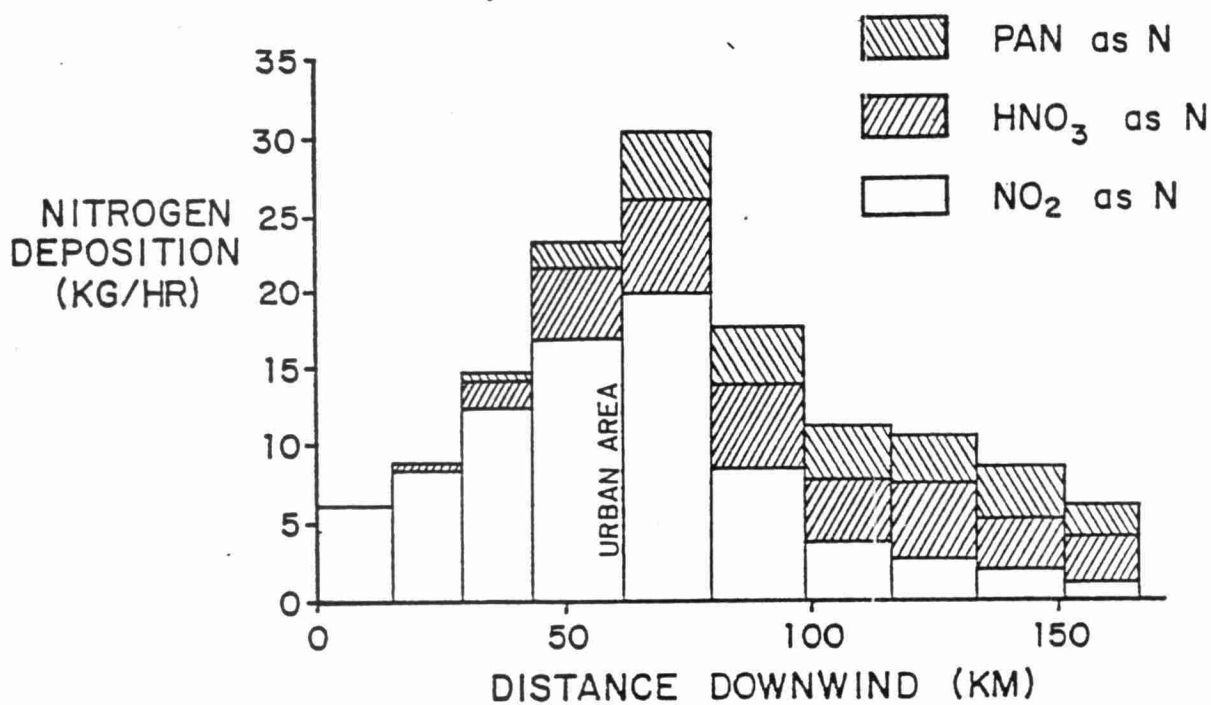
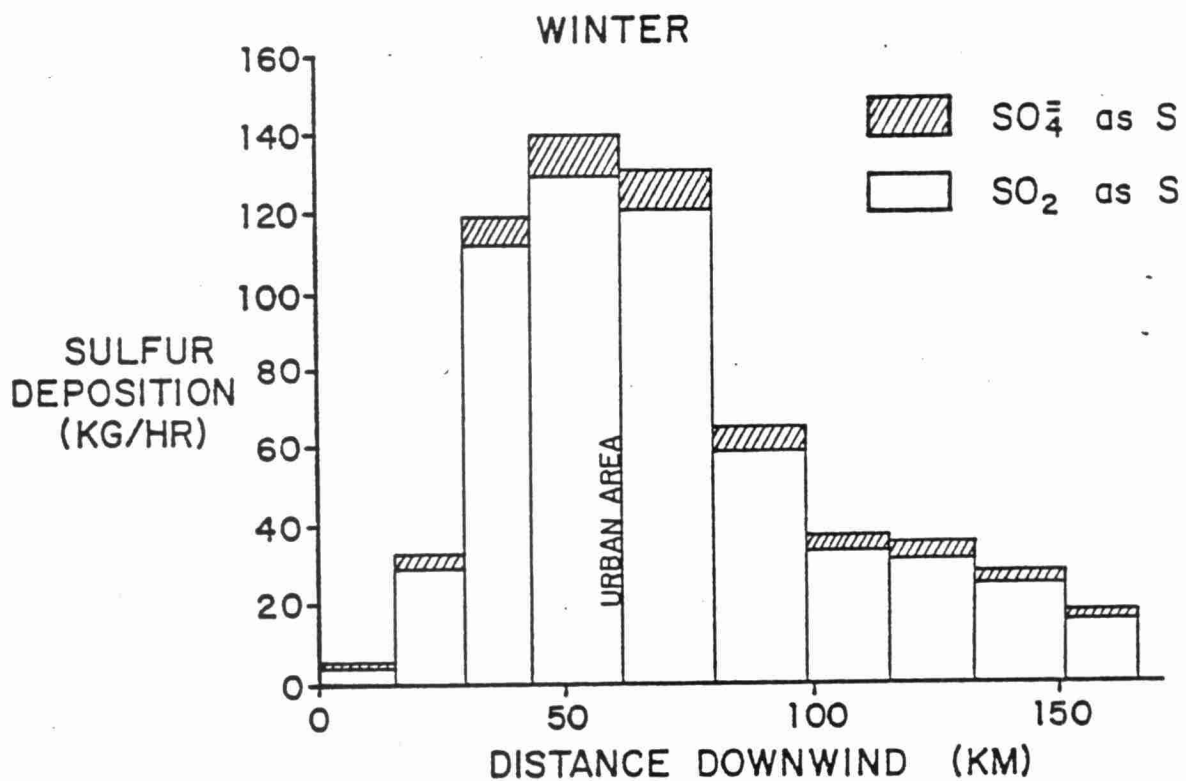


Figure 10-66. Hourly Sulfur and Nitrogen Deposition Rates Predicted by the Complex Model for the Winter Baseline Case.

there are no data to make direct comparisons, yet the predictions for those parameters for which measurements are generally available, indicate the results are within the general range of observation in the Ohio Valley (see Hidy and Mueller 1982).

#### 10.2.4 Mesoscale Model Sensitivity to Model Formulation

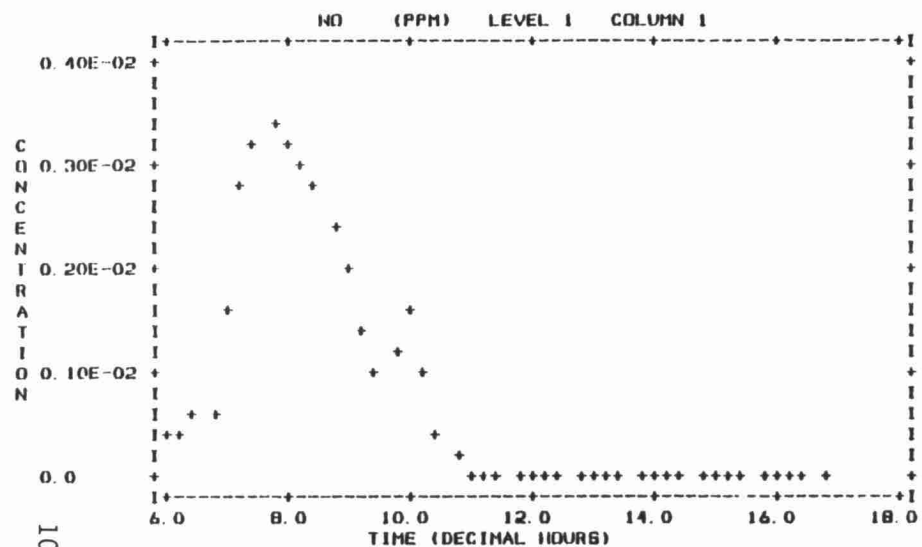
This section describes differences between the predictions of the various simple models' results and the complex model's results. Comparisons are made for the model simulations of both the summer and winter cases with the baseline emissions. The model output parameters selected for the comparison are the maximum surface concentration and final average concentration for ten pollutants, and the cumulative deposition along the trajectory for five pollutants. However, differences in the  $\text{SO}_2$ ,  $\text{SO}_4$ ,  $\text{NO}_x$  and nitrate concentrations and sulfur and nitrogen deposition are emphasized because of their relevance to acid rain questions.

The concentration versus time profiles for the center column surface cell of the alternate model runs (except W4) are shown in Figures 10-67 through 10-75. The maximum surface concentrations and final average concentrations from runs S1 through S6 and runs W1 through W6 are shown in Table 10-24 and 10-25 for  $\text{SO}_2$ ,  $\text{SO}_4$ ,  $\text{NO}_x$ , total nitrate ( $\text{TNO}_3$ ),  $\text{NO}$ ,  $\text{NO}_2$ ,  $\text{O}_3$ , PAN,  $\text{HNO}_3$ , and  $\text{H}_2\text{O}_2$ . The cumulative depositions of sulfur (S),  $\text{SO}_2$ ,  $\text{SO}_4$ , nitrogen (N),  $\text{NO}_2$ , PAN,  $\text{HNO}_3$ , and  $\text{O}_3$  for these runs are shown in Table 10-26. The percentage changes of Model 2's through Model 6's outputs relative to Model 1 are shown in Tables 10-27 through 10-29. Note that the results for Model 3 and 6 include only  $\text{SO}_2$ ,  $\text{SO}_4$ ,  $\text{NO}_x$  and  $\text{TNO}_3$  since the linear chemical mechanism does not include predictions for the other species.

##### 10.2.4.1 Model 2 Performance Relative to Model 1

The results of the single expanding column version of PLMSTAR (runs S2 and W2) show both similarity to and significant differences from the complex model results for the different output parameters.

PLMSTAR - SUMMER - NONLINEAR CHEMISTRY - SINGLE COLUMN - RUN S2



PLMSTAR - SUMMER - NONLINEAR CHEMISTRY - SINGLE COLUMN - RUN S2

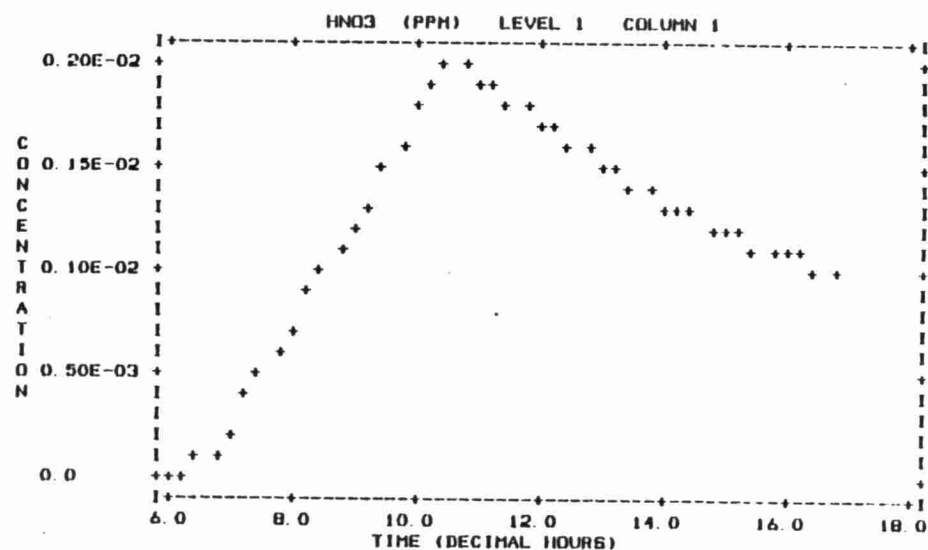
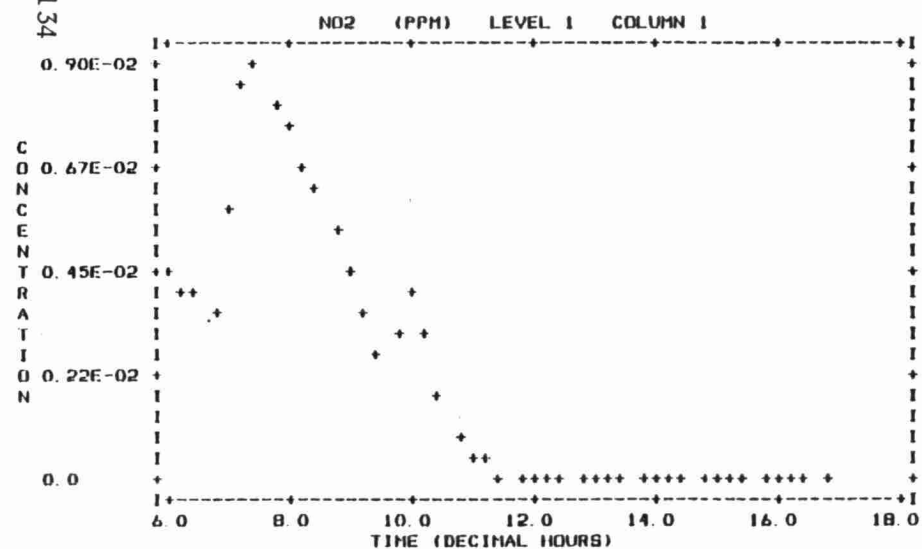
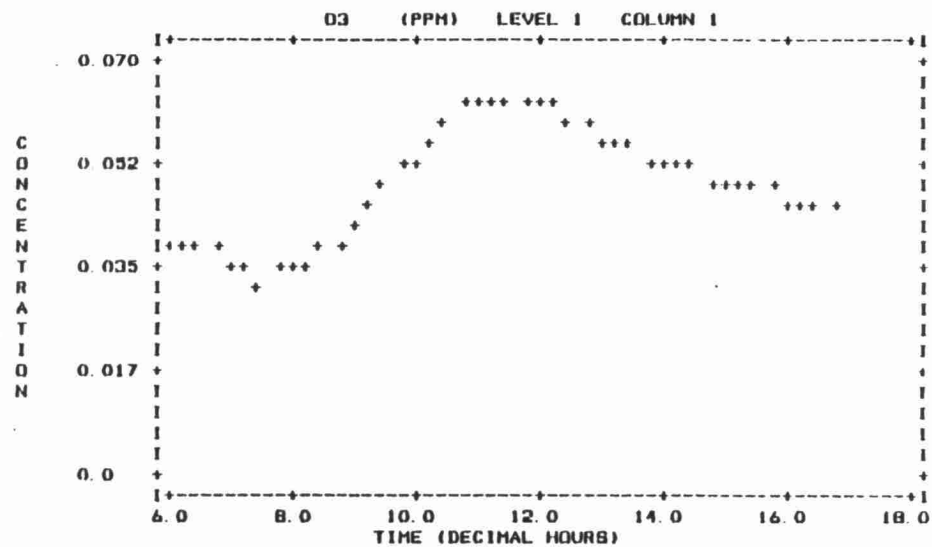
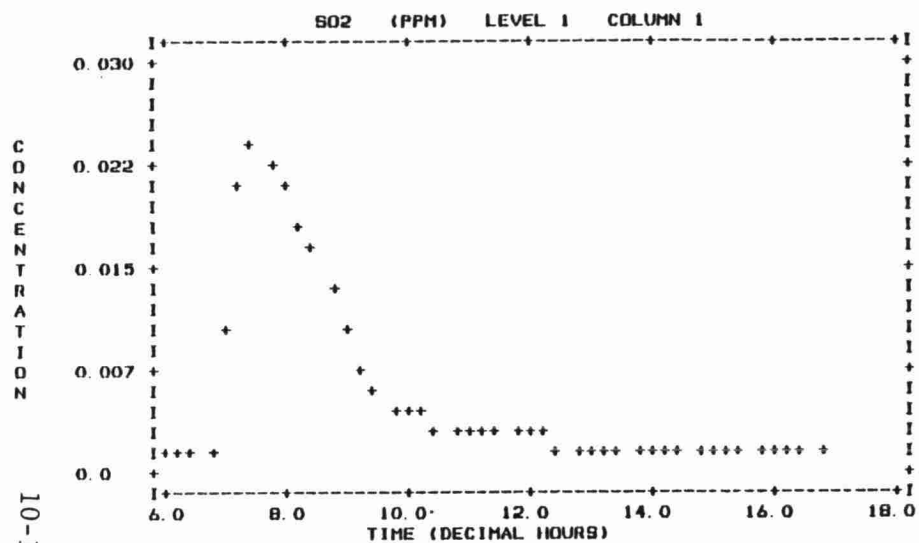
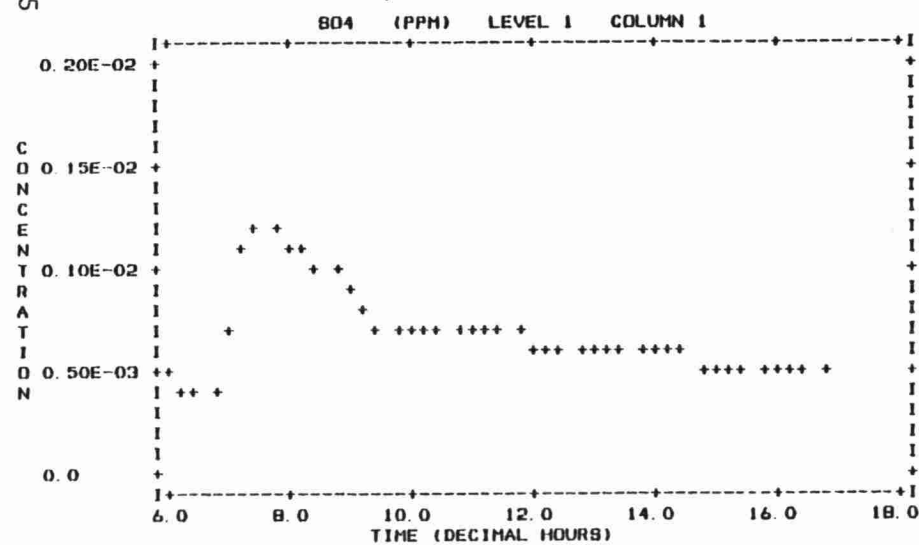


Figure 10-67. Center Column Surface Cell Concentration vs Time Profiles for PLMSTAR run S2.

PLMSTAR - SUMMER - NONLINEAR CHEMISTRY - SINGLE COLUMN - RUN 82



10-135



PLMSTAR - SUMMER - NONLINEAR CHEMISTRY - SINGLE COLUMN - RUN 82

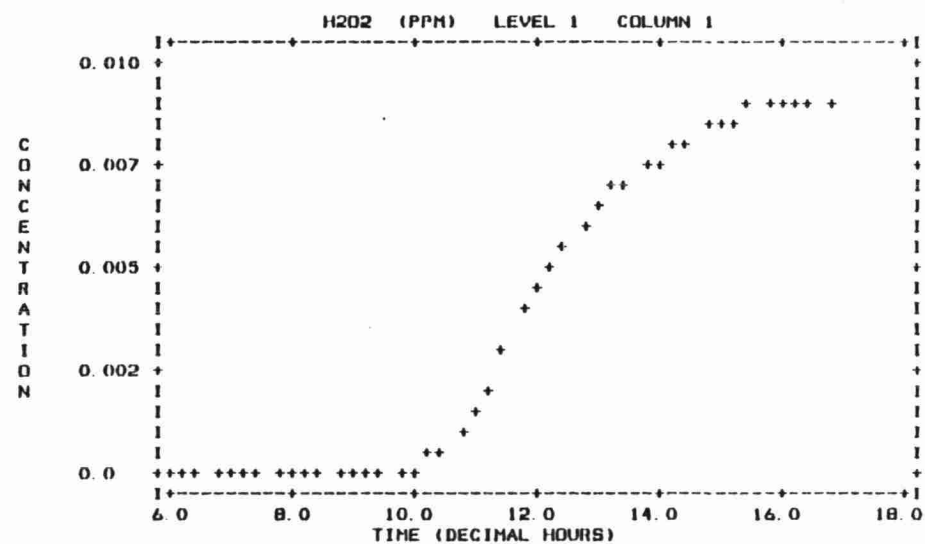
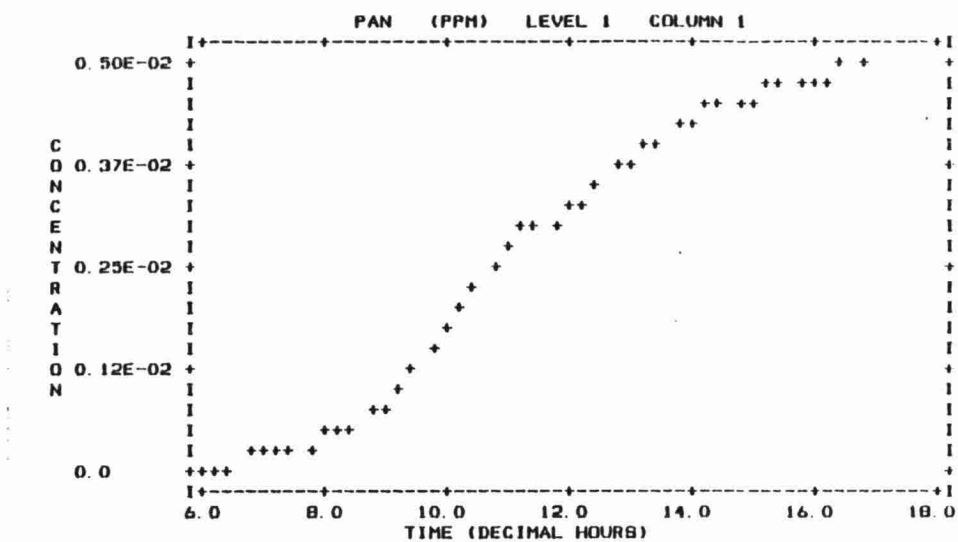
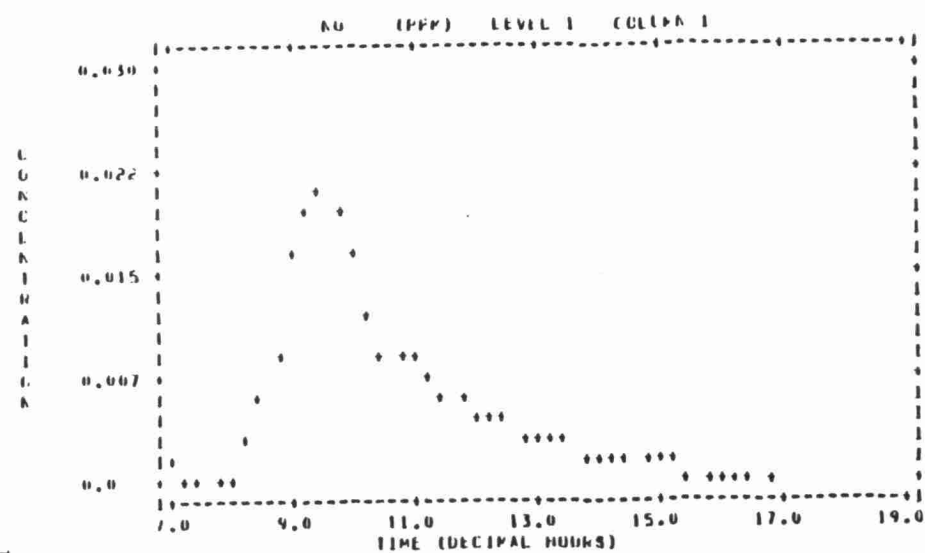


Figure 10-67. (Continued)



PLMSTAR - WINTER - NONLINEAR CHEMISTRY - SINGLE COLUMN - RUN W2



PLMSTAR - WINTER - NONLINEAR CHEMISTRY - SINGLE COLUMN - RUN W2

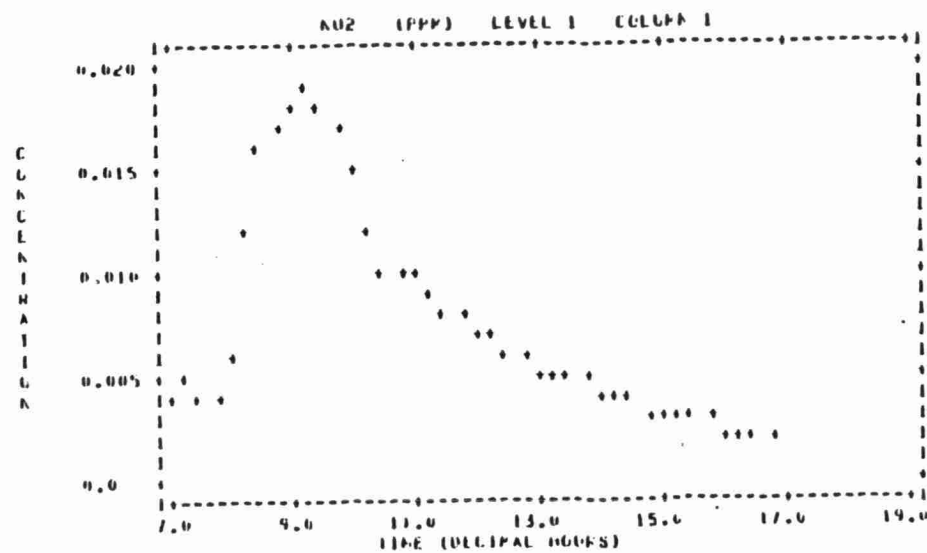
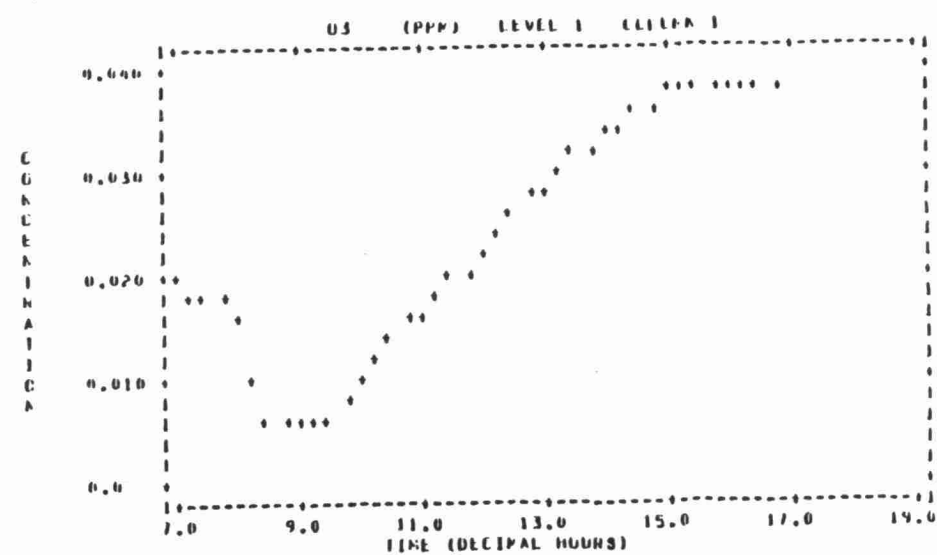


Figure 10-68. Center Column Surface Cell Concentration vs Time Profiles for PLMSTAR run W2.

PLMSTAR - WINTER - NONLINEAR CHEMISTRY - SINGLE COLUMN - RUN #2

PLMSTAR - WINTER - NONLINEAR CHEMISTRY - SINGLE COLUMN - RUN #2

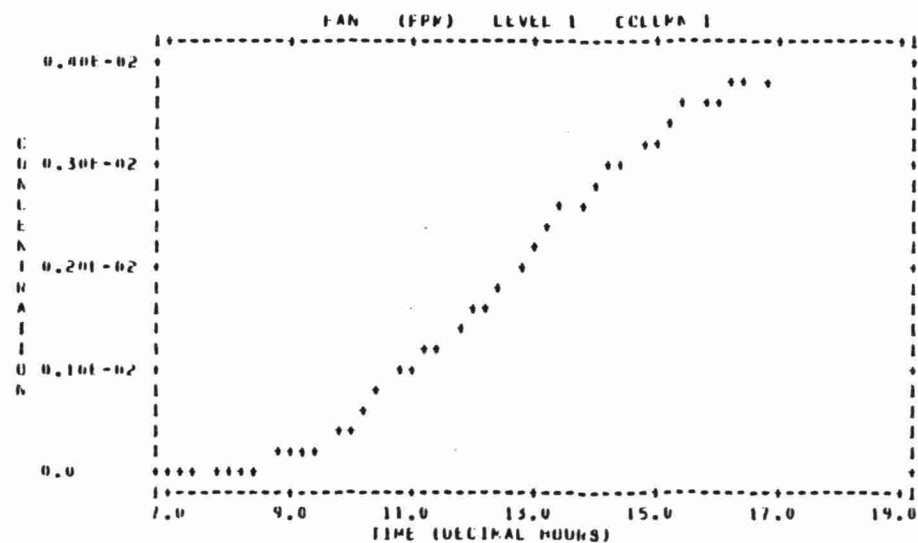
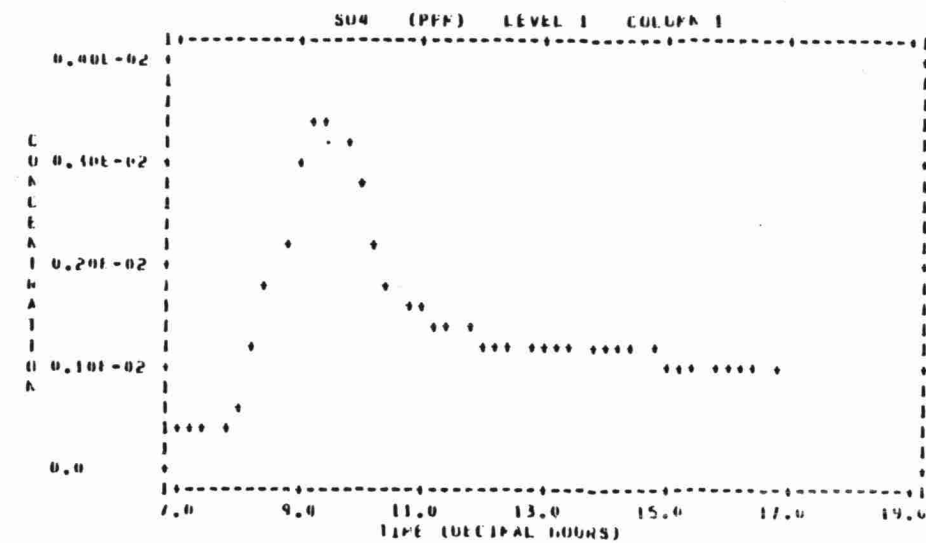
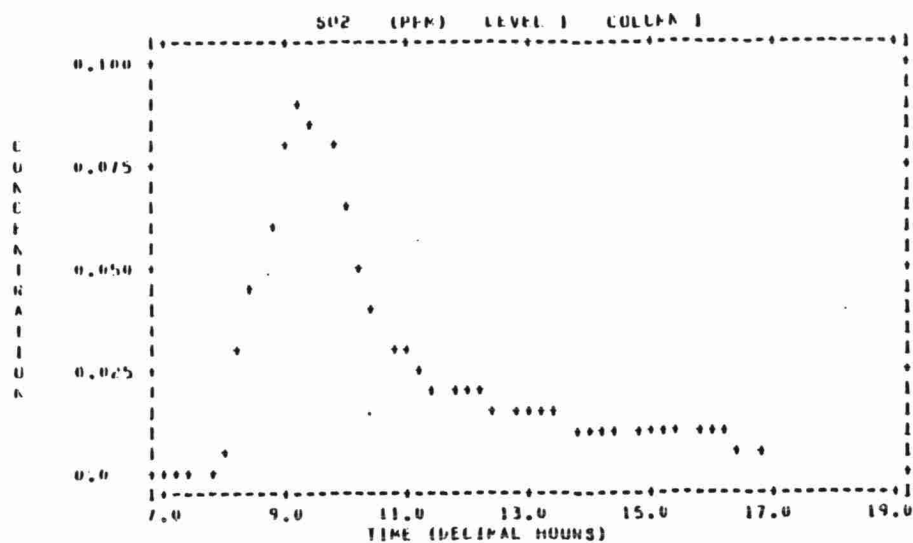
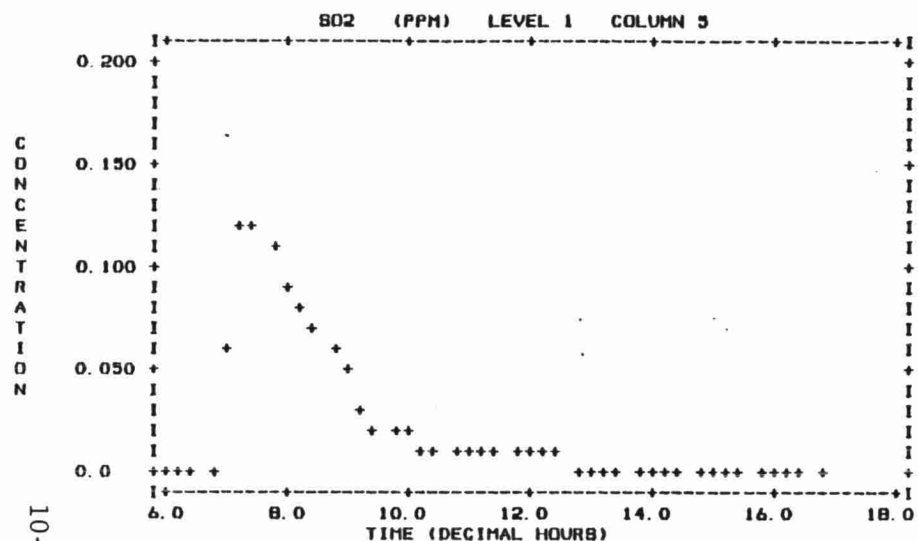


Figure 10-68. (Continued)

PLMSTAR - SUMMER - LINEAR CHEMISTRY - RUN 83



PLMSTAR - SUMMER - LINEAR CHEMISTRY - RUN 83

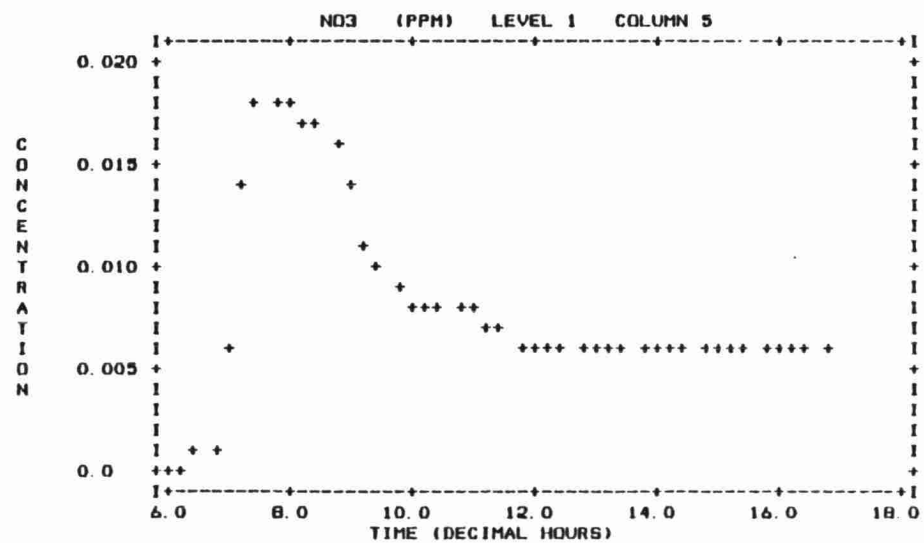
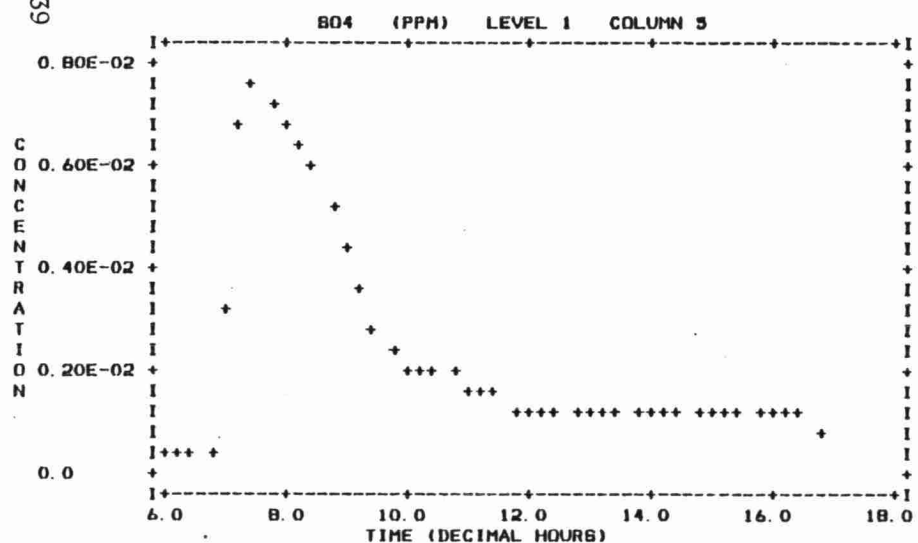
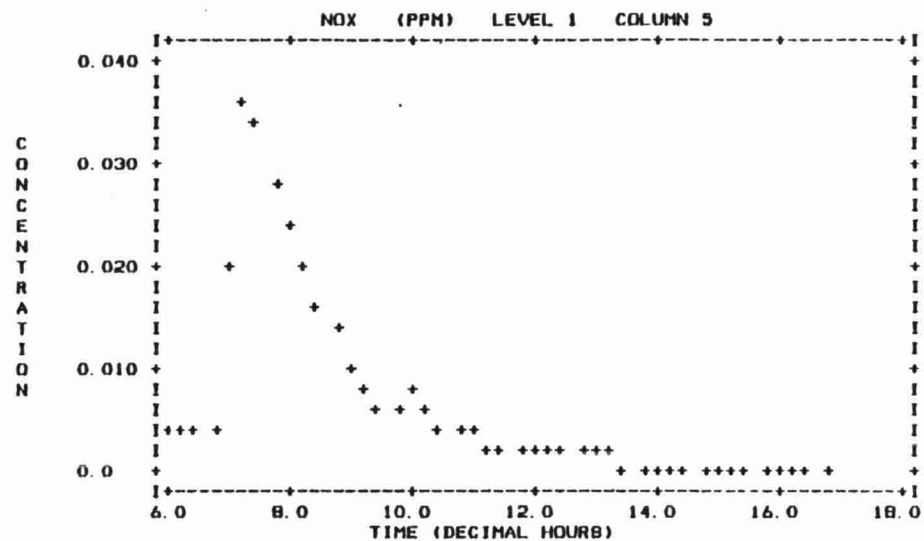
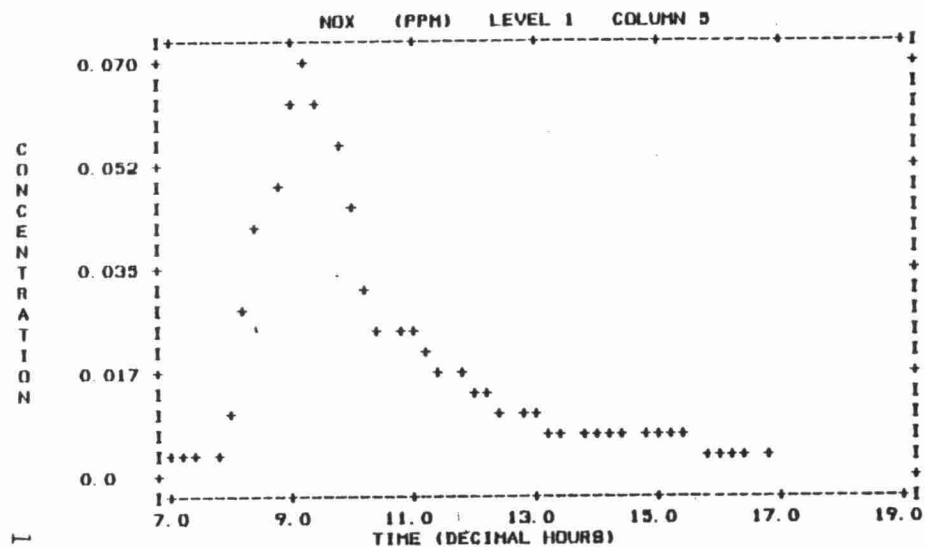


Figure 10-69. Center Column Surface Cell Concentration vs Time Profiles for PLMSTAR run S3.

PLMSTAR - WINTER - LINEAR CHEMISTRY - RUN W3



PLMSTAR - WINTER - LINEAR CHEMISTRY - RUN W3

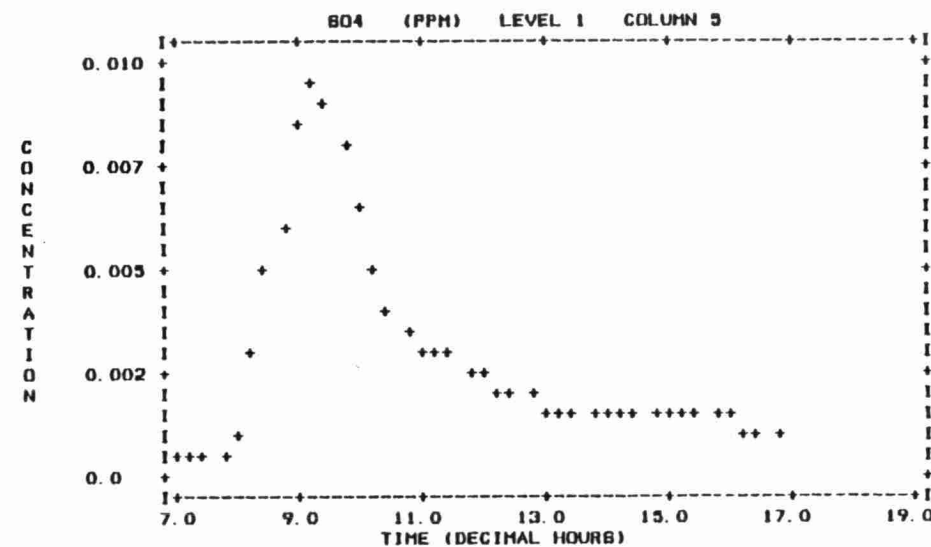
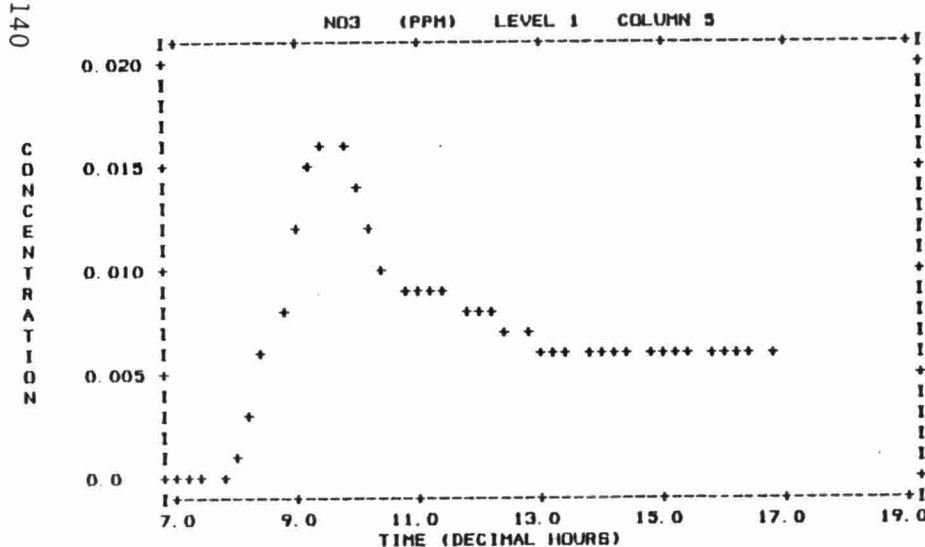
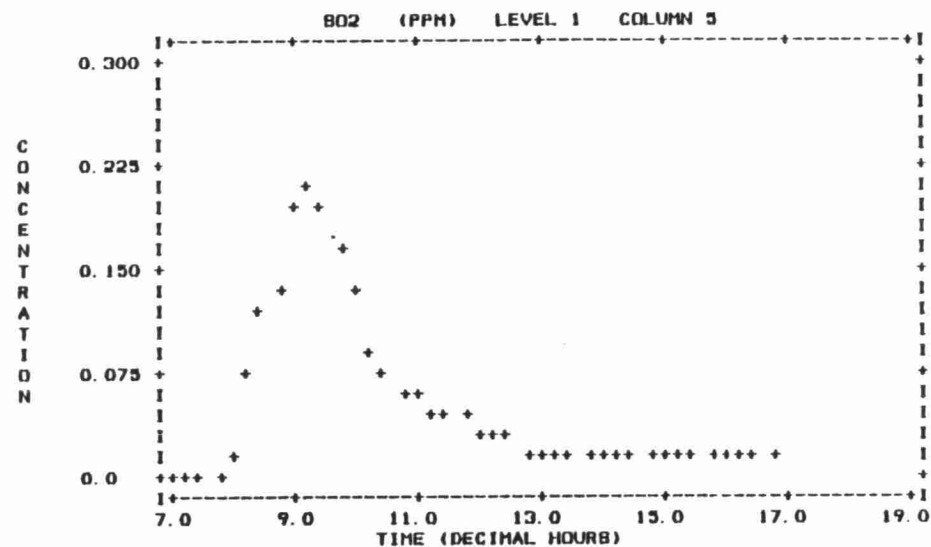


Figure 10-70. Center Column Surface Cell Concentration vs Time Profiles for PLMSTAR run W3.

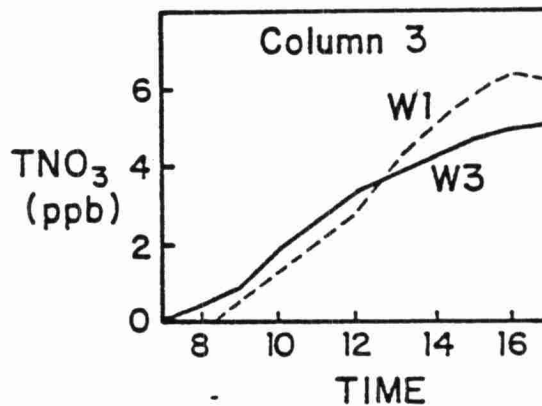
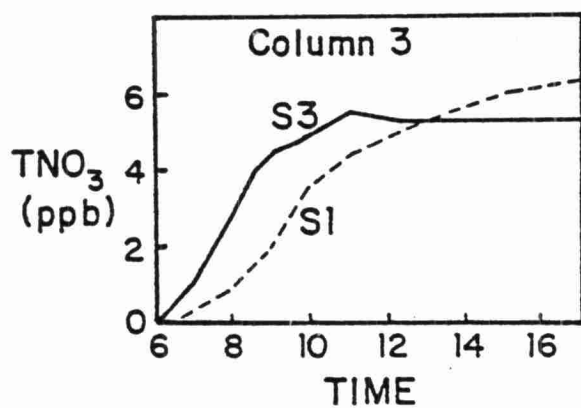
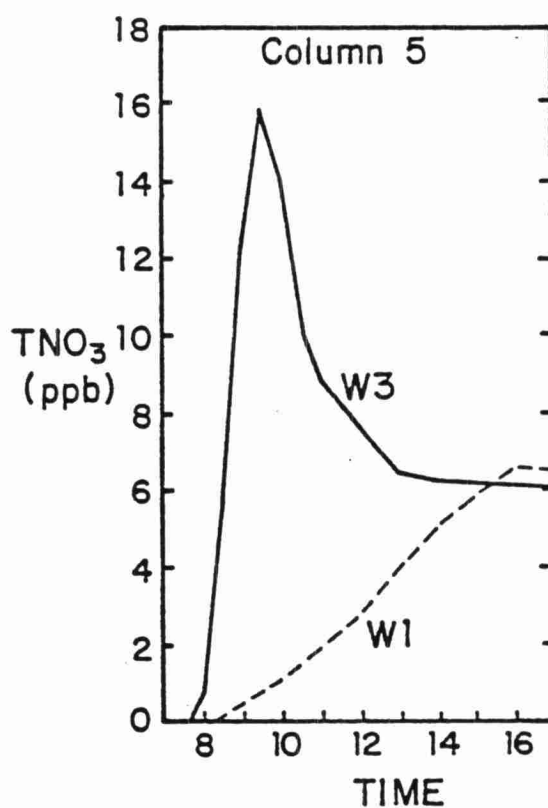
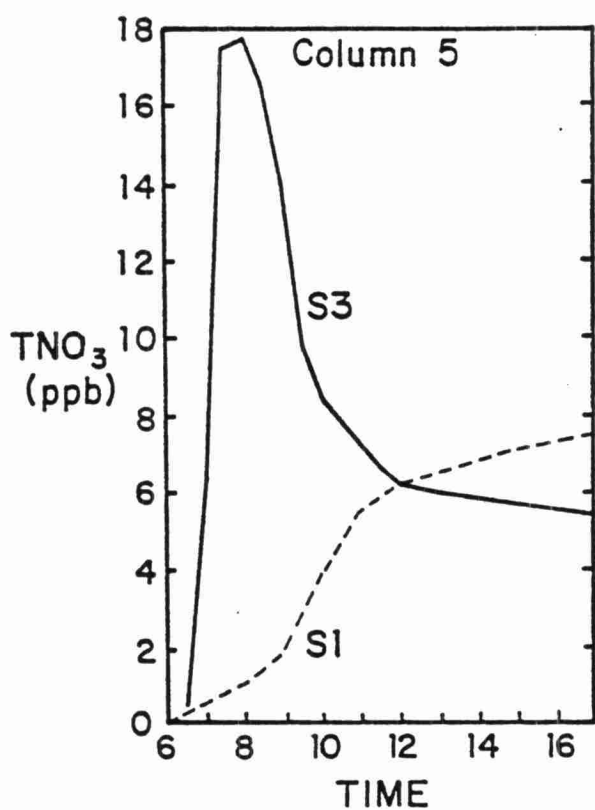
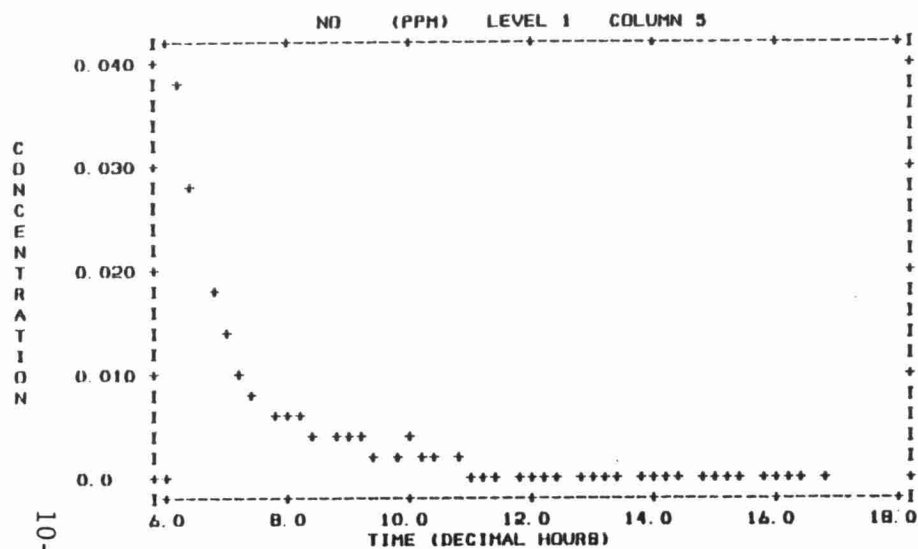


Figure 10-71. Total Nitrate Surface Concentration vs Time Profiles in Model 1 and Model 3 on the Plume Centerline (Col. 5) and 2-3 km off the Plume Centerline (Col. 3).

PLMSTAR - SUMMER - NONLINEAR CHEMISTRY - CONSTANT KZ - RUN S5



PLMSTAR - SUMMER - NONLINEAR CHEMISTRY - CONSTANT KZ - RUN S5

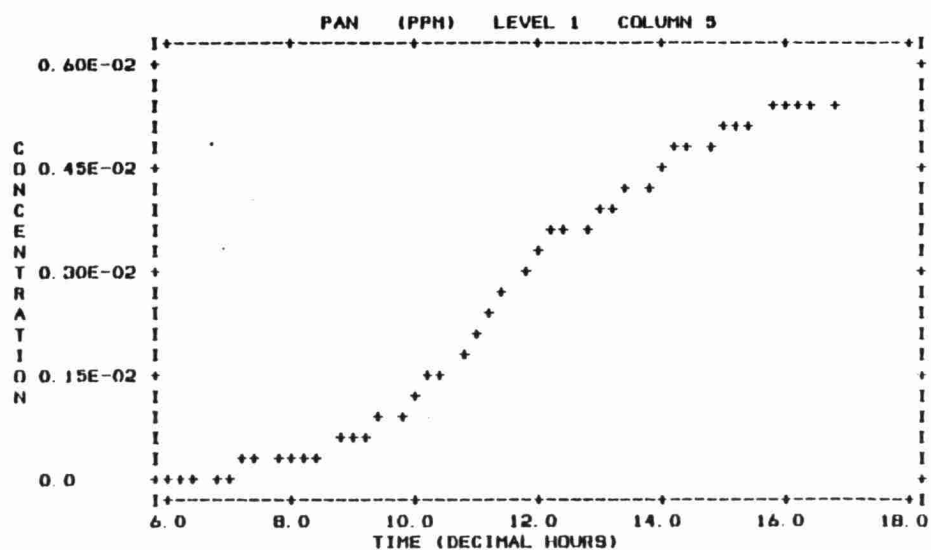
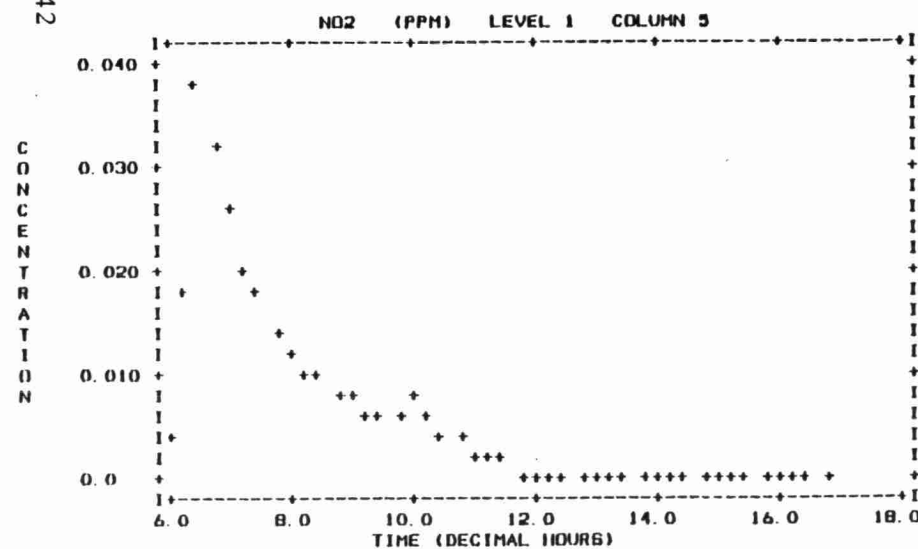
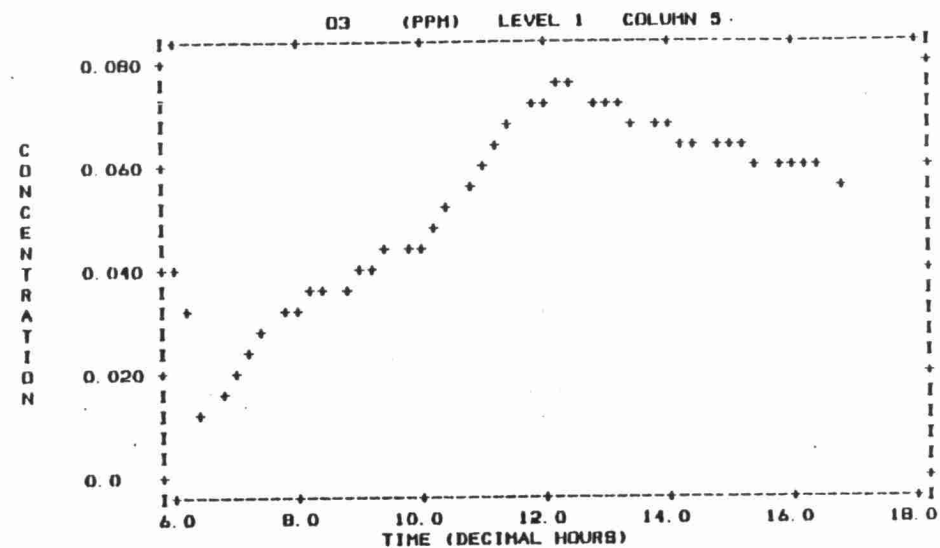
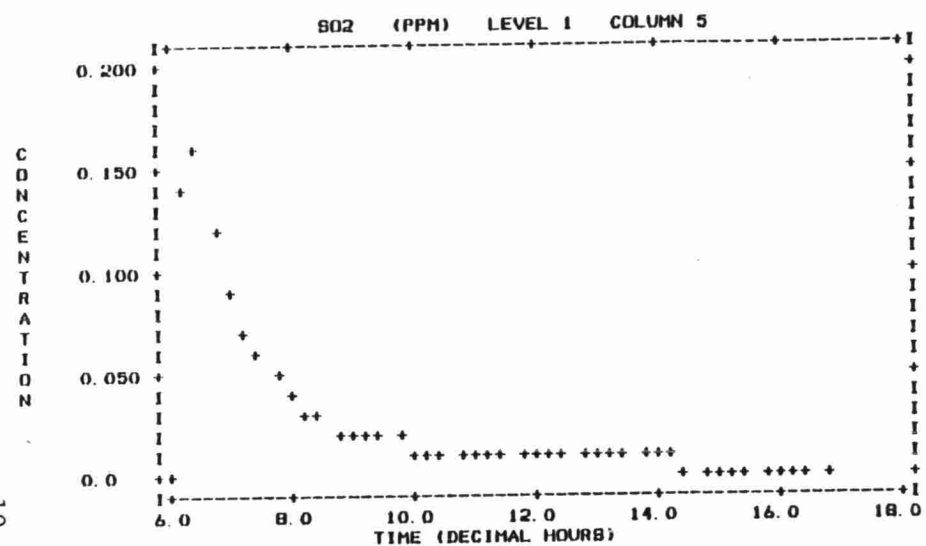


Figure 10-72. Center Column Surface Cell Concentration vs Time Profiles for PLMSTAR run S5.

PLMSTAR - SUMMER - NONLINEAR CHEMISTRY - CONSTANT KZ - RUN 65



PLMSTAR - SUMMER - NONLINEAR CHEMISTRY - CONSTANT KZ - RUN 65

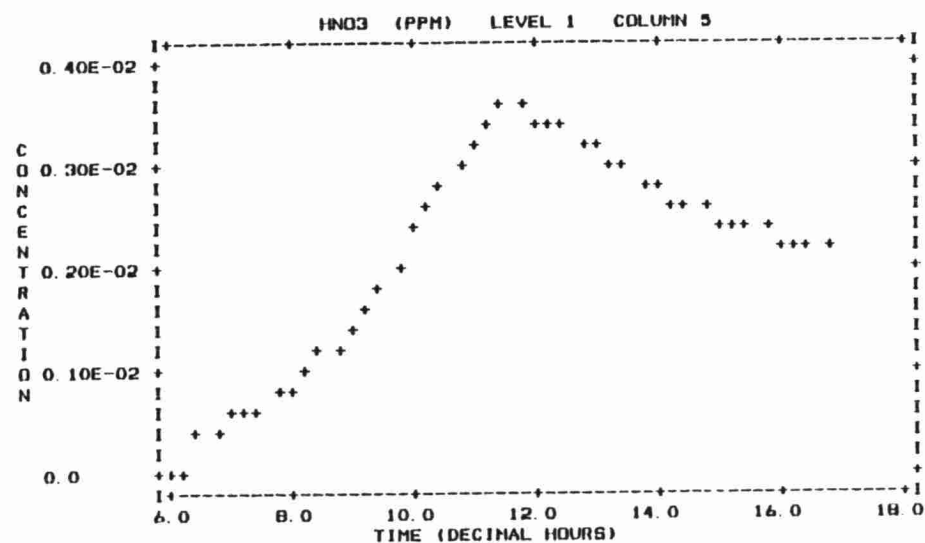
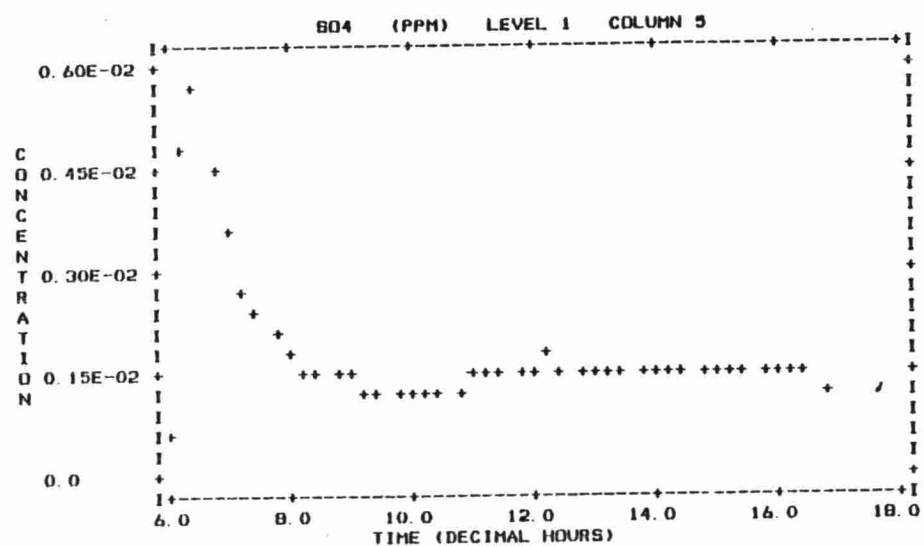
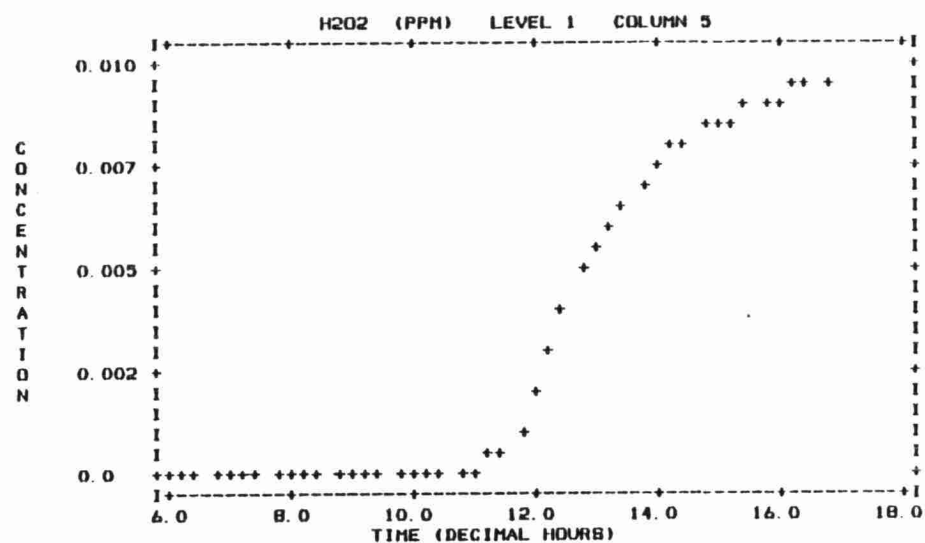
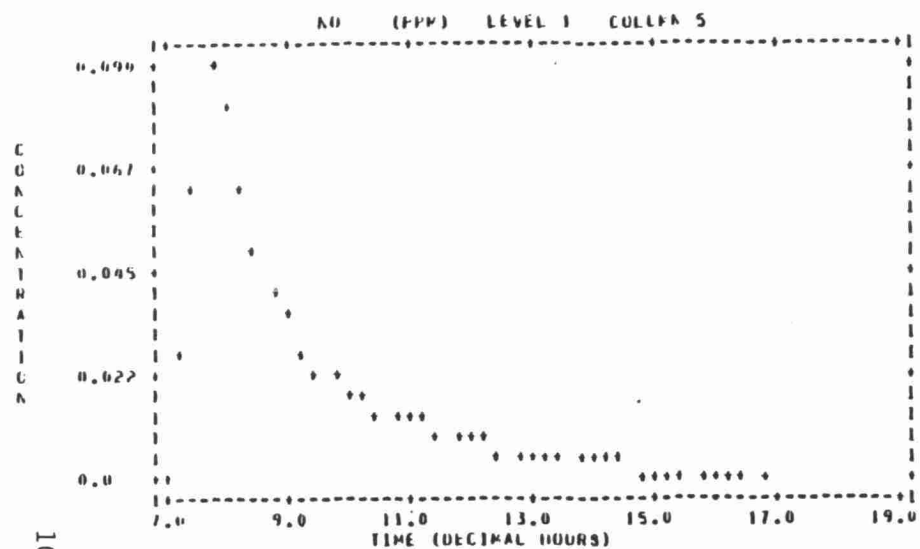
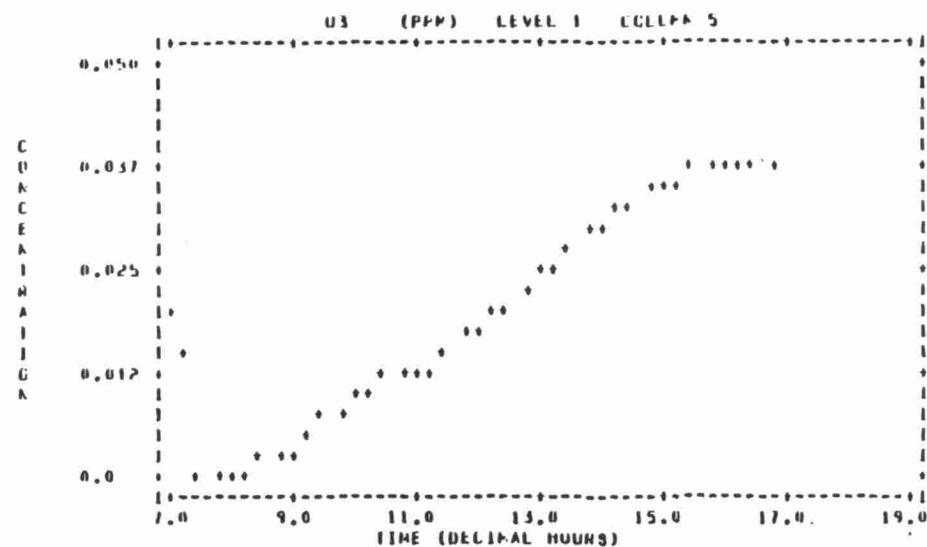


Figure 10-72. (Continued)

PLMSTAR - WINTER - NONLINEAR CHEMISTRY - CONSTANT K2 - RUN W5



PLMSTAR - WINTER - NONLINEAR CHEMISTRY - CONSTANT K2 - RUN W5



10-144

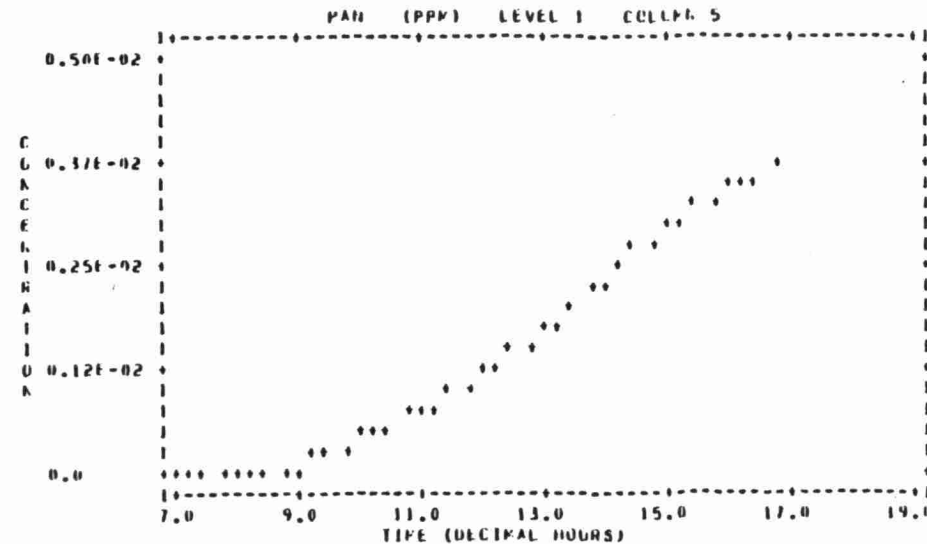
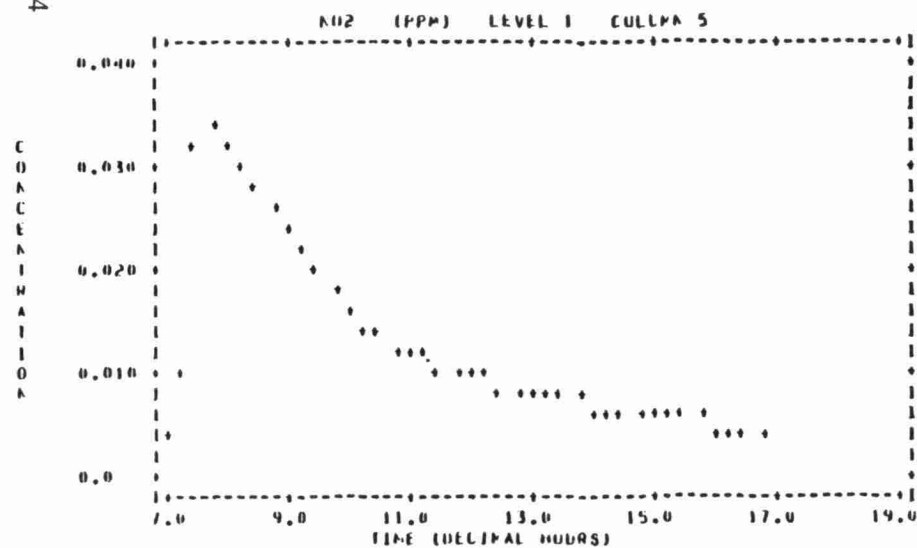
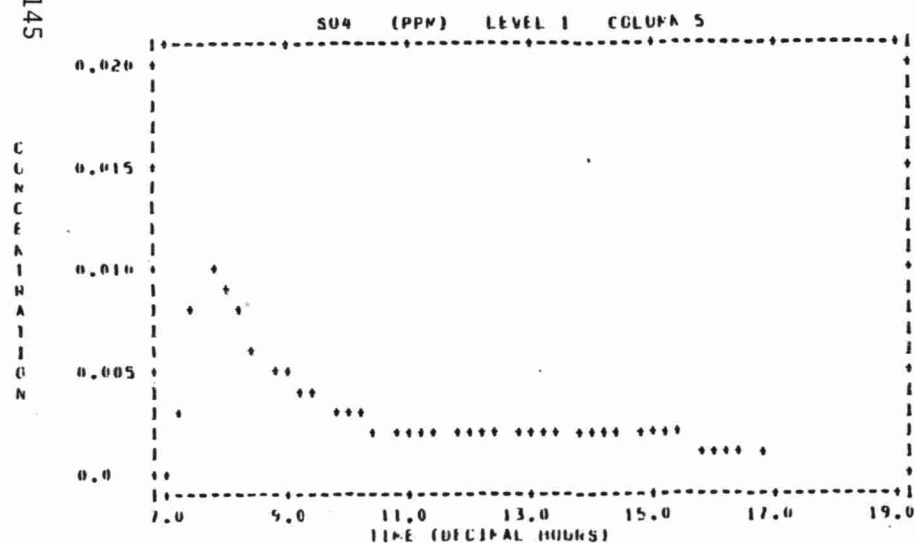
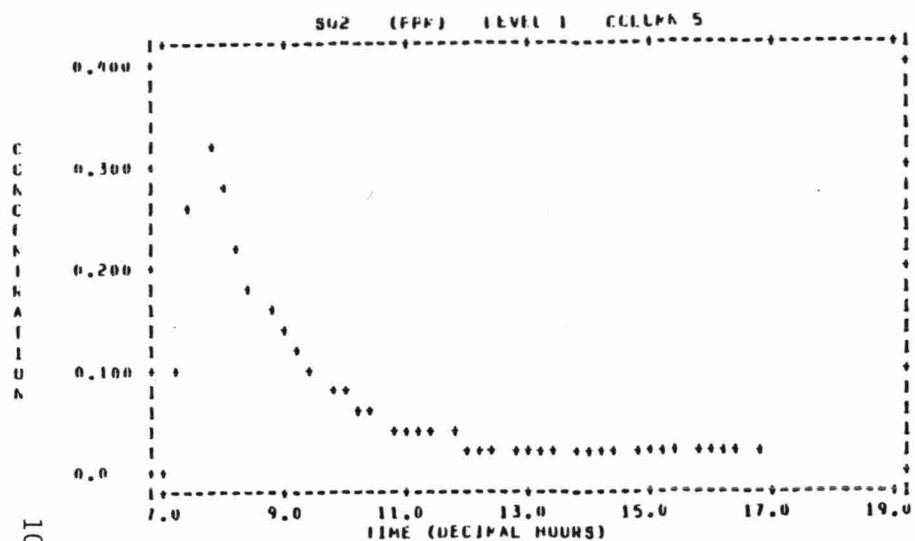


Figure 10-73. Center Column Surface Cell Concentration vs Time Profiles for PLMSTAR run W5.



PLMSTAN - WINTER - NONLINEAR CHEMISTRY - CONSTANT K2 - RUN R5



PLMSTAN - WINTER - NONLINEAR CHEMISTRY - CONSTANT K2 - RUN R5

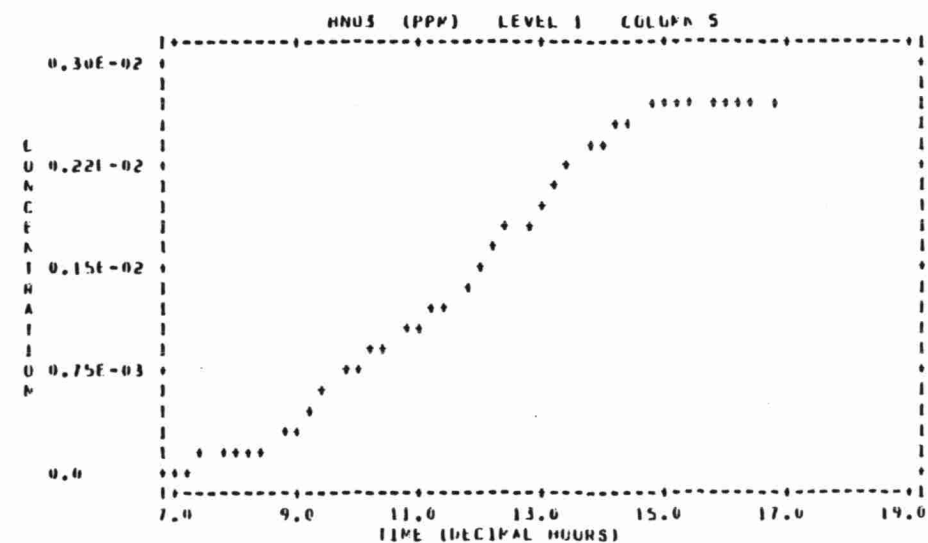
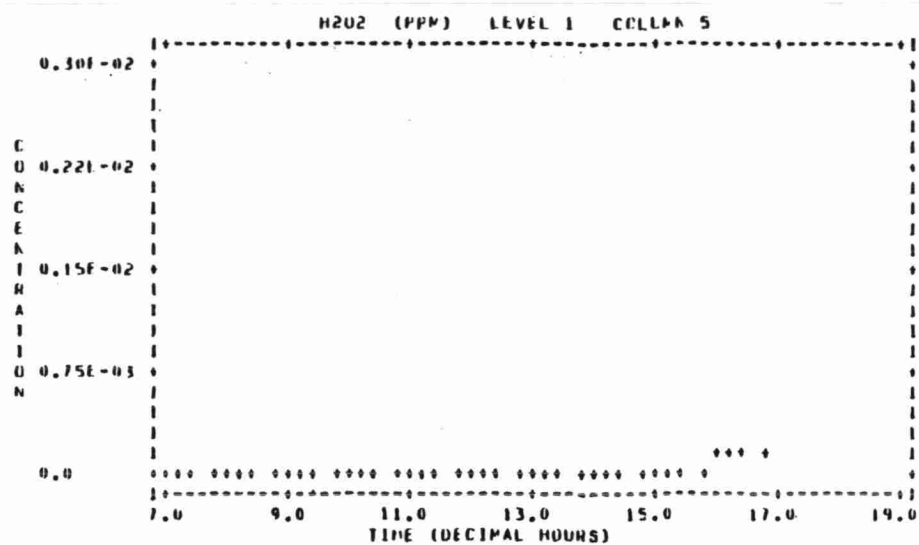


Figure 10-73. (Continued)

PLMSTAR-SUMMER-LINEAR CHEMISTRY-SINGLE COLUMN-CONSTANT DEP VEL & KZ - RUN S6

PLMSTAR-SUMMER-LINEAR CHEMISTRY-SINGLE COLUMN-CONSTANT DEP VEL & KZ - RUN S6

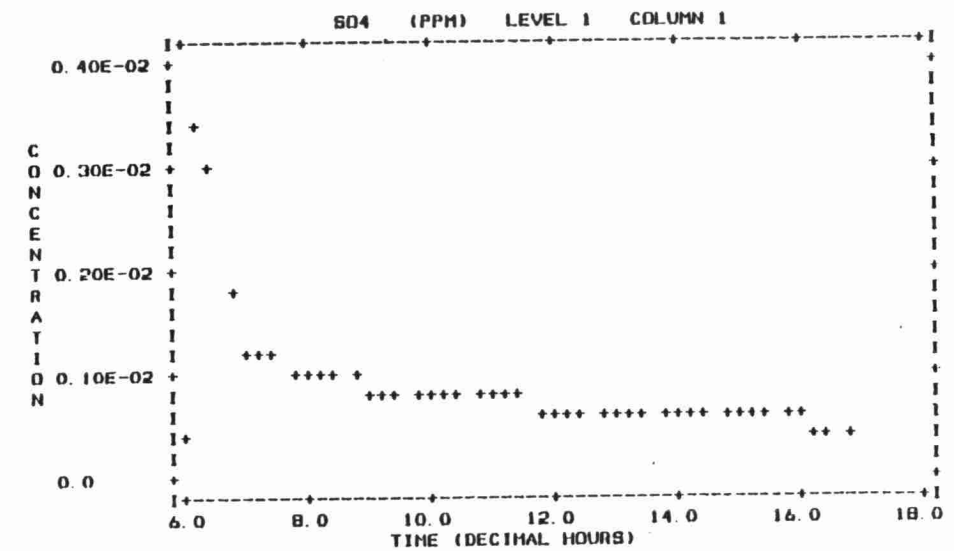
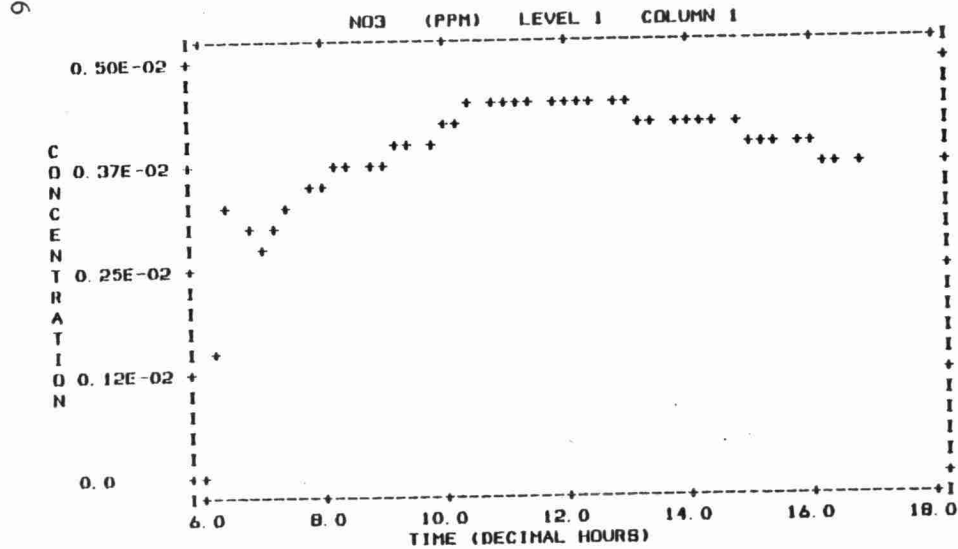
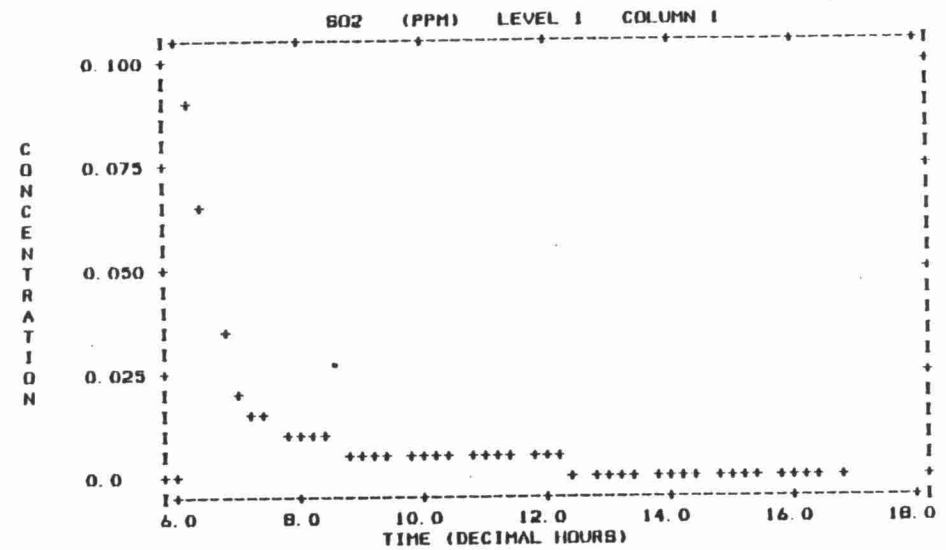
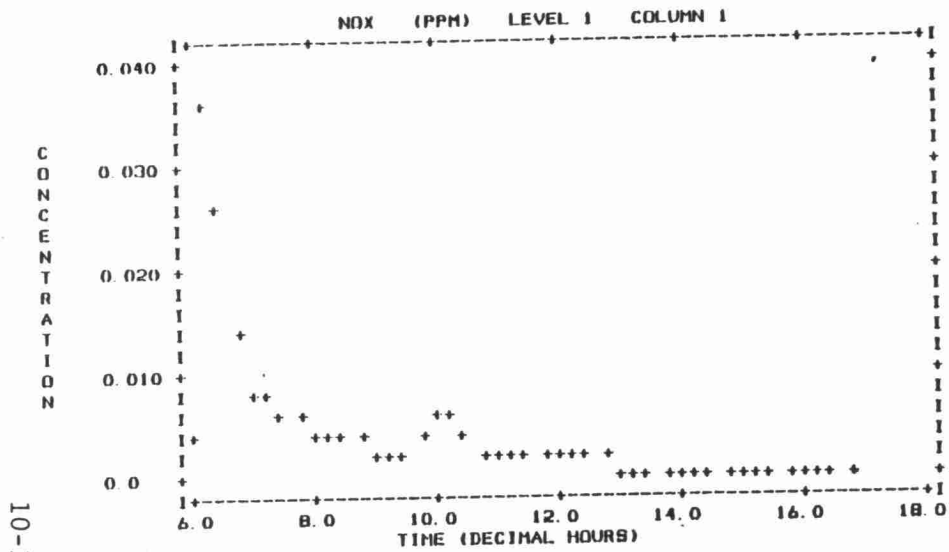
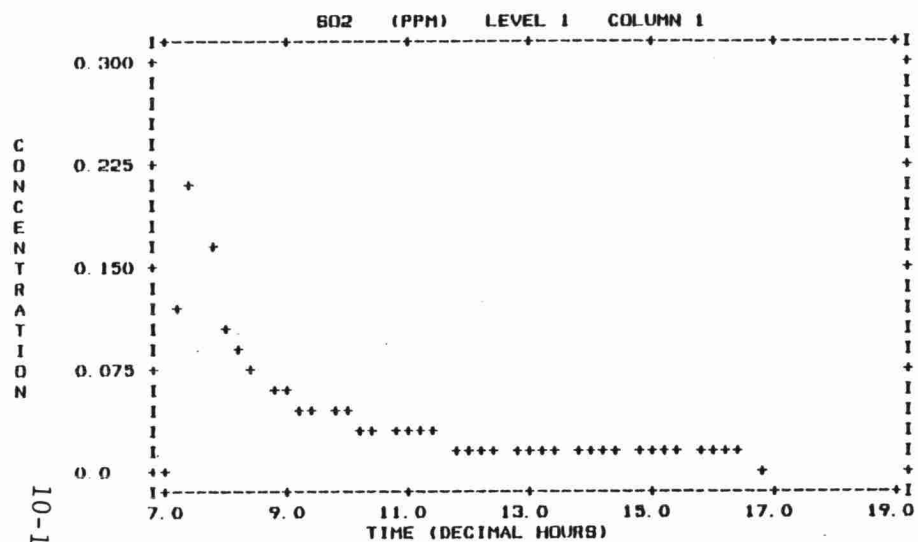


Figure 10-74. Center Column Surface Cell Concentration vs Time Profiles for PLMSTAR run S6.

10-146

PLMSTAR-WINTER-LINEAR CHEMISTRY-SINGLE COLUMN-CONSTANT DEP & KZ- RUN W6



PLMSTAR-WINTER-LINEAR CHEMISTRY-SINGLE COLUMN-CONSTANT DEP & KZ- RUN W6

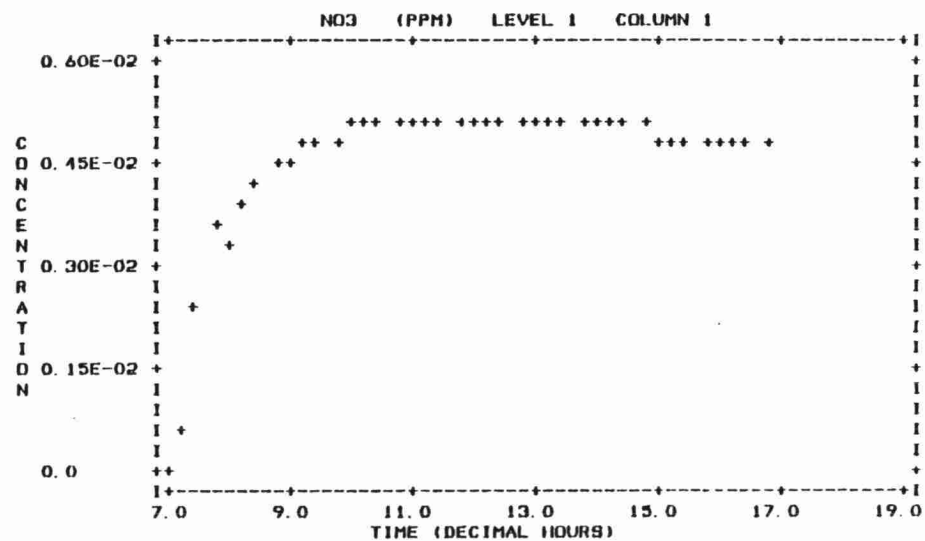
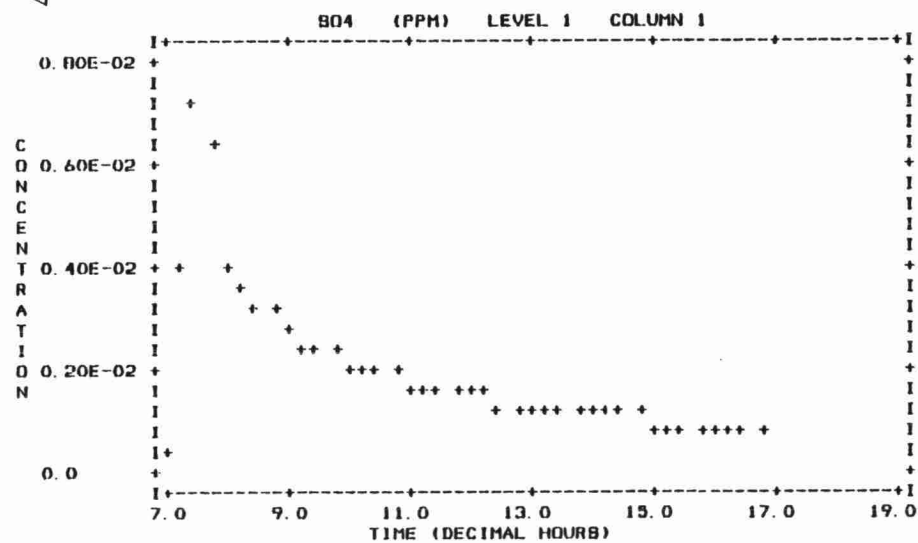
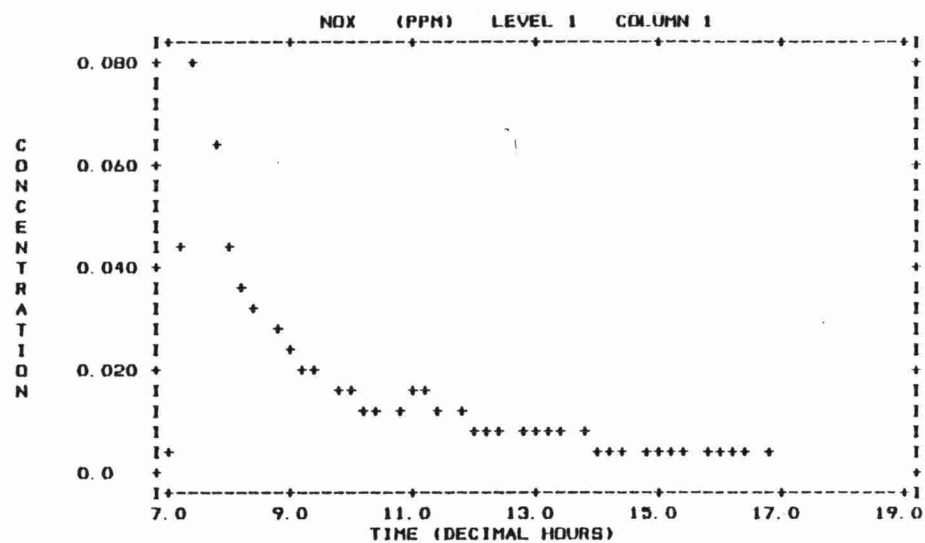


Figure 10-75. Center Column Surface Cell Concentration vs Time Profiles for PLMSTAR run W6.

TABLE 10-24

PLMSTAR MAXIMUM CENTERLINE CONCENTRATIONS (PPB) FOR BASELINE RUNS

RUN #	SO2	SO4	NOX	TNO3	NO	NO2	O3	PAN	HNO3	H2O2
S1	125.00	4.52	51.00	7.60	13.00	28.00	72.90	5.56	3.48	9.82
S2	23.60	1.20	12.30	5.90	3.40	8.90	64.40	4.93	1.97	9.14
S3	122.00	7.62	34.20	18.00						
S4	118.00	4.25	49.80	7.60	23.50	24.30	75.30	5.56	3.93	9.65
S5	144.00	5.71	74.00	7.60	38.00	38.00	74.60	5.55	3.60	9.39
S6	90.00	3.40	36.00	4.45						
W1	210.00	7.20	87.00	6.70	60.00	27.00	40.50	3.91	2.76	0.17
W2	90.00	3.42	38.60	5.80	20.40	18.20	38.20	3.77	2.25	0.73
W3	210.00	9.50	70.00	15.90						
W4	200.00	6.65	84.00	6.50	60.00	24.00	39.30	3.79	2.76	0.16
W5	320.00	10.00	112.00	6.50	79.80	34.00	38.50	3.69	2.77	0.15
W6	209.00	7.28	79.20	5.16						

TABLE 10-25

PLMSTAR FINAL AVERAGE CONCENTRATIONS (PPB) FOR BASELINE RUNS

RUN #	SO2	SO4	NOX	TNO3	NO	NO2	O3	PAN	HNO3	H2O2
S1	1.46	0.69	0.00	6.57	0.00	0.00	49.80	5.11	1.46	9.49
S2	0.95	0.59	0.00	6.87	0.00	0.00	51.60	5.48	1.39	10.20
S3	1.47	0.68	0.21	4.44						
S4	1.49	0.71	0.00	6.62	0.00	0.00	50.10	5.14	1.48	9.46
S5	1.80	0.81	0.00	6.65	0.00	0.00	50.10	5.11	1.54	9.36
S6	0.99	0.60	0.19	4.35						
W1	3.32	0.57	0.78	5.14	0.02	0.74	37.70	3.83	1.31	1.72
W2	3.31	0.63	0.86	5.14	0.02	0.84	37.40	3.77	1.37	1.77
W3	3.33	0.57	2.25	3.49						
W4	3.56	0.60	0.85	5.15	0.02	0.83	37.70	3.83	1.32	1.70
W5	3.97	0.62	0.92	5.08	0.02	0.90	37.20	3.76	1.32	1.71
W6	3.48	0.61	2.17	3.55						

TABLE 10-26

PLMSTAR CUMMULATIVE DEPOSITION (KG) FOR BASELINE RUNS

RUN #	S	N	SO2	SO4	NOX	TNO3	O3	PAN	HNO3
S1	591	207	991	286	238	605	4490	390	402
S2	442	184	719	248	195	561	4410	390	358
S3	591	201	969	319	230	588			
S4	564	201	938	285	228	590	4330	401	381
S5	475	199	761	285	215	599	4540	390	396
S6	434	174	695	259	209	508			
W1	617	137	1120	172	267	252	1470	184	154
W2	865	158	1590	210	327	264	1380	171	175
W3	616	151	1110	184	334	223			
W4	581	131	1039	167	251	247	1450	182	152
W5	508	132	900	150	210	237	1400	180	150
W6	508	132	900	150	210	237	1400	180	150

TABLE 10-27

% CHANGE IN SIMPLE MODELS' MAXIMUM CENTERLINE CONCENTRATIONS  
FOR BASELINE RUNS RELATIVE TO COMPLEX MODEL'S RESULTS

RUN #	SO2	SO4	NOX	TNO3	NO	NO2	O3	PAN	HNO3	H2O2
S2/S1	-81	-73	-75	-22	-85	-68	-11	-11	-43	-6
S3/S1	-2	48	-32	136	0	0	0	0	0	0
S4/S1	-5	-5	-2	0	2	-6	3	0	12	-1
S5/S1	31	26	49	0	65	35	2	0	3	-4
S6/S1	-28	-24	-29	-41	0	0	0	0	0	0
W2/W1	-57	-52	-55	-13	-66	-32	-5	-3	-18	329
W3/W1	0	31	-19	137	0	0	0	0	0	0
W4/W1	-4	-7	-3	-2	0	-11	-2	-3	0	-5
W5/W1	52	38	28	-2	33	25	-4	-5	0	-11
W6/W1	0	1	-8	-22	0	0	0	0	0	0

TABLE 10-28

% CHANGE IN SIMPLE MODELS' FINAL AVERAGE CONCENTRATIONS  
FOR BASELINE RUNS RELATIVE TO COMPLEX MODEL'S RESULTS

RUN #	SO2	SO4	NOX	TNO3	NO	NO2	O3	PAN	HNO3	H2O2
S2/S1	-34	-14	0	4	0	0	3	7	-4	7
S3/S1	0	-1	0	-32	0	0	0	0	0	0
S4/S1	2	2	0	0	0	0	0	0	1	0
S5/S1	23	16	0	1	0	0	0	0	5	-1
S6/S1	-32	-12	0	-33	0	0	0	0	0	0
W2/W1	0	10	10	0	10	10	0	-1	4	2
W3/W1	0	0	188	-32	0	0	0	0	0	0
W4/W1	7	5	8	0	0	9	0	0	0	-1
W5/W1	19	8	17	-1	10	17	-1	-1	0	0
W6/W1	4	7	178	-30	0	0	0	0	0	0

TABLE 10-29

% CHANGE IN SIMPLE MODELS' CUMMULATIVE DEPOSITION  
FOR BASELINE RUNS RELATIVE TO COMPLEX MODEL'S RESULTS

RUN #	S	N	SO2	SO4	NOX	TNO3	O3	PAN	HNO3
S2/S1	-25	-11	-27	-13	-18	-7	-1	0	-10
S3/S1	0	-2	-2	11	-3	-2	0	0	0
S4/S1	-4	-2	-5	0	-4	-2	-3	2	-5
S5/S1	-19	-3	-23	0	-9	0	1	0	-1
S6/S1	-26	-14	-29	-9	-12	-16	0	0	0
W2/W1	40	15	41	22	22	4	-6	-7	12
W3/W1	0	10	0	6	25	-11	0	0	0
W4/W1	-7	-4	-8	-2	-5	-1	-1	-1	-2
W5/W1	-17	-3	-18	-6	-4	-3	0	-2	-4
W6/W1	37	15	39	23	29	-5	0	0	0

Model 2's results for sulfur compounds show some significant differences. The maximum  $\text{SO}_2$  concentration predictions are 57 to 81% lower and the maximum  $\text{SO}_4$  concentrations are 53 to 73% lower than the complex model results, with the largest differences occurring in the summer case. Final average  $\text{SO}_2$  concentration are 35% lower in the summer case, but equal in the winter case. The final average  $\text{SO}_4$  concentrations for Model 2 are predicted to be 14% lower in summer and 11% higher in the winter than Model 1. Similarly, cumulative sulfur deposition is by 25% lower in the summer and 40% higher in the winter run. These differences are substantial for a half-day simulation.

Model 2 predicts lower maximum concentrations for all  $\text{NO}_x$  related pollutants than the complex model. Calculated  $\text{NO}_x$  and  $\text{TNO}_3$  maximum concentrations are lower by 56 to 76% and 13 to 22%, respectively. The maximum PAN concentration is 4 to 11% lower, which is small relative to the 18 to 43% underprediction found for maximum  $\text{HNO}_3$  concentration. Somewhat smaller differences were found in Model 2's final average concentrations. Final average  $\text{NO}_x$  and  $\text{TNO}_3$  are 10 to 14% and 0 to 5% greater than Model 1's predictions, respectively. Final average PAN,  $\text{HNO}_3$ ,  $\text{O}_3$  and  $\text{H}_2\text{O}_2$  are between -5% and +7% of the complex model results. Cumulative deposition of nitrogen is underpredicted by 11% in the summer case and overpredicted by 15% in the winter case.

These results are not surprising considering the conceptual differences between Models 1 and 2. Model 2 does not account for the spatial gradients in concentration across the plume and computes the average concentrations within the  $4.28 \sigma_y$  plume width. Hence, it is expected that the maximum concentrations of plume pollutants would be lower than those predicted by the complex model. The results show that the differences in the first few hours of the calculation influence the overall solution. Final average concentrations of  $\text{SO}_x$  and  $\text{NO}_x$ , which represent the mass available for additional transport, differ significantly. Deposition of S and N can similarly be 40% and 15% different in Model 2. Hence, it is concluded that the expanding column approach to lateral dispersion has serious deficiencies in its ability to simulate plume dynamics relative to the complex model.

#### 10.2.4.3 Model 3 Performance Relative to Model 1

The version of PLMSTAR with linear chemistry for  $\text{SO}_x$  and  $\text{NO}_x$  (Model 3) shows some close similarities to as well as significant differences from the baseline results from Model 1. For  $\text{SO}_x$ , the only measurable differences in Model 3 results are for maximum  $\text{SO}_4$  concentrations. These exceeded the complex model's results by 32 and 69% in winter and summer, respectively. However, the difference does not appear to effect the overall calculation significantly since final average concentrations and cumulative sulfur deposition are within 1% of the complex model's results.

The results with the linear mechanism for  $\text{NO}_x$  transformations show greater differences. Maximum  $\text{NO}_x$  concentrations are by 20 to 33% lower while maximum total nitrate ( $\text{TNO}_3$ ) concentrations are by 137% higher than the corresponding Model 1 values. Examination of Figures 10-62, 10-63, 10-69 and 10-70 indicates that the diurnal  $\text{NO}_x$  concentration profiles are similar for the center column. However, Figure 10-71 shows that the  $\text{TNO}_3$  concentration profiles are very different for the centerline column and somewhat different 2 to 3 km off the centerline. Clearly, the rates used in the linear  $\text{NO}_x$  chemical mechanism cause relative overprediction of chemical conversion along the plume centerline. However, the results for average final concentration show that Model 3 underestimates (21 to 33%) the overall chemical transformation of  $\text{NO}_x$  to nitrates found in the complex model. This difference is believed to be caused by the linear mechanism's inability to account for the increasing  $\text{NO}_2$  conversion to PAN at low  $\text{NO}_x$  concentrations. Model 3's predicted cumulative nitrogen deposition is within -3 to +10% of the complex model's results, which is quite close considering the magnitude of other differences in the predictions.

In summary, the linear chemical mechanism overestimates chemical transformation rates in the first 20 to 40 km of plume travel relative to the nonlinear chemical mechanism. This overprediction results in substantially higher peak  $\text{SO}_4$  and  $\text{TNO}_3$  concentrations. Smaller differences are apparent farther downwind since the final concentrations and deposition amounts are very close for  $\text{SO}_x$  and

moderately close for  $\text{NO}_x$ . Because the  $\text{NO}_x$  conversion depends so strongly on hydrocarbons and photochemistry, it is felt that constant linear transformation rates for  $\text{NO}_x$  cannot account for PAN formation accurately, and the differences exhibited here could be expected to increase with simulation time. More specifically, it would be difficult to choose linear  $\text{NO}_x$  conversion rates that would not substantially overpredict nitrate in the plume's nearfield without significantly underpredicting total conversion to nitrates.

#### 10.2.4.3 Model 4 Performance Relative to Model 1

The sensitivity of the mesoscale model to the use of constant deposition velocities (Model 4), rather than diurnally varying velocities which depend on variations in wind speed and surface roughness, is quite small in the 10- to 11-hour daytime simulations. The diurnal concentration profiles for runs S4 and W4 were almost identical to those for runs S1 and W1.

The net effect of constant deposition velocities for  $\text{SO}_2$  and  $\text{SO}_4$  was 5 to 7% less sulfur deposition over the course of the run. Since the constant deposition velocities were higher than the complex model's values at the time of the peak  $\text{SO}_x$  concentrations (i.e., 0730 to 0930 EST), the peaks were 5 to 8% lower than the complex model's peaks. Correspondingly, lower overall deposition resulted in 2 to 7% more  $\text{SO}_2$  and  $\text{SO}_4$  in the air mass at the end of the run.

The effect of constant deposition velocity formulation showed similar effects for  $\text{NO}_2$ , PAN and  $\text{HNO}_3$ . Overall nitrogen deposition was 3 to 4% lower with constant deposition velocities. Maximum concentrations were slightly lower for  $\text{NO}_x$ , PAN, and  $\text{H}_2\text{O}_2$ , whereas the maximum nitric acid concentration was greater in the summer case because the peak occurred at a time when the average deposition velocity was significantly lower than the time varying deposition velocity. Model 4's final concentrations were very close ( $\pm 1\%$ ) for all pollutants except  $\text{NO}_x$  in the winter case where 9% more final mass was predicted.

In summary, when the constant deposition velocities are derived from the time and space varying velocities, the model calculations are



relatively insensitive to the substitution of average constant deposition velocities. This result may not be true if the simulations were carried out for longer periods (including night time) or if the climatological averages were used rather than trajectory specific averages.

#### 10.2.4.5 Model 5 Performance Relative to Model 1

The use of constant vertical eddy diffusivity ( $K_z$ ) coefficients in Model 5, rather than diurnally varying coefficients which reflect the mixing height dynamics, results in significantly different plume behavior. The constant  $K_z$  coefficients allow for more rapid mixing of the plume to the ground and to the upper levels of the model. Maximum surface concentrations of  $SO_2$ ,  $SO_4$ , and  $NO_x$  are predicted to occur about one half hour downwind of the point source in Model 5 rather than  $1\frac{1}{2}$  to 2 hours downwind in Model 1. Also, the time required for the plume to become well-mixed vertically (to the top of the parcel) is about  $1\frac{1}{2}$  hours with constant  $K_z$ 's and 5 to 6 hours with the diurnally varying  $K_z$ 's. These differences in dispersion rates strongly affect the morning predictions as shown in Figures 10-72 and 10-73.

Maximum  $SO_2$  and  $SO_4$  concentrations were 31 to 52% and 26 to 39% higher in Model 5 than Model 1, respectively. The final  $SO_2$  and  $SO_4$  mass in the air parcel was also 20 to 23% and 9 to 16% higher with the constant  $K_z$ 's, respectively. Cumulative sulfur deposition was underestimated by 18 to 20%. The elevated maximum concentrations are a direct result of the accelerated vertical dispersion in the constant  $K_z$  model. Higher final concentrations and lower cumulative deposition are believed to occur because the constant  $K_z$  model allows the plume to mix rapidly to the upper levels of the model, rather than being confined below the mixing height in the mid-morning hours, and this results in slower transport to the surface for removal by dry deposition processes.

The Model 5 results for  $NO_x$  were similar to those for  $SO_2$  and  $SO_4$ . Maximum  $NO_x$  concentrations were 29 to 49% higher than the Model 1 results. Final  $NO_x$  was 18% higher in the winter case. Much

smaller differences (1 to 3%) were calculated for maximum  $\text{TNO}_3$  concentrations and final  $\text{TNO}_3$  mass. The close agreement between Models 1 and 5 nitrate concentrations are due to the fact that the nitrate concentrations are very low during the morning hours when the two models'  $K_z$  coefficients are most different. Cumulative nitrogen deposition is lower by only 3 to 4% which probably reflects the fact that approximately half of the  $\text{NO}_x$  emissions are injected after the time of greatest differences in  $K_z$  coefficients and that nitrate concentrations, and therefore deposition, increase gradually over the course of the run.

In summary, the constant  $K_z$  model allows for accelerated vertical dispersion of plume material which results in higher relative maximum surface concentrations and final average concentrations, and lower deposition than the complex model. Smaller differences were found for  $\text{NO}_x$  than  $\text{SO}_x$  in these cases because approximately half of the  $\text{NO}_x$  emissions were injected at a time when the constant and diurnally varying  $K_z$ 's were similar. The inability of the constant  $K_z$  model to resolve the mixing height properly is expected to cause major problems in model performance at night when the surface layer is frequently decoupled from elevated layers. Hence, the significant differences demonstrated in these half day simulations would probably be amplified in multiday simulations and, for this reason, the use of a constant  $K_z$  formulation does not appear to be a desirable model characteristic.

#### 10.2.4.6 Model 6 Performance Relative to Model 1

Model 6 included all of the simplifying assumptions incorporated in Models 2 through 5 and, hence, can be thought of as the compound simple model. The Model 6 results show, in general, substantial differences from the Model 1 results, yet the combination of the simplifying assumption, in some cases, offset one another.

The maximum  $\text{SO}_2$  and  $\text{SO}_4$  concentrations predicted by Model 6 are 28 and 25% lower in summer and no different in winter than those calculated by Model 1. These results show better agreement with the complex model than Model 2 or Model 5 because the tendency for under

prediction of peaks in the expanding column formulations is offset by the tendency to overpredict peaks in the constant  $K_z$  formulation. The final average  $SO_2$  and  $SO_4$  concentrations are 32 and 13% lower in summer and 5 to 8% higher in winter than in the complex model's results. Similarly, sulfur deposition is lower by 27% in the summer case and higher by 38% in the winter case. Hence, the compound simple model deviates from the complex model's solution in opposite direction in summer and winter for  $SO_x$ .

The maximum  $NO_x$  and  $TNO_3$  concentrations are 9 to 29% and 23 to 41% lower than the complex model results, respectively. The final average  $TNO_3$  concentrations are also lower by 31 to 34% in the compound simple model. Model 6's results also have substantially more nitrogen mass as  $NO_x$  than the complex model results, which is a characteristic of all the calculations with the linear  $NO_x$  chemical mechanism. Nitrogen deposition is lower by 15% and 40% in the summer and winter cases. These results do not show the opposite sensitivities for the winter and summer cases found in the  $SO_x$  results, most likely because the  $NO_x$  solution involves both point and area source emissions.

In summary, the compound simple model results show substantial differences from the complex model results in almost all the model output parameters. Furthermore, the deviations are not consistently in one direction and are expected to be greater for longer simulations. Little confidence can be placed in the compound simple model's results because of these differences.

#### 10.2.4.7 Summary of Sulfate and Nitrate Concentration Differences

The absolute differences in sulfate and total nitrate concentrations between results of the simple models and the complex model are shown in Figures 10-76 and 10-77 for the summer and winter cases, respectively. The differences are of center column surface cell concentrations for Models 2 through 6 relative to Model 1.

As can be seen in figures, the use of linear conversion rates (Model 3) produces by far the largest deviations of calculated  $TNO_3$  in

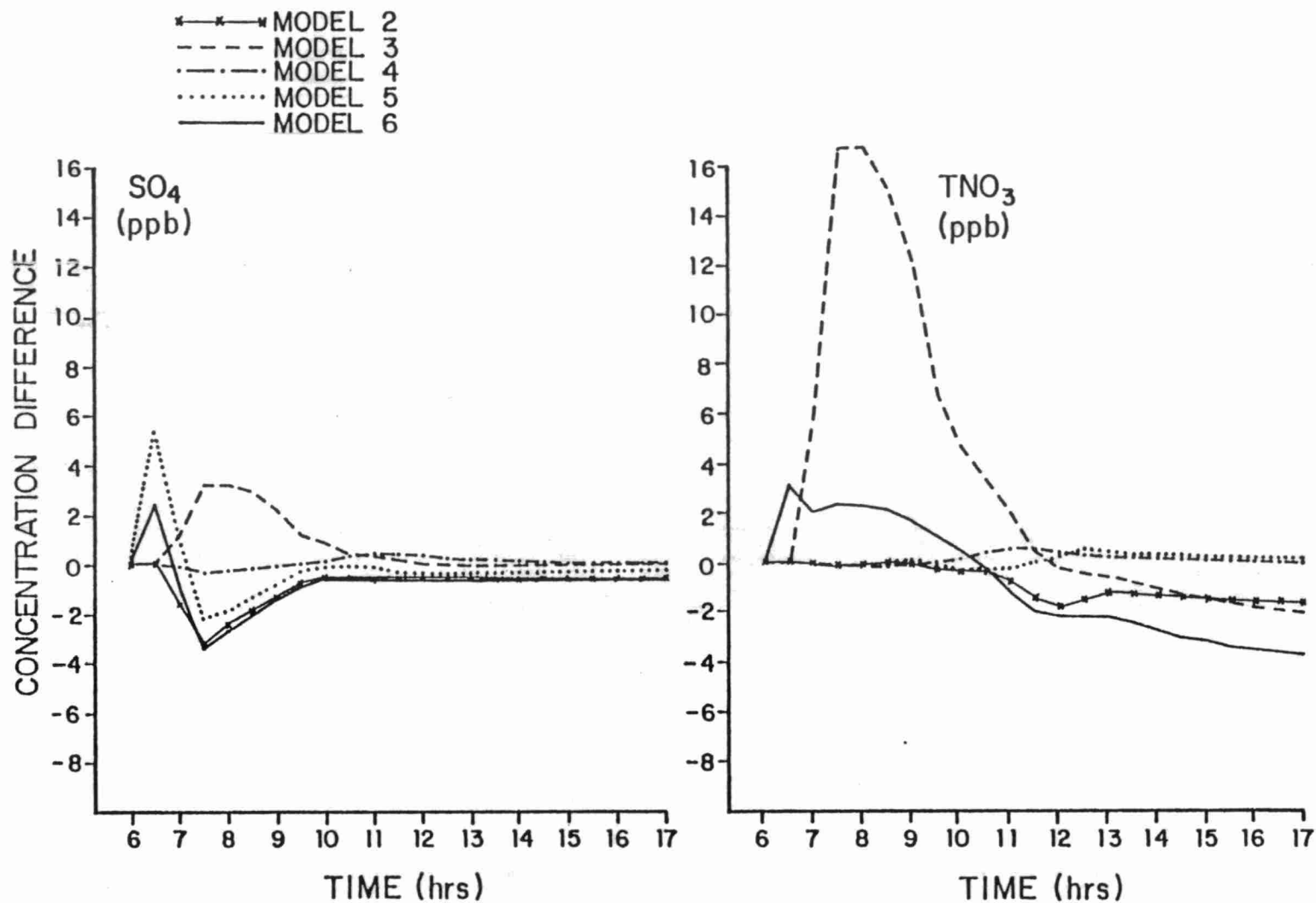


Figure 10-76. Differences in calculated surface concentrations of sulfate ( $\text{SO}_4$ ) and total nitrate ( $\text{TNO}_3$ ) of the simple models' results relative to the complex model's results for the summer simulation.

10-157

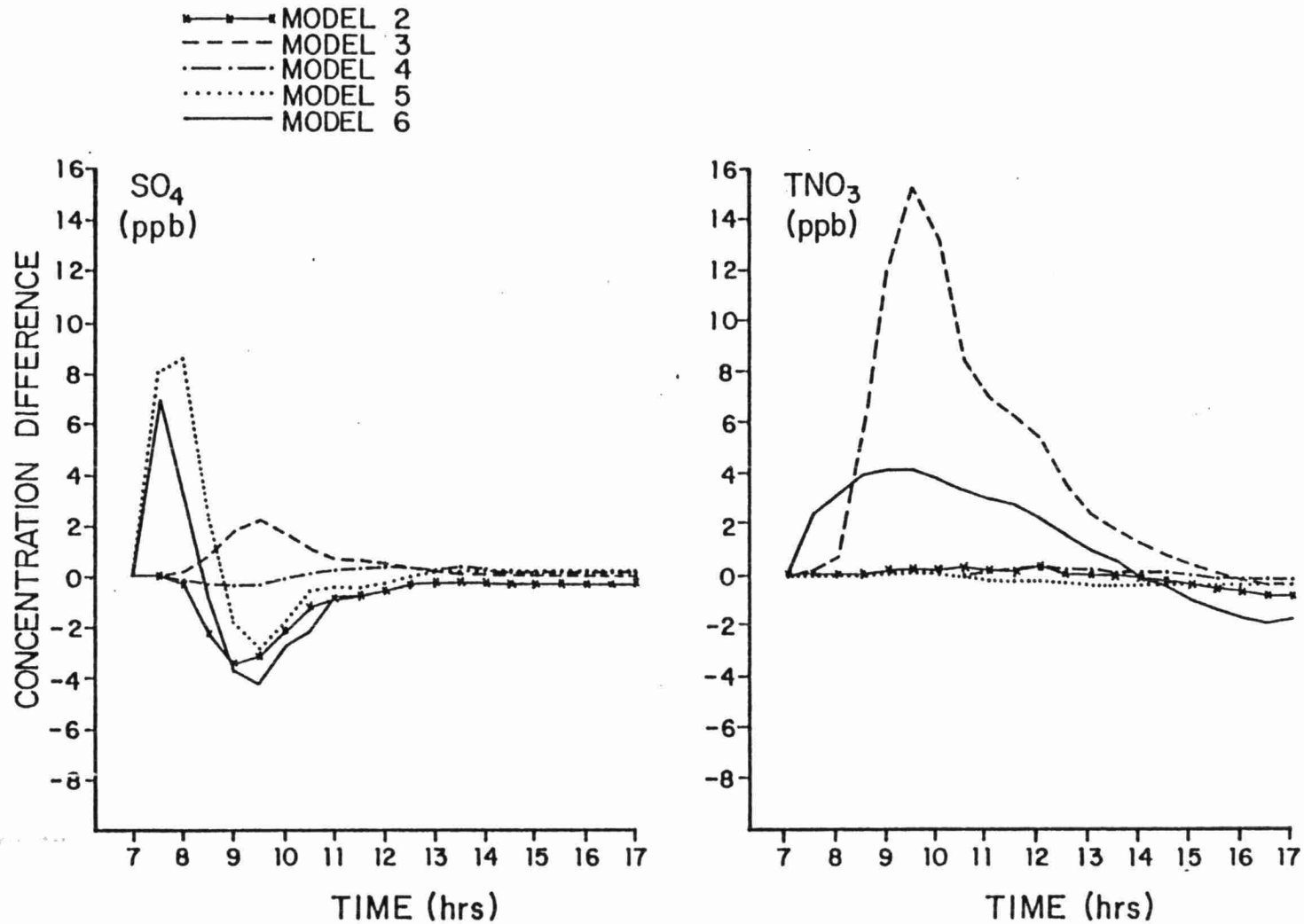


Figure 10-77. Differences in calculated surface concentrations of sulfate (SO<sub>4</sub>) and total nitrate (TNO<sub>3</sub>) of the simple models' results relative to the complex model's results for the winter simulation.

both winter and summers. Moderate differences are also seen with Model 2, which is the single expanding column model, in the summer case.

For  $\text{SO}_4$ , the largest concentration differences relative to the complex model are seen for Model 5, which utilizes constant  $K_z$ 's. However, moderate deviations also result from the use of linear  $\text{SO}_2$ -to- $\text{SO}_4$  conversion rates and the single expanding column. For all simple models, the sulfate concentration differences seen at the end of the runs are small relative to the differences seen in the first four hours of the simulations.

#### 10.2.4.8 Computing Times of the Simple and Complex Models

One of the common rationales for not using complex models is their high computer resource and time requirements. Since some significant differences have been identified between simple and complex models, it is appropriate to discuss their computing time requirements.

The PLMSTAR model used approximately 1 minute of IBM 3033 central processing unit (cpu) time to compute the concentrations of 30 species in 50 cells for 10 hours. This is a relatively small amount of computing time and reflects the economy of Lagrangian models. Model 2 which has nonlinear chemistry, 10 cells and no lateral diffusion algorithm used 19% of the cpu time of Model 1. This shows that computing time is a fairly linear function of the number of cells when nonlinear chemistry is included. Model 3 which has 50 cells and only 4 species required 22% of the cpu time of the complex model. Model 6 which has 10 cells and 4 species required just 3% of the complex model's cpu time. The two latter times are believed to be higher than necessary due to the use of an unnecessarily complex numerical integration algorithm for the linear chemistry. With a simpler algorithm, Model 3 is estimated to require 10 to 15% of the complex model's cpu time. This means that the use of the nonlinear chemistry package increases the computer costs by a factor of 7 to 10 relative to the costs with the linear chemistry. This also suggests

that the computer time is a relatively linear function of the number of chemical species in the chemical mechanism.

#### 10.2.5 Mesoscale Model Sensitivity to Emission Reduction

The response of the complex and simple models to emission reductions are compared in this section. The emission reductions considered include a 50% reduction in point source emissions (Scenario A) and 50% reduction in both point and area source emissions (Scenario B). These emission reductions include RHC emissions, as well as  $\text{NO}_x$  and  $\text{SO}_x$  for the urban areas. Since the baseline case has initial concentrations which, in some cases, dominant the solution, results for simulations with zero emissions are reported as well (Scenario C). Subtraction of the predictions for Scenario C from the other results allows one to examine variations in the "emissions component" of the solutions with emission rate changes.

The results for these runs are presented in tabular form. Tables 10-30 through 10-32 show the maximum concentration, average final concentration, and cumulative deposition predictions of Models 1, 2, 3 and 6 for Scenarios A, B and C. Tables 10-33 through 10-35 show the percent change in the absolute results for Scenarios A, B and C relative to the baseline results for each model (i.e., S1A vs S1, W3A vs W3, etc.). Tables 10-36 through 10-38 show the emissions component of the results for the baseline, Scenario A, and Scenario B runs. Tables 10-39 through 10-41 show the percent change in the emission components of the results for Scenarios A and B. These latter three tables contain the results which are believed to best show the differences in the models' responses to emission reductions.

Because of the relatively large volume of results, a simple evaluation procedure has been used to compare the percent reductions of the simple model's results to the complex model results. The procedure is to assign a score of 2 (for good agreement) to a simple model's percent reductions when they are within 5% of the complex model's percent reductions. Results for percent reduction which are within 5.1% to 10% and greater than 10% of the complex model results are assigned a score of 1 for fair agreement and 0 for poor agreement,

TABLE 10-30

PLMSTAR MAXIMUM CENTERLINE CONCENTRATIONS (PPB) FOR EMISSION SCENARIO RUNS

RUN #	SO2	SO4	NOX	TNO3	NO	NO2	O3	PAN	HNO3	H2O2
S1A	62.90	2.44	27.20	7.40	9.30	17.90	68.70	5.52	2.73	9.81
S2A	12.10	0.79	7.90	5.70	2.00	5.90	62.50	4.89	1.67	9.24
S3A	61.40	4.01	18.40	9.60						
S4A	45.00	2.00	20.00	3.98						
W1A	100.00	3.80	44.00	6.40	24.00	20.00	45.50	4.50	2.06	0.50
W2A	44.00	1.92	20.60	5.50	8.10	12.90	41.00	4.09	1.64	1.18
W3A	95.50	4.75	36.00	8.40						
W4A	105.00	3.86	41.90	3.52						
S1B	62.90	2.44	27.20	6.90	9.30	17.90	66.90	5.33	2.73	9.81
S2B	12.10	0.79	7.90	5.50	2.00	5.90	60.20	4.79	1.49	9.17
S3B	61.40	4.01	18.40	9.60						
S4B	45.00	2.00	20.00	3.70						
W1B	100.00	3.80	44.00	6.10	24.00	20.00	44.90	4.40	1.93	0.66
W2B	44.00	1.92	20.60	5.20	8.10	12.90	40.50	3.99	1.53	1.30
W3B	95.50	4.75	36.00	8.40						
W4B	105.00	3.86	41.90	3.35						
S1C	1.00	0.50	5.00	5.90	0.70	4.50	54.70	4.93	1.10	9.69
S2C	1.00	0.50	5.00	5.10	0.70	4.50	55.00	4.44	1.10	9.14
S3C	1.00	0.50	5.00	3.40						
S4C	1.00	0.50	5.00	2.97						
W1C	1.00	0.50	5.00	3.80	0.70	4.80	34.20	3.29	0.68	2.31
W2C	1.00	0.50	5.00	3.50	0.70	4.80	32.00	3.10	0.60	2.31
W3C	1.00	0.50	5.00	2.10						
W4C	1.00	0.50	5.00	1.78						

TABLE 10-31

PLMSTAR FINAL AVERAGE CONCENTRATIONS (PPB) FOR EMISSION SCENARIO RUNS

RUN #	SO2	SO4	NOX	TNO3	NO	NO2	O3	PAN	HNO3	H2O2
S1A	0.99	0.55	0.00	6.40	0.00	0.00	48.20	5.12	1.28	9.49
S2A	0.77	0.54	0.00	6.78	0.00	0.00	51.00	5.44	1.32	10.25
S3A	0.99	0.55	0.20	4.14						
S4A	0.80	0.55	0.19	4.24						
W1A	1.93	0.46	0.14	4.94	0.00	0.14	38.00	3.88	1.04	1.82
W2A	1.95	0.50	0.14	4.96	0.00	0.14	39.10	3.88	1.08	1.95
W3A	1.95	0.44	1.96	3.02						
W4A	2.04	0.48	1.86	3.04						
S1B	0.98	0.54	0.00	6.20	0.00	0.00	47.10	4.99	1.21	9.41
S2B	0.76	0.54	0.00	6.67	0.00	0.00	50.40	5.38	1.29	10.22
S3B	0.97	0.55	0.17	3.93						
S4B	0.77	0.54	0.17	4.10						
W1B	1.90	0.45	0.11	4.70	0.00	0.11	36.70	3.74	0.96	1.91
W2B	1.93	0.50	0.09	4.87	0.00	0.09	37.90	3.84	1.03	1.99
W3B	1.92	0.43	1.87	2.86						
W4B	2.03	0.48	1.78	2.96						
S1C	0.46	0.38	0.00	5.76	0.00	0.00	43.60	4.79	0.97	9.28
S2C	0.57	0.48	0.00	6.46	0.00	0.00	49.00	5.25	1.21	10.20
S3C	0.47	0.41	0.13	3.42						
S4C	0.56	0.48	0.15	3.84						
W1C	0.51	0.30	0.00	3.93	0.00	0.00	31.50	3.32	0.61	2.29
W2C	0.59	0.34	0.00	4.23	0.00	0.00	33.60	3.51	0.72	2.39
W3C	0.51	0.30	1.28	2.20						
W4C	0.58	0.34	1.38	2.37						



TABLE 10-32

## PLMSTAR CUMMULATIVE DEPOSITION (KG) FOR EMISSION SCENARIO RUNS

RUN #	S	N	SO2	SO4	NOX	TNO3	O3	PAN	HNO3
S1A	379	185	400	238	193	568	4460	395	362
S2A	297	167	456	208	167	522	4370	391	319
S3A	379	170	590	253	207	528			
S6A	293	163	443	215	193	471			
W1A	360	117	627	139	210	241	1500	188	143
W2A	479	123	854	156	229	241	1440	179	148
W3A	360	127	625	142	281	186			
W6A	472	127	841	152	284	184			
S1B	374	175	590	236	176	546	4440	386	345
S2B	292	160	448	205	155	506	4310	380	308
S3B	378	169	579	252	182	513			
S6B	288	155	434	214	177	453			
W1B	355	109	618	139	190	230	1490	184	135
W2B	474	118	849	156	217	236	1440	178	143
W3B	355	118	616	142	256	180			
W6B	469	122	836	152	271	180			
S1C	155	141	191	180	118	474	4250	372	281
S2C	144	135	178	164	119	443	4160	364	253
S3C	156	138	189	186	135	437			
S6C	141	130	173	165	145	386			
W1C	95	78	123	100	111	198	1450	179	105
W2C	88	75	115	93	110	187	1410	175	96
W3C	95	85	123	100	178	138			
W6C	88	82	114	92	178	123			

TABLE 10-33

## % CHANGE IN MAXIMUM CONCENTRATIONS FOR EMISSION SCENARIO RUNS RELATIVE TO BASELINE RESULTS

RUN #	SO2	SO4	NOX	TNO3	NO	NO2	O3	PAN	HNO3	H2O2
S1A	-49	-45	-46	-2	-59	-36	-5	0	-21	0
S2A	-48	-34	-35	-3	-41	-33	-2	0	-15	1
S3A	-49	-47	-46	-46						
S6A	-50	-41	-44	-10						
W1A	-52	-47	-49	-4	-60	-25	12	15	-25	194
W2A	-51	-43	-46	-5	-60	-29	7	8	-27	61
W3A	-54	-50	-48	-47						
W6A	-49	-46	-47	-31						
S1B	-49	-45	-46	-9	-59	-36	-8	-4	-21	0
S2B	-48	-34	-35	-6	-41	-33	-6	-2	-24	0
S3B	-49	-47	-46	-46						
S6B	-50	-41	-44	-16						
W1B	-52	-47	-49	-8	-60	-25	10	12	-30	288
W2B	-51	-43	-46	-10	-60	-29	6	5	-32	78
W3B	-54	-50	-48	-47						
W6B	-49	-46	-47	-35						
S1C	-99	-88	-90	-22	-96	-83	-24	-11	-68	-1
S2C	-95	-58	-59	-13	-79	-49	-14	-9	-44	0
S3C	-99	-93	-85	-81						
S6C	-98	-85	-86	-33						
W1C	-99	-93	-94	-43	-98	-82	-15	-15	-75	1258
W2C	-98	-85	-87	-39	-96	-73	-16	-17	-73	216
W3C	-99	-94	-92	-86						
W6C	-99	-93	-93	-65						

TABLE 10-34

% CHANGE IN FINAL AVERAGE CONCENTRATIONS  
FOR EMISSION SCENARIO RUNS RELATIVE TO BASELINE RESULTS

RUN #	SO2	SO4	NOX	TNO3	NO	NO2	O3	PAN	HNO3	H2O2
S1A	-32	-20		-2			-3	0	-12	0
S2A	-19	-8		-1			-1	0	-5	0
S3A	-32	-19	-5	-6						
S4A	-19	-9	-1	-3						
W1A	-41	-19	-79	-3	-85	-78	0	1	-19	5
W2A	-41	-20	-83	-3	-88	-83	4	2	-21	10
W3A	-41	-22	-12	-13						
W4A	-41	-21	-14	-14						
S1B	-33	-22		-5			-5	-2	-17	0
S2B	-19	-9		-2			-2	-1	-7	0
S3B	-34	-20	-18	-11						
S4B	-21	-9	-11	-5						
W1B	-42	-21	-85	-8	-90	-85	-2	-2	-24	11
W2B	-41	-20	-89	-5	-92	-89	1	1	-24	12
W3B	-42	-24	-16	-18						
W4B	-41	-21	-17	-16						
S1C	-48	-45		-12			-12	-6	-33	-2
S2C	-40	-18		-5			-5	-4	-12	0
S3C	-48	-40	-37	-22						
S4C	-43	-19	-22	-11						
W1C	-84	-47	-100	-23	-100	-100	-14	-13	-53	33
W2C	-82	-44	-100	-17	-100	-100	-10	-6	-47	35
W3C	-84	-47	-43	-34						
W4C	-83	-43	-34	-33						

TABLE 10-35

% CHANGE IN CUMMULATIVE DEPOSITION  
FOR EMISSION SCENARIO RUNS RELATIVE TO BASELINE RESULTS

RUN #	S	N	SO2	SO4	NOX	TNO3	O3	PAN	HNO3
S1A	-35	-10	-39	-14	-18	-6	0	1	-9
S2A	-32	-9	-36	-14	-14	-6	0	0	-10
S3A	-35	-15	-39	-20	-10	-10	0	0	-10
S4A	-32	-7	-36	-16	-7	-7			
W1A	-41	-14	-44	-19	-21	-4	2	2	-8
W2A	-44	-22	-46	-25	-29	-8	4	4	-15
W3A	-41	-15	-43	-22	-15	-16	4	4	-15
W4A	-44	-19	-46	-28	-17	-22			
S1B	-36	-13	-40	-17	-26	-9	-1	-1	-14
S2B	-33	-13	-37	-17	-20	-9	-2	-2	-13
S3B	-36	-15	-40	-21	-20	-12	-2	-2	-13
S4B	-33	-11	-37	-17	-15	-10			
W1B	-42	-20	-44	-19	-28	-8	1	0	-13
W2B	-44	-25	-46	-25	-33	-10	4	4	-18
W3B	-42	-21	-44	-22	-23	-19	4	4	-18
W4B	-44	-22	-46	-28	-21	-24			
S1C	-73	-31	-80	-37	-50	-21	-5	-4	-30
S2C	-67	-26	-75	-33	-38	-21	-5	-6	-29
S3C	-73	-31	-80	-41	-41	-25	-5	-6	-29
S4C	-67	-26	-75	-36	-30	-24			
W1C	-84	-43	-89	-41	-58	-21	-1	-2	-32
W2C	-89	-52	-92	-55	-66	-29	2	2	-45
W3C	-84	-43	-88	-45	-46	-38	2	2	-45

TABLE 10-36

EMISSION COMPONENT OF MAXIMUM CENTERLINE CONCENTRATIONS (PPB)

RUN #	S02	S04	NOX	TNO3	NO	NO2	O3	PAN	HNO3	H2O2
S1	124.00	4.02	46.00	1.70	22.30	23.50	18.20	0.43	2.38	0.13
S2	22.60	0.70	7.30	0.80	2.70	4.40	9.40	0.49	0.87	0.00
S3	121.00	7.12	29.20	14.60	0.00	0.00	0.00	0.00	0.00	0.00
S4	89.00	2.90	31.00	1.48	0.00	0.00	0.00	0.00	0.00	0.00
W1	209.00	6.70	82.00	2.90	59.30	22.20	6.30	0.62	2.08	-2.14
W2	89.00	2.92	33.60	2.30	19.70	13.40	6.20	0.67	1.65	-1.58
W3	209.00	9.00	65.00	13.80	0.00	0.00	0.00	0.00	0.00	0.00
W4	208.00	6.78	74.20	3.38	0.00	0.00	0.00	0.00	0.00	0.00
S1A	61.90	1.96	22.20	1.50	8.60	13.40	14.00	0.59	1.63	0.12
S2A	11.10	0.29	2.90	0.60	1.30	1.40	7.50	0.45	0.57	0.10
S3A	60.40	3.51	13.40	6.20	0.00	0.00	0.00	0.00	0.00	0.00
S4A	44.00	1.50	15.00	1.01	0.00	0.00	0.00	0.00	0.00	0.00
W1A	99.00	3.30	39.00	2.60	23.30	15.20	11.30	1.21	1.38	-1.81
W2A	43.00	1.42	15.60	2.00	7.40	8.10	9.00	0.99	1.04	-1.13
W3A	94.50	4.25	31.00	6.30	0.00	0.00	0.00	0.00	0.00	0.00
W4A	104.00	3.36	36.90	1.74	0.00	0.00	0.00	0.00	0.00	0.00
S1B	61.90	1.96	22.20	1.00	8.60	13.40	12.20	0.40	1.63	0.12
S2B	11.10	0.29	2.90	0.40	1.30	1.40	5.20	0.35	0.39	0.03
S3B	60.40	3.51	13.40	6.20	0.00	0.00	0.00	0.00	0.00	0.00
S4B	44.00	1.50	15.00	0.73	0.00	0.00	0.00	0.00	0.00	0.00
W1B	99.00	3.30	39.00	2.30	23.30	15.20	10.70	1.11	1.25	-1.65
W2B	43.00	1.42	15.60	1.70	7.40	8.10	8.50	0.89	0.93	-1.01
W3B	94.50	4.25	31.00	6.30	0.00	0.00	0.00	0.00	0.00	0.00
W4B	104.00	3.36	36.90	1.57	0.00	0.00	0.00	0.00	0.00	0.00

TABLE 10-37

EMISSIONS COMPONENT OF FINAL AVERAGE CONCENTRATION (PPB)

RUN #	S02	S04	NOX	TNO3	NO	NO2	O3	PAN	HNO3	H2O2
S1	1.00	0.31	0.00	0.81	0.00	0.00	6.20	0.32	0.49	0.21
S2	0.38	0.11	0.00	0.41	0.00	0.00	2.60	0.23	0.18	0.00
S3	1.00	0.28	0.08	1.02	0.00	0.00	0.00	0.00	0.00	0.00
S4	0.44	0.12	0.04	0.51	0.00	0.00	0.00	0.00	0.00	0.00
W1	2.81	0.27	0.78	1.21	0.02	0.74	6.20	0.51	0.70	-0.57
W2	2.72	0.29	0.86	0.91	0.02	0.84	3.80	0.24	0.65	-0.62
W3	2.82	0.27	0.97	1.29	0.00	0.00	0.00	0.00	0.00	0.00
W4	2.90	0.27	0.79	1.18	0.00	0.00	0.00	0.00	0.00	0.00
S1A	0.53	0.17	0.00	0.64	0.00	0.00	4.60	0.33	0.31	0.21
S2A	0.20	0.06	0.00	0.32	0.00	0.00	2.00	0.21	0.11	0.05
S3A	0.52	0.14	0.07	0.72	0.00	0.00	0.00	0.00	0.00	0.00
S4A	0.25	0.07	0.04	0.40	0.00	0.00	0.00	0.00	0.00	0.00
W1A	1.42	0.16	0.16	1.01	0.00	0.16	6.50	0.56	0.45	-0.47
W2A	1.36	0.16	0.14	0.73	0.00	0.14	5.50	0.37	0.36	-0.44
W3A	1.44	0.14	0.68	0.82	0.00	0.00	0.00	0.00	0.00	0.00
W4A	1.46	0.14	0.48	0.67	0.00	0.00	0.00	0.00	0.00	0.00
S1B	0.51	0.16	0.00	0.44	0.00	0.00	3.50	0.20	0.24	0.13
S2B	0.19	0.05	0.00	0.21	0.00	0.00	1.40	0.13	0.08	0.02
S3B	0.50	0.14	0.04	0.51	0.00	0.00	0.00	0.00	0.00	0.00
S4B	0.22	0.06	0.02	0.26	0.00	0.00	0.00	0.00	0.00	0.00
W1B	1.39	0.15	0.11	0.77	0.00	0.11	5.20	0.42	0.35	-0.38
W2B	1.34	0.16	0.09	0.64	0.00	0.09	4.30	0.33	0.31	-0.40
W3B	1.41	0.13	0.59	0.66	0.00	0.00	0.00	0.00	0.00	0.00
W4B	1.45	0.14	0.40	0.59	0.00	0.00	0.00	0.00	0.00	0.00

TABLE 10-38

## EMISSIONS COMPONENT OF CUMMULATIVE DEPOSITION (KG)

RUN #	S	N	SO2	SO4	NOX	TNO3	O3	PAN	HNO3
S1	436	66	800	104	120	131	240	18	121
S2	298	49	541	84	76	118	250	26	105
S3	435	63	780	133	95	151	0	0	0
S4	293	46	522	94	64	122	0	0	0
W1	522	59	997	72	156	54	20	5	51
W2	777	83	1475	117	217	77	-30	-4	79
W3	521	66	987	84	156	85	0	0	0
W4	763	76	1446	120	168	114	0	0	0
S1A	224	44	409	58	75	94	210	23	81
S2A	153	32	278	44	48	79	210	27	66
S3A	223	32	401	67	72	91	0	0	0
S4A	152	33	270	50	48	85	0	0	0
W1A	265	39	504	39	99	43	50	9	38
W2A	391	48	739	43	119	54	30	4	52
W3A	265	42	502	42	103	48	0	0	0
W4A	384	45	727	60	106	61	0	0	0
S1B	219	34	399	56	58	72	190	14	64
S2B	148	25	270	41	36	63	150	16	55
S3B	222	31	390	66	47	76	0	0	0
S4B	147	25	261	49	32	67	0	0	0
W1B	260	31	495	39	79	32	40	5	30
W2B	388	43	734	63	107	49	30	3	47
W3B	260	33	493	42	78	42	0	0	0
W4B	381	40	722	60	93	57	0	0	0

TABLE 10-39

## % CHANGE IN EMISSIONS COMPONENTS OF MAXIMUM CONCENTRATION RELATIVE TO BASELINE RESULTS

RUN #	SO2	SO4	NOX	TNO3	NO	NO2	O3	PAN	HNO3	H2O2
S1A	-50	-51	-51	-11	-61	-42	-23	-4	-31	-7
S2A	-50	-58	-60	-25	-51	-68	-20	-8	-34	
S3A	-50	-50	-54	-57						
S4A	-50	-48	-51	-31						
W1A	-52	-50	-52	-10	-60	-31	79	95	-33	-15
W2A	-51	-51	-53	-13	-62	-39	45	47	-36	-28
W3A	-54	-52	-52	-54						
W4A	-50	-50	-50	-48						
S1B	-50	-51	-51	-41	-61	-42	-32	-36	-31	-7
S2B	-50	-58	-60	-50	-51	-68	-44	-28	-55	
S3B	-50	-50	-54	-57						
S4B	-50	-48	-51	-50						
W1B	-52	-50	-52	-20	-60	-31	69	79	-39	-22
W2B	-51	-51	-53	-26	-62	-39	37	32	-43	-36
W3B	-54	-52	-52	-54						
W4B	-50	-50	-50	-53						

TABLE 10-40

% CHANGE IN EMISSIONS COMPONENTS OF FINAL CONCENTRATION RELATIVE TO BASELINE RESULTS

RUN #	SO2	SO4	NOX	TNO3	NO	NO2	O3	PAN	HNO3	H2O2
S1A	-47	-46		-20			-25	3	-36	0
S2A	-47	-48		-21			-23	-8	-38	
S3A	-47	-48	-15	-29						
S6A	-43	-44	-4	-21						
W1A	-49	-40	-79	-16	-85	-78	4	9	-35	-17
W2A	-50	-44	-83	-19	-88	-83	44	42	-44	-29
W3A	-48	-48	-29	-36						
W6A	-49	-49	-39	-43						
S1B	-48	-48		-45			-43	-37	-51	-38
S2B	-49	-52		-48			-46	-43	-55	
S3B	-50	-49	-50	-50						
S6B	-50	-50	-48	-49						
W1B	-50	-44	-85	-36	-90	-85	-16	-17	-50	-33
W2B	-50	-44	-89	-29	-92	-89	13	26	-52	-35
W3B	-50	-51	-39	-48						
W6B	-50	-50	-49	-50						

TABLE 10-41

% CHANGE IN EMISSIONS COMPONENTS OF CUMMULATIVE DEPOSITION RELATIVE TO BASELINE RESULTS

RUN #	S	N	SO2	SO4	NOX	TNO3	O3	PAN	HNO3
S1A	-48	-32	-48	-45	-37	-28	-12	27	-33
S2A	-48	-34	-48	-47	-36	-33	-16	3	-37
S3A	-48	-34	-48	-49	-24	-39			
S6A	-48	-28	-48	-46	-25	-30			
W1A	-49	-32	-49	-45	-36	-20	150	80	-25
W2A	-49	-44	-49	-46	-45	-29	-200	-200	-34
W3A	-49	-30	-49	-50	-33	-43			
W6A	-49	-40	-49	-50	-36	-46			
S1B	-49	-49	-50	-47	-51	-45	-20	-22	-47
S2B	-50	-48	-50	-51	-52	-46	-40	-38	-47
S3B	-48	-50	-50	-50	-50	-49			
S6B	-49	-45	-50	-47	-50	-45			
W1B	-50	-47	-50	-45	-49	-40	100	0	-41
W2B	-50	-48	-50	-46	-50	-36	-200	-175	-40
W3B	-50	-40	-50	-50	-50	-50			
W6B	-50	-47	-50	-50	-44	-50			

respectively. Sums of the scores for different pollutants in the various models are calculated to provide an overall performance rating for each simple model's responses to emission reductions. These scores are shown in Tables 10-42 and 10-43. This evaluation scheme is simple, yet suffices to illustrate the differences in the models' responses.

#### 10.2.5.1 The Complex Model's Response to Emission Reductions

The complex models response to emission Scenarios A and B for  $\text{SO}_x$  outputs was, in general, fairly close to that predicted by linear rollback (i.e., 48% and 50% reduction on A and B). The absolute and emissions components of maximum  $\text{SO}_2$  concentrations were reduced 50 to 52%. The absolute and emissions component of maximum  $\text{SO}_4$  concentrations were reduced 50-51% and 47-49%, respectively. Although the predicted absolute reduction in final average  $\text{SO}_2$  was greater in winter (42%) than summer (33%), the emissions components of  $\text{SO}_2$  final average concentrations were reduced 47 to 50% in all cases. Similarly, predicted reductions in cumulative sulfur deposition were greater in winter (42%) than summer (36%), however, the emissions components of cumulative sulfur deposition were reduced 48 to 50% in all cases.

It is interesting to note that the average  $\text{SO}_2$ -to- $\text{SO}_4$  transformation rates varied only slightly with the  $\text{RHC}/\text{NO}_x/\text{SO}_x$  emission reductions. The average chemical transformation rates in the summer were 2.02, 1.97, and 1.93% per hour for the baseline, Scenario A and B runs, respectively. In the winter, the complex model's average conversion rate increased from .59% per hour in the baseline run to .68 and .67% per hour in Scenarios A and B. Perhaps larger differences in chemical transformation rates would occur for a situation in which the  $\text{RHC}$  and  $\text{NO}_x$  solutions were less dominated by initial concentrations. Nevertheless, the small variations in chemical transformation rate with emissions reduction in these cases results in  $\text{SO}_2$  and  $\text{SO}_4$  solutions which respond very linearly to emission reductions.

TABLE 10-42

MODEL EVALUATION SCORES FOR PERCENT REDUCTIONS IN ABSOLUTE PREDICTIONS

	<u>Deposition</u> <u>S</u>	<u>Final Avg</u>		<u>Maximum</u>		<u>Dep</u> <u>N</u>	<u>Final Avg</u>		<u>Maximum</u>		<u>Total</u> <u>S's</u>	<u>Total</u> <u>N's</u>	<u>Total</u>
		<u>SO<sub>2</sub></u>	<u>SO<sub>4</sub></u>	<u>SO<sub>2</sub></u>	<u>SO<sub>4</sub></u>		<u>NO<sub>x</sub></u>	<u>TNO<sub>3</sub></u>	<u>NO<sub>x</sub></u>	<u>TNO<sub>3</sub></u>			
S2A	2	0	0	2	0	2	2	2	0	2	4	8	12
S3A	2	2	2	2	2	2	1	2	2	0	10	7	17
S6A	2	0	0	2	2	2	1	2	2	1	6	8	14
W2A	2	2	2	2	2	1	2	2	2	2	10	9	19
W3A	2	2	2	2	2	2	0	1	2	0	10	5	15
W6A	2	2	2	2	2	2	0	0	2	0	19	4	14
S2B	2	0	0	2	0	2	2	2	0	2	4	8	12
S3B	2	2	2	2	2	2	1	1	2	0	10	6	16
S6B	2	0	0	2	2	2	1	2	2	1	6	7	13
W2B	2	2	2	2	2	1	2	2	2	2	10	9	19
W3B	2	2	2	2	2	0	0	1	2	0	10	3	13
W6B	2	2	2	2	2	0	0	1	2	0	10	3	13
Model 2	8	4	4	8	4	6	8	8	4	8	28	34	62
Model 3	8	8	8	8	8	6	2	5	8	0	40	21	61
Model 6	8	4	4	8	8	6	2	5	8	2	32	22	54
Totals	24	16	16	24	20	18	12	18	20	10	100	77	177

TABLE 10-43

MODEL EVALUATION SCORES FOR PERCENT REDUCTIONS IN EMISSION COMPONENTS

	Deposition	Final Avg		Maximum		Dep	Final Avg		Maximum		Total	Total	Total
	S	SO <sub>2</sub>	SO <sub>4</sub>	SO <sub>2</sub>	SO <sub>4</sub>	N	NO <sub>x</sub>	TNO <sub>3</sub>	NO <sub>x</sub>	TNO <sub>3</sub>	S's	N's	
S2A	2	2	2	2	1	2	1	2	1	0	9	6	15
S3A	2	2	2	2	2	0	0	1	2	0	10	3	13
S6A	2	2	2	2	2	2	0	2	1	0	10	5	15
W2A	2	2	2	2	2	1	2	2	2	2	10	9	19
W3A	2	2	1	2	2	2	0	0	2	0	9	4	13
W6A	2	2	1	2	2	1	0	0	2	0	9	3	12
S2B	2	2	2	2	1	2	1	2	1	0	9	6	15
S3B	2	2	2	2	2	2	0	1	2	0	10	5	15
S6B	2	2	2	2	2	2	0	1	1	0	10	4	14
W2B	2	2	2	2	2	2	2	1	2	1	10	8	18
W3B	2	2	1	2	2	2	0	0	2	0	9	4	13
W6B	2	2	1	2	2	2	0	0	2	0	10	4	14
Model 2	8	8	8	8	6	7	6	7	6	3	38	29	67
Model 3	8	8	6	8	8	6	0	2	8	0	38	16	54
Model 6	8	8	6	8	8	7	0	3	6	0	39	16	55
Total	24	24	20	24	22	20	6	12	20	3	115	61	176



The results for pollutants more directly dependent on  $\text{NO}_x$  concentration show less consistent response to the emission reduction than  $\text{SO}_x$ . Linear rollback predicts a reduction of 28 and 50% for  $\text{NO}_x$  related pollutants in Scenarios A and B. Since maximum NO and  $\text{NO}_2$  concentrations occur upwind of the urban area, a 50% reduction would be expected in both scenarios.

The complex model predicts 47 to 49% and 51 to 52% reduction in the absolute and emission components of maximum  $\text{NO}_x$  concentrations, respectively. Final average NO and  $\text{NO}_2$  concentrations are very small in summer, so there is essentially no difference in these values for the scenario runs. In winter, the final average  $\text{NO}_x$  concentration is reduced 79 to 86% in Scenarios A and B, respectively. Accordingly, the total nitrate maximum and final average concentrations show smaller reductions. The maximum and final average  $\text{TNO}_3$  concentrations are reduced only 3 to 4% and 9% in Scenarios A and B. The emission components of the maximum and final average  $\text{TNO}_3$  concentrations show reductions of 10 to 20% and 20 to 45% for Scenarios A and B, respectively. These results suggest that the overall rate of  $\text{NO}_x$  conversion to nitrates increases as the emissions decrease, which is confirmed by the average conversion rates computed by the model. The average conversion rates are 24, 44, 48, 7870, 9160, and 9300 per hour for runs W1, W1A, W1B, S1, S1A and S1B, respectively.

The model's response to emission reductions is different for the two nitrates. Maximum and final average PAN concentrations show small reductions (1 to 4%) for the summer runs and small (2%) reductions to moderate (10 to 13%) increases for the winter runs. This response is consistent with results of other photochemical modeling studies addressing  $\text{NO}_x$  controls (Chock et al 1982; Lurmann et al. 1981). The mechanistic explanation for this response is that  $\text{HC/NO}_x$  systems generate proportionately more PAN-type compounds than  $\text{HNO}_3$  as the  $\text{RHC/NO}_x$  ratio increases. Nitric acid reductions follow the  $\text{NO}_x$  reductions more closely. Maximum  $\text{HNO}_3$  concentrations are reduced 22 to 25% and 22 to 30% in Scenarios A and B, respectively. Final average  $\text{HNO}_3$  concentrations are reduced 12 to 17% and 17 to 27% in Scenarios A and B. The emissions components of final  $\text{HNO}_3$  concentrations are reduced 35 to 50% in Scenarios A and B. Hence,

reductions in  $\text{NO}_x$  emissions results in roughly comparable reduction in  $\text{HNO}_3$  concentrations and smaller reductions in PAN concentrations.

The predicted reductions in nitrogen deposition are 10 to 13% and 14 to 19% for Scenarios A and B, respectively. The emissions components of nitrogen deposition show reductions of 33-34% and 47-48% for Scenarios A and B, respectively, which are fairly close to the emission reductions. These reductions are primarily a result of  $\text{NO}_2$  and  $\text{HNO}_3$ , rather than PAN, deposition reductions. PAN deposition shows small increases on Scenario A and small decreases on Scenario B, whereas  $\text{HNO}_3$  and, especially,  $\text{NO}_2$  show substantial reductions for both scenarios. PAN deposition accounts for only 16 to 21% of the total nitrogen deposition in these 10- to 11-hour simulations. However, at the end of the run 75 to 80% of the nitrogen in the air mass exists as PAN and it represents a substantial fraction of the initial-plus-injected nitrogen in the air mass. Hence, this fairly linear response of the complex model for nitrogen deposition may not hold true for simulations of longer time periods.

Variations in the ozone concentrations were relatively small for all complex model runs. Maximum ozone was decreased about 5 ppb (7%) in the summer scenario runs and increased 5 ppb (12%) in the winter runs. Final average ozone concentrations in the scenario runs were within 2 ppb of the baseline results. The difference in the model's response on the summer and winter cases can be explained by the difference in photochemical activity. The summer runs reach an ozone maximum in midday while the winter runs show increasing ozone concentrations until sunset. Lower absolute levels of  $\text{NO}_x$  in Scenario A, and RHC and  $\text{NO}_x$  in Scenario B result in lower ozone in the summer simulations, because the photochemical system has sufficient sunlight to fully utilize the available  $\text{NO}_x$  for ozone formation. Lower  $\text{NO}_x$  levels in the winter scenario runs results in less ozone scavenging and, therefore, slightly higher ozone concentrations along the plume centerline. However, if the winter cases were extended for two days, the second day ozone maximum would most likely be lower for Scenarios A and B than in the baseline case.

The changes in the predicted hydrogen peroxide concentrations were quite small for the emission scenario runs. Differences in the

maximum and final average  $\text{H}_2\text{O}_2$  concentrations were less than 0.1 ppb (1%) for the summer scenario runs. The winter runs predicted small (<0.5 ppb) increases in  $\text{H}_2\text{O}_2$  maximum and final average concentrations. Only the summer run, which had reduced RHC and  $\text{NO}_x$  emissions (Scenario B), showed a decrease in  $\text{H}_2\text{O}_2$  concentrations. These results suggest  $\text{H}_2\text{O}_2$  concentrations respond to RHC and  $\text{NO}_x$  emission reductions in a manner similar to that of ozone concentrations.

In summary, the complex model's response to  $\text{SO}_x$ ,  $\text{NO}_x$  and RHC emission reductions is approximately linear for  $\text{SO}_2$ ,  $\text{SO}_4$ ,  $\text{NO}_x$  and  $\text{HNO}_3$ , but fairly nonlinear for PAN,  $\text{O}_3$  and  $\text{H}_2\text{O}_2$ .

#### 10.2.5.2 Model 2's Responses to Emissions Reductions

Model 2's response to emission reductions for sulfur compounds is roughly the same as Model 1's response. Predicted percent reductions in maximum and final average  $\text{SO}_2$  concentration are close to Model 1's response. Model 2's percent reductions in absolute maximum and final average  $\text{SO}_4$  concentration are lower, especially in summer, while the percent reduction in emission components of maximum and final average  $\text{SO}_4$  concentration are higher. Although the percent reductions in absolute sulfur deposition differ from Model 1's results, the percent reductions in the emissions component of sulfur deposition for Model 2 are in close agreement. As shown in Tables 10-42 and 10-43, Model 2 scored 23 out of 40 on the accuracy of its percent reductions in absolute sulfur data and 38 out of 40 on the accuracy of its percent reduction in emissions components of sulfur parameters. The former score is the poorest of the simple models scores on sulfur compounds and is probably a result of the substantial differences in absolute predictions of Model 1 and 2 on the baseline cases. However, the latter score shows Model 2's predicted changes in the emission components of sulfur outputs are very similar to Model 1's.

Model 2's response for  $\text{NO}_x$  and  $\text{TNO}_3$  was somewhat mixed. The relative reductions in maximum  $\text{NO}_x$  concentrations are quite similar to Model 1's in winter, while significantly different in summer. Predictions for final average  $\text{NO}_x$  concentration reductions are quite

similar, since there is very little  $\text{NO}_x$  remaining in the system. Percent reduction in maximum and final average  $\text{TNO}_3$  are quite close to Model 1's. Some differences are shown in the response of the emissions components of  $\text{TNO}_3$ , however, since the absolute changes are small, these differences are not meaningful. The results for nitrogen deposition are quite close in the summer case, while showing substantial differences in response for the winter case. Overall, Model 2 scored 34 out of 40 for its accuracy in predicting percent reductions in absolute nitrogen quantities and 29 out of 40 for its predictions of reduction in emissions components. These scores are the best of the simple models for  $\text{NO}_x$  and  $\text{TNO}_3$ .

The response of Model 2's prediction for PAN,  $\text{O}_3$  and  $\text{H}_2\text{O}_2$  with reduced emissions are generally similar to Model 1's. The responses to the emission reductions are always in the same direction as Model 1's, however, smaller changes in PAN,  $\text{O}_3$  and  $\text{H}_2\text{O}_2$  concentrations are predicted. Larger differences between the models are shown for  $\text{HNO}_3$ . These differences may reflect the fact that the baseline solutions for  $\text{HNO}_3$  were significantly different due to the cross-plume averaging in Model 2.

#### 10.2.5.3 Model 3's Response to Emission Reduction

Model 3's predicted reduction in  $\text{SO}_2$  maximum and final concentrations for Scenarios A and B are almost all within 1% of those predicted by the complex model. Similarly, since sulfur deposition is dominated by  $\text{SO}_2$  deposition in these simulations, the Model 3 predictions for reductions in total sulfur deposition agree very well with those predicted by Model 1. The model's response for  $\text{SO}_4$  concentration reductions are slightly less precise than for  $\text{SO}_2$ , but are still good. The only predicted reductions for  $\text{SO}_4$  which differed by more than 3% from the complex model's response occurred for the emissions component of final average  $\text{SO}_4$  concentrations in the winter cases. The linear chemistry in Model 3 responded with 48 and 51% reductions, whereas 40% was predicted by the complex model for both scenarios. This shows a slight tendency for Model 3 to

overestimate the benefits of a  $\text{SO}_x$  emission control measure for  $\text{SO}_4$  reductions relative to the complex model.

Model 3 predictions for  $\text{NO}_x$  and  $\text{TNO}_3$  reductions compare somewhat less favorably than the  $\text{SO}_2$  and  $\text{SO}_4$  results. Reductions in maximum  $\text{NO}_x$  concentrations are very similar, but reductions in final  $\text{NO}_x$  concentrations differ significantly. For example, on the winter trajectory, the emissions components of final average  $\text{NO}_x$  concentrations are reduced 29 to 39% in Model 3 and 79 to 85% in Model 1. Correspondingly, some large differences in predicted reductions are exhibited for  $\text{TNO}_3$ . Predicted reductions in maximum  $\text{TNO}_3$  concentrations are 46 to 47% in Model 3 versus 2 to 9% in Model 1. Predicted reductions in final  $\text{TNO}_3$  concentrations are 6 to 11% versus 2 to 5% in the summer cases and 13 to 18% versus 5 to 8% in the winter cases. The reductions of emissions components of final  $\text{TNO}_3$  concentrations also show significant differences. This is especially true in winter, where the Model 3 versus Model 1 results show 35 versus 16% reduction for Scenario A and 48 versus 36% for Scenario B. Model 3's summer case reductions in emissions components of final  $\text{TNO}_3$  concentration are 29% versus 20% for Scenario A and 50% versus 45% for Scenario B. These results consistently show larger predicted reductions in  $\text{TNO}_3$  concentrations with the linear  $\text{NO}_x$  chemistry in Model 3 than found in the complex model. The differences in nitrogen deposition reductions are smaller. On an absolute basis, nitrogen deposition is reduced 15% in Model 3 versus 10% in Model 1 in the summer cases and 15 to 21% in Model 3 versus 14 to 21% in Model 1 in the winter cases. The reductions in emissions components of nitrogen deposition are very close in all but the winter case for Scenario B, where Model 3 predicts a 40% reduction relative to a 47% reduction in Model 1.

In summary, Model 3's linear chemical mechanisms for  $\text{SO}_x$  reproduced the nonlinear model's response to  $\text{SO}_x$  emissions reduction very well. The linear chemical mechanism for  $\text{NO}_x$  and total nitrates resulted in dissimilar predictions for concentration reductions while providing reasonably close predicted reductions for nitrogen deposition. The most important difference between the linear and nonlinear mechanism's response to  $\text{NO}_x/\text{RHC}$  reductions is that the

linear model appears to overestimate nitrate concentration reductions. These characteristics are reflected in the model's evaluation scores. For sulfur predictions, Model 3 scored 40 out of 40 on an absolute basis and 38 out of 40 on the emission component basis. For nitrogen predictions, Model 3 scored 16 out of 40 on an absolute basis and 21 out of 40 on the emissions component basis.

#### 10.2.5.4 Model 6's Response to Emission Reductions

Model 6's responses for  $\text{SO}_x$  emission reductions were quite similar to both Model 1's and Model 3's responses. In general, good agreement were found between the percent reduction for sulfur outputs, however, the percent reduction in the emissions component of final  $\text{SO}_4$  concentration reduction were overestimated in winter (like Model 3), presumably due to the linear chemistry.

Model 6's predicted reduction for  $\text{NO}_x$  and  $\text{TNO}_3$  are similar to Model 3's and significantly different from the complex model. Predicted reductions for final average  $\text{NO}_x$  concentrations, and both maximum and final average  $\text{TNO}_3$  concentrations differ substantially from the complex model results. The overprediction of total nitrate concentration reductions observed for Model 3 also occurs in Model 6. However, this occurrence is less of a problem in the summer case. Predicted reductions in nitrogen deposition show reasonably close agreement with the complex model's results.

Model 6 scored 39 out of 40 on an absolute basis and 32 out of 40 on the emissions component basis for sulfur compounds. The latter score is poorer than that for Model 3, yet still shows the compound simple model responds accurately to  $\text{SO}_x$  emission reduction. For nitrogen compounds, Model 6 scored 22 and 16 out of 40 on the absolute and emission component basis, respectively. These are essentially the same as Model 3's scores and indicate mediocre comparison of the  $\text{NO}_x$  and  $\text{TNO}_3$  reductions with those in the complex model.

#### 10.2.5.5 Summary of Mesoscale Model Sensitivity to Emission Reduction

The relative response (or percent reductions) of three simple models have been compared to the relative response of the complex model for two meteorological and two emission scenarios. The degree of similarity in responses have been assigned scores to facilitate an overall comparison of the models' responses. Table 10-44 lists the overall scores which are the sums of the scores for the absolute percent reduction predictions and the emission component percent reduction predictions.

The results for percent reductions in sulfur compounds predictions indicate all three simple models respond to emission reductions in a manner similar to that of the complex model. Models 2 and 6 performed somewhat poorer than Model 3, which suggests that differences in dispersion formulation, rather than chemical formulation, are more important for accurate predictions of  $\text{SO}_x$  concentration and deposition reductions. However, it is important to note that the differences in overall scores are too small to place much confidence in this conclusion.

The results for percent reductions in nitrogen compound predictions indicate that Model 2 performance was superior that of Models 3 and 6. In addition, none of the simple models scored as well on nitrogen compounds as they did on sulfur compounds. The difference between the scores for Model 2, and Models 3 and 6 suggest that chemical formulation, rather than dispersion formulation, is more important for accurate nitrogen compound reduction predictions. The differences in the individual predictions and the overall scores are believed to be large enough to place significant confidence in this result. This result is not surprising considering the recognized dependency of  $\text{NO}_x$  chemistry on reactive hydrocarbons and the nonlinearity of the  $\text{RHC}/\text{NO}_x/\text{O}_3$  chemical system. In fact, the complex model calculations indicated that the average  $\text{NO}_x$  conversion rates increased by as much as a factor of 2 when the  $\text{NO}_x$  emissions were reduced by 50%. The linear chemical model for  $\text{NO}_x$  ignores this

TABLE 10-44

## OVERALL MODEL EVALUATION SCORES

	<u>Sulfur</u>	<u>Nitrogen</u>
Perfect Score	80	80
Model 2	66	63
Model 3	78	37
Model 6	71	38



dependency and, therefore, can be expected to respond less accurately to  $\text{NO}_x$  or  $\text{NO}_x$  and RHC emission reductions.

The different results for  $\text{SO}_x$  and  $\text{NO}_x$  can be explained not only by the greater nonlinearity of the  $\text{NO}_x$  chemistry, but also the differences in the chemical transformation scales of the two pollutants.  $\text{NO}_x$  chemical transformations generally occur much faster than  $\text{SO}_x$  chemical transformations. The ratio of chemical transformation to meteorological process time scales is therefore much greater for  $\text{NO}_x$  than  $\text{SO}_x$ . Therefore, it is reasonable to find that meteorological formulation differences are more important for the pollutants with slow chemistry ( $\text{SO}_x$ ) and chemical formulation differences are more important for pollutants with fast chemistry ( $\text{NO}_x$ ).

#### 10.2.6 Mesoscale Model Sensitivity to Sulfate Deposition Velocity

As discussed in Section 10.2, the mesoscale model runs were performed using a sulfate deposition velocity equal to the  $\text{SO}_2$  deposition velocity. This choice of sulfate deposition velocity represents somewhat of an upper limit. In contrast, the baseline SURADS simulations were carried out with sulfate deposition velocities equal to 1/10 the  $\text{SO}_2$  deposition velocities, which is perhaps the lower limit for many situations. A SURADS sensitivity calculation was made using the upper limit  $\text{SO}_4$  deposition velocity and the model's sulfate predictions were found to be quite sensitive to this parameter. The results for a similar sensitivity test using the lower limit  $\text{SO}_4$  deposition velocity in the mesoscale model are discussed below.

For consistency with the SURADS sensitivity tests, these results are presented in terms of the change in the  $\text{SO}_4$  results with the upper limit deposition velocity relative to the lower limit  $\text{SO}_4$  deposition velocity case. Table 10-45 shows the percent changes in the PLMSTAR output parameters. Maximum  $\text{SO}_4$  surface concentrations are 12 to 14% lower with the higher deposition velocity. Final average  $\text{SO}_4$  concentration are 29 and 37% lower in summer and winter, respectively.

TABLE 10-45

PLMSTAR SENSITIVITY TO UPPER LIMIT  $\text{SO}_4$  DEPOSITION VELOCITY

<u>Parameter</u>	<u>Percent Change</u>	
	<u>Summer</u>	<u>Winter</u>
Maximum $\text{SO}_4$ Surface Concentration	-12	-14
Final Average $\text{SO}_4$ Concentration	-29	-37
Cumulative $\text{SO}_4$ Deposition	694	676
Cumulative S Deposition	16	9

Cumulative  $\text{SO}_4$  and total sulfur deposition are predicted to increase 676 to 694% and 9 to 16%, respectively. In addition, the  $\text{SO}_4$  fractions of sulfur deposition are predicted to increase from 1.5 to 9% in the winter case and 2.7 to 16% in the summer case with the upper limit deposition velocity. Hence, these results suggest that there is substantial uncertainty in the predicted fate of  $\text{SO}_4$  in the first 10 to 12 hours of travel due to the uncertainty in the  $\text{SO}_4$  deposition velocity. The differences in final average  $\text{SO}_4$  concentration, which agree quite well with the differences in SURADS 24-hour concentration, suggest potentially large uncertainty exist in modeling atmospheric sulfate lifetimes and the zone of influence of  $\text{SO}_x$  sources due to the uncertainty in  $\text{SO}_4$  deposition velocities. It is important to point out that the model calculations also show substantial sensitivity to  $\text{SO}_2$  deposition velocity variations. Hence, both  $\text{SO}_4$  and  $\text{SO}_2$  deposition velocity need to be specified accurately to achieve accurate modeling results.

#### 10.2.7 Summary of Mesoscale Model Sensitivity Study

The objective of the mesoscale model sensitivity studies was to essentially examine the relative importance of meteorological and chemical model formulations in a model which includes  $\text{SO}_x$ ,  $\text{NO}_x$ , and RHC species. The sensitivity tests were performed for 10-hour daylight periods for winter and summer hypothetical cases using ERT's reactive plume model, PLMSTAR. Because the modeling periods were short and the model ignored aqueous phase chemistry, care must be exercised in extrapolating the results to long range transport time scales and acid precipitation issues. While the quantitative differences in model sensitivity are expected to differ in longer simulations with aqueous phase chemistry, the qualitative differences identified are expected to be similar.

Several interesting chemical characteristics of the baseline simulations worth noting are:

- Gas phase chemical conversion of  $\text{SO}_x$  was generally slow and approximately three times faster in summer than winter.

- Gas phase conversion of  $\text{NO}_x$  was much faster ( $>10$  times) than  $\text{SO}_x$  in both summer and winter.  $\text{NO}_x$  was 100% and 80% converted to nitrates within 10 hours in summer and winter, respectively.
- Gas phase PAN formation lagged several hours behind nitric acid formation; however, PAN was the major  $\text{NO}_x$  product at the end of the 10 to 11 hour simulations.

Testing of simplifying assumptions in the models was conducted using average model inputs calculated from the complex PLMSTAR model. The performance of these simple models is summarized below.

- The single expanding column lateral diffusion formulation predicted substantially different model outputs for  $\text{SO}_x$  and  $\text{NO}_x$  than the K-theory lateral diffusion formulation employed in PLMSTAR. Differences in the simulation of chemical and plume dispersion dynamics in the first 10 to 50 km downwind of the stack appear to affect the overall solutions farther downwind.
- Modeling with constant linear chemical transformation rates was found to work relatively well for  $\text{SO}_x$ , but poorly for  $\text{NO}_x$ . The success of linear chemistry for  $\text{SO}_x$  is believed to occur because the conversion is generally slow and the range of transformation rate is small. The failure of  $\text{NO}_x$  linear chemistry occurs because the range of conversion rate is large and the role of reactive hydrocarbons are ignored. The linear mechanism for  $\text{NO}_x$  overpredicts nitrate formation along the plume centerline and underpredicts the final average nitrate concentration predicted by the complex model. It performs poorly in predicting the PAN component of total nitrates, which is not surprising since the latter is dependent on RHC as well as  $\text{NO}_x$ .
- Modeling with constant instead of time and space varying dry deposition velocity results in small differences in  $\text{SO}_x$  and  $\text{NO}_x$  model outputs. Deposition of sulfur and nitrogen

were 5 to 7% and 3 to 4% lower with constant deposition velocities.

- Modeling with constant vertical diffusivity ( $K_z$ ) coefficients instead of time and space varying  $K_z$  coefficients causes accelerated vertical dispersion and relative underestimation of dry deposition in daytime simulations. The final  $SO_2$  and  $SO_4$  mass in the air parcel was 20 to 23% and 9 to 16% higher, respectively, using constant  $K_z$ 's; final total nitrate was different by less than 3%. Greater differences are expected when nighttime periods are simulated. The failure of the constant  $K_z$  model to simulate the diurnal mixing height variations is believed to be its greatest weakness.
- Modeling results using all of the simplifying assumptions mentioned above compared poorly with the PLMSTAR model results. Although the effects of the individual simplifying assumptions offset one another to a certain extent, the overall results were substantially different from the PLMSTAR results. The final average  $SO_4$  concentration was 13% lower in the summer but 8% higher in the winter. The cumulative sulfur deposition was 27% lower in the summer and 38% higher in the winter. The calculated final total nitrate was lower by 31 to 34%.

Simulations of a 50%  $SO_x$ ,  $NO_x$ , and RHC emission reductions were carried out with and without the simplifying assumptions in the PLMSTAR model. The results of these simulations were compared with the baseline results for each model on a percentage basis. This evaluation protocol basically ignored differences in the baseline simulations (discussed above) and addressed only whether the percent reductions in model outputs were similar in the various models.

The major conclusions from the emission scenario simulation are listed below (see also Section 10.2.5.5).

- The response of the complex PLMSTAR model to emission reduction was within 3% of linear rollback for  $SO_2$  and  $SO_4$ ;

within 2% for the maximum  $\text{NO}_x$  concentrations; and within 15% for final  $\text{HNO}_3$  concentrations. PAN concentrations, however, were reduced by no more than 4% in the summer. In the winter the response of PAN to emission reduction varied from a 2% reduction to a 13% increase in concentrations. For this particular problem,  $\text{NO}_x$  chemical transformation rates increased substantially when  $\text{NO}_x$  emissions were lowered. This results in smaller percent reduction in  $\text{HNO}_3$  and especially PAN concentrations than predicted by linear rollback. Percent reductions in nitrogen deposition tracked emission reductions more closely than  $\text{HNO}_3$  and PAN concentration.

- The expanding column, linear chemistry, and compound simple models' responses to emission reduction for  $\text{SO}_x$  were very similar to the complex PLMSTAR model's response. Differences in the models' meteorological formulations rather than chemical formulations, were found to be somewhat more important in determining their response to  $\text{SO}_x$  emission reductions.
- Overall, the response of the simple models to the emission reductions was less similar to the complex model's response for  $\text{NO}_x$  compounds than for  $\text{SO}_x$ . Comparison of the simple and complex models emission reduction response for  $\text{NO}_x$  species indicated chemical formulation rather than meteorological formulation is more important in determining the model's response. Differences between the linear and nonlinear chemical mechanism for  $\text{NO}_x$  override meteorological differences in the models tested. Overestimation of the percentage reduction in nitrates for  $\text{NO}_x$  emission reductions is the major deficiency of the linear  $\text{NO}_x$  mechanism.

In addition, effects of uncertainties in  $\text{SO}_4$  deposition velocities were investigated. Although the PLMSTAR simulation were too short to quantify the effect well, the trends suggest that the uncertainty in  $\text{SO}_4$  deposition velocities cause substantial uncertainty

in modeling the lifetime of  $\text{SO}_4$  in the atmosphere and zone of influence of  $\text{SO}_x$  emission sources.

### 10.3 Comparison of Findings From the LRT and Mesoscale Sensitivity Studies

In the sensitivity studies performed with the LRT and mesoscale models (described in Sections 10.1 and 10.2, respectively) numerous runs were designed to answer the same questions with both models. This was done to see if both models respond in the same general manner. In this section, comparisons are made between the findings of the mesoscale and LRT model sensitivities. It should be kept in mind that the LRT model results cover a full diurnal cycle, whereas the mesoscale model simulations are for daylight periods only.

Versions of both models were run with constant  $\text{SO}_2$ -to-sulfate conversion rate and compared to the complex models with varying conversion rates. Both models responded similarly in that significant differences were seen in peak sulfate, yet final sulfate concentrations and cumulative sulfur deposition were approximately the same.

Constant vertical diffusivity versions of both models were used to make simulations that were compared to those made with varying  $K_z$ 's. The differences found with the mesoscale model were much larger than those found with the LRT model. For example, cumulative sulfur deposition was 18 to 20% lower than the baseline in the mesoscale model using constant  $K_z$ 's, whereas there was no appreciable difference seen overall with the LRT model. There were, however, significant differences ( $\geq 20\%$ ) seen for individual hours and grid squares with the Eulerian model. That the LRT model is less sensitive to the use of average mixing coefficients is probably due to the fact that the elevated point source emissions do not have the dominating effect on surface concentrations in the LRT model that they do in the mesoscale model. This is because the point source emissions are initially diluted to a much greater extent horizontally when injected into the 80 km x 80 km LRT model grid squares than the 0.5 km x 7.5 km center column of the mesoscale model.

The responses of the two models to the use of constant, rather than varying, deposition velocities were similar. The net effect of constant deposition velocities on sulfur deposition in the mesoscale model was a reduction of 5 to 7%; in the LRT model, the effect was a 6½% reduction. The mesoscale model had 2 to 7% more SO<sub>2</sub> and SO<sub>4</sub> in the air parcel at the end of the simulation, whereas there was 2% more SO<sub>2</sub> and SO<sub>4</sub> in the Eulerian modeling domain at that simulation's end.

The final sensitivity runs employed compound simple versions of the LRT and mesoscale models. These versions used average conversion rate, vertical diffusivities, and deposition velocity. The compound simple version of the mesoscale model also incorporated the single expanding column approach into the formulation, making direct comparison with the LRT results difficult. For the mesoscale model, the results compared poorly with the complex model results, although the effects of the simplifying assumptions were offsetting at times. Though there were significant differences between the LRT model results with the compound simple and complex versions, the agreement was not considered to be poor since the general appearance of the calculated concentration and deposition maps are similar.

In terms of the models' responses to SO<sub>x</sub> emissions reductions, both the complex LRT and mesoscale models responded nearly linearly to the emissions reductions. Furthermore, the responses of the compound simple versions were very similar to the complex models' responses in both cases.

Both the LRT and mesoscale models were also run with an order of magnitude variation in sulfate deposition velocity. The lower limit sulfate depositions were one-tenth the SO<sub>2</sub> deposition velocities; the upper limit set them equal. For the mesoscale model, cumulative sulfate deposition increased about 685% in response to the 900% increase in deposition velocities. The LRT response was very similar, a 650% increase in sulfate deposition. The final average sulfate concentration was reduced by about 33% in the mesoscale model parcel and was reduced by 24% over the LRT model's domain. In short, the LRT and mesoscale models responded similarly to an order of magnitude variation in sulfate deposition velocities.



#### 10.4 Implications of Sensitivity Analyses Results

The results of the sensitivity analyses presented in Sections 10.1 and 10.2 have several important implications for the proposed model design. The results of photochemical analysis performed with the mesoscale model indicates that a reasonable nonlinear chemical mechanism is needed to accurately simulate the behavior of  $\text{NO}_x$  products such as  $\text{HNO}_3$  and PAN in summer or winter meteorological conditions. Even linear conversion rates based on calculated concentrations from the nonlinear chemical mechanism yields poor results.

The mesoscale modeling results also indicate that it is important to simulate the diurnal cycle of vertical mixing, especially for the prediction of surface  $\text{SO}_x$  concentrations due to major point source emissions. The use of constant rather than temporally and horizontally varying  $K_z$ 's in the LRT model had a lesser impact on surface  $\text{SO}_2$  and  $\text{SO}_4$  concentrations than it did in the mesoscale model, presumably because of the considerably lesser resolution of plumes afforded by the grid model. However, the LRT model results indicate that it is important to incorporate temporal and spatial variability in vertical mixing if concentrations in subregions of the grid are to be simulated properly.

The LRT model results also demonstrate the importance of using temporally and horizontally varying deposition velocities in the model. This is crucial to the accurate simulation of sulfur deposition in important subregions of the grid.

Finally, examination of LRT model results has indicated that the use of different advection algorithms (SHASTA and FCT8) can result in major differences in calculated concentration fields. Thus, the selection of an advection algorithm is a very important aspect of model design. The further implication is that unless the advection algorithm controls artificial lateral diffusion, the precise specification of explicit horizontal diffusion parameters is not important to the model design.

## SECTION 10 REFERENCES

- Atkinson, R., A.C. Lloyd, and L. Wings. 1982. An Updated Chemical Mechanism for Hydrocarbon/ $\text{NO}_x$ / $\text{SO}_x$ . Photooxidation Suitable for Inclusion in Atmospheric Simulation Models. Atmospheric Environment, 16, 1341-1355.
- Atkinson, R. and A.C. Lloyd 1982. Evaluation of Kinetic and Mechanistic Data for Modeling of Photochemical Smog. Submitted to Journal of Standard Systems and References.
- Boris, and D.L. Book 1973. Flux-Corrected Transport, I. SHASTA, a Fluid Transport Algorithm that Works. Journal of Computational Physics, 11, 38-69.
- Businger, J.A. 1971. Flux-Profile Relationships in the Atmospheric Surface Layer. Journal of Atmospheric Sciences, 28, 181-189.
- Clark, T.L. and R.E. Eskridge 1977. Non-Divergent Wind Analysis Algorithm for the St. Louis RAPS Network, EPA-600/4-77-049, U.S. EPA, Research Triangle Park, NC.
- Chock, D.P. and A.M. Dunber 1981. A Comparison of Numerical Methods for Solving the Advection Equation, Presented at the Fifth Symposium on Turbulence, Diffusion, and Air Pollution, Atlanta, GA. Sponsored by American Meteorological Society, Boston, MA.
- Crowley, W.P. 1968. Monthly Weather Review, 96, 1.
- Endlich, R.M. 1967. An Iterative Method for Altering the Kinematic Properties of Wind Fields. Journal of Applied Meteorology, 6, 837-847.
- Fulle, D.J. 1975. "A Lapse Rate-wind Shear Classification of Turbulent Diffusion", M.S. Thesis, University of Utah, Department of Meteorology.
- Golder, D. 1972. "Relations Among Stability Parameters in the Surface Layer", Boundary-Layer Meteorology, 3, 45-58.
- Hidy, G.M. and P.K. Mueller 1982. Sulfate Regional Experiment--Report on Findings, Electric Power Research Institute Report EA-1901 (in press), Palo Alto, CA.
- Joseph, D.W. and C.W. Spicer 1978. Chemiluminescence Method for Atmospheric Monitoring of Nitric Acid and Nitrogen Acid and Nitrogen Oxides, Analytical Chemistry, 50, 1400-1403.
- Klemm, H. and R. Brennan 1981. Emissions Inventory for the SURE Region, Electric Power Research Institute, Report No. EA-1913, Palo Alto, CA.

- Kreiss, H. and J. Oliger. Methods for the Approximation Solution of Time Dependent Problems, GARP Publication Series No. 10, World Meteorological Organization.
- Lavery, T.F., R.L. Baskett, J.W. Thrasher, N.J. Lordi, A.C. Lloyd and G.M. Hidy 1980. Development and validation of a regional model to simulate atmospheric concentrations of sulfur dioxide and sulfate. In: Second Joint Conference on Applications of Air Pollution Meteorology, New Orleans, LA. 236-247. Sponsored by American Meteorological Society, Boston, MA.
- Lavery, T.F., G.M. Hidy, R.L. Baskett, P.K. Mueller and K.K. Warren 1981. Regional Air Pollution in Eastern United States I. Descriptive Meteorology of Sulfate Events During 1977 and 1978. Submitted to Journal of Applied Meteorology.
- Lloyd, A.C., F.W. Lurmann, D.A. Godden, J.F. Hutchins, A.Q. Eschenroeder, and R.A. Nordsieck 1979. "Development of the ELSTAR Photochemical Air Quality Simulation Model and Its Evaluation Relative to the LARPP Data Base. ERT Document No. P-5287-500, prepared for the Coordinating Research Council by Environmental Research & Technology, Inc., Westlake Village, CA 91361.
- Long, P.E. and D.W. Pepper 1976. A Comparison of Six Numerical Schemes for Calculating the Advection of Atmospheric Pollutants, IN: Third Symposium on Atmospheric Turbulence, Diffusion and Air Quality, Raleigh, NC. American Meteorological Society, Boston, MA.
- Liu, C.Y. and W.R. Goodin 1976. An Iterative Algorithm for Objective Wind Field Analysis. Monthly Weather Review, 104, 784-792.
- Lurmann, F.W., D.A. Godden and A.C. Lloyd 1982. The Development and Selected Sensitivity Tests of the PLMSTAR Reactive Plume Model. Presented at the Third Joint Conference on Application of Air Pollution Meteorology, San Antonio, TX. Sponsored by American Meteorology Society, Boston, MA.
- McRae, G.J. 1981. Mathematical Modeling of Photochemical Air Pollution, Ph.D. Thesis, California Institute of Technology, Pasadena, CA.
- Mahlman, J.D. and R.W. Sinclair 1977. Advances in Environmental Science and Technology, 8, 12, Wiley, New York.
- Martin, L.R., D.E. Damschen and H.S. Judeikis 1981. The Reactions of Nitrogen Oxides with SO<sub>2</sub> in Aqueous Aerosols, Atmos. Environ., 15, 191-195.
- O'Brien, J.J. 1970. A Note on the Vertical Structure of the Eddy Exchange Coefficient in the Planetary Boundary Layer. Journal of Atmospheric Sciences, 27, 1213-1215.

- Penkett, S.A., B.M.R. Jones, K.A. Brice and A.E.J. Eggleton 1979.  
The Importance of Atmospheric Ozone and Hydrogen Peroxide in  
Oxidizing Sulfur Dioxide in Cloud and Rainwater, Atmos. Environ.  
13, 123-137.
- Pernall, D.K. 1976. Solution of the Advection Equation by Upstream  
Interpolation with a Dubic Spline, Mon. Wes. REv., 104, 42-48.
- Smith, M.E. 1968. Recommended Guide for the Prediction of Dispersion  
from Airborne Effluents, Amer. Soc. Mech. Engineers.
- Wesley, M.L. and B.B. Hicks 1977. Some Factors that Affect the  
Deposition Rates of Sulfur Dioxide and Similar Gases on  
Vegetation. Journal of Air Pollution Control Association, 27,  
1110-1116.
- Winer, Arthyr M., John W. Peters, Jerome P. Smith, and James N.  
Pitts, Jr. 1974. Response of Commercial Chemiluminescent NO-NO<sub>2</sub>  
Analyzers to Other Nitrogen-Containing Compounds.  
Environmental Science and Technology, 8, 1118-1121.
- Zalesak, S.T. 1979. Fully Multidimensional flux-corrected transport  
algorithms for fluids. J. Comp. Phys., 31, 35-362.

## 11. CONCEPTS OF MODEL EVALUATION

### 11.1 Overview

The physical system associated with long-range transport is extremely complex. Our understanding of this system is less than satisfactory and unlikely to improve for some time. Therefore, we cannot expect a long-range transport (LRT) model, constructed by combining a number of submodels, to automatically provide estimates of concentration (or deposition) that compare favorably with observations. In addition to ensuring that the model contains all the "physics," it is necessary to develop the model by comparing the predictions of the complete model (and all its submodels) with observations. A systematic protocol for testing and calibrating the model against data is key to developing a useable LRT model.

It is clear that the evaluation of an LRT model cannot follow a protocol applicable to simpler models. The complexity of the model, inevitable errors in model inputs, and the uncertain quality of the observational data base will force us to formulate model testing methods which are specific to the model. However, it is useful to describe a general model evaluation framework which can guide the development of more sophisticated methods.

Our approach to evaluating models can be categorized as empirical. Model errors are estimated by comparing model predictions with observations. No attempt has been made to make theoretical estimates of "unavoidable" model errors. Preliminary progress in this important subject has been made by Lamb (1982). At a later stage it might be possible to incorporate his results in a model testing program.

### 11.2 The Framework

The observed concentration  $C_o$  associated with a source can be formally written as

$$C_o = f(x_1, x_2) \quad (11-1)$$

where  $x_1$  refers to the known variables and  $x_2$  refers to the variables we know little about. For example,  $x_1$  could denote the set 1-hour averaged wind speed, mixed layer height, precipitation intensity, distance of source from receptor, and turbulent intensities. The set  $x_2$  refers to the turbulent unresolved velocity field and other factors which also affect the observed concentration. Our lack of knowledge of  $x_2$  and the precise form of the function  $f(x_1, x_2)$  prevents us from predicting the observed concentration. Because  $x_1$  represents only part of the information required to predict  $C_o$ , it is associated with an infinite set of possible observations rather than a single observation. In other words, the model inputs  $x_1$  define an ensemble of concentrations. Then the observation  $C_o$  belonging to this ensemble can be written as

$$C_o(x_1, x_2) = \langle C_o(x_1, x_2) \rangle^{x_1} + \epsilon(x_1, x_2) \quad (11-2)$$

where the superscripts indicate that the variables in Equation 11-2 refer to the ensemble defined by  $x_1$ . The carets denote an average over the ensemble. By definition  $\langle \epsilon \rangle^{x_1} = 0$ . Since  $\langle C_o \rangle^{x_1}$  is fixed for a given  $x_1$ , it is the component of  $C_o$  that we can hope to estimate with an air quality model. Then for an adequate model  $\langle C_o \rangle^{x_1} \equiv C_p(x_1)$  where  $C_p$  refers to the model prediction. The presence of the unknown stochastic term  $\epsilon$  in Equation 11-2 implies that the model prediction  $C_p$  is expected to deviate from  $C_o$ . We can rewrite Equation 11-2 as:

$$C_o(x_1, x_2) = C_p(x_1) + \epsilon(x_1, x_2) \quad (11-3)$$

The relationship between a model prediction  $C_p(x_1)$  and observations  $C_o(x_1, x_2)$  is illustrated in Figure 11-1. Each prediction  $C_p(x_1)$  is associated with a "cloud" of observations. The spread of the possible observed values about  $C_p$  is given by  $\sigma_\epsilon$ . A different set of model inputs  $x_1$  is associated with its own ensemble of observations. This general definition of an ensemble

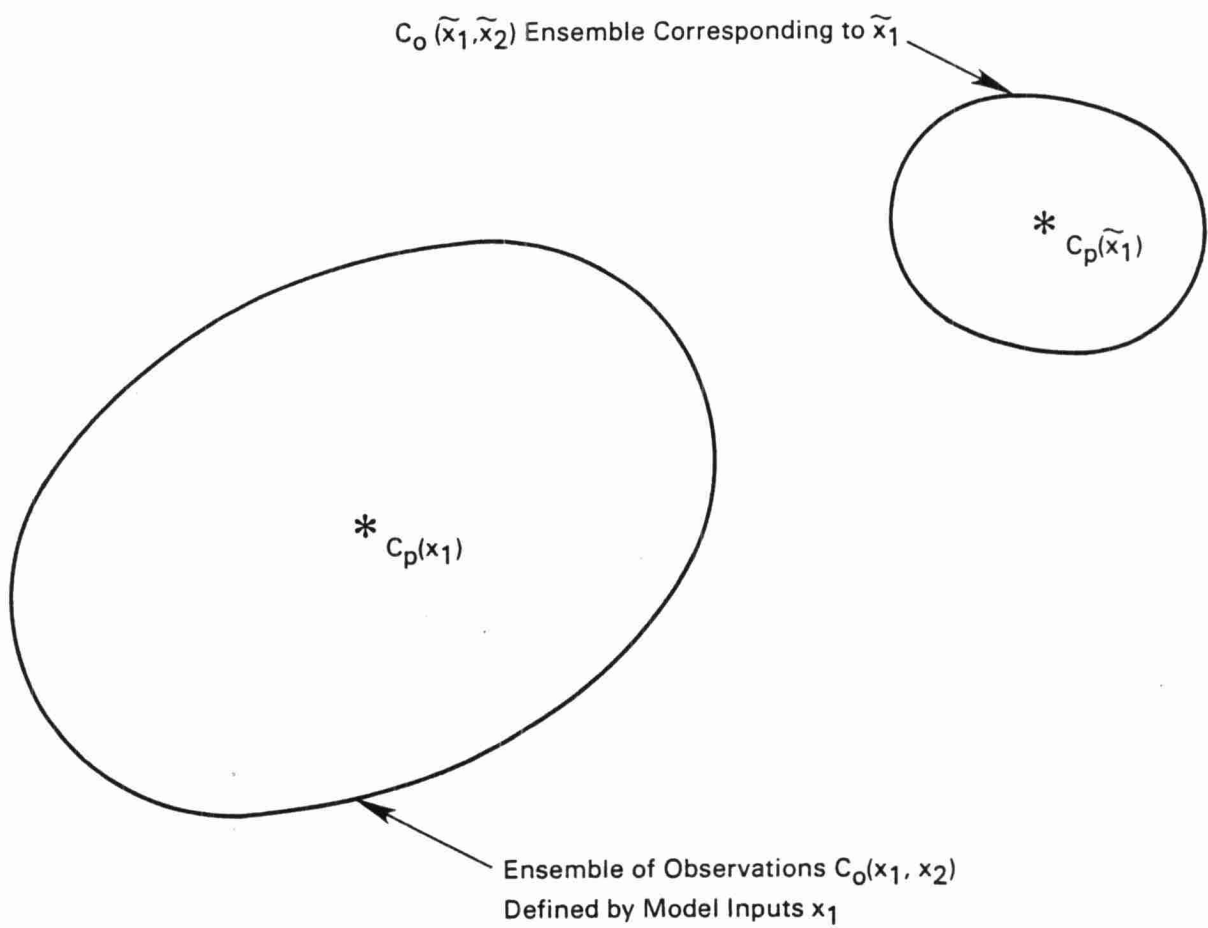


Figure 11-1 Relationship Between a Model Prediction and Observations

implies that  $\epsilon$  can be a function of  $x_1$ . This means that to calculate the statistics of  $\epsilon(x_1, x_2)$ , it is necessary to sample a set of observations keeping  $x_1$  fixed. Because this is impossible in practice, the ensemble must be defined in a special way: The model inputs  $x_1$  should be chosen such that the residual  $\epsilon$  is independent of  $x_1$ . This process allows us to calculate the statistics of  $\epsilon$  by averaging over ensembles corresponding to different  $x_1$ . Thus

$$C_o(x_1, x_2) = C_p(x_1) + \epsilon(x_2) \quad (11-4)$$

It might be necessary to transform  $C_o$  and  $C_p$  in order to make  $\epsilon$  independent of  $x_1$ . To see this let us rewrite Equation 11-3 as follows:

$$C_o(x_1, x_2) = C_p(x_1 + \mu(x_2)\sigma(x_1, x_1^R)) \quad (11-5a)$$

$$\text{where } \epsilon(x_1, x_2) \equiv \mu(x_2)\sigma(x_1, x_1^R) \quad (11-5b)$$

It is easily seen that  $\langle \mu^2 \rangle = 1$  because  $\langle \epsilon^2 \rangle = \sigma^2(x_1, x_1^R)$ . Note that the standard deviation of  $\epsilon$ ,  $\sigma$ , is a function of value  $x_1$  as well as the number of variables which go into making up  $x_1$ . We have denoted this size of the set  $x_1$  by  $x_1^R$ ;  $x_1^R$  does not change with the values of  $x_1$ . To make progress we assume that  $\sigma(x_1, x_1^R)$  can be decomposed as follows:

$$\sigma(x_1, x_1^R) = f(x_1)\tilde{\sigma}(x_1^R) \quad (11-6)$$

With Equation 11-6, Equation 11-5a can be written as

$$\hat{C}_o(x_1, x_2) = \hat{C}_p + \tilde{\epsilon}(x_2, x_1^R) \quad (11-7)$$

where  $\hat{C}_o = C_o/f(x_1)$  and  $\hat{C}_p = C_p/f(x_1)$ . Note that

$$\tilde{\epsilon}(x_2, x_1^R) = \mu(x_2)\sigma(x_1^R) \quad (11-8)$$



In Equation 11-8,  $\sigma(x_1^R)$  represents the "irreducible" error in the model prediction. Its magnitude can be reduced only by expanding  $x_1$  to include more of  $x_2$ .

Now Equation 11-7 is of the form given by Equation 11-4. It is convenient to think of an observation  $C_o(x_1, x_2)$  to consist of a deterministic component,  $C_p(x_1)$ , and a stochastic part,  $\epsilon(x_2)$ . Clearly,  $\epsilon(x_2)$  should be as small as possible. We can clarify this statement by noticing that for a set of predictions, the average "distance" between them is measured by the standard deviation  $\sigma$  of  $C_p$ . This suggests that  $\sigma_\epsilon$  should be small compared to  $\sigma_{C_p}$ . In other words, a "good" model should be able to separate model predictions corresponding to different inputs  $x_1$ .

It is desirable to make the error term  $\epsilon(x_2)$  term in Equation 11-4 as small as possible. In principle, this can be done by expanding the model input set  $x_1$  to include as much of the set  $x_2$  as possible. This increase in information available to make a model prediction should ideally be accompanied by a reduction of the variance  $\langle \epsilon^2 \rangle$  of the stochastic component of  $C_o$ . However, this process of model improvement is limited by our ability to incorporate the extra input information into a more complex model structure. Furthermore, inevitable errors in inputs can counteract the reduction of  $\langle \epsilon^2 \rangle$ . Experience with these problems has given rise to the principle of parsimony in modeling: the model structure should be as simple as possible without making  $\langle \epsilon^2 \rangle$  unacceptably large. Since  $\langle \epsilon^2 \rangle$  is designed to be independent of  $x_1$ , it has to be estimated primarily by empirical means. Much is usually made about the fact that model predictions represent averages over grid squares while measurements represent points; clearly, this is only one of the many reasons that a model prediction deviates from an observation. It is important to realize that with incomplete information  $x_1$ , it is not useful to have preconceived notions about what a model prediction represents before it is compared with an observation.

### 11.3 Model Evaluation Protocol

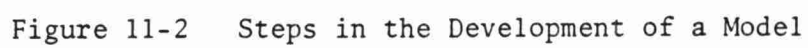
The ideal relationship between an observation  $C_o$  and a prediction  $C_p$  is then given by:

$$C_o(x_1, x_2) = C_p(x_1, p) + \epsilon(x_2) \quad (11-9)$$

In Equation 11-9,  $x_1$  refers to the input variables and  $p$  refers to the parameters of the model. The values of the parameters are obtained by calibrating the model against observations. Calibration refers to choosing the values of  $p$  such that  $\epsilon = 0$  and  $\sigma_\epsilon$  is a minimum for the given set of  $x_1$ . In models in which  $C_p$  depends linearly on  $p$ ,  $p$  is determined by making the vector of residuals perpendicular to the plane containing the vectors  $C_p$  and  $x_1$ . Several methods of achieving this are described in the literature (Box, Hunter, and Hunter 1978). The value of  $p$  will depend on the data used to calibrate the model; therefore, in a sense,  $p$  is a variable derived from data. We can use the "variable"  $p$  as a parameter only if its contribution to the variance of the prediction  $C_p(x_1, p)$  is much less than that of  $x_1$ ; then  $p$  can be treated as a constant in calculating  $C_p$  for different  $x_1$ .

With the background provided by the previous sections, we can describe the steps in developing a model (see Figure 11-2). The first step is postulating a plausible structure for the model. The acceptability of the structure cannot be determined without evaluating it against observations. Furthermore, the structure of the model is not unique; for a complex system like that of long-range transport, several different model structures might provide comparable results.

The postulated model will always have a number of undetermined parameters. These parameters can be estimated by comparing model predictions with available observations. For linear models, this can be accomplished through standard statistical methods. For a complex (non-linear) LRT model, it will be necessary to use non-linear optimization techniques which usually have to be tailored to the problem at hand. At the end of Step 2, we should have a model for which  $\epsilon \approx 0$ , and  $\sigma_\epsilon$  is a minimum for the set of inputs considered.



The next step consists of evaluating the model and determining whether the following conditions are fulfilled:

- 1)  $\epsilon$  is independent of  $x_1$ ,
- 2) the parameters  $p$  are "reasonably stationary," and
- 3)  $s_\epsilon$  is much less than  $s_{C_p}$ .

Draper and Smith (1981) point out that a plot of the residuals  $\epsilon$  against  $C_p(x_1)$  and  $x_1$  is valuable in determining the adequacy of a model. If  $\epsilon$  is not a function of  $x_1$ , the plot should look like a band distributed around  $\epsilon = 0.0$ . Figure 11-3 shows examples of residual plots which might indicate inadequate model structure. Large residuals for a certain range of  $x_1$  can point to improvements in the model in this range of  $x_1$ . A quantitative measure of the relationship between  $\epsilon$  and  $C_p$  is the cross-correlation  $\epsilon C_p$ ; this should be low for an adequate model. The examination of residuals cannot be an objective exercise. Although sample estimates of  $\overline{\epsilon C_p}$  and  $\overline{\epsilon C_p^2}$  can help, there is no substitute to a careful visual examination of the residual plot to judge the adequacy of residual behavior. Note that for a "linear" model, the sample estimate of  $\overline{\epsilon C_p}$  is identically zero.

It is often desirable to transform  $C_o$  and  $C_p$  such that  $\epsilon$  is normally distributed. As described later, this facilitates interpretation of the model predictions.

To find out whether  $p$  is a parameter, it is necessary to estimate  $p$  using different sets of observations. A large variation in  $p$  would tell us to go back to the drawing board and come up with a better model. For models suitable to estimate time series, there is a useful method referred to as extended Kalman filtering (EKF), which allows us to calculate the time variation of  $p$  as a function of  $x_1(t)$ . A non-stationary time series of  $p(t)$  would indicate inadequacy in the model structure. An example of the application of this powerful method is given by Beck and Young (1976).

The next step is to check whether the variance of  $\epsilon$  is small compared to that of  $C_p$ . If this is not fulfilled, it might be necessary to expand the set of model inputs  $x_1$ . Once we have

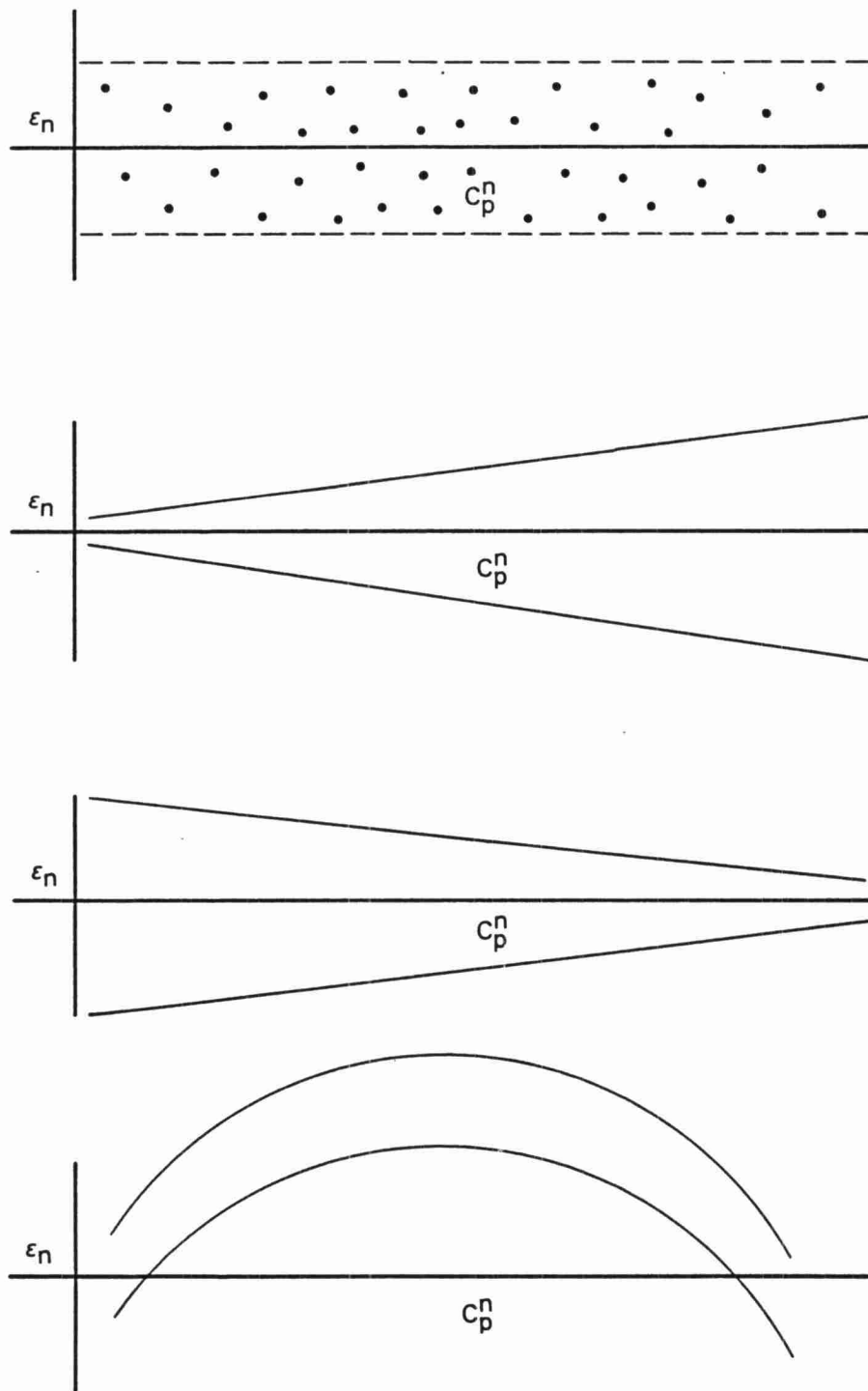


Figure 11-3 Residual behavior as a function of model predictions. Top figure shows adequate behavior while the other three figures show unacceptable residual variation.

satisfied ourselves that the model is adequate, we generate the error statistics required to use the model. The statistics would consist of:

- $\epsilon^2$ ,
- $n$  = number of points used to calculate  $\epsilon^2$ ,
- parameter estimates and the associated variances, and
- plots of  $\epsilon$  versus  $C_p$  and  $x_1$ .

This information can be used to interpret model predictions.

#### 11.4 An Example

In this section we apply the ideas described in the previous sections to the development of a model for the standard deviation of vertical turbulent velocities in the convective boundary layer. The data on which the model is based come from the Minnesota boundary layer experiment conducted in 1973. This data has been analyzed extensively (Kaimal et al. 1976), and several models have been advanced to explain the variation of  $\sigma_w$  in the convective boundary layer. The most recent formulation has been proposed by Lenschow and Stephens (1982).

The proposed model for  $\sigma_w$  differs from the others in that it explicitly accounts for the effect of averaging time on  $\sigma_w$ . In deriving the model we clarify the concepts described in the previous sections. We believe that the approach to the development of the model is as important as the model itself.

Details of the Minnesota experiment together with the processed data are given in the report by Izumi and Caughey (1976). The data are organized in the form of 11 experiments each lasting 75 minutes. Variables such as  $u_*$ ,  $Q_0$ ,  $z_i$ ,  $u(z)$ ,  $\theta(z)$ ,  $\sigma_u$ ,  $\sigma_v$ ,  $\sigma_w$ , and  $\sigma_\theta$  measured during the experiments represent averages over 75 minutes. To build a model for  $\sigma_w$ , we postulate that

$$\sigma_{w0} = Au_f f(z/uT) \epsilon \quad (11-9a)$$

$$\text{where } u_f \equiv (g/T_0 Q_0 z)^{1/3} \quad (11-9b)$$

In Equation 11-9a,  $A$  is a parameter yet to be determined, and  $\epsilon$  is the stochastic function of those variables  $x_2$  not accounted for in the model. Let us assume that  $u_f$  (or  $u_f^2$ ) represents the energy at all scales generated by surface heating. Then it is reasonable to assume that by averaging over a finite time  $T$  ( $\approx 75$  minutes), only a fraction  $f(z/uT)$  of  $u_f$  is seen in the observed standard deviation  $\sigma_{wo}$ . The time scale of the convective eddies is taken to be  $z/u$ . Note that this reasoning has been used to come up with a plausible structure for the  $\sigma_w$  model. We can test its adequacy only by comparing the model estimates with observations. Another way of writing Equation 11-9a is:

$$\ln \sigma_{wo} = \ln \sigma_{wp} + \ln \epsilon \quad (11-10)$$

$$\text{where } \sigma_{wp} = \sigma_{wp}(x_1) = Au_f f(z/uT) \quad (11-11)$$

We hope that this log-transformation will render  $\ln \epsilon$  normal (or  $\epsilon$  log-normal). We can test this hypothesis after constructing the model. Note that

$$x_1 = (Q_o^T, z, g/T_o, u^T, T) \quad (11-12)$$

The values of  $x_1$  define the ensemble of observations  $\sigma_{wo}(x_1)$ . This definition of an ensemble differs from that conventionally used in turbulence literature where an ensemble is defined by "similar" meteorological conditions. There we cannot readily answer the question: What does "similar" mean? The superscripts emphasize that  $Q_o$  and  $u$  represent averages over  $T$ . To make further progress we will assume that

$$f(z/uT) = (z/uT)^\alpha \quad (11-13)$$

where  $\alpha$  is a parameter to be estimated. We can now write Equation 11-10 as

$$\ln \sigma_{wo} = \ln A + \ln u_f + \alpha \ln (z/uT) + \ln \epsilon \quad (11-14a)$$

$$\text{or } \ln (\sigma_{wo}/u_f) = \ln A + \alpha \ln (z/uT) + \ln \epsilon \quad (11-14b)$$

Since T does not vary through the experiment, we are not really justified in including it explicitly in the analysis. It is incorporated in the "integrating" function  $f(z/uT)$  to remind us of the rationale for the formulation. Simple linear regression gives the values of A and  $\alpha$ , and the model for  $\sigma_{wo}$  becomes

$$\sigma_{wo} = \sigma_{wp} \epsilon \quad (11-15)$$

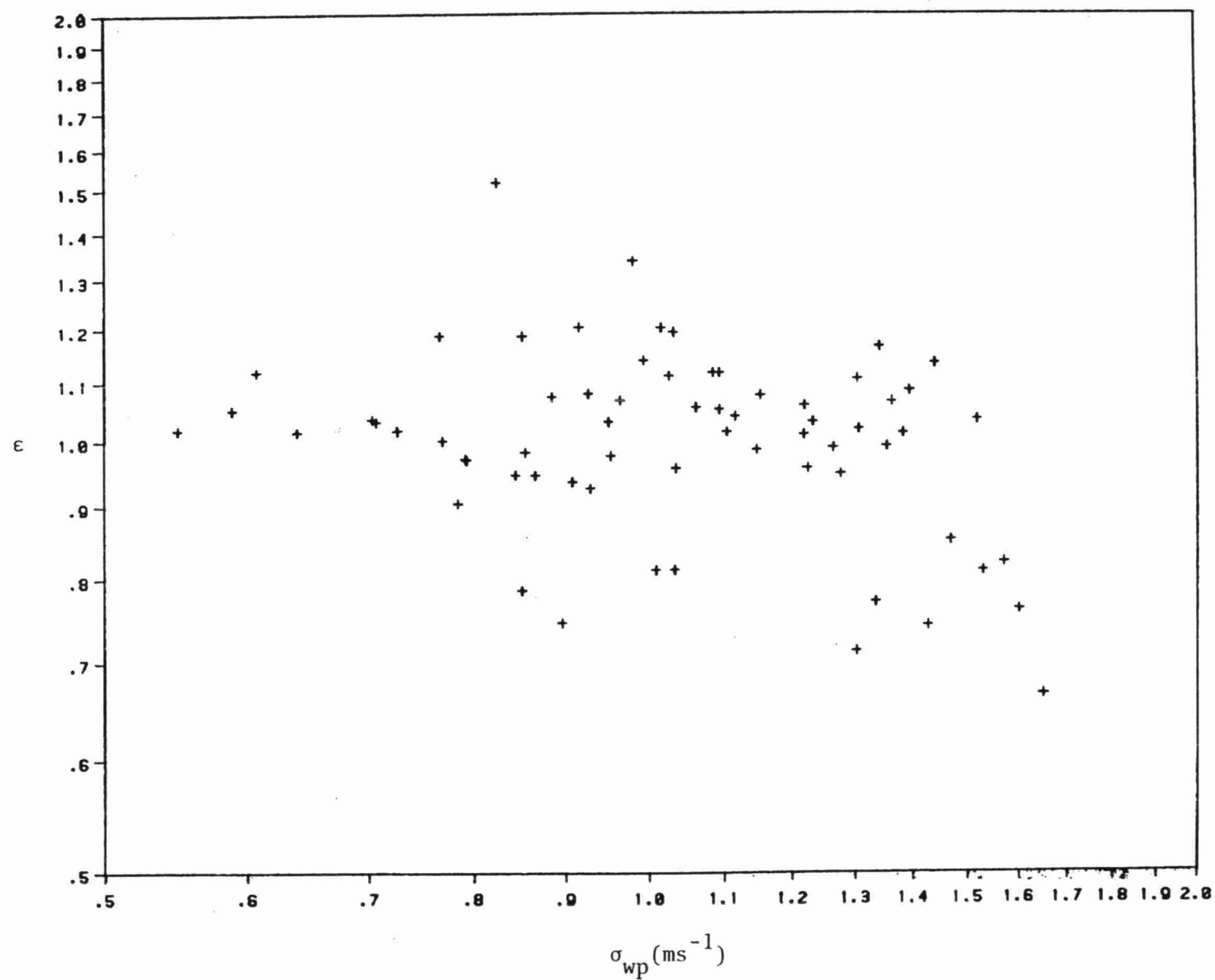
$$\text{where } \sigma_{wp} = 0.41 u_f (z/uT)^{-0.18} \quad (11-16a)$$

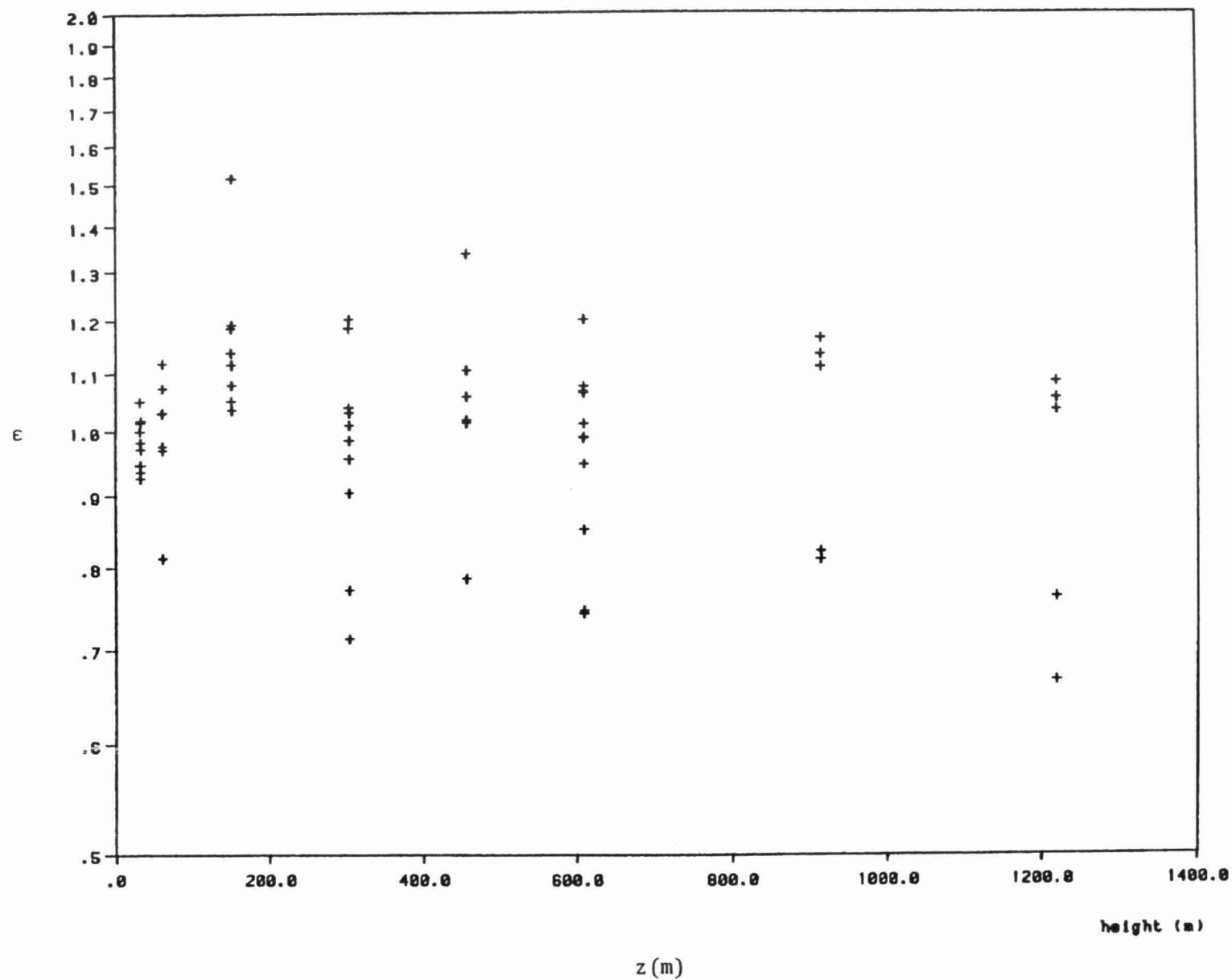
$$\text{and } u_f \equiv (g/T_o Q_o z)^{1/3} \quad (11-16b)$$

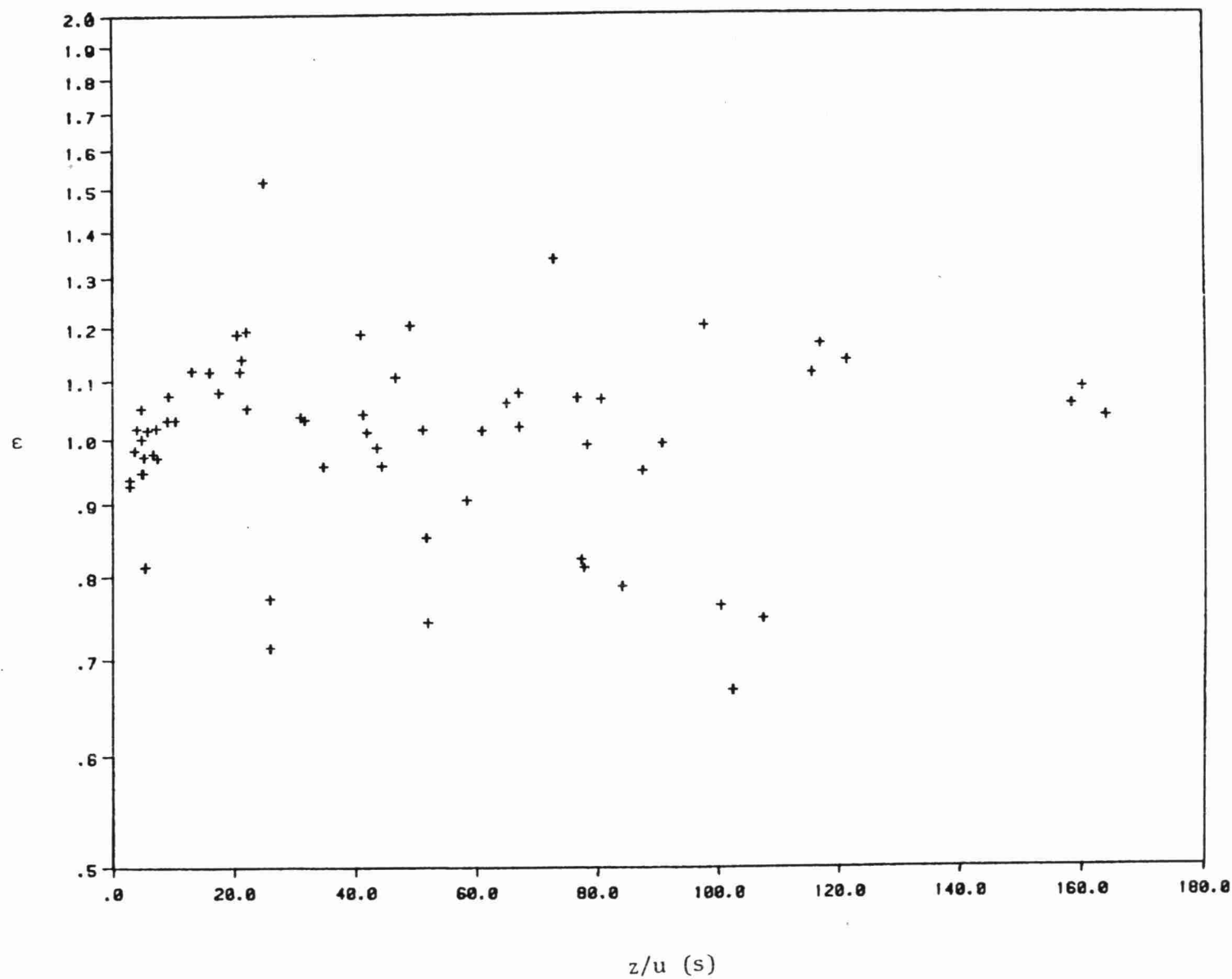
At this stage, we have identified the model and estimated the parameters. The next step is to evaluate the model. In Figure 11-4  $\ln \epsilon$  has been plotted against  $\sigma_{wp}$ . This model overpredicts at values of  $\sigma_{wp} > 1.4 \text{ ms}^{-1}$ , although this is not entirely clear. The plot of  $\epsilon$  versus  $z$  (Figure 11-5) does not indicate any trend. From Figure 11-6 we see that there is no obvious correlation between  $\epsilon$  and  $z/u$ . On the other hand, Figure 11-7 indicates that  $\epsilon$  is less than 1 for wind speeds greater  $11 \text{ ms}^{-1}$ . An examination of the data shows that the circled points come from two distinct experiments (conducted on the same day) during which the wind speeds and heat fluxes were relatively large. Because there is no smooth relationship between  $\epsilon$  and  $u$ , the measurements taken during the two experiments could be in error. This is a tentative conclusion which must be evaluated more carefully.

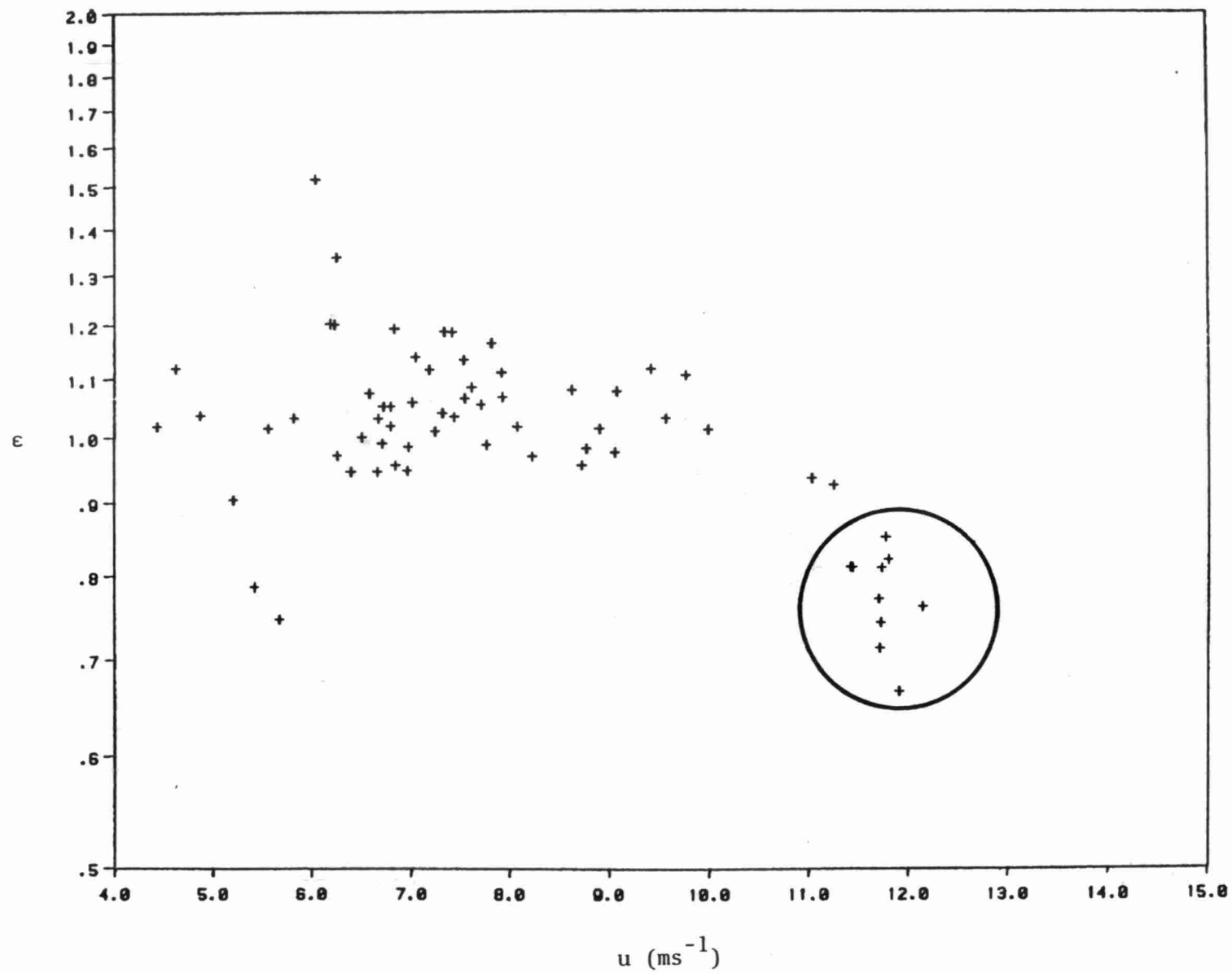
The logarithmic standard deviation of the residuals  $s_{\epsilon}^g$  is 1.16, which should be compared with the standard deviation of the predictions  $s_p^g = 1.31$ . This means that the model accounts for 78% of the variance of the observations. Note that 66 points were used in the computation of  $\epsilon$ , which translates into 64 degrees of freedom. A value of  $s_{\epsilon} = 1.16$  implies that the 95% confidence interval for the ratio of  $\sigma_{wo}/\sigma_{wp}$  ranges from 0.74 to 1.35. This calculation assumes that  $\epsilon$  is log-normally distributed. This



Figure 11-4 Variation of  $\epsilon$  with  $\sigma_{wp}$

Figure 11-5 Variation of  $\epsilon$  with  $z$

Figure 11-6 Variation of  $\epsilon$  with  $z/u$

Figure 11-7 Variation of  $\epsilon$  with  $u$

appears to be borne out in the cumulative distribution plot shown in Figure 11-8. If we wanted to be rigorous, we would account for the variance of  $A$  and  $\alpha$  in estimating the confidence interval. With 64 degrees of freedom, this component of the variance is small compared to that of  $\epsilon$ .

By neglecting the experiments with  $u > 11 \text{ ms}^{-1}$ , a better model for  $\sigma_{wo}$  could be developed. A re-analysis results in

$$\sigma_{wo} = 0.45 u_f (z/UT)^{-0.17} \epsilon \quad (11-17)$$

This model explains about 86% of the variance of the observations;  $s_{\epsilon}^g = 1.11$ , and the 95% confidence interval for  $\sigma_{wo}/\sigma_{wp}$  is approximately 0.81 to 1.23.

Further evaluation of the model would involve recalculating the parameters  $A$  and  $\alpha$  for other sets of data. This has not been done here, although it is clear that the model is acceptable for this range of input variables. The development of a model involves continuous interplay between theory and observation. There is no such thing as a "validated" model applicable to all data. Confidence in a model is a direct function of the number of observations used to evaluate it.

### 11.5 Error Statistics

After evaluating the model, the next step is to compile the error statistics required to use the model. The following statistics provide fairly complete information on the behavior of the model:

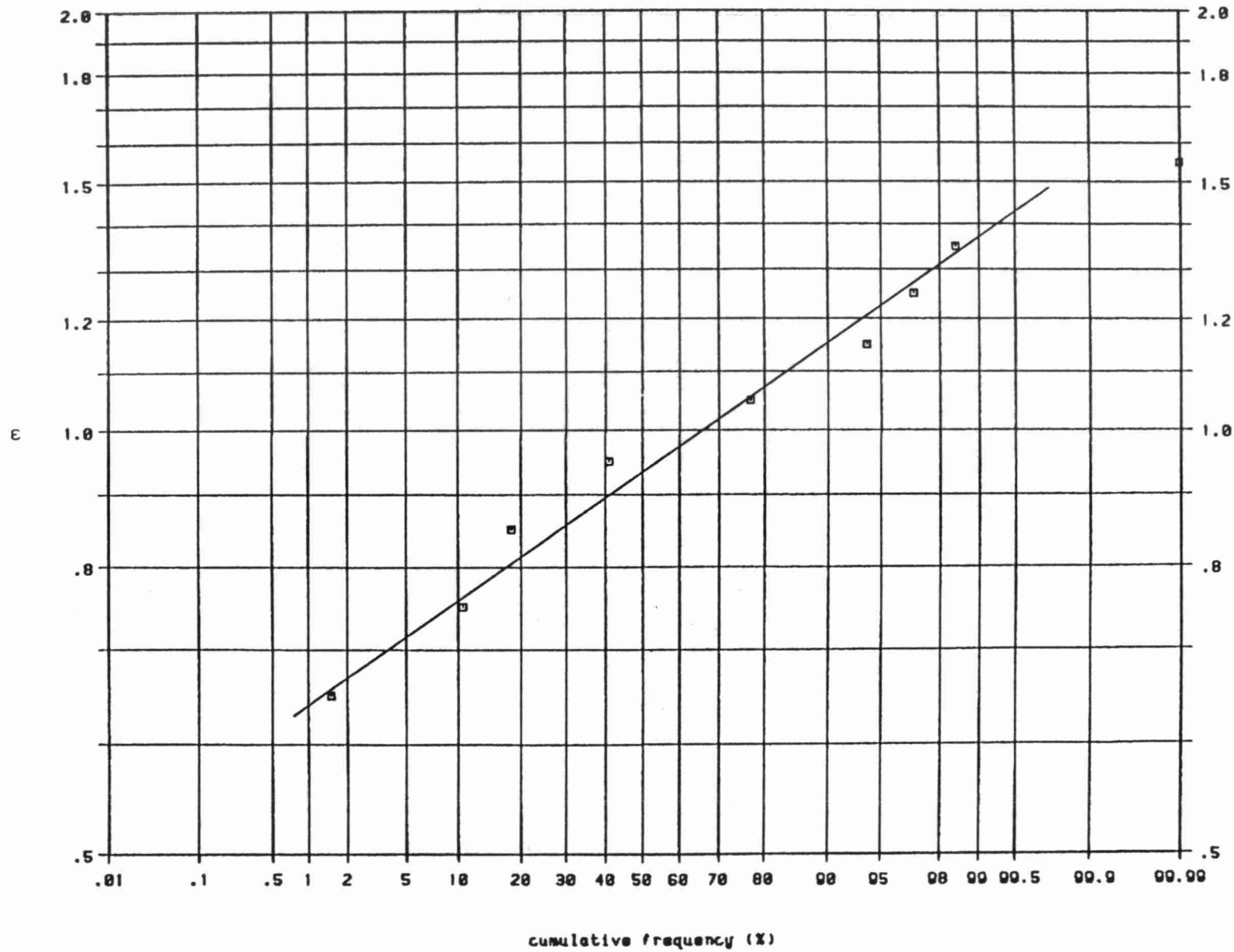
- $\epsilon = \sum \epsilon_i / n$
- $s_{\epsilon} = (\sum \epsilon_i^2 / (n - n_p))^{1/2}$

where  $n$  = number of data points

$n_p$  = number of estimated parameters

- Parameter estimates and the corresponding variances.
- Plots of  $\epsilon$  versus  $C_p$ . This can be supplemented by plots of  $\epsilon$  against input variables  $x_1$  of the model.
- Histogram of  $\epsilon$ .

epsilon vs.  
cumulative frequency



11-18

To illustrate the use of this information, let us consider an example. Let the model prediction corresponding to a set of inputs  $x_1$  be  $C_p(x_1)$ . To interpret this result, we have to first check if  $x_1$  lies within the range of model inputs used to test the model. Otherwise, we would have little confidence in the model prediction. To use  $C_p(x_1)$ , it is necessary to ensure that  $x_1$  does not correspond to a range in which  $\epsilon$  behavior is unacceptable.

Once  $C_p(x_1)$  is accepted, the next question is: What is the probability that the observed concentration corresponding to  $x_1$  exceeds a specified value  $C_o$ ? Recall that we can never predict what the actual observation will be for the reasons given earlier. To answer the question, we calculate the following t-value

$$t_f = (C_o - C_p) / s_\epsilon \quad (11-18)$$

where  $s_\epsilon$  corresponds to the transformed concentrations denoted by carets. Here we assume that the sample of  $\epsilon$  is drawn from a normal population. Using the student-t distribution for  $(n-n_p)$  degrees of freedom, we can readily estimate the required probability  $\Pr(t > t_f)$ .

In order to illustrate the use of the model to make statements about emission control, consider the following example. Assume the model prediction corresponding to a reduced emission scenario is  $C_p$ . The relevant question is: What is the probability that the observed concentration next year will exceed a standard value  $C_s$ ? Since the model inputs for the next year are unknown, we have to consider the variance of  $C_p$  in addition to  $s_\epsilon^2$  to estimate this probability. The expected variance of the observed concentration becomes

$$V(C_o) = V(C_p) + \sigma_\epsilon^2 \quad (11-19)$$

where  $V$  denotes variance. The variance of  $C_p$  corresponds to the variation of the model inputs  $x_1$ . This can be estimated by calculating a sample of  $C_p$ 's corresponding to  $x_1$  chosen with a Monte Carlo procedure from prescribed distribution of  $x_1$ . Note that  $\sigma_\epsilon$  does not change from year to year because  $\epsilon$  is assumed

independent of  $x_1$ . Denoting the standard deviation of  $C_o$  by  $\sigma_o$ , the required probability is  $\Pr(Z > Z_f)$ , where  $Z_f = (C_o - C_p)/\sigma_o$ , and  $Z$  is taken to be normally distributed. A t-distribution would be used if  $V(C_o)$  is estimated from a finite sample of  $C_p$ 's.

The model predictions can be interpreted only in terms of probabilities.  $s_e$  provides the important link between model predictions and observations. This suggests that it is not meaningful to use a model that has not been tested against observations.

## 11.6 Evaluation of the Mesoscale and Long-Range Transport Models

As mentioned before, the general model testing framework described in the previous sections can only serve as a guide to the development of evaluation methods specific to the mesoscale and LRT models. Although it is difficult to anticipate the details of these methods, we can describe some of the minimum requirements for an adequate model testing program.

The objective of model evaluation is to find out whether the model in question is a "useful" surrogate for reality. This process involves two major steps:

- 1) To ensure that the model incorporates a priori knowledge of the processes believed to be important in the physical system. This information usually consists of theory based on laboratory experiments and/or specialized field programs.
- 2) To find out whether model predictions compare with observations. The "goodness" of this comparison is based on specified criteria dependent on the intended use of the model.

The theoretical foundation of a model lends it credibility. Considering the uncertain quality of input data and observations required to run and test the model, this theoretical basis may be the primary reason for accepting or rejecting the model. In practice, once a model is considered acceptable it is used on the assumption that model predictions deviate little from observations.



A crucial test of a model is its ability to provide predictions which agree with corresponding observations within a specified error limit. There are several ways of comparing model predictions with observations. The most severe test of a model consists of pairing model estimates and observations in space and time and calculating the error statistics.

In view of the errors in model inputs, model predictions are usually compared against observations during the same time period but not necessarily at the same location. One version of this approach is to compare patterns of observations against those predicted by the model. In our case, we will derive the observed patterns by fitting empirical orthogonal functions to the deposition and concentration measurements. ERT has extensive experience with this technique (see Henry 1982). For the type of application of interest in long-range transport, this pattern comparison is likely to provide the most useful information.

In comparing observations with model predictions, we propose to divide the available data base into learning and test data sets. The learning set, which will constitute roughly one-third of the total, will be used to conduct sensitivity tests, calibrate the model if necessary, and identify those input parameters which have to be the most accurate. The test data set will be used to test the adequacy of the calibrated parameters. If the testing indicates that the parameters show little variation, the test data set will be used to generate the error statistics required to use the model.

The evaluation of the models will be combined with quality control of the model computer code. Typically this consists of:

- 1) Ensuring that the code matches the corresponding mathematical equation; and
- 2) Running the code for cases for which solutions are well known.

It is not possible to describe all the methods we will use to evaluate the LRT and mesoscale models. In a model development program it will be necessary to tailor the techniques for the models and, if necessary, develop new model testing methods. To a large extent, the acceptability of the two models to the scientific peers will be determined by the expertise and experience of the scientific team working on this project.

REFERENCES: SECTION 11

- Beck, B. and P. Young 1976. Systematic identification of DO-BOD model structure. ASCE J. Env. Eng. Div. 102: 909-927.
- Box, G.E., W.G. Hunter, and J.S. Hunter 1978. Statistics for Experiments. New York: Wiley-Interscience. 653 pg.
- Draper, N. and H. Smith 1981. Applied Regression Analysis (2nd Edition). New York: John Wiley and Sons, Inc. 709 pp.
- Henry, R. 1982. Location of airborne particulate sources by empirical orthogonal functions. Joint AMS/APCA conference on Air Pollution Meteorology, San Antonio, TX. January 11-15. 236-240.
- Izumi, Y. and J.S. Caughey 1976. Minnesota 1973 Atmospheric Boundary Layer Experiment Data Report. Environmental Research Paper No. 547. Air Force Cambridge Research Laboratories, Hanscom AFB, MA 01731.
- Kaimal, J.C., J.C. Wyngaard, D.A. Haugen, O.R. Cote, Y. Izumi, S.J. Caughey and C.J. Readings 1976. Turbulent structure in the convective boundary layer. J. Atmos. Sci. 33: 2152-2169.
- Lamb, R.G. 1982. A regional scale (1,000 km) model of photochemical air pollution. Part I: Theoretical formulation. U.S. EPA, Research Triangle Park, NC.
- Lenschow, D.H. and P.L. Stephens 1982. Mean vertical velocity and turbulence intensity inside and outside thermals. Atmos. Environ. 16: 761-764.
- Venkatram, A. 1981. Model predictability with reference to concentrations associated with point sources. Atmos. Environ. 15: 1517-1522.

LABORATORY LIBRARY



\*96936000119394\*

DATE DUE		

MOE/MOD/ANXC  
 Ontario Ministry of the En  
 Models for long -  
 range and mesoscale <sup>transport</sup> anxc  
 and deposition of atmosphere  
 Vol. II c.1 a aa



Environment Ontario  
 Laboratory Library  
 125 Resources Rd.  
 Etobicoke, Ontario M9P 3V6  
 Canada